中国气象科学研究院年报

ANNUAL REPORT OF CAMS

2021

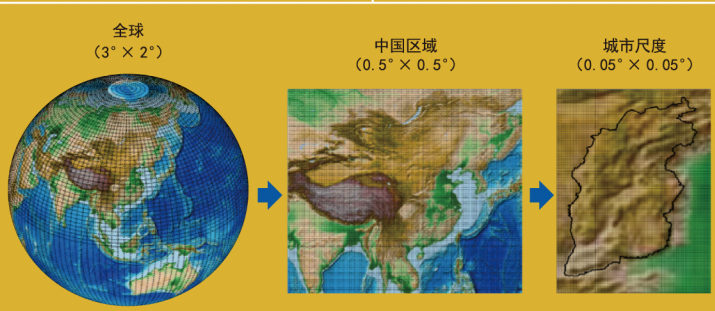

中国气象科学研究院

Chinese Academy of Meteorological Sciences

中国气象科学研究院年报　2021

主办单位：中国气象科学研究院
主　　编：端义宏
执行主编：袁凤杰
编辑出版：《中国气象科学研究院年报》编辑部
制作印刷：北京新华印刷有限公司
地　　址：北京中关村南大街 46 号，邮编 100081
邮　　箱：kjdt@cma.gov.cn
出版日期：2022 年 6 月

ANNUAL REPORT OF CAMS　2021

Sponsor: Chinese Academy of Meteorological Sciences
Chief Editor: Duan Yihong
Executive Chief Editor: Yuan Fengjie
Publication: *Annual Report of CAMS* Editional Division
Design and Printing: Beijing Xinhua Printing Co. , Ltd.
Address: 46 Zhongguancun Nandajie, Beijing, 100081, China
Email: kjdt@cma.gov.cn
Publication date: June 2022

中国气象科学研究院年报
ANNUAL REPORT OF CAMS

2021

中国气象科学研究院
Chinese Academy of Meteorological Sciences

目　　次

Contents

科研成果与进展
Scientific Achievements and Advances

灾害天气
Severe Weather

灾害天气研究进展
Advances in Research on Severe Weather

1 灾害天气监测
1 Severe weather monitoring technology

1.1 A multiscale analysis of a nocturnal extreme rainfall event of 14 July 2017 in Northeast China

A multiscale observational analysis of a nocturnal extreme rainfall event that occurred at Changtu in Northeast China on 14 July 2017 is performed using global analysis, automated surface observations, Doppler radar, rawinsonde, and disdrometer data. Results show that the large-scale environment was characterized by high convective available potential energy and precipitable water, moderate convective inhibition, and a southwesterly low-level jet (LLJ) capped by an inversion layer. The first and subsequent convective cells developed along a quasi-stationary surface convergence zone in a convection-void region of a previously dissipated meso-a-scale convective line. Continuous convective initiation through backbuilding at the western end and the subsequent merging of eastward-moving convective cells led to the formation of a near-zonally oriented meso-β-scale rainband, with reflectivity exceeding 45 dBz (i.e., convective core intensity). This quasistationary rainband was maintained along the convergence zone by the LLJ of warm moist air, aided by local topographical lifting and convectively generated outflows. A maximum hourly rainfall amount of 96 mm occurred during 02:00−03:00 Beijing standard time as individual convective cores with a melting layer of > 55 dBz reflectivity moved across Changtu with little intermittency. The extreme-rain-producing stage was characterized with near-saturated vertical columns, and rapid number concentration increases of all raindrop sizes. It is concluded that the formation of the meso-β-scale rainband with continuous convective backbuilding, and the subsequent echo-training of convective cores with growing intensity and width as well as significant fallouts of frozen particles accounted for the generation of this extreme rainfall event. This extreme event was enhanced by local topography and the formation of a mesovortex of 20−30 km in diameter. (Wang Gaili, Zhang Da-Lin, Sun Jisong)

1.2 Analysis of the vertical air motions and raindrop size distribution retrievals of a squall line based on cloud radar Doppler spectral density data

A squall line is a type of strongly organized mesoscale convective system that can cause severe weather disasters. Thus, it is crucial to explore the dynamic structure and hydrometeor distributions in squall lines. This study analyzed a squall line over Guangdong Province on 6 May 2016 that was observed using a Ka-

band millimeter-wave cloud radar (CR) and an S-band dual-polarization radar (PR). Doppler spectral density data obtained by the CR were used to retrieve the vertical air motions and raindrop size distribution (DSD). The results showed the following: First, the CR detected detailed vertical profiles and their evolution before and during the squall line passage. In the convection time segment (segment B), heavy rain existed with a reflectivity factor exceeding 35 dBz and a velocity spectrum width exceeding 1.3 m s^{-1}. In the PR detection, the differential reflectivity factor (Z_{dr}) was 1−2 dB, and the large specific differential phase (K_{dp}) also represented large liquid water content. In the transition and stratiform cloud time segments (segments B and C), the rain stabilized gradually, with decreasing cloud tops, stable precipitation, and a 0 ℃ layer bright band. Smaller K_{dp} values (less than 0.9) were distributed around the 0 ℃ layer, which may have been caused by the melting of ice crystal particles. Second, from the CR-retrieved vertical air velocity, before squall line passage, downdrafts dominated in local convection and weak updrafts existed in higher-altitude altostratus clouds. In segment B, the updraft air velocity reached more than 8 m s^{-1} below the 0 ℃ layer. From segments C to D, the updrafts changed gradually into weak and wide-ranging downdrafts. Third, in the comparison of DSD values retrieved at 1.5 km and DSD values on the ground, the retrieved DSD line was lower than the disdrometer, the overall magnitude of the DSD retrieved was smaller, and the difference decreased from segments C to D. The standardized intercept parameter (N_w) and shape parameter (μ) of the DSD retrieved at 1.8 km showed good agreement with the disdrometer results, and the mass-weighted mean diameter (D_m) was smaller than that on the ground, but very close to the PR-retrieved D_m result at 2 km. Therefore, comparing with the DSD retrieved at around 2 km, the overall number concentration remained unchanged and D_m got larger on the ground, possibly reflecting the process of raindrop coalescence. Lastly, the average vertical profiles of several quantities in all segments showed that, first of all, the decrease of N_w and D_m with height in segments C and D was similar, reflecting the collision effect of falling raindrops. The trends were opposite in segment B, indicating that raindrops underwent intense mixing and rapid collision and growth in this segment. Then, PR-retrieved D_m profiles can verify the rationality of the CR-retrieved D_m. Finally, a vertical velocity profile peak generated a larger D_m especially in segments C and D. (Ma Ningkun, Liu Liping, Chen Yichen)

1.3 Cloud vertical structure measurements from a ground-based cloud radar over the southeastern Tibetan Plateau

The southeastern Tibetan Plateau (TP) is the critical region of water vapor transport over the TP. Ground-based Ka-band cloud radar (KaCR) measurements collected at the Motuo National Climate Observatory in 2019 were used to analyze the physical properties of clouds at the front of the water vapor channel over the TP. The cloud top heights (CTHs) measured by the KaCR were verified through a comparison with observations from the Fengyun-4A (FY-4A) satellite at the same location. The KaCR-obtained CTHs were generally consistent with the FY-4A-obtained CTHs, although the KaCR slightly overestimated the CTHs of nonprecipitation clouds and underestimated the CTHs of precipitation clouds. Negative deviations between the KaCR- and FY-4A-obtained CTHs increased with rainfall rate. Cloud cover frequently occurred over Motuo, with an annual mean occurrence frequency of 65.3%. Clouds tended to form frequently at night and dissipate gradually in the daytime. Two peaks in the cloud base height (CBH) distribution were observed in Motuo, located at 0−1 km and 2−3 km, corresponding to precipitation and nonprecipitation clouds, respectively. The CTHs reached a peak at 6−7 km, which might be related to precipitation clouds. Moreover, a maximum CTH probability was observed in the midnight-early morning hours during the rainy season, while the CTH frequency peaked in the evening during the dry season. In addition, low and middle clouds were prevalent in Motuo for the period of observation in 2019. Understanding the characteristics of clouds over the TP will provide key validations of satellite measurements and promote research on cloud forces over the TP. (Zhou Renran, Wang Gaili, Zhaxi Suolang)

1.4 Deep learning for polarimetric radar quantitative precipitation estimation during landfalling typhoons in South China

Heavy rain associated with landfalling typhoons often leads to disasters in South China, which can be reduced by improving the accuracy of radar quantitative precipitation estimation (QPE). At present, raindrop size distribution (DSD) -based nonlinear fitting (QPE of DSD) and traditional neural networks are the main radar QPE algorithms. The former is not sufficient to represent the spatiotemporal variability of DSDs through the generalized *Z-R* or polarimetric radar rainfall relations that are established using statistical methods since such parametric methods do not consider the spatial distribution of radar observables, and the latter is limited by the number of network layers and availability of data for training the model. In this paper, we propose an alternative approach to dual-polarization radar QPE based on deep learning (QPENet). Three datasets of dual-polarization radar observations-surface rainfall (DPO-SR) were constructed using radar observations and corresponding measurements from automatic weather stations (AWS) and used for QPENet (V_1), QPENet (V_2), and QPENet (V_3). In particular, 13×13, 25×25, and 41×41 radar range bins surrounding each AWS location were used in constructing the datasets for QPENet (V_1), QPENet (V_2), and QPENet (V_3), respectively. For training the QPENet models, the radar data and AWS measurements from eleven landfalling typhoons in South China during 2017−2019 were used. For demonstration, an independent typhoon event was randomly selected (i.e., Merbok) to implement the three trained models to produce rainfall estimates. The evaluation results and comparison with traditional QPE (DSD) algorithms show that the QPENet model has a better performance than the traditional parametric relations. Only when the hourly rainfall intensity is less than 5 mm ($R < 5$ mm h^{-1}), the QPE (DSD) model shows a comparable performance to QPENet. Comparing the three versions of the QPENet model, QPENet (V_2) has the best overall performance. Only when the hourly rainfall intensity is less than 5 mm ($R < 5$ mm h^{-1}), QPENet (V_3) performs the best. (Zhang Yonghua, Bi Shuoben, Liu Liping)

1.5 Estimating raindrop size distributions and vertical air motions with spectral difference using vertically pointing radar

Doppler spectra measured by vertically pointing radars are inherently linked to raindrop size distributions (DSDs). But accurate estimation of DSDs remains challenging because raindrop spectra are broadened by atmospheric turbulence and shifted by vertical air motions. This paper presents a novel method to estimate vertical air motions in which there is no need to assume a model for DSD at each range gate. The theory of the new method is that the spectral difference between the adjacent range gates is contributed by vertical air motions and the variability of DSDs. The contribution of the change of DSDs is estimated by looking up the prepared tables of raindrop velocity difference and shape function difference. Then the vertical air motions can be estimated by minimizing the cost function of the two spectra between the adjacent range gates. The retrieval algorithm is applied to three cases including a stratiform case and two convective cases observed by a C-band vertically pointing radar in Longmen, Guangdong Province, China, in June 2016. Before that, the spectrum broadening effect is removed by the traditional deconvolution method with a wind profiler. The vertical profiles of precipitation parameters are also retrieved to investigate the microphysical process. The precipitation parameters retrieved near the surface are compared with the ground data collected by a two-dimensional video disdrometer (2DVD), and the results show good agreement. (Pang Suzhou, Ruan Zheng, Yang Ling)

1.6 Raindrop size distribution measurements on the southeast Tibetan Plateau during the STEP project

As part of the Second Tibetan Plateau Scientific Expedition and Research (STEP) field campaign, raindrop size distribution (DSD) measurements were conducted with a laser optical particle size velocity disdrometer in

Motuo on the Tibetan Plateau (TP). The DSD characteristics of five different rain rate classes and convective and stratiform precipitation types were studied using the DSD data from July to September 2019, comprising a total of 47774 1-min raindrop spectra. The average raindrop spectral width and number concentration of large drops increased with the rainfall intensity. Furthermore, the combination of smalland midsize drops dominated the precipitation in Motuo, and their contributions exceeded 99% of the number concentration. The convective precipitation in Motuo was identified as maritime-like precipitation and was characterized by a large normalized intercept parameter $\lg N_w = 4.0 - 4.4$ and small mass-weighted mean diameter $D_m = 1.1 - 1.4$ mm. Empirical relations among the three parameters (intercept N_0, shape μ, and slope λ) of the gamma distribution model, N_w and D_m of the normalized gamma distribution were derived. We also obtained power-law relationships of $Z = AR^b$ for the stratiform and convective precipitation in Motuo, and the empirical relation of $Z = 300R^{1.4}$ significantly underestimated the convective precipitation in Motuo. When the precipitation type transitioned from stratiform into convective precipitation, coefficient A decreased and exponent b increased. Finally, empirical relations between D_m and the radar equivalent reflectivity factor at the Ku and Ka bands were obtained to improve the rainfall retrieval algorithms of the dual-frequency precipitation radar on the southeast TP. (Wang Gaili, Zhou Renran, Zhaxi Suolang)

1.7 Study on radar echo-filling in an occlusion area by a deep learning algorithm

Radar beam blockage is an important error source that affects the quality of weather radar data. An echo-filling network (EFnet) is proposed based on a deep learning algorithm to correct the echo intensity under the occlusion area in the Nanjing S-band new-generation weather radar (CINRAD/SA). The training dataset is constructed by the labels, which are the echo intensity at the 0.5° elevation in the unblocked area, and by the input features, which are the intensity in the cube including multiple elevations and gates corresponding to the location of bottom labels. Two loss functions are applied to compile the network: one is the common mean square error (MSE), and the other is a self-defined loss function that increases the weight of strong echoes. Considering that the radar beam broadens with distance and height, the 0.5° elevation scan is divided into six range bands every 25 km to train different models. The models are evaluated by three indicators: explained variance (EVar), mean absolute error (MAE), and correlation coefficient (CC). Two cases are demonstrated to compare the effect of the echo-filling model by different loss functions. The results suggest that EFnet can effectively correct the echo reflectivity and improve the data quality in the occlusion area, and there are better results for strong echoes when the self-defined loss function is used. (Yin Xiaoyan, Hu Zhiqun, Zheng Jiafeng)

1.8 Supercooled liquid water and secondary ice production in Kelvin-Helmholtz instability as revealed by radar Doppler spectra observations

Mixed-phase clouds are globally omnipresent and play a major role in the Earth's radiation budget and precipitation formation. The existence of liquid droplets in the presence of ice particles is microphysically unstable and depends on a delicate balance of several competing processes. Understanding mechanisms that govern ice initiation and moisture supply are important to understand the life cycle of such clouds. This study presents observations that reveal the onset of drizzle inside a similar to 600 m deep mixed-phase layer embedded in a stratiform precipitation system. Using Doppler spectral analysis, we show how large supercooled liquid droplets are generated in Kelvin-Helmholtz (K-H) instability despite ice particles falling from upper cloud layers. The spectral width of the supercooled liquid water mode in the radar Doppler spectrum is used to identify a region of increased turbulence. The observations show that large liquid droplets, characterized by reflectivity values larger than 20 dBz, are generated in this region. In addition to cloud droplets, Doppler spectral analysis reveals the production of columnar ice crystals in the K-H billows. The

modeling study estimates that the concentration of these ice crystals is 3−8 L^{-1}, which is at least 1 order of magnitude higher than that of primary ice-nucleating particles. Given the detail of the observations, we show that multiple populations of secondary ice particles are generated in regions where larger cloud droplets are produced and not at some constant level within the cloud. It is, therefore, hypothesized that K-H in stability provides conditions favorable for enhanced droplet growth and formation of secondary ice particles. (Li Haoran, Korolev Alexei, Moisseev Dmitri)

1.9 Two-year statistics of columnar-ice production in stratiform clouds over Hyytiala, Finland: Environmental conditions and the relevance to secondary ice production

Formation of ice particles in clouds at temperatures of 10 ℃ or warmer was documented by using ground-based radar observations. At these temperatures, the number concentration of ice-nucleating particles (INPs) is not only expected to be small, but this number is also highly uncertain. In addition, there are a number of studies reporting that the observed number concentration of ice particles exceeds expected INP concentrations, indicating that other ice generation mechanisms, such as secondary ice production (SIP), may play an important role in such clouds. To identify formation of ice crystals and report conditions in which they are generated, W-band cloud radar Doppler spectra observations collected at the Hyytiala station for more than 2 years were used. Given that at these temperatures ice crystals grow mainly as columns, which have distinct linear depolarization ratio (LDR) values, the spectral LDR was utilized to identify newly formed ice particles. It is found that in 5% to 13% of clouds, where cloud top temperatures are 12 ℃ or warmer, production of columnar ice is detected. For colder clouds, this percentage can be as high as 33%, 40% to 50% of columnar-ice-producing events last less than 1 h, while 5% to 15% can persist for more than 6 h. By comparing clouds where columnar crystals are produced and to the ones where these crystals are absent, the columnar-ice-producing clouds tend to have larger values of liquid water path and precipitation intensity. The columnarice-producing clouds were subdivided into three categories, using the temperature difference, ΔT, between the altitudes where columns are first detected and cloud top. The cases where ΔT is less than 2 K are typically single-layer shallow clouds where needles are produced at the cloud top. In multilayered clouds where ΔT is larger tahan 2 K, columns are produced in a layer that is seeded by ice particles falling from above. This classification allows us to study potential impacts of various SIP mechanisms, such as the Hallet-Mossop process or freezing breakup, on columnar-ice production. To answer the question whether the observed ice particles are generated by SIP in the observed single-layer shallow clouds, ice particle number concentrations were retrieved and compared to several INP parameterizations. It was found that the ice number concentrations tend to be 1−3 orders of magnitude higher than the expected INP concentrations. (Li Haoran, Mohler Ottmar, Petaja Tuukka)

1.10 Vertical during snow events in middle latitudes of China observed by a C-band vertically pointing radar

This study applied the C-band vertically pointing radar with frequency-modulation continuous-wave technology to obtain the continuous observation data of four shallow and two deep snow events during the winter of 2015−2016 in the midlatitudes of China. Generating cells (GCs) were found near the echo tops in every event. The ice particle number concentration (N), ice water content (IWC), and median mass diameter (D_m) retrieved from radar Doppler spectra were used to analyze the microphysical properties in the snow clouds. The clouds were divided into upper GC and lower stratiform (St) regions according to their vertical structure. The fall streaks (FSs) associated with GCs were embedded in the St regions. In the GC regions, the N values in shallow events were smaller compared with those in deep events, and D_m and IWC were larger. In the St regions, N decreased compared with that in the GC regions, and D_m and IWC increased, implying the existence of aggregation and deposition growth. The growth of particle size and mass mainly occurred in the St regions.

The increases of N were usually observed near −5 ℃ accompanied by bimodal Doppler spectra, which might be caused by ice multiplication. The average ratios of the median N, D_m, and IWC inside GCs to those outside GCs were 2, 1.3, and 2.5, respectively, for shallow events, with 1.7, 1.2, and 2.3, respectively, for deep events. These values were basically the same as those for the FSs, implying the importance of GCs to the enhanced ice growth subsequently found in FSs. The larger values of N, D_m, and IWC inside GCs could be related to the upward air motions inside GCs. The first Z_e-IWC relationship suitable for snow clouds in the midlatitudes of China was also established. (Cui Ye, Ruan Zheng, Wei Ming)

1.11 Ka/Ku双波段毫米波雷达功率谱数据反演液态水含量方法研究

单波段雷达用Z-LWC关系反演液态水因不同降水类型反演的液态水含量相差较大。利用双波段雷达回波强度偏差反演液态水含量，直接将双波段雷达基数据回波强度相减的差值不仅包括了衰减的偏差也包括散射不同带来的偏差。因此，利用双波段雷达功率谱数据经过小粒子选择计算受Mie散射影响小的粒子，用最小二乘法计算DWR（Dual Wavelength Ratio）的变化率反演液态水含量和液态水积分总量，将双波段雷达基数据和功率谱数据反演结果与微波辐射计测量结果进行对比。结果表明：（1）经过小粒子选择，去掉了双波段雷达的回波强度因散射不同带来的偏差。（2）在高度较低时双波段雷达基数据和功率谱数据经过小粒子选择反演的液态水含量有着较大区别。随着高度的增加，反演的液态水含量比较接近。（3）双波段雷达基数据和功率谱数据反演的液态水含量与微波辐射计进行定性分析，变化趋势能够达到较为一致，微波辐射计液态水含量较强的区域，两者反演的液态水含量也相应较大。（4）双波段雷达基数据和功率谱数据反演的液态水积分总量和微波辐射计的液态水积分总量随着时间的变化趋势较为一致，但双波段雷达功率谱数据总体程度小于基数据反演的液态水积分，双波段雷达基数据与功率谱数据反演的液态水积分总量总体小于微波辐射计的液态水积分总量值。（邹琳，刘黎平）

1.12 Ka/Ku双波段云雷达反演空气垂直运动速度和雨滴谱方法研究及初步应用

在Ka波段云雷达上升级改造建成的Ka/Ku（Ka和Ku波段波长分别为8.9 mm和2.2 cm）双波段云雷达2019年用于华南云降水垂直结构观测，以改进云内动力和微物理参数探测能力。为了利用该双波段云雷达研究华南降水微物理和动力结构，本文提出了基于双波段云雷达回波强度谱密度（SZ）数据和最优估计技术的云内空气垂直运动速度（V_{air}）、雨滴谱（DSD）、液态水含量（LWC）、雨强（R）的反演方法（DWSZ），以及雨区衰减的订正方法。利用2019年在广东龙门观测的一次降水过程数据，对比分析了云雷达反演的微物理参数与雨滴谱直接观测量，并检验了云雷达反演的低层空气垂直运动速度，利用反演结果分析了一次混合云过程的V_{air}与这些微物理参数的垂直结构和相互关系。结果表明：Ka/Ku双波段云雷达合理反演了微降水微物理和动力参数及其垂直分布，经过衰减订正的Ka和Ku波段回波强度偏差明显减小。该双波段云雷达数据可以用于分析0 ～ 30 dBz回波强度的云降水垂直结构。本次过程为混合云降水，对流单体前部存在明显的上升气流，后部存在下沉气流；从平均垂直结构来看，V_{air}和粒子平均直径（D_m）在2 km高度层到达最大，粒子数密度（N_w）、LWC和R在2 km以下明显增强，粒子直径却减小，水汽凝结过程、雨滴碰并云滴是本次过程的主要机制。这一工作验证了Ka和Ku波段组合的双波段云雷达的可行性，为Ka/Ku波段云雷达技术的推广，单波段云雷达反演算法进一步改进，云降水精细结构分析等提供了基础。（刘黎平，张扬，丁晗）

1.13 X波段双偏振雷达相态识别与拼图的关键技术

基于统计的隶属函数参数改进方法和基于衰减程度的拼图融合方法，通过对比改进后可有效提升水凝物相态识别结果的可靠性和多雷达拼图结果的合理性。在2016年汛期北京典型个例中，融合后的X波段雷达网与当地S波段业务雷达相比能够提供更精细的回波结构和水凝物相态分布，有效缓解S波

段雷达在近处探测能力降低的问题，识别的降雹区与地面观测相符。（吴翀，刘黎平，仰美霖）

1.14 毫米波云雷达观测和反演云降水微物理及动力参数方法研究进展

云雷达是探测和反演云降水微物理及动力参数精细结构的重要手段。回顾了世界和我国云雷达观测模式、数据质量控制和数据融合方法，特别是脉冲压缩、相干积累和非相干积累技术在提高云雷达灵敏度的应用，分析了基于回波强度与粒子下落速度关系、单波段云雷达小粒子跟踪方法、双波段云雷达回波强度谱密度比值方法等空气垂直运动速度反演和雨滴谱反演方法，并讨论了这些方法的特色，为今后云雷达观测方法设定和数据分析提供参考。（刘黎平）

1.15 降水条件下的云雷达与微波辐射计反演液态水含量对比分析

为了发展云雷达与微波辐射计联合反演液态水含量的方法，利用2019年4—9月中国气象科学研究院在广东龙门开展的综合观测试验中的双波段云雷达和微波辐射计数据，首先检验了在降水条件下微波辐射计天顶观测和斜路径观测两种探测模式反演温度（T）、相对湿度（RH）、液态水含量（LWC）和液态水路径（LWP）的合理性，然后分析了两种探测设备反演LWC和LWP的差别。得到以下结论：（1）微波辐射计在斜路径观测模式下反演的产品受降水影响较小，其反演结果明显优于天顶观测模式。（2）两种探测设备反演的LWP相关性较好且随时间变化较为一致，但云雷达反演LWP与平均回波强度有明显相关，随着雷达回波强度的增大，云雷达与微波辐射计反演的LWP之比越大。（3）两种探测设备反演的LWC相关性较差且存在明显偏差，在不考虑融化层的情况下单波段云雷达反演LWC与微波辐射计随高度变化趋势相近，双波段云雷达反演LWC与微波辐射计反演结果在1 km及其以上区间存在明显差异。（邹明龙，刘黎平，郑佳锋）

1.16 利用贝叶斯方法改进华南地区冰雹识别效果

使用2019年广东S波段双偏振雷达观测的冰雹和非冰雹数据，统计得到冰雹和非冰雹的雷达反射率Z、差分反射率ZDR和相关系数CC先验概率密度分布，采用贝叶斯方法，根据雷达参量在冰雹和非冰雹条件下的概率以及冰雹和非冰雹的先验概率来确定某一距离库上所测到的（Z、ZDR、CC）所代表冰雹和非冰雹的概率，并用两个个例，比较分析了WSR-88D冰雹识别算法和贝叶斯方法对冰雹识别的效果，分析表明，两种方法都能较准确地识别出冰雹云，但是贝叶斯方法识别范围较大，这可能与华南地区多为雨夹雹有关。（李博勇，胡志群，郑佳锋）

1.17 青藏高原墨脱地区云降水综合观测及初步统计特征分析

为加深对雅鲁藏布大峡谷水汽通道入口处云和降水三维结构及微物理特征的认识，在第二次青藏高原综合科学考察研究专题和国家重点研发计划项目的支持下，中国气象科学研究院于2019年在西藏墨脱地区建立了野外观测试验基地，开展了水汽、云和降水的综合观测，先后布设了先进的Ka波段云雷达、微波辐射计、X波段双偏振相控阵雷达、降水现象仪、K波段微雨雷达等设备，获取了高时、空分辨率的云和降水的宏、微观数据。文中简单介绍了此次观测的情况，并利用云雷达2019年的观测数据和降水现象仪2019年6月至2020年6月的观测数据对云的宏观特征及雨滴谱特征进行了统计分析。从云的宏观特征来看，该地区云的发生率较高，云廓线占2019年云雷达观测廓线的67%，降水云廓线占总云廓线的45%。旱季和雨季云底高度的频率分布在垂直方向均有两个高值区，分别为0 ～ 1 km和2 ～ 3 km，且超过40%的云底高度低于1 km，这可能是墨脱降水云较多造成的。接近60%的云顶高度在4 ～ 7 km。总的来说，墨脱地区以中云和低云为主，云通常在下午到晚上形成，早上到中午慢慢消散；从雨滴谱分布特征来看，该地区平均的雨滴谱谱宽和大雨滴的浓度随雨强的增大而增大，降水以中、小粒子为主，中、小粒子浓度超过粒子数浓度的99%。对流云降水的特点是粒子直径较小，而数浓度较高。粒子质量加权平均直径（D_m）的范围在1.0 ～ 1.6 mm（平均1.38 mm），标准化截距参数（$\lg N_w$）

的范围在3.6 ～ 4.5（平均4.01），表现出海洋性对流降水的特征。此外，该地区降水的lgN_w呈现双峰特征，分别对应于对流云和层状云降水。（王改利，周任然，扎西索郎）

1.18 双偏振相控阵雷达与业务雷达的定量对比及观测精度研究

相控阵天气雷达突破了全机械驱动天线天气雷达的时空分辨率瓶颈，能够提供更加快速、精细的观测资料。但阵列天线存在性能参数随扫描角偏离法向而恶化的情况，使相控阵雷达定量测量存在困难。本文针对中国华南地区最新布网的双偏振相控阵天气雷达，通过与当地S波段业务雷达在相同区域内的定量对比，评估了反射率因子差分反射率因子的误差量级及其随扫描角、观测时间的变化趋势。研究结果表明，相控阵雷达反射率因子的误差不大，约0.82 dB，而差分反射率因子的误差则高达1.04 dB，并且不同仰角、不同时刻之间也存在一定的波动。为此本文提出了基于S波段雷达实时数据的订正方案，能够较好地解决双偏振相控阵天气雷达的定标问题，为相控阵雷达的业务应用提供了保障。（张蔚然，吴翀，刘黎平）

1.19 星载雷达DPR与地基雷达CR的匹配对比及系统偏差初探

将GPM卫星搭载的双频降水雷达DPR和广东龙门观测站的地基Ka/Ku双波段雷达CR在2019年4—9月的观测数据进行时空匹配，结合微雨雷达MRR 的雨滴谱数据对CR衰减订正处理，比较DPR与CR探测回波强度差异，最后对两者的系统偏差进行分析。结果表明：（1）DPR和CR探测到的回波强度随高度变化的趋势大体一致，零度层亮带高度基本一致，同样高度下DPR探测到的回波强度明显大于CR。（2）统计弱的非降水云算得CR双频系统偏差约为3.1 dBz。（3）雨强越强，CR天线罩水膜厚度越大，回波衰减越大。（4）逐库订正过程中利用雨滴谱数据计算衰减系数，CR在Ka与Ku波段的反射率因子订正量不超过4 dBz。（5）综合所有适配数据，CR与DPR的反射率因子在Ka波段内订正后平均系统偏差为15.7 dBz，在Ku波段内订正后平均系统偏差为14.4 dBz。虽然经订正处理后两部雷达间的系统偏差偏大，但对改善地基Ka/Ku双波段雷达的数据质量有明显的改善。（曾震瑜，刘黎平，郑佳锋）

1.20 一次强雹云过程冰雹增长机制分析及防雹探讨

2018年9月29日大连市出现了强雹云天气过程。初始雹云在渤海上空生成，经3 h东移和发展演变，在大连北部沿海登陆并发展为成熟的强雹云。当地作业点及时开展人工防雹与联防作业，并对作业前后雹云雷达特征参数变化及成熟强雹云空间结构特征等进行分析，深入研究和探讨了成熟强雹云有效人工防雹两道防线技术方法，即在重要作物保护区上游空旷地带，或低值作物区增设人工防雹高炮，当成熟强雹云进入该高炮射程，立即实施高炮作业（且仰角≥55°，即打在雹云强回波区），促使冰雹提前和充分降落，从而保护下游的重要作物，将雹灾损失降到最低，达到人工防雹的目的。（李红斌，胡志群，张靖萱）

1.21 风廓线雷达组网观测新型应用研究进展

风廓线雷达具有高的时间和空间分辨率，已经被广泛应用于大气探测、环境气象以及灾害性雷暴天气监测预警等领域。但风廓线雷达组网二次开发产品缺乏，一定程度限制了其在天气气候领域的深度应用。简要介绍中国风廓线雷达网站点分布及其水平风廓线和谱宽等数据产品；阐述基于风廓线雷达观测产生的高时间分辨率边界层高度、垂直风切变、湍流强度和散度等新产品特点，并给出了相应的应用场景或案例。最后，展望了风廓线雷达组网观测的不足及其未来应用前景。（郭建平，刘博铭，郭晓冉）

2 青藏高原天气研究
2 Research on weather over the Tibetan Plateau

2.1 2021年度第二次青藏高原综合科学考察研究进展

中国工程院院士徐祥德承担“第二次青藏高原综合科学考察研究”十大科考任务的第一任务，并负责第5专题。项目科考及研究重点目标是针对亚洲水塔水资源、生态变化的影响因素，研究气候变化及其西风与季风协同作用，拓展青藏高原科考计划实施的多圈层综合观测系统的应用领域；提升科考团队研究成果在青藏高原地球系统前沿领域中的重要地位，着力解决气候变化对青藏高原亚洲水塔水资源与生态环境的影响理论及其应用问题，并提出有助于西藏社会经济高质量发展的科学合理气候应对战略决策；助力深入理解气候变化对青藏高原水资源和生态环境的影响机理，筑牢气象防灾减灾第一道防线。青藏高原科学考察面向国家战略需求，在复杂地形和水循环条件下，构建青藏高原天-地-空一体化的综合观测体系，揭示青藏高原气候和生态变化机理，着力解决青藏高原生态环境、灾害风险、国家重大工程建设安全等方面的问题，推动青藏高原可持续发展，推进国家生态文明建设。

项目除在雅鲁藏布沿江建立微波辐射计、自动气象站与边界层站外，还在水汽输送关键入口区墨脱、珠峰北侧等设立雷达超级站，在墨脱及雅鲁藏布江沿岸实施天-地-空一体化综合观测试验，填补了复杂河谷地形多尺度水汽输送及云降水结构特征综合探测的空白；开展了云、降水粒子微物理特征分析研究，拓展了青藏高原天-地-空一体化的综合观测体系。为获取中国东部地区灾害天气上游“强信号”区青藏高原高时空分辨率的大气温度、湿度和水汽的垂直结构信息。项目还设计和研制了基于车载平台的气象与环境三维结构动态探测系统，首次实施了青藏高原东南部气象与环境三维结构动态探测试验，获取了可靠的高时空分辨率温湿度、水汽、气溶胶等三维结构动态探测数据集。在历史与现今气象观测站网数据、多类再分析与卫星遥感产品大数据助力下，项目提出了亚洲水塔核心区热力驱动下高原区域与全球能量、水分循环“窗口效应”综合相关模型，揭示了青藏高原低云活动、深对流对全球，尤其是南北极水汽输送的重要作用；通过地面观测站与和高分辨率卫星（TRMM）观测相结合的方式，得到高原地区高分辨率降水资料，揭示了青藏高原大气降水“补给”差异对高原南、北冰川消融速率影响。项目研究高原气候变暖背景下冻土退化对生态及国家重大工程建设带来的影响及其风险，并提交气候变暖对青藏高原铁路、公路路基稳定性风险研究成果。此次科学考察拓展了多圈层多元信息观测分析数据集，构建了雅鲁藏布江水循环三维结构数据集、卫星遥感冰川面积数据集、墨脱雷达综合观测数据集、珠峰雷达综合观测数据集、高原湖泊数据集等9个数据集。数据及研究结果应用到数值天气预领域，发展了川藏铁路敏感区数值模式追踪技术，建立了川藏铁路工程区天气雷达资料同化预报系统；搭建了夹卷混合机制的参数化方案，改进了中尺度天气预报模式（WRF）中Mirrison微物理方案，为有效解决模式预报高原降水高估问题提供技术支撑；开展了高原地区卫星协同多元观测的融合技术研究，并实施了我国风云4号气象卫星AGRI和LMI资料协同地面、雷达数据的三维大气和三维云融合技术研究。（徐祥德，张胜军）

2.2 A new inverse modeling approach for emission sources based on the DDM-3D and 3DVAR techniques: An application to air quality forecasts in the Beijing-Tianjin-Hebei region

We develop a new inversion method which is suitable for linear and nonlinear emission source (ES) modeling, based on the three-dimensional decoupled direct (DDM-3D) sensitivity analysis module in the community multiscale air quality (CMAQ) model and the three-dimensional variational (3DVAR) data assimilation technique. We established the explicit observation operator matrix between the ES and receptor concentrations and the background error covariance (BEC) matrix of the ES, which can reflect the impacts

of uncertainties of the ES on assimilation. Then we constructed the inversion model of the ES by combining the sensitivity analysis with 3DVAR techniques. We performed the simulation experiment using the inversion model for a heavy haze case study in the Beijing-Tianjin-Hebei (BTH) region during 27−30 December 2016. Results show that the spatial distribution of sensitivities of SO_2 and NO_x ESs to their concentrations, as well as the BEC matrix of ES, is reasonable. Using a posteriori inversed ES, underestimations of SO_2 and NO_2 during the heavy haze period are remarkably improved, especially for NO_2. Spatial distributions of SO_2 and NO_2 concentrations simulated by the constrained ES were more accurate compared with an apriori ES in the BTH region. The temporal variations in regionally averaged SO_2, NO_2, and O_3 modeled concentrations using a posteriori inversed ES are consistent with in situ observations at 45 stations over the BTH region, and simulation errors decrease significantly. These results are of great significance for studies on the formation mechanism of heavy haze, the reduction of uncertainties of the ES and its dynamic updating, and the provision of accurate virtual emission inventories for airquality forecasts and decision-making services for optimization control of air pollution. (Cheng Xinghong, Hao Zilong, Zang Zengliang)

2.3 Development of three-dimensional variational data assimilation method of aerosol for the CMAQ model: An application for $PM_{2.5}$ and PM_{10} forecasts in the Sichuan Basin

A three-dimensional variational (3DVAR) data assimilation method for the aerosol variables of the community multiscale air quality (CMAQ) model was developed. This 3DVAR system uses $PM_{2.5}$ and $PM_{2.5-10}$ (the difference between PM_{10} and $PM_{2.5}$) as control variables and uses the AERO6 aerosol chemical mechanism in the CMAQ model. Two parallel experiments, one with and one without data assimilation (DA), were performed to evaluate the assimilating effects of surface $PM_{2.5}$ and PM_{10} during a heavy haze episode from 13 to 16 January, 2018 in the Sichuan Basin (SCB) region. The results show that simulations without DA clearly underestimated $PM_{2.5}$ and PM_{10} concentrations, and the analysis field with aerosol DA is skillful at fitting the observations and effectively improving subsequent forecasts of $PM_{2.5}$ and PM_{10}. For the analysis fields of $PM_{2.5}$ and PM_{10} after DA comparing with those without DA, the correlation coefficient (CORR) of $PM_{2.5}$ and PM_{10} increased by 0.59 and 0.65, the bias (BIAS) increased by 82.29 and 125.41 μg m^{-3}, and the root mean square error (RMSE) declined by 73.69 and 116.30 μg m^{-3}, respectively. Improvement of subsequent 24-h forecasts of $PM_{2.5}$ and PM_{10} with DA is also significant. Statistical results of forecasting improvement with DA indicated that the CORR, BIAS, and RMSE for $PM_{2.5}$ and PM_{10} at 78% and 89% of stations in the SCB region are improved, respectively. From the perspective of assimilation duration time, the improvement of $PM_{2.5}$ and PM_{10} can be maintained for similar to 24 h. (Zhang Zhendong, Zang Zengliang, Cheng Xinghong)

2.4 How were the eastward-moving heavy rainfall events from the Tibetan Plateau to the lower reaches of the Yangtze River enhanced?

This study investigates eastward-moving summer heavy rainfall events in the lower reaches of the Yangtze River (LRYR), which are associated with the Tibetan Plateau (TP) vortices. On the basis of rainfall data from gauges and additional atmospheric data from ERA-Interim, the dynamic and thermodynamic effects of moisture transport and diabatic heating are estimated to determine the physical mechanisms that support the eastward-moving heavy rainfall events. As the rainband moves eastward, it is accompanied by anomalous cyclonic circulation in the upper and middle troposphere and enhanced vertical motion throughout the troposphere. In particular, the rainfall region is located in the fore of the upper-level trough, which is ideal for baroclinic organization of the convective system and further development of the eastward-moving vortex. The large atmospheric apparent heat source also contributes to lifting the lower-level air into the upper atmosphere and to enhancing the low-level convective motion and convergence during the heavy rainfall process. Piecewise potential vorticity inversion further verifies the crucial role that the diabatic heating played

in developing the anomalous geopotential height favorable for the enhanced rainfall. The combined action of the dynamic and thermodynamic processes, as well as the rich moisture supply from the seas, synergistically sustained and enhanced the eastward-moving rainfall. (Zhao Yang, Chen Deliang, Deng Yi)

2.5 Intensified moisture sources of heavy precipitation events contributed to interannual trend in precipitation over the Three-Rivers-Headwater region in China

Evidence has indicated an overall wetting trend over the Three-Rivers Headwater region (TRHR) in the recent decades, whereas the possible mechanisms for this change remain unclear. Detecting the main moisture source regions of the water vapor and its increasing trend over this region could help understand the long-term precipitation change. Based on the gauge-based precipitation observation analysis, we find that the heavy precipitation events act as the main contributor to the interannual increasing trend of summer precipitation over the TRHR. A Lagrangian moisture tracking methodology is then utilized to identify the main moisture source of water vapor over the target region for the boreal summer period of 1980−2017, with focus particularly on exploring its change associated with the interannual trend of precipitation. On an average, the moisture sources for the target regions cover vast regions, including the west and northwest of the Tibetan Plateau by the westerlies, the southwest by the Indian summer monsoon, and the adjacent regions associated with the local recycling. However, the increased interannual precipitation trend over the TRHR could be largely attributed to the enhanced moisture sources from the neighboring northeastern areas of the targeted region, particularly associated with the heavy precipitation events. The increased water vapor transport from the neighboring areas of the TRHR potentially related to the enhanced local hydrological recycling over these regions plays a first leading role in the recent precipitation increase over the TRHR. (Zhao Ruiyu, Chen Bin, Xu Xiangde)

2.6 The key supply source of long-distance moisture transport for the extreme rainfall event on July 21, 2012 in Beijing

In this study, the weather research and forecasting (WRF) model and meteorological observation data were used to research the long-distance moisture transport supply source of the extreme rainfall event that occurred on July 21, 2012 in Beijing. Recording a maximum rainfall amount of 460 mm in 24 h, this rainstorm event had two dominant moisture transport channels. In the early stage of the rainstorm, the first channel comprised southwesterly monsoonal moisture from the Bay of Bengal (BOB) that was directly transported to North China along the eastern edge of Tibetan Plateau (TP) by orographic uplift. During the rainstorm, the southwesterly moisture transport was weakened by the transfer of Typhoon Vicente. Moreover, the southeasterly moisture transport between the typhoon and the western Pacific subtropical high (WPSH) became another dominant moisture transport channel. The moisture in the lower troposphere was mainly associated with the southeasterly moisture transport from the South China Sea and the East China Sea, and the moisture in the middle troposphere was mainly transported from the BOB and Indian Ocean. The control experiment well reproduced the distribution and intensity of rainfall and moisture transport. By comparing the control and three sensitivity experiments, we found that the moisture transported from Typhoon Vicente and a tropical cyclone in the BOB both significantly affected this extreme rainfall event. After Typhoon Vicente was removed in a sensitivity experiment, the maximum 24-h accumulated rainfall in North China was reduced by approximately 50% compared with that of the control experiment, while the rainfall after removing the tropical cyclone was reduced by 30%. When both the typhoon and tropical cyclone were removed, the southwesterly moisture transport was enhanced. Moreover, the sensitivity experiment of removing Typhoon Vicente also weakened the tropical cyclone in the BOB. Thus, the moisture pump driven by Typhoon Vicente played an important role in maintaining and strengthening the tropical cyclone in the BOB through its westerly airflow. Typhoon

Vicente was not only the moisture transfer source for the southwesterly monsoonal moisture but also affected the tropical cyclone in the BOB, which was a key supply source of long-distance moisture transport for the extreme rainfall event on July 21, 2012 in Beijing. (Li Juan, Xu Xiang de, Li Yue qing)

2.7 Warm cover: Precursory strong signals for haze pollution hidden in the middle troposphere

Eastern China (EC), located in the downstream region of the Tibetan Plateau (TP), is a large area with frequent haze pollution. In addition to air pollutant emissions, meteorological conditions are a key inducement for air pollution episodes. Based on the study of the Great Smog of London in 1952 and haze pollution in EC over recent decades, it is found that the abnormal warm cover (air-temperature anomalies) in the middle troposphere, as a precursory strong signal, could be connected to severe air pollution events. The convection and vertical diffusion in the atmospheric boundary layer (ABL) were suppressed by a relatively stable structure of warm cover in the middle troposphere leading to ABL height decreases, which were favorable for the accumulation of air pollutants in the ambient atmosphere. The anomalous structure of the troposphere's warm cover not only exists in heavy haze pollution on the daily scale, but also provides seasonal, interannual and interdecadal strong signals for frequently occurring regional haze pollution. It is revealed that a close relationship existed between interannual variations of the TP's heat source and the warm cover strong signal in the middle troposphere over EC. The warming TP could lead to anomalous warm cover in the middle troposphere from the plateau to the downstream EC region and even the entire East Asian region, thus causing frequent winter haze pollution in EC region. (Xu Xiangde, Cai Wenyue, Zhao Tianliang)

2. 8 南海台风生成前48 h环流特征及热力与动力条件

利用1979—2019年4—11月中国气象局上海台风研究所热带气旋最佳路径资料和静止卫星红外云图资料，筛选出189例南海台风，结合欧洲中期天气预报中心1° × 1° 再分析资料，分析南海台风生成前48 h至生成时刻的天气环流和动力、热力条件。结果表明：南海台风生成于热带洋面大范围的高海表温度、高水汽含量和高不稳定层结区，其生成前的主要环境背景环流是赤道辐合带、西南季风或东风波等；台风生成前扰动中心常常处于其北侧风切变小而南侧风切变大的过渡带中，少数扰动中心倾向于风切变小值中心附近，风切变与扰动的发展之间无显著相关；扰动中心一般与垂直涡度中心重合，垂直涡度中心是表征扰动自身强弱的物理量，但垂直涡度自身的大小与未来扰动发展趋势关系不明显，而Okubo-Weiss（OW）指数则对于扰动的发展以及扰动位置确定有较好的指示意义；在扰动发展过程中，扰动中心附近存在一个贯穿整个对流层的位涡柱，低层扰动部分与位涡柱中的中低层位涡相互作用，有利于扰动发展。（高拴柱，张胜军，吕心艳）

3 暴雨和强对流研究
3 Research on heavy rainfall and strong convection

3.1 A double-moment SBU-YLIN cloud microphysics scheme and its impact on a squall line simulation

A double-moment version of the SBU-YLIN cloud microphysical scheme in WRF is introduced. It predicts the mass and number mixing ratios of cloud droplets, rains, cloud ice, and precipitating ice. In addition, a number of physical processes, like rain evaporation, collection between rain and snow are also optimized in the new scheme. The scheme is evaluated and compared with the original one-moment scheme for a squall line case. We found that the double-moment approach gives a better representation of rain evaporation, which is critical for the development, morphology, and evolution of the simulated squall line, especially for the

enhanced trailing stratiform cloud and leading convective line. The relationship between key microphysical processes and squall line dynamics is investigated to identify the driving mechanisms of the descending rear inflow, cold pool, and slantwise updraft. Furthermore, formation of the transition zone in the simulated squall line strongly depends on the flexible description of ice particle properties, such as size, degree of riming and fall speed. (Zhao Xi, Lin Yanluan, Luo Yali)

3.2 A study of the fraction of warm rainfall in a pre-summer rain event over South China

The precipitation is divided into the warm-rain and cold-rain processes according to the microphysical mechanism, but which processes are more important in a heavy precipitation even? An approach that quantitatively separates the warm-rain from total-rain processes is proposed by adding a set of new variables in microphysics schemes of the Weather Research and Forecasting model. The fraction of rainfall that formed by warm-rain processes and the related microphysical characteristic are investigated by a heavy precipitation event in South China on 9 May 2016. The simulation using the Thompson microphysics reasonably reproduces the spatial distribution of precipitation and temporal evolution of rain bands. It is found that when the composite reflectivity is between 25 and 35 dBz, the lowest percentage of warm-rain fraction occurs (median of 20%−30%). While in the strong precipitation area, the contribution of warm-rain steadily increases with the median of −50% due to the continuous moisture supply. The similar characteristics by two other microphysics schemes (Morrison and CAMS) further verify the results. In addition, abundant supercooled water exists above the 0 ℃ level due to the high condensation rate. The strong updrafts in lower-middle layers are closely associated with the areas of water vapor condensation, implying that the phase-change processes should be responsible for the small-scale buoyancy production. The budget of rain water shows that the warm-rain processes play a leading role in the initiating stage of convection, and the weak advection of rain water indicates that the transport of cloud body from surroundings to the precipitation area is quite limited. (Gao Wenhua, Xue Lulin, Liu Liping)

3.3 Analysis of a record-breaking rainfall event associated with a monsoon coastal megacity of South China using multisource data

Monsoon coastal cities often suffer from extreme rain-induced flooding and severe hazard. However, the associated physical mechanisms and detailed storm structures are poorly understood due to the lack of high-resolution data. This study presents an analysis of a thunderstorm that produces extreme hourly rainfall (EXHR) of 219 mm over the Guangzhou megacity on the southern coast of China using integrated multiplatform observations and a four-dimensional variational Doppler radar analysis system. Results indicate that weak environmental flows and convectively generated weak cold pool facilitate the formation of a quasi-stationary storm, while onshore warm and moist flows in the boundary layer (BL) provide the needed moisture supply. The 219-mm EXHR is attendant by a shallow meso-gamma-scale vortex due to stretching of intense latent heating-induced convergence, which, in turn, helps organize convective updrafts into its core region. Lightning and dual-polarization radar observations reveal active warm-rain (but weak mixed-phase) microphysical processes, with raindrop size distribution (RSD) closer to marine convection. In contrast, another storm develops about 4 h earlier and only 35 km to the northwest, but with more lightning, higher cloud tops, more graupels, higher supercooled liquid water content and continental RSD, little evidence of rotation, and much less rainfall. They are attributable to the presence of larger convective available potential energy resulting from the urban heat island effects and less moisture supply in the BL. These results highlight the importance of using multisource remote sensing data sets in understanding the microphysical and kinematic structures of EXHR-producing storms. (Li Mingxin, Luo Yali, Zhang Da-Lin)

3.4 Atmospheric-boundary-layer-height variation over mountainous and urban sites in Beijing as derived from radar wind-profiler measurements

The evolution of the atmospheric boundary layer (ABL) varies greatly with terrain, so that the spatial and temporal variabilities of the ABL height remain poorly understood over complex terrain. Using radar wind-profiler measurements obtained from rural mountainous (Yanqing) and adjoining urban-plain (Haidian) landscapes of Beijing, China in 2019, ABL heights are calculated based on a normalized signal-to-noise-ratio threshold. The seasonally contrasting features of ABL height variation and growth rate over the two sites are revealed for clear-sky conditions. Interestingly, the ABL in spring remains suppressed during the morning and evolves rapidly in the afternoon over Haidian; however, a usual diurnal ABL evolution is observed over Yanqing. During the winter, more rapid evolution of the ABL is observed over Haidian, although on average the daytime ABL height remains less than 800 m above ground level. The growth rate of ABL height is found to undergo a more pronounced seasonal variation over Haidian while being relatively less variable over Yanqing. As expected, the lowest (highest) growth rate of 90 m h^{-1} (188 m h^{-1}) occurs in winter (summer) over Haidian. The analysis of the seasonal variations in wind profiles reveals deeper insights into the development of the local plain-to-mountain flow circulation over the region and possible implications on the contrasting seasonal ABL variations, particularly during the spring and summer. Additionally, the slower ABL evolution over Haidian in autumn and winter could be associated with an aerosol-induced stable ABL as well as stronger urban heat accumulation. The findings have implications for the better understanding of air pollution meteorology in regions with mountainous terrain. (Solanki Raman, Guo Jianping, Li Jian)

3.5 On the anomalous development of a series of heavy rainfall events from central to northern China during 19−21 July 2016

This study examines the development of a series of heavy rainfall events over four different geographical regions from the central to northern China on 19−21 July 2016, with the maximum 48-h-accumulated and hourly rainfall amounts of 875 and 139 mm, respectively. Results show that the heavy rainfall events occurred in an environment with an anomalous deep trough associated with unusual extratropical cyclogenesis during this warm month and a pronounced moisture anomaly compared to a 30-year climatology. The cyclogenesis coincided with dry-air intrusion from the lower stratosphere, and its merging with a northwest and a southwest vortex in the lower troposphere. After its formation, the cyclone moved northward on the east side of Mt. Taihang and then northeastward across Mt. Yanshan. The presence of the southwest vortex and an abnormally strong western Pacific subtropical high contributed to the maintenance and intensification of a southwesterly low-level jet (LLJ) carrying ample moisture, leading to the heavy rainfall in central China. The further enhanced southwesterly LLJ through the cyclogenesis and its accompanying southeasterly LLJ provided much needed precipitable water for the heavy rainfall events over North China. It was the quasi-geostrophic forcing of the extratropical cyclone, together with its cold/warm frontal systems, and especially its northward movement with the approaching airflows near-perpendicular to the general mountain orientations that provided optimized settings for the generation of a series of heavy rainfall events along the windward foothills of the major mountains in the northern China. (Xia Rudi, Zhang Da-Lin, Fu Shenming)

3.6 On the diurnal cycle of heavy rainfall over the Sichuan Basin during 10−18 August 2020

A sustained heavy rainfall event occurred over the Sichuan Basin in Southwest China during 10−18 August 2020, showing pronounced diurnal rainfall variations with nighttime peak and afternoon minimum values, except on the first day. Results show that the westward extension of the anomalously strong western Pacific subtropical high was conducive to the maintenance of a southerly low-level jet (LLJ) in and to the

southeast of the basin, which favored continuous water vapor transport and abnormally high precipitable water in the basin. The diurnal cycle of rainfall over the basin was closely related to the periodic oscillation of the LLJ in both wind speed and direction that was caused by the combination of inertial oscillation and terrain thermal forcing. The nocturnally enhanced rainfall was produced by moist convection mostly initiated during the evening hours over the southwest part of the basin where high convective available potential energy with moister near-surface moist air was present. The convective initiation took place as cold air from either previous precipitating clouds from the western Sichuan Plateau or a larger-scale northerly flow met a warm and humid current from the south. It was the slantwise lifting of the warm, moist airflow above the cold air, often facilitated by southwest vortices and quasi-geostrophic ascent, that released the convective instability and produced heavy rainfall. (Xia Rudi, Luo Yali, Zhang Da-Lin)

3.7 On the localized extreme rainfall over the Great Bay Area in South China with complex topography and strong UHI effects

In this study, high-resolution surface and radar observations are used to analyze 24 localized extreme hourly rainfall (EXHR; > 60 mm h^{-1}) events with strong urban heat island (UHI) effects over the Great Bay Area (GBA) in South China during the 2011−2016 warm seasons. Quasi-idealized, convection-permitting ensemble simulations driven by diurnally varying lateral boundary conditions, which are extracted from the composite global analysis of 3−5 June 2013, are then conducted with a multilayer urban canopy model to unravel the influences of the UHI and various surface properties nearby on the EXHR generation in a complex geographical environment with sea-land contrast, topography, and vegetation variation. Results show that EXHR is mostly distributed over the urban agglomeration and within about 40 km on its downwind side, and produced during the afternoon-to-evening hours by short-lived meso-γ- to meso-β-scale storms. On the EXHR days, the GBA is featured by a weak gradient environment with abundant moisture, and a weak southwesterly flow prevailing in the boundary layer (BL). The UHI effects lead to the development of a deep mixed layer with warm bubbles over the urban agglomeration, in which the lower-BL convergence and BL-top divergence is developed, assisting in convective initiation. Such urban BL processes and associated convective development with moisture supply by the synoptic low-level southwesterly flow are enhanced by orographically increased horizontal winds and sea breezes under the influence of the herringbone coastline, thereby increasing the inhomogeneity and intensity of rainfall production over the pi-shaped urban clusters. Vegetation variations are not found to be an important factor in determining the EXHR production over the region. (Sun Xiaoyan, Luo Yali, Gao Xiaoyu)

3.8 Spatiotemporal characteristics of atmospheric turbulence over China estimated using operational high-resolution soundings

Large-scale in situ observations are sorely lacking, leading to poor understanding of nationwide atmospheric turbulence over China. Nevertheless, high-resolution soundings have become available starting in 2011, providing a unique opportunity to investigate turbulence across China. Here, we calculated the mean turbulence dissipation rate from radiosonde measurements across China for the period 2011−2018 using the Thorpe analysis. The atmospheric layers that had stronger turbulence indicated by larger epsilon generally came with larger Thorpe length but with smaller Brunt-Vaisala frequency. Overall, the clear-air epsilon in the free atmosphere exhibited large spatial variability with a “south-high north-low” pattern. Large clear-air epsilon values were observed in both the lower stratosphere (LS) and upper troposphere (UT), especially over the Tibetan Plateau (TP) and its neighboring regions with complex terrain likely due to large-amplitude mountain waves. Particularly, less frequent but more intense clear-air turbulence was observed in both lower troposphere

(LT) and UT over the TP, while more frequent, less intense clear-air turbulence was found in the northern China. The all-sky turbulence considering the moist-saturation effects was much stronger in the troposphere, notably in the southern China where convective clouds and precipitation of tentimes dominated. In the vertical direction, the altitude of peak clear-air epsilon in the troposphere was found to decrease poleward, broadly consistent with the meridional gradient of tropopause height in the Northern Hemisphere. A double-peak mode stood out for the profiles of clear-air epsilon at midlatitudes to the north of 30°N in winter: one peak was at altitudes of 15−18 km, and another at altitudes of 5−8 km. The strong shear instabilities around the westerly jet stream could account for the vertical bimodal structures. The seasonality of epsilon was also pronounced, reaching maxima in summer and minima in winter. Our results may help understand and avoid clear-air turbulence, as related to aviation safety among other issues. (Lyu Yanmin, Guo Jianping, Li Jian)

3.9 Technical note: First comparison of wind observations from ESA's satellite mission Aeolus and ground-based radar wind profiler network of China

Aeolus is the first satellite mission to directly observe wind profile information on a global scale. After implementing a set of bias corrections, the Aeolus data products went public on 12 May 2020. However, Aeolus wind products over China have thus far not been evaluated extensively by ground-based remote sensing measurements. In this study, the Mie-cloudy and Rayleigh-clear wind products from Aeolus measurements are validated against wind observations from the radar wind profiler (RWP) network in China. Based on the position of each RWP site relative to the closest Aeolus ground tracks, three matchup categories are proposed, and comparisons between Aeolus wind products and RWP wind observations are performed for each category separately. The performance of Mie-cloudy wind products does not change much between the three matchup categories. On the other hand, for Rayleigh-clear and RWP wind products, categories 1 and 2 are found to have much smaller differences compared with category 3. This could be due to the RWP site being sufficiently approximate to the Aeolus ground track for categories 1 and 2. In the vertical, the Aeolus wind products are similar to the RWP wind observations, except for the Rayleigh-clear winds in the height range of 0−1 km. The mean absolute normalized differences between the Mie-cloudy (Rayleigh-clear) and the RWP wind components are 3.06 (5.45), 2.79 (4.81), and 3.32 (5.72) m/s at all orbit times and ascending and descending Aeolus orbit times, respectively. This indicates that the wind products for ascending orbits are slightly superior to those for descending orbits, and the observation time has a minor effect on the comparison. From the perspective of spatial differences, the Aeolus Mie-cloudy winds are consistent with RWP winds in most of East China, except in coastal areas where the Aeolus Rayleigh-clear winds are more reliable. Overall, the correlation coefficient R between the Mie-cloudy (Rayleigh-clear) wind and RWP wind component observation is 0.94 (0.81), suggesting that Aeolus wind products are in good agreement with wind observations from the RWP network in China. The findings give us sufficient confidence in assimilating the newly released Aeolus wind products in operational weather forecasting in China. (Guo Jianping, Liu Boming, Gong Wei)

3.10 The impact of the observation data assimilation on atmospheric reanalyses over Tibetan Plateau and western Yunnan-Guizhou Plateau

Three modern atmospheric reanalyses with different input observation data (NOAA-CIRES 20th century reanalysis (20CR), Japanese 55-year reanalysis (JRA-55) and (JRA-55C) were compared against the independent radiosonde observations over the Tibetan Plateau (TP) and the western Yunnan-Guizhou Plateau (YGP) from the China-Japan Meteorological Disaster Reduction Cooperation (JICA/Tibet) Center Project in the summer of 2018 to investigate the effects of the assimilation of the observation data on the quality and accuracy of the reanalyses in the troposphere. The results indicate that the mean biases and mean root-mean-

square errors of horizontal wind, temperature, and specific humidity significantly decreased when comparing the 20CR reanalysis (assimilating only surface pressure) to the JRA-55C (assimilating conventional surface and upper-air observations) and the JRA-55 (assimilating conventional and satellite observations), and the bias spreads of these aboveground variables in JRA-55C and JRA-55 were cut to almost half of those observed in 20CR. However, the mean biases and uncertainties varied little from JRA-55C to JRA-55. This means that the assimilation of conventional observation data plays a vital role in the quality of reanalyses for the troposphere over these data-sparse plateaus. It was also found that the temperature and specific humidity near the ground over TP showed larger mean biases and bias spans than those over YGP, likely due to the sparser surface observation over TP. (Bao Xinghua, Zhang Fuqing, Zhao Yang)

3.11 The significant role of radiosonde-measured cloud-base height in the estimation of cloud radiative forcing

The satellite-based quantification of cloud radiative forcing remains poorly understood, due largely to the limitation or uncertainties in characterizing cloud-base height (CBH). Here, we use the CBH data from radiosonde measurements over China in combination with the collocated cloud-top height (CTH) and cloud properties from MODIS/Aqua to quantify the impact of CBH on shortwave cloud radiative forcing (SWCRF). The climatological mean SWCRF at the surface (SWCRFSUR), at the top of the atmosphere (SWCRFTOA), and in the atmosphere (SWCRFATM) are estimated to be −97.14, −84.35, and 12.79 W m^{-2}, respectively for the summers spanning 2010 to 2018 over China. To illustrate the role of the cloud base, we assume four scenarios according to vertical profile patterns of cloud optical depth (COD). Using the CTH and cloud properties from MODIS alone results in large uncertainties for the estimation of SWCRFATM, compared with those under scenarios that consider the CBH. Furthermore, the biases of the CERES estimation of SWCRFATM tend to increase in the presence of thick clouds with low CBH. Additionally, the discrepancy of SWCRFATM relative to that calculated without consideration of CBH varies according to the vertical profile of COD. When a uniform COD vertical profile is assumed, the largest SWCRF discrepancies occur during the early morning or late afternoon. By comparison, the two-point COD vertical distribution assumption has the largest uncertainties occurring at noon when the solar irradiation peaks. These findings justify the urgent need to consider the cloud vertical structures when calculating the SWCRF which is otherwise neglected. (Xu Hui, Guo Jianping, Li Jian)

3.12 The synoptic impacts on the convection initiation of a warm-sector heavy rainfall event over coastal South China prior to the monsoon onset: A numerical modeling study

A series of convection-permitting numerical experiments using the weather research and forecasting model with different model configurations are performed to investigate physical mechanisms governing convection initiation (CI) at the coast of South China (SC) during a warm-sector heavy rainfall event occurred before the South China Sea (SCS) monsoon onset. The simulation results are more sensitive to initial state from the different reanalysis products than the microphysics schemes, horizontal resolutions, initialization time, and lateral boundary conditions with the variation examined. It is found that the speeds of easterly to southeasterly winds in the boundary layer (BL) over the northern SCS determine the strength of horizontal convergence of the warm and moist airflows arriving at the coast. The midtropospheric divergence over the west coastal areas of SC and its southwest upstream impact vertical motion of the mid-to-lower tropospheric southwesterly airflows when approaching the coast. Differences in such features of upstream airflows in the experiments lead to distinct temporal evolutions of BL dynamic lifting and temperature stratification in the mid-to-lower levels at the CI location, and thus the level of free convection and convective available potential energy. The modeling evidence presented shows that the synoptic dynamic and thermodynamic characteristics

of the upstream airflows in BL and mid-to-lower troposphere, with local modulation by the coastal mountains, play important roles in determining the time and location of CI, and the distribution and amount of rainfall. Studies on more cases are needed to gain more general and robust conclusions about physical mechanism governing the warm-sector coastal CI. (Bao Xinghua, Luo Yali, Gao Xiaoyu)

3.13 Typhoon disaster risk zoning for China's coastal area

Previous studies on typhoon disaster risk zoning in China have focused on individual provinces or small-scale areas and lack county-level results. In this study, typhoon disaster risk zoning is conducted for China's coastal area, based on data at the county level. Using precipitation and wind data for China and typhoon disaster and social data at the county level for China's coastal area from 2004 to 2013, first we analyze the characteristics of typhoon disasters in China's coastal area and then develop an intensity index of factors causing typhoon disasters and a comprehensive social vulnerability index. Finally, by combining the two indices, we obtain a comprehensive risk index for typhoon disasters and conduct risk zoning. The results show that the maximum intensity areas are mainly the most coastal areas of both Zhejiang and Guangdong, and parts of Hainan Island, which are similar to the distribution of typhoon disasters. The maximum values of vulnerability are in the northwest of Guangxi, parts of Fujian coastal areas and parts of the Shandong Peninsula. The comprehensive risk index generally decreases from coastal areas to inland areas. The high-risk areas are mainly distributed over Hainan Island, south-western Guangdong, most coastal Zhejiang, the coastal areas between Zhejiang and Fujian and parts of the Shandong Peninsula. (Zhu Jing, Lu Yi, Ren Fumin)

3.14 Vertical structures of temperature inversions and clouds derived from high-resolution radiosonde measurements at Ny-Ålesund, Svalbard

The knowledge of the vertical atmospheric structures in the Arctic region remains elusive, due largely to sparse long-term continuous profiling observations. Based on the temporally high-resolution (1 s) radiosonde measurements from April 2017 to September 2019 collected at the Ny-Ålesund (11.92°E, 78.92°N) station in the Arctic, we analyzed the characteristics of temperature inversion (TI) and clouds, including the diurnal and seasonal variabilities under different atmospheric circulations. Clouds mainly appear in the lower troposphere, with the largest contribution by double-layer clouds. The seasonal variation of vertical cloud distribution above 7 km seems closely linked to the seasonal variability of tropopause height. Besides, the diurnal variation of TI frequency exhibits significant seasonality, with a bimodal distribution in the vertical, with stronger TI intensity in summer. The lowest temperatures at the top of bottom of the elevated inversion are observed in winter, whereas the lowest temperature of the surface-based inversion top is observed in spring, which may be related to the seasonal variation of sea surface temperature. The characteristics of cloud and TI are further analyzed under the five typical circulation patterns. It is found that the low-pressure system and southerly wind in front of the trough are favorable for cloud formation in the lower troposphere, while the impact of synoptic pattern on clouds in the upper troposphere seems negligible, likely due to the cold environment. The TI associated with cyclone systems tends to be much thinner and weaker, owning to the conditionally unstable conditions. These findings provide key reference for the vertical structure of the inversion and cloud in the Arctic, which is expected to help improve cloud parameterization in numeric models. (Wang Ding, Guo Jianping, Xu Hui)

3.15 Vorticity and moisture budget analyses on a plateau vortex that cause an intense rainfall event within the Qaidam Basin

As one of the most seriously arid areas in China, the Qaidam Basin (QB) features a notable growing probability of intense rainfall under global warming. Compared to a normal/humid region, intense rainfall usually results in more severe disasters in an arid area. Considering that few studies focused on intense

rainfall within the QB, there is an urgent need to understand the mechanisms governing intense rainfall in this region. A type of Tibetan Plateau vortex (TPV) associated intense rainfall within the QB was investigated in this study, which partly fills the existing research gaps in the field. The main findings are as follows: (a) The intense-rainfall-producing TPV formed and maintained in a favorable background environment which was characterized by a notable upper-level divergence north of a strong upper-level jet and a strong middle-level warm advection ahead of a shortwave trough over the Tibetan Plateau. (b) Vorticity budget indicates that two factors affected the vortex's formation notably, one was the convergence-related vertical stretching, which dominated the vortex's formation and the other was the import of the horizontal transport of anticyclonic vorticity which was the most detrimental factor for the formation of the TPV. Tilting and vertical transport only exerted weak effects on the TPV's formation, since convective activities were relatively weak in this event. (c) Moisture budget shows that the southwestern and southern moisture transport channels, which were mainly driven by the wind field associated with the shortwave trough over the Tibetan Plateau, contributed similar to 70% to the total moisture income of the intense rainfall within the QB. The transport was accomplished primarily through the southern boundary of the QB, with the moisture mainly coming from the Indian Peninsula and Indochina Peninsula. (Li Wanli, Xia Rudi, Zhong Qi)

3.16 Warm-season mesoscale convective systems over eastern China: Convection-permitting climate model simulation and observation

Mesoscale convective systems (MCSs) are important warm-season precipitation systems in the eastern China. However, our knowledge of their climatology and capability in their simulation is still insufficient. This paper examines their characteristics over the 2008−2017 warm seasons using convection-permitting climate simulations (CPCSs) with a 3-km grid spacing that explicitly resolves MCSs, as well as a high-resolution gauge-satellite merged precipitation product. An object-based tracking algorithm is applied to identify MCSs. Results indicate that the MCS genesis and occurrence are closely related to the progression of the East Asian monsoon and are modulated by the underlying topography. On average, about 243 MCSs are observed each season and contribute 19% and 47% to total and extreme warm-season precipitation. The climatological attributes and variabilities are reasonably reproduced in the CPCS. The major model deficiencies are excessive small MCS occurrence and overmuch MCS rainfall, consequently overestimating the precipitation contributions, whereas observational uncertainties may play a role too. Both the observed and simulated MCS precipitation feature a nocturnal or morning maximum and an eastward delayed diurnal peak east of the Tibetan Plateau, in contrast to the dominant afternoon peak of non-MCS precipitation. The favorable comparison with observations demonstrates the capability of CPCSs in simulating MCSs in the Asian monsoon climate, and its usefulness in projecting the future changes of MCSs under global warming. The finding that non-MCS precipitation is responsible for the high biased afternoon precipitation provides helpful guidance for further model improvement. (Yun Yuxing, Liu Changhai, Luo Yali)

3.17 Contrasting effect of soil moisture on the daytime boundary layer under different thermodynamic conditions in summer over China

The investigation is still lacking concerning the effect of soil moisture (SM) on the evolution of planetary boundary layer (PBL) under different land conditions in a huge domain as large as China. We perform an explicit correlation analysis between daytime PBL height (PBLH) and SM for convective, neutral and stable boundary layer regimes (i.e., CBL, NBL, and SBL), respectively. A negative correlation exists between SM and daytime PBLH for CBL and NBL, exhibiting a spatial pattern of east strong west weak, albeit a positive correlation for SBL. The standard deviation of PBLH for CBL and NBL exhibits a spatial pattern of northwest high southeast low. Cloudy, humid, and stable atmosphere result in CBL shoaling. PBLH more correlates

with the sensible heat flux (CBL: r=0.25; NBL: r=0.33) over dry areas, but over Northwest China the PBL depends more on meteorology likely owing to the extremely dry soil. The effect of SM on the evolution of PBL throughout China remains elusive. This study explores the correlation between PBLH and SM under different PBL regimes, using the 5-year record of high-resolution summertime soundings across China. The CBL and NBL heights during daytime are found to negatively correlate with SM. In contrast, the SBL height anticorrelates with SM, likely due to more fluid and moisture intermittent turbulence caused by enhanced SM in SBL. The spatial pattern of the standard deviation of CBL and NBL height exhibits a pronounced northwest high southeast low pattern. Our study also reveals more significant impact of sensible heat flux on CBL and NBL regimes over dry areas, compared to over wet areas, indicating that land surface processes are more coupled to the PBL evolution over dry areas. Besides, less cloud, dry and unstable atmosphere favor the development of CBL in wet areas, and PBLH is more dependent on meteorological quantities, but less on SM in dry areas, likely owing to extremely dry soil and bare land over Northwest China. (Xu Zhiqi, Chen Haishan, Guo Jianping)

3.18 Increased turbulence in the Eurasian upper-level jet stream in winter: Past and future

Anthropogenic activities have been increasingly strengthening the meridional temperature gradient in the upper atmosphere, which has a profound impact on the wind shear and turbulence in mid-latitudes. Here we examined the trends of the wintertime jet stream and clear-air turbulence at 250 hPa over the Eurasian. The zonal wind speed showed a significantly increasing trend in the region between 40°N and 60°N where the meridional temperature gradient between the equator and the pole was increasing sharply in the past 4 decades (1980−2019). In addition, there existed a clear trend toward stronger vertical shear at 250 hPa in the latitudinal zone between 30°N and 40°N where the zonal wind increased, while a declining trend was shown to the south of 30°N, according to three different reanalysis datasets, including ERA5, JRA55, and NCAR/NCEP, which may be related to the poleward shift of the subtropical jet stream. The turbulence, closely related to the occurrence of vertical wind shear, was found to become stronger in the latitudinal zone between 30°N and 40°N consequently. The projections based on phase 6 of Coupled Model Intercomparison Project models show that the zonal wind speed in the mid-latitudes will increase significantly for the period 2015−2100, especially between the latitudinal zone between 40°N and 60°N, and the corresponding vertical wind shear in this area tends to dramatically increase. The findings not only help us better understanding of turbulence occurrence in the past 40 years, but also have profound implications for the projection of turbulence occurrence under global warming over mid-latitude regions of the Northern Hemisphere. (Lyu Yanmin, Guo Jianping, Li Jian)

3.19 Investigation of near-global daytime boundary layer height using high-resolution radiosondes: First results and comparison with ERA5, MERRA-2, JRA-55, and NCEP-2 reanalyses

The planetary boundary layer (PBL) governs the vertical transport of mass, momentum, and moisture between the surface and the free atmosphere, and thus the determination of PBL height (BLH) is recognized as crucial for air quality, weather, and climate analysis. Although reanalysis products can provide important insight into the global view of BLH in a seamless way, the BLH observed in situ on a global scale remains poorly understood due to the lack of high-resolution (1 or 2 s) radiosonde measurements. The present study attempts to establish a near-global BLH climatology at synoptic times (00:00 and 12:00 UTC) and in the daytime using high-resolution radiosonde measurements over 300 radiosonde sites worldwide for the period from 2012 to 2019, which is then compared against the BLHs obtained from four reanalysis datasets, including ERA5, MERRA-2, JRA-55, and NCEP-2. The variations in daytime BLH exhibit large spatial and temporal dependence, and as a result the BLH maxima are generally discerned over the regions such as the western United States and western China, in which the balloon launch times mostly correspond to the afternoon.

The diurnal variations in BLH are revealed with a peak at 17:00 local solar time (LST). The most promising reanalysis product is ERA5, which underestimates BLH by around 130 m as compared to radiosondes released during daytime. In addition, MERRA-2 is a well-established product and has an underestimation of around 160 m. JRA-55 and NCEP-2 might produce considerable additional uncertainties, with a much larger underestimation of up to 400 m. The largest bias in the reanalysis data appears over the western United States and western China, and it might be attributed to the maximal BLH in the afternoon when the PBL has risen. Statistical analyses further indicate that the biases of reanalysis BLH products are positively associated with orographic complexity, as well as the occurrence of static instability. To our best knowledge, this study presents the first near-global view of high-resolution radiosonde-derived boundary layer height and provides a quantitative assessment of the four frequently used reanalysis products. (Guo Jianping, Zhang Jian, Yang Kun)

3.20 Large-scale pattern of the wintertime diurnal temperature range variations over North America during 1979−2018

The atmospheric circulation and remote forcing of SST anomalies play an imporant role in the formation of largescale cloud cover and precipitation anomalies as well as the patterns of diurnal temperature range (DTR) variability. In this study, the dominant patterns of the wintertime DTR variations over North America (NA) and the underlying mechnisms are investigated based on observational and reanalysis datasets during 1979−2018. The first leading mode is characterized by a widespread same-sign loading in the majority of NA. The corresponding principal component (PC) shows an obvious interannual time-scale variations. The second mode displays a north-south dipole-like pattern in the NA and the corresponding PC exhibits a decline trend during 1979−2018. Both patterns of DTR variations are closely associated with the changes in local cloud cover and precipitation. Furthermore, clear effects are identified of El Niño-southern oscillation (ENSO) and Tropical/Northern Hemisphere (TNH) teleconnection on the formation of the two dominant patterns of wintertime DTR variabilty over NA through changing the atmospheric circulation and associated transportation of temperature and moisture. Our findings provide a new insight into understanding the DTR changes during recent decades. (Liu Lin, Chen Wen, Guo Jianping)

3.21 Regional variability of summertime raindrop size distribution from a network of disdrometers in Beijing

Regional raindrop size distribution (DSD) features are poorly understood due to the lack of observations. Here we investigate the regional variability of summertime DSD in Beijing, using the DSD observations from ten disdrometer sites from April to September 2017. The characteristics of DSD are analyzed for both convective and stratiform precipitation, mainly classified by rain rate (R). The shape (μ) and slope (λ) parameters follow a second-degree polynomial regression relationship for both stratiform and convective precipitation. On average, stratiform precipitation is found to have larger values of μ and λ than convective precipitation, whereas convective precipitation has a larger mass-weighted mean diameter (D_m) and a generalized intercept parameter (N_w). Interestingly, the north of Beijing has larger values of μ and λ, as opposed to D_m and N_w that exhibit greater values in the south, which could probably be attributed to terrain differences. The rain rate dependence on DSD is analyzed as well. In general, the D_m-R and N_w-R relationships follow a power-law distribution, and both D_m and N_w increase significantly with R. As the rain rate increases, D_m keeps increasing to around 1.5 mm until an equilibrium state is reached. The findings obtained here could provide useful reference for better estimations of rainfall using the remote sensing techniques. (Han Yi, Guo Jianping, Yun Yuxing)

3.22 The impact of reforestation induced land cover change (1990−2017) on flood peak discharge using HEC-HMS hydrological model and satellite observations: A study in two mountain basins, China

Understanding the effect of land use and land cover (LULC) type change on watershed hydrological response is essential for adopting applicable measures to control floods. In China, the Grain to Green Program (GTGP) and the Natural Forest Conservation Program (NFCP) have had a substantial impact on LULC. We investigate the effect of these conservation efforts on flood peak discharge in two mountainous catchments. We used a series of Landsat images ranging from 1990 to 2016/2017 to evaluate the LULC changes. Further to this, the hydrological responses at the basin and sub-basin scale were generated by the Hydrologic Modeling System (HEC-HMS) under four LULC scenarios. Between 1990 and 2016/2017, both catchments experienced an increase in forest and urban land by 18% and 2% in Yanhe and by 16% and 8% in Guangyuan, respectively. In contrast, the agricultural land decreased by approximately 30% in Yanhe and 24% in Guangyuan, respectively. The changes in land cover resulted in decrease in flood peak discharge ranging from 14% in Yanhe to 6% in Guangyuan. These findings provide a better understanding on the impact of reforestation induced LULC change on spatial patterns of typical hydrological responses of mountainous catchment and could help to mitigate flash flood hazards in other mountainous regions. (Kabeja Crispin, Li Rui, Guo Jianping)

3.23 Assessing the surface-layer stability over China using long-term wind-tower network observations

Surface-layer stability is important in many processes, such as in the surface energy budget, atmospheric pollution, and boundary-layer parametrizations. Most previous studies on stability, however, conducted either theoretical or observational investigations at specific sites, thus leaving a gap with regard to the large-scale pattern. Here, wind-speed and temperature observations at multiple heights from the wind-tower network of China are used to estimate low-level stability during the 2009−2016 period. A series of data-quality-control procedures are conducted and data from 170 wind towers with more than 2 years of valid observations are selected. The degree of stability is classified by the Obukhov length, which is derived from the wind speed and temperature at 10 m and 70 m above ground level, combined with information regarding the roughness length. Overall, the occurrence frequency of surface-layer instability exhibits significant temporal and spatial variability, being particularly larger in spring and summer than in autumn and winter. The maximum frequency of summertime instability occurs in the time period 1000−1200 local solar time, approximately 2 h earlier than in autumn. Geographically, the peak instability frequency occurs much earlier in the day in Northwest China than in other regions, likely owing to the arid and semi-arid land cover. Also noteworthy is the steady increase in instability frequency observed during the period analyzed here, likely resulting from the reduction in the vertical gradient of wind speed. Our findings call for explicit consideration of stability variability in the wind-energy industry and in fundamental boundary-layer investigations in China. (Li Jian, Guo Jianping, Xu Hui)

3.24 Study of the formation of the Arctic cell associated with the two-wave middle-high latitude circulation

The formation of the Arctic cell associated with the two-wave middle-high latitude circulation, which is a major atmospheric circulation common to the three-cell and four-cell mean meridional circulations in the Northern Hemisphere, is analyzed using a long period of reanalysis data. In the context of the two-wave middle-high latitude circulation, when the high near the Arctic region from 120°E to 80°W (AH120E80W) weakens and withdraws eastward and the low near the Arctic region from 80°W to 120°E (AL80W120E) strengthens and expands northeastward, the Arctic tends to be controlled by obvious low pressure and

associated upward motion, leading to the formation of the Arctic cell. The eastward withdrawal of the AH120E80W is attributed to an eastward retreat of the North Pacific Low, because it promotes the strong anticyclonic wind shear associated with the maintenance of the AH120E80W to migrate eastward. The eastward retreat of the North Pacific Low is induced by the decrease in the width of the East Asian Trough, which results from the response of the high terrain in Central Asia to the weakening of middle-latitude westerly winds caused by a northward shift of the Azores high. On the other hand, the eastward withdrawal of the AH120E80W results in the decay of the Arctic high, causing the winds near the Arctic to change from easterly to westerly. At the same time, the northward shift of the Azores high promotes the strong Icelandic Low to expand poleward. The combination of the Arctic westerly winds and the poleward expansion of the strong Icelandic Low leads to the northeastward expansion of the AL80W120E. (Liang Zhaoming, Gao Shouting)

3.25 A dynamical and numerical study of the effects of the topography of the Tibetan Plateau and westerly wind speed on the East Asian Trough

The effects of the topography of the Tibetan Plateau (TP) and westerly wind speed on the East Asian Trough (EAT) are discussed with analysis using a dynamical model, and verified with numerical experiments based on real cases. The dynamical model utilizes a complex terrain function to approximate the TP topography, and derives a stream function generated by the TP terrain. The numerical experiments used for the verification consider the influence of different TP terrain heights and westerly wind speeds. The results show that the topography of the TP has a prominent contribution to the intensity of the EAT, but little effect on its position. The topography of the TP in the westerly winds causes a low-pressure trough to its east, which promotes a deepening of the EAT to the east side of the TP. In contrast, in the context of the TP, westerly wind speed has an important influence on the position of the EAT, but a minor impact on the deepening of the EAT. A larger westerly wind speed causes a more eastern position of the EAT. These findings indicate that the combination of large-scale topography and westerly wind speed plays a key role in the evolution of the EAT, in the terms of intensity and position. (Liang Zhaoming, Xu Pengcheng, Gao Shouting, Zuo Qunjie)

3.26 Organized warm-sector rainfall in the coastal region of South China in an anticyclone synoptic situation: Observational analysis

Organized warm-sector rainfall (OWSR) near the coast of South China tends to occur in certain synoptic situations characterized with either a low-level jet or an anticyclone, with the latter being less investigated. This paper fills the gap by analyzing 15 OWSR events that occurred in an anticyclone synoptic situation during the pre-summer rainy season of 2011–2016, based on high-resolution observational and reanalysis data. The results show that the anticyclone synoptic situation produces marked northerly boundary-layer winds inland and obvious northeasterly, easterly/southwesterly, and southeasterly boundary-layer winds near the coasts of the eastern Guangdong, western Guangdong, and Guangxi, respectively. The coastal boundary-layer winds promote favorable environmental conditions and strong convergence for convection initiation; consequently, OWSR is prone to occur near the coasts of the western Guangdong and Guangxi, but exhibits different formation and propagation features in the following two subareas. (1) The southeasterly boundary-layer winds tend to converge near the border area between Guangxi and Guangdong (BGG), promoting the formation of a stable convective line along the mountains. The convective line persists with support of upper-level southwesterly winds that facilitate convective cells to propagate along the convective line, producing heavy OWSR along the mountains near BGG. (2) In contrast, a west-east convective line tends to form and maintain near the coast of Yangjiang (YJ) area, about 200 km east of BGG, owing to stable convergence between the easterly (or southwesterly) and the northerly boundary-layer winds reinforced by the mountains near YJ.

Moreover, the coupling of upper-level westerly winds with the easterly (southwesterly) boundary-layer winds facilitates expansion (eastward propagation) of the convective line, causing west–east-oriented heavy OWSR near the coast of YJ. In a word, this study reveals refined properties of OWSR initiation and development in the anticyclone synoptic situation, which may help improve the forecast skill of OWSR during the pre-summer rainy season in South China. (Liang Zhaoming, Gao Shouting)

3.27 1980—2017年南海季风爆发前后华南前汛期降水统计特征对比分析

利用1980—2017年华南地区303个国家级地面气象站逐小时降水数据、ERA-Interim再分析资料，分析华南前汛期（4—6月）降水统计特征，定义站点上短时（1～6 h）、中等时长（7～12 h）和长时（＞12 h）降水事件，对比降水量、频次和强度在南海季风爆发前后的变化，以及所定义的西部内陆、东部内陆、沿海地区的异同。结果表明：（1）南海季风爆发后，研究区域平均而言，3类降水事件的降水量增多、小时降水强度增强，短时、长时降水事件发生频次增多，而中等时长降水事件发生频次有所减少。（2）从空间分布来看，南海季风爆发后，小时降水强度在整个华南地区均增强，西部内陆时长大于6 h的降水事件尤为明显；降水事件的发生频次在西部内陆和沿海地区升高，而东部内陆时长大于6 h的降水事件发生频次降低，因此，季风爆发后西部内陆和沿海地区的总降水量均显著增大，而东部内陆的总降水量变化不大。（3）西部内陆降水事件主要在夜间开始发生，持续时间越长的事件越早开始，且由西向东逐渐推迟；东部内陆短时降水事件主要在14:00（北京时，下同）左右开始，季风爆发后更为明显，而时长大于6 h的降水事件的开始时间和峰值时间无明显的分布规律；沿海地区短时降水事件在季风爆发前主要于05:00—08:00时开始，季风爆发后，在海岸线约50 km以内仍然如此，而较远离海岸线的短时降水事件主要于14:00开始，沿海地区长时降水事件在季风爆发前、后都倾向于在夜间开始，并在日间出现峰值。（李争辉，罗亚丽）

3.28 北京地区一次飑线的组织化过程及热动力结构特征

2015年8月7日华北西北部的一次断线状对流系统向东南方向移动，并与平原地区多单体雷暴合并、组织，最终形成强飑线，造成北京地区出现较大范围的风雹和局地短时强降水天气。基于多源资料的研究结果表明：（1）飑线形成有上游线状对流发展移动、平原多个单体雷暴的新生和合并、线状对流并入本地多单体后组织成飑线3个阶段。第2阶段中，城区北部边缘地面热力分布不均，配合局地风场辐合，触发了雷暴。雷暴冷池范围不断扩大，温度梯度区向南扩展，造成新生对流向南传播。（2）飑线的组织化过程，呈现出两支强入流为典型特征的动力结构：一支位于雷暴冷池后侧中层（4500～5000 m），另一支位于低层飑线前侧，由强辐合区垂直于飑线指向云内。这两支强入流分别构成飑线前侧和后侧两个独立的顺时针垂直环流圈。后侧入流和前侧入流在同时加强，造成飑线前侧垂直环流不断加强，与之对应的环境垂直风切变也同步增强。这一动力过程形成了有利于飑线组织化的中尺度垂直切变环境，垂直风切变增大的本质实际上是飑线发展反馈的结果，同时也是驱动飑线快速向前移动和发展的重要因素。当后侧中层入流消失，前侧垂直环流也随之逐渐减弱，预示着飑线从成熟开始减弱消亡。（3）从热力结构看，下山的线状对流冷池与平原地区多单体雷暴的冷池合并，形成了扰动温度低于−8 ℃、厚度加深到1.5 km的强冷池，其前沿的β中尺度锋面附近的辐合上升运动加强，进一步促进了飑线在平原地区发展加强，并出现阵风锋。（雷蕾，孙继松，陈明轩）

3.29 强台风“菲特”（1323）极端降水研究进展

台风暴雨灾害是台风三类灾害（暴雨、大风、风暴潮）之首，而台风极端降水是暴雨灾害的直接原因，对台风极端降水的研究有利于增强对台风极端降水机理的认识和提高极端降水的预报水平。强台风“菲特”（1323）具有登陆强度历史罕见、降雨强度大、影响范围广、引发灾害重等特点，本文对“菲特”极端降水特征及其形成机理研究进行了回顾和总结。“菲特”的强降水过程主要分为两个阶段，

造成了杭州湾一带和浙闽交界处两个强降水中心。“菲特”极端降水的产生主要源于环境因子、地形和内部条件多尺度相互作用：环境因子涉及双台风作用、弱冷空气侵入、台风倒槽、垂直风切变和高空急流等，其中“丹娜丝”台风外围偏东气流源源不断的水汽输送是“菲特”极端降水形成的关键物理因子；山脉等地形增幅作用是浙江余姚等地出现历史性强降水的重要原因；水汽辐合和凝结与霰的融化和对流区雨滴的迁移是暴雨增幅重要的内部因素。（秦思，姚美，任福民）

3.30 山东半岛海风锋在一次飑线系统演变过程中的作用

2016年6月30日生成于华北南部的一次长生命期的强飑线过程，造成了山东地区大范围风雹天气。文中利用常规观测资料、区域自动气象站观测数据及雷达监测产品，分析了山东半岛复杂的海风锋特征在这次飑线系统的断裂、再组织化以及极端大风、冰雹灾害形成过程中的重要作用。结果表明：（1）初始对流是在地面冷锋辐合线上触发的弱对流，在对流系统向更不稳定区域移动时与水平对流卷相交，对流迅速发展，并组织成东西走向的直线型飑线。（2）飑线系统在平原地区继续向前移动的过程中发生断裂，这一过程与渤海湾在黄河三角洲形成的两条移动方向不同的海风锋以及飑线系统的阵风锋有关：向内陆推进的两条海风锋与阵风锋在飑线系统中段的前部相交，诱发新生单体，造成该处对流系统更快地向前传播，最终导致飑线系统断裂;与此同时，断裂后的西段风暴因低层暖湿入流被切断而逐渐减弱。（3）断裂后西段残留风暴系统出流阵风产生的新生风暴向东北方向发展，与断裂后的东段风暴的后向传播（向西南方向发展）机制相互作用，完成了飑线的再次组织化，形成了具有典型弓状特征、水平尺度更大、近似于东北—西南走向的飑线系统。（4）长生命期飑线系统造成的极端雷暴大风和最大冰雹出现在飑线再组织化初期，位于飑线系统“弓部”位置，地面极端雷暴大风是冷池密度流、后侧入流急流和水成物对应的前侧下沉气流共同作用的结果，其中与后侧入流急流几乎完全分离的、与水成物对应的前侧下沉气流在这次极端地面大风发生时可能起到了重要作用。（5）山东半岛东侧的黄海海风锋向内陆推进（东南向西北）过程中与自西北向东南移动的飑线相遇，加强了风暴前侧的抬升、水汽供给和组织化程度，为飑线的长时间维持提供了有利条件。（万夫敬，孙继松，孙敏）

3.31 中小尺度对流系统的高分辨率数值模拟近况和未来挑战

随着高速、大容量、并行计算能力的迅速增长和中尺度数值模式的不断完善，近年来不断涌现使用1 km乃至次千米网格距开展中、小尺度对流系统的数值模拟研究。这些数值模拟工作展现出目前观测手段还无法得到的动力学一致的高分辨率气象信息，大大提高了对一些中、小尺度对流系统内部结构和演变的理解。但高分辨率数值模拟的未来发展也面临着不少问题和挑战。本研究回顾了提高模式分辨率至1 km乃至次千米模拟中、小尺度对流系统的进展，并综述目前在高分辨率数值模拟中的资料同化和物理过程处理方法，同时指出中尺度模式中处理积云对流、大气边界层和辐射过程时值得注意的分辨率“灰色区”，介绍使用1 km和次千米分辨率模拟中、小尺度对流系统的几篇有代表性的工作，最后讨论了高分辨率数值模拟的未来发展和挑战。（黎慧琦，张大林）

4 台风研究
4 Typhoon research

4.1 台风快速更新短临预报系统TRANS v1.0业务运行

聚焦影响我国台风的风雨短临预报，集成“随流型而变”的集合卡尔曼滤波同化方案、空间均匀雷达资料稀疏化算法（ESTM）等台风“973”项目关键技术，气科院牵头发展的台风快速更新短临预

报系统（TRANS）于2021年1月实现业务化运行，实现沿海雷达资料同化，逐小时更新强风雨短临预报。TRANS成为台风逐小时定位、定强的重要依据，强风雨临近预报的重要参考。2020年TRANS系统相比欧洲中心ECMWF模式暴雨以上量级降水和10级大风预报准确率提高16%。该系统的持续升级优化将服务于我国台风业务预报和防灾减灾。（端义宏，冯佳宁，赵大军）

4.2 台风登陆前后强度结构变化机理研究

基于非定常的卡诺热机原理，建立了基于非定常卡诺热机和边界层动力过程的热带气旋（TC）增强的动力系统模型，能定量估计理想数值模拟和实际TC的增强率（即强度变化）。同时，为了弥补TC增强的动力系统模型动力过程缺失的不足，基于TC边界层内切向风的收支方程和热力学熵的准平衡假定，通过引入一个表征等熵面与等角动量面汇合的程度的因子，推导出另外一个时间依赖的TC增强理论模型。虽然基于不同假设，两个模型描述台风加强率的公式形式极为相似，这说明从能量学和动力学考虑，TC增强的基本动力过程具有一致性。这两个协调一致的TC增强率方程可以再现模拟TC生命史中的强度时间演变。将在后续的工作中考虑环境场的影响并试验用于实际TC的强度变率预报。为建立TC登陆后的强度衰减预报模型，系统评估了三个经典的登陆TC强度衰减模型，为后续建立更优化的适用于我国的登陆TC强度衰减模型奠定基础。（王玉清，徐晶，刘璐）

4.3 台风眼墙小尺度精细结构对模式水平分辨率的敏感性研究

利用超高分辨率大涡模拟结果分析，发现次公里级分辨对热带气旋（TC）风圈、垂直上升运动，强度的描述优于中尺度数值模拟。166 m能够开始部分分辨边界层滚涡，55 m分辨率可分辨不同尺度滚涡以及龙卷尺度的相互作用。边界层方案比如YSU方案能够在500 m分辨率上部分分辨滚涡，但是其结构以及波长尺度与大涡模拟结果相差较远。具有尺度依赖的边界层算法能够提高边界层方案对滚涡等小尺度系统的分辨能力，但是对其尺度依赖函数具有较强的敏感性。（王玉清，徐洪雄，赵大军）

4.4 基于台风事件随机模拟新技术的风险评估模型

面向台风防灾减灾需求，建立了基于统计学习方法的热带气旋（TC）风险评估模型，研究提出了一种多变量函数型数据分析方法，用于TC随机事件的全路径模拟，将贯穿TC生命史的各种属性，如中心坐标、最大风速等联合起来视作多元函数型随机变量，构建协同统一的一体化模型，据此进行TC全路径多要素的同步模拟。该方法在TC年发生概率模型、随机模拟模型优化等方面均有创新性的应用。综合评价表明，该方法可与风场模型和工程风险性模型结合使用，为政府和保险/再保险行业估计经济和保险损失提供科学依据。（徐晶）

4.5 吕宋岛地形影响下的台风结构变化及新眼墙形成机制

利用高分辨率模式研究典型台风穿过吕宋岛过程中的眼墙破坏和重组，发现台风登陆吕宋岛后由于摩擦和海面熵通量减小，原始眼墙收缩并且减弱消失，与此同时，在岛外海洋上的外雨带持续增强并且轴对称化，引起岛屿外围大眼墙生成。当台风中心过岛重新进入中国南海后，原始眼墙又重新产生。这种重新产生的眼墙结构是由涡旋内部残余对流和海洋熵通量增加所导致。（王玉清，王慧）

4.6 台风极端降水（TCER）的气候特征及季风涌对登陆台风极端降水的影响

研究发现影响我国的台风极端降水（TCER）频次（强度）有波动增多趋势。造成TCER的台风有两类路径，一是以西北行路径影响（登陆）台湾之后进而登陆我国东南沿海，二是以西北行或西行路径影响（登陆）海南岛及两广地区。研究季风涌对登陆台风极端降水影响发现整层水汽通量积分在极端暴雨发生前1～2天达到峰值；极端暴雨热带气旋（TC）整层水汽通量明显高于非极端暴雨TC，极端暴雨类TC比非极端暴雨类TC水汽通量辐合更强。极端暴雨类TC风场辐合主要是由西南低空急流

叠加TC本体环流引起。动态季风涌指数对ERLTC有较好指示意义，有潜力成为一个业务预报新指标。（李英，赵大军）

4.7 A numerical study of typhoon Megi (2010). Part II: Eyewall evolution crossing the Luzon Island

Typhoon Megi (2010) experienced drastic eyewall structure changes when it crossed the Luzon Island and entered the South China Sea (SCS), including the contraction and breakdown of the eyewall after landfall over the Luzon Island, the formation of a new large outer eyewall accompanied by reintensification of the storm after it entered the SCS, and the appearance of a short-lived small inner eyewall. These features were reproduced reasonably well in a control simulation using the advanced weather research and forecasting (ARW-WRF) model. In this study, the eyewall processes of the simulated Megi during and after landfall have been analyzed. Results show that the presence of the landmass of the Luzon Island increased surface friction and reduced surface enthalpy flux, causing the original eyewall to contract and break down and the storm to weaken. The formation of the new large eyewall results mainly from the axisymmetrization of outer spiral rainbands after the storm core moved across the Luzon Island and entered the SCS. The appearance of the small inner eyewall over the SCS was due to the increased surface enthalpy flux and the revival of convection in the central region of the storm core. In a sensitivity experiment with the mesoscale mountain replaced by flat surface over the Luzon Island, a new large outer eyewall formed over the western Luzon Island with its size about one-third smaller after the storm entered the SCS than that in the control experiment with the terrain over the Luzon Island unchanged. (Wang Hui, Wang Yuqing)

4.8 An investigation of the impact of different turbulence schemes on the tropical cyclone boundary layer at turbulent gray-zone resolution

Accurately resolving turbulence in the tropical-cyclone boundary layer (TCBL) is crucial for realistic simulations of tropical cyclones (TCs), but how well the fine-scale structure of the simulated TCBL can be reproduced at gray-zone resolutions by state-of-the-art planetary boundary layer (PBL) parameterization schemes, and why the simulated fine-scale structure is so sensitive to the PBL scheme, are yet to be evaluated and understood. To address these issues, a series of numerical experiments under idealized conditions were conducted using the advanced research weather research and forecasting (WRF-ARW) model at 500 and 166 m grid spacing. An 18 h WRF-ARW large-eddy simulation (LES) with a 55 m grid spacing based on the nonlinear backscatter and anisotropy subfilter-scale (NBA-SFS) stress scheme was used as reference (RLES). Results from experiments using five different PBL schemes, that is, two conventional schemes-the Yonsei University (YSU) and the original MYNN (termed MYNN1)-two scale-aware schemes-the Shin-Hong (S-H) and the revised MYNN (termed MYNN2)-and the coarse-resolution LES (CLES), were subsequently compared with the RLES. The YSU and S-H not only produced better simulations of TC intensity and structure than the other three PBL schemes, but also produced a fine-scale turbulent structure reasonably well compared with the RLES. Discrepancies in the simulated fine-scale structure among the PBL schemes result primarily from the different strength of vertical mixing, which could be reduced by the scale-aware option. Results from a series of sensitivity experiments with a 166-m grid spacing demonstrate that the scale-aware S-H can significantly improve the finer resolution simulations than the conventional YSU at relatively finer grid spacing at gray zone. (Xu Hongxiong, Wang Hui, Duan Yihong)

4.9 Associations between strong earthquakes and local rainfall in China

Strong earthquakes are a major cause of natural disasters and may also be related to heavy rainfall events. Both phenomena have received considerable attention in seismology and meteorology, two relatively independent disciplines, but we do not yet know whether there is a connection between them. We investigated

the characteristics of daily rainfall over seismic areas in China. Our statistical analyses showed that there was a strong correlation between strong earthquakes (Ms $\geqslant$ 6.0) and rainfall over the seismic area, with 74.9% of earthquakes in China accompanied by seismic epicenter rainfall and 86.6% by seismic area rainfall. The statistics also showed that the daily precipitation over the seismic area, including the epicenter, was mainly light rain, with only a few instances of torrential or storm rain, with 80% of the rainfall events lasting two or more days. The maximum cumulative precipitation corresponded well with the strong earthquakes occurring over steep terrain, such as the Taiwan central mountains and the eastern Tibetan Plateau. The earthquake area rainfall had a higher frequency than the 30-year climatological average and was dominated by earthquake events in the wet season. The WRF-ARW numerical simulation of seismic local rainfall during the devastating Ms 8.0 Wenchuan earthquake in May 2008 showed that the geothermal heat from the earthquake strengthened the local convergence of moisture and vertical motion near the epicenter and the upward transport of the sensible heat flux, which favored seismic rainfall. The results of this study show that rainfall in the seismic area is closely related to strong earthquakes and can be triggered and enhanced by geothermal heat. (Zhao Dajun, Chen Lianshou, Yu Yubin)

4.10 Contribution of the intensity of intraseasonal oscillation to the interannual variation of tropical cyclogenesis over the western North Pacific

The present study compares the contributions of seasonal, intraseasonal, and synoptic variations of environmental factors, i.e., mid-level moisture, vertical instability, and lower-level relative vorticity, to the interannual variation of tropical cyclone (TC) genesis over the western North Pacific (WNP) during July-August-September-October (JASO) of 1979−2015. It is found that the TC genesis frequency has a significant positive correlation with the intensity of intraseasonal oscillation, but a weak correlation with the intensity of synoptic variation of environmental factors during JASO in the WNP. In addition, the intraseasonal components of convection and lower-level vorticity at the location of TC genesis have a larger contribution than the interannual and synoptic components to the differences between more and less TC years over the WNP. The present results indicate that the intensity of intraseasonal oscillation of environmental factors has an important effect on the interannual variation of the TC genesis frequency over the WNP. This study enhances our understanding of the impacts of intraseasonal oscillation on the interannual variation of the WNP TC activity and indicates that the intensity of intraseasonal oscillation has the potential to be used in the seasonal prediction of the WNP TC genesis. (Cao Xi, Wu Renguang, Xu Jing)

4.11 Contribution of vertical advection to supergradient wind in tropical cyclone boundary layer: A numerical study

The existence of supergradient wind in the interior of the boundary layer is a distinct feature of a tropical cyclone (TC). Although the vertical advection is shown to enhance supergradient wind in the TC boundary layer (TCBL), how and to what extent the strength and structure of supergradient wind are modulated by vertical advection are not well understood. In this study, both a TCBL model and an axisymmetric full-physics model are used to quantify the contribution of the vertical advection process to the strength and vertical structure of supergradient wind in TCBL. Results from the TCBL model show that the removal of vertical advection of radial wind reduces both the strength and height of supergradient wind by slightly more than 50%. The removal of vertical advection of agradient wind reduces the height of the supergradient wind core by similar to 30% but increases the strength of supergradient wind by similar to 10%. Results from the full-physics model show that the removal of vertical advection of radial wind or agradient wind reduces both the strength and height of supergradient wind but the removal of that of radial wind produces a more substantial reduction (52%) than the removal of that of agradient wind (35%). However, both the intensification rate

and final intensity of the simulated TCs in terms of maximum 10-m wind speed show little differences in experiments with and without the vertical advection of radial or agradient wind, suggesting that supergradient wind contributes little to either the intensification rate or the steady-state intensity of the simulated TC. (Fei Rong, Wang Yuqing, Li Yuanlong)

4.12 Effect of the vertical diffusion of moisture in the planetary boundary layer on an idealized tropical cyclone

Previous numerical studies have focused on the combined effect of momentum and scalar eddy diffusivity on the intensity and structure of tropical cyclones. The separate impact of eddy diffusivity estimated by planetary boundary layer (PBL) parameterization on the tropical cyclones has not yet been systematically examined. We have examined the impacts of eddy diffusion of moisture on idealized tropical cyclones using the Advanced Research Weather Research and Forecasting model with the Yonsei University PBL scheme. Our results show nonlinear effects of moisture eddy diffusivity on the simulation of idealized tropical cyclones. Increasing the eddy diffusion of moisture increases the moisture content of the PBL, with three different effects on tropical cyclones: (1) a decrease in the depth of the PBL; (2) an increase in convection in the inner rain band and eyewall; and (3) drying of the lowest region of the PBL and then increasing the surface latent heat flux. These three processes have different effects on the intensity and structure of the tropical cyclone through various physical mechanisms. The increased surface latent heat flux is mainly responsible for the decrease in pressure. Results show that moisture eddy diffusivity has clear effects on the pressure in tropical cyclones, but contributes little to the intensity of wind. This largely influences the wind-pressure relationship, which is crucial in tropical cyclones simulation. These results improve our understanding of moisture eddy diffusivity in the PBL and its influence on tropical cyclones, and provide guidance for interpreting the variation of moisture in the PBL for tropical cyclone simulations. (Xu Hongxiong, Zhao Dajun)

4.13 Impact of the monsoonal surge on extreme rainfall of landfalling tropical cyclones

A comparative analysis and quantitative diagnosis has been conducted of extreme rainfall associated with landfalling tropical cyclones (ERLTC) and non-extreme rainfall (NERLTC) using the dynamic composite analysis method. Reanalysis data and the tropical cyclone precipitation dataset derived from the objective synoptic analysis technique were used. Results show that the vertically integrated water vapor transport (Q_{vt}) during the ERLTC is significantly higher than that during the NERLTC. The Q_{vt} reaches a peak 1−2 days before the occurrence of the ERLTC and then decreases rapidly. There is a stronger convergence for both the Q_{vt} and the horizontal wind field during the ERLTC. The Q_{vt} convergence and the wind field convergence are mainly confined to the lower troposphere. The water vapor budget on the four boundaries of the tropical cyclone indicates that water vapor is input through all four boundaries before the occurrence of the ERLTC, whereas water vapor is output continuously from the northern boundary before the occurrence of the NERLTC. The water vapor inflow on both the western and southern boundaries of the ERLTC exceeds that during the NERLTC, mainly as a result of the different intensities of the southwest monsoonal surge in the surrounding environmental field. Within the background of the East Asian summer monsoon, the low-level jet accompanying the southwest monsoonal surge can increase the inflow of water vapor at both the western and southern boundaries during the ERLTC and therefore could enhance the convergence of the horizontal wind field and the water vapor flux, thereby resulting in the ERLTC. On the other hand, the southwest monsoonal surge decreases the zonal mean steering flow, which leads to a slower translation speed for the tropical cyclone associated with the ERLTC. Furthermore, a dynamic monsoon surge index (DMSI) defined here can be simply linked with the ERLTC and could be used as a new predictor for future operational forecasting of ERLTC. (Zhao Dajun, Yu Yubin, Chen Lianshou)

4.14 Increasing lifetime maximum intensity of rapidly intensifying tropical cyclones over the western North Pacific

The long-term trend in the annual mean lifetime maximum intensity (LMI) of rapidly intensifying tropical cyclones (RI-TCs) over the western North Pacific (WNP) is investigated in this study. During 1970−2019, a notable upward trend is observed in the average RI-TC LMI, which is primarily linked to a significant increase in the mean intensification rate prior to LMI. This intensification rate increase is caused by an increase in the mean magnitude of RI cases. By contrast there is no significant change in the RI ratio, which is calculated as the proportion of 24 h RI records to all 24 h records before a RI-TC reaches its LMI. Furthermore, there is a significantly greater RI magnitude at the west of 155°E, where the vast majority of RI cases occur on average. Over this region, there are significant increases in sea surface temperatures, TC heat potential, 700−500 hPa relative humidity and 200 hPa divergence during 1970−2019. Only a small region of significantly reduced 850−200 hPa vertical wind shear is observed to the northeast of the Philippines during 1970−2019. These results imply that both thermodynamic and dynamic variables play an important role in modulating RI magnitude over the WNP. (Song Jinjie, Klotzbach Philip J., Duan Yihong)

4.15 Modulation of tropical cyclone formation over the western North Pacific by the ENSO combination mode

Previous studies have shown that a combination mode (C-mode) is formed by nonlinear interactions between the western Pacific warm pool annual cycle and El Niño-southern oscillation variability. We find a significant inverse relationship between the western North Pacific (WNP) tropical cyclone (TC) frequency and the C-mode index on monthly timescales from 1970 to 2019. During positive C-mode phases, TC formation is significantly suppressed over a region spanning 5°−20°N and 140°−175°E, primarily due to reduced 850 hPa relative vorticity and increased 850-200-hPa vertical wind shear. By contrast, there is significantly enhanced TC genesis over the region spanning 25°−30°N and 125°−135°E, mainly due to increased 850 hPa relative vorticity and 600 hPa relative humidity. All of these changes in atmospheric conditions are further linked to an anomalous large-scale anticyclone over the WNP generated by the C-mode. Our results suggest that C-mode variability can serve as a potential predictor for forecasting monthly WNP TC activity. (Song Jinjie, Klotzbach Philip J., Duan Yihong)

4.16 Monsoon surges enhance extreme rainfall by maintaining the circulation of landfalling tropical cyclones and slowing down their movement

Extreme rainfall induced by landfalling tropical cyclones (ERLTCs) in China can cause flash floods and other disastrous impacts, so investigating their genesis and mechanism of enhancement has been attracting considerable attention. This study demonstrates that the extreme rainfall of landfalling tropical cyclones (LTCs) possesses two key properties, namely, maintenance of the LTC circulation and a lagging (slowing down or looping) of its movement, and the monsoon surge can provide a positive contribution to these properties. Specifically, diagnostics show that the low-level cyclonic vorticity and upper-level divergence of ERLTCs are significantly stronger than those of NERLTCs (non-extreme-rainfall-producing LTCs). The continuous intensification of the cyclonic rotation in the lower troposphere before the occurrence of extreme rainfall is a significant feature that distinguishes ERLTCs from NERLTCs. Vorticity budget analysis further shows that the relative vorticity advection term contributes the most to the local increase and maintenance of vorticity in the middle and lower troposphere of ERLTCs under the influence of the southwest monsoonal surge, thus demonstrating that the monsoonal surge favors the maintenance of LTC circulation. On the other hand, the activity of the southwest monsoonal surge is mainly manifested in the zonal wind anomaly, and the

corresponding strong westerly transport can significantly reduce the zonal component of the steering flow. As a result, the total steering flow can be weakened, which decreases the northwestward translation speed of ERLTCs, and thus the monsoonal surge favors a lagging (slowing down or looping) of LTC movement. These results reveal the mechanism of influence through which the monsoonal surge affects ERLTCs via its direct impacts on the maintenance of their circulation and lagging of their movement-two distinct evolutionary characteristics. (Zhao Dajun, Chen Lianshou, Yu Yubin)

4.17 Recent weakening of the interannual relationship between ENSO Modoki and boreal summer tropical cyclone frequency over the western North Pacific

This study shows that the impact of El Niño-southern oscillation (ENSO) Modoki on boreal summer tropical cyclone (TC) formation over the western North Pacific (WNP) has experienced decadal changes during the past few decades. The correlation between the ENSO Modoki index and TC frequency over the WNP was weak during 1975−1989, becomed strong and significant during 1990−2004, and becomed weak again during 2005−2019. Over the eastern part of the WNP, ENSO Modoki enhanced TC formation during 1990−2004 but did not significantly impact on the TC formation during 1975−1989 and 2005−2019. The difference in correlation strength primarily results from changes in large-scale features related to ENSO Modoki among the three subperiods (1975−1989, 1990−2004, and 2005−2019). El Niño Modoki during 1990−2004 was characterized by a tripole sea surface temperature (SST) pattern with maximum SST anomalies in the equatorial central Pacific, while during 1975−1989 and 2005−2019, the maximum SST anomalies were located over the subtropical northeastern Pacific. The two primary environmental variables likely leading to these observed relationships between ENSO Modoki and TCs were mid-level moisture (RH600) and low-level vorticity (VOR850). During 1990−2004, TC formation was enhanced both at the south of 20°N and north of 20°N. The increase in TC activity during El Niño Modoki at the south of 20°N was likely tied to greater RH600 and north of 20°N to larger cyclonic VOR850. In contrast, ENSO Modoki's impacts on both VOR850 and RH600 were weak during 1975−1989 and 2005−2019. (Song Jinjie, Klotzbach Philip J., Duan Yihong)

4.18 Sensitivity of fine-scale structure in tropical cyclone boundary layer to model horizontal resolution at sub-kilometer grid spacing

In view of the increasing interest in the explicit simulation of fine-scale features in the tropical cyclone (TC) boundary layer (TCBL), the effects of horizontal grid spacing on a 7−10 h simulation of an idealized TC are examined using the weather research and forecasting (ARW-WRF) mesoscale model with one-way moving nests and the nonlinear backscatter with anisotropy (NBA) sub-grid-scale (SGS) scheme. In general, reducing the horizontal grid spacing from 2 km to 500 m tends to produce a stronger TC with lower minimum sea level pressure (MSLP), stronger surface winds, and smaller TC inner core size. However, large eddies cannot be resolved at these grid spacings. In contrast, reducing the horizontal grid spacing from 500 to 166 m and further to 55 m leads to a decrease in TC intensity and an increase in the inner-core TC size. Moreover, although the 166-m grid spacing starts to resolve large eddies in terms of TCBL horizontal rolls and tornado-scale vortex, the use of the finest grid spacing of 55 m tends to produce shorter wavelengths in the turbulent motion and stronger multi-scale turbulence interaction. It is concluded that a grid spacing of sub-100-meters is desirable to produce more detailed and fine-scale structure of TCBL horizontal rolls and tornado-scale vortices, while the relatively coarse sub-kilometer grid spacing (e.g., 500 m) is more cost-effective and feasible for research that is not interested in the turbulence processes and for real-time operational TC forecasting in the near future. (Xu Hongxiong, Wang Yuqing)

4.19 Statistical linkage between coastal El Niño-southern oscillation and tropical cyclone formation over the western North Pacific

This study investigates the modulation of tropical cyclone (TC) formation over the western North Pacific (WNP) by coastal El Niño-southern oscillation (ENSO). There is a significant inverse relationship between WNP TC frequency during July−October from 1961 to 2019 and simultaneous Nino 1+2 sea surface temperature anomalies. TC formation is significantly suppressed and enhanced over the subtropical and equatorial WNP during coastal El Niño, respectively, while TC formation exhibits opposite-signed anomalies during La Niña. This north-south dipolar pattern during coastal ENSO is distinct from the pattern observed in basin-wide ENSO events. Additional analyses show that coastal ENSO influences WNP TC formation through modulation of the large-scale environment. Changes in mid-level moisture and low-level vorticity appear to be the primary large-scale influences on TC formation during both coastal ENSO phases. These changes can be further linked to the anomalous large-scale circulation over the WNP during coastal ENSO. (Song Jinjie, Klotzbach Philip J., Duan Yihong)

4.20 Stochastic simulation of tropical cyclones for risk assessment at one go: A multivariate functional PCA approach

A multivariate functional principal component analysis approach to the full-track simulation of tropical cyclones (TCs) is developed for risk assessment. Elemental variables of TC along the track necessary for risk assessment, such as center coordinates, maximum wind speed, minimum central pressure and ordinal dates, can be simulated simultaneously at one go, using solely the best-track data with no data supplemented from any other sources. The simulation model is optimally determined by means of the ladle estimator. A TC occurrence model using the Conway-Maxwell-Poisson distribution is proposed as well, by which different dispersion features of annual occurrence can be represented in a unified manner. With the occurrence model, TCs can be simulated on an annual basis. The modeling and simulation process is programmed and fully automated such that little manual intervention is required, which greatly improves the modeling efficiency and reduces the turnaround time, especially when newly available TC data are incorporated periodically into the model. Comprehensive evaluation shows that this approach is capable of generating high-performance synthetic TCs in terms of distributional and extreme value features, which can be used in conjunction with wind field and engineering vulnerability models to estimate economic and insurance losses for governments and insurance/reinsurance industry. Tropical cyclones (TCs) are one of the biggest threats to life and property around the world. However, the infrequent nature of catastrophic TCs invalidates the standard actuarial loss estimation approaches. TC risk assessment requires estimation of catastrophic TCs having a very low occurrence probability, or equivalently a very long return period spanning up to thousands of years. Since reliable TC data are available only for recently decades, stochastic modeling and simulation turned out to be an effective approach to achieve more stable TC risk estimates for regions where little or no historical TC records exist. Here we present a novel model for the full-track simulation of TCs for risk assessment, via a machine learning approach called multivariate functional principal component analysis. Using this model, high-performance synthetic TCs can be generated in a fully automated manner such that little manual intervention is required, which greatly improves the modeling efficiency and reduces the turnaround time, especially when newly available TC data are incorporated periodically into the model. These synthetic TCs can be used in conjunction with wind field and engineering vulnerability models to estimate economic and insurance losses for governments and insurance/reinsurance industry. (Yang Chi, Xu Jing, Yin Jianming)

4.21 The cold avoidance of typhoons in their north turning over the South China Sea

Based on the typhoon best tracks of the China Meteorological Administration (CMA), ERA5 reanalysis data of ECMWF at 0.25° horizontal resolution, and NOAA optimal interpolated sea surface temperature (OISST V2) data, the dynamical compositing analysis is used to study the north turning at nearly 90° of 4 westward typhoons over the South China Sea (SCS). The composite analysis results show that: (1) As the typhoon goes westward into the SCS, the upper-level westerly trough moves eastward to the vicinity of 110°E in the mainland of China, and the western North Pacific subtropical high (SH) retreats eastward at the same time, which weakens the steering flow of typhoon and slowes down its movement. (2) The cold air guided by the westerly trough invades southwardly into the western part of SCS from the mainland leading to a descending and divergent airflow in the lower-to-middle atmospheric layers and enhancing the eastward pressure gradient force (PGF) in the west quadrant of the typhoon, which blocks and repesls the typhoon from moving any further westward. (3) Due to the cold air intrusion, the vertical atmospheric stratification in the west quadrant of the typhoon becomes static and stable, which may suppress the convection, impeding a typhoon's westward motion. (4) With the cold air involving to the south of the typhoon, the direction of the PGF on the typhoon switches from eastward to northward, and the SH falling southward enhances the southwesterly airflow on the south of the typhoon at the same time. The remarkable increase of the northward steering airflows of the typhoon results in an abrupt northward turn. (5) In addition, the sea surface temperature (SST) and the ocean heat content (OHC) on the western part of the SCS are also reduced, attributed to the cold air cooling, and the typhoon is likely to avoid the cold ocean and approachs a relatively warmer region. This study suggests that cold avoidance during the westward movement of typhoons is worthy of consideration in the operational forecast of typhoon tracks. (Lai Shaojun, Li Ying, He Fen, Wang Yufei)

4.22 The intensity dependence of tropical cyclone intensification rate in a simplified energetically based dynamical system model

In this study, a simple energetically based dynamical system model of tropical cyclone (TC) intensification is modified to account for the observed dependence of the intensification rate (IR) on the storm intensity. According to the modified dynamical system model, the TC IR is controlled by the intensification potential (IP) and the weakening rate due to surface friction beneath the eyewall. The IP is determined primarily by the rate of change in the potential energy available for a TC to develop, which is a function of the thermodynamic conditions of the atmosphere and the underlying ocean, and the dynamical efficiency of the TC system. The latter depends strongly on the degree of convective organization within the eyewall and the inner-core inertial stability of the storm. At a relatively low TC intensity, the IP of the intensifying storm is larger than the frictional weakening rate, leading to an increase in the TC IR with TC intensity in this stage. As the storm reaches an intermediate intensity of 30−40 m s^{-1}, the difference between IP and frictional weakening rate reaches its maximum, concurrent with the maximum IR. Later on, the IR decreases as the TC intensifies further because the frictional dissipation increases with TC intensity at a faster rate than the IP. Finally, the storm approaches its maximum potential intensity (MPI) and the IR becomes zero. The modified dynamical system model is validated with results from idealized simulations with an axisymmetric nonhydrostatic, cloud-resolving model. (Wang Yuqing, Li Yuanlong, Xu Jing)

4.23 The performance of three exponential decay models in estimating tropical cyclone intensity change after landfall over China

In this study, the performance of three exponential decay models in estimating intensity change of tropical cyclones (TCs) after landfall over China is evaluated based on the besttrack TC data during 1980–2018.

Results indicate that the three models evaluated can reproduce the weakening trend of TCs after landfall, but two of them (M1 and M2) tend to overestimate TC intensity and one (M3) tends to overestimate TC intensity in the first 12 h and underestimate TC intensity afterwards. M2 has the best performance with the smallest errors among the three models within 24 h after landfall. M3 has better performance than M1 in the first 20 h after landfall, but its errors increase largely afterwards. M1 and M2 show systematic positive biases in the southeastern China likely due to the fact that they have not explicitly included any topographic effect. M3 has better performance in the southeastern China, where it was originally attempted, but shows negative biases in the eastern China. The relative contributions of different factors, including landfall intensity, translational speed, 850-hPa moist static energy, and topography, to model errors are examined based on classification analyses. Results indicate that the landfall intensity contributes about 18%, translational speed, moist static energy and topography contribute equally about 15% to the model errors. It is strongly suggested that the TC characteristics and the time-dependent decay constant determined by environmental conditions, topography and land cover properties, should be considered in a good exponential decay model of TC weakening after landfall. (Liu Lu,Wang Yuqing,Wang Hui)

4.24 The role of boundary layer dynamics in tropical cyclone intensification. Part I: Sensitivity to surface drag coefficient

This study examines the role of boundary layer dynamics in tropical cyclone (TC) intensification using numerical simulations. The hypothesis is that although surface friction has a negative effect on TC intensification due to frictional dissipation (direct effect), it contributes positively to TC intensification by determining the amplitude and radial location of eyewall updrafts/convection (indirect effect). Results from a boundary layer model indicate that TCs with a larger surface drag coefficient (CD) can induce stronger and more inwardly penetrated boundary layer inflow and upward motion at the top of the boundary layer. This can lead to stronger and more inwardly located condensational heating inside the radius of maximum wind with higher inertial stability and is favorable for more rapid intensification. Results from full-physics model simulations using TC Model version 4 (TCM4) demonstrate that the intensification rate of a TC during the primary intensification stage is insensitive to CD if CD is changed over a reasonable range. This is because the increased/reduced positive contribution by the indirect effect of surface friction to TC intensification due to increased/reduced CD is roughly offset by the increased/reduced negative (direct) dissipation effect due to surface friction. However, greater surface friction can significantly shorten the initial spinup period through stronger frictional moisture convergence and Ekman pumping and thus expedite moistening of the inner-core column of the TC vortex but is likely to lead to a weaker storm in the mature stage. (Li Tsung-Han, Wang Yuqing)

4.25 The role of boundary layer dynamics in tropical cyclone intensification. Part II: Sensitivity to initial vortex structure

In Part I of this series of studies, we demonstrated that the intensification rate of a numerically simulated tropical cyclone (TC) during the primary intensification stage is insensitive to the surface drag coefficient. This leads to the question of what is the role of the boundary layer in determining the TC intensification rate given sea surface temperature and favorable environmental conditions. This part attempts to answer this question based on a boundary layer model and a full-physics model as used in Part I. Results from a boundary layer model suggest that TCs with a smaller radius of maximum wind (RMW) or of lower strength (i.e., more rapid radial decay of tangential wind outside the RMW) can induce stronger boundary layer inflow and stronger upward motion at the top of the boundary layer. This leads to stronger condensational heating inside the RMW

with higher inertial stability and is thus favorable for a higher intensification rate. Results from full-physics model simulations indicate that the TC vortex initially with a smaller RMW or of lower strength has a shorter initial spinup stage due to faster moistening of the inner core and intensifies more rapidly during the primary intensification stage. This is because the positive indirect effect of boundary layer dynamics depends strongly on vortex structure, but the dissipation effect of surface friction depends little on the vortex structure. As a result, the intensification rate of the simulated TC is very sensitive to the initial TC structure. (Li Tsung-Han, Wang Yuqing)

4.26 The simulation of five tropical cyclones by sample optimization of ensemble forecasting based on the observed track and intensity

The quality of ensemble forecasting is seriously affected by sample quality. In this study, the distributions of ensemble members based on the observed track and intensity of tropical cyclones (TCs) were optimized and their influence on the simulation results was analyzed. Simulated and observed tracks and intensities of TCs were compared and these two indicators were combined and weighted to score the sample. Samples with higher scores were retained and samples with lower scores were eliminated to improve the overall quality of the ensemble forecast. For each sample, the track score and intensity score were added as the final score of the sample with weight proportions of 10 to 0, 9 to 1, 8 to 2, 7 to 3, 6 to 4, 5 to 5. These were named as tr, 91, 82, 73, 64, and 55, respectively. The WRF model was used to simulate five tropical cyclones in the northwestern Pacific to test the ability of this scheme to improve the forecast track and intensity of these cyclones. The results show that the sample optimization effectively reduced the track and intensity error, 55 usually had better performance on the short-term intensity prediction, and tr had better performance in short-term track prediction. From the overall performance of the track and intensity simulation, 91 was the best and most stable among all sample optimization schemes. These results may provide some guidance for optimizing operational ensemble forecasting of TCs. (Li Jihang, Zhang Zhiyan, Liu Lu)

4.27 川藏高原一次混合型强对流天气的观测特征

利用中国气象局地面自动气象站、探空、天气雷达等观测资料和ERA-Interim再分析资料，分析2016年9月8日川藏高原一次强对流天气过程。结果表明：该过程多站出现8级雷暴大风、10 mm以上小时强降水且伴有最大直径为18 mm的冰雹，是川藏高原一次混合型强对流过程。对流系统发生在500 hPa弱冷平流和低层切变线影响下，中低层深厚湿层、环境中等强度对流有效位能和垂直风切变为超级单体的形成和维持提供有利条件。初始北侧多单体和南侧弱对流在地面辐合线上生成，向东南移入适宜环境后，北侧多单体发展成线状对流系统，与南侧单体合并且促使其迅速发展成超级单体。成熟超级单体低层具有清晰的前侧入流缺口、钩状回波和中气旋特征。强回波区随高度前倾，呈显著的上冲云顶突起、回波悬垂和有界弱回波区。风暴内中层径向辐合、上升气流减弱和反射率因子核心快速下降预示下击暴流的产生。中层干空气的夹卷和水凝物快速下落的拖曳作用加强下沉气流，结合峡谷地形的狭管效应，引起地面大风。（王黉，李英，文永仁）

4.28 台风“山竹”（2018）远距离暴雨的成因分析

热带气旋远距离暴雨（TRP）往往成为高影响天气，是业务预报难点。本文用地面、探空观测资料、雷达遥感资料以及NCEP一日四次0.5°×0.5°再分析资料，对2018年第22号台风“山竹”登陆广东期间在长江三角洲（简称长三角）地区引起的远距离暴雨过程进行分析。结果表明：（1）这是一次发生在副热带高压（简称副高）控制范围内的热带气旋远距离暴雨，低层受台风倒槽影响。（2）这次过程第一阶段暴雨主要是在强的对流不稳定条件下，由对流层低层“山竹”倒槽中的辐合线触发对流产生，同时对流层高层“山竹”的极向流出汇入加大了中纬度西风风速，在长三角地区上空产生辐散，

有利于上升运动的维持。第二阶段，对流不稳定条件有所减弱，但前一阶段强回波产生的低层偏北外出气流与东南风形成辐合线，辐合线上还有中γ尺度的涡旋产生，又促进了对流发展。850 hPa台风倒槽北端形成一个低涡，500 hPa副高边缘发展出一个短波槽，暴雨的动力条件更为有利。（3）长三角的3个强降水中心分别在长江口、杭州湾北岸的嘉兴沿海及宁波沿海，都是在水陆边界附近。（4）远距离暴雨区的涡度收支诊断发现：暴雨的初始扰动主要由近地层水平辐合辐散项提供，850 hPa的水平辐合辐散项和扭曲项共同作用形成和加强低涡，并通过垂直运动上传使中层700 ～ 500 hPa附近涡度增长，进而发展出500 hPa短波槽。850 hPa涡度来自于台风倒槽和副高边缘的偏南急流。（5）在这次远距离暴雨过程中，台风“山竹”与海上西太平洋副高之间形成偏南低空急流，向长三角输送水汽，这与典型TRP事件相似。不同之处在于：典型TRP中暴雨的初始扰动一般由西风槽提供，而这次过程主要由低空台风倒槽和偏南急流提供，涡度上传形成高空短波槽，是不同于典型TRP事件的一个物理过程。（陈淑琴，李英，范悦敏）

4.29 台风“利奇马”（1909）双眼墙特征及长时间维持机制

利用CIMSS微波卫星产品和多普勒天气雷达资料，分析超强台风“利奇马”（1909）的长时间双眼墙特征，并采用集合卡尔曼滤波方法同化雷达径向风资料，诊断台风“利奇马”双眼墙的三维结构演变特征。结果表明：在双眼墙演变过程初期，受强垂直风切变和中高层干空气入侵的影响，外眼墙对流减弱，呈非对称特征。Sawyer-Eliassen方程诊断结果显示：台风“利奇马”（1909）内、外眼墙次级环流之间的相互作用不明显，不同于发生眼墙替换过程的台风，其外眼墙处非绝热加热引起的下沉运动发生在内眼的眼心，内眼墙的上升运动并未受到外眼墙次级环流抑制。另外，在强垂直风切变条件下，非对称的外眼墙不能持续增强收缩并取代内眼墙，因此双眼墙结构得以长时间维持。可见，台风“利奇马”（1909）外眼墙的非对称结构和特殊的次级环流分布是其双眼墙能够长期维持的重要原因。（刘涛，端义宏，冯佳宁）

5 雷电研究
5 Lighting research

5.1 雷电野外科学试验

雷电团队克服新冠疫情影响，于5—8月在广州从化开展了第16年度的人工触发闪电试验。期间建设了新型人工引雷平台，成功触发闪电8次，改进了弱电流测试方案；围绕引雷试验场建设了低功耗太阳能供电的闪电中低频电场探测阵列；完成了针对广州塔雷电流直接测量的方案设计和工程建设；升级实时低频电场探测阵列，引入混合基线GPU三维定位算法实现快速全闪定位；在海南和西藏那曲新建了新一代三维全闪探测网络，关注海陆雷暴和高原雷暴的闪电活动探测。通过上述技术发展和试验开展，显著提升了雷电团队对闪电过程的综合数据获取能力和数据质量。（吕伟涛，郑栋，张阳，樊艳峰，马颖）

5.2 雷电探测技术研发

在VHF闪电探测和定位方面，提出了利用DBM_EEMD方法对宽带干涉仪VHF信号进行带通截断等质量控制，通过广义互相关、信号阈值和相似度约束等方法实现不同天线信号的精准匹配的方法，对闪电通道解析能力获得显著提升。在低频闪电探测和定位方面，引入深度学习技术，提出了基于编码特征的脉冲匹配新方法，大大提高了匹配效率和定位速度。评估了粤港澳闪电定位系统和广东电网地闪定位系统在粤港澳大湾区范围内的地闪探测性能。提出了一种考虑辐射源密度和通道重复放电的

辐射源连接方法，能够获得体现时间和空间信息的闪电放电尺度参量，更好地描述闪电放电过程和受影响区域。（张阳，范祥鹏，刘恒毅）

5.3 雷电物理研究

发现广州塔触发式上行闪电的正极性连续先导产生之前，普遍存在先导企图发展过程，并指出触发式上行正先导在初始速度上比人工触发闪电高一个量级；发现有14%的高建筑物负地闪回击事件其继后回击光脉冲峰值大于首次回击。提出了一种闪击距离估算方法，发现雷击建筑物的高度和顶部几何形状是影响闪击距离的关键因素；在正地闪回击后的水平通道上发现了类“针”状结构，指出其是正地闪回击后期和连续电流期间大量负电荷被输送至水平通道上的结果。提出了以集合经验模态分解方法为基础的高能云内脉冲（EIP）放电事件电场波形分解方法，指出EIP的发生机制是逃逸电子雪崩产生的大电流过程；发现EIP与地源伽马射线闪（TGF）之间的密切关系，将任一EIP亦是TGF的可能性由原来的超过37%提到了74% ～ 100%。（樊艳峰，武斌，齐奇，吕凡超）

5.4 雷暴电学研究

给出了高原、中国中东部和喜马拉雅山南麓雷暴结构、电荷区大小以及起电效率概念图，提出闪电频次随着雷暴对流增强持续增大而闪电尺度则先增大再减小的观点，指出闪电频次和尺度的反向关系出现在当对流强度超过一定阈值时，发现冬季雷暴正地闪主要发生在正常极性和反极性电荷结构中，不支持先前的倾斜偶极子假说和雷暴消亡阶段的单层正电荷区假说。利用闪电数据以及卫星云顶亮温和云分类数据建立了亚太区域雷暴特征数据集，揭示我国陆地和毗邻海域以及西太平洋地区的雷暴活动和雷暴云结构特征。发现全球闪电探测网（WWLLN）和星基光学成像仪（LIS）探测的高原闪电活动时空分布存在差异，指出高原雷暴云电属性存在区域差异和季节性变化。发现一类只发生在高原山地雷暴环境中的山顶与其上部雷暴主负电荷区之间的一种特殊放电过程，它可以产生上百kA的瞬态电流；揭示中尺度对流系统层云区闪电分布位置、尺度以及相互之间的关系。（郑栋，张文娟，王飞）

5.5 雷电预警预报技术研发与应用

发现湍流耗散率是指示闪电初生以及区分雷暴和非雷暴的有效参量；针对闪电活动短时预报，发展了基于自动气象站、历史闪电观测和WRF模式模拟的多源时空数据深度神经网络闪电预报框架（LightNet+）。针对闪电活动临近预警，利用闪电监测数据以及雷达数据，构建了一个基于主从时空预测网络模型（MSTNet）的雷电临近预警方法；对比Gatlin算法和σ算法，指出2σ闪电跃增算法更适于基于闪电资料预警北京冰雹天气；实现基于CMA-meso的中国南海区域闪电活动预报，30 km邻域半径下，6 ～ 24 h预报时效下的CSI评分超过0.2。初步完成基于人工智能的雷电短时预报系统的研制，找到适合不同评估标准的预报概率阈值，并于2021年5月起在广东省气象安全技术支持中心开展运行试验，取得较好效果。（姚雯，孟青，徐良韬）

5.6 A comprehensive study on the improved radio-frequency magnetic field measurement for the initial upward leader of a negative rocket-triggered lightning flash

The spectrum analysis of the lightning current in the experiment campaign of 2019 reveals that the lightning current waveform contains rich medium-frequency (MF) radiation signals in the initial stage. However, there is a lack of resolution for MF signals by using conventional magnetic sensors. The bandwidth of radio-frequency magnetic field measurement is improved by extending to 20 kHz to 1.2 MHz in the Guangdong Comprehensive Observation Experiment on Lightning Discharge (GCOELD). During the previously noticed quiet period that can only maintain the upward propagation with relatively small-scale breakdown, magnetic pulses of quiet period (MPQPs) are discerned more clearly than the previous experiment

in GCOELD. Aided by the improvement of a magnetic sensor, this paper captures richer magnetic field signals radiated from the weak discharge of the precursory phase than previous experiments in GCOELD. The analysis shows that both aborted UPLs and UPLs are caused by weak discharge pulses called initial precursor pulses (IPPs), which are very similar to the amplitude of the streamer discharge obtained in the laboratory. In summary, the signals detected by an improved magnetic sensor will provide an important reference for exploring the pulse characteristics of the whole discharge process and formation mechanism of the UPL in the initial stage of triggered lightning. (Shi Tao, Lu Gaopeng, Fan Yanfeng)

5.7 A new method for connecting the radiation sources of lightning discharge extension channels

The connections of lightning radiation sources along channels are greatly affected by the radiation source density, and the channel length is geometrically scaled when neglecting repeated discharges in the same channel. Based on lightning mapping array (LMA) three-dimensional radiation source location data of two lightning flashes, this study presents a radiation source connection method considering the source density and repeated discharges in channels that includes two steps: the connection of radiation sources and the connection of segments. After increasing the spatial connection threshold determined by the source density, the stability of the channel scale under different detection capabilities (source densities) is improved compared with that of the traditional fixed spatial threshold method. The channel growth rate of the low-density case reaches 120.99%, which is close to the real situation, and the connection shape is consistent with the real situation. For repeated discharge paths, by limiting the time interval of the radiation source connection, the optimized threshold obtained in this paper can distinguish between discharges occurring in the same channel at different times. Compared with the geometric scale, the discharge scale is significantly larger (similar to 2.8 times the geometric scale in one case) and can better characterize both the lightning discharge process and the affected area. These comprehensive results show that the proposed method can reduce the number of incorrect connections, increase the channel length, and obtain a more realistic discharge scale. (Li Yurui, Zhang Yang, Zhang Yijun)

5.8 A positive cloud-to-ground flash caused by a sequence of bidirectional leaders that served to form a ground-reaching branch of a pre-existing horizontal channel

High-speed video and electric field change data were used to analyze the initiation and propagation of four predominantly vertical bidirectional leaders making connection to a predominantly horizontal channel previously formed aloft. The four bidirectional leaders sequentially developed along the same path and served to form a positive branch of the horizontal in-cloud channel, which became a downward positive leader producing a 135-kA positive cloud-to-ground (+CG) return stroke. The positive (lower) end of each bidirectional leader elongated abruptly at the time of connection of the negative (upper) end to the pre-existing channel aloft. Thirty-six negative streamer-like filaments (resembling recently reported needles) extended sideways over similar to 110 to 740 m from the pre-existing horizontal channel at speeds of similar to $(0.5-1.9)\times10^{7}$ m s^{-1}, in response to the injection of negative charge associated with the +CG. (Wu Bin, Lyu Weitao, Qi Qi)

5.9 Application of ensemble empirical mode decomposition in low-frequency lightning electric field signal analysis and lightning location

The application of empirical mode decomposition (EMD) in the analysis and processing of lightning electric field waveforms acquired by the low-frequency e-field detection array (LFEDA) in China has significantly improved the capabilities of the low-frequency/very-low-frequency (LF/VLF) time-of-arrival technique for studying the lightning discharge processes. However, the inherent mode mixing and the endpoint

effect of EMD lead to certain problems, such as an inadequate noise reduction capability, the incorrect matching of multistation waveforms, and the inaccurate extraction of pulse information, which limit the further development of the LFEDAs positioning ability. To solve these problems, the advanced ensemble EMD (EEMD) technique is introduced into the analysis of LF/VLF lightning measurements, and a double-sided bidirectional mirror (DBM) extension method is proposed to overcome the endpoint effect of EMD. EEMD can effectively suppress mode mixing, and the DBM extension method proposed in this article can effectively suppress the endpoint effect, thus greatly improving the accuracy of a simulated signal after a 25500-kHz bandpass filter. The resulting DBMEEMD algorithm can be used in the LFEDA system to process and analyze the detected electric field signals to improve the systems lightning location capabilities, especially in terms of accurate extraction and location of weak signals from lightning discharges. In this article, a 3-D image of artificially triggered lightning obtained from an LF/VLF location system is reported for the first time, and methods for further improving the location capabilities of the LF/VLF lightning detection systems are discussed. (Fan Xiangpeng, Zhang Yijun, Krehbiel Paul R.)

5.10 Characteristics of negative leader propagation area of lightning flashes initiated in the stratiform regions of mesoscale convective systems

To investigate the characteristics of extension areas (mainly the propagation areas of negative leaders in this study), the lightning location data of 254 lightning flashes initiated in the stratiform regions (stratiform lightning flashes) of 14 mesoscale convective systems (MCSs) are analyzed. The results show that most of the flashes have a relatively small lightning area (LA) ($\leqslant 100$ km^2), although they are initiated in the stratiform regions. In small or developing MCSs, most negative leaders of stratiform lightning flashes concentrate within the 9−12 km altitude range. In other MCSs with a large-sized and developed stratiform region, besides being in this high-altitude range, the negative leaders are also found to propagate more frequently in a low-altitude range of 5−7 km. Further analysis indicates that most of the stratiform lightning flashes with a large LA (>100 km^2) propagate their negative leaders within the high-altitude range, no matter where they are initiated. Moreover, the stratiform lightning flashes with or near the largest LA tend to be initiated 4−6 km below their negative leaders, while most of the stratiform lightning flashes usually propagate their negative leaders horizontally within ± 1 km of the first detected very-high-frequency (VHF) radiation source. It is inferred that some in-situ electrifications occurring before and during the formation of the high reflectivity layers in the low-altitude range contribute to these flashes, although the influence of the advection charges from the convective regions still cannot be totally ruled out. (Wang Fei, Zhang Yijun, Dong Wansheng)

5.11 Electromagnetic characteristics of upward leader initiated from the Canton Tower: A comparison with rocket-triggered lightning

By using the synchronous observation data obtained at the Tall-Object Lightning Observatory in Guangzhou (TOLOG) of 2019, the electromagnetic characteristics of upward positive leader (UPL) ascending from the 600 m high Canton Tower are examined, and are compared with the magnetic field (B-field) radiation of UPL in rocket-triggered lightning. Before the inception of sustained UPL, small electric field (E-field) pulses are superposed on the fast E-field changes. The timescale of B-field pulses corresponding to the E-field pulses ranges from 5 to 9 μs, and the inter-pulse interval is about 30 μs, which are both similar to the B-field pulses associated with the precursors of rocket-triggered lightning. Measurements show that the precursor-like stage is likely common for upward lightning initiated from the Canton Tower. Moreover, the UPL channel of tower-initiated upward lightning extends significantly in the first several ms with the initial average two-dimensional (2-D) velocity of 8.77×10^5 m s^{-1} (3-D velocity of 11.0×10^5 m s^{-1}), which is one order of magnitude faster

than the UPL initiated from the wire tip of rocket-triggered lightning, indicating that initiation of UPL from Canton Tower benefits from a substantial E-field enhancement of nearby lightning discharges. However, this favorable condition is rapidly consumed during the UPL development, causing the average 2-D velocity of UPL to decrease rapidly and maintain at about 0.5×10^5 m s^{-1}. It is noted that the variation in the 2-D speed of sustained UPL differs from tower-initiated upward lightning reported in the literature, which is possibly associated with the physical and geometric properties of the tower. (Fan Yanfeng, Lyu Weitao, Lu Gaopeng)

5.12 Fast and fine location of total lightning from low frequency signals based on deep-learning encoding features

Lightning location provides an important means for the study of lightning discharge process and thunderstorms activity. The fine positioning capability of total lightning based on low-frequency signals has been improved in many aspects, but most of them are based on post waveform processing, and the positioning speed is slow. In this study, artificial intelligence technology is introduced for the first time to lightning positioning, based on the low-frequency electric-field detection array (LFEDA). A new method based on deep-learning encoding features matching is also proposed, which provides a means for fast and fine location of total lightning. Compared to other LFEDA positioning methods, the new method greatly improves the matching efficiency, up to more than 50%, thereby considerably improving the positioning speed. Moreover, the new algorithm has greater fine-positioning and anti-interference abilities, and maintains high-quality positioning under low signal-to-noise ratio conditions. The positioning efficiency for return strokes of triggered lightning was 99.17%, and the standard deviation of the positioning accuracy in the *X* and *Y* directions was approximately 70 m. (Wang Jingxuan, Zhang Yang, Tan Yadan)

5.13 First documented downward positive cloud-to-ground lightning initiated by an upward negative lightning

An interesting downward positive cloud-to-ground lightning (DPCG) initiated by an upward negative cloud-to-ground lightning (UNCG) was recorded by the instruments installed at the Tall-Object Lightning Observatory in Guangzhou. The characteristics of the discharges before and after the DPCG return stroke were investigated in detail using both optical and electric field change data. The UNCG was triggered from the tip of the Canton Tower (600 m high) by a distant +CG lightning. A sequence of intracloud (IC) discharges developed toward and connected to several pre-existing channels of the UNCG. As a result, some positive charge was pumped from remote thundercloud regions to the region around the intersection of the pre-existing and new channels. A branch of one IC channel developed from the intersection point toward the ground, transformed into a downward positive leader, terminated on the ground, and resulted in a positive return stroke. After that, the discharge processes in the cloud continued to neutralize the remaining positive charge. The UNCG served to facilitate the IC discharges that supplied positive charges for the DPCG. Most of the charge involved in the UNCG-initiated DPCG originated from remote positively charged regions in the cloud. These observations constitute evidence for a new scenario of the initiation of +CG lightning. Key Points A downward +CG initiated by an upward tall-object –CG was recorded for the first time. The characteristics of the discharges before and after the +CG were investigated using optical and electric field change data. The observed sequence of events constitutes evidence for a new scenario of the initiation of downward +CG (Jiang Ruijiao, Lyu Weitao, Wu Bin)

5.14 Lightning fatalities in China, 2009−2018

The statistical characteristics of 1789 deaths, 1552 injuries and 1904 disasters caused by lightning based on the 2009 to 2018 National Lightning Disaster Compilation of Mainland China were analyzed. The results

showed that males accounted for 53% of casualties. Lightning disasters were more common in the east and south than in the west and north. The number of lightning disasters and casualties in the south accounted for 82.98% and 82.94% of the totals, respectively. May to August of each year is the intensive period of lightning disasters in China, and the number of deaths, injuries and disasters caused by lightning during these four months accounted for 84.80%, 79.45% and 82.77% of the total numbers per year, respectively. From 2009 to 2018, the annual injury and death rates per million people in China were 0.13 and 0.12, respectively. After population weighting, the high death rate of lightning disaster shows a certain trend of transferring from the concentrated area to the sparsely populated area, and after area weighting, the casualty density was higher in small provinces and lower in large provinces. The analysis of the environments in which lightning disaster casualties occurred found that environments closely related to agriculture, such as farmland (35%) and paddy fields or ponds (4%), accounted for nearly 40% of the casualties; accordingly, rural farmers were the main victims, accounting for 80.96% of the total casualties. Lightning protection and disaster reduction measures in rural agricultural areas should be the focus of future work. (Yin Qiyuan, Liu Hengyi, Fan Xiangpeng)

5.15 New insights into the correlation between lightning flash rate and size in thunderstorms

Thunderstorms over the Tibetan Plateau (TP), Central and Eastern China (CEC), and southern foothills of the Himalayas (SHF), have the correlations between lightning flash rate and size disagreeing with the previously published negative correlation in thunderstorms with different dynamics. There is a positive correlation when comparing TP and CEC thunderstorms. Compared with SHF thunderstorms, TP thunderstorms have much lower flash rate and similar flash size. It is explored that the TP and SHF thunderstorms have the weakest and strongest convection, respectively, and both have small effective charge regions (ECRs). The CEC and SHF thunderstorms contain more ECRs than TP thunderstorms. The weak convection in TP thunderstorm should be responsible for the common occurrence of small flash rate and size. The results suggest that the negative correlation between flash rate and size may require the dynamic intensity of compared thunderstorms to exceed a certain threshold. (Zheng Dong, Zhang Yijun)

5.16 Spatiotemporal lightning activity detected by WWLLN over the Tibetan Plateau and its comparison with LIS lightning

Herein, we compared data on the spatiotemporal distribution of lightning activity obtained from the World Wide Lightning Location Network (WWLLN) with that from the lightning imaging sensor (LIS). The WWLLN and LIS both suggest intense lightning activity over the central and southeastern Tibetan Plateau (TP) during May–September. Meanwhile, the WWLLN indicates relatively weak lightning activity over the northeastern TP, where the LIS suggests very intense lightning activity, and it also indicates a high-density lightning center over the southwestern TP that is not suggested by the LIS. Furthermore, the WWLLN lightning peaks in August in terms of monthly variation and in late August in terms of 10-day variation, unlike the corresponding LIS lightning peaks of July and late June, respectively. Other observation data were also introduced into the comparison. The blackbody temperature (TBB) data from the Fengyun-2E geostationary satellite (as a proxy of deep convection) and thunderstorm-day data support the spatial distribution of the WWLLN lightning more. Meanwhile, for seasonal variation, the TBB data are more analogous to the LIS data, whereas the cloud-to-ground (CG) lightning data from a local CG lightning location system are closer to the WWLLN data. It is speculated that the different WWLLN and LIS observation modes may cause their data to represent different dominant types of lightning, thereby leading to differences in the spatiotemporal distributions of their data. The results may further imply that there exist regional differences and seasonal variations in the electrical properties of thunderstorms over the TP. (Ma Ruiyang, Zheng Dong, Zhang Yijun)

5.17 Turbulence characteristics of thunderstorms before the first flash in comparison to non-thunderstorms

This study evaluates how clouds evolve into thunderstorms in terms of the turbulence characteristics producing the first flash. Observations of 57 (39) isolated thunderstorm (non-thunderstorm) cells during 2016–2017 in South China are provided by an S-band polarimetric radar and three independent lightning location systems. The vertical turbulence characteristics of clouds associated with thunderstorms are obviously different from non-thunderstorms. For thunderstorms, the maximum of the eddy dissipation rate (mean value in each height layer) in the entire height is 0.19 $m^2 s^{-3}$, which occurs at the first flash stage, and the achievable height of turbulence exceeds the −30 ℃ layer. For non-thunderstorms, however, the maximum is 0.12 $m^2 s^{-3}$, and the achievable turbulence height hardly exceeds the −10 ℃ layer. Additionally, the turbulence intensities of the locations where the initial discharge pulse events of the first flashes occur are weak. These turbulence characteristics are useful for lightning nowcasting. (Zhao Chuanhong, Zheng Dong, Zhang Yijun)

5.18 Two-dimensional striking distance of lightning flashes to a cluster of tall buildings in Guangzhou

Based on the high-speed video records of 54 lightning flashes striking on a cluster of tall buildings in Guangzhou and the return stroke peak currents provided by lightning location systems, this paper analyzed the two-dimensional (2D) first-return-stroke striking distances (SD) of lightning flashes to buildings with a height ranging from 100 to 600 m. Three methods, including one proposed in this study, have been used to estimate the 2D SD. The results with different methods basically agree with each other and show that the height and the top geometry of the structure on which lightning terminates are key factors that affect the SD. The correlation between the SD and the peak return stroke current appeared very scattered, particularly in the cases when each building was considered separately. Besides, we found that: (a) the estimated 2D average initiation speed of upward connecting leader (UCL) on different buildings are similar, ranging from 4.9 to 23×10^4 m s^{-1}, with an average of 13.4×10^4 m s^{-1}; (b) about 87% (27/31) flashes that struck on buildings with simple top shape only have one upward leader observed, while for buildings with complicated top shape, only 26% (6/23) flash cases have one upward leader observed; (c) for the 36 flashes to four tall buildings with heights higher than 300 m, the 2D average speed ratio of the downward leader and the UCL is 0.74 during the last 0.1 ms before the first return stroke. (Qi Qi, Lyu Weitao, Wang Daohong.)

5.19 Winter positive cloud-to-ground lightning flashes observed by LMA in Japan

Using a lightning mapping array (LMA), we have observed 24 positive cloud-to-ground (CG) flashes occurred in three thunderstorm days. These flashes can be apparently grouped into 5 clusters according to their occurrence times. We have obtained the charge structures for both the individual flashes and clusters. It was found that 4 out of 5 clusters of positive CG flashes exhibited either inverter dipolar or tri-polar charge structures. This result indicates that the high percentage of positive CG flashes in Hokuriku winter thunderstorms originated from the inverted charge structure rather than the various deformations of normal charge structures widely accepted in literatures. The flash positive charge appeared to distribute usually in a layer with its thickness of around 1 km, its horizontal area of more than 100 km^2 and its bottom altitude of around 1–2 km above the ground. For each of the flash, we have also obtained its duration, length, duration before the first stroke and convex area. It was found that all flashes with a large peak return stroke current had short durations before their first return strokes. (Wang Daohong, Zheng Dong, Wu Ting)

5.20 CMA_FEBLS低频三维全闪探测技术研究及观测10年进展

三维全闪探测已经成为了深入认识闪电物理机制和雷暴电活动规律的重要手段。中国气象局雷电

野外科学试验基地（CMA_FEBLS）自主研发了低频电场探测阵列（LFEDA），并持续开展了针对广东地区雷暴全闪电活动的综合观测试验，在精细化三维定位算法和基于三维全闪数据的闪电放电过程研究方面取得了若干研究结果。（1）LFEDA具备雷暴电活动的无死时间捕获能力以及优于百米的定位精度和一定的通道定位能力。（2）发展了基于简单脉冲特征的三维全闪定位算法，并进一步将经验模态分解及衍生方法引入到闪电信号处理中，提高了定位的精细化水平；发展了融合到达时差和时间反转技术的定位方法，提升了抗干扰能力、降低了对站网的要求。（3）实现了典型放电事件的电流波形反演，获得了窄偶极性放电事件（NBE）、初始击穿脉冲（IBP）和爆发式脉冲簇（RBPs）的放电特征；研究发现绝大多数闪电始发于IBP，而作为始发的NBE则具有更大的孤立性、更大的相对幅度和更快的发展速度。（4）发现随着起始放电高度增加，初始阶段持续时间和步长增加，发展速度和脉冲丰度下降；始发于强对流区时始发阶段通常有更大的速度和脉冲丰度。（张阳，王敬轩，郑栋）

5.21 FY-4A LMI观测的“利奇马”（2019）台前飑线闪电活动及其与对流演变的关系

为研究风云四号A星闪电成像仪（FY-4A LMI）闪电资料在强对流天气的监测预警能力，以2019年台风“利奇马”台前飑线为例，利用FY-4A LMI闪电资料、FY-4A云顶亮温资料（TBB）、地基闪电定位资料（ADTD）、组网雷达组合反射率因子资料和东南沿海自动站风雨资料，研究“利奇马”台前飑线全闪电活动的时空分布特征及其与飑线内对流演变的关系。结果表明：FY-4A LMI闪电频次的时空变化与台前飑线的演变过程相一致，LMI闪电爆发对台前飑线强度增强具有提早约1 h的指示作用。在闪电活动与台前飑线对流的演变关系上，LMI闪电与卫星TBB深对流及雷达强回波的时空演变存在较好的相关性。LMI观测的闪电频数与强回波（35 ～ 55 dBz）顶高具有对应关系，与–72 ℃冷云区面积及35 dBz以上雷达组合反射率因子面积的变化特征相同。闪电活动集中位于TBB低值区的左侧和前部的亮温梯度大值区，对地面雷暴大风和强降水的可能发生位置具有判识作用。LMI与ADTD的比较发现二者所揭示的“利奇马”台前飑线闪电活动特征基本一致。（林小红，张文娟，范能柱）

5.22 不同闪电跃增算法在北京地区应用效果对比

基于S波段多普勒天气雷达基数据、北京闪电定位网全闪定位数据和北京地区降雹的人工观测结果，对比分析Gatlin和σ两种闪电跃增算法在不同配置下对北京地区2015—2018年共177次冰雹天气过程的预警效果。结果表明：不同倍数的σ算法预警结果差别很大，2σ（要求当前闪电频数变化率超过之前平均闪电频数变化率两倍标准差）在σ算法中的预警效果最佳；不同N（总闪频数变化率的数量）配置下的Gatlin算法的预警结果差别不大，其中当N = 6时的预警效果最佳。2σ算法的命中率、虚警率和临界成功指数分别为80.2%，41.6%和51.1%，N = 6的Gatlin算法的相应结果分别为82.5%，62.0%和35.2%。另外，详细分析了一次多单体雷暴过程和一次飑线过程中两种算法的应用情况，结果也表明Gatlin算法比2σ算法的命中率略高，但虚警率偏高很多，临界成功指数偏低。综合Gatlin算法和σ算法对冰雹预报结果评估情况，发现2σ闪电跃增算法更适于对北京冰雹天气的预警，对提升闪电数据在北京地区冰雹预报业务的可用度有一定参考价值。（田野，姚雯，尹佳莉）

5.23 广州高建筑物雷电回击光脉冲特征分析

为了深入认识负地闪放电过程中光辐射信号的特性，对广州高建筑物雷电观测站所获得的回击光脉冲波形进行了分析。对观测到的88例负地闪事件中的184次回击（包括60次下行闪电首次回击、58次下行闪电继后回击、66次上行闪电继后回击）的光脉冲特征进行了统计分析。结果表明：下行闪电首次回击光脉冲10% ～ 90%上升时间T_1的算术平均值/中值为32.5/31.4 μs，20% ～ 80%上升时间T_2的算术平均值/中值为22.6/22.4 μs，半峰宽度T_3的算术平均值/中值为131.1/117.0 μs。下行闪电继后回击光脉冲T_1的算术平均值/中值为30.4/27.7 μs，T_2的算术平均值/中值为19.5/17.6 μs，T_3的算术平均值/

中值为153.6/142.6 μs。在21例下行多回击负地闪事件中，光脉冲回击间隔时间在12.6 ～ 368.6 ms范围之间，算术平均值为78.7 ms，有14%闪电事件存在继后回击光脉冲峰值大于首次回击的情况。上行闪电继后回击光脉冲T_1的算术平均值/中值为27.5/24.3 μs，T_2的算术平均值/中值为17.0/15.7 μs，T_3的算术平均值/中值为132.2/124.5 μs。总体上，下行闪电首次回击的光脉冲上升时间最长、下行闪电继后回击次之、上行闪电继后回击最小;下行闪电继后回击脉冲半峰宽度比下行闪电首次回击及上行闪电继后回击的更大。（黄晓磊，吕伟涛，武斌）

5.24 华南飑线系统对流与层云区闪电起始和通道位置处的云微物理特征

利用广州S波段双偏振雷达观测数据和低频电场探测阵列三维闪电定位数据，分析了2017年5月4日和5月8日华南地区两次飑线过程中闪电起始和通道位置处的雷达偏振参量和降水粒子特征。两次飑线中约80%的闪电起始和通道（统称闪电放电）定位于对流区。对流区闪电放电位置处的雷达反射率（Z_H）要比层云区平均大4 ～ 5 dBz，其它偏振参量的平均值较为接近。闪电放电位置处的Z_H中值随高度增加而减小，但差分反射率（Z_{DR}）、差分传播相移率（K_{DP}）和共极化相关系数（CC）在–10 ℃层以上随高度变化不大；–10 ℃层以下，对流区闪电放电位置对应Z_{DR}和K_{DP}随高度下降明显增大。闪电起始位置的平均Z_H比闪电通道位置处的平均Z_H大1 ～ 2 dBz，但前者在对流区内对应Z_H分布峰值区间为25 ～ 30 dBz，弱于后者的30 ～ 35 dBz；同时，它们的对比关系在–20 ℃层上下不同。对流区内闪电放电位置处的主导性粒子是霰和冰晶，它们的区域占比接近。在层云区内，闪电放电位置主要是干雪和冰晶，干雪区域的占比显著大于冰晶。（赵川鸿，郑栋，张义军）

5.25 基于闪电聚类方法的西北太平洋区域雷暴活动特征

利用2010—2018年全球闪电探测网（WWLLN）观测资料，采用基于闪电密度的空间聚类算法（DBSCAN）建立了西北太平洋地区雷暴数据集，研究了该区域雷暴的时空分布特征，并进行海陆差异对比。研究结果表明，在合理设定DBSCAN参数阈值的条件下，基于WWLLN闪电聚类的雷暴与天气雷达观测在时空分布和过程演变上具有一致性。西北太平洋区域的日均雷暴数为3869，雷暴的闪电密集区平均面积为557.91 km^2，平均延展尺度为31.99 km，平均每小时每个雷暴闪电频次为33次。在空间分布上，东南亚沿海地区与热带岛屿的雷暴活动最强，南海的雷暴活动强于深海。距离海岸线越近的海域其雷暴面积越大。在季节分布上，整个区域雷暴活动在夏季（6—8月）达到全年最强，南海雷暴活动6月达到峰值，而日本东部近海海域的雷暴活动则在冬季达到最强。我国内陆南方地区雷暴3月开始显著增多，雷暴平均面积达到最大，但雷暴平均闪电频次5月才达到峰值。在日变化方面，陆地雷暴活动呈现典型的单峰型特征，大部分雷暴发生在午后及傍晚。海洋雷暴日变化则较为平缓，南海具有其独特的雷暴日变化特征。（周鑫，张文娟，张义军）

5.26 雷暴闪电活动特征研究进展

从一般雷暴、灾害性雷暴和台风的闪电活动特征以及雷暴闪电尺度特征四个方面对相关研究进行梳理。一般雷暴通常具有正常极性电荷结构，云/地闪比例在3左右（中纬度地区），地闪中正地闪占比为10%左右，负地闪位置往往更集中于对流区。灾害性雷暴倾向具有活跃的云闪，低比例的地闪，易出现反极性电荷结构，正地闪比例偏高。闪电活动与灾害性天气现象之间存在关联性，部分雹暴过程具有两次闪电活跃阶段。台风中大部分闪电发生在外雨带，眼壁/外雨带闪电爆发很可能预示气旋强度的增强以及路径的改变。由闪电持续时间、通道空间扩展所表征的闪电尺度与雷暴对流强度相关。弱对流雷暴或雷暴的弱对流区域可能由水平扩展、垂直分层的电荷分布形态主导，闪电频次低，闪电空间尺度大；强对流雷暴或雷暴的强对流区域可能由交错分布的小电荷区主导，闪电频次高，闪电尺度小。（郑栋，张文娟，姚雯）

5.27 雷暴云特征数据集及我国雷暴活动特征

基于FY-2E气象卫星相当黑体亮度温度（TBB）和云分类数据（CLC）及全球闪电探测网（WWLLN）闪电数据，通过对TBB不超过–32 ℃的云区进行椭圆拟合，定义1 h内上述云区或椭圆区域有WWLLN闪电发生的个例为雷暴云，获得雷暴云时间、位置、形态、结构、闪电活动等特征参量，构建雷暴云特征数据集，并基于该数据集初步分析了我国陆地和毗邻海域的雷暴活动特征。研究表明：我国华南、西南、青藏高原东、中部和南海雷暴最为活跃，华北和东北地区是北方雷暴活动较强的区域。雷暴活动时间变化海陆差异明显，陆地雷暴活动峰值出现在6—8月，南海雷暴活动一个峰值出现在5月左右，另一峰值出现在8月后，且纬度越低出现越晚。陆地大部分地区雷暴活动在14:00—20:00（北京时）达到峰值，毗邻海域雷暴活动峰值主要出现在早上。雷暴云TBB不超过–32 ℃面积符合对数正态分布，峰值区间位于$1\times10^3\sim1\times10^4$ km^2，平均值为3.0×10^4 km^2。南海雷暴云面积最大，陆地上大于雷暴云面积平均值1.2×10^5 km^{2}的区域主要分布于我国地形的第一阶梯和柴达木盆地。（马瑞阳，郑栋，姚雯）

5.28 热带气旋闪电活动特征研究综述

针对热带气旋（TC）闪电已有研究，首先从闪电活动分布特征、眼壁闪电爆发对TC强度和路径的指示、外雨带闪电活动与雨带对流结构的关系3个方面进行了总结；其次从动力–微物理方面对TC闪电的形成原因和特征机理进行了梳理；最后提出当前研究中存在的两个关键问题，并对后续研究内容进行了展望。基于地基和空基相结合的综合闪电探测得到的闪电属性特征参量，有望建立一个明确的、具有代表性的闪电活动–TC强度变化关系。利用沿海地区架设的三维闪电定位系统结合地基双偏振雷达，针对登陆台风强对流过程开展的综合观测研究，将有助于推进闪电观测资料在台风中小尺度强对流监测、预警和资料同化中的应用。（张文娟，张义军，郑栋）

5.29 铷原子簇自发磁矩的试验观测及理论分析

在碱金属原子簇磁性的研究中，存在自由原子簇含有的原子个数及其磁矩难以准确确定的问题，本文采用光磁共振光谱检测手段，对工作温度约为328 K的饱和铷蒸汽样品中单原子分子$^{87}Rb_1$和14种簇粒子（^{87}Rb）$_{n'}$（n' = 2，3，…，15）的磁矩进行了深入研究。试验结果表明：在同一外磁场下，14种簇粒子（^{87}Rb）$_{n'}$的共振频率$f_{n'}$与$^{87}Rb_1$的共振频率f^*之间存在$f_{n'}=f^*/n'$的数值关系，并且各簇粒子的磁矩值与振幅值均随n'的大小和奇、偶性呈现不同性质的变化规律。运用分子轨态理论通过$^{87}Rb_n=87Rb_{n-1}+{}^{87}Rb$联合原子簇构造模式，给出14种簇粒子$^{87}Rb_n$（$n$ = 2，3，…，15）的基态和最低激发态的电子组态和分子态项型，分析了各分子态的稳定性和发生可见塞曼效应的可能性。进一步基于双原子分子磁矩公式计算，发现当$n=n'$时$^{87}Rb_n$的磁矩值与（^{87}Rb）$_{n'}$的磁矩值严格吻合（平均相对误差仅为0.6765%），证实了（^{87}Rb）$_{n'}$和$^{87}Rb_n$的对应关系。（邸淑红，张阳，杨会静）

5.30 粤港澳大湾区两套闪电定位系统地闪探测性能的对比分析

根据2014—2018年粤港澳闪电定位系统（GHMLLS）和广东电网地闪定位系统（GDLLS）两套闪电定位系统的观测资料，对粤港澳大湾区范围内二者的地闪探测性能进行评估和对比。结果表明：在粤港澳大湾区，对于地闪回击记录，从各月份记录和空间密度的分布上来看，GDLLS的探测数都多于GHMLLS，二者的比值为1.24；两套系统总回击、负回击、正回击的月分布和日变化特征基本一致；两系统地闪回击的匹配记录在大湾区大部分区域内的偏差量都在1.5 km内；对于匹配后的负、正回击电流峰值，二者有较强的相关性，相关系数分别为0.99和0.98，GDLLS的负、正回击电流峰值分别为GHMLLS的1.47倍和1.45倍。（张悦，吕伟涛，陈绿文）

6 模式和再分析资料
6 Model and reanalysis data

6.1 A large-eddy simulation study on the diurnally evolving nonlinear trapped lee waves over a two-dimensional steep mountain

The diurnally evolving trapped lee wave over a small-scale two-dimensional steep mountain is investigated in large-eddy simulations based on a fully compressible and nonhydrostatic model (Icosahedral Nonhydrostatic, ICON) with triangular grids of 50-m-edge length. An idealized atmospheric profile derived from a realistic case is designed to account for influences from the stagnant layer near the surface, the stability of the atmospheric boundary layer (ABL) and the upper-level jet. First, simulations were done to bridge from the linear regime to the nonlinear regime by increasing the mountain height, which showed that larger-amplitude lee waves with longer wavelength can be produced in the nonlinear regime than in the linear regime. Second, the effects of the stagnant layer near the surface and the ABL stability were explored, which showed that the stagnant layer or the stable ABL can play a similar wave-absorbing role in the nonlinear regime as in linear theories or simulations. Third, the role of the upper-level jet was explored, indicating that a stronger (weaker) upper-level jet can help to produce longer (shorter) lee waves. The stable ABL with a stagnant layer can more (less) efficiently absorb the longer (shorter) lee waves due to the stronger (weaker) jet, so that the wave response is more sensitive to the wave-absorption layer when an upper-level jet is present. Finally, the momentum budget was analyzed to explore the interaction between the upper and lower levels of the troposphere, which showed that the momentum flux due to the upward-propagating waves and trapped waves varies with the upper-level jet strength and low-level stagnancy and ABL stability. (Xue Haile, Giorgetta Marco A.)

6.2 A new perspective on evaluating high-resolution urban climate simulation with urban canopy parameters

The “state-of-the-art” urban climate models have not been evaluated against dense meteorological networks under various weather conditions. In this study, we conducted high-resolution urban climate simulations in Beijing and investigated the relationship between their performances and urban canopy parameters (UCPs). The latest version of single-layer (UCM) and multi-layer (BEP) urban canopy models were tested separately. Results show that model performances are insensitive to rainfall events in summer, but change significantly with wind conditions in winter. Inclusion of UCPs has a limited impact on air temperature simulations. In terms of wind speed simulations, consistent overestimations by UCM and BEP are found in both summer and winter. The overestimation by BEP reduces significantly when UCPs are available, especially on windy days in winter. On the other hand, performance of UCM can degrade over urban areas with canopy parameters. Wind speed biases are found to correlate significantly with UCPs. The accuracy of wind speed simulations by UCM and BEP increases with urban fraction and building surface ratio. This indicates poor model performances over low-density urban areas, which requires enhanced aerodynamic parameterizations to better account for UCPs. This study reveals the limitation of current urban climate simulations and provides guidance for future model developments. (Yu Miao, Chen Xuan, Yang Jiachuan)

6.3 A study of extrapolation nowcasting based on IVAP-retrieved wind

In this study, we propose a new way to obtain motion vectors using the integrating velocity-azimuth process (IVAP) method for extrapolation nowcasting. Traditional tracking methods rely on tracking radar

echoes of a few time slices. In contrast, the IVAP method does not depend on the past variation of radar echoes; it only needs the radar echo and radial velocity observations at the latest time. To demonstrate it is practical to use IVAP-retrieved winds to extrapolate radar echoes, we carried out nowcasting experiments using the IVAP method, and compared these results with the results using a traditional method, namely, the tracking radar echoes by correlation (TREC) method. Comparison based on a series of large-scale mature rainfall cases showed that the IVAP method has similar accuracy to that of the TREC method. In addition, the IVAP method provides the vertical wind profile that can be used to anticipate storm type and motion deviations. (Luo Yi, Liang Xudong, Wang Gang)

6.4 Advances in research on the ITCZ: Mean position, model bias, and anthropogenic aerosol influences

The zonal-mean position of the intertropical convergence zone (ITCZ) and its shift in the meridional direction significantly influence both the tropical and even global climate. This work reviews three aspects of the progress in ITCZ-relevant research: 1) the mechanism behind the asymmetry of the ITCZ annual- and zonal-mean positions relative to the equator; 2) causes of the double-ITCZ problem (pervasive in climate models) and the efforts to solve it; and 3) the physical mechanisms by which anthropogenic aerosols affect the location of the zonal-mean ITCZ. According to recent studies, the north-of-the-equator location of the annual- and zonal-mean ITCZ is mainly driven by the cross-equatorial energy transports in the ocean, induced by the Atlantic overturning circulation. A quantitative relationship between the ITCZ shift and the anomalous cross-equatorial energy transport in the atmosphere has been found. Presently, the double-ITCZ problem is still the most common and pronounced bias in tropical precipitation simulations with climate models. Recently, some studies have found that simply correcting the biases in hemispheric energy contrast does not improve the simulation of the ITCZ with climate models; whereas others have found that improving model resolutions and convective parameterizations in climate models, such as entrainment rate, rain-droplet re-evaporation, and convection triggering function, can alleviate the double-ITCZ bias. Therefore, it seems that the double-ITCZ problem in climate models is rooted in the complex physics of the models, which is not yet well-understood. In addition, anthropogenic aerosols are suggested to be able to induce meridional shifts of the ITCZ, but through various physical mechanisms. Absorbing aerosols like black carbon influence the ITCZ position basically via instantaneous absorption of shortwave radiation in the atmosphere, whereas scattering aerosols like sulfate affect the location of the ITCZ through the cloud lifetime effect and the subsequent response of surface evaporation. (Zhang Hua, Ma Xinyu, Zhao Shuyun)

6.5 An investigation into the vertical structures of low-altitude atmosphere over the Central Taklimakan Desert in summer

In this study, 1-month continuous radiosonde observational data were applied to present the low-altitude vertical structures and their evolutions over the Central Taklimakan Desert (CTD). The primary focus is to highlight the vertical structures near the ground with the high-resolution (10 m in height and 6 h in time) radiosonde data. One of the unique features evident in our results is an obvious diurnal transition in lower layers near the ground due to strong surface heating or cooling. Unlike a traditional vertical structure in the boundary layer observed over a nondesert surface, both superadiabatic and inversion layers are distinct during the day. More specifically, the superadiabatic layer is obvious in the daytime because of strong solar radiation over the desert, and the superadiabatic can reach up to 0.2 km. In contrast, an apparent inversion layer forms in the nighttime due to the surface cooling. It is found that the surface forcing mainly dominates the structures in the boundary layer. At last, the vertical structures from the observations are compared with those from the ERA-Interim and MERRA2 reanalysis data sets. The results indicate that both reanalysis products can provide

similar vertical profile patterns and diurnal variations. However, the diurnal transitions of temperature and wind profiles over the CTD are underestimated severely by both reanalysis data. Besides, the reanalysis data sets completely miss the superadiabatic near the ground in the daytime. (Yin Jinfang, Gu Haodong, Huang Jie)

6.6 Challenges in developing finite-volume global weather and climate models with focus on numerical accuracy

High-resolution global non-hydrostatic gridded dynamic models have drawn significant attention in recent years in conjunction with the rising demand for improving weather forecasting and climate predictions. By far it is still challenging to build a high-resolution gridded global model, which is required to meet numerical accuracy, dispersion relation, conservation, and computation requirements. Among these requirements, this review focuses on one significant topic—the numerical accuracy over the entire non-uniform spherical grids. The paper discusses all the topic-related challenges by comparing the schemes adopted in well-known finite-volume-based operational or research dynamical cores. It provides an overview of how these challenges are met in a summary table. The analysis and validation in this review are based on the shallow-water equation system. The conclusions can be applied to more complicated models. These challenges should be critical research topics in the future development of finite-volume global models. (Xie Yuanfu, Qin Zilong)

6.7 Changes in anthropogenic particulate matters and resulting global climate effects since the Industrial Revolution

In order to quantify air pollution effects on climate change, we investigated the climate response associated with anthropogenic particulate matters (PMs) by dividing fine PM ($PM_{2.5}$, particle size $\leqslant 2.5$ μm) and coarse particulate matter (CPM, particle size >2.5 μm) in great detail in this work, with an aerosol-climate coupled model. We find that the changes in $PM_{2.5}$ and CPM are very different and thus result in different, even opposite effects on climate, especially on a regional scale. The column burden of $PM_{2.5}$ increases globally from 1850 to the present, especially over Asia's southern and eastern parts, whereas the column concentration of CPM increases over high-latitude regions and decreases over South Asia. The resulted global annual mean effective radiative forcing (ERF) values due to $PM_{2.5}$ and CPM changes are −1.21 W m^{-2} and −0.24 W m^{-2}, respectively. Increases in $PM_{2.5}$ result in significant cooling effects on the climate, whereas changes in CPM produce small and even opposite effects. The global annual mean surface air temperature (SAT) decreases by 0.94 K due to $PM_{2.5}$ increase. Coolings caused by increased $PM_{2.5}$ are more apparent over the Northern Hemisphere (NH) terrain and ocean at mid- and high- latitudes. Increases in SATs caused by increased CPM are identified over high latitudes in the NH, whereas decreases are identified over mid-latitude regions. Strong cooling due to increased $PM_{2.5}$ causes a southward shift of the Intertropical Convergence Zone (ITCZ), whereas the Hadley circulation associated with CPM is enhanced slightly over both hemispheres, along with the weak movement of corresponding ITCZ. The global annual mean precipitation decreases by approximately 0.11 mm day^{-1} due to the increased $PM_{2.5}$. Generally, $PM_{2.5}$ concentration changes contribute more than 80% of the variation caused by all anthropogenic aerosols in ERF, SAT, cloud fraction, and precipitation. (Yang Dongdong, Zhang Hua, Wang Zhili)

6.8 Discontinuous Galerkin isogeometric analysis of convection problem on surface

The objective of this work is to study finite element methods for approximating the solution of convection equations on surfaces embedded in R-3. We propose the discontinuous Galerkin (DG) isogeometric analysis (IgA) formulation to solve convection problems on implicitly defined surfaces. Three numerical experiments shows that the numerical scheme converges with the optimal convergence order. (Wang Liang, Xiong Chunguang, Yuan Xinpeng)

6.9 Effects of mosaic representation of land use/land cover on skin temperature and energy fluxes in Noah-MP land surface model over China

The representations of land use/land cover (LULC) play an important role in land surface models (LSMs) for the simulation of the energy flux partition, soil moisture redistribution, and runoff generation. This study was designed to investigate the regional effects of mosaic LULC representations on skin temperature (T_s) and energy fluxes over China at three horizontal resolutions and how these effects changed with climate regimes, using Noah with multiparameterization (Noah-MP) LSM. The current officially released Noah-MP only considered the most abundant LULC type within one model grid. In this study, the mosaic method considering all the LULC types existing in one model grid was implemented into Noah-MP. Against the reference data (including MODIS land surface temperature products, FLUXCOM energy flux data and Numerical Terra dynamic Simulation Group evapotranspiration data), the mosaic method generally performed better than the default method and reduced the root-mean-squared-error of T_s and energy fluxes significantly over urban region. The mosaic method affected the T_s and energy fluxes by changing leaf area index and soil moisture, mainly by the former. The warm (monthly mean air temperature larger than 10 ℃) and relatively humid climate (annual total precipitation larger than 200 mm) could enlarge the effect of mosaic method on T_s and energy fluxes. The mosaic method reduced discrepancies of T_s and energy fluxes among three horizontal resolutions (0.0625°, 0.25°, and 0.50°), especially over the heterogeneous vegetated and urban region. Key Points Mosaic representation of land use/land cover was implemented in Noah-MP to obtain more accurate land surface information Noah-MP incorporated with the mosaic method improved the skin temperature and energy fluxes. Warm climate regimes enlarged the effect of mosaic method on skin temperature and energy fluxes through LAI changes. (Zhang Guo, Li Jianduo, Zhou Guangsheng)

6.10 Effects of organic soil in the Noah-MP land-surface model on simulated skin and soil temperature profiles and surface energy exchanges for China

Inclusion of the thermal and hydraulic effect of soil organic matter plays an important role in land-surface models (LSMs) for simulating soil temperature and surface energy exchanges. The current officially released Noah with multiparameterization (Noah-MP) LSM, implemented in the community weather research and forecasting (WRF) model, does not include a parameterization for soil organic matter. In this study, the thermal and hydraulic effect of soil organic matter was parameterized into Noah-MP LSM. Based on the profiled soil organic matter data for China and the observations of skin temperature and soil temperature profiles from more than 2000 surface meteorological stations, we investigated the effects of organic soil using the Noah-MP LSM with and without the profiled soil organic matter at the regional scales. Compared with the simulation without the inclusion of organic soil parameterization, the Noah-MP LSM simulation with the profiled soil organic matter improved the skin temperature and soil temperature profiles, especially soil temperature in deep soils under cold and arid regions. The realistic representation of snow depth and the snow insulation dependency on snow depth were confirmed to be a pre-requisite in Noah-MP in the high latitudes. By incorporating the profiled soil organic matter, the Noah-MP LSM enlarged the regional mean sensible heat flux (SH) and lower the regional mean latent heat flux (LH). In the warm and humid regions, a relatively smaller effect of organic soil on soil temperature could lead to a larger effect on SH and LH, especially LH. (Zhang Guo, Chen Yueli, Li Jianduo)

6.11 Evaluating the impacts of cloud microphysical and overlap parameters on simulated clouds in global climate models

The improvement of the accuracy of simulated cloud-related variables, such as the cloud fraction, in

global climate models (GCMs) is still a challenging problem in climate modeling. In this study, the influence of cloud microphysics schemes (one-moment versus two-moment schemes) and cloud overlap methods (observation-based versus a fixed vertical decorrelation length) on the simulated cloud fraction was assessed in the BCC_AGCM2.0_CUACE/Aero. Compared with the fixed decorrelation length method, the observation-based approach produced a significantly improved cloud fraction both globally and for four representative regions. The utilization of a two-moment cloud microphysics scheme, on the other hand, notably improved the simulated cloud fraction compared with the one-moment scheme; specifically, the relative bias in the global mean total cloud fraction decreased by 42.9%−84.8%. Furthermore, the total cloud fraction bias decreased by 6.6% in the boreal winter (DJF) and 1.64% in the boreal summer (JJA). Cloud radiative forcing globally and in the four regions was improved by 0.3%−1.2% and 0.2%−2.0%, respectively. Thus, our results showed that the interaction between clouds and climate through microphysical and radiation processes is a key contributor to simulation uncertainty. (Wang Haibo, Zhang Hua, Xie Bing)

6.12 Evaluation of a flexible single ice microphysics and a Gaussian probability-density-function macrophysics scheme in a single column model

Scale-aware parameterizations of subgrid scale physics are essentials for multiscale atmospheric modeling. A single-ice (SI) microphysics scheme and Gaussian probability-density-function (Gauss-PDF) macrophysics scheme were implemented in the single-column global-to-regional integrated forecast system model (SGRIST) and they were tested using the Tropical Warm Pool-International Cloud Experiment (TWP-ICE) and the Atmospheric Radiation Measurement Southern Great Plains Experiment in 1997 (ARM97). Their performance was evaluated against observations and other reference schemes. The new schemes simulated reasonable precipitation with proper fluctuations and peaks, ice, and liquid water contents, especially in lower levels below 650 hPa during the wet period in the TWP-ICE. The root mean square error (RMSE) of the simulated cloud fraction below 200 hPa was 0.10/0.08 in the wet/dry period, which showed an obvious improvement when compared to that, i.e., 0.11/0.11 of the original scheme. Accumulated ice water content below the melting level decreased by 21.57% in the SI. The well-matched average liquid water content displayed between the new scheme and observations, which was two times larger than those with the referencing scheme. In the ARM97 simulations, the SI scheme produced considerable ice water content, especially when convection was active. Low-level cloud fraction and precipitation extremes were improved using the Gauss-PDF scheme, which displayed the RMSE of cloud fraction of 0.02, being only half of the original schemes. The study indicates that the SI and Gauss-PDF schemes are promising approaches to simplify the microphysics process and improve the low-level cloud modeling. (Li Jiabo, Peng Xindong, Li Xiaohan)

6.13 Evaluation of CMIP6 global climate models for simulating land surface energy and water fluxes during 1979−2014

This study examined the overall performance of the climate models in the Coupled Model Intercomparison Project phase 6 (CMIP6) in simulating the key energy and water fluxes over land. For this purpose, this study selected multiple land flux products as reference data sets and assessed the global spatial means, patterns, trends, seasonal cycles, and regional mean estimates of the sensible heat (SH), latent heat (LH), net radiation (RN), runoff (RF), and precipitation (PR) simulated by 32 CMIP6 models in recent decades. The global (Antarctica, Greenland, and hot deserts are not included) mean SH, LH, RN, RF, and PR simulated by the CMIP6 models are 37.55 ± 4.81 W m^{-2}, 49.88 ± 5.31 W m^{-2}, 89.10 ± 4.45 W m^{-2}, 351.31 ± 95.28 mm yr^{-1}, and 948.35 ± 88.77 mm yr^{-1}, respectively. The ensemble median of CMIP6 simulations (CMIP6-MED) can provide robust estimates of global and regional land fluxes, which are within the ranges given by the reference

data sets, and highly consistent spatiotemporal patterns of these fluxes. The comparison of CMIP6-MED with the first preferred reference data sets shows that CMIP6-MED generally overestimates the water and energy fluxes over land, except for the simulated RF and PR in the Amazon region. The most disagreements between CMIP6-MED and the reference data sets occur in South America (particularly the Amazon region) and the Tibetan Plateau. Finally, the sources of model biases are discussed. It is suggested that current land flux products should be widely used to optimize the structures and parameters of climate models in future work. (Li Jianduo, Miao Chiyuan, Wei Wei)

6.14 Evaluation of five reanalysis products with radiosonde observations over the Central Taklimakan Desert during summer

To provide guidance for the use of reanalysis data in the Central Taklimakan Desert (CTD), five reanalysis products are evaluated based on the radiosonde data obtained from two field experiments during summer for the first time in the CTD, including the European Center for Medium-Range Weather Forecasts (ECMWF) reanalysis version 5 (ERA5), ECMWF reanalysis-interim (ERA-Interim), Japanese 55-years reanalysis (JRA55), modern-era retrospective analysis for research and applications version 2 (MERRA2), and the National Centers for Environmental Prediction-Department of Energy reanalysis version 2 (NCEP2). The results show that reanalysis temperature (T), specific humidity (Q), geopotential height (GPH), and wind field (U and V components) are consistent with the radiosonde observations in terms of the vertical distribution. In general, ERA5 has the best performance in the CTD during the study period, followed closely by ERA-Interim. However, NCEP2 produces the largest error. The errors of all the reanalysis data show significant diurnal variations, and the diurnal variations differ from each other. Moreover, the results indicate that the reanalysis datasets have the largest deviation at 850 hPa (near the ground), which means that in the desert region complex interactions may exist between the land surface and the atmosphere. Therefore, more attention should be paid to the description of complex interactions between land and atmosphere over the moving-sand desert region in the numerical models. (Huang Jie, Yin Jinfang, Wang Minzhong)

6.15 High-order conservative and oscillation-suppressing transport on irregular hexagonal grids

A third-order numerical scheme was developed for 2D irregular hexagonal meshes for the advection problems in this study. The scheme is based on a multi-moment constrained finite-volume method (MCV) in Cartesian coordinates and entails the introduction of a general integration method over a hexagonal cell. Unlike in the conventional finite-volume method, various discrete moments, that is, point value and volume-integrated average, are adopted as computational constraints to achieve high-order computation. The high-order spatial reconstruction can therefore be built in a local space, which considerably reduces the stencil length. The numerical scheme is tested using various idealized experiments. Compared with the existing schemes, this scheme is demonstrated to be flexible for application in irregular hexagonal meshes without increasing cost or compromising on accuracy. The general integration formulation based on a third-order polynomial helps to expand the application to arbitrary hexagons that does not require the use of centroids as computational points or Voronoi tessellation. It is also convenient to define the orthogonal wind components in the Cartesian system to directly drive the atmospheric transport. (Jiao Han, Peng Xindong, Che Yuzhang)

6.16 Impact of parameterizing the turbulent orographic form drag on convection-permitting simulations of winds and precipitation over South China during the 2019 pre-summer rainy season

A turbulent orographic form drag (TOFD) parameterization, which accounts for the unresolved drag induced by the subgrid orographic variance, is implemented in the Weather Research and Forecasting (WRF) model with a horizontal grid spacing of 3 km. Its impact on the surface wind and precipitation forecasts over

South China during a pre-summer rainy season (April–June 2019) is evaluated based on 3-hour observations from more than 2500 stations, by comparing the results from two series of parallel simulation with the TOFD parameterization turned on or off, respectively. Results show that the seasonal mean root mean square error (RMSE) and bias of the surface wind have been significantly reduced by more than 7% and 5%, respectively. The low-level wind is also shown improved by comparing the two series of simulations with 12-hour observations from 26 sounding stations. Consequently, the equitable threat score (ETS) is increased by the TOFD parameterization for most rainfall-intensity categories, and the six-category mean ETS shows an improvement of more than 3%. The mechanism of the TOFD impact on low-level wind and precipitation is investigated as well. The low-level southwesterlies from the South China Sea flow over the rough land in South China are found to be weakened, which leads to the low-level wind convergence and more precipitation over those regions. Moreover, this effect is more apparent during the daytime. (Xue Haile, Zhou Xu, Luo Yali)

6.17 Modulation of snow on the daily evolution of surface heating over the Tibetan Plateau during winter: Observational analyses

Studying the daily evolution of turbulent fluxes modulated by snowfall over the Tibetan Plateau (TP) is of great importance to understand the features of the change in the TP heat source/sink and its contribution to Asian atmospheric circulation and weather processes. However, the lack of data over the TP restricts the detailed studies. Based on observations from four sites of the Third TP Atmospheric Scientific Experiment, the process of surface energy balance impacted by snow is investigated. The results show that the surface albedo largely increases on the first day of snow and then slowly decreases. Correspondingly, the sensible heat (H) flux sharply decreases after snow and then gradually recovers to the original level during the following approximately 10 days. The latent heat (LE) flux becomes more active and stronger after snowfall and persists for a longer period than H, since the soil moisture may still contribute to a high LE after snowmelt. As the synergistic result of H and LE modulated by snow, the surface turbulent heating (i.e., the sum H and LE) of the TP decreases at the early period of snow events and then even enhances to a higher level after the snowmelt than before snow. Comparison analyses reveal that the impact of snow on the H and LE over the TP is much stronger than over similar latitude low-altitude regions in North America and Europe, which may be partly attributed to the larger and more drastic change of the surface net solar radiation associated with snow processes in the TP. The ERA5 and CFS reanalysis data sets fail to reproduce the modulation of snow on the heat fluxes, which suggests that the physical schemes of the models should be further improved based on the observational analyses over TP. This study may help further understand the detailed physical processes of modulation of snow events on Asian weather processes during winter and is also conducive to the improvement of surface parameterization schemes of models. (Xin Yufei, Liu Ge, Chen Yueli)

6.18 Potential driving factors on surface solar radiation trends over China in recent years

The annual mean surface solar radiation (SSR) trends under all-sky, clear-sky, all-sky-no-aerosol, and clear-sky-no-aerosol conditions as well as their possible causes are analyzed during 2005–2018 across China based on different satellite-retrieved datasets to determine the major drivers of the trends. The results confirm clouds and aerosols as the major contributors to such all-sky SSR trends over China but play differing roles over sub-regions. Aerosol variations during this period result in a widespread brightening, while cloud effects show opposite trends from south to north. Moreover, aerosols contribute more to the increasing all-sky SSR trends over the northern China, while clouds dominate the SSR decline over the southern China. A radiative transfer model is used to explore the relative contributions of cloud cover from different cloud types to the all-types-of-cloud-cover-induced (ACC-induced) SSR trends during this period in four typical sub-regions over

China. The simulations point out that the decreases in low-cloud-cover (LCC) over the North China Plain are the largest positive contributor of all cloud types to the marked annual and seasonal ACC-induced SSR increases, and the positive contributions from both high-cloud-cover (HCC) and LCC declines in summer and winter greatly contribute to the ACC-induced SSR increases over East China. The contributions from medium-low-cloud-cover (mid-LCC) and LCC variations dominate the ACC-caused SSR trends over the southwestern and South China all year round, except for the larger HCC contribution in summer. (Wang Qiuyan, Zhang Hua, Yang Su)

6.19 Reconstruction of missing data in weather radar image sequences using deep neuron networks

Missing data in weather radar image sequences may cause bias in quantitative precipitation estimation (QPE) and quantitative precipitation forecast (QPF) studies, and also the obtainment of corresponding high-quality QPE and QPF products. The traditional approaches that are used to reconstruct missing weather radar images replace missing frames with the nearest image or with interpolated images. However, the performance of these approaches is defective, and their accuracy is quite limited due to neglecting the intensification and disappearance of radar echoes. In this study, we propose a deep neuron network (DNN), which combines convolutional neural networks (CNNs) and bi-directional convolutional long short-term memory networks (CNN-BiConvLSTMs), to address this problem and establish a deep-learning benchmark. The model is trained to be capable of dealing with arbitrary missing patterns by using the proposed training schedule. Then the performances of the model are evaluated and compared with baseline models for different missing patterns. These baseline models include the nearest neighbor approach, linear interpolation, optical flow methods, and two DNN models three-dimensional CNN (3DCNN) and CNN-ConvLSTM. Experimental results show that the CNN-BiConvLSTM model outperforms all other baseline models. The influence of data quality on interpolation methods is further investigated, and the CNN-BiConvLSTM model is found to be basically uninfluenced by less qualified input weather radar images, which reflects the robustness of the model. Our results suggest good prospects for applying the CNN-BiConvLSTM model to improve the quality of weather radar datasets. (Gao Lihao, Zheng Yu, Wang Yaqiang, Xia Jiangjiang, Chen Xunla, Li Bin, Luo Ming, Guo Yuchen)

6.20 Classification of the circulation patterns related to strong dust weather in China using a combination of the Lamb-Jenkinson and K-means clustering methods

Sand and dust storms (SDSs) cause major disasters in the northern China. They have serious impacts on human health, daily life, and industrial and agricultural production, in addition to threatening the regional ecological environment and social economy. Based on meteorological observational data and the European Centre for Medium-Range Weather Forecasts (ECMWF) ERA5 dataset for spring 2000–2021, we used the Lamb-Jenkinson circulation classification method to classify the three major areas influencing SDSs in the northern China. We also used the K-means clustering method to classify the overall circulation pattern in the northern China. Our results show that the circulation types favoring SDSs in the southern basin of Xinjiang are southwesterly winds (SW), cyclones (C), and anticyclones (A). The circulation types favoring SDSs in the western Inner Mongolia and southern Mongolia are northwesterly winds (NW), northerly winds (N), cyclones (C), and anticyclones (A). The circulation types favoring SDSs in the central Inner Mongolia are northwesterly winds (NW), northerly winds (N), southwesterly winds (SW), and anticyclones (A). The 500 hPa and surface circulation patterns in China can be divided into nine types. Among them, five dominant circulation patterns favor strong SDSs: a cold high-pressure region and cold front (T1), a Mongolian cyclone (T2), a mixed type of Mongolian cyclone and cold front (T3), a thermal depression and cold front (T5), and a cold front (T8). During

2000–2004, the T8 circulation pattern occurred most frequently as the main influencing circulation. From 2005 to 2010, the T3 and T8 circulation patterns dominated. Circulation patterns T1 and T3 dominated during 2011–2015 and 2016–2020, respectively. We analyzed the main circulation patterns for four SDS events occurring in 2021 by combining the Lamb-Jenkinson and k-means methods. The SDS events in 2021 were closest to the T3 circulation pattern and were mainly influenced by Mongolian cyclones and surface cold fronts. The main propagation paths were westerly and northwesterly. (Yi Ziwei, Wang Yaqiang, Chen Wencong, Guo Bin, Zhang Bihui, Che Huizheng, Zhang Xiaoye)

6.21 IPCC AR6对地球气候系统中反馈机制的新认识

气候反馈反映了气候系统内部对外界干扰的适应过程，在很大程度上影响对未来气候变化的预估。本文对政府间气候变化专门委员会（IPCC）第六次评估报告（AR6）中有关气候反馈的内容进行了梳理。相比第五次评估报告（AR5），AR6对云反馈的认识有了较大的提高，尤其是副热带海洋上空低云的反馈。AR6认为在高信度上云反馈参数为正值，即对气候变化起到一种放大效应。不过，云反馈的不确定范围在所有反馈机制中依然是最大的。除了普朗克反馈外，其他反馈机制（包括水汽、温度直减率、地表反照率、云、生物地球物理和非CO_2生物地球化学反馈）均在正值区间或零附近，总体上对气候变化起到放大效应。AR6对总的气候反馈的估计值为–1.16 W/（m^2·℃），5% ～ 95%的置信区间为（–1.81 ～ –0.51）W/（m^2·℃）。随着气候平均态的增暖，气候反馈参数很可能会更靠近正值。（赵树云，孔铃涵，张华）

6.22 IPCC AR6报告解读：地球能量收支、气候反馈和气候敏感度

文中对IPCC第六次评估报告（AR6）第一工作组（WGI）报告的第七章关于地球能量收支、气候反馈和气候敏感度中的重要内容进行了凝练，并简要总结该方面的最新研究成果和结论。评估显示，自工业革命以来，人类活动造成的有效辐射强迫（ERF）为2.72（1.96 ～ 3.48）W/m^2，其中，均匀混合温室气体的贡献为3.32（3.03 ～ 3.61）W/m^2，气溶胶的贡献为–1.1（–1.7 ～ –0.4）W/m^2。净的气候反馈参数为–1.16（–1.81 ～ –0.51）W/（m^2·℃），云仍然是气候反馈整体不确定性的最大来源。平衡态气候敏感度（ECS）和瞬态气候响应（TCR）可用于评估全球平均地表温度对强迫的响应，是衡量全球气候响应的有效手段。ECS和TCR的最佳估计分别为3.0（2.0 ～ 5.0）℃和1.8（1.2 ～ 2.4）℃。（张华，王菲，赵树云）

6.23 尺度自适应大气边界层参数化改进及其对一次海雾的数值模拟研究

大气边界层湍流运动是地球大气运动最重要的能量输送过程之一。当数值模式分辨率接近活跃含能湍涡长度尺度时，湍流运动被部分解析，被称为“灰色区域”，传统的边界层方案不适合此时模式湍流问题的描述。为了提高模式边界层方案在包括“灰色区域”的不同网格尺度上的描述能力，适应不同分辨率模式的需要，在雷诺平均湍流理论基础上，修正Mellor-Yamada-Nakanishi-Niino（MYNN）方案湍流长度尺度参数和非局地湍流的参数表达，改进湿度和温度在“灰色区域”的湍流输送参数化及对网格尺度的自适应能力。利用改进的MYNN尺度自适应方案，分别采用3 km和1 km、1.5 km和0.5 km分辨率单向嵌套网格WRF中尺度模式，对2014年2月26日的一次黄海海雾过程进行模拟试验，检验不同分辨率下改进后的MYNN大气边界层参数化方案的合理性和对海雾的模拟效果。尺度自适应MYNN大气边界层参数化方案在千米级网格尺度上获得稳定、合理的湍流垂直输送计算结果。参照雾区卫星云图，不同分辨率模式低层云水混合比模拟结果具有稳定表现，模拟的雾区分布和温度、湿度等物理量结构都较好地再现了再分析“观测事实”，初步表明该参数化方案有较高的网格尺度自适应能力。（卢绪兰，彭新东）

6.24 次季节波动对青藏高原及其下游东亚季风区降水的影响

影响青藏高原及其下游季风区的次季节波动对我国乃至亚洲地区的洪涝灾害起着不容忽视的作用。本文回顾了近40年来在青藏高原及下游东亚季风区的次季节降水方面取得的进展，主要从影响降水的次季节尺度波动的特征、来源和传播机制对研究成果进行了归纳。回顾表明，青藏高原及下游东亚季风区的降水主要受到来自欧亚大陆及孟加拉湾——南海地区30～60天及准双周次季节波动的强烈影响，同时高原次季节波动能够直接与间接地影响下游季风区降水。本文有助于系统理解高原及下游东亚季风区次季节大气振荡及降水，并基于现有研究提出了该领域值得进一步研究的重点和方向，具有一定的科学意义和参考价值。（杨琳韵，王淑瑜，符淙斌）

6.25 复杂地形对大理地区风场的影响研究——兼论观测、理论和数值模拟配合解答科学问题

引用了一次基于真实地形和大气背景的大涡模拟，阐述了大理大风成因并就如何配合使用观测资料、理论研究和模式模拟来研究小尺度高影响天气现象进行了讨论。通过大涡模拟的方式补充了观测的稀疏和理论的缺失，解答了大理三处地方大风形成的机制。同时又反过来分别对观测、理论和模式发展提出了新要求。（1）背风波是否真实存在，具有何种日变化和季节变化特征，如要提供更加坚实的证据，就必须要有长期的三维流场观测。（2）背风波为什么会有周期性增强伸展和减弱缩短的现象，这要求对这种特殊的大振幅背风波的机理进行研究，而机理研究要求进行理论研究和理想模拟研究，因此本次大涡模拟对模式和理论也提出了新要求。（3）背风波的这种周期性变化会对动量在垂直和水平方向上的分布造成何种影响，其导致的背风波转子会对水汽和热量通量造成何种影响，这要求建立这种大振幅背风波的参数化方案或者使用超高分辨率大范围模拟，这对模式研发也提出了新要求。（薛海乐）

6.26 基于功率谱的风廓线雷达回波强度定标方法

风廓线雷达已在我国得到大范围的业务布网应用，现有业务产品主要为风场信息。为了充分发挥风廓线雷达的作用，获取更多的天气过程信息，该文提出仅使用风廓线雷达返回信号功率谱进行数据定标（DCNP）的方法。使用雷达系统噪声功率对返回信号功率谱单位幅度进行标校计算，基于标校后的雷达探测功率谱分布数据计算回波强度功率谱密度分布、回波强度、大气折射率结构常数。利用2017年北京风廓线雷达、2016年南京风廓线雷达和2018年梅州风廓线雷达观测数据，对我国业务运行的3种主要型号风廓线雷达进行算法评估试验。定标方法的计算结果稳定，风廓线雷达不同探测模式之间的一致性较好。使用每个测站定标结果与相邻天气雷达数据进行比较，风廓线雷达回波强度定标结果与天气雷达也有较好的一致性。DCNP方法与基于信噪比（SNR）的强度计算方法进行比较，与SNR方法相比，DCNP方法定标结果更加稳定可靠。（李丰，阮征，王红艳）

6.27 冬季稳定性降水相态预报研究进展

冬季降水无论对地面的人类生产生活还是对高空飞机航行都可能造成严重灾害，降水相态预报的准确性决定了冬季降水预报的成功。该文较系统地回顾了近几十年来降水相态的预报方法与技术的研究成果。降水相态预报的方法大致分为3类：第1类是基于观测或者数值预报建立的指标或回归方程，其中某些方法高度依赖于数值预报模式的准确率；第2类是数值模式预报微物理方案法和集合预报法；第3类是基于观测和数值预报资料的人工智能预报法。近年来降水相态模式预报产品的预报准确率不断提高，成为降水相态预报中一个重要的产品支撑。但如何将降水相态形成机制的微物理研究成果用于改善数值预报模式降水相态预报的技巧以及利用人工智能等技术提高降水相态预报的准确率等方面还需不断努力。（赵琳娜，慕秀香，马翠平，王秀娟，李缔华）

6.28 中国气象局野外科学试验基地管理服务平台

中国气象局野外科学试验基地管理服务平台是中国气象局气象科学决策支撑应用集约化建设项目的一个子系统，由中国气象科学研究院承担建设。平台开发采用前后端分离技术，通过nginx+tomcat方式有效解耦。前端开发采用vue+ElementUI框架，使用异步调用后端接口方式实现前后端数据交互和呈现。后端采用快速、敏捷的Springboot开发框架，应用tomcat服务实现接口发布，与前端实现数据交互。平台提供了两类管理服务：（1）面向基地工作人员和各级管理人员等内部注册用户，平台提供了基地管理信息、设备信息和数据信息的填报、审核与共享服务。通过预置的数据分析模型，生成分类或综合数据分析图、表，也可按需生成数据查询结果。（2）面向普通用户，平台网站提供了基地综合信息展示、基地短视频宣传和基地全景科普服务。通过浏览器呈现野外试验基地全景的视觉效果。用户使用鼠标控制环视方向，犹如置身现场环境中，在三维窗口中浏览外场试验基地的环境、场景、仪器设备、观测数据和集成的研究成果。2021年该平台完成了与气政通平台的集成，实现了31个基地在线信息填报，多个基地全景虚拟现实展示和短视频制作。（高梅）

7 卫星研究与应用
7 Satellite research and application

7.1 An observational study on the local climate effect of the Shangyi Wind Farm in Hebei Province

Zhangjiakou is an important wind power base in Hebei Province, China. The impact of its wind farms on the local climate is controversial. Based on long-term meteorological data from 1981 to 2018, we investigated the effects of the Shangyi Wind Farm (SWF) in Zhangjiakou on air temperature, wind speed, relative humidity, and precipitation using the anomaly or ratio method between the impacted weather station and the non-impacted background weather station. The influence of the SWF on land surface temperature (LST) and evapotranspiration (ET) using MODIS satellite data from 2003 to 2018 was also explored. The results showed that the SWF had an atmospheric warming effect at night especially in summer and autumn (up to 0.95 ℃). The daytime air temperature changes were marginal, and their signs were varying depending on the season. The annual mean wind speed decreased by 6%, mainly noted in spring and winter (up to 14%). The precipitation and relative humidity were not affected by the SWF. There was no increase in LST in the SWF perhaps due to the increased vegetation coverage unrelated to the wind farms, which canceled out the wind farm-induced land surface warming and also resulted in an increase in ET. The results showed that the impact of wind farms on the local climate was significant, while their impact on the regional climate was slight. (Liu Yonghong, Dang Bing, Xu Yongming)

7.2 Comparing the thermal structures of tropical cyclones derived from Suomi NPP ATMS and FY-3D microwave sounders

Accurate information on the thermal structures of tropical cyclones (TCs) is essential for monitoring and forecasting their intensity and location. In this study, a scene-dependent 1-D variation (SD1DVAR) algorithm is developed to retrieve atmospheric temperature and moisture profiles under all-weather conditions. In SD1DVAR, the background and observation error matrix varies according to the scattering intensity. Especially, the observation error matrix increases in precipitating atmospheres due to a larger uncertainty in the forward operator. With the data from the advanced technology microwave sounder (ATMS) onboard the Suomi National Polar-orbiting Partnership (NPP) satellite, SD1DVAR can retrieve better thermal structures in the storm life cycle than the NOAA Microwave Integrated Retrieval System (MIRS). Comparing with the

aircraft dropsonde observations, the temperature and humidity errors from SD1DVAR are about 3 K and 20%, respectively, whereas those from MIRS are around 4−5 K and 30%, respectively. SD1DVAR is also applied for microwave temperature sounder (MWTS) and microwave humidity sounder (MWHS) onboard the FengYun3D (FY-3D) satellite. The MWTS and MWHS data sets are first combined into a single comprehensive microwave suite (CMWS) data stream and then used to retrieve the hurricane thermal structures. It is shown that the hurricane structure from CMWS is very similar to that from ATMS. However, due to the availability of 118-GHz measurements from the CMWS, the hurricane temperature vertical structure is better resolved, and the humidity error is also reduced by about 5%. (Hu Hao, Han Yang)

7.3 Discrete ordinate adding method (DOAM), a new solver for advanced radiative transfer modeling system (ARMS)

Satellite data assimilation requires a computationally fast and accurate radiative transfer model. Currently, three fast models are commonly used in the numerical weather prediction (NWP) models for satellite data assimilation, including the Radiative Transfer for TIROS operational vertical sounder (RTTOV), community radiative transfer model (CRTM), and advanced radiative transfer modeling system (ARMS). ARMS was initiated in 2018 and is now becoming the third pillar supporting many users in NWP and remote sensing fields. Its radiative transfer solvers (e.g. doubling adding method) are inherited from CRTM. In this study, we propose a discrete ordinate adding method (DOAM) to solve the radiative transfer equation including both solar and thermal source terms. In order to accelerate the DOAM computation, the single scattering approximation is used in the layer with an optical depth less than 10^{-8} or a single scattering albedo less than 10^{-10}. From principles of invariance, the adding method is then applied to link the radiances between the layers. The accuracy of DOAM is evaluated through four benchmark cases. It is shown that the difference between DOAM and the DIScrete ordinate radiative transfer (DISORT) decreases with an increase of stream number. The relative bias of the 4-stream DOAM ranges from −5.03% to 5.92% in the triple layers of a visible wavelength case, while the maximum bias of the 8-stream DOAM is only about 1%. The biases can be significantly reduced by the single scattering correction. Comparing to the visible case, the accuracy of the 4-stream DOAM is much higher in the thermal case with a maximum bias −1.69%. Similar results are also shown in two multiple-layer cases. In the MacBook Pro (15-inch, 2018) laptop, the 2-stream DOAM only takes 1.68 seconds for calculating azimuthally independent radiance of 3000 profiles in the hyper-spectral oxygen A-band (wavelength ranges from 0.757 μm to 0.775 μm), while the 4-stream DOAM takes 4.06 seconds and the 16-stream DOAM takes 45.93 seconds. The time of the 2-, 4- and 16-stream DOAM are 0.86 seconds, 1.09 seconds and 4.34 seconds for calculating azimuthally averaged radiance. DISORT with 16 streams takes 1521.56 seconds and 127.64 seconds under the same condition. As a new solver, DOAM has been integrated into ARMS and is used to simulate the brightness temperatures at the microwave humidity sounder (MWHS) as well as the microwave radiation imager (MWRI) frequencies. The simulations by the DOAM are compared to those by the Doubling Adding method and the accuracy of both solvers shows a general agreement. All the results show that the DOAM is accurate and computational efficient for applications in NWP data assimilation and satellite remote sensing. (Shi Yining, Yang Jun, Weng Fuzhong)

7.4 Impact of hematite on dust absorption at wavelengths ranging from 0.2 to 1.0 μm: An evaluation of literature data using the T-matrix method

Hematite is the absorbing mineral component of dust aerosols in the shortwave spectral region. However, dust shortwave absorption related to hematite suffers from significant uncertainties. In this study, we evaluated available hematite complex refractive index data in the literature on determining the dust effective refractive

index at wavelengths ranging from 0.2 to 1.0 μm using rigorous T-matrix methods. Both spherical and super-spheroidal dust with hematite inclusions were examined to compute the dust optical properties and associated effective refractive indices. We found that the imaginary part of the effective refractive index retrieved from all available hematite complex refractive index data is larger than the measured effective values from Di Biagio et al. The result obtained using the hematite refractive index from Hsu and Matijevic is closest to but approximately two times larger than Di Biagio et al. Our results emphasize the importance of accurate measurements of mineral refractive indices to clarify the dust absorption enigma. (Zong Ruirui, Weng Fuzhong, Bi Lei)

7.5 Impacts of urban spatial layout and scale on local climate: A case study in Beijing

Based on the meteorological data (2009−2018) acquired by high-density automatic meteorological stations (AMSs) in Beijing, the influences of urbanization on urban heat island (UHI), wind, and humidity were described by UHI, wind speed ratio (W_{sr}), and specific humidity ratio (q_r), respectively. For the 37 AMSs in central Beijing, the relationships between UHI, W_{sr}, and q_r and six spatial morphological parameters (building height (BH), building density (BD), floor area ratio, sky view factor, frontal area index, and roughness length (RL)) and two land surface parameters (vegetation coverage and impervious cover) in the range of 200−3000 m from the station were studied. The scale effect of each parameter on local climate was also studied. The results showed that individually, these parameters account for 46.8%−79.6% of the change in UHI, 25.6%−52.8% of the change in W_{sr}, and 25.7%−29.3% of the change in q_r. The impact of spatial morphological parameters on local climate has surpassed that of land surface parameters. The parameters that make the largest contributions to the annual average UHI, W_{sr}, and q_r are RL, BH, and BD, respectively. The optimal influencing ranges of the spatial morphological parameters on UHI, W_{sr}, and q_r are 800−1000 m, 1600−2600 m, and 1200−1400 m, respectively. (Liu Yonghong, Xu Yongming, Weng Fuzhong)

7.6 Influence of the urban spatial layout of central Beijing on the atmospheric humidity field

Based on the meteorological data (2009−2018) acquired by high-density automatic meteorological stations in the central urban area (CUA) of Beijing, this study adopted an urban-rural ratio method to construct a q_r to quantify the impact of urbanization on the spatial and temporal distribution of specific humidity (q). And the urban morphological parameters such as building height (BH), building density (BD), floor area ratio (FAR), sky view factor (SVF), and land surface parameters including vegetation coverage (VC) and impervious coverage (IC) with 500-m spatial resolution in CUA were calculated, and furthermore, the relationships between the six spatial layout parameters and another indicator, urban heat island (UHI) intensity, and q_r were studied. The results show that q of CUA is 81% to 114% of that of the suburbs, and the urban dry island (UDI) effect and urban wet island (UWI) effect coexist throughout the year. The maximum UDI occurs during autumn daytime and the maximum UWI appears at night in winter. The UDI effect is prone to occur in areas with VC < 11%, IC >85%, BH > 15 m, and BD > 24%, while the UWI effect is more likely to appear in areas with VC > 35% and FAR < 0.3. The contributions of the six urbanization parameters to the spatial change of q_r in different time periods are 6.2% to 33.5%, and VC is the largest (33.5%), followed by BD (31.9%) and SVF (29.9%), and the main factor affecting the annual average q_r is BD with the contribution of 18.9%. Compared with the urbanization parameters, the UHI is more important and the contribution to the change of q can be up to 35.7%. The results show that these spatial layout parameters are not sufficient to explain the main change in q, and more other parameters need to be considered. (Liu Yonghong, Xu Yongming, Han Xiuzhen)

7.7 Retrieval of oceanic total precipitable water vapor and cloud liquid water from Fengyun-3D microwave sounding instruments

Fengyun-3D (FY-3D) satellite is the latest polar-orbiting meteorological satellite launched by China and carries 10 instruments onboard. Its microwave temperature sounder (MWTS) and microwave humidity sounder (MWHS) can acquire a total of 28 channels of brightness temperatures, providing rich information for profiling atmospheric temperature and moisture. However, due to a lack of two important frequencies at 23.8 and 31.4 GHz, it is difficult to retrieve the total precipitable water vapor (TPW) and cloud liquid water path (CLW) from FY-3D microwave sounder data as commonly done for other microwave sounding instruments. Using the channel similarity between Suomi National Polar-orbiting Partnership (NPP) advanced technology microwave sounder (ATMS) and FY-3D microwave sounding instruments, a machine learning (ML) technique is used to generate the two missing low-frequency channels of MWTS and MWHS. Then, a new dataset named as combined microwave sounder (CMWS) is obtained, which has the same channel setting as ATMS but the spatial resolution is consistent with MWTS. A statistical inversion method is adopted to retrieve TPW and CLW over oceans from the FY-3D CMWS. The intercomparison between different satellites shows that the inversion products of FY-3D CMWS and Suomi NPP ATMS have good consistency in magnitude and distribution. The correlation coefficients of retrieved TPW and CLW between CMWS and ATMS can reach 0.95 and 0.85, respectively. (Han Yang, Yang Jun, Hu Hao)

7.8 The potential of satellite sounding observations for deriving atmospheric wind in all-weather conditions

Atmospheric wind is an essential parameter in the global observing system. In this study, the water vapor field in Typhoon Lekima and its surrounding areas simulated by the weather research and forecasting (WRF) model is utilized to track the atmospheric motion wind through the Farneback Optical Flow (OF) algorithm. A series of experiments are conducted to investigate the influence of temporal and spatial resolutions on the errors of tracked winds. It is shown that the wind accuracy from tracking the specific humidity is higher than that from tracking the relative humidity. For fast-evolving weather systems such as typhoons, the shorter time step allows for more accurate wind retrievals, whereas for slow to moderate evolving weather conditions, the longer time step is needed for smaller retrieval errors. Compared to the traditional atmospheric motion vectors (AMVs) algorithm, the Farneback OF wind algorithm achieves a pixel-wise feature tracking and obtains a higher spatial resolution of wind field. It also works well under some special circumstances such as very low water vapor content or the region where the wind direction is parallel to the moisture gradient direction. This study has some significant implications for the configuration of satellite microwave sounding missions through their derived water vapor fields. The required temporal and spatial resolutions in the OF algorithm critically determine the satellite revisiting time and the field of view size. The brightness temperature (BT) simulated through community radiative transfer model (CRTM) is also used to track winds. It is shown that the error of tracking BT is generally larger than that of tracking water vapor. This increased error may result from the uncertainty in simulations of brightness temperatures at 183 GHz. (Zhang Yijia, Hu Hao, Weng Fuzhong)

7.9 北京城市空间形态对热岛分布影响研究

在城市尺度上探究城市空间形态布局对城市热岛（UHI）影响研究，对于城市规划中通风环境改善、生态宜居城市建设具有重要意义。以北京为例，利用2009—2018年高密度自动气象站逐小时气温资料和2018年NPP/VIIRS夜光卫星资料，分析了UHI时空分布特征；利用2017年1∶2000基础地理信息和Landsat8卫星资料，开展了北京主城区建筑高度（BH）、建筑密度（BD）、建筑高度标准差（BSD）、容积率（FAR）、迎风截面积指数（FAI）、粗糙度长度（RL）、天空开阔度（SVF）、城市分数维（FD）

等8个空间形态参数和植被覆盖度（VC）、不透水盖度（IC）、反照率（AB）等3个陆表参数的提取，并在城市尺度上开展了这些参数与UHI之间空间相关性及对UHI变化影响研究。结果显示：2009—2018年北京主城区年均、四季以及夜晚02:00 UHI均存在一个较为固定的形态，年均、春、夏、秋、冬、白天14:00和夜晚02:00UHI分别为1.81 ℃、1.50 ℃、1.43 ℃、2.16 ℃、2.17 ℃、0.48 ℃和2.77 ℃；8个空间形态参数在一年中大部分时段与UHI存在明显空间相关性，这种相关性在冬季强于其他季节，在夜晚02:00强于白天14:00，排名前三的分别为SVF、FAR和BD。空间形态参数已超越陆表参数成为UHI变化的重要驱动因子，11种参数对UHI变化的单独贡献为13.7% ～ 63.7%，其中夏季、冬季和全年时段贡献最大的空间形态参数分别是BD（43.7%）、SVF（63.7%）和SVF（45.4%），贡献最大的陆表参数分别是VC（42.6%）、AB（57.1%）和VC（45.3%）；夏季、冬季和全年时段多个参数对UHI变化的综合贡献分别为51.4%、69.1%和55.3%，主导要素分别为BD、SVF和BD。（刘勇洪，徐永明，张方敏）

7.10 卫星微波大气遥感温湿廓线及应用进展

简要回顾了星载微波探测仪对大气温湿廓线遥感应用技术进展，对统计回归反演方法、一维变分反演方法以及最新的场景自适应反演方法的发展进行了介绍。最后通过介绍新型微波探测仪搭载平台，对可能的新反演产品和技术进行展望。（胡皓，翁富忠）

气候与气候变化
Climate and Climate Change

气候与气候变化研究进展
Progress in Research on Climate and Climate Change

1 次季节至季节变化特征与机理
1 Features and mechanism of the subseasonal to seasonal variability

1.1 Diversity of the coupling wheels in the East Asian summer monsoon on the interannual time scale: Challenge of summer rainfall forecasting in China

Two types of three-dimensional circulation of the East Asian summer monsoon (EASM) act as the coupling wheels determining the seasonal rainfall anomalies in China during 1979–2015. The first coupling mode features the interaction between the Mongolian cyclone over North Asia and the South Asian high (SAH) anomalies over the Tibetan Plateau at 200 hPa. The second mode presents the coupling between the anomalous low-level western Pacific anticyclone and upperlevel SAH via the meridional flow over Southeast Asia. These two modes are responsible for the summer rainfall anomalies over China in 24 and 7 out of 37 years, respectively. However, the dominant SST anomalies in the tropical Pacific, the Indian Ocean, and the North Atlantic Ocean fail to account for the first coupling wheel's interannual variability, illustrating the challenges in forecasting summer rainfall over China. (Zhu Congwen, Liu Boqi, Xu Kang, Jiang Ning, Liu Kai)

1.2 Seasonal evolution of anomalous rainband over East China regulated by sea surface temperature anomalies in the Northern Hemisphere

A seasonal evolution of rainbands over East China is evident and shows remarkable year-to-year variations. The present study identifies two dominant interannual modes of the seasonal evolution of rainbands over East China from 1981 to 2018: 1) the sudden change pattern, in which the anomalous rainfall changes abruptly from boreal spring to summer, especially over South China; and 2) the northward migration pattern, which shows a gradual poleward migration of the anomalous rainband over East China with the East Asian summer monsoon (EASM). Both of them are regulated by the sea surface temperature anomalies (SSTAs) in the Northern Hemisphere from spring to summer. In the sudden change pattern, the SSTAs in the Pacific modulate spring rainfall over South China via the ENSO-EASM teleconnection. By contrast, the North Atlantic SSTAs change the midlatitude wave train and modify summer rainfall over South and North China, in conjunction with the anomalous tropical circulation due to the Indian Ocean SSTAs. In the northward migration pattern, the North Pacific SSTAs alter spring rainfall over South China by varying the low-level western North Pacific subtropical high and the zonal land-sea thermal contrast over East Asia. Afterward, the ENSO-like SSTAs induce a Pacific-Japan teleconnection and shift the anomalous rainband northward to the Yangtze-Huai River and North China in summer. The seasonal switch of the SSTAs regulating these two modes is physically linked from boreal spring to summer. This mechanism provides potential seasonal predictability of the seasonal evolution of the anomalous rainband over East China. (Liu Boqi, Zhu Congwen, Jiang Ning, Guo Li)

1.3 Subseasonal-to-seasonal predictability of onset dates of South China sea summer monsoon: A perspective of meridional temperature gradient

The onset of the South China Sea summer monsoon (SCSSM) has traditionally been ascribed to El Niño-southern oscillation (ENSO) on an interannual time scale, but the two do not correspond in some years. The present study applies harmonic analysis on the meridional temperature gradient (MTG) in the mid-upper troposphere over the South China Sea (SCS) and decomposes the onset process to be a slow-varying seasonal cycle and transient subseasonal component. The ENSO-related air temperature anomaly in the southern SCS provides seasonal predictability of SCSSM onset by a stable and robust relationship between ENSO and MTG seasonal cycle. However, in the northern SCS, the MTG is regulated by an intraseasonal oscillation (ISO) of extratropical air temperature with a significant 10–30-day period. This ISO originates over the western Tibetan Plateau (TP) and then propagates eastward and gets enhanced by anomalous diabatic heating due to spring rainfall anomaly over South China as a result of subseasonal thermal forcing of TP. When the ISO arrives to the north of the SCS, it directly changes the tropospheric temperature to modulate the MTG. Meanwhile, the upper-level circulation associated with the ISO alters themeridional potential vorticity advection and pumping effect, followed by the anomalous low-level westerly wind andmonsoon convection over the SCS. The SCSSM onset is evidently disrupted from its seasonal cycle when this ISO is more active. Since the independence of its intensity from ENSO, this extratropical ISO over TP and South China provides additional subseasonal predictability of the onset dates of the SCSSM. (Liu Boqi, Zhu Congwen)

1.4 Regulation of the subseasonal variability of winter rainfall in South China by the diversity of El Niño-southern oscillation

Winter precipitation over South China tends to increase with enhancement of the 10–30-day intraseasonal oscillation (ISO) during El Niño-southern oscillation (ENSO) events from 1981 to 2017. This study shows that, in contrast with central Pacific El Niño and La Niña events, the 10–30-day ISO of rainfall particularly intensify during eastern Pacifc (EP) El Niño events. The seasonal evolution of the anomalous circulation, indicated as the annual cycle (AC), bridges the slow-varying ENSO and the transient 10–30-day ISO of winter rainfall over South China. As to the AC component, the EP El Niño events not only enhance the Philippine Sea anticyclone to provide a wetter low-level background over South China, but also develop the mid-latitude cyclone and westerly winds in the upper-level over East Asia by changing tropical convection. The moisture over South China further increases due to the low-level wind convergence on a 10–30-day timescale. In the upper troposphere, the AC component of the anomalous westerly redistributes the 10–30-day relative vorticity by modulating the subseasonal mid-latitude wave train to strengthen the positive vorticity advection and ascending motion over South China. Their collaboration amplifes the subseasonal variance of winter precipitation in situ. By contrast, the AC component of the upper level circulation at mid-latitudes is not well organized in other ENSO subsets, corresponding to their lack of infuence on the ISO variability of rainfall over South China. (Guo Li, Zhu Congwen, Liu Boqi)

1.5 Combined impacts of sea surface temperature in tropical Pacific and North Atlantic oceans on the winter rainfall in southern China under decadal background

The sea surface temperature anomalies (SSTAs) in the tropical Pacific (TP) and North Atlantic (NA) are both important factors regulating the winter rainfall over the southern China (SC). Our results show the combined impact of SSTAs exhibitd an offset effect before 1985, after a decadal transition period, the two SSTAs patterns formed an additive effect on the interannual timescale after 1995. These distinct impacts of the TP and NA result in the southward shift of the winter rainfall variability, which is associated with the decadal

change of the TP and NA. Both the background modes in TP and NA show a phase transition during the period 1985–1995, accompanied by the interannual variations of the SSTAs in two ocean basins before 1985 and after 1995. Before 1985, the canonical El Niño-related southerly winds of the anticyclone over the western North Pacific transport sufficient water vapour and enhance rainfall in SC. While the concurrent dipole NA SSTA-related wave train propagates to Eurasia, causing a cyclone and divergence of water vapour fluxes suppressing the local rainfall. After 1995, the El Niño-related warm SSTAs move westward and strengthen the rainfall anomalies in the Yangtze River basin. Meanwhile, a tripole mode of SSTAs replaces the dipole counterpart in NA, resulting in the anomalous cyclonic circulation over South Asia with more rainfall in the south edge of SC. The decadal changes of the TP and NA mode combination could affect the seasonal distribution and prediction of China winter rainfall. (Yu Minjie, Jiang Ning, Zhu Congwen, Su Jingzhi)

1.6 Atmospheric circulation regime causing winter temperature whiplash events in North China

Temperature whiplash events, which are characterized by a rapid transition between persistent and extreme warm and cold conditions, usually damage natural systems and human communities and can even have catastrophic impacts. To more deeply understand the severe winter temperature whiplash events in North China, in this study, the atmospheric circulation regime that is primarily responsible for such events is investigated based on Japanese 55-year reanalysis data. The results show that the drastic temperature shifts during winter temperature whiplash events are closely correlated with the southeastward propagation of the dipolar anomalous temperature in the middle and lower troposphere over the Eurasian continent. The dipolar structure of the temperature signals features an initial cold anomaly over the West Siberian Plain and a warm anomaly over East Asia during negative (extremely warm to extremely cold) events and the opposite pattern during positive (extremely cold to extremely warm) events. This dipolar temperature anomaly is tightly coupled with the southeastward development of an upper-level wave-like anomalous circulation pattern over the Eurasian continent, which is associated with a Rossby wave originating near the Kara Sea during negative events and in the northern Europe during positive events. Based on the calculation of the temperature budget, the drastic temperature drop during negative events is mainly dominated by anomalous meridional temperature advection, and adiabatic heating due to vertical motion is negligible. In contrast, adiabatic heating due to sinking plays a dominant role in the drastic temperature increase during positive events, while anomalous meridional temperature advection also makes a substantial contribution to the temperature increase. (Ma Shuangmei, Zhu Congwen)

1.7 Subseasonal forecast barrier of the North Atlantic oscillation in S2S models during the extreme Meiyu rainfall event in 2020

Enhanced predictability of high-impact weather events is a Subseasonal to Seasonal (S2S) Prediction Project priority. In early summer 2020, a record-breaking heavy rainfall event occurred over the Yangtze River valley during the Meiyu season (June and July). Here we evaluate the S2S model forecast performance concerning the summer 2020 extreme Meiyu event over the Yangtze River valley. Our results show all operational S2S models exhibit fluctuating high-low-high forecast skill patterns during this three-stage Meiyu event, determined by different dominant circulations. In particular, the poor midlatitude circulation forecast (low trough over the northern China) in the North Atlantic oscillation (NAO) negative phase, with relative more contribution than that of the low-latitude circulation (western North Pacific subtropical high and South Asian high), decreases the model forecast skill for Meiyu rainfall in early-mid July. The prediction barrier of the NAO pattern and its downstream response, via the eastward-propagating wave train, jointly decrease the rainfall forecast skill during the NAO active negative period. Therefore, the skillful model prediction of the active summer NAO could help predict mei-yu events in the East Asian summer monsoon, suggesting further

model improvements to the S2S forecasting of summertime mid-latitude variations are urgently needed. (Yan Yuhan, Liu Boqi, Zhu Congwen, Lu Riyu, Jiang Ning, Ma Shuangmei)

1.8 Subseasonal predictability of South China Sea summer monsoon onset with the ECMWF S2S forecasting system

Accurate forecasting of the South China Sea summer monsoon (SCSSM) onset is critical for water resource management in the rainy season across East Asia. The present work evaluates the skill of the ECMWF subseasonal-to-seasonal (S2S) forecasting system in predicting SCSSM onset dates using a hindcast experiment. The model provides accurate predictions of the SCSSM onset date 10 days in advance. The predictability mainly arises from the sea surface temperature anomaly (SSTA) in the northern Indian Ocean and central-eastern tropical Pacific, which usually coincides with moderate and extreme decaying El Niño, thus creating windows of opportunity for SCSSM onset forecasting. The model can reasonably reproduce the SCSSM-related SSTA and its induced atmospheric teleconnections. However, when anomalous Ural blocking influences the mid-high latitudes, the ECMWF model forecasts of the SCSSM onset are trapped in the synoptic timescale because of the limited ability of the model to consider blocking in forecasting. (Yan Yuhan, Liu Boqi, Zhu Congwen)

1.9 Annual cycle of East Asian precipitation simulated by CMIP6 models

Annual cycle is fundamental in the East Asian monsoon (EAM) systems, profoundly governing the spatiotemporal distribution of the East Asian rainfall. The present study identified the dominant modes of the annual cycle in the East Asian rainfall based on the fourier harmonic analysis and the empirical orthogonal function (EOF) decomposition. We evaluated the performance of the first two leading modes (i.e., EOF-1 and EOF-2) in historical experiments (1979–2014) of the 21 released climate models of the Coupled Model Intercomparison Project phase 6 (CMIP6). Comparing with the observation, although the CMIP6 models yield the essential fidelity, they still show considerable systematic biases in the amplitude and phase of the annual cycle, especially in East and South China. Most models exhibit substantial phase delays in the EOF-2 mode of the annual cycle. Some specific models (BCC-ESM1, CanESM5, and GFDL-CM4) exhibiting better performance could capture the observed annual cycle and the underlying physics in climatology and interannual variability. The limited fidelity of the EOF-2 mode of the EAM annual cycle primarily hinders the monsoon variability simulation and thus the reliable future projection. Therefore, the dominant modes of the EAM annual cycle act as the evaluate benchmark in the EAM modelling framework. Their improvement could be one possible bias correction strategy for decreasing the uncertainty in the CMIP6 simulation of the EAM. (Yan Yuhan, Zhu Congwen, Liu Boqi, Jiang Song)

1.10 Relations between the quasi-biweekly oscillation over the East Asian monsoon region and the East Asian tropical monsoon depressions

An empirical orthogonal function analysis was applied to 34 years of anomalous daily 10–20 day filtered outgoing longwave radiation data to determine the north-westward propagating mode of quasi-biweekly oscillations (QBWOs) over tropical East Asia during boreal summer. The centres of active QBWO convection coincided with positive potential vorticity (PV) anomalies at 500 hPa and cyclonic gyres at 850 hPa, whereas the centres of suppressed convection were superimposed upon negative PV anomalies and anticyclonic gyres. These circulations formed an inclined northwest-southeast wave train. The vertical dynamic and thermodynamic structures of the QBWO mode evince two centres of PV at 500 and 750 hPa, respectively, and an almost upright structure in the troposphere up to 300 hPa. The QBWO's convective cell has a warm-over-cold structure in the troposphere. These features have several similarities to East Asian tropical monsoon

depressions (EAMDs), implying a close relationship between the north-westward propagating mode of QBWOs and EAMDs. Further investigation indicates that EAMDs are prone to appear in the region of deep convection and move north-westward with the QBWO circulation. The westernmost position of the western Pacific subtropical high (WPSH), which is linked to the QBWO phase, strongly influences the route of EAMDs. An EAMD generated in the easterly winds to the south of WPSH moves westward under the influence of the horizontal adiabatic advection of PV. More eastward-moving and turning EAMDs appear when WPSH weakens and retreats eastward due to enhancement of QBWO convection over the South China Sea (SCS) and western North Pacific. Most EAMDs reach peak intensity when moving over the SCS, and show a strong relation to the vigorous convection. However, there is no significant relation between the QBWO convection and the points of disappearance of the EAMDs. (Li Jingyi, Wen Min, Wang Zunya, Hu Yi)

1.11 Trends in the differences between homogenized ground surface temperature and surface air temperature in China during 1961–2016 and its possible causes

Based on the latest series of homogenized ground surface temperature (GST) and surface air temperature (SAT) data for China, this study performed a detailed analysis of the trend of the differences between the two homogenized series during 1961–2016. The differences, referred to as surface–air temperature differences (SATDs) in this study, were separately averaged by month, season, and year. The long-term and spatial changes in the trends of SATDs were investigated. Moreover, interdecadal trend breakpoints were identified to understand the characteristics of trends in fluctuation. The possible influences of precipitation, Pacific decadal oscillation (PDO) and global warming on SATDs were also analyzed. The results showed that during the 12 months of a year, only three months, March, April, and May, exhibited increasing trends of station-averaged monthly mean SATDs while the other nine months exhibited decreasing trends. In addition, the station-averaged annual and seasonal mean SATDs of summer, autumn, and winter all showed significant decreasing trends, while the spring mean SATDs showed a significant increasing trend. The spatial distribution pattern of the linear trends of monthly, seasonal and annual SATDs in meteorological stations indicated that SATDs had more obviously increasing trends in the northern regions than in the southern regions of China. The trends of station-averaged monthly mean SATDs (except for April) and station-averaged seasonal and annual mean SATDs experienced interdecadal breakpoints, fully indicative of obvious interdecadal fluctuations with temporal complexity among China's SATD trends. By the regression analysis of monthly STADs against simultaneous precipitation, as well as the comparative analysis of their linear trends, we found that both amount of precipitation and the change of precipitation type have important influences on SATDs. The results of convergent cross mapping analysis also revealed the causal effect of precipitation on SATDs. (Shi Xiaohui, Chen Jinqiu)

1.12 Remote forcing effect of sea surface temperatures in the northern tropical Atlantic on tropical cyclone genesis over the western North Pacific in July

In July 2020, neither genesis nor landfall of typhoons occurred in the western North Pacific (WNP). This was the first time that the "no-typhoon" phenomenon had occurred since 1949. This study analyzed the variation in the tropical cyclone genesis frequency (TCGF) in the WNP in July over the past 40 years, including the corresponding atmospheric background circulation and the possible influence of tropical sea surface temperature (SST). The results revealed that the eastward and northward location of the western Pacific subtropical high (WPSH), the deepened and eastward expanded tropical monsoon trough (TMT) in the WNP, the active convection in the main body of TMT, the weakened southwest water vapor transport of the East Asian summer monsoon, as well as the strengthened and eastward expanded equatorial westerly wind were conducive to the tropical cyclone genesis in the WNP in July. Furthermore, we used regression analysis to

explore the possible impact of tropical SSTs. We found that the relatively high SSTs in the northern tropical Atlantic (NTA) in June and July triggered a cyclonic circulation over the tropical East Pacific and NTA, resulting in strong upward motion. The airflow subsidence in the tropical central Pacific then caused the WPSH to extend westward and the easterly airflow on the south side of WPSH to strengthen, which weakened the WNP monsoon trough. Besides, the influence of warming NTA SSTs could be conveyed to the Indian Ocean and indirectly induce the enhancement of WPSH. Such a series of the large-scale circulation variations were not favorable for tropical cyclone genesis in the WNP. As a result, the TCGF was relatively low in July. Thus, one of the causes of the July 2020 "no-typhoon" phenomenon in the WNP could be the remote forcing effect of SST in NTA. (Shi Xiaohui, Fang Yin)

1.13 Diverse inter-annual variations of winter Siberian high and link with Eurasian snow in observation and BCC-CSM2-MR coupled model simulation

An observational study illustrates that three distinct modes of winter Siberian high variability exist in observations at the inter-annual time scale. In this paper, we compare the connection between these diverse Siberian high variation modes with pre-autumn and simultaneous Eurasian snow cover in an observation and BCC-CSM2-MR coupled climate model run under pre-industrial conditions from the CMIP6 project. Our analyses indicate that the inter-annual variation of observed Siberian high modes do have a connection with pre-autumn and simultaneous Eurasian snow cover anomalies, but the BCC-CSM2-MR coupled climate model does not capture the observed diverse Eurasian snow–Siberian high relationships well. The BCC-CSM2-MR coupled climate model can partly reproduce the observed Siberian high variation modes, but fail to capture the spatial distribution and statistics of boreal fall and winter Eurasian snowpack, which is a key facet of simulated diverse Siberian high variability irrespective of the influence of Eurasian snow cover. (Sun Chenghu, Zuo Zhiyan, Shi Xiaohui)

1.14 Effect of upper-level air temperature changes over the Tibetan Plateau on the genesis frequency of Tibetan Plateau vortices at interannual timescales

Tibetan Plateau vortices (TPVs) are important rainfall producers over the Tibetan Plateau in summer and can also influence wide areas east of the Tibetan Plateau when emigrating from the plateau. The effects of the variations in air temperature over the Tibetan Plateau on the genesis frequency of TPVs at interannual timescales are explored in this work to understand the interannual variations in TPVs and the resultant precipitation. The results indicate that the interannual variations in the genesis frequency of TPVs are significantly related to that in the air temperature at 250 hPa over the Tibetan Plateau. The upper-level air temperature affects the genesis of TPVs by modulating the large-scale circulations at 200 hPa. In warm (cold) years, an anomalous high (low) at 200 hPa is observed over the eastern Tibetan Plateau and central China, and a strong (weak) westerly jet is found north of the Tibetan Plateau. The upper-level westerly jet is considered to have a direct influence on TPVs. Impact of 250-hPa air temperature over the Tibetan Plateau on the westerly jet is further explained from two perspectives. First, the air temperature at 250 hPa regulates the thermal wind between 250 and 200 hPa, thereby affecting the wind at 200 hPa. Second, the air temperature at 250 hPa changes the geopotential height gradient at 200 hPa north of the Tibetan Plateau, which results in variations in the westerly jet there. Consequently, more TPVs are generated over the Tibetan Plateau in warm years, and vice versa for cold years. (Li Lun, Zhang Renhe)

1.15 Regionally different precipitation trends over the Tibetan Plateau in the warming context: A perspective of Tibetan Plateau vortices

Precipitation over the Tibetan Plateau (TP) significantly affects both the local ecology and the downstream

water resources. In this study, it is found that there exists an increasing precipitation trend over the northern TP but not in the southern TP, which is interpreted from the perspective of the activities of Tibetan Plateau vortices (TPVs). In the context of recent warming over the TP, the increasing rate of genesis frequency of TPVs over the northern TP is remarkably larger than that over the southern TP, which is responsible for different precipitation trends in the northern and southern TP, respectively. That is, the most significant warming over the TP appears in the upper troposphere, which intensifies the 200 hPa westerly jet north of the TP, hereby produces more favorable conditions for the genesis of TPVs over the northern TP than over southern TP, and contributes to regional difference in precipitation trends. (Li Lun, Zhang Renhe, Wen Min, Lyu Junmei)

1.16 Roles of the Tibetan Plateau vortices in the record Meiyu rainfall in 2020

Meiyu rainfall in June–July of 2020 hit the Yangtze-Huaihe River basin, and the precipitation at lots of observational stations broke the records, inducing severe disasters there. Tibetan Plateau vortices (TPVs) generated over the Tibetan Plateau are local major rainfall triggers. In previous knowledge, TPVs can affect the rainfall in the eastern China, only after emigrating from the Tibetan Plateau. In this work, roles of TPVs in the record Meiyu are revealed, implying that the effects of TPVs may be underestimated previously. Firstly, TPVs dying out over the Tibetan Plateau may be transformed into troughs and continue to move eastward, influencing the rainfall in Yangtze-Huaihe River basin. Secondly, southwest vortices, the important rainfall producers in China, tend to be generated and maintained when TPVs are located over eastern plateau. The results give extended knowledge on the effects of TPVs, which are beneficial for the rainfall prediction in the eastern China. (Li Lun, Zhu Congwen, Zhang Renhe, Liu Boqi)

1.17 Climatological intraseasonal oscillation in the middle-upper troposphere and its effect on the northward migration of the East Asian westerly jet and rain belt over eastern China

Using daily atmospheric circulation data for 1981–2010, we identify the climatological intraseasonal oscillation (CISO) in the mid-upper troposphere and reveal its critical role in anchoring the Meiyu season to the period from mid-June to mid-July and the rainfall episode of northeastern China to begin in late July. Wavelet analysis shows a significant 20–90-day period in the climatological 200- and 500-hPa zonal winds during boreal summer, indicating the existence of the zonal wind CISO in the mid-upper troposphere. The leading mode of zonal wind CISO features a dipole pattern along the coast of East Asia controlled by convection over the southeastern China-western North Pacific (SC-WNP). In mid-June, suppressed convection over the SC-WNP induces the negative phase of intraseasonal Pacific-Japan pattern, leading to the strong anticyclone with a poleward tilt with height to dominate over the WNP. Consequently, more moisture are transported to the middle and lower reaches of the Yangtze River Valley (YRV), and the mid-tropospheric (upper-tropospheric) East Asian westerly jet (EAWJ) is shifted north of 32°N (36°N), which further increases the YRV rainfall through enhancing warm advection and upper-tropospheric divergence, thus facilitating the initiation of Meiyu season. In mid-July, active convection occupies the SC-WNP instead, with the reversed circulation pattern terminating the Meiyu season. In late July, active convection shifts from the equator to the tropical western Pacific, leading to the second mode of zonal wind CISO, which is characterized by a quasi-barotropic Mongolian anticyclone in the mid-upper troposphere. The upper-tropospheric EAWJ is further shifted to 45°N, displacing the induced upper-tropospheric divergence northward, thus initiating the rainfall episode of the northeastern China. (Li Jianying, Liu Boqi, Mao Jiangyu)

1.18 The influence of atmospheric intraseasonal oscillations on terrestrial biospheric CO_2 fluxes in Southeast China forest

With its strong carbon sequestration capacity and significantly expanding trend, forest over Southeast

China (SEC) is an important biospheric carbon sink. As intraseasonal oscillation (ISO) is a remarkable variability of the East Asian summer monsoon—the major climate system influencing the carbon exchange of SEC forest, the objective of this study is to examine the impact of atmospheric intraseasonal oscillation on CO_2 fluxes in SEC forest based on daily CO_2 fluxes and meteorological data. Significant 15–60-day ISO of CO_2 fluxes is identified in SEC forest during May–August of 1980–2013. The 15–60-day ISO of net ecosystem exchange between atmosphere and biosphere mainly results from that of gross primary productivity (GPP), with the explained variances greater than 50% over most SEC forest areas. Due to the high drought-resistance of SEC forest, the 15–60-day ISO of its GPP is controlled primarily by local solar radiation, which is in turn associated with the northward-propagating atmospheric ISO. Suppressed (active) convection anomaly and the thermally induced anomalous anticyclone (cyclone) on its northwestern side initiate from the southern South China Sea and then propagate northward to SEC coherently in the form of a Rossby wave-like pattern. Decreased (increased) cloud cover associated with the suppressed (active) convection anomaly leads to more (less) solar radiation reaching the SEC forest canopy, thus promoting (impairing) forest productivity. (Li Jianying, Jong-Seong Kug, Mao Jiangyu)

1.19 Synergistic effect of the 25–60-day tropical and midlatitude intraseasonal oscillations on the persistently severe Yangtze floods

Significant 25–60-day intraseasonal oscillations (ISOs) in rainfall over the middle-lower reaches of the Yangtze River (MLYR) are found for eight summers during 1979–2020. These 25–60-day ISOs of MLYR rainfall account for 66.7% of persistently severe floods (PSFs) during 1979–2020, indicating their major role in inducing PSFs and the potential for extended-range forecasting of PSFs. The 25–60-day ISO in MLYR rainfall results from the synergistic effect of tropical and midlatitude ISOs. During the eight identified summers, more barotropic energy is transferred from summer-mean to 25–60-day circulation, thus forming a midlatitude ISO wave train, which cooperates with the tropical ISO in triggering twin vertical cells. Phase locking of ascending branch from the vertical cell induced by the tropical ISO with that from the reversed vertical cell triggered by the midlatitude ISO brings about the wet phase of 25–60-day ISO of MLYR rainfall. (Li Jianying, Zhai Panmao, Mao Jiangyu, Song Lili)

1.20 2019年4—6月云南持续性高温天气的大气环流异常成因

2019年4—6月云南省发生了历史罕见的持续性极端高温天气，并引发了严重气象干旱。本文利用1961—2019年逐日温度和大气再分析等资料以及CESM-LE（Community Earth System Model Large Ensemble Project）计划模式模拟结果，分析了历史同期云南极端高温天气发生的环流特征，探讨了2019年云南破纪录持续性高温的成因。历史极端高温日的合成分析表明，云南地区对流层上层显著异常反气旋伴随的强下沉异常和到达地表太阳辐射增加，是引发该区域极端高温天气的主要成因。该异常反气旋的形成主要源自北大西洋经东欧平原、西西伯利亚平原向东亚传播的高纬度罗斯贝波和经北非、黑海、伊朗高原向东亚传播的中纬度罗斯贝波之间的相互作用。2019年极端高温的强度和与之相应异常反气旋出现自1961年以来的最强。外强迫导致的增暖对2019年极端暖异常强度的贡献约为37.51%，同时对类似2019年以及更强极端暖事件发生概率的贡献为56.32%，内部变率对该事件也具有重要贡献。2019年4—6月北极涛动（AO）和ENSO事件分别处于历史极端负位相和暖位相。一方面，在AO强负位相影响下，极地上空深厚的位势高度正异常向南伸至东欧平原，有利于高纬度波列和云南上空的反气旋异常增强。另一方面，ENSO事件暖位相加强了西北太平洋异常反气旋环流，令西北太平洋副热带高压增强西伸至我国内陆地区，维持了云南上空反气旋异常。两者的共同作用，造成了2019年4—6月云南上空持续的深厚异常反气旋，云南地区继而出现持续性极端高温事件。（马双梅，祝从文，刘伯奇）

1.21 北太平洋异常高压对京津冀地区PM2.5污染影响分析

以2021年3月2—5日京津冀地区持续4 d的$PM_{2.5}$重污染过程为例，使用$PM_{2.5}$质量浓度格点资料、城市空气质量指数（AQI）资料、NCEP再分析资料、海温资料以及HYSPLIT轨迹追踪模式，重点分析了北太平洋异常高压对京津冀地区$PM_{2.5}$污染的影响。结果表明：（1）500 hPa北太平洋异常暖性高压系统的稳定维持是京津冀地区污染发生的有利环流形势，当该地区处于此异常高压后部并受偏南风控制时，不利于该地区污染物扩散。（2）低层850 hPa异常高压系统引导来自西北太平洋暖湿气流向京津冀地区输入使低层增温增湿，不利于污染物垂直扩散，并使污染物快速吸湿增长。（3）北太平洋异常高压与北太平洋中西部海温呈正相关，与赤道中东太平洋海温呈现负相关。北太平洋异常高压配合京津冀地面南风对该地区空气污染的发生具有一定的指示意义。（陈运，蒋宁，朱莉莉）

1.22 次季节至季节气候预测业务支撑与决策服务

气候所次季节至季节（S2S）研究团队先后参加国家气候中心、东北区域气候中心、国家海洋局海洋环境预报中心、水利部黄河委员会和北京冬奥气象中心等部门组织的全国和区域/流域气候预测会商共计17次，并提供预测意见，服务效果得到相关部门认可。基于自主研发的统计预测方法（CAMS-ASPS）和气科院动力预测系统（CAMS-CSM），在3月份不仅准确给出今年夏季我国北方地区和长江流域降水明显偏多、黄河流域防洪压力大的预测结果，还准确预测出初夏东北地区降水异常偏多、气温偏低的气候格局，为国家和区域汛期防灾减灾工作提供了重要参考。（刘伯奇、鄢钰函、祝从文、蒋宁、马双梅、苏京志）

在决策气象服务方面，S2S团队针对2021年国内、外高影响天气气候事件，先后开展了多次复盘工作，包括：春季北方沙尘暴天气、2020/2021年冬季气温冷暖急转、6月东北冷涡异常活跃、“7·21”郑州暴雨、盛夏北美极端高温热浪、华北超长汛期和降水异常以及美国超级龙卷事件。以院专报形式上报决策服务材料4份。气候与气候变化研究所获得2021年度中国气象局“重大气象服务先进集体”称号。（刘伯奇、蒋宁、马双梅、鄢钰函、鲁萌萌、祝从文、孙丞虎、齐艳军）

2 气候特征与气候变化
2 Climate characteristics and climate change

2.1 Anthropogenic emissions and urbanization increase risk of compound hot extremes in cities

Urban areas are experiencing strongly increasing hot temperature extremes. However, these urban heat events have seldom been the focus of traditional detection and attribution analysis designed for regional to global changes. Here we show that compound (day-night sustained) hot extremes are more dangerous than solely daytime or nighttime heat, especially to female and older urban residents. Urban compound hot extremes across the eastern China have increased by 1.76 days per decade from 1961 to 2014 with fingerprints of urban expansion and anthropogenic emissions detected by a stepwise detection and attribution method. Their attributable fractions are estimated as 0.51 (urbanization), 1.63 (greenhouse gases) and −0.54 (other anthropogenic forcings) days per decade. Future emissions and urbanization would make these compound events two to five times more frequent (the 2090s versus 2010s), leading to a threefold-to-sixfold growth in urban population exposure. Our findings call for tailored adaptation planning against rapidly growing health threats from compound heat in cities. (Wang Jun, Chen Yang, Zhai Panmao)

2.2 Detectable anthropogenic changes in daily-scale circulations driving summer rainfall shifts over eastern China

Wetting in the south while drying in the north during the last few decades constitutes the well-known

"southern flood-northern drought" (SFND) precipitation pattern over the eastern China. The fingerprint of anthropogenic influence on this dipole pattern of regional precipitation trends has not been confirmed, especially for forced changes in relevant dynamics at the synoptic scale. Using a process-based approach involving model experiments both with and without anthropogenic inputs, it is demonstrated that the occurrences of daily circulation patterns (CPs) governing precipitation over the eastern China during 1961−2013 have been altered by human influence. Due to anthropogenic forcing, CPs favoring SFND have become more likely to occur at the expense of CPs unfavorable to SFND. Regression analysis shows that changes recorded in the occurrence of CPs from the factual simulations could explain a large part of the precipitation trends over the eastern China. CP frequencies driven by purely natural forcing do not reproduce this dipole pattern nor the inferred magnitude of precipitation trends over the eastern China. These results suggest that human influence has played a critical role in shaping the contrasting north-south precipitation trends. (Zhou Baiquan, Zhai Panmao)

2.3 Detectable intensification of hourly and daily scale precipitation extremes across East China

Detecting long-term changes in precipitation extremes over monsoon regions remains challenging due to large observational uncertainty, high internal variability at the regional scale, and climate models' deficiency in simulating monsoon physics. This is particularly true for East China, as illustrated by limited yet controversial detection results for daily scale precipitation extremes and the lack of detection analysis on hourly scale extremes there. Relying on high-quality gauge observations, two complementary techniques are used to detect the footprint of anthropogenic forcings in observed changes in both hourly and daily scale precipitation extremes across East China. Results show that, scaled with global mean surface temperature during 1970–2017, the regional-scale intensification nearly doubles the Clausius-Clapeyron rate (C-C; 6.5% 8C21) for the wettest 10 h in the period and almost triples the C-C rate for the top 10 heaviest daily precipitation extremes. The intensification at both time scales, as well as the resulting increase in frequency, is discernibly stronger and more widespread than expected due to random internal variability. This not only lends supports to the model-based detection of forced trends for daily scale precipitation extremes, but it also suggests that anthropogenic warming has already been intensifying hourly scale precipitation extremes in this monsoon region. The magnitude and detectability of observed changes arise primarily from systematic intensification of non-tropical-cyclone-related precipitation extremes in response to the past warming. (Chen Yang, Li Wei, Jiang Xiaoling, Zhai Panmao, Luo Yali)

2.4 Hourly extreme precipitation changes under the influences of regional and urbanization effects in Beijing

Short duration extreme precipitation has devastating impacts on city area. Local urbanization effects, superimposed upon regional climate change, complicate examination of long-term changes in short duration precipitation extremes in urban areas. Based on high-quality rain gauge observations of summer time hourly precipitation in Beijing region over 1977–2013, this study reveals that despite the general drying tendency for North China, the urban area of Beijing has experienced more hourly precipitation extremes (HPE) than the suburban area since 2004, coinciding with the surge in the growth of urban built-up areas. These hourly urban precipitation extremes are increasingly inclined to occurring during night-time, especially during 18:00 LST to 02:00 LST (UCT+8). On the one hand, the amplified urban heat inland effect, which was more significant at night-time, seems to have facilitated formation of more intense small scale thermal-low and resultant ascending branch; on the other hand, it has favoured in establishing unstable stratification in the lower level. This possible mechanism explains the preference of HPE in urban areas during night-time and climate change diversity under the influence of megacity superposition. (Yuan Yufeng, Zhai Panmao, Chen Yang, Li Jian)

2.5 Detectable increases in sequential flood-heatwave events across China during 1961−2018

Traditional univariate analysis on weather and climate extremes failed to consider temporally compounding events and the resulting cascading impacts. A case in point is a sequence of flood and heatwave within a week, which slows recovery and amplifies damages. We show that across China, floods and heatwaves seldom occurred serially within seven days in the past, but after 2000 the probability is five-to-ten times higher in the southern, northwestern and northeastern sectors. It is the significant increase in heatwaves that alters the clustering of independent extremes, and facilitates the emergence of sequential extremes. Typhoon-participating sequential extremes have also increased significantly in frequency in both inland and coastal areas, with the fastest rate at around 200% per decade registered within the 30°–35°N latitudinal band. The observed increases in sequential flood-heatwave events are discernibly stronger and more widespread than what would be expected from pure random variability, implying a detectable role of anthropogenic forcings. (Chen Yang, Liao Zhen, Shi Yan, Tian Yangmei, Zhai Panmao)

2.6 Fine-scale characteristics of summer precipitation over Cang Mountain

Fine-scale characteristics of summer precipitation over Cang Mountain, a long and narrow mountain with a quasi-north–south orientation in Southwest China, are studied using station and radar data. Three kinds of rainfall processes are classified according to the initial stations of regional rainfall events (RREs) by utilizing minute-scale rain gauge data. RREs initiating in the western part of Cang Mountain exhibit eastward evolution and tend to reach their maximum rainfall intensity on the mountaintop. The results indicate differences in the precipitation evolution characteristics between short-duration (1–3 h) and long-duration (at least 6 h) events. Short-duration events begin farther from the mountaintop and then propagate eastward, whereas long-duration events remain longer around the mountaintop. RREs that initiate from the eastern part of Cang Mountain display westward propagation and frequently reach their maximum rainfall intensity over the eastern slope of the mountain. Among them, short-duration events tend to propagate farther west of Cang Mountain at high speeds, but the westward evolution of long-duration events is mainly confined to the eastern part of Cang Mountain. For mountaintop-originated RREs, precipitation quickly reaches its maximum intensity after it starts and then continues for a long time around the mountaintop during the period from late afternoon to early morning. These findings provide references for the fine-scale prediction of precipitation evolution in small-scale mountainous areas. (Zhang Mengke, Li Jian, Li Nina)

2.7 Application of an improved analog-based heavy precipitation forecast model to the Yangtze–Huai River Valley and its performance in June–July 2020

Precipitation extremes, such as the record-breaking Meiyu characterized by frequent occurrences of rainstorms that resulted in severe flooding over the Yangtze-Huai River Valley (YHRV) in June–July 2020, are always attracting considerable interest, highlighting the importance of improving the forecast accuracy at the medium-to-long range. To elevate the skill in forecasting heavy precipitation events (HPEs) with both long and short durations, the key influential systems based analog model (KISAM) was further improved and brought into operational application in 2020. Verification and comparison of this newly adapted analog model and ensemble mean forecasts from the ECMWF at lead times of up to 15 days were carried out for the identified 16 HPEs over the YHRV in June–July 2020. The results demonstrate that KISAM is advantageous over ECMWF ensemble mean for forecasts of heavy precipitation $\geqslant 25$ mm day^{-1} at the medium-to-long (6–15-day) lead times, based on the traditional dichotomous metrics. At short lead times, ECMWF ensemble mean outperforms KISAM due largely to the low false alarm rates (FARs) benefited from an underestimation of the frequency of heavy precipitation. However, at the medium-to-long forecast range, the large fraction of misses induced by

the high degree of underforecasting overwhelms the fairly good FARs in the ECMWF ensemble mean, which partly explains its inferiority to KISAM in terms of the threat score. Further assessment on forecasts of the latitudinal location of accumulated heavy precipitation indicates that smaller displacement errors also account for a part of the better performance of KISAM at lead times of 8–12 days. (Zhou Baiquan, Zhai Panmao, Niu Ruoyun)

2.8 Investigation of the effects of dynamic vegetation processes on global climate simulation using the NCEP GFS and SSiB4/TRIFFID

To investigate the effects of dynamic vegetation processes on numerical climate simulation, two experiments are conducted globally by integrating the National Centers for Environmental Prediction global forecast system (GFS) coupled with a biophysical model, simplified simple biosphere model (SSiB) version 2 (referred to as GFS/SSiB2) and with a biophysical and dynamic vegetation model, SSiB version 4/TRIFFID (referred to as GFS/SSiB4/TRIFFID) from 1948 to 2008. By assessing GFS/SSiB4T/TRIFFID and GFS/SSiB2 results against satellite-derived leaf area index (LAI) and albedo, as well as observed land surface temperature and precipitation, we identify the effects of dynamic vegetation processes on the simulations of precipitation, near-surface temperature and the surface energy budget at monthly and annual scales. The results show that compared to the GFS/SSiB2, the temporal correlation coefficients between globally averaged monthly simulated LAI and the GIMMS/GLASS LAI in the GFS/SSiB4/TRIFFID increase from 0.31/0.29 (SSiB2) to 0.47/0.46 (SSiB4). Meanwhile, the correlation coefficients between simulated and observed monthly mean near-surface air temperature increase from 0.58 (over Africa), 0.47 (over Southeast Asia) and 0.50 (over South America) to 0.66, 0.55 and 0.58 respectively. While the correlation coefficients between model-simulated and observed monthly mean precipitation increase from 0.31 (over Africa), 0.41 (over East Asia) and 0.21 (over Australia) to 0.38, 0.47 and 0.24 respectively. The most improvement occurs over arid and semi-arid areas. The spatial-temporal variability and changes in vegetation and ground surface albedo modeled by GFS with dynamic vegetation model are more consistent with observations, which contribute to the surface energy and water balances, and in turn improve the annual variations in simulated regional temperature and precipitation. The dynamic vegetation processes have the greatest influences on the temporal and spatial changes of latent heat fluxes. This study demonstrates that the dynamic vegetation processes in the Earth system model are capable to improve the climate mean status simulation significantly. (Zhang Zhengqiu, Xue Yongkang, Zhai Panmao)

2.9 Changes in summer persistent precipitation over the middle-lower reaches of the Yangtze River and associated atmospheric circulation patterns

Persistence is an important property of precipitation and its related impacts. However, changes in persistent precipitation and the possible underlying mechanisms in the context of global warming have not yet been discussed in sufficient depth. In this study, the changes in persistent precipitation in summer and related atmospheric circulation patterns over the middle-lower reaches of the Yangtze River (MLRYZR)—a typical monsoon region frequently hit by consecutive rainfall events—are analyzed based on observed daily precipitation and NCEP/NCAR reanalysis data from 1961 to 2019. The results reveal that persistent precipitation events (PPs) tend to happen in a more persistent way, with increased frequency and intensity in the MLRYZR region. Mechanism analyses show that persistent precipitation has happened along with simultaneous enhancement of some large-scale atmospheric circulation patterns, including the Lake Baikal blocking (BB), the Okhotsk Sea blocking (OB), and the western Pacific subtropical high (WPSH). Such enhanced anomalous circulation patterns could persistently reinforce the convergence and supply of water vapor in the MLRYZR region, contributing to the increase in PPs in this region. Based on the above results,

we are able to offer some new insights into the long-term changes in precipitation structure and the possible causes. This study is also expected to support attribution studies on regional precipitation changes in the future. (Yu Rong, Zhai Panmao)

2.10 Divergent responses of ecosystem water use efficiency to drought timing over Northern Eurasia

Warming has resulted in increases in frequency, intensity and/or duration of droughts in most land regions over the globe. Nevertheless, knowledge on how ecosystem water use efficiency (WUE) responds to extreme drought stress and whether the responses are affected by drought timing is still limited. In this study, we examined the changes in ecosystem WUE under extreme drought years over Northern Eurasia during 1982–2011 and further assessed WUE responses to droughts with separate groupings designed to characterize the timing of extreme drought stress. We found that drought timing indeed influenced the responses of ecosystem WUE under extreme drought years. Negative impacts of extreme drought stress during the dry season on ecosystem WUE were more remarkable than those from extreme drought stress during the wet season. Particularly, impacts of droughts on ecosystem carbon-water interactions differed among ecosystem types due to the specific hydrothermal condition of each biome. The information provided by our analyses plays an importance role in identifying water use strategies of terrestrial vegetation in response to drought stress and will help improve our understanding and predictions of the response of ecosystem WUE to global environmental change. (Huang Mengtian, Zhai Panmao, Piao Shilong)

2.11 Performance of the CRA-40/Land, CMFD, and ERA-Interim datasets in reflecting changes in surface air temperature over the Tibetan Plateau

We analyzed the spatiotemporal variations in surface air temperature and key climate change indicators over the Tibetan Plateau during a common valid period from 1979 to 2018 to evaluate the performance of different datasets on various timescales. We used observations from 22 in-situ observation sites, the CRA-40/Land (CRA) reanalysis dataset, the China meteorological forcing dataset (CMFD), and the ERA-Interim (ERA) reanalysis dataset. The three datasets are spatially consistent with the in-situ observations, but slightly underestimate the annual mean surface air temperature. The daily mean surface air temperature estimated by the CRA, CMFD, and ERA datasets is closer to the in-situ observations after correction for elevation. The CMFD shows the best performance in simulating the annual mean surface air temperature over the Tibetan Plateau, followed by the CRA and ERA datasets with comparable performances. The CMFD is relatively accurate in simulating the daily mean surface air temperature over the Tibetan Plateau on an annual scale, whereas both the CRA and ERA datasets perform better in summer than in winter. The increasing trends in the annual mean surface air temperature over the Tibetan Plateau from 1979 to 2018 reflected by the CRA dataset and the CMFD are 0.5 ℃ $(10year)^{-1}$, similar to the in-situ observations, whereas the warming rate in the ERA dataset is only 0.3 ℃ $(10year)^{-1}$. The trends in the length of the growing season derived from the in-situ observations, the CRA, CMFD, and ERA datasets are 5.3, 4.8, 6.1, and 3.2 day $(10year)^{-1}$, respectively. Our analyses suggest that both the CRA dataset and the CMFD perform better than the ERA dataset in modeling the changes in surface air temperature over the Tibetan Plateau. (Yang Jiaxi, Huang Mengtian, Zhai Panmao)

2.12 Achieving Paris Agreement temperature goals requires carbon neutrality by middle century with far-reaching transitions in the whole society

The concept of carbon neutrality is much emphasized in IPCC Spatial Report on Global Warming of 1.5 ℃ in order to achieve the long-term temperature goals as reflected in Paris Agreement. To keep these goals within reach, peaking the global carbon emissions as soon as possible and achieving carbon neutrality

are urgently needed. However, global CO_2 emissions continued to grow up to a record high of 43.1 Gt (CO_2) during 2019, with fossil CO_2 emissions of 36.5 Gt (CO_2) and land-use change emissions of 6.6 Gt (CO_2) . In such case, the global carbon emissions must drop 32 Gt (CO_2) (7.6% per year) from 2020 to 2030 for the 1.5 ℃ warming limit, which is even larger than the COVID-induced reduction (6.4%) in global CO_2 emissions during 2020. Recently, China has announced scaling up its national commitments, aiming to peak its CO_2 emissions before 2030 and achieve carbon neutrality before 2060. Achieving these goals requires rapid and far-reaching transitions in the whole society. On the one hand, deeper emissions reduction in all sectors includes decarbonization of energy, electrification, increasing share of renewables, energy efficiency, sustainable land management, decarbonization of transport, reducing food loss and waste, as well as behavior and lifestyles changes. On the other hand, possible actions by removing CO_2 from the atmosphere involves enlarging land and ocean net carbon sink, CO_2 removal technologies (such as bioenergy with carbon capture and storage), and CO_2 capture, utilization and storage technologies, but should be caution for their scales and tradeoffs. (Huang Mengtian, Zhai Panmao)

2.13 Change in drought conditions and its impacts on vegetation growth over the Tibetan Plateau

Understanding climate change as well as its impacts on vegetation growth over the Tibetan Plateau has important implication for ecosystems. This study investigated changes in drought conditions and their impacts on vegetation growth over the Tibetan Plateau. The results reveal that the precipitation in growing season (May−September) shows a significant increase over most parts of the central and eastern Tibetan Plateau during 1961−2019. Consequently, drought conditions have generally relieved except in the south and northeast where precipitation has decreased. Combining analyses of gridded-dataset-derived drought indices with vegetation indices during 1982−2015, vegetation improvement in most regions of the Plateau is mainly due to lessened drought conditions. Noticeably, vegetation degradation is also found in part of the southern Tibetan Plateau mainly resulting from drought enhancement. This study is expected to provide scientific basis for understanding of change in drought condition and its impacts on vegetation over different regions of TP under global warming background. (Wang Chenpeng, Huang Mengtian, Zhai Panmao)

2.14 Growing threats from unprecedented sequential flood-hot extremes across China

When multiple extremes occur in rapid sequence, their impacts cascade to cause disproportionate damages. However, the prevalence of univariate definitions and inability to identify low-likelihood events in short observations/simulations leave the knowledge on sequential extremes sparse. Leveraging two initial-condition large ensembles, we project future changes in historically unprecedented sequential flood-hot extremes in China. Results show that despite dozens of 1 in 50-year floods and hot extremes in more than 2000 years of historical simulations, their sequenced occurrence within a week has no historical precedent. This out-of-ordinary configuration is projected to be increasingly possible across China, with earlier emergence and larger frequency increases expected in Southwest and Southeast China. The direction, spatial extent, and magnitude of projected changes in unprecedented sequential extremes cannot be explained by internal variability alone, though it has the potential to modulate human-caused changes in emergence timing and magnitude. (Liao Zhen, Chen Yang, Li Wei, Zhai Panmao)

2.15 Investigating the influence of synoptic circulation patterns on regional dry and moist heat waves in North China

Summer (June–August) heat waves in North China are found to be either primarily dry or moist, based on surface meteorological observations. This study characterizes synoptic circulation patterns (i.e., 500 hPa geopotential height) using the self-organizing map (SOM) method and investigates the influence of synoptic

circulation patterns on these two types of heat waves. Results show that regional dry and moist heat waves are associated with different circulation patterns, which significantly modulate the advection of water vapor within the low-level atmosphere, and soil moisture and evaporation conditions at the surface. Regional dry heat waves are associated with times when a continental high pressure ridge is situated to the northwest of North China, and when the northern edge of the western North Pacific subtropical high (WNPSH) is south of 30°N. Regional moist heat waves are associated with a northward shift of the WNPSH. Long term variations of dry and moist heat wave occurrences correlated significantly with the occurrences of their associated circulation patterns at 0.38 (p = 0.02) and 0.71 (p = 0.00), respectively. On sub-seasonal time scales, the dominant heat wave type transforms from dry in June to moist in late July, which is in accordance with summer north–south WNPSH shifts. In addition, training the SOM with absolute geopotential height results in representative circulation patterns that are closely related to surface heat wave conditions in North China rather than the anomaly field, which mixes different circulation regimes. (An Ning, Zuo Zhiyan)

2.16 Changing structures of summertime heatwaves over China during 1961–2017

Despite the prevalence of artificial separation of daytime and nighttime hot extremes, they may actually co-occur or occur sequentially. Considering their potential lead-lag configuration, this study identified an entire heatwave period as consecutive days with either daytime or nighttime hot extremes and investigated the changes of the prevalence and sequence of daytime and nighttime hot extremes during heatwaves over China from 1961 to 2017. It was found that the majority (82%) of heatwaves were compound heatwaves that had both daytime and nighttime hot extremes exceeding the 90th percentile-based thresholds, while only 7% (11%) were purely daytime (nighttime) heatwaves that contained only daytime (nighttime) hot extremes. During the entire periods of compound heatwaves, daytime hot extremes usually occurred one day or a few days before nighttime hot extremes, which was in accordance with the daily variations in radiation and meteorological conditions, such as the increasing surface humidity and cloud cover, and decreasing solar radiation during the entire heatwave periods. From 1961 to 2017, compound heatwave numbers exhibited the sharpest increase with a statistically significant trend of 0.44 times per decade, in contrast to an insignificant trend of 0.00 times per decade for purely daytime heatwaves and a significant trend of 0.09 times per decade for purely nighttime heatwaves. Within the compound heatwave periods, hot nights were starting earlier and ending later, and numbers of concurrent daytime-nighttime hot extremes increased significantly at 0.20 days per decade. In particular, urban areas were not only subject to increasingly more frequent and longer compound heatwaves, but also to more occurrences of concurrent daytime-nighttime hot extremes with more serious impact. This study provides instructions for researchers to customize and select appropriate heatwave indices. (An Ning, Zuo Zhiyan)

2.17 Evaluating boreal summer circulation patterns of CMIP6 climate models over the Asian region

Our confidence in future climate projection depends on the ability of climate models to simulate the current climate, and model performance in simulating atmospheric circulation affects its ability of simulating extreme events. In this study, the self-organizing map (SOM) method is used to evaluate the frequency, persistence, and transition characteristics of models in the Coupled Model Intercomparison Project phase 6 (CMIP6) for different ensembles of daily 500 hPa geopotential height (Z500) in Asia, and then all ensembles are ranked according to a comprehensive ranking metric (MR). Our results show that the SOM method is a powerful tool for assessing the daily-scale circulation simulation skills in Asia, and the results will not be significantly affected by different map sizes. Positive associations between each two of the performance in frequency, persistence and transition were found, indicating that a good ensemble of simulation for one metric is good for the others. The r10i1p1f1 ensemble of CanESM5 best simulates Z500 in Asia comprehensively, and

it is also the best of simulating frequency characteristics. The MR simulation of the highest 10 ensembles for the western North Pacific subtropical high (WNPSH) and the South Asia high (SAH) are far better than those of the lowest 10. Such differences may lead to errors in the simulation of extreme events. This study will help future studies in the choice of ensembles with better circulation simulation skills to improve the credibility of their conclusions. (Bu Lulei, Zuo Zhiyan, An ning)

2.18 气候变化科学方面的几个最新认知

IPCC第六次评估报告（AR6）第一工作组报告主要从以下几个方面的进展提升了我们对气候系统变化、气候变化原因以及预估未来气候系统变化等方面的认知，对过去气候变化及其与人类活动的关系有了更加清晰、可靠的认识。综合多重证据评估指出，全球气候正经历着前所未有的变化；包括极端事件在内的归因进展已把人类活动对气候系统影响的认识从大气圈扩展到水圈、冰冻圈和生物圈，进一步强化了人类活动影响全球和区域气候的认识；有关区域气候变化信息的内容更加丰富，与各行业和敏感地区的气候变化影响联系更加紧密，使这些信息能更好地为气候变化风险评估和气候变化区域适应提供支持；气候模式和约束预估方法的发展以及对气候敏感度认识的深化，减少了未来不同排放情景下全球地表温度（GST）、海平面上升和海洋热含量的变化预估的不确定性。这份最新报告对我国提升气候变化研究水平和防灾减灾应对能力具有十分重要的指导意义。（翟盘茂，周佰铨，陈阳，余荣）

2.19 IPCC第六次气候变化评估中的气候约束预估方法

得益于第五次评估报告（AR5）以来约束预估研究的迅速发展，观测约束成为政府间气候变化专门委员会（IPCC）第一工作组（WGI）第六次评估报告（AR6）提升对未来预估约束的证据链中的重要一环。IPCC 第一工作组第六次评估报告首次利用包括根据历史模拟温度升高幅度得到的观测约束、多模式预估以及第六次评估报告中更新的气候敏感度在内的多条证据链来约束全球地表温度未来变化的预估，减小了多模式预估的不确定性。文中回顾并介绍了IPCC 第一工作组第六次评估报告中涉及的几种主要观测约束方法（多模式加权方法、基于归因结论的约束方法（ASK方法、萌现约束方法）及其应用情况。在IPCC 第一工作组第六次评估报告以及很多针对不同区域不同变量的预估研究中，观测约束方法均显示出了订正模式误差、改善模式预估的潜力。相比而言，目前中国在观测约束预估方面的研究还不多，亟待加强观测约束方法研究以及在中国区域气候变化预估中的应用，为中国应对气候变化的政策制定和适应规划提供更丰富、不确定性更小的未来气候信息。（周佰铨，翟盘茂）

2.20 IPCC第六次评估报告中的《图集》

决策者和公众正在越来越多地关注气候变化带来的影响，而这需要更加丰富的、区域尺度上的当前和未来气候状况的精细信息。《图集》与IPCC第六次评估报告第一工作组报告中其他章节相协调，评估区域气候变化的观测、归因、预估的基本信息，并建立了在线交互图集系统。《图集》包含图集章节和交互图集两部分，图集章节基于新的区域划分，评估了各区域的气候变化，重点关注地表温度和降水的观测趋势、归因以及预估的未来变化。交互图集是AR6 WGI报告的一个新组成部分，基于观测、全球（CMIP5和CMIP6）和区域（CORDEX）模式数据，以互动地图的形式提供观测和预估时间段的气候变化和归因的综合信息。（李建，陈昊明）

2.21 关于复合型极端事件的新认识和启示

近年来，极端天气气候事件频繁发生，且常常是由多种事件交织形成的复合型极端事件。为了更好地认识复合型极端事件，IPCC AR6 基于现有的新证据评估了复合型极端事件的最新研究成果，并取得一些新认识：扩展了有关复合型极端事件的定义，重点围绕高温干旱复合型极端事件、复合洪水和

野火，评估了复合型极端事件的变化特征，探讨了复合型极端事件多因子之间的依赖性，对人类活动的影响进行了归因分析并给出了未来可能的变化。这些评估结果丰富了对复合型极端事件的基本认识，但根据现有的评估可以看出目前在复合型极端事件发生发展机理认识方面还存在不足；同时，未来仍需进一步完善跨学科跨部门跨区域研究，加强对复合型极端事件形成机理、预估及其对生态系统、经济社会影响风险的评估，提高对区域气候变化的适应能力。（余荣，翟盘茂）

2.22 基于CMIP6模式优化集合平均预估21世纪全球陆地生态系统总初级生产力变化

利用国际耦合模式比较计划第六阶段（CMIP6）中18个地球系统模式总初级生产力（GPP）模拟数据，基于传统的多模式集合平均（MME）和可靠集合平均方法（REA），在4个未来情景（SSP1-2.6，SSP2-4.5，SSP3-7.0和SSP5-8.5）下预估了21世纪全球陆地生态系统GPP的变化量，并分析了GPP变化的驱动因子。研究结果表明：在4个未来情景下，基于REA方法预估的全球陆地生态系统年GPP在未来时期（2068—2100年）比历史时期（1982—2014年）分别增长了（14.85 ± 3.32）、（28.43 ± 4.97）、（37.66 ± 7.61）和（45.89 ± 9.21）Pg C，其增量大小和不确定性都明显低于MME方法。在4个情景下，大气CO_2浓度增长对GPP变化的贡献最大，基于REA方法计算的贡献占比分别为140%、137%、115%和75%；除了SSP5-8.5（24%）外，其他情景下升温均导致全球陆地生态系统GPP降低（–42%、–37%、–16%），部分抵消了CO_2施肥效应的正面贡献。温度的影响存在纬度差异：升温在低纬度地区对GPP有负向贡献，在中高纬度地区为正向贡献。降水和辐射变化对GPP变化的贡献相对较小。（黄禄丰，朱再春，黄萌田）

2.23 气候动力诊断和分析系统设计与应用

气候动力诊断和数值模拟是认识气候变化规律、提高短期气候预测与科学决策服务水平的重要手段。但基于气候模拟的动力诊断技术在气候预测业务中还未得到广泛应用，缺乏支撑科研成果转化为业务应用的中试平台。为此，通过集成多种现代计算机通信协议、可视化编辑和气象数值计算等技术，研发可视化交互气候动力诊断和分析系统（CDDAS），以促进气候模拟的动力诊断技术在气候业务中的广泛应用。该系统具有结构开放、诊断方法集成度高、方便易用等特点，包括数据更新备份、气候动力诊断、多模式数值模拟、结果分析 4 个功能模块，并设计了一种远程交互控制脚本语言，为用户二次开发提供语言环境，可实现本地客户端、服务器端和超级计算机三者交互通信控制可视化管理。该系统使用便捷，目前已在国家级业务和科研单位获得应用，在气候异常成因分析、气候预测和气候决策服务中可显著提高工作效率。（张正秋，祝从文，苏京志，刘伯奇，蒋宁，陈昊明）

2.24 IPCC工作支撑

气候变化团队成员圆满完成本年度IPCC第一工作组（WGI）联合主席技术支撑工作任务，通过网络会议、亲自出访等多种方式，为IPCC WGI第六次评估报告（AR6）的撰写、评审、批准、发布及后续科学传播活动以及IPCC综合报告的准备、撰写等相关工作提供技术支持。团队成员作为副主编、主要作者、技术支持等角色参与《中国气候与生态环境演变：2021》《青藏高原气候变化、影响与应对》《新疆气候变化科学评估报告》等国内气候变化评估报告的编写工作中。（翟盘茂，黄萌田，陈阳，余荣）

2.25 气候变化决策服务

气候变化团队分别围绕气候变化的影响与应对、极端天气气候事件的变化及风险等方面展开专题研究，并报送多份决策服务材料，受到高度重视，获得良好的决策支撑效果。（翟盘茂，陈阳，余荣，黄萌田，廖圳）

3 气候模式研发
3 Climate model development

3.1 The CMIP6 historical simulation datasets produced by the climate system model CAMS-CSM

This paper describes the historical simulations produced by the Chinese Academy of Meteorological Sciences (CAMS) climate system model (CAMS-CSM), which are contributing to the Coupled Model Intercomparison Project phase 6 (CMIP6). The model description, experiment design and model outputs are presented. Three members' historical experiments are conducted by CAMS-CSM, with two members starting from different initial conditions, and one excluding the stratospheric aerosol to identify the effect of volcanic eruptions. The outputs of the historical experiments are also validated using observational data. It is found that the model can reproduce the climatological mean states and seasonal cycle of the major climate system quantities, including the surface air temperature, precipitation, and the equatorial thermocline. The long-term trend of air temperature and precipitation is also reasonably captured by CAMS-CSM. There are still some biases in the model that need further improvement. This paper can help the users to better understand the performance and the datasets of CAMS-CSM. (Rong Xinyao, Li Jian, Chen Haoming, Su Jingzhi, Hua Lijuan, Zhang Zhengqiu, Xin Yufei)

3.2 Seasonal prediction skills in the CAMS-CSM climate forecast system

The seasonal prediction skills in the CAMS-CSM (the acronym stands for the Chinese Academy of Meteorological Sciences climate system model) climate forecast system is evaluated with a set of retrospective forecast experiments during the period of 1981−2019. The CAMS-CSM, which has been registered for the Coupled Model Intercomparison Project phase 6 (CMIP6), is an atmosphere-ocean-land-sea ice fully coupled general circulation model. The assimilation scheme used in the forecast system is the 3-dimentional nudging, including both the atmospheric and oceanic components. The analyses mainly focus on the seasonal predictable skill of sea surface temperature, 2-m air temperature, and precipitation anomalies. The analyses revealed that the model shows a good prediction skill for the SST anomalies, especially in the tropical Pacific, in association with El Niño-southern oscillation (ENSO) events. The anomaly correlation coefficient (ACC) score for ENSO can reach 0.75 at 6-month lead time. Furthermore, the extreme warm/cold Indian Ocean dipole (IOD) events are successfully predicted at 3- and even 6-month lead times. The whole ACC of IOD events between the observation and the prediction can reach 0.51 at 2-month lead time. There are reliable seasonal prediction skills for 2-m air temperature anomalies over most of the Northern Hemisphere, where the correlation is mainly above 0.4 at 2-month lead time, especially over the East Asia, North America and South America. However, the seasonal prediction for precipitation still faces a big challenge. The source of precipitation predictability over the East Asia can be partly related to strong ENSO events. Additionally, the anomalous anticyclone over the western North Pacific (WPAC) which connects the ENSO events and the East Asian summer monsoon (EASM) can be well predicted at 6-month lead time. (Liu Bo, Su Jingzhi, Ma Libin, Tang Yanli, Rong Xinyao, Li Jian, Chen Haoming, Liu Boqi, Hua Lijuan)

3.3 AMIP simulations of a global model for unified weather-climate forecast: Understanding precipitation characteristics and sensitivity over East Asia

A global model formulation for unified weather-climate forecast is evaluated, with emphasis on the climate simulations at typical hydrostatic resolutions. The internal sensitivity is explored by considering different dynamical configurations (resolution, solver type, transport scheme). After a basic assessment of the

global mean climate, a detailed analysis of precipitation characteristics is extended to East Asia. The model shows a reasonable mean state, seasonal variation, frequency-intensity structure, and diurnal phase time. The artificial rainfall around the steep slopes of the Tibetan Plateau can be improved through choices in the dynamical configuration. The regional features characterized by "afternoon versus nocturnal-to-early-morning peaks" are properly distinguished. The hourly climatic features are comparable to super-parameterized CAM5. Different dynamical configurations demonstrate unique sensitivities related to underling physical mechanisms, which are studied from the perspective of the diurnal cycle for three representative regions. Over South China, the higher-resolution models decrease the weak-precipitation while increase intense rainfall, thus reducing the dry biases. This is contributed by enhanced grid and sub-grid scale motions associated with daytime convection progression. Over the central western China, the variable-resolution model better simulates the eastward propagating episodes characterized by a transition from convective to stratiform rainfall along the eastern slope of the Plateau. This reduces the positive biases at the high topography of the Plateau and alleviates the negative biases at the lower foot. Over the central eastern China, the model replicates the dominant role of large-scale governing factors in regulating the early morning rainfall peaks, and produces stratiform heating patterns. (Zhang Yi, Yu Rucong, Li Jian, Li Xiaohan, Rong Xinyao, Peng Xindong)

3.4 Evaluation of CMIP6 HighResMIP models in simulating precipitation over Central Asia

The High Resolution Model Intercomparison Project (HighResMIP) experiment within the Coupled Model Intercomparison Project phase 6 (CMIP6), for the first time, has provided an opportunity to evaluate the performance of climate models over complex topographies. Based on the HighResMIP's historical simulations of atmospheric general circulation models, the performances of global high-resolution models, with a horizontal resolution finer than 50 km, in representing precipitation over Central Asia were evaluated using rain gauge observation datasets. All the models successfully reproduce the large precipitation regions that are located over the mountainous areas and the northern Central Asia. However, nearly all the models overestimate precipitation frequency over Central Asia and large overestimations of precipitation amount and frequency are located over the mountainous areas. Although the HighResMIP multi-model ensemble mean performs better than all individual models at simulating the spatial pattern of precipitation frequency, it is inferior to HadGEM3-GC31-HM and ECMWF-IFS-HR at simulating that of precipitation amount. The simulation performance exhibits remarkable regional differences. Over the Qilian Mountains, the relationship between precipitation and elevation is totally captured by climate models. In contrast, over the Tianshan Mountains, the models fail to simulate the decrease in precipitation frequency after elevation higher than the maximum precipitation elevation. Most models successfully reproduce the annual cycle shape of precipitation amount over the southern Central Asia, Qilian Mountains and Tianshan Mountains, but fail to reproduce it over the northern Central Asia. More than half of the high-resolution GCMs have a reduced bias relative to the corresponding low-resolution GCMs. The performances of most high-resolution GCMs in simulating precipitation pattern are well over the Tianshan Mountains. (Li Liangliang, Li Jian, Yu Rucong)

3.5 Convection-permitting modelling improves simulated precipitation over the central and eastern Tibetan Plateau

The Tibetan Plateau (TP) plays an essential role in influencing the global climate, and precipitation is one of its most important water-cycle components. However, accurately simulating precipitation over the TP is a long-standing challenge. In this study, a convection-permitting model (CPM, with 4 km grid spacing) that covers the entire TP was conducted and compared to two mesoscale models (MSMs, with model horizontal resolutions of 13 and 35 km) over the course of a summer. The results showed that the two MSM shave notable wet biases over the TP and can overestimate the summer precipitation by more than 4.0 mm day^{-1}

in some parts of the Three Rivers Source region. Moreover, both MSMs have more frequent light rainfall; increasing horizontal resolution of the MSMs alone does not reduce the excessive precipitation. Further investigation reveals that the MSMs have a spurious early-afternoon rainfall peak, which can be linked to a strong dependence on convective available potential energy (CAPE) that dominates the wet biases. Herein, we highlight that the sensitivity of CAPE to surface temperatures may cause the MSMs to have a spurious hydrological response to surface warming. Users of climate projections should be aware of this potential model uncertainty when investigating future hydrological changes over the TP. In comparison, the CPM removes the spurious afternoon rainfall and thus significantly reduces the wet bias simulated by the MSMs. In addition, the CPM also better depicts the precipitation frequency and intensity, and is therefore a promising tool for dynamic downscaling over the TP. (Li Puxi, Kalli Furtado, Zhou Tianjun, Chen Haoming, Li Jian)

3.6 Reevaluating the impacts of oceanic vertical resolution on the simulation of Madden-Julian oscillation eastward propagation in a climate system model

The upper ocean plays a critical role in determining the Madden-Julian oscillation (MJO) characteristics through modulating the tropical atmosphere-ocean interaction. By increasing the oceanic vertical resolution, its impacts on the MJO eastward propagation are discussed in this study by using a climate system model. With a refined vertical resolution in the upper ocean, warmer surface ocean and shallower mixed layer depth are produced in the tropics, which induces associated atmospheric changes as the response to the ocean feedbacks. Enhanced November–April-mean vertically-integrated specific humidity is found around the equatorial region with the increased vertical resolution, which strengthens the zonal and meridional moisture gradients. The lead-lag correlation of MJO precipitation demonstrates that the simulated MJO eastward propagation is improved with increased oceanic vertical resolution by improving the simulations of convective instability at the east of the MJO convective center, the boundary layer moisture convergence, the low- and upper-level circulation, and the vertical structure of equivalent potential temperature and diabatic heating. Moreover, the zonal asymmetry of the tendency of specific humidity is also improved by increasing the oceanic vertical resolution. The vertically-integrated moisture budget analysis is applied to further investigate the dominance of the moistening and drying processes. Results reveal that the drying processes are successfully reproduced over the central Indian Ocean in the case of increased oceanic vertical resolution, whilst the moistening processes are not well captured over the Maritime Continent and the MJO "detour" region. It suggests that additional modifications are needed to further improve the MJO simulation. (Ma Libin, Jiang Zijun)

3.7 Sensitivity of ENSO simulation to the convection schemes in the NESM3 climate system model: Atmospheric processes

The El Niño-southern oscillation (ENSO) is the most prominent climate system in the tropical Pacific. However, its simulation, including the amplitude, phase locking, and asymmetry of its two phases, is not well reproduced by the current climate system models. In this study, the sensitivity of the ENSO simulation to the convection schemes is discussed using the Nanjing University of Information Science and Technology Earth System version 3.0 (NESM3) model. Three convection schemes, including the default, the default coupled with the stochastic multicloud model (SMCM), and the default used in the Coupled Model Intercomparison Project phase 6 (CMIP6), are implemented. The model results reveal that the low-level cloud cover and surface net shortwave radiation are best represented over the tropical Pacific in the model containing the SMCM. The simulations of the ENSO behavior's response to changes in the convection scheme are not uniform. The model results reveal that the model containing the SMCM performs best in terms of simulating the seasonal cycle of the sea surface temperature anomaly along the equatorial Pacific, the phase locking, and the power spectrum of ENSO but with a modest ENSO amplitude. Compared to the model containing the default convection scheme,

the coupling of the default scheme and the SMCM provides a good simulation of the ENSO's asymmetry, while the model containing the CMIP6 convection scheme outperforms the others in terms of the simulation of the ENSO's amplitude. Two atmospheric feedback processes were further discussed to investigate the factors controlling the ENSO's amplitude. The analyses revealed that the strongest positive atmospheric Bjerknes feedback and the thermodynamic damping of the surface net heat flux occurred in the model containing the CMIP6 convection scheme, suggesting that the atmospheric Bjerknes feedback may overwhelm the heat flux damping feedback when determining the ENSO's amplitude. The results of this study demonstrate that perfectly modeling and predicting the ENSO is not simple, and it is still a large challenge and issue for the entire model community in the future. (Ma Libin, Jiang Zijun)

3.8 基于GWR模型的中国中东部降水与海拔高度关系特征分析

利用中国国家级地面气象站逐时降水资料，采用地理加权回归（GWR）模型系统分析了中国中东部暖季降水与海拔高度的关系，并将二者关系作为一种客观标准，评估了ECMWF-IFS 模式对2017年暖季降水的预报能力。主要结论如下：（1）总体来看，中国中东部降水频率（强度）随海拔高度升高而增加（减小），二者在不同地区的贡献程度不同导致降水量与海拔高度关系的区域差异显著。（2）通过对比午后短时和夜间长时降水事件与海拔高度关系的差异，发现午后短时降水事件的降水量主要随海拔高度升高而增加，且以降水频率与海拔高度关系的贡献为主。而夜间长时降水事件的降水量与海拔高度关系的区域一致性较差。相较于午后短时降水事件，夜间长时降水事件中有更多站点表现出降水量随海拔高度升高而减小的特征，在大地形周边陡峭地形处的站点所表现出的此种差异较东部孤立地形处更加显著。（3）根据ECMWF-IFS 模式的评估结果，模式能够较好地刻画出中国中东部2017年暖季降水气候态的空间分布特征，且与观测具有较大的空间相关系数。但从降水与海拔高度关系来看，观测与模式的空间相关性偏弱。此外，模式能够表现出降水强度（频率）主要随海拔高度升高而减小（增加）的特征，但绝大多数站点在模式中的降水强度（频率）与海拔高度的负（正）回归关系要弱（强）于观测结果。（张铭明，李建，甘玉婷，李妮娜）

3.9 千米尺度数值预报模式对泰山地区暖季降水预报性能的评估

为深入认识对流可分辨模式对小尺度孤立地形区降水的预报性能，使用2017 年暖季（5—9 月）台站逐时降水观测数据，以小时尺度降水特征为指标，细致评估了千米尺度分辨率（3 km）的北京“睿图”短期数值预报子系统（RMAPS-ST）对泰山及其周边地区降水特征的预报能力，并对比了不同起报时次（北京时08:00和20:00）的预报差异。评估发现，RMAPS-ST可以再现泰山站的局地降水中心，但区域西南侧降水预报小于观测，而泰山站及其东北侧则相反。清晨和午后时段的降水预报与观测相比存在较大偏差。以泰山站为例，RMAPS-ST易于低估夜间至清晨时段的降水频率，这可能与模式对降水系统发展演变过程的预报偏差以及清晨泰山站弱降水事件的漏报有关；清晨泰山站降水强度的预报在不同起报时次的结果中存在差异，20:00起报存在大幅度高估的问题，进而导致其暖季平均降水量预报大于观测，而08:00起报对于清晨降水强度的高估不明显；08:00起报易高估泰山站午后的降水频率，这与其午后短历时降水事件数预报偏多有关，模式对山区热动力场的预报偏差是午后降水空报的可能原因。小时尺度降水特征已应用于中国气象局区域数值预报模式的业务评估体系中，本研究结果也表明，此类评估有助于深入认识千米尺度数值预报模式对降水日内变化的预报能力，从而为精细化降水产品的订正提供更详实的科学依据。（甘玉婷，陈昊明，李建）

3.10 2020年夏季江淮流域降水ECMWF模式预报偏差分析

基于CMPAS 多源融合降水和ERA5 再分析产品，评估全球高分辨率确定性预报产品（ECMWF）对2020 年梅汛期（6月10日至7月20日）极端强降水过程的预报性能。同时，基于面向对象的诊断评

估方法（MODE），揭示ECMWF 模式对强降水落区的质心经纬度、面积、长度、宽度、轴角等空间特征的预报性能。结果表明：ECMWF 模式对于梅雨期的日降水量预报，在雨带的空间位置上，模式预报偏北、偏西的偏差较多；在落区形态上，模式预报的雨带面积偏大，轴角倾斜度更大。观测中江淮流域区域平均降水的日变化主峰值出现在清晨至上午，ECMWF 预报能够再现降水日变化特征。针对模式对主雨带南北落区质心位置预报偏差的评估表明，模式预报主雨带位置偏北的频次呈现出双峰分布的日变化特征，峰值出现在夜间和午后。雨带位置预报偏南的频次为单峰分布，峰值在上午。低空急流的日变化特征明显，且峰值时刻超前降水峰值时刻3 h，而ECMWF 预报急流峰值时刻则较观测早3 h。ECMWF 预报降水落区位置偏差与预报低层南风分量的强弱偏差相关，当对流层低层南风分量偏强时，雨带位置预报易偏北；南风分量较弱时雨带位置预报易偏南。针对ECMWF 预报位置偏北和偏差较小的两次典型强降水事件的对比分析，结果表明在小时尺度上急流与降水的日变化一致，ECMWF 预报降水落区的偏北与前3 h 内强度更强的急流有关。（卜文惠，陈昊明，李普曦）

3.11　千米尺度模式降水的检验评估进展及展望

数值模式检验评估是理解模式偏差、完善数值模式和提升预报服务产品质量的有效方法，是现代数值模式发展的基础环节之一。传统的降水业务检验主要基于累积降水量的评估，较少考虑降水的发展演变过程。随着模式分辨率和降水精细化预报需求的提升，仅基于降水量的检验评估已不能满足定时、定点、定量的降水预报服务需求。在回顾已有降水检验评估方法的基础上，重点介绍基于降水频次、强度等小时尺度特征量及其日变化峰值时间的新评估方法，并示例给出此类评估结果对于深入认识日内降水预报偏差的应用价值。初步结果表明，相关方法和结论为丰富和深化数值模式评估，改进客观预报方法具有有益的启发作用。随着千米尺度模式在降水精细化预报业务中的广泛应用，未来仍需进一步发展和完善针对不同区域降水过程分类、分型的细致评估方法，并进一步研发面向快速更新循环系统和对流可分辨集合预报模式应用的检验评估指标，为千米尺度数值模式的改进和模式产品的合理应用提供科技支撑。（陈昊明，李普曦，赵妍）

3.12　基于GRIST模式的多年气候积分

确认了模式动力求解器的多尺度计算和物理性能的合理性。进而通过耦合物理过程，实现了全球模式准均匀网格（120 km）和变分辨率网格（120 ～ 30 km）的长期稳定气候积分，验证了前期所开发的模式动力框架在真实下垫面条件下的计算性能和稳定性。在小时尺度降水特征方面，GRIST模式具有和超级参数化模式相当的效果，准确区分了东亚地区以“午后v.s.午夜至清晨”为特点的的降水气候模拟。（张祎，李晓涵，王蕾，李建）

3.13　基于非结构网格的海洋模式动力框架研发和球面三维海洋平坦地形基准测试

在GRIST浅水框架的基础上研发了并行的球面海洋模式的三维动力框架。完成了三维正压海洋的无地形Rossby Wave测试和理想地形平流测试，确认了三维海洋模式离散的正确性。同时，开展了三维理想地形的斜压的Baroclinic Channel测试。（刘波，容新尧）

3.14　CAMS-CSM的大气分量更新为GRIST模式及多年稳定积分

基于ESMF底层耦合软件自主开发了适用于全球公里级分辨率以及多种网格结构的耦合框架，并基于新一代非结构网格大气模式GRIST和海洋模式MOM6建立了不同分辨率的新一代海陆气冰多圈层耦合模式，实现不同分辨率的稳定积分。其中，G6（120 km）分辨率大气+50 km海洋模式，实现稳定积分超过40年（20年spinup积分+20年freerun积分）；G5B3×4变分辨率（120 ～ 30 km）大气+25 km海洋稳定积分20年（spinup积分）；G8分辨率（15 km）大气+10 km海洋稳定积分40天。（容新尧，华莉娟，唐彦丽，马利斌，苏京志，刘波）

3.15 CAMS-CSM的集合资料同化系统研发及资料同化和回报试验

大气分量采用nudging方法，海洋分量采用考虑偏差订正的集合卡尔曼滤波方法，建立了CAMS-CSM的集合资料同化系统。大气同化CRA40再分析资料，海洋同化海表温度、卫星高度计、海表流速和温盐剖面数据，共20个集合成员，完成了10年的资料同化和回报试验。（马利斌，容新尧）

3.16 区域数值预报检验评估系统的完善及业务运行

面向区域数值预报系统发展和灾害天气精细化预报服务的业务需求，持续完善面向精细化预报的模式检验评估方法和指标体系，针对区域模式特点研发了降水时空演变过程的检验评估方法。基于此建立的区域高分辨率数值预报检验评估系统，通过局预报与网络司组织的业务化评审，实现业务运行。承担区域模式检验评估业务，针对“7·21”河南暴雨等多次强降水过程进行了系统评估，发布区域模式检验评估报告4期，评估结果得到数值预报中心、华北、华东和华南等模式研发团队以及国家气象中心和上海中心气象台等国家级和省级业务单位的认可。（陈昊明，李普曦，陆天舒，杨琳韵，周佰铨）

4 其他
4 Others

4.1 Wind characteristic in the complex underlying terrain as studied with CALMET system

In the present study, the wind data during two synoptic processes observed by the surface wind tower in the Tibetan Plateau and the high spatial resolution model data simulated by CALMET were be evaluated, the horizontal and vertical distribution characteristics of the model wind data around the region of the wind tower point and the reference point were be analysed. Results showed that the wind observation data during the two processes in the near-surface boundary were a well consistency. The horizontal distribution of the wind fields were consistent at the moment of the maximum wind speed during the two processes. The trend of the ten minute mean wind speed was upward with time variations during the two strong wind weather systems. The air was flowed from the mountain ridge to the mountain valley over the complex region. The vertical distribution of the wind speed had more relevant that the correlation coefficients were 0.6811 (α = 0.05) in the observation tower point and 0.8304 (α = 0.05) in the reference point between 16:00 pm Jan 30th and 16:00 pm Jan 31st. The advantages of using the advanced numerical models will be reflected over the extremely complex underlying terrain where the lack of observation stations. (Liao Rongwei, Fang Xiaoyi, Liu Huaiyu, Zhou Rongwei, Zhang Lei, Zhu Yuzhou, Zhang Dongbin, Meng Fanchao)

4.2 Study of wind characteristic in Tibet with numerical simulation

In order to analyse the model simulation results and study the impact of the horizontal resolution in model during different weather process in complicated topography areas in Tibet, the mean wind observation data from wind tower and high-resolution numerical model data were used, the characteristics of the mean wind and the turbulent kinetic energy (TKE) in the near-surface boundary layer around the region of the wind tower point and comparison point were analyzed. The results showed that the mean wind observation data were a well consistency. With time variations, the mean values of ten minute wind speed had an upward trend over time during different strong wind weather systems. The air flow and the spatial distribution of TKE were consistent around the region of the wind tower point and comparison point. The air flowed from high elevation areas (mountain ridge) to the low elevation areas (mountain valley) during different resolution numerical model data. Comparative analysis of different resolutions simulation results, the higher-resolution simulation result

showed more clear in the characteristics of the air flow. The correlation had increased considerably between the different times of the mean value of the ten minute wind speed or TKE on the vertical layers, and the bias was decreased. (Liao Rongwe, Fang Xiaoyi, Zhang Dongbin, Zhu Yuzhou, Zhang Lei, Meng Fanchao)

4.3 A view for atmospheric unpredictability

Based on chaotic dynamics, this paper illustrated the necessity of research and the objective existence of atmospheric unpredictability. Actually, inaccurate forecast happens all the time in both operational weather forecasting and climate prediction in which atmospheric unpredictability hides. By means of discrete mathematics, this paper also defined the degree of hesitation and the predictable days with which to discuss and compare the relationship between the predictability and unpredictability of several different forecast objects. In addition, this paper discussed the approaches of evaluating the atmospheric predictability and unpredictability, emphatically showed the experience assessment method. At the last, this paper also proved the existence of atmospheric unpredictability by an example. (Cai Xiuhua, Cao Hongxing, Fang Xiaoyi, Sun Jingli, Yu Ying)

4.4 Identification of regional drought processes in North China using MCI analysis

Comprehensive identification of drought events is of great significance for monitoring and evaluating drought processes. Based on the data of daily precipitation, temperature and drought-affected areas of 403 meteorological stations in North China from 1960 to 2019, the comprehensive drought process intensity index (CDPII) has been developed by using the meteorological-drought composite index (MCI) and regional drought process identification method, as well as the EIDR theory method. The regional drought processes in the past 60 years in North China, including Beijing, Tianjin, Hebei, Shanxi and middle Inner Mongolia, were analyzed and identified. The result shows that the distribution characteristics of droughts with different intensities are as follows: The number of days of all annual-average mild droughts, moderate droughts and severe droughts was the highest in Tianjin and that of extreme droughts was the highest in Shanxi. The number of days of mild droughts was the highest in May and the lowest in January. The number of days of moderate droughts was highest in June. The number of days with mild and moderate droughts showed an overall increasing trend, while the number of days with severe droughts and above showed an overall decreasing trend (through a 0.05 significance test). The number of drought days was the highest in the 1990s. The annual frequency of drought was between 66.7% and 86.7%; the drought frequency in Hebei was the highest at 86.7%, followed by Beijing at 80%. There were 75 regional drought processes in North China from 1960 to 2019, and the correlation coefficient between process intensity and the drought-affected area was 0.55, which passed the 0.01 significance test. The comprehensive intensity of drought process from 27 April to 1 September 1972 was the strongest. From 18 May to 31 October 1965, the drought lasted 167 days. The overall drought intensity had a slight weakening trend in the past 60 years. A total of 75 regional drought processes occurred in North China, and the process intensity showed a trend of wavy decline with a determination coefficient (R^2) of 0.079 (0.05 significance test). Overall, the regional drought process identification method and strength assessment result tally with the drought disaster, which can better identify the regional drought process. Furthermore, including the last days, the average intensity, and average scope comprehensive strength, there are many angles to monitor and evaluate the droughts and drought processes. These provide a reference for drought control and decision-making. (Cai Xiuhua, Zhang Wenqian, Fang Xiaoyi, Zhang Qiang, Zhang Cunjie, Chen Dong, Chen Cheng, Wen Jiefan, Yu Ying)

4. 5 我国城市通风廊道研究与实践进展

城市通风廊道作为协同解决城市气候问题的一种有效手段被纳入国土空间规划中。本文回顾了城

市通风廊道规划的由来，总结了其功能与机理，重点梳理了我国通风廊道规划研究与实践进展，旨在为国土空间规划中科学、合理地开展廊道划定工作提供参考。通风廊道的主要功能是为气流进入城市建成区内部提供通道，引导城市空间形态优化以减少风的损耗，结合科学保护城市开敞空间，促进局地空气流通，对缓解城市热岛效应、减轻空气污染、降低建筑物能耗和提高城市宜居性也有积极作用；而城市内部的功能布局、用地类型、空间形态、建筑高度和密度等因素会很大程度上对这种功能的发挥造成影响。我国通风廊道规划研究与实践经历了4个发展阶段，分别为古代风水与营城、新中国成立至20世纪90年代末的恢复阶段、21世纪初期的发展阶段和2012年至今生态优先的新阶段。全国超过2/3的省开展了相关工作，在技术方法、应用策略和政策法规3个方面取得了重要进展。通风廊道规划体现了快速城镇化进程背景下中国城市对发展质量的追求，但在规划过程中的介入时间、跨领域融合、与城市设计衔接及廊道绩效评估机制等工作途径层面仍存在问题，在气象观测分析、仿真模拟、效果评估等技术层面也有诸多提升空间。（房小怡，李磊，刘宛，任超，王佳文，程宸，于瀛，张硕，杜吴鹏）

4.6　福清核电厂厂址区域龙卷风设计基准参数的估算

基于1959—2017年福清核电厂区龙卷风的调查资料，采用Rankine 涡模型估算该区域超过某一特定风速的概率分布，通过概率值导出设计基准龙卷风和基准设计风速，按照压降模型计算出龙卷风的压降，研究结果表明：福清核电评价区域龙卷风的总压降为4.29 kPa；平移速度为13.8 m/s，最大旋转风速为57.6 m/s，最大压降速率为1.18 kPa/s，基准设计风速为71.4 m/s，属于F3 级别的龙卷风；在125 kg 下落的穿甲弹类和2.5 cm 实心钢球两种不同情景下计算出的龙卷风产生的飞射物的最大水平碰撞速度均为24.99 m/s、碰撞动量依次为3123.75 kg/（m/s）和1.615 kg/（m/s）。这些计算结果，从龙卷风的角度，为政府相关部门在规划和建设福清核电厂时提供了可靠的理论依据。（蔡秀华，吕文忠，陈龙泉）

4.7　影响福清厂址区域热带气旋工程参数估算

统计和分析了福清核电厂区热带气旋的分布特征及极值气压和风速。以1949—2017年影响福清核电厂区的台风资料为基础，利用Gumbel-Ⅰ型极值分布概率方法和Pearsonl-Ⅲ型分布函数方法及梯度风公式对影响福清核电厂区最低中心气压和最大风速进行经验拟合，估算出可能最大热带气旋的强度参数，并经比较后得出更加合理的数值，百年一遇的可能最低气压估值为887 hPa。在此基础上估算出的10 m和200 m高度百年一遇的10 min平均最大风速和3 s阵风的极大风速依次为52.7、68.4、87.7和113.8 m/s。（蔡秀华，吕文忠，陈龙泉，范雯杰）

4.8　1961—2019年河南秋季连阴雨气候特征分析

利用河南省103个地面气象站1961—2019年逐日资料，采用滑动平均、小波分析、EOF分解等方法分析了河南秋季区域性连阴雨降水的时空分布特征，采用自组织神经网络方法对河南秋季区域性连阴雨环流进行客观分型。结果表明：（1）河南区域性秋季连阴雨以7～9天的过程居多，其次为10天以上过程。20世纪60年代和80年代是河南区域性秋季连阴雨多发期，90年代为连阴雨少发期，70年代和21世纪10年代发生次数与近59年年均频次基本持平，21世纪10年代河南区域性秋季连阴雨比其它年代强，20世纪90年代强度最弱。20世纪70年代区域性秋季连阴雨年平均过程降水量存在准5年周期，21世纪00年代前半期及10年代区域性秋季连阴雨年平均过程降水量存在2～3年周期。（2）近59年河南区域性秋季连阴雨平均降水量分布上，黄河以南地区比黄河以北地区降水多，山区比平原地区多，降水大值区与山区分布基本一致。河南区域性秋季连阴雨降水空间分布型上，最主要的特征是全省一致变化型，其次是南北反相型。（3）SOM方法不仅可以区分出环流形态上的差别，还可以区分出

环流型的发生时间和连阴雨期间环流的阶段性演变特征。SOM分型得到8类区域性连阴雨环流型，从天气学意义上可归结为阻塞型、低槽型和平直环流型。大部分河南秋季区域性连阴雨过程为2～3种环流型的组合，不同环流型之间存在转换关系。（杜明哲，鲁坦，朱玉周，廖荣伟，房小怡）

4.9 界壳论探讨生态环境安全

从界壳论来探讨生态环境安全问题，介绍了界壳的概念及其理论，指出界壳论在该安全问题中的可应用性。就古文明衰落、全球增暖、生物入侵等问题进行了论述。界壳现象广泛存在于自然界和人类社会中，如栅栏、国界、防火墙、人的衣服等，例如蜗牛长有一个坚硬的壳用以保护自己。界壳被定义为处在系统外围能卫护系统且与环境进行交换的中介体，它是系统的一部分，又和环境相毗邻。界壳论研究界壳的普适性规律，从一般意义上研究界壳的结构、功能和行为。生物入侵是典型的界壳论问题，一个物种离开原来的栖息地，进入到另一个原不是它生息的地方，即从一个该物种生存的界壳进入到另一个新界壳中生活。若大量繁殖，会造成生态环境危害。（蔡秀华，于瀛，曹鸿兴，彭誉葆，范雯杰，吕文忠）

大气成分与环境气象
Atmospheric Composition and Environmental Meteorology

大气成分与环境气象研究进展
Advances in Research on Atmospheric Composition and Environmental Meteorology

1 大气成分及相关特性变化观测研究
1 Observational studies of atmospheric composition and related properties

1.1 Advances in sunphotometer-measured aerosol optical properties and related topics in China: Impetus and perspectives

Aerosol is a critical trace component of the atmosphere. Many processes in the Earth's climate system are intimately related to aerosols via their direct and indirect radiative effects. Aerosol effects are not limited to these climatic aspects. They are also closely related to human health, photosynthesis, new energy, etc., which makes aerosol a central focus in many research fields. A fundamental requirement for improving our understanding of the diverse aerosol effects is to accumulate high-quality aerosol data by various measurement techniques. Sunphotometer remote sensing is one of the techniques that has been playing an increasingly important role in characterizing aerosols across the world. Much progress has been made on this aspect in China during the past decade, which is the work reviewed in this paper. Three sunphotometer networks have been established to provide high-quality observations of long-term aerosol optical properties across the country. Using this valuable dataset, our understanding of spatiotemporal variability and long-term trends of aerosol optical properties has been much improved. The radiative effects of aerosols both at the bottom and at the top of the atmosphere are comprehensively assessed. Substantial warming of the atmosphere by aerosol absorption is revealed. The long-range transport of dust from the Taklimakan Desert in Northwest China and anthropogenic aerosols from South Asia to the Tibetan Plateau is characterized based on ground-based and satellite remote sensing as well as model simulations. Effective methods to estimate chemical compositions from sunphotometer aerosol products are developed. Dozens of satellite and model aerosol products are validated, shedding new light on how to improve these products. These advances improve our understanding of the critical role played by aerosols in both the climate and environment. Finally, a perspective on future research is presented. (Che Huizheng)

1.2 The dominant mechanism of the explosive rise of $PM_{2.5}$ after significant pollution emissions reduction in Beijing from 2017 to the COVID-19 pandemic in 2020

The Chinese government implemented strict emission reduction measures of air pollution between 2013 and 2017. However, from the winter of 2017 until February 2020, during the COVID-19 pandemic, the twenty explosive rise (ER) events of $PM_{2.5}$ mass in twelve heavy aerosol pollution episodes (HPEs) still appeared in Beijing and its vicinity (BIV). To explore the controlling mechanism for the ER under the condition of drastically reduced emissions, the vertical structure of meteorological elements by L-band

second-level sounding and aerosol properties by Lidar were investigated associating with the analysis of surface concentration in $PM_{2.5}$ mass, its main precursor gases, as well as black carbon (BC) by seven-wavelength Aethalometer. The planetary boundary layer height (BLH) was also estimated together with an analysis of the unfavorable meteorological index (PLAM) that can quantify the impact of unfavorable meteorological conditions to cause the change of $PM_{2.5}$ concentration. The results suggested that the ER reoccurrence's fundamental cause is that the emissions have not yet fallen sufficiently to a level to decouple HPEs from unfavorable meteorological conditions. During the ER period, the BLH dropped significantly. The fact that $PM_{2.5}$, its precursor gases, and black carbon increased almost in a similar proportion, indicating that the boundary layer structure change caused by aerosol accumulation is the dominant reason for the ER phenomenon compared to the chemical conversion factor. The two-way feedback effect between the further worsened meteorological conditions and the accumulation of $PM_{2.5}$ typically interpreted 54%–93% of the ER. An HPE starting 8 Feb. 2020 during the COVID-19 period underwent one of the worst meteorological conditions, quantified by PLAM, in BIV since 2013. However, with a similar level of unfavorable meteorological conditions, the average $PM_{2.5}$ concentration during the HPE in 2020 was only about 66% of that of a similar HPE in 2016. It shows that the substantial reduction of emissions reduces the $PM_{2.5}$ pollution level primarily as before when facing an equivalent level of unfavorable meteorological conditions. These results combined suggest that China's continuous efforts to reduce emissions proceed in the right direction and have achieved the desired results. (Che Huizheng)

1.3 Robust prediction of hourly $PM_{2.5}$ from meteorological data using LightGBM

Retrieving historical $PM_{2.5}$ data is a key for evaluating the long-term impacts of $PM_{2.5}$ on the environment, human health, and climate change. Satellite-based aerosol optical depth has been used to estimate $PM_{2.5}$, but estimations have largely been undermined by massive missing values, low sampling frequency, and weak predictive capability. Here, using a novel feature engineering approach to incorporate spatial effects from meteorological data, we developed a robust LightGBM model that predicts $PM_{2.5}$ at an unprecedented predictive capacity on hourly (R^2 = 0.75), daily (R^2 = 0.84), monthly (R^2 = 0.88), and annual (R^2 = 0.87) timescales. By taking advantage of spatial features, our model can also construct hourly gridded networks of $PM_{2.5}$. This capability would be further enhanced if meteorological observations from regional stations were incorporated. Our results show that this model has great potential in reconstructing historical $PM_{2.5}$ datasets and real-time gridded networks at high spatial-temporal resolutions. The resulting datasets can be assimilated into models to produce long-term reanalysis that incorporates interactions between aerosols and physical processes. (Zhong Junting, Zhang Xiaoye, Gui Ke)

1.4 Attribution of the worse aerosol pollution in March 2018 in Beijing to meteorological variability

Fine particle matter ($PM_{2.5}$) pollution frequently occurs in winter with increased consumption for heating and decreased radiation and boundary-layer height. Under strict emission controls since 2013, the mass concentrations of $PM_{2.5}$ in Beijing decreased substantially in Winter 2017/2018. However, in March 2018, the mean $PM_{2.5}$ concentration doubled from about 40 to 87 μg m^{-3}, the reason for which is still unclear in the context of significant emission reductions. Here, using $PM_{2.5}$ measurements, vertical observations, and reanalysis data, we found that this worsening was attributed to increasingly stable stratification characterized by temperature differences between 850 hPa and 1000 hPa, which reached the maximum value (−4 ℃) for March from 1951 to 2018. Not limited to Beijing, positive anomalies in temperature differences occurred widely as a result of a westward transition in the center of the polar vortex. Away from the cold center and dominated by anomalous zonal westerlies, the northern China was intruded by warm southerly winds. The warm regional

advection increased positive anomalies in low-level temperature differences, and in turn, enhanced geopotential thickness throughout the troposphere. The adverse impact on pollution was also confirmed in comparison to the vortex pattern in January. The vortex changed from the elongated one with a split-flow pattern in January to the annular vortex with a major center over Novaya Zemlya in March. Correspondingly, Beijing was less affected by cold air masses and thereby under relatively stable stratification, which is unfavorable for pollution dispersion in March. Additionally, this aerosol pollution was further worsened by aerosol-induced deteriorating meteorological conditions. (Zhong Junting, Zhang Xiaoye)

1.5 Three-dimensional climatology, trends, and meteorological drivers of global and regional tropospheric type-dependent aerosols: Insights from 13 years (2007–2019) of CALIOP observations

Globally gridded aerosol extinction data from the Cloud-Aerosol Lidar with Orthogonal Polarization (CALIOP) during 2007–2019 are utilized to investigate the three-dimensional (3D) climatological distribution of tropospheric type-dependent aerosols and to identify the trends in column aerosol optical depth (AOD), partitioned within different altitude regimes, and their meteorological drivers. Using detection samples of layer aerosols, we also yield a 3D distribution of the frequency of occurrence (FoO) of aerosol subtypes classified by CALIOP. The results show that the aerosol extinction coefficient (AEC) shows contrasting vertical distribution patterns over land and ocean, with the former possessing significant geographical dependence, while the enhancement of AEC in the latter is mainly located below 1 km. The vertical structures of the type-dependent AECs, however, are strongly dependent on altitude. When the total AOD (TAOD) is partitioned into the planetary boundary layer (PBL) and the free troposphere (FT), results demonstrate that the PBL and FT contribute 62.08% and 37.92%, respectively, of the global tropospheric TAOD averaged over daytime and nighttime. Yet this CALIOP-based partitioning of the different aerosol subtypes in the PBL and FT varies significantly. Among all 12 typical regions of interest analyzed, more than 50% of TAOD is located in the lower troposphere (0–2 km), while the contribution is less than 2% above 6 km. In global average terms, we found the aerosol FoO averaged over all layers is 4.45%, with the largest contribution from “clean marine” (1.79%) and the smallest from “clean continental” (0.05%). Overall, the FoO vertical structures of the aerosol layer exhibit a distribution pattern similar to that of AEC. The resulting trend analyses show that CALIOP accurately captures significant regional anomalies in TAOD, as observed in other satellite measurements and aerosol reanalysis. Our correlation analysis between meteorological factors and TAOD suggests the interannual variability of TAOD is related to the variability of precipitation (PPT), volumetric soil moisture (VSM), and wind speed (WS) in the particular regions. For instance, the positive TAOD trend over the equatorial central Pacific is mainly attributable to the increased PPT and decreased WS. In contrast, in dry convective regions dominated by dust and smoke, the interannual variability/trend in TAOD is largely modified by the VSM driven by the PPT. Additionally, we further found that these significant regional correlations are more robust within the PBL and significantly weakened or even reversed within the FT. This highlights the superiority of using the TAOD partitioned within the PBL as a proxy variable for the widely applied TAOD to explore the relationships between atmospheric pollution and meteorology. (Gui Ke)

1.6 Seasonal variability and trends in global type-segregated aerosol optical depth as revealed by MISR satellite observations

This study utilized a long-term (2001–2018) aerosol optical component dataset retrieved from the Multiangle Imaging Spectroradiometer (MISR), Version 23, to perform comprehensive analyses of the global climatology of seasonal AODs, partitioned by aerosol types (including small-size, medium-size, large-size,

spherical, and non-spherical). By dividing eight different AOD bins and performing trend analysis, the seasonal variability and trends in these type-segregated AODs, as well as in the frequency occurrences (FOs) for different AOD bins, globally and over 12 regions of interest, were also investigated. In terms of particle size, small-size aerosol particles (diameter < 0.7 μm) contribute the largest to global extinction in all three seasons except winter. A similar globally dominant role is exhibited by spherical aerosols, which contribute 68.5%, 73.3%, 71.6% and 70.2% to the global total AOD (TAOD) in spring, summer, autumn and winter, respectively, on a global average scale. FOs with different aerosol loading levels suggested that the seasonal FOs tend to decrease progressively with increasing aerosol loading, except for Level 1 (TAOD < 0.05). Examination of the seasonal distribution of FOs revealed that the FO at Level 1 (Level 2, 0.05 < TAOD < 0.15) is much larger in summer/winter (winter/autumn) than in spring/autumn (spring/summer) over most areas of the world. However, the FOs for Level 3 (0.15 < TAOD < 0.25) to Level 8 (TAOD > 1.0) generally exhibit greater intensity in spring/summer than in autumn/winter. Temporal trend analyses showed that the seasonal TAOD experiences a significant decline during 2001–2018 in most regions globally, except in South Asia, the Middle East, and North Africa. Opposite seasonal trends in the above regions are closely related to the increase in FOs in the range of 0.4 < TAOD < 1.0. The global average TAOD shows the most pronounced decline in spring, falling by −10.4% ($P < 0.05$). Examination of the trends in type-segregated AODs further revealed that the decreases in size-segregated (shape-segregated) AODs all contribute to the decrease in seasonal TAOD, with small-size AOD (spherical AOD) contributing most significantly. (Gui Ke)

1.7 A global-scale analysis of the MISR Level-3 aerosol optical depth (AOD) product: Comparison with multi-platform AOD data sources

This study analyses the applicability of the recently released Level-3 (L3) daily and monthly aerosol optical depth (AOD) products (version F15_0032) over land retrieved from the Multiangle Imaging Spectroradiometer (MISR) instrument. For this purpose, daily AOD data from 427 Aerosol Robotic Network (AERONET) sites worldwide during 2001–2018 and 39 China Aerosol Remote Sensing Network (CARSNET) sites across China during 2002–2014 were selected for comparison. Also, MISR-based size-segregated AODs were collected to compare with the coarse- and fine-mode AODs retrieved from AERONET to reveal the particles size modes that mainly contribute to the offset of MISR total AOD relative to observations. By comparing with five other monthly AOD datasets, including two MODIS (Moderate resolution Imaging Spectroradiometer) retrieval products, a multi-satellite merged product, and two aerosol reanalysis, MERRA-2 (Modern-Era Retrospective Analysis for Research and Applications) and CAMS (Copernicus Atmosphere Monitoring Service), we then explored the applicability of MISR for characterizing the climatology, interannual variations, and long-term (2003–2017) trends in regional aerosol loadings over the 12 regions of interest. Overall, about 80% (60%) of the daily AOD values retrieved by MISR fall within expected error bounds of ± [0.05 + 0.2 × AOD] (± [0.03 + 0.1 × AOD]), with a high correlation ($R = 0.87$). Our comparison results show that although the V23 algorithm addresses several issues in L2 AOD retrieval relative to the previous version, the L3 data aggregated from L2 data tends to on average overestimate low AOD values and underestimate high AOD values. These offsets relative to observations are mainly attributed to the overestimation of coarse-mode AOD and the underestimation of fine-mode AOD by MISR. Intercomparison of 2003–2017 AOD trends from multiple data sources indicates that MISR can capture well the increases occurring in South Asia, as well as the decreases occurring in the eastern China, eastern United States, and western Europe. Our study confirmed that MISR L3 product performs reliably at regional scales, particularly in typically polluted areas, but caution is still needed when applied to areas where sparse sampling is encountered. (Gui Ke)

1.8 Identifying the dominant local factors of 2000–2019 changes in dust loading over East Asia

East Asian dust aerosols play a vital role in the local and regional climate through its direct, indirect, and semidirect effects, but the dominant factors affecting the interannual variation of dust aerosols over East Asia and their regional differences remain unclear. This study verified the accuracy of MEERA-2 dust data in East Asia, analyzed the interannual trends of dust in East Asia from 2000 to 2019 using the MERRA-2 dust column mass density (DCMD) and identified the dominant factors affecting the interannual variation during the dusty season (March–July) by developing the regional multiple linear regression models, combined with correlation and partial correlation analysis. The comparison with the dust index (DI) calculated from ground-based observations of dust events frequency indicated that MERRA-2 DCMD exhibited high spatial agreement (R >0.8) with ground-based observations in most regions (especially in the dust source region of North China). The trend analysis revealed that DCMD in East Asia decreased significantly after 2000, particularly in the dusty season (March–July). These significant decreases were generally highly correlated with increases in normalized differential vegetation index (NDVI), volumetric soil moisture (VSM), and precipitation (PPT) and with decreases in wind speed (WS). Furthermore, WS dominated the interannual variation in the dust concentration over the East Asian dust source regions and their downstream. By contrast, PPT, through its wet deposition effect, dominated the variation in the rest of the regions away from the dust source regions. The study findings may help clarify the associations between local meteorological and surface factors and long-term variations in dust aerosols over East Asia. (Gui Ke)

1.9 Aerosol optical properties and its type classification based on multiyear joint observation campaign in North China Plain megalopolis

Since haze and other air pollution are frequently seen in the North China Plain (NCP), detail information on aerosol optical and radiative properties and its type classification is demanded for the study of regional environmental pollution. Here, a multiyear ground-based synchronous sun photometer observation at seven sites on North China Plain megalopolis from 2013 to 2018 was conducted. First, the annual and seasonal variation of these characteristics as well as the intercomparsion were analyzed. Then the potential relationships between these properties with meteorological factors and the aerosol type classification were discussed. The results show: Particle volume exhibited a decreasing trend from the urban downtown to suburban and the rural region. The annual average aerosol optical depth at 440 nm (AOD_{440}) varied from 0.43 to 0.86 over the NCP. Annual average single-scattering albedo at 440 nm (SSA_{440}) varied from 0.89 to 0.93, indicating a moderate to slight absorption capacity. Average absorption aerosol optical depth at 440 nm ($AAOD_{440}$) varied from 0.07 to 0.10. The absorption Ångström exponent (AAE) (0.89–1.40) indicated the multi-types of absorptive matters originated form nature and anthropogenic emission. The discussion of aerosol composition showed a smaller particle size of aerosol from biomass burning and/or fossil foil consumption with enhanced aerosol scattering and enlarged light extinction. Aerosol classification indicated a large percentage of mixed absorbing aerosol (20%–49%), which showed increasing trend between relative humidity (RH) with aerosol scattering and dust was an important environmental pollutant compared to the southern China. (Zheng Yu)

1.10 Simultaneous measurements of PM_1 and PM_{10} aerosol scattering properties and their relationships in urban Beijing: A two-year observation

The aerosol scattering properties of submicron (PM_1) and sub-10-μm particles (PM_{10}) under dry conditions (RH < 30%) were investigated in Beijing from 2018 to 2019. Using the simultaneous measurement of PM_1 and PM_{10}, the scattering properties of super micron (PM_{10-1}) particles were also calculated. At 550 nm, the average of scattering coefficient (σ_{sp}) and asymmetry parameter (g) were 208.7 ± 204.9 Mm^{-1} and 0.61 ± 0.04 for PM_{10},

140.6 ± 130.2 Mm^{-1} and 0.60 ± 0.04 for PM_1, and 69.8 ± 82.2 Mm^{-1} and 0.62 ± 0.04 for PM_{10-1}, respectively, while the backscattering ratio (b) values were 0.13 ± 0.02 for PM_{10} and PM_1, and 0.12 ± 0.02 for PM_{10-1}. The mass scattering efficiencies (MSE) for PM_{10}, PM_1 and PM_{10-1} were 2.43 ± 2.37, 3.67 ± 0.96, and 1.73 ± 1.82 $m^2\ g^{-1}$, respectively. In 2019, σ_{sp} decreased by approximately 18.4% for PM_{10}, and 16.7% for PM_1 compared with those in 2018, which was quite similar to the decrease of 17% and 19% for PM_{10} and $PM_{2.5}$ mass concentrations during the same time period. The scattering Ångström exponent (SAE450/700), which was 1.88 ± 0.29 for PM_1 and 1.50 ± 0.27 for PM_{10} indicated size distributions dominated by fine mode aerosols. This is also evidenced by the high submicron scattering ratio (R_{sp}) (71.1% ± 7.9%). The high SAE, R_{sp}, and high PM_1 σ_{sp} in the study suggest that control of fine particle pollution is important to reduce overall PM pollution in urban Beijing. In addition, with an increase in σ_{sp}, b, R_{sp}, and SAE gradually decreased, while g and MSE increased. The clearly scattering coefficient-dependent MSE suggests that high aerosol loading and high MSE both play an important role in degraded visibility during heavy pollution periods. (Sun Junying)

1.11 Reduced volatility of aerosols from surface emission to the top of planetary boundary layer

Aerosols from surface emission can be transported upwards through convective mixing in the planetary boundary layer (PBL), which subsequently interact with clouds, serving as important sources to nucleate droplets or ice particles. However, the evolution of aerosol composition during this vertical transport has yet to be explicitly understood. In this study, simultaneous measurements of detailed aerosol compositions were conducted at both sites, urban Beijing (50 m a.s.l.) and Haituo mountain (1344 m a.s.l.) during wintertime, representing the anthropogenically polluted surface environment and the top of the PBL respectively. The pollutants from surface emissions were observed to reach the mountain site on daily basis through daytime PBL convective mixing. From surface to the top of PBL, we found efficient transport or formation for lower-volatile species, black carbon, sulfate and low-volatile organic aerosol (OA); however notable reduction of semi-volatile substances, such as the fractions of nitrate and semi-volatile OA reduced by 74% and 76% respectively, during the upward transport. This implied the mass loss of these semi-volatile species was driven by the evaporation process, which repartitioned the condensed semi-volatile substances to gas-phase, when aerosols were transported and exposed to a cleaner environment. In combination with the oxidation processes, these led to enhanced oxidation state of OA at the top of the PBL compared to surface environment, with an increase of oxygen to carbon atomic ratio by 0.2. Such reduction of aerosol volatility during vertical transport may be important in modifying its viscosity, nucleation activity and atmospheric lifetime. (Liu Quan)

1.12 Aerosol component retrievals from satellite observations

The multi-angle polarimetric satellite observations are helpful for improving the retrievals of aerosol parameters. However, practical applications of polarization technology are still limited because of complexity of measurement and interpretation of polarimetric observations. In this study, we analyze the performance of a new component approach developed in the frame of the Generalized Retrieval of Atmosphere and Surface Properties (GRASP) algorithm. In addition to aerosol optical properties including particle size distribution, non-sphericity and index of refraction that are commonly derived from multi-angle radiance and polarization measurements, the GRASP/Component approach also provides some information about aerosol composition. Specifically, in this approach aerosol is modeled as an internal mixture of several components with distinctly different chemical compositions and known refractive indices. The approach is intended not only to provide additional insight on aerosol composition but also to improve retrieval of basic aerosol optical properties. This study presents comprehensive validation and evaluation of aerosol optical depth (AOD)s, Ångström exponent (AE), fine mode AOD (AODF), coarse mode AOD (AODC), and single scattering albedo (SSA) as retrieved by the GRASP/Component approach. The GRASP/Component products include aerosol retrievals using

two different aerosol component mixing rules, i.e., Maxwell-Garnett (MG) effective medium approximation and a simple Volume-Weighted averaging (VW). The differences between the results obtained using these two assumptions are also discussed. The obtained results show that the aerosol optical property products of GRASP/Component approach have good agreement with the ground-based AERONET measurements, which is comparable to other PARASOL/GRASP approaches. Specifically, the AOD retrieved by GRASP/Component approach show high correlation and nearly no bias both over land and ocean, as compared with AERONET. The more detailed aerosol properties such as AE, AODF, AODC and SSA also show one of the best comparisons with AERONET. These improvements can probably be attributed to the use of the additional physical constraints on spectral dependence of the complex refractive index and the reduction of total number of aerosol parameters directly retrieved in the GRASP/Component approach. In addition, the choice of mixing rules had no significant effect on optical retrievals. With the exception of SSA, the results obtained based on the MG mixing rule were found to be slightly better over those obtained using VW mixing rule, especially for bias. (Li Lei)

1.13 The influence of stagnant and transport type weather on heavy pollution in the Yangtze-Huaihe Valley, China

The ambient atmospheric $PM_{2.5}$ concentrations in Anhui Province, China, which links the Yangtze River Delta region, China's fastest growing economy area, with the Beijing-Tianjin-Hebei (BTH) region, China's most polluted region, are influenced not only by local emissions, but also by changes in regional circulation. During the period 2013−2017, when China adopted a series of pollution abatement measures, there were still occasional pollution episodes with significant increases in $PM_{2.5}$ concentrations. $PM_{2.5}$ rose instead during the period 2013−2017 in Anhui (the Center of the Yangtze-Huaihe, YH), when pollution emissions continued to decrease. What is the controlling mechanism behind these? By analyzing elements such as ground-based $PM_{2.5}$ concentration and the planetary boundary layer (PBL) structure affecting it as well as larger scale circulation, combined with the analysis of a parameterized index, one can find that aerosol pollution in the YH region can usually be classified into three types. (1) There is a short-term transport stage (TS) in the initial stage of pollution; then as the pollutant concentrations increase, the PBL height decreases; the temperature inversion is gradually formed or strengthened; the wind speed decreases and the relative humidity of the lower layer increases, forming a two-way feedback mechanism in the cumulative stage (CS). (2) The pollutant concentrations will not drop rapidly in the later stage of CS, while a short-term TS will occur again. (3) The explosive rise (ER) events are mainly affected by transportation in the YH. The first of these types tends to be accompanied by the emergence and maintenance of heavy pollution periods (HPEs), and in some phases is accompanied by explosive rises (ERs) in $PM_{2.5}$ that at least double in a short period of time. To sum up, deterioration of meteorological conditions explains approximately 68% to the increase in $PM_{2.5}$ in the ER. (Jia Wenxing, Zhang Xiaoye)

1.14 Assessing the pollutant evolution mechanisms of heavy pollution episodes in the Yangtze-Huaihe Valley: A multiscale perspective

The Yangtze-Huaihe (YH) region experiences heavy aerosol pollution, characterized by high $PM_{2.5}$ concentration. To unravel the pollutant evolution mechanism during the heavy pollution episodes (HPEs), this study combined observational data analysis and three-dimensional WRF-Chem simulations. From 2 December 2016 to 15 January 2017, the YH region experienced 4 HPEs under the control by synoptic system, normally associated with a transport stage (TS) and a cumulative stage (CS). During the TS, pollutants are transported to the north of the YH region through the near-surface, and then transported to the "mountain corridor" through the residual layer (RL) under the influence of prevailing wind. For the RL transport mechanism, the

change of pollutant concentration can consider not only the net flux in the horizontal direction, but also the role of the vertical movement, which is extremely important and cannot be ignored. By analyzing the mass conservation equation of pollutant, the results show that the advection transport and turbulent diffusion have a synergistic effect on the change of pollutant in the CS of three HPEs. The change of turbulence characteristics is also affected by topography. The "mountain corridors", which is accompanied by variable wind direction and turbulence diffusion, is easily affected by wind shear. In addition, the turbulence characteristics are different during the TS and CS, especially the strong stable conditions in the CS at nighttime. The turbulence, is intermittent, and the model has insufficient performance for turbulence, which will lead to differences for the simulation of pollutant concentration. In short, as the $PM_{2.5}$ concentration linearly increases, the friction velocity (turbulent diffusion coefficient) decreases by 63% (80%), 61% (78%) and 45% (68%), respectively. Therefore, the change of pollutants is less sensitive to the change of turbulence during the HPEs. The contribution of regional transport (local emissions) reaches 43% (47%), thus we need pay attention to the contribution of each part during the HPEs, which will help us to build a certain foundation for the emission reduction work in the future. (Jia Wenxing, Zhang Xiaoye)

1.15 A novel method of retrieving low visibility during heavily polluted episodes in the North China Plain

The prediction of visibility is an ongoing problem in air quality models, particularly that of low visibility during heavily polluted episodes. In this study, a new method of calculating visibility based on the data of particle mass concentration of $PM_{2.5}$ (particles with diameter $\leqslant$ 2.5 μm) and relative humidity (RH), which are generally available in most regions of China, is developed. The method also considers the particle number size distribution (PNSD) and hygroscopic parameter (κ), and focuses on visibility below 10 km. First, the PNSD was re-constructed under dry condition (PNSDdry) based on the relationship between $PM_{2.5}$ and the particle volume size distribution modal parameters obtained in a previous study conducted in the North China Plain. Then, the ambient PNSD was retrieved based on the PNSDdry and κ, and the light extinction was calculated by applying the Mie code ($\sigma_{ext,\ amb}$). Finally, the visibility was calculated based on the Koschmieder experimental equation, and denoted as V_{iscal}. A parameterization scheme was proposed based on the $\sigma_{ext,\ amb}$, $PM_{2.5}$, and RH to simulate the visibility (V_{issimu}), which is more applicable than the theoretical calculation described above. This method was validated at different locations in different regions in China. The values calculated by the scheme showed agreeable well with the observed data in general, especially for low visibility of $\leqslant$ 5 km, associated with severe haze. Although a large bias occurred at some sites, both the hourly and daily averages for almost every event with visibility lower than 5 km were captured. The method reported in this work exhibited smaller bias below 2 km than the other visibility parameterization scheme, and will be available for improving the prediction of visibility in air quality models. (Shen Xiaojing)

1.16 Drivers of the rapid rise and daily-based accumulation in PM_1

Submicron particle matter (PM_1) that rapidly reaches exceedingly high levels in several or more hours in the North China Plain (NCP) has been threating about 400 million individuals' health for decades. The precise cause of the rapid rise in PM_1 remains uncertain. Based on sophisticated measurements in PM_1 characterizations and corresponding boundary-layer (BL) meteorology in the NCP, it is demonstrated that this rising is mainly driven by BL meteorological variability. Large increases in near-ground inversions and decreases in vertical heat/momentum fluxes during the day-night transition result in a significant reduction in mixing space. The PM_1 that is vertically distributed before accumulates at the near-ground and then experiences a rapid rise. Besides meteorological variability, a part of the rise in organics is ascribed to an increase of coal combustion at midnight. The daily-based accumulation of PM_1 is attributed to day-to-day

vertical meteorological variability, particularly diminishing mixing layer height exacerbated by aerosol-radiation feedback. Resolved by a multiple linear regression model, BL meteorological variability can explain 71% variances of PM_1. In contrast, secondary chemical reactions facilitate the daily-based accumulation of PM_1 rather than the rapid rise. Our results show that BL meteorological variability plays a dominant role in PM_1 rising and day-to-day accumulation, which is crucial for understanding the mechanism of heavy pollution formation. (Zhong Junting, Zhang Xiaoye, Zhang Yangmei)

1.17 Enhancement of nanoparticle formation and growth during the COVID-19 lockdown period in urban Beijing

Influenced by the spread of the global 2019 novel coronavirus (COVID-19) pandemic, primary emissions of particles and precursors associated with anthropogenic activities decreased significantly in China during the Chinese New Year of 2020 and the lockdown period (24 January–16 February 2020). The 2-month measurements of the number size distribution of neutral particles and charged ions showed that during the lockdown (LCD) period, the number concentration of particles smaller than 100 nm decreased by approximately 40% compared to the pre-LCD period in January. However, the accumulation mode particles increased by approximately 20% as several polluted episodes contributed to secondary aerosol formation. In this study, new particle formation (NPF) events were found to be enhanced in the nucleation and growth processes during the LCD period, as indicated by the higher formation rate of 2 nm particles (J2) and the subsequent growth rate (GR). The relevant precursors, e.g., SO_2 and NO_2, showed a clear reduction, and O_3 increased by 80% during LCD period, as compared with pre-LCD. The volatile organic vapors showed different trends due to their sources. The proxy sulfuric acid during the LCD period increased by approximately 26%, as compared with pre-LCD. The major oxidants (O_3, OH, and NO_3) of VOCs were also found to be elevated during LCD. That indicated higher J2 and GR (especially below 5 nm) during the LCD period were favored by the increased concentration level of condensing vapors and decreased condensation sink. Several heavy haze episodes have been reported by other studies during the LCD period; however, the increase in nanoparticle number concentration should also be considered. Some typical NPF events produced a high number concentration of nanoparticles that intensified in the following days to create severe aerosol pollution under unfavorable meteorological conditions. Our study confirms a significant enhancement of the nucleation and growth process of nanoparticles during the COVID-19 LCD in Beijing and highlights the necessity of controlling nanoparticles in current and future air quality management. (Shen Xiaojing)

1.18 Simultaneous observation of atmospheric peroxyacetyl nitrate and ozone in the megacity of Shanghai, China: Regional transport and thermal decomposition

Atmospheric peroxyacetyl nitrate (PAN) and ozone (O_3) are two typical indicators for photochemical pollution that have adverse effects on the ecosystem and human health. Observation networks for these pollutants have been expanding in developed regions of China, such as North China Plain (NCP) and Pearl River Delta (PRD), but are sparse in Yangtze River Delta (YRD), meaning their concentration and influencing factors remain poorly understood. Here, we performed a one-year measurement of atmospheric PAN, O_3, particulate matter with aerodynamic diameter smaller than 2.5 mm ($PM_{2.5}$), nitrogen oxides (NO_x), carbon monoxide (CO), and meteorological parameters from December 2016 to November 2017 in Shanghai. Overall, high hourly maximum PAN and O_3 were found to be 7.0 and 185×10^{-9} (V) in summer, 6.2 and 146×10^{-9} (V) in autumn, 5.8 and 137×10^{-9} (V) in spring, and 6.0 and 76.7×10^{-9} (V) in winter, respectively. Continental air masses probably carried atmospheric pollutants to the sampling site, while frequent maritime winds brought in less polluted air masses. Furthermore, positive correlations (R: 0.72−0.85) between PAN and O_3 were found in summer, indicating a predominant role of photochemistry in their formation. Unlike in summer, weak

or no correlations between PAN and O_3 were featured during the other seasons, especially in winter, due to their different loss pathways. Unexpectedly, positive correlations between PAN and $PM_{2.5}$ were found in all seasons. During summer, moderate correlation could be attributed to the strong photochemistry acting as a common driver in the formation of secondary aerosols and PAN. During winter, high $PM_{2.5}$ might promote PAN production through HONO production, hence resulting in a good positive correlation. Additionally, the loss of PAN by thermal decomposition (TPAN) only accounted for a small fraction (about 1%) of the total (PAN+TPAN) during a typical winter episode, while it significantly reached 14.4×10^{-9} (V) (71.1% of the total) in summer. (Zhang Gen)

1.19 Measurement report: Chemical characteristics of $PM_{2.5}$ during typical biomass burning season at an agricultural site of the North China Plain

Biomass burning activities are ubiquitous in China, especially in North China, where there is an enormous rural population and winter heating custom. Biomass burning tracers (i.e., levoglucosan, mannosan and potassium (K+)), as well as other chemical components were quantified at a rural site (Gucheng, GC) in North China from 15 October to 30 November, during a transition heating season, when the field burning of agricultural residues was becoming intense. The measured daily average concentrations of levoglucosan, mannosan and K+ in $PM_{2.5}$ during this study were 0.79 ± 0.75 μg m^{-3}, 0.03 ± 0.03 μg m^{-3} and 1.52 ± 0.62 μg m^{-3}, respectively. Carbonaceous components and biomass burning tracers showed higher levels at nighttime than daytime, while secondary inorganic ions were enhanced during daytime. An episode with high levels of biomass burning tracers was encountered at the end of October, 2016, with high levoglucosan at 4.37 μg m^{-3}. Based on the comparison of chemical components during different biomass burning pollution periods, it appeared that biomass combustion can obviously elevate carbonaceous components levels, whereas no essentially effect on secondary inorganic aerosols in the ambient air. Moreover, the levoglucosan/mannosan ratios during different biomass burning pollution periods remained at high values (in the range of 18.3−24.9); however, the levoglucosan/K+ ratio was significantly elevated during the intensive biomass burning pollution period (1.67) when air temperatures decrease, substantially higher than those in other biomass burning periods (averaged at 0.47). (Liang Linlin)

1.20 Characteristics and potential sources of wintertime air pollution in Linfen, China

Linfen in China's Shanxi Province suffers severe air pollution in winter. Understanding the characteristics of air pollution and providing scientific support to mitigate such pollution are urgent matters. This study investigated the variations of $PM_{2.5}$, PM_{10}, NO_2, SO_2, O_3, and CO in Linfen between December 1, 2019 and February 29, 2020. The mean concentrations of $PM_{2.5}$, PM_{10}, NO_2, SO_2, MDA8 (the maximum daily 8-h average) O_3, and CO were 106.2, 139.4, 47.2, 41.0, 57.0 μg m^{-3}, and 1.8 mg m^{-3}, respectively. Large amounts of pollutants emitted by coal burning, industry, vehicles, and residents contributed to air pollution. Unfavorable meteorological conditions, such as lower temperature, weaker wind, higher relative humidity, and reduced planetary boundary layer height, made the situation worse. Fireworks and firecrackers set off to celebrate traditional Chinese festivals caused the concentration of PM pollutants to spike, with the maximum daily mean concentration of $PM_{2.5}$ reaching 314 μg m^{-3} and the peak hourly value reaching 378.0 μg m^{-3}. Suspensions of commercial and social activities due to COVID-19 reduced anthropogenic emissions, mainly from industry and transportation, which decreased the level of air pollutants other than O_3. Analyses involving backward trajectory cluster, the potential source contribution function, and concentration weighted trajectory demonstrated that $PM_{2.5}$ pollution mainly came from local emissions in Shanxi Province and regional transport from Inner Mongolia, Shaanxi, Hebei, Henan, and Gansu provinces. Shanxi and its surrounding provinces

should adopt measures such as tightening environmental management standards, promoting the use of renewable energy, and adjusting the transportation structure to reduce regional emissions. This study will help policy-makers draft plans and policies to reduce air pollution in Linfen. (Liu Lei)

1.21 Aerosol promotes peroxyacetyl nitrate formation during winter in the North China Plain

Peroxyacetyl nitrate (PAN) is an important indicator for photochemical pollution, formed similar to ozone in the photochemistry of certain volatile organic compounds (VOCs) in the presence of nitrogen oxides, and has displayed surprisingly high concentrations during wintertime that were better correlated to particulate rather than ozone concentrations, for which the reasons remained unknown. In this study, wintertime observations of PAN, VOCs, $PM_{2.5}$, HONO, and various trace gases were investigated to find the relationship between aerosols and wintertime PAN formation. Wintertime photochemical pollution was affirmed by the high PAN concentrations (average: $(1.2 \pm 1.1) \times 10^{-9}$, maximum: 7.1×10^{-9}), despite low ozone concentrations. PAN concentrations were determined by its oxygenated VOC (OVOC) precursor concentrations and the NO/NO_2 ratios and can be well parameterized based on the understanding of their chemical relationship. Data analysis and box modeling results suggest that PAN formation was mostly contributed by VOC aging processes involving OH oxidation or photolysis rather than ozonolysis pathways. Heterogeneous reactions on aerosols have supplied key photochemical oxidants such as HONO, which produced OH radicals upon photolysis, promoting OVOC formation and thereby enhancing PAN production, explaining the observed $PM_{2.5}$-OVOC-PAN intercorrelation. In turn, parts of these OVOCs might participate in the formation of secondary organic aerosol, further aggravating haze pollution as a feedback. Low wintertime temperatures enable the long-range transport of PAN to downwind regions, and how that will impact their oxidation capacity and photochemical pollution requires further assessment in future studies. (Zhang Gen)

1.22 Unexpected deep mixing layer in the Sichuan Basin, China

In the Sichuan Basin (SCB), one of the four major basins in China, a one-year continuous observation study was performed using a ceilometer in Chengdu (November 2018–December 2019). The results show that the mixing layer height (MLH) in the SCB exhibits a bimodal seasonal variation pattern, with peaks in June (842 m) and October (704 m) and valleys in September (535 m) and January (607 m). Stable atmospheric conditions in September were the main reason for the decrease in MLH. Through comparison to other regions in China, it is found that the seasonal evolution of the MLH in the SCB is similar to that in the Yunnan-Guizhou Plateau region and more pronounced than that in the central and eastern plain regions of China. This indicates that the change in MLH is influenced by both the Western Pacific subtropical high and South Asian high. Combined with an analysis of the fine-particulate matter concentration, it is found that the main influence factor of the air pollution in the SCB is not the atmospheric dilution capability, and the local contribution should be paid more attention. The MLH as a meteorological index for air quality prediction varies from place to place. This study is of great importance to the understanding of the mixing layer structure in the basin and its influence on air pollution. (Liu Yusi)

1.23 Impact of residual layer transport on air pollution in Beijing, China

The residual layer (RL) stores a large amount of pollutants, but its effect on near-surface pollution is unknown. In this study, a two-year continuous observation was performed in Beijing using a ceilometer. The generalized boundary layer includes the mixing layer and RL. The results showed that there is no significant seasonal difference in the generalized boundary layer height (GBLH). The average GBLHs in spring, summer, autumn and winter are 1155, 1139, 1036 and 1195 m, respectively. The diurnal variation characteristics of spring, summer and autumn are similar, and the RL disappears when the mixing layer height reaches its peak

in the afternoon. In winter, the development of the mixing layer is weak, and there is a 33.8% chance that the RL cannot be breached, thus making the mixing layer height at noon much lower than the GBLH. The concentrations of $PM_{2.5}$ in the mixing layer and RL are 89 and 52 mg m^{-3}, respectively, and the probability that the $PM_{2.5}$ concentration in the RL was higher than that near the ground was 38.9%. RL transport represents an important beginning of the pollution event during the winter mornings and afternoons in Beijing. This study is helpful to better understand the structure of the RL and its influence on air pollution. (Liu Yusi)

1.24 基于航测的云底气溶胶活化率和过饱和度估算

2016年11月13日在北京地区上空存在持续稳定的层状云天气背景下，利用飞机开展了气溶胶粒径谱、化学组成、云滴谱等参量的垂直观测，研究了本次个例中云底气溶胶的活化能力。结果表明，探测期间北京地区为轻度污染天气，地面气溶胶浓度（0.11 ～ 3 μm）达到了4600 cm^{-3}。云层高度为800 ～ 1200 m，云底气溶胶数浓度相对于近地面大幅度降低，而有效粒径显著增大（0.3 ～ 0.6 μm）。同时，近地面气溶胶中疏水性的一次有机气溶胶POA贡献显著，而云底气溶胶中POA的贡献大幅降低，无机组分和二次有机气溶胶SOA的贡献明显增大，造成吸湿性参数κ由0.25（地面）增大至0.32（云底）。云中气溶胶和云滴的谱分布可很好地衔接，且两者的数浓度之和与云底气溶胶浓度一致，可分别代表未活化和已活化的粒子。基于云底气溶胶粒径谱和吸湿性参数计算得到不同过饱和比下云凝结核（CCN）的活化率，通过与实测的云中结果对比，反推得到此次个例的云中的过饱和度约为0.048%。（刘全）

1.25 江西景德镇站大气CH_4和CO季节变化及源解析

基于江西景德镇温室气体站2017年12月至2018年11月筛分获得的CH_4及CO大气本底和污染浓度数据，对大气CH_4和CO浓度季节变化及其排放源特征进行研究，结果表明，大气CH_4和CO本底浓度季节变化特征与浙江临安本底站类似，即夏季低而冬季高，而夏季江西地区水稻田和湿地排放导致CH_4污染浓度显著抬升，相比本底浓度抬升幅度可达133.9×10^{-9}，冬季受西北部地区取暖排放的区域输送的影响，1月CO污染平均浓度较本底浓度抬升达227.2×10^{-9}。基于本底数据及污染数据，结合后向轨迹模型分析发现景德镇站大气CO潜在排放源主要分布在湖北东南部（四季）、安徽（秋冬季）、山东中部（秋季）、长三角上海及杭州（夏秋季）、湖南东部和江西地区（冬季）等区域，其中冬季湖南东部和江西地区贡献率达53.7%，CH_4排放源主要集中在江西地区（夏季）、长江三角洲杭州、南京及安徽南部覆盖区域（夏季）、湖北东南部（夏秋季）以及安徽（秋季）、山东中部（秋季）等区域，夏季南京、杭州及安徽南部覆盖区域的CH_4排放对景德镇站CH_4浓度抬升的贡献率达到69.5%。大气CH_4及CO呈现较好的相关性，冬季其相关系数可达0.86，受CH_4和CO源汇季节变化影响，CH_4/CO排放比呈现冬季低值（0.31）、夏季高值（1.06）。（张根）

2 环境气象数值预报模式发展及大气成分与天气、气候相互作用研究
2 Development of environmental meteorological numerical prediction model and studies of interactions between atmospheric compositions and weather/climate

2.1 Biological crust in sand and dust storm source areas of Asia and its impact on dust emission

Even though the biological crusts are critical to dust emissions, no sand and dust forecast model have considered the impacts of the biological crust in dust emission scheme. This situation mainly comes from two scientific difficulties: there is no large scale regional biological crust data available that can be used in the forecast model; there is no quantification of how biological crusts impact on sand emission. In this way, we

studied the distribution of biological soil crust in sand and dust storm (SDS) source areas of the Central and East Asia using moderate resolution imaging spectroradiometer satellite surface reflectance data collected in 2000−2019 to determine its potential impact on dust emission according to two empirical schemes. We further evaluated the relationships between soil crust coverage, roughness length, and dust emission to study SDS source areas. We found that biological crust is widely distributed in SDS source areas of the Central and East Asia, with coverage rates of 19.8% in Central Asian deserts, 23.1% in the Gobi Desert, and 17.3% to 32.8% in Chinese deserts ($p > 0.05$). Cyanobacteria and lichen coverage has increased in Chinese deserts, reflecting the recent impacts of the Project of Returning Farmland to Grassland and Farmland to Forests. However, biological soil crust coverage has not increased in Central Asian deserts or the Gobi Desert, and that in Central Asian deserts continues to decrease, demonstrating the complexity of the combined effects of human activities and climate change on its distribution. Biological soil crust increased the roughness length of Central and East Asian SDS source areas by 0.14−0.62 mm. The suppression of dust emission due to biological soil crust did not change among years during the study period. The horizontal and vertical dust flux inhibition coefficient (DFIC) were 2.0−11.0 and 1.7−2.9 ($p > 0.05$), respectively, clearly showing a suppressive effect. Improvement of the ecological environment in some deserts can lead to the ability of these crusts to inhibit dust erosion errors that must be considered in the dust emission scheme for areas where crust coverage has improved. (Zhou Chunhong)

2.2 Development of key physicochemical mechanisms in CUACE model

The development of chemical transport models with advanced physics and chemical schemes could improve air-quality forecasts. In this study, the China Meteorological Administration unified atmospheric chemistry environment (CUACE) model, a comprehensive chemistry module incorporating gaseous chemistry and a size-segregated multicomponent aerosol algorithm, was coupled to the weather research and forecasting (WRF) framework with chemistry (WRF-Chem) using an interface procedure to build the WRF/CUACE v1.0 model. The latest version of CUACE includes an updated aerosol dry deposition scheme and the introduction of heterogeneous chemical reactions on aerosol surfaces. We evaluated the WRF/CUACE v1.0 model by simulating $PM_{2.5}$, O_3, NO_2, and SO_2 concentrations for January, April, July, and October (representing winter, spring, summer and autumn, respectively) in 2013, 2015, and 2017 and comparing them with ground-based observations. Secondary inorganic aerosol simulations for the North China Plain (NCP), Yangtze River Delta (YRD), and Sichuan Basin (SCB) were also evaluated. The model captured well the variations of $PM_{2.5}$, O_3, and NO_2 concentrations in all seasons in the eastern China. However, it is difficult to accurately reproduce the variations of air pollutants over SCB, due to its deep basin terrain. The simulations of SO_2 were generally reasonable in the NCP and YRD with the bias at 15.5% and 24.55%, respectively, while they were poor in the Pearl River Delta (PRD) and SCB. The sulfate and nitrate simulations were substantially improved by introducing heterogeneous chemical reactions into the CUACE model (e.g., change in bias from 95.0% to 4.1% for sulfate and from 124.1% to 96.0% for nitrate in the NCP). Additionally, The WRF/CUACE v1.0 model was revealed with better performance in simulating chemical species relative to the coupled fifth-generation Penn State/NCAR mesoscale model (MM5) and CUACE model. The development of the WRF/CUACE v1.0 model represents an important step towards improving air-quality modeling and forecasts in China. (Zhang Lei, Gong Sunling)

2.3 Development of four-dimensional variational assimilation system based on the GRAPES-CUACE adjoint model (GRAPES-CUACE-4D-Var V1.0) and its application in emission inversion

In this study, a four-dimensional variational (4DVar) data assimilation system was developed based on the GRAPES-CUACE (global/regional assimilation and prediction system-CMA unifified atmospheric

chemistry environmental forecasting system) atmospheric chemistry model, GRAPES-CUACE adjoint model and L-BFGSB (extended limited-memory Broyden-Fletcher-Goldfarb-Shanno) algorithm (GRAPES-CUACE-4D-Var) and was applied to optimize black carbon (BC) daily emissions in the northern China on 4 July 2016, when a pollution event occurred in Beijing. The results show that the newly constructed GRAPES-CUACE-4D-Var assimilation system is feasible and can be applied to perform BC emission inversion in the northern China. The BC concentrations simulated with optimized emissions show improved agreement with the observations over the northern China with lower root-mean square errors and higher correlation coeffificients. The model biases are reduced by 20%–46%. The validation with observations that were not utilized in the assimilation shows that assimilation makes notable improvements, with values of the model biases reduced by 1%–36%. Compared with the prior BC emissions, which are based on statistical data of anthropogenic emissions for 2007, the optimized emissions are considerably reduced. Especially for Beijing, Tianjin, Hebei, Shandong, Shanxi and Henan, the ratios of the optimized emissions to prior emissions are 0.4–0.8, indicating that the BC emissions in these highly industrialized regions have greatly reduced from 2007 to 2016. In the future, further studies on improving the performance of the GRAPES-CUACE-4D-Var assimilation system are still needed and are important for air pollution research in China. (Wang Chao, An Xingqin)

2.4 Application of turbulent diffusion term of aerosols in mesoscale model

The presence of unfavorable meteorological conditions triggers pollution, and then further weakens turbulence, especially in the stable boundary layer (SBL), which is a frequent situation in heavy pollution episodes in China. The inapplicability of the classical Monin-Obukhov similarity theory (MOST) and the uncertainty of the planetary boundary layer height can lead to large deviation of turbulent diffusion in the SBL in numerical simulations. However, in current mesoscale models, no term has been used to accurately describe the turbulent diffusion of aerosols. Therefore, we use the Mixing-Length theory to obtain the turbulent diffusion term of aerosols based on high-resolution observational data, and, for the first time, embed this term into a mesoscale model, which makes the turbulent diffusion process of aerosols more truly depicted. Results from a two-way coupled atmospheric-chemistry mesoscale model demonstrate that the turbulent diffusion term of aerosols can improve the problem of overestimated $PM_{2.5}$ concentration in the eastern China. (Jia Wenxing, Zhang Xiaoye)

2.5 Impact of modified turbulent diffusion of $PM_{2.5}$ aerosol in WRF-Chem simulations in eastern China

Correct description of the boundary layer mixing process of particle is an important prerequisite for understanding the formation mechanism of pollutants, especially during heavy pollution episodes. Turbulent vertical mixing determines the distribution of momentum, heat, water vapor and pollutants within the planetary boundary layer (PBL). However, what is questionable is that turbulent mixing process of particles is usually denoted by turbulent diffusion of heat in the WRF-Chem model. With mixing-length theory, the turbulent diffusion relationship of particle is established, embedded into the WRF-Chem and verified based on long-term simulations from 2013 to 2017. The new turbulent diffusion coefficient is used to represent the turbulent mixing process of pollutants separately, without deteriorating the simulation results of meteorological parameters. The new turbulent diffusion improves the simulation of pollutant concentration to varying degrees, and the simulated results of $PM_{2.5}$ concentration are improved by 8.3% (2013), 17% (2014), 11% (2015) and 11.7% (2017) in the eastern China, respectively. Furthermore, the pollutant concentration is expected to increase due to the reduction of turbulent diffusion in mountainous areas, but the pollutant concentration did not change as expected. Therefore, under the influence of complex topography, the turbulent diffusion process is insensitive

to the simulation of the pollutant concentration. For mountainous areas, the evolution of pollutants is more susceptible to advection transport, because of the simulation of obvious wind speed gradient and pollutant concentration gradient. In addition to the $PM_{2.5}$ concentration, the concentration of CO as a primary pollutant, has also been improved, which shows that the turbulent diffusion process is extremely critical for variation of the various aerosol pollutants. Additional joint research on other processes (e.g., dry deposition, chemical and emission processes) may be necessary to promote the development of the model in the future. (Jia Wenxing, Zhang Xiaoye)

2.6 Development and application of a street-level meteorology and pollutant tracking system

A multi-model simulation system for street level circulation and pollutant tracking (S-TRACK) has been developed by integrating the weather research and forecasting (WRF), the STAR-CCM+ (computational fluid dynamics model, CFD) and the flexible particle (FLEXPART) models. The winter wind environmental characteristics and the potential contribution of traffic sources on nearby receptor sites in a city district of China are analysed with the system for January 2019. It is found that complex building layouts change the structure of the wind field and thus have an impact on the transport of pollutants. The wind speed inside the building block is smaller than the background wind speed due to the dragging effect of dense buildings. Ventilation is better when the dominant airflow is in the same direction as the building layout. Influenced by the building layout, the local circulations show that the windward side of the building is mostly the divergence zone and the leeward side is mostly the convergence zone, which is more obvious for high buildings. With the hypothesis that the traffic sources are uniformly distributed on each road and with identical traffic intensity, the potential contribution ratios (PCR) of four traffic sources to certain specific sites under the influence of the street-level circulations are estimated with the method of residence time analysis. It is found that the contribution ratio varies with the height of the receptor site. As a result of the generally upward motion in the airflow, the position with the greatest PCR from the four road traffic sources is located on a certain height which is commonly influenced by the distance of this location from the traffic source and the background wind field (about 15 m in this study). The potential contribution of a road to one of the receptor sites is also investigated under different wind directions. The established system and the results can be used to understand the characteristics of urban wind environment and to help the air pollution control planning in urban areas. (Zhang Huan, Gong Sunling)

2.7 A new parameterization of uptake coefficients for heterogeneous reactions on multi-component atmospheric aerosols

Based on laboratory studies and field observations, a new parameterization of uptake coefficients for heterogeneous reactions on multi-component aerosols is developed in this work. The equivalent ratio (ER) of inorganic aerosol is used to establish the quantitative relationship between the heterogeneous uptake coefficients and the composition of aerosols. Incorporating the new ER-dependent scheme, the WRF-CUACE model has been applied to simulate sulfate mass concentrations during December 2017 in the Beijing-Tianjin-Hebei region and evaluate the role of aerosol chemical components played in the sulfate formation. Simulated temporal variations and magnitudes of sulfate show good agreement with the observations by using this new scheme. From clean to polluted cases, although both dominant cations and anions increase significantly, the equivalent ratio decreases gradually and is closer to unity, representing the variation of aerosol compositions, which inhibits the heterogeneous uptake of SO_2, with the uptake coefficient decreasing from 1×10^{-4} to 5.3×10^{-5}. Based on this phenomenon, a self-limitation process for heterogeneous reactions with the increasing secondary inorganic aerosol from clean to polluted cases is proposed. (Zhou Yike, Gong Sunling)

2.8 Impact of Arctic oscillation anomalies on winter $PM_{2.5}$ in China via a numerical simulation

The impact of Arctic oscillation (AO) anomalies on winter $PM_{2.5}$ variability in China was investigated using a numerical modeling system (WRF-CUACE). The model results showed that the influence of AO anomalies on winter $PM_{2.5}$ concentration was mainly concentrated in the eastern China, especially in the Central China (CEN), Beijing-Tianjin-Hebei (BTH), the Yangtze River Delta (YRD), and Pearl River Delta (PRD) and was mostly consistent with the conclusions of a previous analysis using haze data. Winter $PM_{2.5}$ concentrations in CEN and BTH increased under abnormally high AO and decreased under abnormally low AO due to the subsequent changes in specific meteorological conditions, such as temperature, wind speed, and boundary layer height. Winter $PM_{2.5}$ decreased in the YRD and PRD in both abnormally high and low AO years due to more favorable vertical transport conditions and regional transport capacity compared with those of other regions. In addition to meteorological factors, AO anomalies also impacted $PM_{2.5}$ depositions in winter, with more apparent effects in the southern China. It is found that AO had a larger impact on dry deposition than on wet deposition, and dry deposition was a dominant factor affecting $PM_{2.5}$ concentrations in CEN. (Lu Shuhua, Gong Sunling)

2.9 Impacts of long-range transports from Central and South Asia on winter surface $PM_{2.5}$ concentrations in China

A quantitative analysis of the impacts of particulate matter transported from Central and South Asia on winter surface $PM_{2.5}$ concentrations in China is investigated from 2013 to 2017. The chemical boundary conditions generated by the MOZART4 global model (MOZ-CBC) are used to drive WRF-Chem regional model as the long-range transport inflow to China. The long-range transport effects of $PM_{2.5}$ were estimated by the difference caused by primary aerosol (PA), secondary aerosol (SIA), and dust separately from the corresponding component changes in MOZ-CBC. On the five-year average, the long-range transports of particulate matter increase the winter surface dust concentrations by 6–30 μg m^{-3}, PA concentrations by 0–2 μg m^{-3}, and SIA concentrations by 0–1.2 μg m^{-3}. Except for Xinjiang, which is closest to the western border, North China Plain is the most significant region in the mainland of China that could be affected by the long-range transport, indicated by the average increase at 1.6 μg m^{-3} (4.5%) in PA, 0.9 μg m^{-3} (1.8%) in SIA, and 16 μg m^{-3} (35%) in dust. The average increment in PA, SIA, and dust is decreased during El Niño and increased during La Niña. Wind anomalies in the El Niño event weaken prevailing westerly wind but favor the meridional circulation, increasing the precipitation and wet scavenging contribution in the eastern seaboard and resulting in the decrease of the $PM_{2.5}$ concentration in China caused by long-range transport, while these phenomena are opposite in La Niña events. However, the MOZART4 model might overestimate the frequency of dust storms in winter and the vertical height that dust could reach. (Mo Jingyue, Gong Sunling)

2.10 Assessment of meteorology vs. control measures in the China fine particular matter trend from 2013 to 2019 by an environmental meteorology index

A framework was developed to quantitatively assess the contribution of meteorology variations to the trend of fine particular matter ($PM_{2.5}$) concentrations and to separate the impacts of meteorology from the control measures in the trend, based upon the environmental meteorology index (EMI). The model-based EMI realistically reflects the role of meteorology in the trend of $PM_{2.5}$ and is explicitly attributed to three major factors: deposition, vertical accumulation and horizontal transports. Based on the 2013–2019 $PM_{2.5}$ observation data and re-analysis meteorological data in China, the contributions of meteorology and control measures in nine regions of China were assessed separately by the EMI-based framework. Monitoring network observations show that the $PM_{2.5}$ concentrations have declined by about 50% on the national average and by

about 35% to 53% for various regions. It is found that the nationwide emission control measures were the dominant factor in the declining trend of China $PM_{2.5}$ concentrations, contributing about 47% of the $PM_{2.5}$ decrease from 2013 to 2019 on the national average and 32% to 52% for various regions. The meteorology has a variable and sometimes critical contribution to the year-by-year variations of $PM_{2.5}$ concentrations, 5% on the annual average and 10%–20% for the fall-winter heavy pollution seasons. (Gong Sunling)

2.11 Development and application of an automated air quality forecasting system based on machine learning

As one of the most concerned issues in the modern society, air quality has received extensive attentions from the public and the government, which promotes the continuous development and progress of air quality forecasting technology. In this study, an automated air quality forecasting system based on machine learning has been developed and applied for daily forecasts of six common pollutants ($PM_{2.5}$, PM_{10}, SO_2, NO_2, O_3, and CO) and pollution levels, which can automatically find the best "Model + Hyperparameters" without human intervention. Five machine learning models and an ensemble model (Stacked Generalization) were integrated into the system, supported by a knowledge base containing the meteorological observed data, pollutant concentrations, pollutant emissions, and model reanalysis data. Then five-year data (2015–2019) of Beijing, Shanghai, Guangzhou, Chengdu, Xi'an, Wuhan, and Changchun in China, were used as an application case to study the effectiveness of the automated forecasting system. Based on the analysis of seven evaluation criteria and pollution level forecasts, combined with the forecasting results for the next 3-days, it is found that the automated system can achieve satisfactory forecasting performance, better than most of numerical model results. This implied that the developed system unveils a good application prospect in the field of environmental meteorology. (Ke Huabin, Gong Sunling)

2.12 Incorrect Asian aerosols affecting the attribution and projection of regional climate change in CMIP6 models

Anthropogenic aerosol (AA) forcing has been shown as a critical driver of climate change over Asia since the mid-20th century. Here we show that almost all Coupled Model Intercomparison Project phase 6 (CMIP6) models fail to capture the observed dipole pattern of aerosol optical depth (AOD) trends over Asia during 2006–2014, the last decade of CMIP6 historical simulation, due to an opposite trend over the eastern China compared with observations. The incorrect AOD trend over China is attributed to problematic AA emissions adopted by CMIP6. There are obvious differences in simulated regional aerosol radiative forcing and temperature responses over Asia when using two different emissions inventories (one adopted by CMIP6; the other from Peking University, a more trustworthy inventory) to drive a global aerosol-climate model separately. We further show that some widely adopted CMIP6 pathways (after 2015) also significantly underestimate the more recent decline in AA emissions over China. These flaws may bring about errors to the CMIP6-based regional climate attribution over Asia for the last two decades and projection for the next few decades, previously anticipated to inform a wide range of impact analysis. (Wang Zhili)

2.13 Reduction in European anthropogenic aerosols and the weather conditions conducive to $PM_{2.5}$ pollution in North China: a potential global teleconnection pathway

Frequent and severe $PM_{2.5}$ pollution over China seriously harms natural environment and human health. Changes in meteorological conditions in recent decades have been recognized to contribute to the long-term increase in $PM_{2.5}$ pollution in North China (NC). However, the dominant climatic factors driving the interdecadal changes of the weather conditions conducive to $PM_{2.5}$ pollution remain unclear. Here we identify a potential global teleconnection mechanism: the decadal reduction in European aerosol emissions since the

1980s may have partially contributed to the interdecadal increase in weather conditions conducive to $PM_{2.5}$ pollution in NC, measured by an emission-weighted air stagnation index (ASIE) that increases at a rate of 6.2% per decade (relative to the 1981–1985 level). By regression analysis, we show that the decreased European aerosol loadings can warm the lower atmosphere and induce anomalous ascending motion in Europe, which potentially stimulates two anomalous Rossby wave trains in the upper troposphere travelling eastward across Eurasia. The teleconnection patterns project on NC by weakening the near-surface horizontal dispersion, which may be favorable to the increase in local ASIE and air pollution build-up. The suggested mechanism is further supported by the results from a set of large-ensemble simulations, showing that the European aerosol emission decline since the 1980s excites similar local heating and ascending motion and leads to increasing trends of 0.1–0.5 μg m^{-3} per 38 years in surface sulfate concentrations over most of NC. This proposed "West-to-East Aerosol-to-Aerosol" teleconnection mechanism helps resolve opposite views on the impact of global versus local aerosol forcing on $PM_{2.5}$ pollution weather in NC. The policy implication is that the sustained decline in European aerosol emissions in coming decades, in conjunction with unabated global and regional warming, could further exacerbate air pollution in NC, thus imposing stronger pressure to reduce local emission sources quicker and deeper. (Wang Zhili)

2.14 Responses of the East Asian summer monsoon to aerosol forcing in CMIP5 models: The role of upper-tropospheric temperature change

We quantitatively distinguish the fast and slow responses of the East Asian summer monsoon (EASM) to aerosol forcing using the outputs from 16 Coupled Model Intercomparison Project phase 5 (CMIP5) models. The mechanism of the EASM change due to aerosol forcing is then evaluated from the perspective of upper-tropospheric temperature change. The results show that aerosol forcing leads to the weakening of the EASM circulation and decreases in precipitation. The aerosol-induced fast atmospheric response dominates the weakening of EASM and the decreased precipitation over the eastern China. In the fast response, upper-tropospheric cooling in the midlatitudes of East Asia during summer changes the circulation structure, thereby causing the weakening of the EASM. The formation of upper-tropospheric cooling is closely related to the eastward propagation of atmospheric cooling caused by aerosol forcing in Europe and the resulting change in local meridional heat transport. The slow ocean-mediated response to aerosol forcing partially offsets the weakening of the EASM over the eastern China in the fast response. In the slow response, southwesterly wind is enhanced and precipitation is increased over the eastern China, while southwesterly wind is weakened over the northwestern Pacific and the South China Sea, which dominates the decrease in precipitation over the oceans. The aerosol-induced changes of land–sea thermal contrasts further confirm that the decrease of upper-tropospheric land-sea thermal contrasts over East Asia in the fast response plays a key role in driving the weakening of the EASM. (Wang Zhili)

2.15 Simulation of the influence of a fine-scale urban underlying surface on the urban heat island effect in Beijing

In this study, the weather research and forecasting (WRF) model coupled with slab model and single-layer urban canopy model (SLUCM) was used to simulate the urban heat island effect in Beijing. The effects of the refined local climate zone (LCZ) urban underlying surface and Moderate resolution Imaging Spectroradiometer (MODIS) land use data on temperature simulated results were compared through sensitivity tests. These two types of underlying surface data present similar simulation error tendencies, showing an overestimation of the 2 m temperature at night. The simulated temperature results using MODIS land use data are closer to the observations than those simulated using the LCZ data. However, the MODIS land use data provide one

classification for urban surface, which cannot reflect the complex urban morphology, whereas the LCZ concept divides urban land surface into ten categories that can reflect the surface characteristics more accurately. The sensitivity of different urban canopy parameters on temperature simulation provides priority parameters for model improvement. Real data were used to improve the parameter table setting in the urban canopy model and thus enhance the simulation ability of the LCZ test. The urban fraction, emissivity, and albedo in the parameter table were calculated and replaced. It was found that the use of the accurate emissivity provided the best simulation results. There are negative correlations between near-surface temperature and emissivity/albedo, and a positive correlation between near-surface temperature and urban fraction. The influence of the parameters on the simulated temperature at night was more evident than that during the daytime. (He Jianjun)

2.16 The impact of the variation in weather and season on WRF dynamical downscaling in the Pearl River Delta region

In this study, the National Centers for Environmental Prediction (NCEP) final operational global analysis data and meteorological observation data from 2013 to 2017 were used to evaluate the impact of seasonal changes and different circulation classifications on the dynamical downscaling simulation results of weather research and forecasting (WRF) in the Pearl River Delta (PRD) region. The results show that the dynamical downscaling method can accurately simulate the time variation characteristics of the near-surface meteorological field and the hit rates of a 2-m temperature, 2-m relative humidity, 10-m wind speed, and 10-m wind direction are 92.66%, 93.98%, 26.78%, and 76.78%, respectively. The WRF model slightly underestimates the temperature and relative humidity, and overestimates the wind speed and precipitation. For precipitation, the WRF model can better simulate the variation characteristics of light rain and heavy rain, with the probability of detection are 0.59 and 0.69, respectively. For seasonal factors, the WRF model can conduct a perfect simulation in autumn and winter, followed by spring, while summer is vulnerable to extreme weather, so the result of the simulation is relatively poor. The circulation type is an important parameter of downscaling assessment. When the PRD is controlled by high pressure, the simulated results of WRF are good, and when the PRD is affected by low pressure or extreme weather, the simulation results are relatively poor. (He Jianjun)

2.17 Simulation study on regional atmospheric oxidation capacity and precursor sensitivity

In this study, an evaluation index of atmospheric oxidation capacity (AOIe) was established. A typical pollution event from October 3 to 8, 2015, and the WRF-Chem air quality model were used to simulate the distribution characteristics of atmospheric oxidation capacity (AOC) in Beijing and the influence of reducing emissions (NO_x and VOCs) on regional AOC. The results showed that urban areas have stronger (approximately 11% higher on average) AOC than suburban areas. AOIe_G (the process of valence change in gaseous oxidants) contributed more to the regional AOC during the clean period. AOIe_G also contributed more in the daytime whereas AOIe_P (the process of valence change in particulate state) contributed more at nighttime, with the highest contribution accounting for 72% and 69%, and the corresponding peak concentrations appearing at 14:00 and 06:00, respectively. In addition, compared with NO_x reduction, the effect of reducing VOCs on reducing AOC was more significant. (Li Jiangtao, An Xingqin)

2.18 Simulated sensitivity of ozone generation to precursors in Beijing during a high O_3 episode

This study uses the WRF-Chem model combined with the empirical kinetic modeling method (EKMA curve) to study the compound pollution event in Beijing that happened in 13−23 May 2017. Sensitivity tests are conducted to analyze ozone sensitivity to its precursors, and to develop emission reduction measures. The results suggest that the model can accurately simulate the compound pollution process of photochemistry and haze. When VOCs and NO_x were reduced by the same proportion, the effect of O_3 reduction at peak time was

more obvious, and the effect during daytime was more significant than at night. The degree of change in ozone was peak time > daytime average. When reducing or increasing the ratio of precursors by 25% at the same time, the effect of reducing 25% VOCs on the average ozone concentration reduction was most significant. The degree of change in ozone decreased with increasing altitude, the location of the ozone maximum change shifted westward, and its range narrowed. As the altitude increases, the VOCs-limited zone decreases, VOCs sensitivity decreases, and NO_x sensitivity increases. The controlled area changed from near-surface VOCs-limited to high-altitude NO_x-limited. Upon examining the EKMA curve, we have found that suburban and urban are sensitive to VOCs. The sensitivity tests indicate that when VOCs in suburban are reduced about by 60%, the O_3 1 h concentration could reach the standard, and when VOCs of the urban decreased by about 50%, the O_3 1 h concentration could reach the standard. Thus, these findings could provide references for the control of compound air pollution in Beijing. (An Xingqin)

2.19 Influence of East Asian winter monsoon on particulate matter pollution in typical regions of China

This study uses the NCEP/NCAR monthly average reanalysis and number of haze day data during 1958–2017, and the average daily $PM_{2.5}$ mass concentration data during 2013–2017, to calculate the East Asian winter monsoon index (EAWMI) and statistically analyze the correlation between the winter monsoon index and air quality in China, particularly for the five typical regions (Beijing-Tianjin-Hebei, Fen-Wei Plain, Sichuan Chongqing Delta, Yangtze River Delta, and Pearl River Delta). Thereafter, the strong and weak winter monsoon years were classified based on the EAWMI, and the atmospheric circulation and temperature fields over China and the five regions in different winter monsoon years were spatially compared. Finally, the study also investigated the various distribution features of the climatic circulation background responsible for the strong and weak winter monsoons and their impact mechanisms on air quality in the five typical regions in China. The results show that the effect of the winter monsoon on the air quality of China may be represented by a north-south boundary line located at approximately 30°N. During strong winter monsoon years, pollution was lower in the area north of the boundary but higher to its south. By contrast, the opposite phenomenon was observed during the weak monsoon years. During the strong winter monsoon years, the Beijing-Tianjin-Hebei region and Fen-Wei Plain to the north of the boundary line were less polluted, while the Yangtze River, Chengdu-Chongqing, and Pearl River delta regions to the south of the boundary were more polluted. Diagnostic analysis of the circulation field indicated that during the strong winter monsoon years, an abnormal downward airflow occurred to the south of the boundary, limiting convective diffusion and thereby causing the increased pollution. However, during the weak winter monsoon years, ascending airflows occurred, which favored pollutant diffusion. Furthermore, during the strong winter monsoon years, an abnormal southeast airflow with weak horizontal wind speed occurred in the lower atmosphere of the Chengdu-Chongqing region, causing localized pollutant accumulation, thereby aggravating the pollution. In the Pearl River Delta region, a descending abnormal westerly flow inhibited the local uplift and diffusion of air. Moreover, importing pollutants occurred from the north, aggravating the pollution in the region. (Li Yanjun, An Xingqin)

2.20 Key factors determining heterogeneous uptake kinetics of NO_2 onto alumina: Implication for the linkage between laboratory work and modeling study

Heterogeneous reactions on mineral dust play pivotal roles in the removal/production of gaseous pollutants and the formation of secondary particles. However, the uptake coefficient (γ), a key kinetic parameter for a heterogeneous reaction, could vary by several orders of magnitude in different laboratory analyses and give rise to great uncertainties in modeling studies. Thus, a detailed understanding of heterogeneous uptake

kinetics is vital to accurately evaluate the impacts of heterogeneous reactions on atmospheric chemistry. In order to reveal the key factors affecting uptake kinetics, heterogeneous reaction of NO_2 on surfaces of typical mineral component alumina (α-Al2O3, γ-Al2O3, δ-Al2O3, AlOOH) was comprehensively studied using two widely used methods, including diffuse reflectance infrared Fourier transform spectroscopy (DRIFTS) and flow tube reactor. The discrepancy between the true uptake coefficients (γ_{BET}) obtained via two techniques was within 1 to 2 orders of magnitude for alumina samples. The γ_{BET} depended positively on NO_2 concentration in the DRIFTS measurements but negatively on NO_2 concentration in the flow tube experiments, and the discrepancy might be attributed to different calculation methods of γ_{BET}, which was calculated based on nitrate formation kinetics in DRIFTS experiments while based on NO_2 consumption kinetics in flow tube experiments. The results implied that an accurate selection of the uptake coefficient for modeling studies should base on the consideration of factors such as the measurement method, the concentration range of the reaction gas, and the characteristics of the sample such as crystal structure and effective surface area. (Liu Chang)

2.21 Relationship between summertime concurring $PM_{2.5}$ and O_3 pollution and boundary layer height differs between Beijing and Shanghai, China

The rapid development in the economy during past decades has caused serious air pollution issues in China with high concentrations of $PM_{2.5}$ and O_3, particularly in the densely populous cities. To integrate $PM_{2.5}$ and O_3 controls, it is necessary to understand the impacts of meteorology on both pollutants. Thereby, the complex linkages between planetary boundary layer (PBL), synoptic forcing, regional transport, and heavy pollution in Beijing and Shanghai during summer were investigated using long-term measurements, simulations, and reanalysis. Influenced by the unfavorable meteorological conditions, $PM_{2.5}$ pollution and O_3 pollution often simultaneously occurred. In Beijing, the heavy concurring pollutions usually happened on the days with shallow afternoon PBL and southerly/southwesterly prevailing winds. Within the PBL, the pollutants emitted from the southern plains can be transported to Beijing and accumulated on the windward side of the mountains. At the top of PBL, the synoptic southerly warm advections can strengthen the elevated thermal inversion layer and suppress the development of PBL, leading to worse pollution. Contrarily, the heavy pollutions in Shanghai usually occurred on the days with deep afternoon PBL and southwesterly warm advections within the PBL. Although the warm advections were more favorable to the PBL development than the movements of cool marine air mass, the input of pollutants from the southwest can overweigh this advantage, resulting in poor air quality in Shanghai. The occurrence of heavy pollution or clean condition in Shanghai was primarily determined by the synoptic forcing rather than the local PBL structure. This comparative study indicates that the relationship between PBL height and pollution level is changeable and complicated, which needs to be elucidated from the synoptic perspective. (Miao Yucong)

2.22 On the heavy aerosol pollution and its meteorological dependence in Shandong Province, China

Partly due to the lack of fine-resolution measurements of the planetary boundary layer (PBL), the impacts of PBL on the aerosol pollution in the densely populous Shandong Province were not well understood. On the basis of long-term $PM_{2.5}$ measurements, fine-resolution radiosonde data, and meteorological reanalysis from April 2016 to March 2019, the aerosol pollution in Jinan and Qingdao and its complex relationships with the multi-scale meteorological conditions were investigated in this study. During an annual cycle, prominent seasonal variations of $PM_{2.5}$ concentrations can be observed in both cities, with heaviest pollution in the heating season and relatively low concentrations in summer. Significant positive correlation was found between the monthly $PM_{2.5}$ concentrations and thermal stability of the lower troposphere, indicating that the seasonal shifts

of PBL play an important role in regulating the variations of aerosol pollution, in addition to the seasonal changes in the emissions. In the heating season, influenced by unfavorable synoptic patterns, heavy pollution often simultaneously happened in Jinan and Qingdao. Utilizing an objective synoptic classification approach with reanalysis data, two dominant synoptic types led to heavy pollution in Jinan and Qingdao were identified, which were featured by 900-hPa warm advections from the west or southwest with weaker prevailing winds. These synoptic types not only strengthened the elevated thermal inversion and inhibited the vertical dilution of pollutants locally, but also caused the regional transports of pollutants to Jinan and Qingdao from high-emission upstream regions, such as the Beijing-Tianjin-Hebei region, Henan Province and Jiangsu Province. Therefore, to prevent heavy pollution in Jinan and Qingdao, regional joint measures should be implemented with full consideration of synoptic impact. (Miao Yucong)

2.23 Impacts of synoptic forcing and topography on aerosol pollution during winter in Shenyang, Northeast China

Northeast China frequently experiences aerosol pollution episodes in winter. In addition to the pollutant emissions, synoptic pattern and topography can impact the air quality in complex ways, which are still not well understood in Northeast China. Therefore, the impacts of synoptic forcing and topography on aerosol pollution in Shenyang were investigated combining surface observations, sounding measurements, and three-dimensional air quality simulations. The studied pollution episode occurred from January 1 to 5, 2020, along with poor meteorological dispersion conditions characterized by weak winds, strong thermal stabilities, and shallow planetary boundary layers (PBLs). During the formation of pollution, strong elevated thermal inversion layers were observed over Shenyang, induced by the large-scale synoptic pattern, which suppressed the PBL growth and the vertical dispersion of aerosols. Moreover, the blocking effect of mountains to the east of Shenyang further worsened the pollution when northwesterly/westerly flows prevailed in shallow PBLs. A numerical sensitive experiment was conducted to estimate the contribution of blocking effect of mountains to the near-surface $PM_{2.5}$ concentration in Shenyang, and it was found that around one third of $PM_{2.5}$ concentration during January 1–4 was relevant to the terrain effect. These findings can facilitate a comprehensive understanding of the physical formation of aerosol pollution in Northeast China and be helpful for the pollution controls. (Miao Yucong)

2.24 Study on the variation of air pollutant concentration and its formation mechanism during the COVID-19 period in Wuhan

To prevent the spread of COVID-19 (2019 novel coronavirus), from January 23 to April 8 in 2020, the highest Class 1 Response was ordered in Wuhan, requiring all residents to stay at home unless absolutely necessary. This action was implemented to cut down all unnecessary human activities, including industry, agriculture and transportation. Reducing these activities to a very low level during these hard times meant that some unprecedented naturally occurring measures of controlling emissions were executed. Ironically, however, after these measures were implemented, ozone levels increased by 43.9%. Also worthy of note, $PM_{2.5}$ decreased by 31.7%, which was found by comparing the observation data in Wuhan during the epidemic from 8 February to 8 April in 2020 with the same periods in 2019. Utilizing CMAQ (the community multiscale air quality modeling system), this article investigated the reason for these phenomena based on four sets of numerical simulations with different schemes of emission reduction. Comparing the four sets of simulations with observation, it was deduced that the emissions should decrease to approximately 20% from the typical industrial output, and 10% from agriculture and transportation sources, attributed to the COVID-19 lockdown in Wuhan. More importantly, through the CMAQ process analysis, this study quantitatively analyzed

differences of the physical and chemical processes that were affected by the COVID-19 lockdown. It then examined the differences of the COVID-19 lockdown impact and determined the physical and chemical processes between when the pollution increased and decreased, determining the most affected period of the day. As a result, this paper found that (1) $PM_{2.5}$ decreased mainly due to the reduction of emission and the contrary contribution of aerosol processes. The northeast wind was also in favor of the decreasing of $PM_{2.5}$. (2) O_3 increased mainly due to the slowing down of chemical consumption processes, which made the concentration change of O_3 pollution higher in 16:00–19:00. of the day, while increasing the concentration of O_3 at night during the COVID-19 lockdown in Wuhan. The higher O_3 concentration in the northeast of the main urban area also contributed to the increasing of O_3 with unfavorable wind direction. (NiuTao)

2.25 Study on the causes of heavy pollution in Shenyang based on the contribution of natural conditions, physical processes, and anthropogenic emissions

This study investigated the impacts of meteorological and geographical conditions, the roles of individual physical processes, and the contribution of emissions during severe $PM_{2.5}$ (fine particulate matter) pollution events in Shenyang, one of the largest industrial cities in China. Simulations of six severe $PM_{2.5}$ pollution events that occurred in 2015 and 2016 revealed that unfavorable meteorological conditions, including high relative humidity, low depth of the planetary boundary layer, low wind speed, changes in wind direction, and unfavorable geographical conditions underly severe $PM_{2.5}$ pollution events in Shenyang. Regarding individual physical processes, emission and aerosol processes increased the concentration of $PM_{2.5}$, while horizontal advection, vertical advection, and vertical diffusion processes dominated the decrease in $PM_{2.5}$. Analysis of source apportionment found that residential (37%) and transportation (30%) dominated $PM_{2.5}$ pollution as categories, and Shenbei New District contributed 75% of regional emissions. The main causes of the severe $PM_{2.5}$ pollution events in Shenyang are complex, including local emissions associated with transportation emissions from Shenbei New District, local emissions associated with agricultural emissions and low northwesterly winds, long-range transport with a southeasterly wind, and middle-range transport with a northerly wind. (NiuTao)

2.26 Application of morrison cloud microphysics scheme in GRAPES_Meso model and the sensitivity study on CCN's impacts on cloud radiation

The Morrison double-moment cloud microphysics scheme is implemented into the GRAPES_Meso model. Sensitivity experiments of different cloud condensation nuclei (CCN) values are conducted to study the impacts of CCN on cloud microphysical processes and radiation processes in East China. The model evaluations illustrate the effectiveness (R = 0.6) of the Morrison scheme for the cloud processes simulations in East China. For the study period of 8 to 12 October 2017, with initial CCN number concentration (CCN0) increasing from 10 to 3000 cm^{-3}, the maximum value of the daily average mixing ratio of cloud water, cloud liquid water path (CLWP), and cloud optical depth (COD) increases by 133%, 100%, and 150%, respectively. However, the maximum value of the daily average mixing ratio of rain decreases by 44%. These impacts on the cloud result in about a 65% increase of the maximum value of daily average cloud downward shortwave radiative forcing (CDSRF). This study indicates the significant impacts of CCN on cloud properties and radiation effects. (Wang Hong)

2.27 Aerosol impacts on cloud physical characteristics and radiation effect

The radiative forcing caused by aerosol-cloud interaction (ACI) is one of the most critical factors that lead to climate research uncertainty. In East China and the adjacent sea areas, the severe air pollution makes the ACI effect stronger than in other regions, but few observational studies focus on the effect of different

aerosol components. This study estimates the shortwave radiation effect at the top of the atmosphere (TOA) caused by the interaction between the increased four aerosol components (black carbon, dust, organic carbon, and sulfate) and the warm liquid cloud in East China and the East China Sea, by applying the multiple linear regression to two ACI effect calculating methods proposed by Quaas et al. (2008; Method 1) and Chen et al. (2014; Method 2). The results suggest a cooling effect of aerosol, with sulfate showing the strongest cooling effect and dust showing the strongest warming effect. The meteorological factor has a significant influence on the distribution of the aerosol effect. Regions with higher relative humidity and low-tropospheric stability have a more significant cooling effect due to the suppression of droplet evaporation and entrainment. Meanwhile, in the heavily polluted East China, a relatively higher warm cloud altitude could reduce the in-cloud aerosol and avoid the droplet evaporation caused by absorbing aerosol and the over much cloud condensation nuclei. This research contributes to a better understanding of the aerosol-cloud radiative effect and its mechanism in East China and the East China Sea. (Wang Hong).

2.28 Comparative analysis of $PM_{2.5}$ and O_3 source in Beijing using a chemical transport model

For many years, Beijing has suffered from severe air pollution. At present, fine particulate matter ($PM_{2.5}$) pollution in the winter and ozone (O_3) pollution in the summer constitute serious environmental problems. In this study, the combination of a comprehensive air quality model with particulate matter source apportionment technology (CAMx-PAST) and monitoring data was used for the high-spatial resolution source apportionment of secondary inorganic components (SNA: SO_4^{2-}, NO_3^-, and NH_4^+) in $PM_{2.5}$ and their corresponding precursor gases (SO_2, NO_2, and NH_3) and O_3 in the winter and summer over Beijing. Emissions from residents, industry, traffic, agriculture, and power accounted for 54%, 25%, 14%, 5%, and 2% of $PM_{2.5}$ in the winter, respectively. In the summer, the emissions from industry, traffic, residents, agriculture, and power accounted for 42%, 24%, 20%, 10%, and 4% of $PM_{2.5}$, respectively. The monthly transport ratio of $PM_{2.5}$ was 27% and 46% in the winter and summer, respectively. The regional transport of residential and industrial emissions accounted for the highest proportion of $PM_{2.5}$. The regional transport of emissions had a significant effect on the SO_4^{2-} and NO_3^- concentrations, whereas SO_2 and NO_2 pollution were mainly affected by local emissions, and NH_4^+ and NH_3 were mainly attributed to agricultural emissions. Industrial and traffic sources were two major emission sectors that contributed to O_3 pollution in Beijing. The monthly transport ratios of O_3 were 31% and 65% in the winter and summer, respectively. The high-spatial resolution regional source apportionment results showed that emissions from Langfang, Baoding, and Tangshan had the greatest impact on Beijing's air pollution. This work's methods and results will provide scientific guidance to support the government in its decision-making processes to manage the $PM_{2.5}$ and O_3 pollution issues. (Liu Lei)

2.29 A reliability assessment of the NCEP/FNL reanalysis data in depicting key meteorological factors on clean days and polluted days in Beijing

In this study, based on the National Centers for Environmental Prediction (NCEP) final analysis (FNL) data, the reliability and performances of their application on clean days and polluted days (based on the $PM_{2.5}$ mass concentrations) in Beijing were assessed. Conventional meteorological factors and diagnostic physical quantities from the NCEP/FNL data were compared with the L-band radar observations in Beijing in the autumns and winters of 2017−2019. The results indicate that the prediction reliability of the temperature was the best compared with those of the relative humidity and wind speed. It is worth noting that the relative humidity was lower and the near-surface wind speed was higher on polluted days from the NCEP/FNL data than from the observations. As far as diagnostic physical quantity is concerned, it was revealed that the temperature inversion intensity depicted by the NCEP/FNL data was significantly lower than that from the

observations, especially on polluted days. For example, the difference in the temperature inversion intensity between the NCEP/FNL data and the observation ranged from −0.56 to −0.77 ℃ on polluted days. In addition, the difference in the wind shears between the NCEP/FNL reanalysis data and the observations increased to 0.40 m/s in the lower boundary layer on polluted days compared with that on clean days. Therefore, it is suggested that the underestimation of the relative humidity and temperature inversion intensity, and the overestimation of the near-surface wind speed should be seriously considered in simulating the air quality in the model, particularly on polluted days, which should be focused on more in future model developments. (Liu Chao, Guo Jianping, Zhang Bihui)

2.30 Characteristics of surface energy balance and atmospheric circulation during hot-and-polluted episodes and their synergistic relationships with urban heat islands over the Pearl River Delta region

This study analyzed the nature, mechanisms and drivers for hot-and-polluted episodes (HPEs) in the Pearl River Delta, China. Numerical model simulations were conducted for the summer and autumn of 2009−2011. A total of eight HPEs were identified, mainly occurring in August and September. *k*-means clustering was applied to group the HPEs into three clusters based on their characteristics and mechanisms. We found three HPEs were driven by weak subsidence and convection induced by approaching tropical cyclones (TC-HPE) and two HPEs were controlled by calm (stagnant) conditions (ST-HPE) with low wind speed in the lower atmosphere, whereas the remaining three HPEs were driven by the combination (hybrid) of both aforementioned systems (HY-HPE). A positive synergistic effect between the HPE and urban heat island (UHI; similar to 1.1 ℃ increase) was observed in TC-HPE and ST-HPE, whereas no discernible synergistic effect was found in HY-HPE. Total aerosol radiative forcing (TARF) caused a reduction in temperature (0.5−1.0 ℃) in TC-HPE and ST-HPE but an increase (0.5 ℃) in HY-HPE. (Nduka Ifeanyichukwu C., Tam Chi-Yung, Guo Jianping)

2.31 Distinct spatiotemporal variation patterns of surface ozone in China due to diverse influential factors

A better knowledge of surface ozone variations and the relevant influential factors is of great significance for controlling frequent ozone pollution events. In this study, we first examined the primary variation patterns of surface ozone in space and time across China via a clustering analysis on the basis of daily maximum 8 h average surface ozone (MDA8) between 2015 and 2018. Statistical models were then established between MDA8 and a set of influential factors to pinpoint dominant factors contributing to regional MDA8 variations. The clustering results revealed four typical variation patterns of MDA8 in China given distinct pollution levels, seasonality, and long-term trends. Statistical modeling results indicated that the seasonal variability of MDA8 was closely associated with UV radiation and meteorological factors like boundary layer height, temperature and relative humidity. In contrast, the long-term trends of MDA8 were largely linked to ozone precursors and meteorological variables including temperature, relative humidity, and total cloud cover. Moreover, the phenomenal increasing trends of MDA8 in North China were found to be statistically associated with the depletion of nitrogen dioxide (NO_2) and carbon monoxide (CO). Specifically, substantial increases in volatile organic compounds (VOCs) along with depletions in NO_2 and CO significantly boosted the photochemical ozone formation chain process in a VOC limited regime like the North China Plain. Overall, the inferred linkage in this study provides evidence and clues to help control increasing ozone pollution events in North China. (Ma Mingliang, Yao Guobiao, Guo Jianping)

2.32 Impacts of biomass burning in Peninsular Southeast Asia on $PM_{2.5}$ concentration and ozone formation in southern China during springtime—A case study

Biomass burning (BB) affects fine particulate matter ($PM_{2.5}$) concentration and ozone (O_3) formation by emitting gaseous precursors and primary aerosols. The Impacts of BB in peninsular Southeast Asia (BB-PSEA) on $PM_{2.5}$ concentration and O_3 formation in the southern China are evaluated using a source-oriented WRF-Chem model to simulate an air pollution episode from March 21 to March 25, 2015. The source-oriented model separates the emissions from BB-PSEA and other sources and can evaluate the effects of aerosol-radiation interactions (ARIs) and aerosol-photolysis interactions (APIs) from BB-PSEA. Comparisons with observations reveal that the model performs well in simulating the air pollution episode. Sensitivity experiments show that BB-PSEA increases $PM_{2.5}$ concentrations on the regional average by 39.3 μg m^{-3} (68.0%) in Yunnan Province (YNP) and 8.4 μg m^{-3} (24.1%) in other downwind areas (ODAs) in the southern China, including the provinces of Guizhou, Guangxi, Hunan, Guangdong, Jiangxi, Fujian, and Zhejiang. $PM_{2.5}$ enhancement is mainly attributed to primary aerosols in YNP and to secondary aerosols in ODA. BB-PSEA increases O_3 concentrations by 18.1 μg m^{-3} (19.4%) in YNP and decreases O_3 concentrations by 3.7 μg m^{-3} (5.3%) in ODA. The O_3 increase in YNP is attributed to the gaseous emissions of BB-PSEA, and the O_3 decrease in ODA is caused by the effects of ARI and API from BB-PSEA. NH_3 emissions from BB-PSEA play a key role in enhancing secondary inorganic aerosols in the southern China and determining increases in $PM_{2.5}$ concentrations in ODA. (Xing Li, Bei Naifang, Guo Jianping)

2.33 Satellite-derived long-term estimates of full-coverage PM_1 concentrations across China based on a stacking decision tree model

Fine particles with aerodynamic diameters less than 1 μm (PM_1) often exert a greater threaten on human health, and thus it is highly imperative to accurately characterize the spatiotemporal variation of PM_1 concentrations and to assess the potential health risks. Our study attempted to predict the long-term full-coverage PM_1 concentrations across China during 2004−2018 using a stacking decision tree model based on satellite data, meteorological variables, and other geographical covariates. The result suggested that the stacking model captured strong prediction capability with a higher cross-validation (CV) R^2 value (0.64), and the lower root-mean-square error (RMSE: 18.60 μg m^{-3}) and mean absolute error (MAE: 11.96 μg m^{-3}) compared with the individual model. The higher PM_1 concentrations were mainly concentrated on North China Plain (NCP), Yangtze River Delta (YRD), and Sichuan Basin due to intensive anthropogenic activities and poor meteorological conditions especially in winter. The annual mean PM_1 concentration in China exhibited a remarkable increase during 2004−2007 by 1.34 μg m^{-3} $year^{-1}$ ($p < 0.05$), followed by a gradual decrease during 2007−2018 by 1.61 μg m^{-3} $year^{-1}$ ($p < 0.05$). After 2013, the mean PM1 concentration at the national scale experienced a dramatic decrease by 2.96 μg m^{-3} $year^{-1}$ ($p < 0.05$). The persistent increase of PM_1 concentration across China during 2004−2007 was mainly caused by the rapid increases of energy consumption and inefficient emission control measures, while the dramatic decrease since 2013 was attributed to increasingly strict control measures, particularly the implementation of the Air Pollution Prevention and Control Action Plan (the Action Plan). The long-term PM_1 estimates obtained here provide a key scientific basis and data support for epidemiological research and air pollution mitigation. (Li Rui, Guo Jianping, Geng Guannan)

2. 34 温室气体对亚洲夏季风影响的数值研究

利用NCEP/NCAR再分析资料检验全球气候模式CAM5.1模拟亚洲夏季风的能力，CAM5.1模式能够较好再现亚洲夏季风的基本特征。通过工业革命前、后温室气体排放情景的敏感性试验探讨近现代温室气体增加对亚洲夏季风的影响机制，结果显示：温室气体增加导致亚洲大部分区域地面气温增加，

印度半岛中部、中南半岛和中国东部地区季风增强，印度半岛中部及北部、中南半岛中北部和中国东部地区降水增加。分析大气能量收支和转换发现，温室气体增加通过增强大气对流凝结潜热释放的方式加强大气热源；夏季陆地为暖区，不均匀加热引起全位能增加，从而增强全位能向辐散风动能的转换和辐散风动能向无辐散风动能的转换，最终导致这些区域夏季风增强。其中，对流凝结潜热增加是温室气体增加造成大气稳定度降低，对流活动加强，对流云厚度加大，对流降水增加的结果；同时，对流降水增加是总降水增加的主要原因。（刘煜）

2.35 2016—2019年江西省臭氧污染特征与气象因子影响分析

本文利用2016—2019年生态环境部环境监测总站提供的江西省11个设区市的监测数据及同期的国家气象观测站常规观测资料，研究江西省臭氧污染特征与气象因子的关系。结果表明，江西省近几年臭氧污染日益严重，2016年全省臭氧（日最大8 h滑动平均值）平均浓度为80.1 μg/m^3，到2019年上升至98.2 μg/m^3，平均年增长率为6 μg/m^3。2019年江西省11个设区市O_3超标总天数为475 d，占总超标天数的72.6%。2016—2018年O_3月平均浓度具有典型的季节变化特征：夏季＞春季＞秋季＞冬季，2019年秋季由于降水量显著减少、日照时数增多、气温升高等气象条件导致秋季近地面臭氧浓度异常升高，其平均浓度高于其他季节。臭氧质量浓度总体与气温、日照时数呈正相关，与相对湿度呈负相关，当气温高于30 ℃、相对湿度在20% ～ 40%区间、风速在2 ～ 3 m/s区间时易出现高浓度臭氧污染。江西省臭氧浓度呈现一定的空间分布特征：赣东北城市低于其他地区，南部城市高于北部城市。其中，赣州市臭氧污染较为严重，其2019年平均浓度居全省最高，为104.2 μg/m^3。基于后向轨迹HYSPLIT模型和潜在源解析PSCF对赣州市进行分析，研究结果表明赣州市臭氧污染的主要潜在贡献源区存在一定的季节差异：春季臭氧污染的外来输送源主要来自广东中部和江西北部地区，夏季主要来自江西北部地区，而秋季则主要来自广东北部和安徽中部地区。（张根）

2.36 基于XGBoost算法的WRF-Chem模式优化模拟研究

采用人工智能算法XGBoost结合大气化学模式WRF-Chem，利用北京地区大气污染物的模拟结果及站点监测数据，构建XGBoost统计预报算法模型，并对两种大气污染物$PM_{2.5}$和O_3进行优化模拟，同时分析其特征贡献要素。结果表明，该统计预报模型能够很好地优化大气化学模式模拟的大气污染物浓度，降低模拟误差，对于北京地区站点模拟浓度优化呈现出城区＞近郊＞远郊的优化特点，且算法模型对O_3浓度优化程度更高，优化后相关系数提高达128%。此外，通过特征要素的贡献量分析表明，CO是影响O_3优化的重要特征变量，城郊区特征贡献得分均高达1000以上，Q_2（近地面2 m比湿）是影响$PM_{2.5}$优化的重要气象特征变量，城郊区特征贡献得分分别为950和824。该研究结果为深入分析优化算法模型对大气污染物的优化原理及其影响因素的定量研究提供一种新思路。（李江涛，安兴琴）

2.37 精细化下垫面对海南地区气象场模拟的影响

使用WRF模式对2013年海南地区气象场进行了模拟研究，并对比分析使用不同精度的陆面资料［WRF默认的陆面资料（土地利用、植被覆盖度、地形和土壤类型），2013年MODIS土地利用和植被覆盖度资料，SRTM3地形资料，HWSD土壤类型资料］对WRF模式模拟结果的影响。结果表明：采用WRF模式默认或高精度的陆面资料都能够较为准确地模拟出当地气象场的时空分布特征；采用高精度且时效性更好的陆面资料可显著地改进WRF模式对2 m温度和2 m相对湿度的模拟，冬（夏）季的均方根误差（RMSE）分别降低了7.2%（6.5%）和6.1%（7.7%），准确率（HR）分别提高了3.7%（2.8%）和3.2%（2.9%）；陆面资料的分辨率及时效性对风场模拟的影响较不敏感，总体上WRF模式仍能较为准确地模拟出研究区域内风场的特征，更新陆面资料后WRF模拟冬（夏）季的风速的RMSE降低了3.8%（4.5%），HR提升了2.1%（2.9%）。（何建军）

2.38 北京边界层参数化敏感性模拟研究

利用中尺度数值天气预报模式WRF模拟晴天条件下北京边界层的气象场特征，并通过敏感性试验研究4组边界层参数化方案（YSU、ACM2、MYJ和BL）对辐射、地表能量、近地面气象要素以及边界层结构的模拟差异。结果表明，4种边界层参数化方案都可以准确模拟向下短波辐射，对长波辐射的模拟能力相似。YSU方案模拟的感热通量最低，4种参数化方案对地表净辐射通量的模拟差异主要受到短波辐射的影响。MYJ方案模拟的2 m温度效果最好，YSU方案对2 m比湿以及10 m风速的模拟效果最优，综合而言，YSU方案对近地面气象要素的模拟效果较好。与探空数据对比，得到4种边界层参数化方案模拟的高层温度廓线偏冷，湿度偏高，风速偏低。与气象铁塔观测数据对比，白天4组试验都能够较为准确地反映温度垂直廓线，YSU方案在15 m以上模拟的相对湿度结果最接近观测值。YSU方案模拟的边界层高度最高，非局地方案模拟的边界层高度相对局地方案更高，MYJ方案模拟的边界层高度误差较大。（何建军）

2.39 江西省冬季大气典型污染过程的气象成因研究

选取2019年1月江西省两次大气污染过程为研究对象，利用常规气象观测资料、美国国家环境预报中心（NCEP）再分析资料、全球资料同化系统（GDAS）气象数据和空气质量数据，分别从局地气象要素变化、地面天气形势、大气动力和热力条件及污染潜在源区等进行分析，对比两次污染过程形成机制。两次污染过程地面天气形势分别为冷锋前部型和低压倒槽型。冷锋前部型污染形成主要原因为冷空气南下在江西省减弱辐合导致上游细颗粒物输送并堆积，西北风增大细颗粒物浓度降低。低压倒槽型污染形成原因为较长时间处于高湿、小风或静风、逆温下的污染累积。对两次过程中污染较为严重的九江市进行分析，冷锋前部型九江市近地面主要受西风影响，低压倒槽型主要受东北风影响，低压倒槽型九江市风速明显低于冷锋前部型，风速多在2 m/s以下。两次污染期间大于3 m/s的风速有利于污染物清除。长时间高湿、小风（＜2 m/s）及风场辐合，是低压倒槽型九江市重污染维持较长时间的重要原因。低压倒槽型大气垂直结构较冷锋前部型稳定。低压倒槽型垂直湍流弱、低层风速小于2 m/s，且存在多层逆温和深厚的湿区，冷锋前部型存在明显下沉运动，逆温强度明显弱于低压倒槽。九江市$PM_{2.5}$污染潜在贡献源主要来自河南东部、山东西部和安徽西北部；低压倒槽型九江市潜在源区主要位于江西省内及与江西省接壤的湖北东南部、安徽西南部。（张根）

2.40 新疆地区大气环境容量系数的气候特征及其在空气质量变化中的作用

新疆在我国属于冬半年大气环境容量系数（*A*值）显著偏低的区域。研究了1975—2019年新疆大气环境容量系数的时空变化特征。新疆的低*A*值区主要分布在塔里木盆地北部和新疆东部；研究期间新疆的大气环境容量系数在随机波动中整体呈下降趋势，这与新疆平均风速的变化较为一致，主要是由气候变化引起。新疆*A*值的季节差异大，春夏高、秋冬低；*A*值的冬季均值远小于年均值，说明新疆冬季的大气自净能力很弱。新疆4个地级市的月均*A*值与$PM_{2.5}$浓度具有显著的负相关，*A*值能够较好地反映当地空气污染的气象条件特征。南疆城市则由于沙尘天气的影响，大气颗粒物浓度很高，但*A*值与$PM_{2.5}$浓度的相关性较差。还基于*A*值，利用城市大气环境荷载指数对新疆4个地级市的大气污染排放变率进行了评估。（王郁）

生态与农业气象
Ecological and Agricultural Meteorology

生态与农业气象研究进展
Progress in Ecological and Agricultural Meteorology Research

1 生态气象
1 Ecological meteorology

1.1 Critical leaf water content for maize photosynthesis under drought stress and its response to rewatering

Crop photosynthesis is closely related to leaf water content (LWC), and clarifying the LWC conditions at critical points in crop photosynthesis has great theoretical and practical value for accurately monitoring drought and providing early drought warnings. This experiment was conducted to study the response of LWC to drought and rewatering and to determine the LWC at which maize photosynthesis reaches a maximum and minimum and thus changes from a state of stomatal limitation (SL) to non-stomatal limitation (NSL). The effects of rehydration were different after different levels of drought stress intensity at different growth stages, and the maize LWC recovered after rewatering following different drought stresses at the jointing stage; however, the maize LWC recovered more slowly after rewatering following 43 days and 36 days of drought stress at the tasseling and silking stages, respectively. The LWC when maize photosynthesis changed from SL to NSL was 75.4% ± 0.38%, implying that the maize became rehydrated under physiologically impaired conditions. The LWCs at which the maize V_{cmax25} reached maximum values and zero differed between the drought and rewatering periods. After exposure to drought stress, the maize exhibited enhanced drought stress tolerance, an obviously reduced suitable water range, and significantly weakened photosynthetic capacity. These results provide profound insight into the turning points in maize photosynthesis and their responses to drought and rewatering. They may also help to improve crop water management, which will be useful in coping with the increased frequency of drought and extreme weather events expected under global climate change. (Zhou Guangsheng)

1.2 Quantitative response of maize V_{cmax25} to persistent drought stress at different growth stages

Drought stress has adverse effects on crop growth and yield, and its identification and monitoring play vital roles in precision crop water management. Accurately evaluating the effect of drought stress on crop photosynthetic capacity can provide a basis for decisions related to crop drought stress identification and monitoring as well as drought stress resistance and avoidance. In this study, the effects of different degrees of persistent droughts in different growth stages (3rd leaf stage, 7th leaf stage and jointing stage) on the maximum carboxylation rate at a reference temperature of 25 ℃ (V_{cmax25}) of the first fully expanded leaf and its relationship to the leaf water content (LWC) were studied in a field experiment from 2013 to 2015. The results indicated that the LWC decreased continuously as drought stress continued and that the LWC decreased faster in the treatment with more irrigation. V_{cmax25} showed a decreasing trend as the drought progressed but had no

clear relationship to the growth stage in which the persistent drought occurred. V_{cmax25} showed a significantly parabolic relationship (R^2 = 0.701, p < 0.001) with the LWC, but the different degrees of persistent drought stress occurring in different growth stages had no distinct effect on the LWC values when V_{cmax25} reached its maximum value or zero. The findings of this study also suggested that the LWC was 82.5 ± 0.5% when V_{cmax25} reached its maximum value (42.6 ± 3.6 μmol m^{-2} s^{-1}) and 67.6 ± 1.2% (extreme drought) when V_{cmax25} reached zero. These findings will help to improve crop drought management and will be an important reference for crop drought identification, classification and monitoring as well as for the development of drought monitoring and early warning systems for other crops or maize varieties. (Zhou Guangsheng)

1.3 The interrelationship between water use efficiency and radiation use efficiency under progressive soil drying in maize

The maximizing of water use efficiency (WUE) and radiation use efficiency (RUE) is vital to improving crop production in dryland farming systems. However, the fundamental question as to the association of WUE with RUE and its underlying mechanism under limited-water availability remains contentious. Here, a two-year field trial for maize designed with five progressive soil drying regimes applied at two different growth stages (three-leaf stage and seven-leaf stage) was conducted during the 2013–2014 growing seasons. Both environmental variables and maize growth traits at the leaf and canopy levels were measured during the soil drying process. The results showed that leaf WUE increased with irrigation reduction at the early stage, while it decreased with irrigation reduction at the later stage. Leaf RUE thoroughly decreased with irrigation reduction during the progressive soil drying process. Aboveground biomass (AGB), leaf area index (LAI), a fraction of absorbed photosynthetically active radiation (fAPAR), and light extinction coefficient (k) of the maize canopy were significantly decreased by water deficits regardless of the growth stages when soil drying applied. The interrelationships between WUE and RUE were linear across the leaf and canopy scales under different soil drying patterns. Specifically, a positive linear relationship between WUE and RUE is unexpectedly found when soil drying was applied at the three-leaf stage, while it turned out to be negative when soil drying was applied at the seven-leaf stage. Moreover, the interaction between canopy WUE and RUE was more regulated by fAPAR than by LAI under soil drying. Our findings suggest that more attention must be paid to fAPAR in evaluating the effect of drought on crops and may bring new insights into the interrelationships of water and radiation use processes in dryland agricultural ecosystems. (Zhou Guangsheng)

1.4 Capability of leaf water content and its threshold values in reflection of soil-plant water status in maize during prolonged drought

Leaves play an important role in plant growth and development through photosynthesis and transpiration. Many studies have explored the effects of short-term drought stress on leaf water status; however, few studies have focused on the leaf water content capacity as an indicator of soil-plant water status during prolonged droughts. The results of a field experiment with various irrigation regimes that was conducted during two consecutive maize growing seasons from 2013 to 2014, indicated that the water content of the first fully expanded leaf (LWCtop1) was representative of the soil–plant water status with the development of drought. LWCtop1 was closely linked to the water condition of other leaves and different plant parts in response to progressive water stress. LWCtop1 shared a quadratic relationship with the photosynthetic rate (P_n), and P_n peaked when LWCtop1 approached 84.11% and decreased to zero when LWCtop1 dropped to 68.26%. Moreover, three stages (slow-fast-slow) were observed as leaf water content responded to soil drying, and two important threshold values (minimum: 70.86 ± 0.80%, maximum: 84.58 ± 1.10%) of the leaf water content were determined. The results of this study may provide a physiological and ecological basis for the identification and monitoring of crop drought. (Zhou Guangsheng)

1.5 Increasing temperature shortened the carbon uptake period and decreased the cumulative net ecosystem productivity in a maize cropland in Northeast China

Phenology—mainly associated with climatic factors—is crucial for the accurate estimation of cumulative annual carbon exchange between terrestrial ecosystems and the atmosphere. However, the effects of changes in phenology on annual vegetation productivity and its regulatory mechanisms remain unclear, particularly in agricultural ecosystems. Therefore, in this study, we examined the associations among cumulative net ecosystem productivity (NEP), phenological metrics, and climatic factors based on long-term (2005–2014) eddy covariance flux and meteorological observations in a maize cropland in Northeast China. The results showed that carbon uptake period (CUP) was mainly determined by the end date of CUP (ECUP) in autumn. Cumulative NEP from May to September (NEP5-9), a period generally corresponding to the growing season, significantly increased with NEP_{max} (defined in this study as the 90th percentile of daily NEP during CUP) and CUP. NEP_{max} explained greater interannual variation in NEP5-9 than CUP. The start date of CUP (SCUP) and ECUP were both advanced with increasing winter temperature, but ECUP was more temperature-sensitive than SCUP. Thus, CUP tended to shorten with increasing temperature, ultimately decreasing cumulative NEP. In addition, NEP_{max} decreased with increasing precipitation in summer and autumn. The Greenup and MidGreendown dates from the MODIS Global Vegetation Phenology (MCD12Q2) product generally captured the interannual variation in the carbon flux-based SCUP and ECUP, respectively, well. The results of this study would be of great significance for predicting the response of ecosystem productivity to plant phenology shifts in agricultural ecosystems in future climate change scenarios. (Zhou Guangsheng)

1.6 Climatic warming enhances soil respiration resilience in an arid ecosystem

Precipitation plays a vital role in maintaining desert ecosystems in which rain events after drought cause soil respiration (R_s) pulses. However, this process and its underlying mechanism remain ambiguous, particularly under climatic warming conditions. This study aims to determine the magnitude and drive R_s of R_s resilience to rewetting. We conducted a warming experiment in situ in a desert steppe with three climatic warming scenarios—ambient temperature as the control, long-term and moderate warming treatment, and short-term and acute warming treatment. Our findings showed that the average R_s over the measurement period in the control, moderate and acute warming plots were 0.51, 0.30 and 0.30 μm(CO_2) m^{-2} s^{-1}, respectively, and significantly increased to 1.72, 1.41 and 1.72 μm(CO_2) m^{-2} s^{-1}, respectively, after rewetting. Both microbial and root respiration substantially increased by rewetting; microbial respiration contributed more than root respiration to total R_s. The R_s significantly increased with microbial biomass carbon and soil organic carbon (SOC) contents. The R_s increase by rewetting might be due to the greater microbial respiration relying heavily on microbial biomass and the larger amount of available SOC after rewetting. A trackable pattern of R_s resilience changes occurred during the daytime. The resilience of R_s in acute warming plots was significantly higher than those in both moderate warming and no warming plots, indicating that R_s resilience might be enhanced with drought severity induced by climatic warming. These results suggest that climatic warming treatment would enhance the drought resilience of soil carbon effluxes following rewatering in arid ecosystems, consequently accelerating the positive feedback of climate change. Therefore, this information should be included in carbon cycle models to accurately assess ecosystem carbon budgets with future climate change scenarios in terrestrial ecosystems, particularly in arid areas. (Zhou Guangsheng)

1.7 Resistance, recovery, and resilience of desert steppe to precipitation alterations with nitrogen deposition

Precipitation fluctuations with high nitrogen (N) deposition severely impact terrestrial ecosystem

functioning, particularly in arid areas. Here, with rainout shelter facility, a field experiment with a large variation in precipitation and N addition was conducted to disentangle the responses of the plant community to normal precipitation, less precipitation, and rewetting conditions in a desert steppe, Inner Mongolia, the northern China. The field experiment established a unique annual precipitation change cycle across normal precipitation, less precipitation, and rewetting processes to quantify drought resistance, recovery, and resilience by calculating functional differences among three years. Furthermore, the relationships between plant community functional traits and response indices (i.e., the resistance, recovery, and resilience) were tested to clarify the mechanisms driving their responses to precipitation regimes and N addition. The aboveground net primary production (ANPP) increased with annual precipitation and was enhanced by N addition. ANPP with reduced precipitation regimes was less resistant to drought but recovered significantly greater than that with increased precipitation regimes. The perennial species, C3 plants, and forbs mainly contributed to the variations in vegetation productivity in response to drought and wet status cycles. Drought resistance and the recovery of species' functional diversity, evenness, and ANPP stability were closely associated with precipitation changes. The present findings suggested that altered precipitation patterns, community composition, and functional stability contribute to ecosystem stability during water change cycles and are mediated slightly by N deposition. These findings advance understanding of the mechanisms of ecosystem functioning underlying the responses to climatic change. (Zhou Guangsheng)

1.8 Vertical distribution of gas exchanges and their integration throughout the entire canopy in a maize field

Fluxes of carbon and water along a vertical profile within a canopy, particularly the associations between canopy and ecosystem levels, are not well studied. In this study, gas exchange along the vertical profile in a maize canopy was examined. The relationships between leaf- and ecosystem-level carbon and water fluxes were compared. The results from research conducted over two growing seasons showed that during vegetative growth, the top and middle leaf layers in the canopy contribute most to the carbon and water fluxes of the entire canopy. During the grain-filling stage, gas exchange processes were performed mostly in the middle leaves with and near the ears. Significant relationships were observed between the net ecosystem CO_2 exchange rate (NEE) plus soil respiration and the assumed canopy levels (Acanopy) and between evapotranspiration rates at the ecosystem (ET) and assumed canopy levels (Ecanopy). This highlights the close associations between these parameters by integrating the leaf gas exchange rates measured in a conventional leaf cuvette and those at the ecosystem level via the eddy covariance technique. These results improve our understanding of how carbon assimilation varies vertically within a canopy, highlighting the critical role of ear leaves. (Zhou Guangsheng)

1.9 Effects of mosaic representation of land use/land cover on skin temperature and energy fluxes in Noah-MP land surface model over China

The representations of land use/land cover (LULC) play an important role in land surface models (LSMs) for the simulation of the energy flux partition, soil moisture redistribution, and runoff generation. This study was designed to investigate the regional effects of mosaic LULC representations on skin temperature (T_s) and energy fluxes over China at three horizontal resolutions and how these effects changed with climate regimes, using Noah with multi-parameterization (Noah-MP) LSM. The current officially released Noah-MP only considered the most abundant LULC type within one model grid. In this study, the mosaic method considering all the LULC types existing in one model grid was implemented into Noah-MP. Against the reference data (including MODIS land surface temperature products, FLUXCOM energy flux data and numerical terra dynamic simulation group evapotranspiration data), the mosaic method generally performed better than the

default method and reduced the root-mean-squared-error of T_s and energy fluxes significantly over urban region. The mosaic method affected the T_s and energy fluxes by changing leaf area index and soil moisture, mainly by the former. The warm (monthly mean air temperature larger than 10 ℃) and relatively humid climate (annual total precipitation larger than 200 mm) could enlarge the effect of mosaic method on T_s and energy fluxes. The mosaic method reduced discrepancies of T_s and energy fluxes among three horizontal resolutions (0.0625º, 0.25º, and 0.50º), especially over the heterogeneous vegetated and urban region. (Zhou Guangsheng)

1.10 Climate warming-induced drought constrains vegetation productivity by weakening the temporal stability of the plant community in an arid grassland ecosystem

An investigation of the influences of climatic warming on ecosystem function and stability is crucial to project the impact of global climate change on terrestrial ecosystems. However, few studies have applied multiple warming treatments in arid ecosystems, which play a critical role in the global carbon cycle and are among the ecosystems most sensitive to future climatic change. To explore the effects of climatic warming on plant community function and stability, moderate warming and acute warming treatments were conducted in desert grassland, Inner Mongolia, China, using free-air temperature increase facilities. Aboveground net primary production (ANPP) of plant community significantly decreased with climatic warming, particularly in warmer years with drier conditions. The decrease in ANPP was mainly caused by decreased soil moisture induced by climatic warming. Climatic warming reduced the temporal stability of the plant community by weakening plant species asynchrony and shifting key functional groups, such as perennial vs annual grass and C3 vs C4 species. Our findings indicate that climatic warming could hamper plant community productivity via decreased soil moisture and constrain plant community functioning by weakening community stability. This result highlights that shifts in plant community composition and consequent functional changes can play a key role in predicting the responses of arid ecosystems to climatic change. (Zhou Guangsheng)

1.11 Photosynthetic resistance and resilience under drought, flooding and rewatering in maize plants

Abnormally altered precipitation patterns induced by climate change have profound global effects on crop production. However, the plant functional responses to various precipitation regimes remain unclear. Here, greenhouse and field experiments were conducted to determine how maize plant functional traits respond to drought, flooding, and rewatering. Drought and flooding hampered photosynthetic capacity, particularly when severe and/or prolonged. Most photosynthetic traits recovered after rewatering, with few compensatory responses. Rewatering often elicited high photosynthetic resilience in plants exposed to severe drought at the end of plant development, with the response strongly depending on the drought severity/duration. The associations of chlorophyll concentrations with photosynthetically functional activities were stronger during post-tasseling than during pre-tasseling, implying an involvement of leaf age/senescence in responses to episodic drought and subsequent rewatering. Coordinated changes in chlorophyll content, gas exchange, fluorescence parameters (PSII quantum efficiency and photochemical/non-photochemical radiative energy dissipation) possibly contributed to the enhanced drought resistance and resilience and suggested a possible regulative trade-off. These findings provide fundamental insights into how plants regulate their functional traits to deal with sporadic alterations in precipitation. Breeding and management of plants with high resistance and resilience traits could help crop production under future climate change. (Zhou Guangsheng)

1.12 Quantitative evaluation of the trade-off growth strategies of maize leaves under different drought severities

The leaf is one of the most drought-sensitive plant organs. Investigating how leaf traits change and their

trade-off growth during a drought would contribute to developing targeted drought-resistance measures. We investigated changes in five key maize leaf traits (leaf area, dry mass, effective number, water content, and specific weight) and their trade-off growth based on a drought simulation experiment. We also developed an indicator (0, 1) to quantitatively evaluate drought severity. The results showed a trade-off growth between different leaf traits of maize plants under drought conditions. Maize maintained relatively high leaf water content to maintain high leaf metabolic activity until drought severity was greater than 0. When drought severity was (0, 0.48), maize tended to adopt rapid growth strategy by maintaining regular leafing intensity and investing more energy into leaf area rather than specific leaf weight so that more energy could be absorbed. When the drought severity exceeded 0.48, maize conserved its resources for survival by maintaining relatively lower metabolic activity and thicker leaves to minimize water loss. The results provide an insight into the acclimation strategies of maize under drought, and contribute to targeted drought prevention and relief measures to reduce drought-induced risks to food security. (Zhou Guangsheng)

1.13 Growth variations of dahurian larch plantations across Northeast China: Understanding the effects of temperature and precipitation

Climate change is affecting the growth and distribution of trees in the Chinese boreal forest. Such changes in China, the southern terminus of the extensive Eurasian boreal forests, reflect on the changes that could occur further north under a warming climate. Most studies have found that tree growth increases with increasing temperature and precipitation in boreal forests, but there is little observational evidence of the climate thresholds that might slow these growth rates at the more extreme temperatures which are predicted to occur under future global warming. Here, we examine growth responses of this dominant boreal tree species (Larix gmelinii) to climate based on the data from plantation sample plots across a broad region (40º51'–52º58' N, 118º12'E−133º42' E) in Northeast China. From statistically significant fits to quadratic equations, temperature and precipitation are the important climatic factors determining tree growth in L. *gmelinii* plantations at two age classes (<10 year and 10–30 years-old stands). The maximum rates of tree height and diameter at breast height (DBH) were about 0.53 m year^{-1} and 0.46 cm year^{-1} at <10 year stands, and about 0.63 m/year and 0.60 cm/year at 10–30-year stands, respectively. For stands with the highest values of mean annual increment (MAI), the corresponding optimal mean annual temperature (MATopt) focused between 0.66 ℃ and 1.57 ℃. The optimal mean annual precipitation (MAPopt) between 663 mm and 708 mm produced the maximal growth increments. With mean annual temperature of −2.4 ℃ and precipitation of 470 mm averaged over 1954–2005 in Chinese boreal forest region as baseline, we conservatively estimated that trees in Chinese boreal forest appear to have higher growth potentials with the maximum temperature increase of 3.6 ℃ and precipitation increase of 40%. (Zhou Guangsheng)

1.14 Responses of plant biomass and yield component in rice, wheat, and maize to climatic warming: A meta-analysis

The responses of crop yields to climatic warming have been extensively reported from experimental results, historical yield collections, and modeling research. However, an integrative report on the responses of plant biomass and yield components of three major crops to experimental warming is lacking. Here, a meta-analysis based on the most recent warming experiments was conducted to quantify the climatic warming responses of the biomass, grain yield (GY), and yield components of three staple crops. The results showed that the wheat total aboveground biomass (TAGB) increased by 6.0% with general warming, while the wheat GY did not significantly respond to warming; however, the responses shifted with increases in the mean growing season temperature (MGST). Negative effects on wheat TAGB and GY appeared when the MGSTs

were above 15 ℃ and 13 ℃, respectively. The wheat GY and the number of grains per panicle decreased by 8.4% and 7.5%, respectively, per ℃ increase. Increases in temperature significantly reduced the rice TAGB and GY by 4.3% and 16.6%, respectively, but rice straw biomass increased with increasing temperature. However, the rice grain weight and the number of panicles decreased with continuous increasing temperature (ΔT_a). The maize biomass, GY, and yield components all generally decreased with climatic warming. Finally, the crop responses to climatic warming were significantly influenced by warming time, warming treatment facility, and methods. Our findings can improve the assessment of crop responses to climatic warming and are useful for ensuring food security while combating future global climate change. (Zhou Guangsheng)

1.15 ChinaSpec: A network for long-term ground-based measurements of solar-induced fluorescence in China

Remotely sensed solar-induced fluorescence (SIF) has emerged as a novel and powerful approach for terrestrial vegetation monitoring. Continuous measurements of SIF in synergy with concurrent eddy covariance (EC) flux measurements can provide a new opportunity to advance terrestrial ecosystem science. Here, we introduce a network of ground-based continuous SIF observations at flux tower sites across the mainland China referred to as ChinaSpec. The network consists of 16 tower sites until 2019 including six cropland sites, four grassland sites, four forest sites, and two wetland sites. An automated SIF system was deployed at each of these sites to collect continuous high-resolution spectra for high-frequency SIF retrievals in synergy with EC flux measurements. The goal of ChinaSpec is to provide long-term ground-based SIF measurements and promote the collaborations between optical remote sensing and EC flux observation communities in China. We present here the details of instrument specifications, data collection and processing procedures, data sharing and utilization protocols, and future plans. Furthermore, we show the examples how ground-based SIF observations can be used to track vegetation photosynthesis from diurnal to seasonal scales, and to assist in the validation of fluorescence models and satellite SIF products (e.g., from OCO-2 and TROPOMI) with the measurements from these sites since 2016. This network of SIF observations could improve our understanding of the controls on the biosphere-atmosphere carbon exchange and enable the improvement of carbon flux predictions. It will also help integrate ground-based SIF measurements with EC flux networks which will advance ecosystem and carbon cycle researches globally. (Zhou Guangsheng)

1.16 Grated remote sensing and model approach for impact assessment of future climate change on the carbon budget of global forest ecosystems

At present, global warming is an indisputable fact, and more and more attention has been paid to the impacts of climate warming on global ecological environments. Forests play increasing significant roles in regulating global carbon balance and mitigating climate change. Therefore, to understand the response mechanisms of the carbon budget of global forest ecosystems to future climate change, an improved version of the FORest ecosystem Carbon budget model for CHiNa (FORCCHN) and future Representative Concentration Pathway (RCP) scenario RCP4.5 and RCP8.5 were applied in this study. The results demonstrated that the global forest ecosystems will play a major role in the carbon sink under the future two climate change scenarios. In particular, the average carbon budget of global forest ecosystems under RCP4.5 scenario was estimated to be 0.017 kg(C) m^{-2} yr^{-1} from 2007 to 2100. The future carbon sink areas of global forest ecosystems will increase significantly. Under RCP4.5 and RCP8.5 climate scenarios, the carbon sink areas of global forest ecosystems during 2026–2100 would be significantly been expanded than those in 2007–2025, with increases of 83.16%–87.26% and 23.53%–29.70%, respectively. The impacts of future climate change on carbon budget of global forest ecosystems will significantly vary between different regions. The carbon budget of forests will be enhanced in the Northern Hemisphere and significantly weakened in the Southern

Hemisphere under the future two climate change scenarios. The carbon sink regions of global forests will be mainly distributed in the middle and high latitudes of the Northern Hemisphere. In particular, the forests' carbon budget in the northeastern and central Asia, northern Europe and western North America will increase by 40% to 80%. However, the carbon budget of forests will decrease by 20% to 40% in the most regions of the Southern Hemisphere. In northern South America and central Africa, the forests' carbon budget will be reduced by more than 40%. In the future, in some areas of Southern Hemisphere, where the forests' carbon budget was predicted to be reduced, some measures for improving forest carbon sink, such as strengthening forest tending, enforcing prohibiting deforestation laws and scientific forest management, and so on, should be implemented to ensure immediate mitigation and adaptation to climate change. (Zhao Junfang)

1.17 Analysis of wheat yield losses at the county level in mainland China

There have been few pieces of research focused on quantifying wheat yield loss risk based on high-resolution long-term historical data. What is more, the existence of the area scale effect reduces the certainty and spatial comparability of results. In this study, long-term wheat yield and planting area data at the county level from 1981 to 2010 were used. The spatial distribution of wheat yield loss risks was analyzed in the mainland of the People's Republic of China (China for short). An improved comprehensive risk index of yield loss risk was established by integrating the reduction rate, coefficient of variation, and the probability of occurrence for different yield reduction rates after removing the effect of area scale. The main wheat-growing areas of 874 counties in the mainland of China were divided into lowest, lower, moderate, higher, and highest risk areas based on it. The high-risk areas are located in the Yellow-Huai-Hai Plain, including Shandong, Henan, northern Anhui, and parts of Jiangsu Province. (Fang Shibo)

1.18 Using long-term earth observation data to reveal the factors contributing to the early 2020 desert locust upsurge and the resulting vegetation loss

Massive desert locust swarms have been threatening and devouring natural vegetation and agricultural crops in East Africa and West Asia since 2019, and the event developed into a rare and globally concerning locust upsurge in early 2020. The breeding, maturation, concentration and migration of locusts rely on appropriate environmental factors, mainly precipitation, temperature, vegetation coverage and land-surface soil moisture. Remotely sensed images and long-term meteorological observations across the desert locust invasion area were analyzed to explore the complex drivers, vegetation losses and growing trends during the locust upsurge in this study. The results revealed that (1) the intense precipitation events in the Arabian Peninsula during 2018 provided suitable soil moisture and lush vegetation, thus promoting locust breeding, multiplication and gregarization; (2) the regions affected by the heavy rainfall in 2019 shifted from the Arabian Peninsula to West Asia and Northeast Africa, thus driving the vast locust swarms migrating into those regions and causing enormous vegetation loss; (3) the soil moisture and NDVI anomalies corresponded well with the locust swarm movements; and (4) there was a low chance the eastwardly migrating locust swarms would fly into the Indochina Peninsula and Southwest China. (Fang Shibo)

1.19 Analyzing the probability of acquiring cloud-free imagery in China with AVHRR cloud mask data

Optical remote sensing data are used widely in many fields (such as agriculture, resource management and the environment), especially for the vast territory of China; however, the application of these data is usually limited by clouds. Although it is valuable to analyze the probability of acquiring cloud-free imagery (PACI), PACI using different sensors at the pixel level across China has not been reported. In this study, the PACI of China was calculated with daily advanced very high resolution radiometer (AVHRR) cloud mask data from 1990 to 2019. The results showed that (1) PACI varies dramatically in different regions and months in China.

The value was larger in autumn and winter, and the largest figure reached 49.55% in October in Inner Mongolia (NM). In contrast, relatively small values occurred in summer, and the minimum value (5.26%) occurred in June in South China (SC). (2) As the climate changes, the PACI has increased significantly throughout the country, especially in North China (NC), with a growth rate of 1.9% per decade. The results can be used as a reference for selecting appropriate optical sensors and observation times in areas of interest. (Fang Shibo)

1.20 Analysis of variation in reference evapotranspiration and its driving factors in mainland China from 1960 to 2016

Understanding the variation in reference evapotranspiration (ET_0) is vital for hydrological cycles, drought monitoring, and water resource management. With 1507 meteorological stations and 130 radiation-measured stations, the annual and seasonal ET_0 were calculated at each site from 1960 to 2016 in mainland China. The phenomenon of coefficient *a* being less than 0.25 and coefficient *b* being greater than 0.50 in the Angstrom–Prescott model occurred in almost the whole country, except for a small area of western and northeastern China. Moreover, the Xiao's method was more applicable to calculate the net longwave radiation (R_{nl}) and then improve the estimation accuracy of ET_0. The annual ET_0 varied from 538.8 to 1559.8 mm and had a high-value center located in the plateau and desert of the northwestern China and a low-value center located in Northeast China and near the Sichuan Basin. The spatial distribution of seasonal ET_0 was roughly similar to that of annual ET_0, except for that in winter when ET_0 was high in the south and low in the north. In mainland China, the annual ET_0 decreased by 21.2 mm per decade because of the declining sunshine duration before 1993 and increased by 21.1 mm per decade due to the decreased relative humidity (RH) after 1993. Generally, the abrupt change of ET_0 mainly occurred in the southern China rather than northern China (except for Qinghai Tibet Plateau). Basically, the dominant driving factors of annual and seasonal ET_0 were RH and/or T_{max} after the abrupt change in most parts of China. (Fang Shibo)

1.21 New aricultural drought index for monitoring the water stress of winter wheat

Timely and effectively monitoring agricultural droughts for winter wheat production is crucial for water resource management, drought mitigation and even national food security. With soil moisture and actual evapotranspiration (ET) products from 2001 to 2018 supplied by the European Centre for Medium-Range Weather Forecasts (ECMWF) and moderate resolution imaging spectroradiometer (MODIS) data, respectively, two agricultural drought indices, i.e., the univariate soil moisture and evapotranspiration index (USMEI) and bivariate soil moisture and evapotranspiration index (BSMEI), were developed to reflect water stress for winter wheat. Our case study on the North China Plain (NCP) indicated that the USMEI could effectively monitor agricultural drought, especially in autumn and winter from October to January. Furthermore, compared with the evaporative stress index (ESI) and soil moisture anomaly percentage index (SMAPI), the correlations between the USMEI and climatic yields were acceptable at the county level or site scale. However, for the rest of the winter wheat growing season, the ESI and SMAPI performed better than the USMEI. In addition, the BSMEI was not suitable for monitoring droughts for winter wheat because this index overestimated the drought intensity. (Fang Shibo)

1. 22 生态气象：起源、概念和展望

生态气象是应人类面临的生存环境危机而兴起的地球系统科学新兴学科，已经成为大气科学的二级学科。本文阐述了生态气象的学科起源、概念、主要研究内容与特征，指出生态气象是研究生态系统与气象条件之间相互关系的科学，是地球系统多圈层相互作用的核心，服务于人与自然和谐发展；探讨了生态气象观测的主要指标与可能的业务服务产品；阐释了生态气象研究与生态文明气象保障、

气象防灾减灾和应对气候变化的关系。当前生态气象迫切需要开展的重点研究任务如下：（1）生态气象长期观测联网研究；（2）基于大数据与人工智能的生态气象信息提取与分析技术；（3）生态系统对气候变化的适应性及其变化归因；（4）生态系统主要气象灾变机制及其致灾临界气象条件；（5）陆地生态系统关键物候期对多环境要素响应的生理生态机制与模拟模型研究；（6）耦合生物–物理–化学–管理过程的生态气象数值模式研发；（7）陆地生态系统变化对气候系统的反馈作用与可持续发展对策研究。（周广胜）

1.23　河水生态承载力的流域整体性和时空连通性

黄河是中华民族的母亲河，黄河流域是中华文明的重要发育地。在中国5000多年的历史长河中，黄河流域作为全国政治、经济和文化中心占据了3000多年，孕育了河洛文化、河湟文化、关中文化等，分布有西安、郑州、洛阳、开封等古都，诞生了四大发明和《诗经》《老子》《史记》等经典著作。黄河流域是连接青藏高原、黄土高原和华北平原的生态廊道，是西北和华北地区的重要水源，以其占全国2.2%的径流量灌溉了占全国15%的耕地，哺育了流域9省近23.3%的全国人口（2019年），贡献了21.6%的全国GDP（2018年）。不仅如此，黄河流域还是中国最重要的煤炭生产地带。中国排名前14的大型煤炭生产基地中有9个地处黄河流域，已经探明的煤炭储量累计达7292亿吨（原煤）。特别是，煤炭工业已经成为黄河流域中、上游晋陕蒙宁甘地区（即山西、陕西、内蒙古、宁夏和甘肃五省区）经济发展的主要经济支柱产业，煤炭年产量约28亿t，占全国总产量的近70%。因此，黄河流域生态保护和高质量发展直接关系到中国生态文明建设的成败。长期以来，黄河存在水土流失、泥沙淤积和洪水威胁等问题。特别是近几十年来，黄河流域气温升高、极端事件及自然灾害频发，径流减少；同时，大规模的能源开发、煤炭开采也需要大量的水资源。气候变化和不合理人类活动使得黄河上游部分生态系统质量退化、水源涵养功能下降；中游水土流失严重；下游生态流量偏低，部分河口湿地萎缩。目前，黄河流域水资源短缺、自然生态脆弱、经济社会发展相对滞后，是中国生态安全保障和经济社会发展的重点和难点地区。为此，需要梳理制约黄河流域生态保护与高质量可持续发展存在的问题，凝炼关键科学问题，提出当前迫切需要开展的任务。（周广胜）

1.24　中国生态与农业气象研究进展

目前中国生态与农业气象研究主要关注气候变化的影响，而脆弱性与风险预估研究仍存在很大不确定性，甚至无法进行预估研究。以生态/农业气象的脆弱性和风险为切入点，从生态/农业的地理/种植分布、物候/生育期和生产力/产量等方面，综述了中国生态/农业气象的研究进展，指出现有研究成果难以满足高质量生态保护与粮食安全的需求，为此提出了未来拟重点开展的研究任务，即生态/农业气象承载力及其优化布局、生态/农业气象的灾变过程与调控机制、生态/农业变化的气象条件贡献率评估及其适应技术、高质量生态保护与粮食提质增效的气候资源高效利用和定向调控研究，以推进中国生态与农业气象脆弱性与风险研究，为中国生态/农业气象科学应对气候变化提供依据。（周广胜）

1.25　2000—2019年秦岭地区植被生态质量演变特征及驱动力分析

为了阐明2000—2019年秦岭地区植被生态质量变化的空间异质性，以及植被生态质量变化的驱动力，该文采用模型模拟和卫星观测的方法对植被生态质量演变及其驱动力进行研究。结果显示：（1）秦岭地区植被生态质量整体显著改善，植被净初级生产力（NPP）和植被覆盖度（VFC）的平均增加速率分别为8 g（C）/（m^2·a）和0.0054/a。空间上，秦岭地区85% ～ 95%区域的植被生态质量明显改善，但是以西安市为代表的局部地区植被NPP和VFC显著下降。（2）秦岭地区80% ～ 85%区域的降水量和气温呈上升趋势，与植被NPP和VFC增加的空间范围大体一致，证实气候暖湿化对改善植被质量有重

要驱动作用。（3）人类保护活动（天然林保护、退耕还林还草等）使秦岭地区大范围植被生态系统得到抚育，林地、草地和水域面积大幅度增加。以秦岭北麓为代表的建设用地扩张是秦岭部分地区植被生态质量恶化的主要原因，但是人类破坏活动被限制在局部区域。（周广胜）

1.26　增温背景下克氏针茅枯黄期物候对降水响应的光合生理机制

基于红外线辐射增温与控水相结合的原位模拟试验资料，分析了克氏针茅（*Stipa krylovii*）枯黄期对水热变化响应的光合生理机制。结果表明，增温背景下降水是枯黄期的主要影响因子，增水（减水）导致枯黄始期和枯黄盛期的发生时间均延迟（提前），枯黄期持续时间均延长，减水处理对枯黄期持续时间的延长作用更显著。增温背景下，降水变化显著影响枯黄期的生理生态特性，且在枯黄始期最为显著，净光合速率、气孔导度、蒸腾速率、核酮糖-1,5-二磷酸（RuBP）羧化的最大速率（V_{cmax}）、RuBP再生能力的最大速率（J_{max}）均与降水量呈显著正相关。通径分析表明，克氏针茅枯黄期的光合生理机制因水热变化的不同而异。当前环境条件下，枯黄期物候变化的主要影响因子是J_{max}，主要限制因子是V_{cmax}。未来暖干和暖湿气候下枯黄期物候变化的主要影响因子均是V_{cmax}；但在暖干气候下主要限制因子为J_{max}，而在暖湿气候下则无限制因子。这表明克氏针茅枯黄期物候的变化取决于气候环境条件变化对其光合能力的影响。（周广胜）

1.27　温度和光周期协同作用对蒙古栎幼苗春季物候的影响

植物物候对气候变化非常敏感，但关于物候对不同气候因子协同作用的响应机制仍不清楚。为此，以蒙古栎为研究对象，针对蒙古栎物候的主要影响因子温度和光周期，利用大型人工气候室，模拟研究了温度与光周期协同作用（对照、增温1.5 ℃、增温2.0 ℃，不同光周期（10 h、14 h、18 h）及其协同作用（对照处理、增温1.5 ℃ ×18 h、增温1.5 ℃ ×10 h、增温2.0 ℃ ×18 h、增温2.0 ℃ ×10 h））对蒙古栎春季物候的影响与机制。结果表明，（1）相同水分条件下，不同升温程度对蒙古栎幼苗春季物候的影响不同。温升1.5 ℃促进蒙古栎幼苗春季物候（芽膨大期、芽开放期、展叶始期和展叶盛期）提前；而温升2.0 ℃则对不同春季物候的影响不同，表现为促进芽休眠解除和芽开放，但抑制叶片展开。（2）相同水分条件下，不同光周期对蒙古栎幼苗不同春季物候的影响存在差异。长光周期对蒙古栎幼苗展叶盛期影响最大，短光周期对芽膨大期影响最大，但均表现为抑制作用。（3）相同水分条件下，温度升高与光周期增加协同作用有助于促进蒙古栎幼苗春季物候提前，但温度升高与光周期缩短协同作用则对春季物候有抑制作用。（4）蒙古栎幼苗春季物候变化与前期气候胁迫程度存在显著正相关，表明前期气候因子也是物候变化的重要影响因子。研究结果丰富了蒙古栎物候响应多气候因子协同作用的认知，有助于促进物候模型的完善。（周广胜）

1.28　1969—2018年金华市舒适度和冷/热日特征分析

利用1969—2018年气象观测资料对金华市年、季尺度的舒适度和冷/热日数进行分析。结果表明：金华市全年和各季节的平均有效温度均呈显著上升趋势，2000年前后稳定超过平均值且上升趋势增加；年均气候倾向率为0.67 ℃/10a，各季节的上升趋势不同，其中冬季最大，夏季最小。暖冬或冷冬的概率呈先增后减再略增的N型变化趋势，热夏或凉夏的概率呈弱增加趋势。舒适期呈双峰型分布，主要集中在4—6月和9—10月，其中5月的舒适日数最多。舒适期的50 a平均初、终日分别为4月4日和11月8日，随时间推移，初日呈显著提前趋势(约5.7 d/10a)，终日呈显著延后趋势(约4 d/10a)，气候舒适率总体呈不显著的弱上升趋势。年舒适日数和热日数呈显著增加趋势，分别为5.08 d/10a和2.31 d/10a，冷日数呈显著下降趋势，达7.39 d/10a。整体来看，金华市冬季气温较以往更为温暖，夏季更热，春季舒适时间明显增多，秋季的冷不舒适体感时间明显减少。（周广胜）

1.29 基于大气–土壤–植被系统干旱发生发展过程的综合干旱指标构建与应用

适宜的干旱指标和高分辨率数据是准确监测干旱的基础。本研究从气象干旱和土壤干旱以及植被对干旱的响应出发，整合中国国家气象观测站、中国气象局陆面数据同化系统（CLDAS）土壤湿度0.0625°×0.0625°）和MODIS叶面积指数（500 m×500 m）等多源数据信息，构建了基于气象干旱指数（标准化降水蒸散指数）、土壤干旱指数（土壤湿度百分位）和植被干旱指数（叶面积指数百分位）的综合干旱指数，并在中国东北地区开展了典型站点和区域10 km×10 km空间分辨率干旱监测试验。结果表明，综合干旱指数克服了单一气象干旱指数不能准确反映农业旱情及单一植被长势指数会将其他灾害引起的植被长势变差误判为干旱的不足，能够反映灌溉对干旱的影响，实现对大气–土壤–植被系统干旱发生、发展及其影响的监测。（周广胜）

1.30 蒙古栎展叶盛期变化的光谱特征及其影响因素研究

植物生长状况是反映环境变化的重要指标，在全球环境变化格局下，研究多环境因子及交互作用对植物的影响尤为重要。为探究植物光谱特征响应环境变化，从而探究环境变化对植物生长状况的影响，同时实现遥感对植物的监测，该研究以东北地区优势树种蒙古栎为研究对象，分析研究了不同光周期、温度和氮沉降交互作用引起的蒙古栎展叶盛期冠层光谱反射特征变化。基于大型人工气候室模拟试验，设置3个温度，3个光周期和2个氮沉降交互处理，每个处理4个重复。当蒙古栎进入展叶盛期时，每个处理选择差异较小的3个重复，使用Fieldspec Pro FR2500型背挂式野外高光谱辐射仪测量光谱反射率。对不同处理的蒙古栎冠层光谱反射率进行分析，选取NDVI（归一化植被指数）、Chl NDI（归一化叶绿素指数）和PRI（光化学反射指数）3个常用的光谱指数作为辅助分析，同时计算一阶导数光谱以得到红边斜率、红边位置、红边面积等参数。不同处理展叶盛期的蒙古栎光谱反射率趋势大体一致，均符合植物特有的光谱反射特征，在350～680 nm范围内有一个小的波峰，680～750 nm反射率显著上升，750 nm后进入反射平台。结果表明：（1）光周期对于蒙古栎冠层的光谱反射率没有明显的影响；（2）增温会减小蒙古栎冠层在350～750 nm波段处的光谱反射率；（3）施氮会导致蒙古栎展叶盛期350～750 nm波段和750～1100 nm波段处的光谱反射率降低；（4）增温和施氮的交互作用会显著减小蒙古栎的光谱反射率；（5）通过一阶导数光谱可清晰地指示植物的红边特征。研究结果可为物候变化的监测与影响因素分析提供理论依据。（周广胜）

1.31 横断山区地表真实面积与垂直投影面积差异分析——以雅江县为例

横断山脉地形起伏复杂，以垂直投影面积作为地表真实面积进行定量计算会产生较大误差。本文以横断山脉中部雅江县为例，基于DEM数据和地表覆盖产品数据集，利用地表粗糙度的地学意义，计算了雅江县不同土地利用类型地表真实面积，并分析了地表真实面积与垂直投影面积之间的差异。结果表明：雅江县地表面积与投影面积的差异与DEM分辨率呈正相关，与海拔呈负相关，坡度是地表面积与投影面积差异的主要影响因素，坡度越大，差异越大，差异的增长速率越大；不同土地利用类型对面积差异有不同程度的影响。（周广胜）

1.32 不同灌溉量夏玉米叶绿素含量的高光谱特征及其反演

植物叶绿素含量直接影响其光合作用，并与植物的光谱特征密切相关。以夏玉米为研究对象，采用人工控水方法研究了夏玉米七叶期不同灌溉量下冠层叶绿素含量特征及其与光谱特征之间的关系。结果表明：灌溉量越少，夏玉米叶片叶绿素含量越低，冠层光谱反射率越高，绿峰位置“红移”，而红边位置“蓝移”。叶绿素含量与光谱特征参数、植被光谱指数之间存在极显著相关关系，据此建立了冠层叶绿素含量高光谱估算模型，且基于植被指数模型较基于单一光谱特征参数模型模拟效果更好。研究结果可为夏玉米叶绿素含量的快速无损测定以及夏玉米干旱监测提供依据。（周广胜）

1.33 中国毛葡萄和刺葡萄分布的气候适宜性

毛葡萄和刺葡萄是起源于中国且用于葡萄酒酿造的两大野生葡萄品种。本研究基于已有中国毛葡萄和刺葡萄的气候影响因子研究成果，利用最大熵原理从充分性与必要性方面确定了影响中国毛葡萄和刺葡萄种植分布的主导气候因子，并基于这些因子综合作用反映的毛葡萄和刺葡萄种植分布的存在概率分析了中国毛葡萄和刺葡萄分布区的气候适宜性。结果表明，影响中国毛葡萄、刺葡萄分布的主导气候因子是年日照时数、开花期5月降水量、年极端最低气温、最冷月平均气温。中国毛葡萄、刺葡萄气候高适宜区分布在湖南西部和南部、广西中北部、贵州东南部、重庆中部。气候高适宜区、适宜区、低适宜区面积分别占研究区域总面积的2%、14%和16%。毛葡萄、刺葡萄气候适宜及以上区域的年日照时数阈值为1200 ～ 1800 h，年极端最低气温–8 ℃以上，最冷月平均气温阈值为2 ～ 13 ℃，5月降水量为110 ～ 320 mm。（周广胜）

1.34 中国欧亚种酿酒葡萄种植分布的主要气候影响因子与气候适宜性

开展酿酒葡萄气候适宜性研究对于优化酿酒葡萄布局、气候资源开发利用具有重要意义。基于欧亚种酿酒葡萄（*Vitis vinifera* L.）分布数据和影响其分布的气候因子，利用最大熵模型（MaxEnt）和地理信息系统（ArcGIS），研究影响欧亚种酿酒葡萄种植分布的主导气候因子及其气候适宜性。结果表明：MaxEnt 模型能够很好地模拟我国欧亚种酿酒葡萄的潜在分布，模拟效果达到“非常好”（AUC 平均值0.936）的水平。基于气候因子对欧亚种酿酒葡萄地理分布影响的贡献确定了主导气候因子，即无霜期、干燥度、极端最低气温、年降水量、生长季日照时数、≥10 ℃活动积温。当前，我国欧亚种酿酒葡萄种植分布的气候高适宜区、适宜区、次适宜区分别占次适宜及以上区域总面积的2.9%、20.4%和76.7%。欧亚种酿酒葡萄气候高适宜区主要分布在宁夏、山西、陕西、内蒙古、山东、河北、新疆、甘肃等省，只考虑气候因子，陕西、山西、内蒙古具有较大的发展空间。（周广胜）

1.35 基于微波数据与光学数据集成的机器学习技术在作物产量估算中的应用

各类光学植被指数已成功地应用于各种植被监测与作物产量估算中，但这些指数易受大气状况的影响。由星载微波辐射计得到的植被光学厚度数据（VOD）与植被密度、含水量密切相关，数据可全天候获得，在农业遥感监测中呈现着巨大的潜力。作为来自不同传感器的遥感数据，微波遥感数据与光学遥感数据可以提供不同波长范围内的植被信息。为了更准确地进行作物产量估算，本研究提出将微波遥感数据与光学遥感数据共同应用于冬小麦单产估算中。研究选择L波段微波辐射计SMAP卫星的VOD数据与MODIS的标准归一化植被指数NDVI、增强型植被指数EVI、叶面积指数LAI、光合有效辐射分量FPAR数据作为研究变量，分别使用BP神经网络、GA-BP神经网络和PSO-BP神经网络建立冬小麦产量估算模型。结果表明，3种神经网络回归模型的P值均小于0.001，通过了显著性检验。GA-BP神经网络回归模型的估算值与真实值在3种神经网络回归模型中表现了最高的相关性（R = 0.755）与最低的均方根误差（RMSE = 529.145 kg/hm^2），平均绝对误差（MAE = 425.168 kg/hm^2）和平均相对误差（MRE = 6.530%）。为了分析多源遥感数据的结合在作物产量估算中的优势，研究同时构建了仅使用NDVI和LAI，使用NDVI、EVI、LAI、FPAR等光学数据进行冬小麦产量估算的3种GA-BP神经网络回归模型作为对比。结果表明，使用微波遥感数据与光学遥感数建立的GA-BP神经网络回归模型较上述3种作为对比的GA-BP神经网络回归模型的相关系数R值分别提高了0.163，0.229与0.056，均方根误差RMSE分别降低了122.334、158.462和46.923 kg/hm^2，使用多源遥感数据的组合可以很好地提高作物产量估算的准确性。（房世波）

2 农业气象
2 Agricultural meteorology

2.1 Integrated remote sensing and crop model approach for impact assessment of aerosols on biomass accumulation of maize

The remote sensing data and crop model were used to explore the dynamic changes and accumulation of maize biomass in China caused by aerosols in this study. Maize varieties were divided into spring maize and summer maize. Two spring maize and three summer maize stations were selected. The results indicated that the solar radiation through all stages of maize development was reduced by aerosols, with daily average reductions of 3.23 MJ m^{-2} d^{-1} for spring maize and 8.96 MJ m^{-2} d^{-1} for summer maize from 2001 to 2014. Aerosols reduced the daily actual maize biomass in the study area, with an average daily decrease of 3.78 g m^{-2} d^{-1} from 2001 to 2014. Moreover, the changes in daily actual biomass caused by aerosols varied in different growth stages. The reduction in daily actual biomass caused by aerosols in the stage of emergence–flowering was larger than that in the stage of flowering–maturity. For spring maize, the changes in daily actual biomass caused by aerosols were –2.12 to –2.29 g m^{-2} d^{-1} from emergence to flowering and –0.72 to 0.08 g m^{-2} d^{-1} from flowering to maturity. For summer maize, the changes in daily actual biomass caused by aerosols were –8.94 to –3.45 g m^{-2} d^{-1} from emergence to flowering and –6.50 to –2.24 g m^{-2} d^{-1} from flowering to maturity. In addition, the annual maize biomass from 2001 to 2014 at five stations clearly decreased owing to aerosols. Moreover, the decrease in the annual biomass of summer maize was greater than that of spring maize, with an average decrease of 27.77% in summer maize biomass and 10.94% in spring maize biomass. (Zhao Junfang)

2.2 Long-term variations in solar radiation, diffuse radiation, and diffuse radiation fraction caused by aerosols in China during 1961–2016

The effects of atmospheric aerosols on the terrestrial climate system are more regional than those of greenhouse gases, which are more global. Thus, it is necessary to examine the typical regional effects of how aerosols affect solar radiation in order to develop a more comprehensive understanding. In this study, we used global AErosol RObotic NETwork (AERONET) data and robust radiation observational evidence to investigate the impact of aerosols on total radiation, diffuse radiation, and the diffuse radiation fraction in China from 1961 to 2016. Our results showed that there were different temporal changes in the aerosol optical depth (AOD), total solar radiation, diffuse radiation, and diffuse radiation fraction over the past 56 years. Specifically, the 550 nm AOD from 2005 to 2016 decreased significantly, with annual average AOD of 0.51. Meanwhile, the average total solar radiation reduced by 2.48%, while there was a slight increase in average diffuse radiation at a rate of 3.10 MJ m^{-2} yr^{-1}. Moreover, the spatial heterogeneities of AOD, total radiation, diffuse radiation, and the diffuse radiation fraction in China were significant. Aerosol particle emissions in the developed eastern and southern regions of China were more severe than those in the western regions, resulting in higher total radiation and diffuse radiation in the western plateau than in the eastern plain. In addition, aerosols were found to have negative effects on total radiation and sunshine hours, and positive effects on diffuse radiation and diffuse radiation fraction. Further, the diffuse radiation fraction was negatively correlated with sunshine hours. However, there was a positive correlation between AOD and sunshine hours. These results could be used to assess the impacts of climate change on terrestrial ecosystem productivity and carbon budgets. (Zhao Junfang)

2.3 Assessment of seasonal variability of extreme temperature in mainland China under climate change

Some studies have suggested that variations in the seasonal cycle of temperature and season onset could

affect the efficiency in the use of radiation by plants, which would then affect yield. However, the study of the temporal variation in extreme climatic variables is not sufficient in China. Using seasonal trend analysis (STA), this article evaluates the distribution of extreme temperature seasonality trends in mainland China, describes the trends in the seasonal cycle, and detects changes in extreme temperature characterized by the number of hot days (HD) and frost days (FD), the frequency of warm days (TX90p), cold days (TX10p), warm nights (TN90p), and cold nights (TN10p). The results show a statistically significant positive trend in the annual average amplitudes of extreme temperatures. The amplitude and phase of the annual cycle experience less variation than that of the annual average amplitude for extreme temperatures. The phase of the annual cycle in maximum temperature mainly shows a significant negative trend, accounting for approximately 30% of the total area of China, which is distributed across the regions except for northeast and southwest. The amplitude of the annual cycle indicates that the minimum temperature underwent slightly greater variation than the maximum temperature, and its distribution has a spatial characteristic that is almost bounded by the 400 mm isohyet, increasing in the northwest and decreasing in the southeast. In terms of the extreme air temperature indices, HD, TX90p, and TN90p show an increasing trend, FD, TX10p, and TN10p show a decreasing trend. They are statistically significant ($p < 0.05$). This number of days also suggests that temperature has increased over mainland China in the past 42 years. (Zhao Junfang)

2.4 Indicator-based spatiotemporal characteristics of apple drought in North China

Frequent occurrences of drought stress caused by dry weather create severe destroy in apple yield and quality in North China. Although appropriate drought stress is beneficial to apple planting, it might change to apple drought disaster when dry weather continues and reaches to a certain magnitude. So, precisely identification of apple drought based on weather condition is of great merit to provide a basis for targeted apple drought monitoring, early warning and evaluation. To explore the trigger dry weather condition of an apple drought event, apple drought index (ADI) was firstly constructed by the consideration of physiological water demand and precipitation characteristics. The ADIs in historical apple drought disaster samples were reanalysed in North China, and the distribution-type fitting and confidence interval method were used to identify the drought trigger thresholds in the apple drought indicators. Afterwards, spatiotemporal characteristics of apple drought in North China from 1981 to 2018 were explored based on the apple drought indicators. Drought trigger thresholds were ADI 0.86, 0.84 and 0.76 for apple tree germinating to bud brush (P1), bud brush to flowering (P2) and flowering to maturity (P3), respectively. A percentage of 81.82% of drought indicator-based results were strongly consistent with historical records about apple drought disasters. Indicator-based regional average apple drought ratios in North China from 1981 to 2018 were 28.27%, 28.33% and 20.82% in P1, P2 and P3, respectively. 2009, 2000 and 2001 were detected the highest drought frequency years for P1, P2 and P3, with drought ratio 57.07%, 60.00% and 40.98%, respectively. The results can provide technical and theoretical support for targeted apple drought detection, and information and measures for apple drought prevention and mitigation can be implemented according to the indicator-based results. (Yang Jianying)

2.5 Process-based indicators for timely identification of apricot frost disaster on the warm temperate zone, China

Frequent occurrences of late spring frost disaster create severe agricultural/forest damage, even given the background of global warming. In the warm temperate zone of China, which is the largest planting area for fresh apricot, late spring frost disaster has become one of the major meteorological hazards during flowering. To prevent cold weather-induced apricot frost disaster and reduce potential losses in related fruit economic value, it is vital to establish a meteorological indicator for timely and accurate identification of cold weather

process-based apricot frost disaster, to provide support for timely apricot frost monitoring and warning in late spring. In this study, daily minimax temperature (T_{min}) and apricot frost disaster data during flowering were combined to establish meteorological identification indicators of apricot frost based on cold weather processes. A process-based apricot frost model f (D,T T_{cum}) was firstly constructed, and characteristics of T_{cum} (accumulated harmful temperature) were explored under different D (duration days) based on the representation of historical apricot frost processes. Thresholds for the T_{cum} for apricot frost in 1, 2, 3, 4 and more than 5 days of apricot frost process were determined as −1.5, −2.9, −4.4, −5.8 and −7.3 °C, respectively. Validation results by reserved independent disaster samples were generally consistent with the historical records of apricot frost disasters, with 89.00% accuracy for indicator-based identification results. Typical process tracking of the proposed identification indicator to an apricot frost event that occurred in North Hebei during April 3−9, 2018 revealed that the indicator-based identification result basically coincides with the historical disaster record and can reflect more detailed information about the apricot frost process. (Yang Jianying)

2.6 Threshold-based characteristics of apricot frost exposure at young fruit in the warm temperate zone, China

Late spring frost stress is one of the major environmental limiting factors for apricot in the warm zoon in China. Investigation of frost exposure of apricot is of particular interest for estimating the frost risk, thus representing the potential damage for apricot production. In this study, daily minimum temperature (T_{min}), disaster and phenological data of apricot from 1981 to 2020 in the warm zoon were integrated to explore the temperature threshold on apricot at young fruit, facilitating the assessment of apricot frost exposure under the background of climate warming. The daily T_{min} was firstly extracted according to the historical disaster records, to identify the per- and ongoing weather conditions of the low-temperature events. The overall accuracy and receiver operating characteristics curve (ROC) were combined to identify the trigger threshold of apricot frost. The temperature of 1.9 ℃ was identified as the apricot frost trigger threshold in regional assessment, with relatively higher correct rate for disaster (90.2%) and lower incorrect rate for none-disaster (23.4%). An area under the ROC curve (AUC) of 0.88 was obtained, demonstrating a good performance of T_{min} as the trigger factor in discriminating between apricot frost and no frost. High frequency of days suffered from apricot and frost exposure (E) at young fruit were mainly found in the northwestern and middle parts of the region, with frequencies of more than 2 days and E more than 3. Regional days suffered from apricot frost and E were found to have a negative trend with slope −0.0317 and −0.789, respectively, whereas the northwest and middle part of the study region were found to have an increasing trend. The results can provide technical and theoretical support for targeted apricot frost detection and risk assessment, and measures for apricot frost prevention and mitigation can be implemented according to the threshold-based results. (Yang Jianying)

2.7 Dryland maize yield potentials and constraints: A case study in western Kansas

Water-limited environments account for half of the earth's land surface and dryland agriculture acreage is projected to expand due to climate changes. Examining typical dryland yield potentials and yield improvement measures is crucial for developing future dryland crop production systems. This case study used crop modeling to analyze dryland maize yield potential (YPd), farmers' yield potential (YPf), and actual farm yields (Ya) in 1990−2015 in three counties in western Kansas (i.e., Thomas, Greeley and Finney in the U.S. Great Plains region). The calibrated APSIM-Maize model along with actual yields was used to estimate yield gaps attributed to: (1) agronomic factors (YG1 = YPd − YPf) and, (2) socio-economic constraints (YG2 = YPf − Ya). Observed climate conditions during maize growing seasons showed warming, brightening, and drying trends for all three counties in western Kansas from 1990 to 2015. Our results showed that the current actual farm yields (Ya) in western Kansas represented only 34%, 32%, and 28% of YPd in Thomas, Greeley, and Finney

counties respectively, indicating significant exploitable yield gaps. Agronomic factors (YG1) contributed the greatest to the yield gap in Greeley and Finney counties whereas socioeconomic constraints (YG2) offered the greatest opportunity for improvement in Thomas county. Our analysis suggested that improving agronomic management could be a greater priority for further yield improvement in Greeley county but selecting an appropriate hybrid was a greater priority in Finney county. (Sun Shuang)

2.8 Standardized relative humidity index can be used to identify agricultural drought for summer maize in the Huang-Huai-Hai Plain, China

Maize (*Zea mays* L.) is a staple food in most parts of the world, and is also one of the most important food crops in China. Frequent occurrences of drought events can lead to summer maize drought disasters. The air relative humidity has the predominant superiority in spatio-temporal continuity compared to precipitation. In this study, meteorological data, phenophase observations, and disaster records of summer maize in the Huang-Huai-Hai Plain (the HHH Plain) were jointly used to establish a standardized relative humidity index (SRHI) to identify and characterize summer maize drought disasters and to provide support for summer maize drought monitoring, prevention, and mitigation. Results showed that the threshold values of SRHI10 (at ten-day scale) during the V0-VT (planting-tasseling) and VT-R6 (tasseling-physiological maturity) periods were −0.05 and −0.25, and the values of SRHI30 (at monthly scale) during the V0-VT and VT-R6 periods were −0.10 and −0.50, respectively. Both SRHI10 and SRHI30 could reasonably identify the actual drought conditions of summer maize in the HHH Plain. Validation with independent drought samples showed that SRHI10 was the most effective among SRHI10, SRHI30, and SPI10. The province-wide validation within 55 years also revealed that the drought of summer maize identified with SRHI10 was basically consistent with historical disaster records, with the average identification accuracy being of 94.0%. Additionally, SRHI10 could indicate the occurrence of drought relatively earlier than actual drought records during both the V0-VT and VT-R6 periods of summer maize. Therefore, the spatio-temporal distribution characteristics of drought for summer maize in the HHH Plain were mapped based on SRHI10. Drought occurred in 38% and 25% of the years during the V0-VT and VT-R6 periods, respectively, from 1961 to 2015. The drought extent during the V0-VT period was greater than that during the VT-R6 period in 64% of the study years, indicating that summer maize in the HHH Plain was more exposed to drought during the vegetative growth period. The spatial distribution pattern of drought severity increased from the south to north during the V0-VT period, while during the VT-R6 period it exhibited the same spatial pattern to drought frequency. The drought in both the V0-VT and VT-R6 periods of summer maize showed the increasing trend in most of the HHH Plain of China. SRHI10 can be a useful indicator for monitoring and assessing summer maize drought disasters at regional scale. This index can also provide a new method for agricultural drought analysis. (Wang Peijuan)

2.9 Spring frost damage to tea plants can be identified with daily minimum air temperatures estimated by MODIS land sur-face temperature products

Tea (*Camellia sinensis*) is one of the most dominant economic plants in China and plays an important role in agricultural economic benefits. Spring tea is the most popular drink due to Chinese drinking habits. Although the global temperature is generally warming, spring frost damage (SFD) to tea plants still occurs from time to time, and severely restricts the production and quality of spring tea. Therefore, monitoring and evaluating the impact of SFD on tea plants in a timely and precise manner is a significant and urgent task for scientists and tea producers in China. The region designated as the middle and lower reaches of the Yangtze River (MLRYR) in China is a major tea plantation area producing small tea leaves and low shrubs. This region was selected to study SFD to tea plants using meteorological observations and remotely sensed products. Comparative analysis between minimum air temperature (T_{min}) and two MODIS nighttime land

surface temperature (LST) products at six pixel-window scales was used to determine the best suitable product and spatial scale. Results showed that the LST nighttime product derived from MYD11A1 data at the 3×3 pixel window resolution was the best proxy for daily minimum air temperature. A T_{min} estimation model was established using this dataset and digital elevation model (DEM) data, employing the standard lapse rate of air temperature with elevation. Model validation with 145210 ground-based T_{min} observations showed that the accuracy of estimated T_{min} was acceptable with a relatively high coefficient of determination (R^2=0.841), low root mean square error (RMSE=2.15 °C) and mean absolute error (MAE=1.66 °C), and reasonable normalized RMSE (NRMSE=25.4%) and Nash-Sutcliffe model efficiency (EF=0.12), with significantly improved consistency of LST and T_{min} estimation. Based on the T_{min} estimation model, three major cooling episodes recorded in the "Yearbook of Meteorological Disasters in China" in spring 2006 were accurately identified, and several highlighted regions in the first two cooling episodes were also precisely captured. This study confirmed that estimating T_{min} based on MYD11A1 nighttime products and DEM is a useful method for monitoring and evaluating SFD to tea plants in the MLRYR. Furthermore, this method precisely identified the spatial characteristics and distribution of SFD and will therefore be helpful for taking effective preventative measures to mitigate the economic losses resulting from frost damage. (Wang Peijuan)

2.10 Mapping threats of spring frost damage to tea plants using satellite-based minimum temperature estimation in China

Spring frost damage (SFD), defined as the disaster during the period of newly formed tea buds in spring caused by lower temperature and frost damage, is a particular challenge for tea plants (*Camellia sinensis*), whose capacity to adapt to extreme weather and climate impacts is limited. In this paper, the region of the middle and lower reaches of the Yangtze River (MLRYR) in China was selected as the major tea plantation study area, and the study period was focused on the concentrated occurrence of SFD, i.e., from March to April. By employing the standard lapse rate of air temperature with elevation, a minimum temperature (T_{min}) estimation model that had been previously established was used based on reconstructed MYD11A1 nighttime LST values for 3×3 pixel windows and digital elevation model data. Combined with satellite-based T_{min} estimates and ground-based T_{min} observations, the spatiotemporal characteristics of SFD for tea plants were systematically analyzed from 2003 to 2020 in the MLRYR. The SFD risks at three scales (temporal, spatial, and terrain) were then evaluated for tea plants over the MLRYR. The results show that both SFD days at the annual scale and SFD areas at the daily scale exhibited a decreasing trend at a rate of 2.7 days decade^{-1} and 2.45×10^4 ha day^{-1}, respectively (significant rates at the 0.05 and 0.01 levels, respectively). The period with the highest SFD risk appeared mainly in the first twenty days of March. However, more attention should be given to the mid-to-late April time period due to the occurrence of late SFD from time to time. Spatially, areas with relatively higher SFD days and SFD risks were predominantly concentrated in the higher altitude areas of northwestern parts of MLRYR for both multi-year averages and individual years. Fortunately, in regions with a higher risk of SFD, the distribution of tea plants was relatively scattered and the area was small. These findings will provide helpful guidance for all kinds of people, including government agencies, agricultural insurance agencies, and tea farmers, in order that reasonable and effective strategies to reduce losses caused by spring frost damage to tea plants may be recommended and implemented. (Wang Peijuan)

2.11 GHCN-CAMS和CMFD两种尺度再分析资料对宁夏气温反映能力评估

再分析资料能有效弥补实际观测数据时空分布不均的缺陷，开展再分析资料区域适应性评估对地气过程研究、气候分析等具有重要意义。论文利用宁夏24 个气象观测站的平均气温，从2种空间尺度（0.5°×0.5°和0.1°×0.1°）和2种时间尺度（年、月），采用偏差、绝对偏差、均方根误差和相

关系数等多个统计指标，评估了再分析资料对宁夏地区地面气温的反映能力。结果表明：（1）GHCN-CAMS（Global Historical Climatology Network and the Climate Anomaly Monitoring System）和CMFD（China Meteorological Forcing Dataset）2套再分析资料对宁夏气温的反映能力整体上均较强，前者对宁夏气温略高估，后者略低估。（2）年和月2种时间尺度上，2种尺度的再分析资料存在阶段性正偏差和负偏差，且年尺度上的相关性好于月尺度的。（3）2套再分析资料对下垫面主要为农田(压砂种植)的气温均存在冷季高估、暖季低估的情况，对城镇两者总体均低估，对草地整体表现为CMFD在冷季低估、暖季略高估，而GHCN-CAMS在冷季高估、暖季低估。总体看，空间分辨率较高的CMFD再分析资料对宁夏气温的反映能力更好一些。(赵俊芳)

2.12 作物发育模式重构及基于甘蔗的模拟检验

发育进程是作物的生理年龄，发育模式是作物生长模型的时间指针。但目前的发育模式只关注某时段（日）气象条件对作物发育的影响，其准确率也难以满足作物生长模拟的需求。根据作物发育速率不仅与气象条件有关、还与其所处发育期有关的理论假设，重构发育进程模式，并利用1980—2019年我国甘蔗发育实测数据进行模式适应性分析，比较传统模式与重构模式的模拟能力。结果表明：重构模式中，发育单位日序模式和温度日序模式对甘蔗发育进程的适应性均较好，尤其在后期温度不断降低的发育进程以及低温年型的模拟中，其适应能力明显优于传统模式。重构及传统模式模拟能力从强到弱依次为发育单位日序模式、温度日序模式、响应适应模式、发育单位模式、发育单位温度修正模式、热量单位模式，均方根误差计算的模拟能力值依次为4.3、3.9、3.7、3.3、3.0、2.8。（马玉平）

2.13 中国普通油茶种植气候适宜性区划

发展油茶产业可有效增加农民收益，促进精准扶贫并改善生态环境。对油茶进行全国尺度的气候适宜性区划，可以为油茶产业的发展提供科学依据。本研究以中国分布面积最广、产量最高的普通油茶为对象，选择年平均气温、1月和7月平均气温、年降水量和日照时数为关键气候因子，计算主产区（即种植面积在6667 hm^2以上的县市）的关键因子值。基于这些因子值，采用改进的气候相似距法进行全国1 km × 1 km网格的普通油茶种植气候适宜性区划。结果表明：中国普通油茶的最适宜区面积为98×10^4 km^2，主要分布在湖南、江西、福建和浙江四省及周围省的相邻区域；适宜区面积和次适宜区分别为52×10^4 km^2和80×10^4 km^2，依次分布在最适宜区的外围；次适宜区北界约为北纬33.5°，西界约为东经111.5°，南界和东界不明显；湖南省的最适宜区面积最大，其次是江西、广西、浙江和福建，五省合计约占全国最适宜区面积的70%；与多种来源实际种植面积资料对比表明，区划较好地反映了普通油茶的种植状况；与主产区气候特征对比表明，区划较为准确地区分了普通油茶最适宜区、适宜区和次适宜区的气候特征。本研究明确了普通油茶种植气候适宜区的分布，可为油茶产业的规划布局提供科学支撑。(邬定荣)

2.14 中国电线积冰灾害研究进展

电线积冰灾害是导致电力系统发生事故的重要自然灾害之一。基于已有研究成果，从电线积冰相关概念与分类出发，对电线积冰的影响与危害、时空分布、成因、影响因子、预报模型、风险评估以及预防措施等方面进行归纳。我国电线积冰灾害以雾凇型积冰和雨凇型积冰为主，主要环境成因包括准静止锋、大气垂直结构和逆温层，同时还受到地形、高度和导线自身特性等的影响。电线积冰灾害总体上呈现北方多雾凇而南方多雨凇的分布特征，20世纪80—90年代的积冰日数较多，90年代后呈下降趋势。为更好地实现电线积冰灾害的模拟与预测，预报模型也在不断完善，包括物理数值模型和统计预测模型；而对于电线积冰灾害风险评估的研究较少，主要集中在电线积冰灾害的危险性和线路的脆弱性。基于多学科指标构建的电线积冰综合性指标、基于灾变过程的综合风险评估及气候变化对电

线积冰的影响将是今后重点研究方向。（霍治国）

2.15 中国北方冬小麦蚜虫气候风险评估

基于1958—2018年中国北方冬小麦主产区8个主产省（市）小麦蚜虫发生面积、防治面积和小麦播种面积、产量损失、561个气象站点逐日气象资料和典型农业气象站小麦发育期资料，采用相关分析、主成分分析和回归分析等方法，构建华北、黄淮及苏皖地区小麦蚜虫分区域的气候致灾指数。以小麦蚜虫年代际气候致灾指数所划分不同致灾等级发生频次作为小麦蚜虫气候危险性指标，采用小麦蚜虫发生面积率作为脆弱性指标，防治面积与发生面积比值作为防灾减灾能力指标，综合评估小麦蚜虫气候风险趋势。结果表明：北方冬小麦主产区小麦蚜虫气候危险性呈增加态势，年代际差异明显；小麦蚜虫发生脆弱性随年代变化也呈逐步加重态势；小麦蚜虫防灾减灾能力总体呈逐步增强趋势，20世纪90年代提升显著；90年代起小麦蚜虫气候风险逐步加重，高风险范围逐渐扩大，华北、黄淮分别于21世纪初、2011—2018年风险等级达最高；小麦蚜虫气候风险高的区域主要分布在北京、天津、河北中南部大部、山东北部部分地区，较高区域分布在山东大部、河南北部等地。（霍治国）

2.16 季节性冻土的分布与变化特征及对多样性农区农业生产的影响

研究季节性冻土的分布与变化对多样性农区农业生产的影响，对于合理利用气候资源，指导当地农业生产具有重要的意义。文章以临汾市为例，选用1960—2019年临汾市17个观测站逐日的冻土深度、温度、地温、降水量和蒸发量等资料数据，采用克里金空间插值法分析研究区冻土的空间分布，并运用M-K检验、一元线性回归、相关分析等方法分析研究区不同海拔高度季节性冻土的变化趋势及影响因素。（1）临汾市季节性冻土深度在山区大于盆地，北部大于南部，冻土深度与海拔高度正相关显著，相关系数为0.712（$P<0.01$）具有明显的垂直分布特征。（2）近年来最大冻土深度呈明显下降趋势，变化倾向率平均为–2.304 cm/10a，高海拔地区变化趋势尤为显著，1982年冻土深度发生突变，突变后从一个相对偏深期跃变为相对较浅期。（3）冻土始冻日山区早于平川，北部早于南部，解冻日刚好相反，冻土持续期平均相差1个月左右；多年来临汾市土壤表面始冻日推迟，解冻日提前，冻土期明显减少，平均变化率分别为2.088 d/10a、1.762 d/10a和4.069 d/10a，低海拔地区变化趋势更为明显。（4）相关分析表明，冻土深度受冬季地面最低气温影响极显著，其中1月的地面最低气温升高对冻土深度变化起到主要的促进作用，这种影响在高海拔地区更为明显；春、秋两季的地面最低气温升高，使研究区始冻日推迟，解冻日提前，相关系数分别为–0.741、–0.408（$P<0.01$），冻土期明显缩短，蒸发量的相对减少对冻土期和冻土深度变化起到一定抑制作用，降水量对冻土期和冻土深度影响甚微。临汾市冻土期缩短，冻土深度变浅，使越冬农作物干旱加剧，病虫害发生几率增加，同时增加了植物安全越冬系数，使作物生长季延长，对农业增产起到一定作用。（霍治国）

2.17 山西省干旱灾害风险评估与区划

分析山西省干旱灾害风险的关键作用因子，并进行风险评估和区划，对于提升该地干旱灾害风险管理和决策水平、减轻干旱损失具有重要指导意义。文章利用改进的相对湿润度指数、DEM资料、地形坡度资料和1990—2016年以县（市）为单元的行政区域的人口密度、GDP、人均GDP、耕地面积等社会经济数据来定量化评价山西干旱风险，从干旱灾害致灾因子的危险性、孕灾环境的脆弱性、承灾体的易损性和防灾减灾能力4个方面选取因子，构建相应的指数模型并分析其空间分布状况，在此基础上进一步构建山西省干旱灾害风险综合评估模型，并基于GIS绘制山西省干旱灾害风险区划图。山西省干旱致灾因子危险性呈北高南低的趋势，大同、朔州、忻州北部和西部、太原南部的干旱致灾因子危险性最强；孕灾环境脆弱性呈东西两侧高、中间低的趋势，而承灾体易损性和防灾减灾能力均呈东西两侧低、中间高的趋势；从干旱灾害风险区划图可以看出，山西省干旱风险总体呈北高南低，从

西北向东南递减的趋势。高风险区主要分布在大同、朔州东部，较高风险区包括朔州西部、忻州中西部、太原大部，吕梁大部、晋中西部、临汾中部、运城西部为中风险区，临汾西部、晋中大部、长治东北部为较低风险区，临汾东部、运城东部、晋城大部、长治西部和南部风险最低。山西省干旱灾害的精细化风险区划，可为相关区域有效地开展抗旱活动提供定量化依据，增强干旱灾害防御的科学性、实用性和可操作性。（霍治国）

2.18 山西省主要粮食作物气候资源利用率评估

分析和评价区域农业气候资源状况，找出影响农业气候资源有效匹配的限制因子，提高农业气候资源利用率，对促进农业生产、提升农业产能具有重要的实践意义。本文基于山西省1981—2018年108个地面气象观测站的逐日气温、降水、日照等气象资料及31个农业气象观测站春玉米、夏玉米和冬小麦的发育期观测资料，采用平均资源适宜指数、平均效能适宜指数和平均资源利用指数分析了山西省不同作物种植区的气候资源适宜程度、匹配状况和利用率，结果表明：（1）山西省春玉米种植区大部气候资源适宜程度、匹配程度和利用率均较高，西部呈增加趋势、中东部大部呈降低趋势；朔州和忻州中西部温度偏低，制约了该区域光、温、水的合理匹配，利用率较低。（2）山西省夏玉米种植区气候资源适宜度较高，但匹配一般，尤其是运城中西部受降水偏少的影响，气候资源利用率相对较低；全区大部夏玉米气候资源适宜程度、匹配状况及利用率均呈下降趋势。（3）山西省冬小麦种植区平均资源适宜指数、平均效能适宜指数和平均资源利用指数均呈西北低、东南高的空间分布格局，西北部降水偏少导致光、温、水匹配不佳，利用率较低，长治、晋城、临汾中部和运城东部等地资源利用率呈上升趋势，吕梁、太原、晋中和运城西部等地呈下降趋势。由此可见，晋北地区提高农业气候资源利用率的有效途径重点是提升热量资源的利用率，晋中盆地区域以提高水资源利用率为主，晋南运城及临汾盆地区域除提升水资源利用率外，还需考虑温度持续增高对作物生长发育带来的不利影响。（郭建平）

2.19 中国主产区玉米冠层对降水的截留研究

基于13个农业气象试验站2010—2017年逐日气象观测数据和玉米观测数据，采用针对玉米的截留模型，研究自然降雨条件下中国主产区玉米冠层截留及其变化规律。结果表明：在不同气候条件和生长状况下，玉米全生育期冠层截留差异较大。玉米冠层生长季平均截留量为4.3 ～ 23.5 mm，拔节到成熟期降水量≤ 70 mm时，截留量不足8 mm，随着降水量增加，截留量先是同时受降水量和最大面积指数制衡，后变为对最大叶面积指数更敏感。平均截留率为1.9% ～ 11.6%，中国四大玉米主产区中的黄淮海夏播玉米区截留率最稳定，生长季降水量＜ 120 mm的地区截留率超过10%，按玉米主产区和气候干湿度两种分类提供平均截留率范围。依据拔节到成熟期降水量、最大叶面积指数及截留变化规律可以估算不同地区玉米冠层截留量和截留率，为有效降水评估、干旱指标修正、农田水分循环等方面提供科学依据。（郭建平）

2.20 中国北方苹果干旱等级指标构建及危险性评价

构建苹果干旱等级指标体系，评估苹果干旱危险性，对开展苹果干旱防灾减灾、灾害保险意义重大。本文以中国北方苹果主产区为研究对象，利用气象资料、苹果干旱灾情史料和发育期资料，在干旱指数（DI）构建的基础上，以历史灾情反演、灾害样本重建和历史灾害过程解析为主线，采用独立样本T检验、K-S检验、累积概率反函数值等方法，构建适用于中国北方苹果主产区的苹果干旱等级指标体系，并在此基础上开展苹果干旱危险性评价，结果表明：构建的干旱指数（DI）能有效表征苹果干旱灾害；同一等级苹果干旱指标阈值果树萌动–萌芽期＞萌芽–盛花期＞盛花–成熟期；苹果危险性萌芽–盛花期＞果树萌动–萌芽期＞盛花–成熟期，渤海湾产区及黄土高原产区北部是苹果干旱的高危险区

域。基于历史灾情资料加工与再分析的苹果干旱等级指标体系构建方法可为经济林果气象灾害研究提供新的思路，研究结果可为中国北方苹果干旱防灾减损气象服务、灾害保险提供基础支撑。（杨建莹）

2.21 从土壤气候视角解析农业文化遗产地的自然禀赋——以宽城传统板栗栽培系统为例

宽城传统板栗栽培系统是中国重要农业文化遗产，宽城板栗栽培历史悠久，品质优良，为了从土壤气候角度解析宽城板栗栽培系统的自然禀赋和不足，本文利用宽城县基本气象站和自动气象站的观测资料以及专项进行的土壤取样分析数据全面分析了宽城板栗栽培的土壤和气候条件，综合评价了宽城板栗栽培的气候适宜性及其空间分布。结果表明：宽城板栗林土壤酸碱度适宜，有机质丰富，N、K含量和Fe、Mn、Mg等微量元素含量较高，宽城光热资源完全满足板栗生长成熟需要，果实生长期水分供应充足，果实成熟期气温日较差大，板栗主要栽培区域综合气候条件优于板栗栽培适宜指标。总之，宽城板栗栽培系统拥有较好的土壤气候环境，具备栽培高产优质板栗的条件和潜力，春季降水偏少是宽城板栗高产的一个限制因素，适当的春季灌溉可较大幅度地促进板栗高产优质潜力的发挥。（谭凯炎）

2.22 华北平原不同等级干旱对冬小麦产量的影响

华北平原是中国重要的粮食生产基地，其中冬小麦播种面积和产量均居中国首位，在国家粮食安全中具有重要作用，干旱是影响该区域冬小麦产量的最主要农业气象灾害。该研究基于华北平原44个气象站点1981—2017年的逐日气象数据以及作物、土壤和田间管理资料，以作物水分亏缺指数为农业干旱指标，基于调参验证后的农业生产系统模型（APSIM），评估了冬小麦生长发育中后期各生育阶段不同等级干旱对冬小麦单产和总产的影响。结果表明，冬小麦拔节–开花和开花–成熟阶段干旱造成冬小麦减产率空间上均呈北高南低的分布特征，且开花–成熟阶段干旱引起的减产率（26.8%）高于拔节–开花阶段干旱引起的减产率（19.1%），区域间比较均表现为干旱对京津冀地区冬小麦单产影响最大，对河南省冬小麦单产影响最小；随着干旱等级的加重减产率增大，开花–成熟阶段轻旱、中旱和重旱的减产率分别为16.5%、32.8%和44.9%，拔节–开花阶段轻旱、中旱和重旱的减产率分别为10.3%、18.8%和28.6%。结合冬小麦实际播种面积得到各生育阶段干旱对总产的影响，区域间比较均表现为干旱对山东省冬小麦总产影响最大，对河南省冬小麦总产影响最小。（孙爽）

2.23 我国北方一作区马铃薯高产稳产区分布特征

北方一作区马铃薯种植面积和总产居我国首位，明确其高产稳产区分布，对马铃薯合理布局具有重要意义。基于研究区域内234个气象站点1981—2019年逐日气象数据以及作物、土壤资料，利用APSIM-Potato模型，以产量平均值和变异系数为高产性和稳产性评价指标，将研究区域划分为高产高稳、高产低稳、低产高稳和低产低稳4个亚区，明确了过去39年不同生产水平下我国北方一作区马铃薯高产稳产区分布特征，解析了降水和土壤对马铃薯高产性和稳产性的影响。结果表明：过去39年不同生产水平下马铃薯高产区比例呈下降趋势；随着限制因素增加，高产高稳区面积比例逐渐降低，气候–土壤潜在生产水平下高产高稳区面积比例仅占研究区域总面积的13%；高产低稳区是潜在的高产高稳区，需重点关注，及时采取有效措施提升稳产性。降水对马铃薯高产性和稳产性的影响大于土壤因素。实际生产中，降水和土壤限制下高产性和稳产性降低的区域，应注意结合当地灌溉条件配合耕作措施，以确保马铃薯高产稳产。（孙爽）

2.24 中国大陆茶树种植气候适宜性区划

基于1961—2019年全国1903个气象站点的气候数据以及1115条茶树分布站点记录，利用最大熵模型和GIS技术筛选影响茶树种植的主导气候因子，根据自然间断点分级法将中国大陆茶树气候适宜性划分为不适宜区、次适宜区、适宜区和高适宜区4个等级，厘定不同区划等级的主导气候因子阈值。结果表明，影响中国大陆地区茶树种植分布的主导气候因子为多年平均极端最低气温、春霜冻频率、

年平均气温、年降水量和3—9月平均相对湿度。模型区划结果与名茶之乡、地理标志茶叶所在地吻合较好。茶树适生区的北界总体呈现出由东部高纬度向西部低纬度降低的分布态势，北界界限移动较明显地区主要分布在东部高纬度省份。整体茶树适生区质心的年代际变化较为平缓，除20世纪60—70年代和80—90年代的适生区范围有所缩小外，其他相邻年代际间茶树适生区的面积均呈现出不同程度的增长趋势，与质心迁移情况相吻合。（王培娟）

2.25 中国茶树春霜冻害研究进展

茶树作为我国主要的经济作物，在早春萌发时易遭受霜冻害。本文系统归纳了茶树春霜冻害的研究进展和取得的主要成果，并对未来茶树春霜冻害研究进行展望。我国茶树春霜冻多发于长江中下游，霜冻灾害指标可按照获取方法、数据类别、气象数据的时间尺度进一步细分。在全球变暖的背景下，茶树春霜冻发生次数虽呈下降趋势，但其危害不可忽视；其中，江南茶区茶树春霜冻的发生频率呈现出由南向北逐渐增加的纬向分布以及随海拔的升高而增大的地形分布特征。茶树春霜冻影响评估目前多集中于江苏、浙江、安徽、江西等茶区，且逐步由定性向定量发展；风险评估主要基于自然灾害风险形成机制划分不同的风险等级。今后，完善茶树春霜冻的气象指标、构建基于茶园小气候的茶树春霜冻灾害指标、阐明国家尺度上茶树春霜冻的时空分布特征、开展精细化茶树春霜冻风险评估将备受关注。（王培娟）

2.26 基于多种算法的果树果实生长模型研究——以云南昭通苹果为例

针对果树果实与生长过程中的气象因子关联密切，且生长过程多为非线性、非平稳序列，直接对其连续测定难度较大的问题，对比多种模型对果实直径的模拟能力，为果树及其果实的生长发育监测和预测、适时灌溉施肥、生长环境调控等提供科学参考。以云南昭通苹果为例，分析2019和2020年果实生长期间直径变化特征及其与环境气候因子的关系。引入深度学习中的长短期记忆模型（LSTM），使用LSTM模型对苹果果实直径进行模拟及预测，与多元线性回归模型（MLR）和机器学习模型中的决策树（DT）及随机森林（RF）模型的模拟结果进行对比分析，并使用3种采样方法对不同模型模拟的结果进行评估。苹果果实直径有明显日变化特征，呈夜间直径增长而白天缩小为主的规律，一般早晨直径达到最大，然后逐渐微缩，在日落前后直径到达当日最小。苹果果实直径的增长速率在果实膨大初期较高，在果实生长后期降低。苹果果实小时和日平均直径与土壤温度和土壤湿度呈中度或高度正相关，与紫外线指数（UVI）呈高度负相关。苹果果实直径的日平均增长量（FMDG）、日增长量（FDG）、日最大变化量（MDFS）与60 cm土壤温度和20、40 cm土壤湿度呈低负相关（$-0.5 \leqslant R < -0.3$）。4个模型的模拟结果相比，LSTM模型的模拟精度高于MLR、DT和RF模型。LSTM模型比MLR模型在相关系数R增加3% ～ 20%的情况下，RMSE和MAE下降50% ～ 75%，而机器学习模型DT和RF对苹果果实直径的预测相对较差，可能存在过度拟合。对比统计学、机器学习和深度学习等方法，LSTM模型在苹果果实直径的模拟中表现出更高的精度和可靠性，能更好地解决果实生长过程中的复杂非线性问题。（孙擎）

青藏高原与极地气象
Tibetan Plateau and Polar Meteorology

青藏高原与极地气象研究进展
Progress in the Tibetan Plateau and Polar Meteorology Research

1 青藏高原气象
1 Tibetan Plateau meteorology

1.1 Precursory signals (SST and soil moisture) of summer surface temperature anomalies over the Tibetan Plateau

Understanding the variability of surface air temperature (SAT) over the Tibetan Plateau (TP) and its precursory signals is of great benefit to climate change adaptation and socioeconomic development. This study explores the precursory signals of summer SATs over the TP in oceanic and land boundary conditions. The results show that the summer eastern TP SAT is significantly correlated with three precursors in April: the high-latitude North Atlantic sea surface temperature (SST), the northern Indian Ocean SST, and the Indian soil moisture (SM). The April SST anomalies (SSTAs) in the high-latitude North Atlantic can exert a cross-season impact on the summer SAT over the TP through two processes. The SSTAs in the high-latitude North Atlantic maintain from April to summer and modulate atmospheric circulation over the eastern TP through exciting a downstream wave train during summer, and finally modulate the summer SAT over the eastern TP. In addition to the above process, the April SSTAs in the high-latitude North Atlantic may remotely regulate simultaneous SM in the Indian subcontinent through stimulating a downstream wave train pattern. Through a persistent SM-precipitation interaction, the April Indian SM anomaly can affect the local precipitation and associated condensation heating anomalies during the ensuing summer, which forces an anomalous cyclone-anticyclone pattern around the TP and accordingly affects the summer SAT over the eastern TP. Additionally, the SSTAs in the northern Indian Ocean can persist from April to summer and adjust the intensity and location of the western North Pacific subtropical high through the Kelvin-wave-induced Ekman divergence during summer, eventually affecting the summer eastern TP SAT. The three precursory signals, which synergistically contribute to the variability of the summer eastern TP SAT, can be applied in predicting the summer SAT over the eastern TP. (Wang Hui, Liu Ge, Wang Sai, He Kejun)

1.2 Retrieval of O_3, NO_2, BrO and OClO columns from ground-based zenith scattered light DOAS measurements in summer and autumn over the northern Tibetan Plateau

Ground-based zenith scattered light differential optical absorption spectroscopy (DOAS) measurements were performed in summer and autumn (27 May to 30 November) 2020 at Golmud (94°54′ E, 36°25′ N; 2807.6 m altitude) to investigate the abundances and temporal variations of ozone (O_3) and its depleting substances over the northern Tibetan Plateau (TP). The differential slant column densities (dSCDs) of O_3, nitrogen dioxide (NO_2), bromine monoxide (BrO), and chlorine dioxide (OClO) were simultaneously retrieved from scattered solar spectra in the zenith direction during the twilight period. The O_3 vertical column densities

(VCDs) were derived by applying the Langley plot method, for which we investigated the sensitivities to the chosen wavelength, the a-priori O_3 profile and the aerosol extinction profile used in O_3 air mass factor (AMF) simulation as well as the selected solar zenith angle (SZA) range. The mean O_3 VCDs from June to November 2020 are 7.21×10^{18} molecules m^{-2} and 7.18×10^{18} molecules m^{-2} at sunrise and sunset, respectively. The derived monthly variations of the O_3 VCDs, ranging from a minimum of 6.9×10^{18} molecules m^{-2} in October to 7.5×10^{18} molecules m^{-2} in November, well matched the OMI satellite product, with a correlation coefficient $R = 0.98$. The NO_2 VCDs at SZA = 90°, calculated by a modified Langley plot method, were systematically larger at sunset than at sunrise as expected with a pm/am ratio of about 1.56. The maximum of the monthly NO_2 VCDs, averaged between sunrise and sunset, was 3.40×10^{15} molecules m^{-2} in July. The overall trends of the NO_2 VCDs were gradually decreasing with the time and similarly observed by the ground-based zenith DOAS and OMI. The average level of the BrO dSCD 90°–80° (i.e., dSCD between 90° and 80° SZA) was 2.06×10^{14} molecules m^{-2} during the period of June–November 2020. The monthly BrO dSCD 90°–80° presented peaks in August and July for sunrise and sunset, respectively, and slowly increased after October. During the whole campaign period, the OClO abundance was lower than the detection limit of the instrument. This was to be expected because during that season the stratospheric temperatures were above the formation temperature of polar stratospheric clouds. Nevertheless, this finding is still of importance, because it indicates that the OClO analysis works well and is ready to be used during periods when enhanced OClO abundances can be expected. As a whole, ground-based zenith DOAS observations can serve as an effective way to measure the columns of O_3 and its depleting substances over the TP. The aforementioned results are helpful in investigating stratospheric O_3 chemistry over the third pole of the world. (Cheng Siyang, Ma Jianzhong, Zheng Xiangdong)

1.3 Monsoon clouds control the summer surface energy balance on east Rongbuk glacier (6,523 m above sea level), the northern of Mt. Qomolangma (Everest)

To identify the atmospheric controls of the summertime glacier surface energy balance in the Himalayas, in situ meteorological data collected at 6,523 m above sea level during May–July 2005 were obtained and analyzed. Our results showed that net shortwave radiation (103 W m^{-2}) and turbulent sensible heat flux (12 W m^{-2}) acted as energy sources, and net longwave radiation (−62 W m^{-2}) and turbulent latent heat flux (−20 W m^{-2}) represented heat sinks. Cloud cover controlled the summer surface energy balance. During the active period of the South Asian summer monsoon, the frequent cloud coverage increased the incoming longwave radiation more than it decreased the incident solar radiation. Intensification (weakening) of the South Asian summer monsoon strengthened (suppressed) surface melting. The melt energy measured during the nonmonsoon period was small due to the energy consumption associated with glacier volume warming, energy loss from sublimation, and large heat loss through net longwave radiation due to the low amount of incoming longwave radiation caused by the low cloudiness. The comparison of glacier surface energy balances on the Tibetan Plateau shows that on continental glaciers, net radiation is lower and accounts for a smaller contribution to energy sources, and the dominant energy sinks are sublimation and evaporation, rather than melting, which is the primary energy sink for maritime/subcontinental glaciers. This implies an important spatial variability in glacial sensitivity to different climatic conditions on the Tibetan Plateau. (Liu Weigang, Zhang Dongqi, Ding Minghu)

1.4 Links between the thermal condition of the Tibetan Plateau in summer and atmospheric circulation and climate anomalies over the Eurasian continent

We examine the links between the thermal condition of the troposphere over the Tibetan Plateau with the atmospheric circulation and climate over the Eurasian continent. The temperature of the troposphere over the Tibetan Plateau is higher than the temperature in other regions at the same latitude and is consistent with the

temperature of the Eurasian troposphere on an interannual timescale. The higher temperature of the troposphere over the Tibetan Plateau leads to anomalous south–north temperature gradients from mid-latitudes over the Eurasian continent to its two flanks, accompanied by anomalous easterly and westerly winds in the upper troposphere in the subtropics and at higher latitudes. Anomalous anticyclonic circulations and subsidence motions appear between the anomalous easterly and westerly winds and contribute to the high surface air temperature over West Asia, Central Asia and East Asia via anomalous vertical temperature advection in the troposphere and change in the amount of solar radiation incident on the surface. The enhanced East Asian summer monsoon associated with the high temperature of the troposphere over the Tibetan Plateau also partly contributes to the high surface air temperature over East Asia via horizontal temperature advection. The westerly wind anomalies in the north of the mid-latitudes over the Eurasian continent indicate the enhancement and northward shift of the mid-latitude westerly jet. This is related to anomalous upward motion and higher precipitation in Northeast China and North China. Sensitivity experiments based on an atmospheric model verify the impact of anomalous tropospheric heating over the Tibetan Plateau in summer on the atmospheric circulation over the Eurasian continent. (Nan Sulan, Zhao Ping, Chen Junming, Liu Ge)

1.5 台站建设

2021年4月，于西藏自治区墨脱县新建方舱式风廓线雷达（型号CFL-03，北京无线电测量研究所）观测站，位于墨脱县气象局观测场旁，海拔1305 m，地理环境为郊外山腰，可实现0～6 km风廓线的探测。2021年7月，于云南贡山新建微波辐射计（型号MP-3000A，Radiometer）观测站，位于贡山县气象局楼顶，海拔1590 m，地理环境为郊外山腰，测量从地面至天空10 km高度垂直剖面上的温度、湿度廓线，液态水含量，云参数及有无降水等大气信息。2021年8月，于西藏自治区嘉黎县新建边界层梯度通量观测系统，位于嘉黎县气象局观测场旁，海拔4489 m，地理环境为河谷，观测要素包含5层空气温湿、5层土壤温湿、5层风速、风向、光合有效辐射、净辐射、土壤热通量、地表温度、雨量、雪深、CO_2/H_2O汽通量。

1.6 青藏高原大气环境立体综合观测试验

根据中国气象科学研究和西藏自治区双边协议，联合推进青藏高原野外科学试验。双方在拉萨站开展了多轴差分吸收光谱（MAX-DOAS）和大气水汽–气溶胶激光雷达地基主被动遥感观测，提升了提升青藏高原地区大气环境多组分垂直廓线观测能力，为开展青藏高原气候变化研究、青藏高原立体生态环境研究、青藏高原臭氧低谷研究等重大前沿科学问题奠定了数据基础。首次在青藏高原北部（西宁–达日–玉树线）和南部（拉萨–林芝–波密线）同时协作开展基于车载平台的青藏高原大气环境多组分三维结构动态遥感探测试验，有望对三江源地区和藏东南水汽通道上的大气环境有新认识。

1.7 第二次青藏高原水环境科学考察

2021年进行了一次青藏高原水环境科学考察，在青海曲麻莱、西藏错那的冻土安装了冻土温度、水热通量和气象观测仪器；在西藏浪卡子枪勇冰川和申扎甲岗山冰川安装了水位计和自动气象站；在在青海玉树隆宝湿地安装了水位计并进行观测。根据西风季风作用范围，选取了3个位于不同气候区的典型站点（错那、若尔盖、普兰）进行降水采样，将通过分析降水样品的同位素来确定西风–季风作用时间，并在甘肃省玛曲县进行水汽稳定氢氧同位素在线观测。参加了“藏东南大峡谷河谷关键区野外观测现场考察”和“高原气候资料稀缺地区气候变化及其影响应对”的野外考察，对沿途冰冻圈及其变化情况进行了文献查阅和现场考察。

1.8 推进青藏高原区域气候监测、诊断与预测业务系统建设

中国气象科学研究院与国家气候中心基于青藏高原相关科研成果，筛选、构建出了在我国气候诊

断、预测中具有实际业务应用意义的系列指标和预测模型，共同建立了“青藏高原区域气候监测诊断预测系统（TPMAPS）”，为国家气候中心汛期气候趋势预测业务提供了参考，发挥了积极作用。2021年11月9日，经专家论证，TPMAPS进入准业务运行。

2 极地气象
2 Polar meteorology

2.1 Two atmospheric responses to winter sea ice decline over the Barents-Kara Seas

The intraseasonal atmospheric responses to winter sea ice decline over the Barents-Kara Seas are examined by dividing rapid sea ice decline events into two categories, based on the direction (upward vs. downward) of the anomalous surface turbulent heat flux (ASTHF) after the sea ice loss. The upward ASTHF events, which could potentially have a large impact on the overlying atmosphere, are characterized by anomalously negative total column water and surface air temperature minus skin temperature, and anomalously positive surface wind speed following the sea ice loss. The downward ASTHF events show opposite features. Both types of events are linked to the Madden-Julian oscillation and subsequent circulation anomalies. This result indicates that on the intraseasonal time scale, not all sea ice decline events influence the atmosphere. (Jiang Zhina, Steven B. Feldstein, Sukyoung Lee)

2.2 Potential mechanisms governing the variation in rain/snow frequency over the northern Antarctic Peninsula during austral summer

Precipitation with different phases can exert different influences on the Antarctic mass balance. Using the observational rain and snow days from the Great Wall Station, ERA-interim reanalysis, and other data, this study investigates the mechanisms governing the year-to-year variability of precipitation phase (i.e., rainfall and snowfall) over the northern Antarctic Peninsula (AP) during austral summer (December, January, and February; abbreviated as DJF) for the period 1985–2016. The results reveal that the rainfall and snowfall anomalies are controlled mainly by the change in the proportion of precipitation occurring as rain and snow, and the latter is strongly influenced by the change in air temperature. Through regulating the air temperature, different atmospheric circulation anomalies affect the variability of the rainfall and snowfall over the northern AP during summer. Specifically, a circulation pattern with an anomalous anticyclone over the Malvinas Islands and an anomalous cyclone over the Amundsen-Bellingshausen Seas (ABS) can increase summer rainfall, whereas an anomalous cyclone over the Weddell Sea facilitates more snowfall. The summertime atmospheric circulation anomalies, which modulate the variability of rainfall over the northern AP, are primarily caused by an atmospheric teleconnection pattern persisting from austral spring (September–November, SON) to summer. Such a persistent teleconnection pattern can be attributed to the long-time maintenance of sea surface temperature anomalies due to air-sea interaction processes. (Wang Sai, Liu Ge, Ding Minghu, Chen Wen, Zhang Wenqian, Lyu Junmei)

2.3 Impact of internal variability on recent opposite trends in wintertime temperature over the Barents-Kara Seas and central Eurasia

The large ensembles of the IPSL-CM6A-LR model output for the historical forcing experiment were employed to investigate the role of internal variability in the formation of the recent “warm Arctic-cold Eurasia” trend pattern in winter surface air temperature (SAT). The ensemble-mean SAT shows a positive trend over Arctic during 1990–2014, indicating a positive contribution of anthropogenic forcing to the warming

Arctic. Over the region of central Eurasia, the ensemble-mean SAT trend is opposite to the observed trend. The winter SAT trends display remarkable inter-member diversity over the Barents-Kara Seas (BKS) region and central Eurasia, suggesting an important role played by internal variability. In addition to anthropogenic forcing, the results suggest that the barotropic anticyclone over northern Eurasia arising from internal variability can also contribute positively to the warming anomalies over the BKS region. On the other hand, through a fingerprint pattern matching method, it is found that the observed cooling trend over central Eurasia tends to be predominantly due to the internal variability. Finally, the results estimate that the internal variability can contribute to about 50%–60% of the observed warming trend over the BKS region. (Wang Sai, Chen Wen)

2.4 Evaluation of multiple density-dependent empirical snow conductivity relationships in East Antarctica

Nine density-dependent empirical thermal conductivity relationships for firn were compared against data from three automatic weather stations at climatically different sites in East Antarctica (Dome A, Eagle, and LGB69). The empirical relationships were validated using a vertical, 1D thermal diffusion model and a phase-change-based firn diffusivity estimation method. The best relationships for the abovementioned sites were identified by comparing the modeled and observed firn temperature at a depth of 1 and 3 m, and from the mean heat conductivities over two depth intervals (1–3 and 3–10 m). Among the nine relationships, that proposed by Calonne et al. (2011) appeared to show the best performance. The density- and temperature-dependent relationship given in Calonne et al. (2019) does not show clear superiority over other density-dependent relationships. This study provides a useful reference for firn thermal conductivity parameterizations in land modeling or snow–air interaction studies on the Antarctica ice sheet. (Ding Minghu)

2.5 On the differences in precipitation type between the Arctic, Antarctica and Tibetan Plateau

Under the effect of global warming, more precipitation will shift to rainfall in cryospheric regions. Considering the influence of the precipitation type on surface energy and mass cycles, it is important to determine the specific precipitation features and to classify the precipitation type in key areas correctly. We analyzed the monthly distribution, variations in annual days of each precipitation type, and trends based on daily precipitation and air temperature observations from six tripolar stations. The results indicated that snow dominated the precipitation type at Zhongshan Station (69.4°S, 76.4°E) throughout the year, while the Greatwall Station (62.2°S, 59.0°W) exhibited a relatively diverse precipitation type distribution and significant seasonal cycles. Compared to the Greatwall Station, every precipitation type was less frequently encountered at the Barrow (71.3°N, 156.8°W), Coral Harbour (64.2°N, 83.4°W), Linzhi (29.6°N, 94.5°E), and Maqu stations (34°N, 102.1°E), in which all the sites demonstrated classical reverse seasonal variation. A consistent trend across the years was found regarding the trends of the different precipitation types, except at the Greatwall and Coral Harbour stations. Due to snow/rain conditions partly converting into sleet conditions, which may be related to air temperature changes and synoptic atmospheric activities, inconsistent increasing trends of the sleet days were observed compared to the snow/rain days. Furthermore, a hyperbolic parameterized model was also fitted to determine the air temperature threshold of precipitation type transitions in this paper. According to the threshold comparison results, a warm bias in the temperature threshold was found at the warm stations. We also proposed that high relative humidity and low freezing levels were the likely reasons for the ERA5 reanalysis datasets. Finally, this paper's fitted parameterized model was proven to perform better than the ERA5 reanalysis datasets through validation. This preliminary research provides observational evidence and possible interpretation of the mechanism of precipitation type changes in tripolar areas. (Yang Diyi, Ding Minghu)

2.6 The shallowing surface temperature inversions in the Arctic

Temperature inversion plays an important role in various physical processes by affecting the atmospheric stability, regulating the development of clouds and fog, and controlling the transport of heat and moisture fluxes. In the past few decades, previous studies have analyzed the spatiotemporal variability of Arctic inversions, but few studies have investigated changes in temperature inversions. In this study, the changes in the depth of Arctic inversions in the mid-21st century are projected based on a 30-member ensemble from the Community Earth System Model Large Ensemble (CESM-LE) project. The ERA-Interim, JRA-55, and NCEP-NCAR reanalyses were employed to verify the model results. The CESM-LE can adequately reproduce the spatial distribution and trends of present-day inversion depth in the Arctic, and the simulation is better in winter. The mean inversion depth in the CESM-LE is slightly underestimated, and the discrepancy is less than 11 hPa within a reasonable range. The model results show that during the mid-21st century, the inversion depth will strongly decrease in autumn and slightly decrease in winter. The shallowing of inversion is most obvious over the Arctic Ocean, and the maximum decrease is over 65 hPa in the Pacific sector in autumn. In contrast, the largest decrease in the inversion depth, which is more than 45 hPa, occurs over the Barents Sea in winter. Moreover, the area where the inversion shallows is consistent with the area where the sea ice is retreating, indicating that the inversion depth over the Arctic Ocean in autumn and winter is likely regulated by the sea ice extent through modulating surface heat fluxes. (Zhang Lin, Ding Minghu, Lyu Junmei)

2.7 Characteristics of low-level temperature inversions over the Arctic Ocean during the CHINARE 2018 campaign in summer

Across the Arctic Ocean, the semi-permanent sea-ice layer insulates the atmosphere from the Arctic Ocean, thereby influencing the lower boundary conditions of the atmosphere in this region. The presence of a temperature inversion predominantly characterizes the Arctic lower troposphere throughout the year. The 9th Chinese National Arctic Research Expedition took place in the Pacific Sectors of the Arctic Ocean from July to September 2018, gathering high-resolution radiosonde data to provide a detailed structure of the low-level temperature inversion (LLI) over the summer months. Statistical analyses showed that LLIs occurred most frequently below 500 m and were generally weaker and shallower than those occurring during the winter months. Low-level inversions are influenced by both local meteorology and large scale synoptic conditions. The continual presence of low-level clouds or fog tends to lift the inversion layer at the local scale, transferring it from a surface-based inversion (SBI) to an elevated inversion (EI). By contrast, SBIs were found to dominate over regions of melting sea-ice. Regimes, where the cloud top penetrated the inversion base were more frequently observed than where regimes cloud capped by inversion. Inversions tended to be deeper, stronger, and with a lower base during cloud top penetrating inversion base regimes. At the synoptical scale, the intense poleward intrusions of warm air brought moist air to the top of low-level inversions, creating a robust thermal stratification between layers and promoting extensive and frequency occurrences of low cloud/fog. Moreover, the polar high contributed to establishing a multilayer inversion structure at relatively high altitudes by subsidence. These findings contribute to an improving understanding of low-level vertical temperature structures and their influence on a rapidly warming Arctic. (Zhang Lei, Li Jian, Ding Minghu)

2.8 Estimation and long-term trend analysis of surface solar radiation in Antarctica: A case study of Zhongshan Station

Long-term, ground-based daily global solar radiation (DGSR) at Zhongshan Station in Antarctica can quantitatively reveal the basic characteristics of Earth's surface radiation balance and validate satellite data for the Antarctic region. The fixed station was established in 1989, and conventional radiation observations started

much later in 2008. In this study, a random forest (RF) model for estimating DGSR is developed using ground meteorological observation data, and a high-precision, long-term DGSR dataset is constructed. Then, the trend of DGSR from 1990 to 2019 at Zhongshan Station, Antarctica is analyzed. The RF model, which performs better than other models, shows a desirable performance of DGSR hindcast estimation with an R^2 of 0.984, root-mean-square error of 1.377 MJ m^{-2}, and mean absolute error of 0.828 MJ m^{-2}. The trend of DGSR annual anomalies increases during 1990–2004 and then begins to decrease after 2004. Note that the maximum value of annual anomalies occurs during approximately 2004/2005 and is mainly related to the days with precipitation (especially those related to good weather during the polar day period) at this station. In addition to clouds and water vapor, bad weather conditions (such as snowfall, which can result in low visibility and then decreased sunshine duration and solar radiation) are the other major factors affecting solar radiation at this station. The high-precision, long-term estimated DGSR dataset enables further study and understanding of the role of Antarctica in global climate change and the interactions between snow, ice, and atmosphere. (Zeng Zhaoliang, Ding Minghu)

2.9 The surface energy balance of Austre Lovénbreen, Svalbard, during the ablation period in 2014

The ability to simulate the surface energy balance is key to studying land-atmosphere interactions; however, it remains a weakness in Arctic polar sciences. Based on the analysis of meteorological data from 1 June to 30 September 2014 from an automatic weather station on the glacier Austre Lovénbreen, near Ny-Ålesund, Svalbard, we established a surface energy balance model to simulate surface melt. The results reveal that the net shortwave radiation accounts for 87% (39 W m^{-2}) of the energy sources, and is controlled by cloud cover and surface albedo. The sensible heat equals 6 W m^{-2} and is a continuous energy source at the glacier surface. Net longwave radiation and latent heat account for 31% and 5% of heat sinks, respectively. The simulated summer mass balance equals –793 mm w.e., agreeing well with the observation by an ultrasonic ranger. (Zou Xiaowei, Ding Minghu)

2.10 Skillful prediction of winter Arctic oscillation from previous summer in a linear empirical mode

The winter Arctic oscillation (WAO), as a primary atmospheric variability mode in the Northern Hemisphere, plays a key role in influencing mid-high-latitude climate variations. However, current dynamical seasonal forecasting systems have limited skills in predicting WAO with lead time longer than two months. In this study, we design a linear empirical model using two effective precursors from anomalies of the Arctic sea ice concentration (SIC) and the tropical sea surface temperature (SST) initiated in preceding late summer (August) which are both significantly correlated with WAO in recent four decades. This model can provide a skillful prediction of WAO at about half-year lead started from previous summer and perform much better than the dynamical models. Such a significantly prolonged lead time is owed to the stable precursor signals extracted from the SIC and SST anomalies over specific areas, which can persist from previous August and be further enhanced through autumn months. Validation results show that this model can produce a 20-year independent-validated prediction skill of 0.45 for 1999–2018 and a 39-year cross-validated skill of 0.67 for 1980–2018, providing a potentially effective tool for earlier predictions of winter climate variations at mid-high latitudes. (Ren Hongli, Yu Nie)

2. 11 南极冰盖地表能量平衡的研究进展

南极冰盖地表能量平衡研究，是耦合冰冻圈，大气圈和水圈过程的基础之一，对了解冰盖表面物质平衡过程、提升极地天气气候预报水平有着极其重要的意义。随着近年来极地观测水平的提升，南极冰盖地表能量平衡研究取得了长足的进步，特别是在辐射参数化和有效热传导系数模拟等方面。但

在南极广袤的地域和多样的天气条件下，已有的研究大都适用于局地环境，限制了我们的模拟和预测能力。因此，适用于极地特殊环境的传感器的研发、关键气候区的科学试验的开展和基础的气象站网建设，能加深我们对冰/雪–气相互作用过程的理解，进而改进已有的参数化方案，应用于多圈层模式的耦合。（杨堤益，丁明虎）

2.12 “暖北极–冷欧亚”模态的年代际变化及其与北大西洋海温的联系

本文利用美国航空航天局戈达德空间研究所地表气温，美国国家海洋和大气局–环境科学协作研究所20世纪再分析资料，以及第六次国际耦合模式比较计划的多模式Historical试验结果，去除外强迫影响后，研究1910/1911—2019/2020年冬季（DJF）欧亚中高纬地区“暖北极–冷欧亚”（WACE）模态的年代际变化特征及其物理原因。结果表明：WACE具有显著的年代际变化，在WACE正位相时期，乌拉尔阻塞发生频率偏高，有利于热量向极区输送使得极区出现异常暖平流，且水汽向极区输送导致极区水汽辐合，向下长波辐射增加，另外对流活动增强导致潜热释放，进而极区温度上升。与此同时，极涡及欧亚大陆西风减弱且乌拉尔阻塞发生频率偏高，有利于冷空气侵袭欧亚大陆造成异常冷平流，且欧亚地区水汽辐散，向下长波辐射减少，对流活动减弱进而潜热释放减少，导致欧亚大陆温度降低。最后利用CAM3.0大气环流模式模拟了北大西洋海温正异常对WACE的影响，模式结果与统计结果相符合，进一步说明了北大西洋海温正异常可以通过强迫低层与高层大气环流异常，导致极区水汽辐合，欧亚大陆水汽辐散，进而影响WACE的年代际变化。（王婧，吕俊梅）

2.13 冬季北半球大气对秋冬季巴伦支海海冰异常的敏感性研究

基于ERA-Interim再分析资料，借助大气模式CAM4，分析了北半球冬季不同月份的平均大气对巴伦支海不同振幅及不同季节海冰扰动的敏感性，并考察了中高纬度典型大气模态的分布变化情况。结果表明，冬季巴伦支海海冰的减少，会导致湍流热通量异常向上、局地异常变暖及水汽含量的异常升高，且相关异常的强度和范围随着海冰减少幅度的减小而减弱。这种局地响应会通过大气环流调整扩散开来，产生远程影响。具体地，冬季大气环流与欧亚地面温度异常对于不同幅度海冰异常的响应是非线性的，且在不同月份也呈现出不同特征。秋季巴伦支海海冰减少虽未引起局地显著的温度异常，但欧亚大陆温度及环流场异常响应的强度更强、范围更广，这表明秋季海冰可以独立地对冬季中纬度大气产生影响。此外，冬季不同月份西伯利亚高压强度、位置对巴伦支海海冰减少的响应是不同的，北大西洋涛动位相的倾向变化对不同季节、不同振幅海冰减少的响应也不相同。冬季海冰减少时，12月和1月，西伯利亚高压强度更易偏强、位置易偏东，2月则与之相反。与冬季相比，秋季海冰偏少时，西伯利亚高压更易稳定维持在欧亚大陆，晚冬时发生北大西洋涛动负位相的概率增大，但出现极端负位相概率降低。这为了解巴伦支海海冰异常对北半球天气、气候的影响提供了参考。（段升妮，姜智娜）

2.14 过去2000年北极地区气候变化特征及其对AMO的响应

北极地区对全球变暖十分敏感，分析北极地区过去2000年历史气候对揭示全球气候变化极其重要，也是国际过去全球变化计划（PAGES）的重要目标。然而，过去2000年北极不同区域的气候随时间变化是否存在一致性仍有待检验。文章基于北极地区及其3个子扇区（北大西洋扇区、阿拉斯加扇区和西伯利亚扇区）的温度序列，对过去2000年北极的气候变化进行了趋势分析与频谱特征分析，初步探讨了大西洋多年代涛动（AMO）作为驱动因子对北极地区温度的影响。结果表明，公元1—1800年间北极地区存在着普遍的降温过程（–0.47 ℃ /ka），但温度变化区域差异显著，其中北大西洋扇区与北极地区整体温度间呈现显著的相关性（0.82）。北大西洋扇区温度呈现“平稳–下降–陡升”的趋势，阿拉斯加扇区温度呈现“下降–缓升–下降–陡升”的趋势，西伯利亚扇区温度呈现“平稳波动–陡升”的趋势。在过去200年间北极地区及其3个子扇区气候均出现了快速变暖。频谱分析表明，北极地区温

度存在着准14年、准26年、准62年、准75年和准186年周期，其中北极地区温度的LFV谱在准62年与准75年周期与AMO周期大致吻合。综合交叉谱与小波分析的结果，公元1100年后，AMO以准74年的周期影响北极的气候变化，其中，北大西洋扇区受影响最为明显。阿拉斯加扇区与西伯利亚扇区虽然存在着显著的年代际周期特征，但可能与AMO的关联并不显著，这些区域气候变化的影响机理需要进一步深入研究。(祁威，丁明虎)

2.15 BCC_CSM北极海冰模拟性能的改进对东亚冬季气候模拟的影响

国家气候中心气候系统模式（BCC_CSM）将美国Los Alamos国家实验室发展的海冰模式CICE5.0替代原有的海冰模式SIS，形成一个新版本耦合模式，很好地提高了模式对北极海冰和北极气候的模拟能力。在此基础上，本文评估新耦合模式对1985—2014年东亚冬季气候的模拟性能，检验北极海冰模拟性能的改进对东亚冬季气候模拟性能的影响。结果表明，引入CICE5.0后，新耦合模式能较好地模拟出东亚冬季海平面气压、850 hPa风场以及辐射通量，进而改善东亚气温以及降水的气候态空间分布模拟效果。进一步分析发现，与原有耦合模式相比，新耦合模式更好地抓住了东亚冬季海平面气压、总降水量和气温异常对同期巴伦支海–喀拉海海冰密集度异常的响应，进而提高了模式对东亚冬季中高纬度地区气温以及降水变率的模拟能力。（邓汝漳，储敏，任宏利，刘景鹏，陈权亮）

2.16 第三极地区气温和积雪的季节–年际气候预测研究

第三极地区气候多样、灾害频发，是影响全球和亚洲气候异常的关键区域，针对此地区开展季节–年际气候预测研究对于提高区域预报技巧以及减少灾害造成的影响具有重要的科学和指导意义。基于国家气候中心气候预测业务模式（BCC_CSM1.1m）的历史回报和预测数据，对第三极地区2 m气温和积雪的预测结果进行了确定性技巧评估，并分析了海洋因子对于预测技巧的调制作用。研究表明：该模式对于青藏高原及其周边地区气温和积雪的季节–年际气候预测具有一定的预测能力，对夏季气温的预测效果整体上好于冬季气温和积雪深度预测；预测技巧随着模式起报时间的提前而下降，但是存在技巧回升现象。研究也发现，海温异常因子对第三极地区的气候预测技巧具有不同程度的调制作用，厄尔尼诺等海洋信号能够通过直接和间接作用影响第三极地区的气候预测。（汪芋君，任宏利，王琳）

2.17 长城气象站、中山气象台观测业务

2021年，中国气象科学研究院继续执行极地气象业务化观测任务，陕西省气象局武维刚、安徽省气象局凌新锋和山西省气象局董剑3位同志在南极长城站和中山站进行地面气象、臭氧洞及大气成分等观测，获取合乎WMO规范的气象数据并报送中国气象局国家气象信息中心和WMO。在南极冰盖内陆及边缘地区、格陵兰冰盖等地区维护运行的17个自动气象站继续稳定获取自动气象观测数据。选拔并培训了第38次南极考察队员，已前往南极执行下一年度观测任务。

2.18 南极泰山气象站、昆仑气象站正式业务化

在昆仑站、泰山站稳定准业务运行5年和近9年之后，经过对接收到的数据的分析，两站数据质量稳定，数据到报率分别超过99.58%和99.73%，指标超过国家基本气象站业务运行要求。为体现中国气象全球观测、全球预报和全球服务的战略目标，我们积极向院和局观测司、预报司以及国际司等业务主管部门申请，使两站升级为国家基本气象站（站号：89572、89576），自2021年12月1日（北京时间11月30日20:00）起正式开展业务运行，凸显极地特殊环境观测水平。该工作受到WMO和国际关注。

2.19 受疫情影响，开展北冰洋和黄河站考察

由于疫情原因，2020年度无法派人去黄河站现场工作。目前国内接收到截至2020年2月2日数据，内部存储卡可存储一年数据，其余数据需现场取回。2021年，气科院积极参与极地考察工作，在第12

次北极科学考察中继续进行走航路线上大气成分的观测，观测内容包括黑碳气溶胶、CH_4、CO_2、CO、地面臭氧。

3 其他
3 Others

3.1 Effect of preceding soil moisture-snow cover anomalies around Turan Plain on June precipitation over the southern Yangtze River Valley

This study investigates precursory signals of the June precipitation over the southern Yangtze River Valley (SYRV). It is found that the synergistic anomalies of the Turan Plain soil moisture and northern Iranian Plain snow cover (TPSM-IPSC) during April can modulate the June SYRV precipitation. Through the persistence/memory effect of soil moisture anomalies, lower soil moisture around the Turan Plain-Iranian Plain region can maintain from April to June. Because of drier soil (i.e., lower soil moisture), higher surface air temperature (SAT) appears over the Turan Plain during June. The higher SAT anomaly stimulates anomalous upward motion and associated overlying and downstream atmospheric circulation anomalies through modulating the downstream dispersion of Rossby wave energy. As a part of these atmospheric circulation anomalies, the blocking-like anomaly to the west of the Okhotsk Sea facilitates more June precipitation over the SYRV. Additionally, June SYRV precipitation is significantly correlated with sea surface temperature (SST) anomalies in the tropical eastern Pacific (TEP) during the preceding winter. The TPSM-IPSC can compensate for the defect of prediction using the TEP SST (i.e., ENSO) signal in recent years since the former (latter) shows a strengthened (weakened) relationship with SYRV precipitation recently. Considering jointly the traditional pacific SST and new TPSM-IPSC precursors, we establish a physics-based statistical prediction model, which shows a good skill in predicting June SYRV precipitation. (He Kejun, Liu Ge, Wu Renguang, Nan Sulan, Li Jingxin, Yue Xiaoyuan, Wang Huimei, Wei Xinchen, Li Rongrong)

3.2 A tripole pattern of summer surface air temperature anomalies over northern Eurasia and its precursory signals in the tropical Atlantic and northern Asian land

This study investigates the variability of summer surface air temperature (SAT) over northern Eurasia and its precursory signals in the tropical Atlantic and northern Asian land. The leading mode of summer SAT variations features a northern Eurasian SAT tripole (NEST) pattern, with two same-sign SAT anomaly regions over eastern Europe-western Siberia and the Far East region and an opposite-sign SAT anomaly region around the Baikal Lake. It is found that sea surface temperature (SST) or SAT anomalies in the tropical Atlantic and rainfall-soil moisture anomalies around the Baikal Lake during May can modulate the NEST pattern. The SST anomalies in the tropical Atlantic persist from May to summer and induce a downstream zonal wave train across northern Eurasia, consequently causing the variation in the summer NEST pattern. May rainfall anomalies around the Baikal Lake affect the overlying atmospheric circulation during summer through the "memory" effect of soil moisture and the soil moisture-rainfall interaction, correspondingly modulating the downstream wave train and the associated NEST pattern. Based on the above results, a statistical prediction model is established using the two precursory signals, that is, SAT in the tropical Atlantic and rainfall around the Baikal Lake during May. The leave-three-out cross-validation shows that the model has a high skill in predicting the summer NEST pattern, with a correlation coefficient of 0.51 (significant at the 99.8% confidence level) between observation and prediction during the period 1980–2016. (He Kejun, Liu Ge, Wu Renguang, Li Jingxin, Wang Huimei, Yue Xiaoyuan)

3.3 RO_x budgets and O_3 formation during summertime at Xianghe suburban site in the North China Plain

Photochemical smog characterized by high concentrations of ozone (O_3) is a serious air pollution issue in the North China Plain (NCP) region, especially in summer and autumn. For this study, measurements of O_3, nitrogen oxides (NO_x), volatile organic compounds (VOCs), carbon monoxide (CO), nitrous acid (HONO), and a number of key physical parameters were taken at a suburban site, Xianghe, in the NCP region during the summer of 2018 in order to better understand the photochemical processes leading to O_3 formation and find an optimal way to control O_3 pollution. Here, the radical chemistry and O_3 photochemical budget based on measurement data during 1–23 July using a chemical box model is investigated. The daytime (06:00–18:00 LST) average production rate of the primary radicals referred to as RO_x ($OH + HO_2 + RO_2$) is 3.9×10^{-9} (V) h^{-1}. HONO photolysis is the largest primary RO_x source (41%). Reaction of NO_2 + OH is the largest contributor to radical termination (41%), followed by reactions of RO_2 + NO_2 (26%). The average diurnal maximum O_3 production and loss rates are 32.9×10^{-9} (V) h^{-1} and 4.3×10^{-9} (V) h^{-1}, respectively. Sensitivity tests without the HONO constraint lead to decreases in daytime average primary RO_x production by 55% and O_3 photochemical production by 42%, highlighting the importance of accurate HONO measurements when quantifying the RO_x budget and O_3 photochemical production. Considering heterogeneous reactions of trace gases and radicals on aerosols, aerosol uptake of HO_2 contributes 11% to RO_x sink, and the daytime average O_3 photochemical production decreases by 14%. The O_3-NO_x-VOCs sensitivity shows that the O_3 production at Xianghe during the investigation period is mainly controlled by VOCs. (Xue min, Ma Jianzhong)

3.4 Reduction in extreme climate events and potential impacts by the use of technological advances

Technological advances have the potential to balance climate change mitigation and economic development. However, it remains unclear how much technological advances alone can mitigate climate change and the associated economic losses in the future. Through designing a suite of technological advances scenarios and using an earth system model with an integrated assessment model, we illustrate that rapid technological progress without production control might achieve the 2 ℃ global warming target in the 2100s. Relative to a world of stagnant technology, the frequency (intensity) of extreme warm events at the end of the 21st century (2081–2100) would be reduced by about 21% (5.5 ℃) via rapid technological advances, with a reduction in extreme precipitation (droughts) by about 41% (10 times). Furthermore, fast technological advances may reduce the global economic losses linked with climate change at 2081–2100 by about 21% and those in China related to floods (droughts) by 86% (67%). Our results highlight the potential of technological advances to fill the emission gap between the Paris Agreement and unconditional Nationally Determined Contributions and hence to efficiently mitigate global warming. (Wei Ting, Liu Changxin, Dong Wenjie)

3.5 Effects of organic soil in the Noah-MP land-surface model on simulated skin and soil temperature profiles and surface energy exchanges for China

Inclusion of the thermal and hydraulic effect of soil organic matter plays an important role in land-surface models (LSMs) for simulating soil temperature and surface energy exchanges. The current officially released Noah with multiparameterization (Noah-MP) LSM, implemented in the community weather research and forecasting (WRF) model, does not include a parameterization for soil organic matter. In this study, the thermal and hydraulic effect of soil organic matter was parameterized into Noah-MP LSM. Based on the profiled soil organic matter data for China and the observations of skin temperature and soil temperature profiles from more than 2000 surface meteorological stations, we investigated the effects of organic soil using the Noah-MP LSM with and without the profiled soil organic matter at the regional scales. Compared with the simulation without

the inclusion of organic soil parameterization, the Noah-MP LSM simulation with the profiled soil organic matter improved the skin temperature and soil temperature profiles, especially soil temperature in deep soils under cold and arid regions. The realistic representation of snow depth and the snow insulation dependency on snow depth were confirmed to be a pre-requisite in Noah-MP in the high latitudes. By incorporating the profiled soil organic matter, the Noah-MP LSM enlarged the regional mean sensible heat flux (SH) and lowered the regional mean latent heat flux (LH). In the warm and humid regions, a relatively smaller effect of organic soil on soil temperature could lead to a larger effect on SH and LH, especially LH. (Zhang Guo, Chen Yueli, Li Jianduo)

3.6 Asymmetry and pathways of inter-hemispheric transport in the upper troposphere and lower stratosphere

Inter-hemispheric transport may strongly affect the trace gas composition of the atmosphere, especially in relation to anthropogenic emissions, which originate mainly in the Northern Hemisphere. This study investigates the transport from the boundary surface layer of the Northern Hemispheric (NH) extratropics (30º–90º N), Southern Hemispheric (SH) extratropics (30º–90º S), and tropics (30º S–30º N) into the global upper troposphere and lower stratosphere (UTLS) using simulations with the chemical Lagrangian model of the stratosphere (CLaMS). In particular, we diagnose inter-hemispheric transport in terms of the air mass fractions (AMFs), age spectra, and the mean age of air (AoA) calculated for these three source regions. We find that the AMFs from the NH extratropics to the UTLS are about 5 times larger than the corresponding contributions from the SH extratropics and almost 20 times smaller than those from the tropics. The amplitude of the AMF seasonal variability originating from the NH extratropics is comparable to that from the tropics. The NH and SH extratropical age spectra show much stronger seasonality compared to the seasonality of the tropical age spectra. The transit time of NH-extratropical-origin air to the SH extratropics is longer than vice versa. The asymmetry of the inter-hemispheric transport is mainly driven by the Asian summer monsoon (ASM). We confirm the important role of ASM and westerly ducts in the inter-hemispheric transport from the NH extratropics to the SH. Furthermore, we find that it is an interplay between the ASM and westerly ducts which triggers such cross-equator transport from boreal summer to fall in the UTLS between 350 and 370 K. (Yan Xiaolu, Paul Konopka, Marius Hauck, Aurélien Podglajen, Felix Ploeger)

3.7 Frequent locally absent rings indicate increased threats of extreme droughts to semi-arid *Pinus tabuliformis* in North China

Global climatic change indicates that some climate systems have passed tipping points, e.g. the inner East Asia; however it's still uncertain when the tipping point of forest mortality could be triggered. Absent rings are early warnings of irreversible mortality. They widely exist in Northern Hemisphere forests, but they're locally rare and under-discussed in previous studies. We reported a tree ring network, including 17 collections among the extensive distribution of *Pinus tabuliformis* in North China. Locally absent rings (LAR) were counted and logistic models were built to determine biotic and abiotic driving forcings of LAR. *Pinus tabuliformis* suffered increasing LAR frequency in recent decades, and the highest LAR frequency occurred at the driest distributional margin. At the semi-arid region, LAR frequency increased along with increasing age, decreasing previous September moisture, and decreasing May moisture. LAR risk would gradually increase, and older trees would suffer quite high LAR risk in the future. We highlight the connection between frequent LAR and extreme droughts in semi-arid pine forests, and propose that LAR can be a proxy of the potential tipping points of forest systems. (Zhao Shoudong, Jiang Yuan, Wen Yan, Jiao Liang, Li Wenqing, Xu Hui, Ding Minghu)

3.8 Spatiotemporal variation of precipitation on a global scale from 1960 to 2016 in a new normalized daily precipitation dataset

Increases in total and extreme precipitation have been investigated worldwide using limited spatiotemporal data based on surface observations and satellite remote sensing during recent decades. However, it remains unclear whether rain gauge daily precipitation records also show a significant increase in global precipitation. In this study, we first apply the transformed version of the penalized maximum *F* test ("transPMFred") to homogenize daily precipitation (*P*) records from 10629 stations around the world during 1960–2016 from a dataset (GHCN-CMA) that combines the daily precipitation data from the Global Historical Climatology Network (GHCN-Daily) dataset and the China Meteorological Administration (CMA), and then utilize the homogenized data to study the frequency of daily precipitation on a global scale. The results indicate that precipitation frequency exhibited significant increasing trends from 1960 to 2016 across most of the globe, except for East Asia. Moreover, the variability of global precipitation frequency was more pronounced in wet regions than dry regions, especially in North America, Europe and East Asia based multiple daily precipitation datasets. The regional average frequency for moderate (30th $< P \leqslant$ 60th percentile), heavy (60th $< P \leqslant$ 90th percentile) and very heavy ($P >$ 90th percentile) precipitation increased in North America and Europe. Changes in precipitation frequency decreased for light ($P \leqslant$ 30th percentile) and moderate precipitation but increased for heavy and very heavy precipitation, which mainly occurs in dry regions of Australia. Moreover, precipitation frequency in wet and dry regions of East Asia showed opposite trends, with a decrease in wet regions and an increase in dry regions. (Liu Jun, Wu Dongyou, Li Yue, Ren Hongli, Zhao Yongtao, Sun Xiaoyu, Zhang Haitao, Ji Mingxia)

3.9 The UK-China climate science to service partnership

We present results from the first 6 years of this major UK government funded project to accelerate and enhance collaborative research and development in climate science, forge a strong strategic partnership between UK and Chinese climate scientists, and demonstrate new climate services developed in partnership. The development of novel climate services is described in the context of new modeling and prediction capability, enhanced understanding of climate variability and change, and improved observational datasets. Selected highlights are presented from over 300 peer reviewed studies generated jointly by UK and Chinese scientists within this project. We illustrate new observational datasets for Asia and enhanced capability through training workshops on the attribution of climate extremes to anthropogenic forcing. Joint studies on the dynamics and predictability of climate have identified new opportunities for skillful predictions of important aspects of Chinese climate such as East Asian summer monsoon rainfall. In addition, the development of improved modeling capability has led to profound changes in model computer codes and climate model configurations, with demonstrable increases in performance. We also describe the successes and difficulties in bridging the gap between fundamental climate research and the development of novel real-time climate services. Participation of dozens of institutes through subprojects in this program, which is governed by the Met Office Hadley Centre, the China Meteorological Administration, and the Institute of Atmospheric Physics, is creating an important legacy for future collaboration in climate science and services. (Scaife Adam A., Good Elizabeth, Sun Ying, Yan Zhongwei, Dunstone Nick, Ren Hongli)

3.10 Change of East-Asian summer precipitation associated with strong El Niño under the future emission scenarios

Strong Eastern-Pacific type El Niño (EP-El Niño) events have significant impacts on the decaying-summer precipitation over East Asia (EA). It has been demonstrated that frequency of strong EP-El Niños will increase

and associated precipitation will become more severe and complex under future high emission scenarios. In this study, using simulations of CMIP5 and CMIP6, changes of the summer precipitation pattern related to strong EP-El Niño during its decay phase and the possible mechanism as responding to high emission scenarios are examined. Precipitation anomaly patterns over EA of strong EP events show a large inter-model spread in historical simulations between the CMIP models where CMIP6 is not superior to CMIP5. Under high emission scenarios, changes of summer precipitation anomalies related to strong EP events tend to increase over the southern EA and decrease around the northern EA from CMIP5, while there is an overall increase in the whole EA from CMIP6. The common change is featured by the increase of precipitation over southeastern China under high emission scenarios. This could be mainly attributed to the anticyclonic circulation from the South China Sea to the western North Pacific as a delayed response to more frequent strong EP-El Niños, which favors an increase in water vapor fluxes converging into the southeastern China. (Huang Yu, Ren Hongli, Liu Minghong)

3.11 Impacts of late-spring North Eurasian soil moisture variation on summer rainfall anomalies in Northern East Asia

This paper reports findings from a diagnostic and modeling analysis that investigates the impacts of the boreal late-spring soil moisture anomalies over North Eurasia on the summer rainfall over the northern East Asia (NEA). The soil moisture in May from the Kara-Laptev Sea coasts to Central Siberian Plateau is found to be negatively correlated with the summer rainfall from Mongolia to Northeast China. The atmospheric circulation anomalies associated with the anomalously dry soil are characterized by a pressure dipole with the high-pressure center located over North Eurasia and low-pressure center over NEA, where an anomalous water vapor convergence occurs, favoring rainfall formation. Diagnoses and modeling experiments demonstrate that the effects of the spring lower soil moisture over North Eurasia may persist into the following summer, then increase the low-level air temperature at higher latitudes through modulating local surface latent and sensible heat fluxes, and effectively reduce the meridional temperature gradient north of NEA. The weakened temperature gradient could induce the decreased vertical shear of zonal wind and generate an anomalously cyclonic center over NEA by affecting the baroclinicity around 60° N, associated with a favorable condition of local synoptic activity to increase rainfall. The above relationships and mechanisms are vice versa for the prior wetter North Eurasian soil and decreased NEA rainfall. These findings suggest that the soil moisture anomalies at higher latitudes may act as a new precursor providing an additional predictability source for better predicting the summer rainfall in NEA. (Sang Yinghan, Ren Hongli, Deng Yi, Xu Xiaofeng, Shi Xueli, Zhao Shuo)

3.12 Climatic factors contributing to interannual and interdecadal variations in the meridional displacement of the East Asian jet stream in boreal winter

We employ the fifth generation of the European Centre for medium-range weather forecasts reanalysis to investigate the leading mode of the East Asian zonal wind and the contribution of associated climatic factors in boreal winter during 1979–2020. The dominant mode, accounting for 46% of the explained variance, indicates that the East Asian subtropical jet (EASJ) and East Asian polar frontal jet (EAPJ) are meridionally displaced in opposite directions. The corresponding first principal component (PC1) shows clear interannual and interdecadal variations, with a regime shift in the year 1997. The dominant mode is significantly related to the Niño3.4 sea surface temperature (SST), the Barents-Kara Seas (BKS) sea ice concentration (SIC), the Arctic oscillation (AO) and the Tibetan Plateau (TP) surface air temperature (SAT) on interannual and interdecadal timescales. Multiple linear regression with these variables reproduces PC1 well. The interdecadal variation of PC1 is dominated by the BKS SIC and Niño3.4 SST. The Niño3.4 SST explains more than half of the variance of PC1 on an interannual time scale, which is more than all of the other factors combined.

The El Niño phase and BKS SIC are associated with the distance between the EASJ axis (EASJA) and the EAPJ axis (EAPJA). The AO and TP SAT may influence the meridional migration of the EASJA and EAPJA, respectively. The distance between the EASJA and EAPJA also depends on the configuration of the southern Asian cyclone and Siberian anticyclone. (Dong Xiao, Zhao Ping, Ren Hongli)

3.13 Diagnosing SST error growth during ENSO developing phase in BCC_CSM1.1m prediction system

In this study, the predictability of the El Niño-south oscillation (ENSO) in an operational prediction model from the perspective of initial errors is diagnosed using the seasonal hindcasts of the Beijing Climate Center system model, BCC_CSM1.1m. Forecast skills during the different ENSO phases are analyzed and it is shown that the ENSO forecasts appear to be more challenging during the developing phase, compared to the decay phase. During ENSO development, the SST prediction errors are significantly negative and cover a large area in the central and eastern tropical Pacific, thus limiting the model skill in predicting the intensity of El Niño. The large-scale SST errors, at their early stage, are generated gradually in terms of negative anomalies in the subsurface ocean temperature over the central-western equatorial Pacific, featuring an error evolutionary process similar to that of El Niño decay and the transition to the La Niña growth phase. Meanwhile, for short lead-time ENSO predictions, the initial wind errors begin to play an increasing role, particularly in linking with the subsurface heat content errors in the central-western Pacific. By comparing the multiple samples of initial fields in the model, it is clearly found that poor SST predictions of the Niño3.4 region are largely due to contributions of the initial errors in certain specific locations in the tropical Pacific. This demonstrates that those sensitive areas for initial fields in ENSO prediction are fairly consistent in both previous ideal experiments and our operational predictions, indicating the need for targeted observations to further improve operational forecasts of ENSO. (Tian Ben, Ren Hongli)

3.14 Understanding the causes of rapidly declining prediction skill of the East Asian summer monsoon rainfall with lead time in BCC_CSM1.1m

Dynamical prediction of monsoon rainfall has been an important topic and a long-standing issue in both research and operational community. This paper provides a comprehensive evaluation of the subseasonal-to-seasonal (S2S) prediction skill of the East Asian summer monsoon (EASM) rainfall using the hindcast record from the Beijing Climate Center climate system model, BCC CSM1.1m, during the period 1983–2019. The model exhibits reasonable skills for predicting the EASM rainfall at all lead times with the skill dropping dramatically from the shortest lead time of about 2 weeks (LM0) to 1-month lead (LM1), and then fluctuating remarkably throughout 2-month to 12-month lead times. Over the EASM domain, the rapid decline of the S2S rainfall prediction skill from LM0 to LM1 is mainly caused by the inferior skills over Central China in July and over Northeast China in August. Composite analysis based on hindcast records suggests that these inferior skills are directly tied to the model's difficulties in capturing above-normal precipitation over the eastern Central China and Northeast China in the respective months, which are further shown to be associated with anomalous weakening and meridional movement of the Northwestern Pacific subtropical high and the activity of large-scale teleconnection pattern hard to be predicted over the northeastern Asia in summer, respectively. These findings inform the intrinsic limits of the S2S predictability of the EASM rainfall by a dynamical model, and strongly suggest that the level of confidence placed upon S2S forecasts should be stratified by large-scale circulation anomalies known to significantly affect the prediction skill, e.g., the subtropical high and high-latitude teleconnection patterns for summer monsoon rainfall prediction in this region. (Wang Na, Ren Hongli, Deng Yi, Zhao Siyu)

3.15 A dynamical and machine learning hybrid seasonal prediction of summer rainfall in China

Seasonal prediction of summer rainfall is crucial to reduction of regional disasters, but currently it has a low prediction skill. We developed a dynamical and machine learning hybrid (MLD) seasonal prediction method for summer rainfall in China based on circulation fields from the Chinese Academy of Sciences (CAS) flexible global ocean-atmosphere-land system model finite volume version 2 (FGOALS-f2) operational dynamical prediction model. Through selecting optimum hyperparameters for three machine learning methods to obtain the best fit and least overfitting, an ensemble mean of the random forest and gradient boosting regression tree methods was shown to have the highest prediction skill measured by the anomalous correlation coefficient. The skill has an average value of 0.34 in the historical cross-validation period (1981–2010) and 0.20 in the 10-year period (2011–2020) of independent prediction, which significantly improves the dynamical prediction skill by 400%. Both reducing overfitting and using the best dynamical prediction are important in applications of the MLD method and in-depth analysis of these warrants a further investigation. (Wang Jialin, Yang Jing, Ren Hongli, Li Jinxiao, Bao Qing, Gao Miaoni)

3.16 Interdecadal changes in synoptic transient eddy activity over the Northeast Pacific and their role in tropospheric Arctic amplification

Arctic amplification refers to the greater surface warming of the Arctic than of other regions during recent decades. A similar phenomenon occurs in the troposphere and is termed "tropospheric Arctic amplification" (TAA). The poleward eddy heat flux and eddy moisture flux are critical to Arctic warming. In this study, we investigate the synoptic transient eddy activity over the North Pacific associated with TAA and its relationship with the subtropical jet stream, and propose the following mechanism. A poleward shift of the subtropical jet axis results in anomalies of the meridional gradient of zonal wind over the North Pacific, which drive a meridional dipole pattern of synoptic transient wave intensity over the North Pacific, referred to as the North Pacific synoptic transient wave intensity dipole (NPSTD). The NPSTD index underwent an interdecadal shift in the late 1990s accompanying that of the subtropical jet stream. During the positive phase of the NPSTD index, synoptic eddy heat flux transports more heat to the Arctic circle, and the eddy heat flux diverges, increasing Arctic temperature. This mechanism highlights the need to consider synoptic transient eddy activity over the North Pacific as the link between the mean state of the North Pacific subtropical upper jet and TAA. (Dong Xiao, Ren Hongli)

3.17 ENSO phase-locking behavior in climate models: From CMIP5 to CMIP6

The phase-locking behavior of El Niño-southern oscillation (ENSO) in models from Coupled Model Intercomparison Project (CMIP) phase 5 to phase 6 is assessed in terms of the locking-month of ENSO peak and the sharpness of locking tendency. Overall, a robust improvement exists in CMIP6. Compared to CMIP5, more CMIP6 models truly reproduce the locking-month in November-January. Meanwhile, the sharpness of phase-locking in CMIP6 models also improves, though most of them are still far from the observations. The locking-month is verified to be highly corresponding to the phase of seasonal modulation of ENSO's instabilities. The sharpness is mainly controlled by the intensity of this modulation and noise. Compared to CMIP5, CMIP6 models generally simulate these affecting factors better. Besides, models displaying an exaggerated semi-annual variation of ENSO's instabilities simulate the ENSO phase-locking relative-poorly, and these models show no reduction from CMIP5 to CMIP6. (Liu Minghong, Ren Hongli, Zhang Renhe, Sarah Ineson, Wang Run)

3.18 Improving long-lead seasonal forecasts of precipitation over southern China based on statistical downscaling using BCC_CSM1.1m

Long-lead precipitation forecasts for 1–4 seasons ahead are usually difficult in dynamical climate models due to the model deficiencies and the limited persistence of initial signals. But, these forecasts could be empirically improved by statistical approaches. In this study, to improve the seasonal precipitation forecast over the southern China (SC), the statistical downscaling (SD) models are built by using the predictors of atmospheric circulation and sea surface temperature (SST) simulated by the Beijing Climate Center climate system model version 1.1 m (BCC_CSM1.1 m). The different predictors involved in each SD model is selected based on both its close relationship with the target seasonal precipitation and its reasonable prediction skill in the BCC_CSM1.1 m. Cross and independent validations show the superior performance of the SD models, relative to the BCC_CSM1.1 m. The temporal correlation coefficient of SD models could reach over 0.4, exceeding the 95% confidence level. The SC precipitation index can be much better forecasted by the SD models than by the BCC_CSM1.1 m in terms of the interannual variability. In addition, the errors of the precipitation forecast in all four seasons are significantly reduced over most of SC in the SD models. For the 2015/2016 strong El Niño event, the SD models outperform the dynamical BCC_CSM1.1 m model on the spatial and regional-average precipitation anomalies, mostly due to the effective SST predictor in the SD models and the weak response of the SC precipitation to El Niño-related SST anomalies in the BCC_CSM1.1 m. (Liu Ying, Ren Hongli, N. P. Klingaman, Liu Jingpeng, Zhang Peiqun)

3.19 Intercomparison of MJO column moist static energy and water vapor budget among six modern reanalysis products

This study conducts an intercomparison of the column-integrated moist static energy (MSE) and water vapor budget of the Madden-Julian oscillation (MJO) among six modern global reanalysis products (RAs). Inter-RA differences in the mean MSE, MJO MSE anomalies, individual MSE budget terms, and their relative contributions to the propagation and maintenance of MJO MSE anomalies are examined. Also investigated is the relationship between the MJO column water vapor (CWV) budget residuals with the other CWV budget terms as well as with the two parameters that characterize cloud-radiation feedback and moisture–convection coupling. Results show a noticeable inter-RA spread in the mean-state MSE, especially its vertical structure. In all RAs, horizontal MSE advection dominates the propagation of the MJO MSE while column-integrated longwave radiative heating and vertical MSE advection are found to be the key processes for MJO maintenance. The MSE budget terms directly affected by the model parameterization schemes exhibit high uncertainty. The differences in anomalous vertical velocity mainly contribute to the large differences in vertical MSE advection among the RAs. The budget residuals show large inter-RA differences and have nonnegligible contributions to MJO maintenance and propagation in most RAs. RAs that underestimate (overestimate) the strength of cloud-radiation feedback and the convective moisture adjustment time scale tend to have positive (negative) MJO CWV budget residual, indicating the critical role of these processes in the maintenance of MJO CWV anomalies. Our results emphasize that a correct representation of the interactions among moisture, convection, cloud, and radiation is the key for an accurate depiction of the MJO MSE and CWV budget in RAs. (Ren Pengfei, Daehyun Kim, Min-Seop Ahn, Daehyun Kang, Ren Hongli)

3.20 Decomposition of projected summer rainfall change over East Asia based on timeslice experiments

The summer rainfall change over East Asia in response to CO_2 forcing and the associated processes are investigated via a set of pilot timeslice piSST experiments from the Cloud Feedback Model Intercomparison

Project phase 3 (CFMIP-3). The total response of rainfall to 4 × CO_2 in coupled models is decomposed into components associated with uniform SST warming, SST pattern change, the direct radiative effect of increased CO_2, and the plant physiological response. In general, the contributions of the individual responses of summer rainfall to different forcings are subject to a regional dependence. The uniform SST warming reduces rainfall in many land regions in East Asia, but increases rainfall over the northern East Asia. The spatial patterns of the rainfall change as the result of SST pattern change are nearly opposite to those of the uniform SST warming, which account for most inter-model uncertainty in the simulations. The direct radiative effect of increasing CO_2 is largely responsible for an increase of rainfall across the East Asian continent, especially over the central China and southern Tibetan Plateau, and the plant physiological effect appears to increase rainfall over the eastern and southern China. Also discussed are the atmospheric circulation changes that are driven by the distinct aspects of CO_2 forcing and directly tied to the summer rainfall changes. (Huang Yu, Ren Hongli, Robin Chadwick, Deng Yi)

3.21 Improvement of soil moisture simulation in Eurasia by the Beijing Climate Center Climate System Model (BCC-CSM) from CMIP5 to CMIP6

This study provides a comprehensive evaluation of historical surface soil moisture simulation (1979–2012) over Eurasia at annual and seasonal time scales between two medium-resolution versions of the Beijing Climate Center climate system model (BCC-CSM)—one that is currently participating in the Coupled Model Intercomparison Project phase 6 (CMIP6), i.e., BCC-CSM2-MR, and the other, BCC-CSM1.1m, which participated in CMIP5. We show that BCC-CSM2-MR is more skillful in reproducing the climate mean states and standard deviations of soil moisture, with pattern correlations increased and biases reduced significantly. BCC-CSM2-MR performs better in capturing the first two primary patterns of soil moisture anomalies, where the period of the corresponding time series is closer to that of reference data. Comparisons show that BCC-CSM2-MR performs at a high level among multiple models of CMIP6 in terms of centered pattern correlation and "amplitude of variation" (relative standard deviation). In general, the centered pattern correlation of BCC-CSM2-MR, ranging from 0.61 to 0.87, is higher than the multi-model mean of CMIP6, and the relative standard deviation is 0.75, which surmounts the overestimations in most of the CMIP6 models. Due to the vital role played by precipitation in land-atmosphere interaction, possible causes of the improvement of soil moisture simulation are further related to precipitation in BCC-CSM2-MR. The results indicate that a better description of the relationship between soil moisture and precipitation and a better reproduction of the climate mean precipitation by the model may result in the improved performance of soil moisture simulation. (Sang Yinghan, Ren Hongli, Shi Xueli, Xu Xiaofeng, Chen Haishan)

3.22 Leading modes of Asian-Australian monsoon interannual variability as represented in CMIP5 models

The Asian-Australian monsoon (AAM) exerts a strong impact on the regional climate. The ability of climate models to simulate the AAM is of great importance. This study evaluates the performance of 26 models, which participate in the Coupled Model Intercomparison Project phase 5 (CMIP5), in representing features of the leading modes of the AAM interannual variability. This is achieved by diagnosing quantitative metrics derived from a season-reliant empirical orthogonal function (S-EOF) analysis, and plausible external forcing contributing to the simulation results are presented. Our results show that the CMIP5 models can generally capture the spatial patterns of the leading modes of AAM interannual variability during El Niño development periods because of strong air–sea interactions. The variance percentage explained by the first two S-EOF modes is found to be closely related to the amplitude of the El Niño-southern oscillation (ENSO) in the models. In contrast, simulation of the periodicity remains challenging, and the models show deficiencies in the

accurate capture of periodic characteristics. Models with realistic ENSO simulations typically perform well in simulating S-EOF1, and the key to improving the simulation of S-EOF2 is the greater intensity of the simulated field of background heating over the Northwest Pacific warm pool. The multimodel ensemble (MME) performs better than most of the 26 individual models. Models in the MME with better ENSO simulation and stronger warm pool heating are found to be better able to represent the relationships between the first two leading S-EOF modes and ENSO, although biases remained. (Zhou Fang, Ren Hongli, Liu Minghong, Wang Run, Huang Kai)

3.23 Evaluation of simulation capability for multiple tropical cyclone events in the western North Pacific of the UH_HCM model

The intraseasonal variability of multiple tropical cyclone (MTC) events in the western North Pacific (WNP) during 1979–2015 is analyzed using the best-track dataset archived at the Joint Typhoon Warning Center. MTC events are divided into three phases according to the time intervals of the tropical cyclone (TC) genesis, that is, active, normal, and inactive phases. Composite analysis results indicate that MTC events tend to occur in the active phase when the monsoon trough is stronger and located farther north than at other times. Initialized by the data from a 10-year stable running result, a 12-year control experiment is carried out using the hybrid atmosphere-ocean coupled model developed at the University of Hawaii (UH_HCM model) to evaluate its simulation capability. Compared with the climate observations, the model shows good skill in simulating the large-scale environmental conditions in the WNP, especially the subtropical high and the monsoon trough. In addition, the model can well simulate the climate characteristics of TCs in the WNP, as well as the differences in each MTC phase. However, the simulated frequency of TCs is less and their locations are more northeast, compared with the observations. The vorticity and moisture in the model appear to be the two main factors affecting MTC activity based on analyses of the genesis potential index. (Li Tianhang, Ren Hongli, Wu Yujie, Gao Jianyun)

3.24 Improvement in the prediction of summer precipitation in the North China-Hetao region using the tropospheric temperature over the Tibetan Plateau in spring

We investigated the relationship between the spring tropospheric temperature over the Tibetan Plateau (TPT) and summer precipitation in the eastern China on an interannual timescale using the monthly mean ERA-Interim reanalysis dataset, the HadISST dataset and the daily mean precipitation dataset for China. We found that there is a significant positive correlation between the spring TPT and summer precipitation in the North China-Hetao region. The relationship is manifested in the context of the East Asia-Pacific pattern teleconnection. In the high spring TPT index years, the geopotential height anomalies over East Asia and the western North Pacific present a negative phase of the East Asia-Pacific pattern teleconnection in the subsequent summer. This circulation pattern is beneficial for the water vapor transport from the western Pacific to inland, which further transport to the North China-Hetao region from the Yangtze River-Yellow Rivers region. Anomalous upward motion occurs in the North China-Hetao region, which increases precipitation. The East Asian subtropical westerly jet shifts further north and the South Asian high weakens and shrinks westward. These conditions all favor an increase in precipitation over the North China-Hetao region. The spring TPT plays an important part in the prediction of summer precipitation in the North China-Hetao region. The improvement in the use of the spring TPT to predict summer precipitation in the North China-Hetao region is examined by comparing the prediction equations with and without the prediction factor of the spring TPT on the basis of the sea surface temperatures in key regions. After considering the impact of the spring TPT, the explanatory variance of the prediction equation for precipitation in the North China-Hetao region increases by 17.3%. (Chen Dan, Nan Sulan, Liu Ge)

3.25 GRAPES-GEPS环流集合预报的分类释用方法研究与检验

集合预报在数值天气预报体系中具有重要地位，因此如何有效提取集合样本信息以提高集合预报技巧一直是一个重要课题。基于中国全球集合预报业务系统（GRAPES-GEPS）的500 hPa高度场集合资料开展对环流集合预报的分类释用方法研究，并对集合聚类预报结果进行了检验分析。通过在传统Ward聚类法中引入动态聚类的“手肘法”方案，发展了环流集合预报分类释用方法。针对该方法的个例分析表明，对于中国中东部地区环流集合预报的聚类释用方法能够有效地划分出最有可能发生的环流形势类型并提供发生概率。确定性预报综合检验结果显示，集合预报聚类结果中发生概率最高的集合大类相对于集合平均的预报技巧有明显提升，并随着预报时效的延长提升更明显。总体来看，通过集合预报的分类释用方法划分环流形势类型可以为天气预报提供参考依据，具有实际应用价值。（罗月琳，高丽，陈权亮，蔡宏珂，任宏利）

3.26 热带大西洋海温异常季节内演变对中国江南地区夏季持续性高温事件影响的初步研究

中国江南地区是高温热浪灾害的高影响区。以往的一些研究发现了不同海域海温异常在年际或年代际尺度上的变化对中国南方夏季平均温度异常的影响效应。但是，关于这些关键海域海温季节内尺度变化对江南地区高温事件发生和维持影响的研究尚不多见。为此，本文利用中国站点观测、美国气象环境预报中心和美国国家大气研究中心（NCEP/NCAR）再分析以及美国国家海洋大气管理局（NOAA）海温等资料，首先以2016年江南地区夏季2次高温事件为例（分别发生在7月21—31日和8月15—25日），重点探讨了热带大西洋海温季节内变化的可能贡献。在此基础上，基于1981—2016年多高温事件合成结果，进一步分析了热带大西洋海温季节内变化影响江南高温事件的可能链接过程。研究发现，热带西大西洋暖海温异常在季节内尺度上的发展与维持有利于在欧亚大陆激发出较为稳定的Rossby波列结构，使东亚及其沿海地区为深厚的高压系统控制，进而引发江南地区持续性高温事件。这种热带大西洋暖海温的阶段性增强与维持及其相应的稳定Rossby波列结构超前于持续性高温事件：在热带大西洋海温显著升高1个月之内，江南地区可能出现持续性高温事件。在季节内尺度上，热带大西洋显著暖海温异常出现明显的阶段性增强之后10天左右，北印度洋暖海温也出现了阶段性增强。这暗示热带大西洋热力异常除通过直接激发欧亚大陆 Rossby 波列之外，还有可能通过影响热带印度洋海温的阶段性异常，进而对江南地区高温事件的发生和维持产生一定影响。另外，在厄尔尼诺衰减并向拉尼娜转变阶段，热带中东太平洋冷海温异常和北印度洋暖海温异常在季节内的协同阶段性变化可能也对持续性高温事件有贡献。上述关键区海温的季节内变化对中国江南地区高温事件具有一定的前期指示意义，但它们的具体影响过程，特别是在季节内尺度上的协同影响效应和物理过程，尚需未来进一步研究。(王慧美，刘舸，彭京备，纪立人)

3.27 地面观测资料地形高度订正对我国东部暴雨数值模拟的影响

采用中尺度气象模式WRFv3.8.1和GSI同化系统，建立了一套循环同化系统，开展了一个月的地面观测资料、探空资料、雷达资料和卫星资料的同化试验。在试验结果基础上，针对我国西部地区复杂地形，根据模式地形高度与实际测站地形高度的差异对地面观测资料进行订正，以2016年6月30日至7月6日长江中下游地区一次暴雨天气过程为例开展了数值模拟试验，并对比分析地面观测资料的高度订正及同化对我国东部暴雨数值模拟的可能影响。模拟结果表明：（1）批量循环同化试验模拟的地面变量较ERA-Interim再分析资料的均方根误差普遍减小，对地面气象要素的模拟有一定的改善。（2）地面观测资料经地形差异订正后同化到模式中，模拟的降雨落区和量级与观测雨带更为接近，TS评分、散度和垂直速度方面都有一定的改进，表明西部地区地面观测资料经地形高度订正后再同化到数值模式中能改进数值模式对我国东部暴雨的模拟效果。（曹润东，陈军明，赵平）

大气物理与人工影响天气
Atmospheric Physics and Weather Modification

云物理与人工影响天气研究进展
Advances in Research on Cloud Physics and Weather Modification

1 人工影响天气机理与方法
1 Mechanism and method of weather modification

1.1 Cable-car measurements of vertical aerosol profiles impacted by mountain-valley breezes in Lushan Mountain, East China

In-situ field observations of vertical aerosol profiles for one month in complex terrain (Lushan Mountain, China) were carried out using a cable car, which resolved detailed vertical distributions of mountain aerosols with lowcost operation. Cable-car observations were conducted during the early morning and late afternoon, when mountain and valley winds dominated, respectively. The diurnal aerosol variations at the top and foot of Lushan Mountain were analyzed based on environmental and meteorological stations. The observations indicated that the mountain-valley breezes notably impacted the mountain-area aerosol distribution under weak weather conditions. More uniform aerosol profiles for the afternoon than the morning, with their decreasing rates of $PM_{2.5}$ (particles with diameters less than 2.5 μm) were 1.64 and 2.28 μg m^{-3} hm^{-1}, respectively. The $PM_{2.5}/PM_{10}$ ratio at the mountain top increased from 0.69 to 0.81, and that at the mountain base decreased from 0.75 to 0.70 from morning to afternoon. The $PM_{2.5}$ concentration decreased in and around Lushan Mountain from daytime to nighttime, with the impacted diameter of the 300-m topography line being smaller than about 5 km, while the concentration increased in Jiujiang City. The relative decreasing rate of $PM_{2.5}$ was higher at the mountain top site (about 20%) than at the base site (about 2%) from daytime to nighttime. Moreover, uniform aerosol profiles could have been caused by regional transport through a relatively strong low-level synoptic flow (about 5 m s^{-1}) and the mountain's dynamic lifting effect.（Duan Jing, Chen Yong, Wang Wenling, Li Jun, Zhang Xiaopeng, Lu Guangxian, Che Yunfei, Zhong Shujun, Ma Shupo, Li Peng, An Junling, Fu Pingqing）

1.2 Radiative effects of clouds and fog on long-lasting heavy fog events in northern China

In the last decade, heavy fog events have been found to last from several days to more than a week and frequently occur in the northern China. The mechanism responsible for the long-lasting heavy fog events has not been fully understood. In this study, the radiative effects of the clouds and fog on two persistent heavy fog events on December 3–6, 2011 (Case-2011) and January 28–31, 2013 (Case-2013) are investigated based on both observations and weather research and forecasting (WRF) model. The results indicate that the radiative effects of clouds formed at middle and high levels and fog may play an important role in sustaining long-lasting fog events in the northern China. The clouds formed above the fog primarily consist of ice and snow particles with a thickness of more than 3–4 km and cloud base of 3–6 km. During the daytime, the increase in solar radiation reflection caused by both clouds and fog can reduce the mean surface solar radiation by 71% in Case-2011 and 84% in Case-2013, and the contribution from clouds accounts for 18%, which may significantly

weaken the surface heating from solar radiation and prevent the dissipation of fog events. While during the nighttime, the greenhouse effect of clouds and fog can increase the mean surface net radiation by 77 W m^{-2} in Case-2011 and 68 W m^{-2} in Case-2013, which may reduce the surface long-wave radiative cooling and prevent the further development of fog events. However, the greenhouse effect of clouds and fog during both daytime and nighttime may enhance turbulent processes and cause the fog to rise, and remain in the stable inversion layer.（Guo Lijun, Guo Xueliang, Luan Tian, Zhu Shichao, Lyu Kai）

1.3 Characteristics of raindrop size distributions during Meiyu season in Mount Lushan, East China

Meiyu front precipitation makes the region prone to frequent floods, mudslides, landslides, and other disasters, and has been the focus of ongoing and challenging meteorological research. Investigation of the raindrop size distribution (RSD) is essential for exploring the characteristics and underlying physical precipitation processes. This study investigated the precipitation characteristics in Lushan mountainous areas during the Meiyu season using laser disdrometer observed RSD data from 2016 to 2019. For the average spectra of five rain rate classes, the concentrations of large raindrops (> 0.5 mm) increased with rain rate (R), while the concentrations of small raindrops (< 0.5 mm) increased only under rain rates higher than 10 mm h^{-1}. The gamma distribution parameters of N_0 (intercept parameter) and λ (slope parameter) increased/decreased with rain rate, and the shape parameter μ exhibited negative values in different rain rate classes. The distribution pattern features were $N(D) = 721D^{-1.79}e^{-1.20D}$. Distributions of the frequency for mass-weighted mean diameter (D_M) and the logarithm of the generalized intercept parameter ($\lg N_w$) both showed a unique bimodal type, and an exceptionally high N_W ($\lg N_w > 4.5$) subset with small D_M was determined. The stratiform and convective rain of RSD were also investigated. D_M-R and N_W-R showed similar variations in two types of precipitation. The lower μ values resulted in higher primary and constant coefficients in the quadratic polynomial fitting for the μ-λ relationship ($\lambda = 0.0347\mu^2 + 1.180\mu + 2.495$). The Z-R relationship (Z for radar reflectivity factor) in stratiform precipitation characteristics was $Z = 203R^{1.59}$. Further investigations showed that high N_W values usually occurred in persistent precipitation. The RSD can be characterized as high concentrations of the first two diameter classes with narrow spectrum width (< 1 mm), which were captured during in-cloud rain with a low but continuous rain rate (< 5 mm h^{-1}). The mountainous topography plays an important role in reshaping the characteristics of RSD and the physical processes of precipitation.（Chang Yi, Ma Qianrong, Guo Lijun, Duan Jing, Li Jun, Zhang Xiaopeng, Guo Xueliang, Lou Xiaofeng, Chen Baojun）

1.4 Aerosol and cloud properties over a coastal area from aircraft observations in Zhejiang, China

Using in-situ aircraft observations from six flights over Zhejiang on September 1 and September 4, 2016, this study investigates differences in aerosol and cloud properties between daytime and nighttime. The samples were divided into marine type and continental type based on the backward air mass trajectories and aerosol characteristics. The results show that the aerosol number concentration (N_a) near the ground during daytime is higher than that at nighttime. During daytime, N_a has a significant decreasing trend near the top of the planetary boundary layer (PBL), which is not obvious during nighttime. There may be still a relative high concentration of aerosols remaining in the transition zone between the PBL and the free troposphere. Under similar liquid water content (LWC) conditions, the cloud droplet number concentration (N_c) at night is lower, and the cloud droplet effective diameter (cloud ED) is larger. The total N_a of marine type aerosols is generally lower than that of continental type aerosols, but for aerosols with particle diameters greater than 1 μm, the marine type aerosols are higher. The study shows a strong negative N_a-cloud ED relationship for marine type aerosols, but no obvious N_a-cloud ED relationship for continental type aerosols. The number of cloud condensation nuclei (CCN) is higher under high-N_a conditions; the ratio of CCN to N_a reveals that the activation efficiency of marine type aerosols is higher than that of continental type aerosols. There is no obvious difference in activation efficiency

between day and night. (Che Yunfei, Zhang Jing, Fang Chungang, Zhou Xu, Xue Wenhao, Hu Xiaomin, Duan Jing, Li Wei, Gao Yang, Lu Guangxian, Zhao Delong, Zhao Chuanfeng)

1.5 An airborne study of the aerosol effect on the dispersion of cloud droplets in a drizzling marine stratocumulus cloud over eastern China

Detailed airborne measurements were carried out to explore aerosol-cloud interactions and cloud microphysical properties in a drizzling marine stratocumulus cloud deck over the eastern China. Results show that the collisioncoalescence of cloud droplets, the condensation of small droplets, and the collision-induced break-up of drizzle were the dominant microphysical processes in the sampled water cloud parcel. The region in the vicinity of the cloud's lateral boundary was spatially divided into sub-regions to better understand aerosol and droplet interactions. Relationships between the relative dispersion (ε) and the cloud's microphysical and dynamical characteristics were also examined. A negative relation was found between ε and the cloud droplet number concentration, with ε showing a close relationship with the liquid water content (LWC) and updraft velocity. When LWC was greater than about 0.75 g kg^{-1}, the range of ε values narrowed, and updrafts dominated. By introducing ε in the cloud droplet effect radius (R_e) parameterization, we find that ε can further affect indirect forcing by changing the R_e distribution for the cloud examined in this study. The dispersion effect (DE) was estimated using the effective radius ratio and the specific cloud water content. An in-depth analysis indicates that DE may offset the Twomey effect by about 12%. Two different methods of estimating the indirect effect (IE) yielded close values (0.084 and 0.077), suggesting that introducing DE into the estimation had a small influence on the IE calculation in the drizzling marine stratocumulus cloud of this study. Note that the estimated IE has a large uncertainty, given the large biases in the cloud properties measured. (Wang Fei, Li Zhanqing, Zhao Delong, Ma Xincheng, Gao Yang, Sheng Jiujiang, Tian Ping, Maureen Cribb)

1.6 Revisiting the size of nonspherical particles recorded by optical array probes with a new method based on the convex hull

In recent years, the cloud imaging probe (CIP) and precipitation imaging probe (PIP) produced by droplet measurement technologies (DMT) have been introduced by a number of meteorological research and operation centers in China. The supporting software provided by DMT, i.e., PADS (particle analysis and display system), cannot output detailed information on each individual particle, which definitely limits the in-depth utilization of cloud and precipitation particle image data in China. In this paper, particle-by-particle information was extracted by decompressing the CIP and PIP original particle image data, based on which a new definition of the dimension for nonspherical particles is proposed by using the area of the convex hull enclosing a particle to obtain the equivalent diameter of a circle with equal area. Based on the data detected during one flight in Inner Mongolia, the particle size distribution obtained using the new particle size definition and that used by the other four existing definitions are compared. The results show that the particle number concentration calculated using different particle size definitions can vary by up to an order of magnitude. The result obtained based on the new particle size definition is closest to that calculated with the area-equivalent diameter definition.（Zhang Rong, Zhou Xu, Li Hongyu, Li Hanchao, Wei Lei, Gao Yang, Xia Qiang, Wang Xiangyu）

1.7 Satellite estimates and subpixel variability of rainfall in a semi-arid grassland

Uncertainties in satellite rainfall estimation may derive from both the local rainfall characteristics and its subpixel variability. To study this issue, micro rain radars and a rain gauge network were deployed within a 9-km satellite pixel in the semi-arid Xilingol grassland of China in summer 2009. The authors characterized the subpixel variability with the coefficient of variation (CV) and evaluated the satellite rainfall estimation for this semi-arid area. The results showed that rainfall events with a high CV were mostly convective with a small

amount of rainfall. Spatially inhomogeneous rainfall was most likely to occur at the edges of small clouds producing rain. The performance of the TRMM (tropical rainfall measuring mission) 3B42V7 product for daily rainfall was better than that of the CMORPH (Climate Prediction Center morphing technique) and PERSIANN (precipitation estimation from remotely sensed information using artificial neural networks) products, although the TRMM product tended to overestimate rainfall in a lake area of the semi-arid grassland. (Chen Yong, Duan Jing, An Junling, Liu Huizhi, Ulrich Görsdorf, Franz H. Berger)

1.8 A hypergraph-embedded convolutional neural network for ice crystal particle habit classification

In the field of weather modification, it is important to accurately identify the ice crystal particles in ice clouds. When ice crystal habits are correctly identified, cloud structure can be further understood and cloud seeding and other methods of weather modification can be used to change the microstructure of the cloud. Consequently, weather phenomena can be changed at an appropriate time to support human production and quality of life. However, ice crystal morphology is varied. Traditional ice crystal particle classification methods are based on expert experience, which is subjective and unreliable for the identification of the categories by threshold setting. In addition, existing deep learning methods are faced with the problem of improving classification performance on datasets with unbalanced sample distributions. Therefore, we designed a convolutional neural network (CNN) embedded with a hypergraph convolution module, named Hy-INet. The hypergraph convolution module can effectively capture information from hypergraphs constructed from local and global feature spaces and learn the features of small samples in ice crystal datasets that have unbalanced sample numbers. Experimental results demonstrate that the proposed method can achieve superior performance in the classification task of ice crystal particle habits.（Liao Mengyuan, Duan Jing, Zhang Rong, Zhou Xu, Wu Xi, Wang Xin, Hu Jinrong）

1.9 Temporospatial distribution and trends of thunderstorm, hail, gale, and heavy precipitation events over the Tibetan Plateau and associated mechanisms

Temporospatial distribution and trends of thunderstorm, hail, gale, and heavy precipitation events over the Tibetan Plateau (TP) as well as the associated mechanisms with observational data from 1979 to 2016 are investigated, which have not been fully studied under a changing climate. The results indicate that thunderstorm, hail, and gale events over the whole TP show significant decreasing trends, while heavy precipitation events have an insignificant increasing trend. The southeast and central south subregions have obvious significant decreasing trends in thunderstorm, hail, and gale events, while the northeast subregion has a significant increasing trend in heavy precipitation events. It is found that the atmospheric circulation anomaly caused by the northwestern Atlantic sea surface temperature (SST) anomaly associated with the North Atlantic oscillation (NAO) should be responsible for these changes. A strong wave train triggered by the northwestern Atlantic SST anomaly propagates from the northern Atlantic to East Asia through Europe, and induces a more upper-level warming over the TP and an anomalous anticyclonic circulation near the Lake Baikal, resulting in a more stable atmosphere and blocking effect, which forces the midlatitude westerlies and associated cold air to shift poleward. The weakened cold-air advection over the TP decreases the baroclinic instability and convection initiation, and finally causes the significant decreasing trends in severe weather events. On the other hand, the enhanced easterly winds in the southern flank of the anticyclonic circulation can significantly increase the water vapor flux from the eastern boundary of the TP and heavy precipitation events in the northeast subregion. (Tang Jie, Guo Xueliang, Chang Yi, Lu Guangxian, Qi Peng)

1.10 Microphysical characteristics of precipitating cumulus cloud based on airborne Ka-band cloud radar and droplet measurements

Based on cloud-probe data and airborne Ka-band cloud radar data collected in Baoding on 5 August 2018, the microphysical structural characteristics of cumulus (Cu) cloud at the precipitation stage were investigated. The cloud droplets in the Cu cloud were found to be significantly larger than those in stratiform (STF) cloud. In the Cu cloud, most cloud particles were between 7 and 10 μm in diameter, while in the STF cloud the majority of cloud particles grew no larger than 2 μm. The sensitivity of cloud properties to aerosols varied with height. The cloud droplet effective radius showed a negative relationship with the aerosol number concentration (N_a) in the cloud planetary boundary layer (PBL) and upper layer above the PBL. However, the cloud droplet concentration (N_c) varied little with decreased N_a in the high liquid water content region above 1500 m. High N_a values between 300 and 1853 cm^{-3} were found in the PBL, and the maximum N_a was sampled near the surface in August in the Hebei region, which was lower than that in autumn and winter. High radar reflectivity corresponded to large FCDP (fast cloud droplet probe) particle concentrations and small aerosol particle concentrations, and vice versa for low radar reflectivity. Strong updrafts in the Cu cloud increased the peak radius and N_c, and broadened the cloud droplet spectrum; lower air temperature was favorable for particle condensational growth and produced larger droplets.（Wei Lei, Huang Mengyu, Zhang Rong, Lyu Yuhuan, Hou Tuanjie, Lei Hengchi, Zhao Delong, Zhou Wei, Fu Yuan）

1.11 Characteristics of raindrop size distributions in Chongqing observed by a dense network of disdrometers

This study investigates the characteristics of raindrop size distribution (RSD) including the temporal and spatial variabilities and the summer rain RSD features using 34 Parsivel disdrometers data from January 2015 to January 2016 in Chongqing, an inland municipality in Southwest China. The observed RSDs are fitted with the gamma distribution ($N(D) = N_0 D^{\mu} e^{-\lambda D}$) in this study. Rainfall in summer differs greatly from winter with larger rain rate, rain water content and variabilities. From winter to summer, raindrop sizes increase as the frequency of convective rain increases, and the diurnal variabilities of raindrop sizes are greatly enlarged. The spatial variabilities of N_0, λ and μ are relatively weak and change little in summer. The summer rainfall RSD characteristics and parameter relationships in Chongqing are different from other regions (Nanjing, Beijing, Zhuhai and Daocheng) in China. A novel diagnosed relation between the shape parameter of the gamma distribution (μ) and the mean volume diameter (D_v) is proposed based on the large amount of observations, which allows for a wider range of the mean volume diameter of raindrops compared to traditional μ-λ relations in microphysics parameterizations. (Liu Xuancheng, Xue Lulin, Chen Baojun, Zhang Yixuan)

1.12 Numerical simulation and the underlying mechanism of a severe hail-producing convective system in East China

A severe convective system that produced egg-sized hail in Jiangsu Province in East China on April 28, 2015 was simulated using a cloud-resolving weather research and forecasting model with the spectral bin microphysics scheme. The simulation reproduced the two stages of the convective system: the linear convective system (LCS) and the bow echo system (BES) stages. During the LCS stage, the intensity of updrafts was slightly stronger than that in the BES stage, with abundant supercooled water above the −20 ℃ layer, and graupel and hail mainly generated in this period. The microphysical budget analyses and size distribution characteristics of hail were studied within one cell that produced hail during the LCS. It was suggested that hail mainly formed through water-graupel collision and increased in size by collecting liquid water. Hail particles with smaller diameter were located around the perimeter of the main updrafts, while larger ones were

distributed at the left edge of the updrafts. Trajectories and size growth processes of hailstones within the chosen cell were calculated by a three-dimensional hail growth model, and it was found that hails originated from the middle levels on the east side of the updrafts, and were transformed westward and downward to the lower levels. They continued to ascend along the left edge of the updrafts and experienced one or more up-down recycles and fell down to the ground on the west side of the updrafts. (Lei Yin, Fan Ping, Xu Huanbin, Chen Baojun)

1.13 Characteristics of deep convective systems and initiation during warm seasons over China and its vicinity

The spatiotemporal statistical characteristics of warm-season deep convective systems, particularly deep convective systems initiation (DCSI), over China and its vicinity are investigated using Himawari-8 geostationary satellite measurements collected during April-September from 2016 to 2020. Based on a satellite brightness temperature multiple-threshold convection identification and tracking method, a total of 47593 deep convective systems with lifetimes of at least 3 h were identified in the region. There are three outstanding local maxima in the region, located in the southwestern, central and eastern Tibetan Plateau and Yunnan-Guizhou Plateau, followed by a region of high convective activities in South China. Most convective systems are developed over the Tibetan Plateau, predominantly eastward-moving, while those developed in Yunnan-Guizhou Plateau and South China mostly move westward and southwestward. The DSCI occurrences become extremely active after the onset of the summer monsoon and tend to reach a maximum in July and August, with a diurnal peak at 11:00–13:00 LST in response to the enhanced solar heating and monsoon flows. Several DCSI hotspots are identified in the regions of inland mountains, tropical islands and coastal mountains during daytime, but in basins, plains and coastal areas during nighttime. DCSI over land and oceans exhibits significantly different sub-seasonal and diurnal variations. Oceanic DCSI has an ambiguous diurnal variation, although its sub-seasonal variation is similar to that over land. It is demonstrated that the high spatiotemporal resolution satellite dataset provides rich information for understanding the convective systems over China and vicinity, particularly the complex terrain and oceans where radar observations are sparse or none, which will help to improve the convective systems and initiation nowcasting. (Li Yang, Liu Yubao, Chen Yun, Chen Baojun, Zhang Xin, Wang Weisheng, Shu Zhuozhi, Huo Zhaoyang)

1.14 Hydrometeor and latent heat nudging for radar reflectivity assimilation: Response to the model states and uncertainties

Radar data are essential to convection nowcasting and nudging-based radar data assimilation through diabatic initialization is one of the most effective approaches for forecasting convective systems with numerical weather prediction (NWP) models, used at several advanced global weather centers. It is desired to assess the uncertainty and physical consistency of this assimilation process. This paper investigated impacts of relaxation coefficient, radar data update intervals and continuous assimilation time duration and addressed the key issues and possible solutions of the radar data assimilation based on the WRF hydrometeor and latent heat nudging (HLHN) developed at the National Center for Atmospheric Research (NCAR). It is revealed that excessively large re-laxation coefficient forced the model to observations with a tendency greater than the physical terms of the convection, causing the dynamic imbalances and serious convection “ramp-down” right after the free forecast starts. Assimilating high update frequency radar data can make the tendency terms moderate and sustained thereby maintaining the assimilation effect and reducing fortuitous convection. HLHN requires a minimum continuous assimilation duration to contain the initial forced disturbance of the model. For a summer Meiyu precipitation case studied, the minimum duration is about 1 h. Appropriate selection of the HLHN parameters is able to effectively improve the temperature, humidity, and dynamic fields of the model. In

addition, several issues still remain to be solved to further enhance HLHN.（Huo Zhaoyang, Liu Yubao, Wei Ming, Shi Yueqin, Fang Chungang, Shu Zhuozhi, Li Yang）

1.15 Vertical distributions of aerosol microphysical and optical properties based on aircraft measurements made over the Loess Plateau in China

Aerosol microphysical properties, scattering and absorption characteristics, and in particular, the vertical distributions of these parameters over the eastern Loess Plateau, were analyzed based on aircraft measurements made in 2020 during a summertime aircraft campaign in Shanxi, China. Data from six flights were analyzed. Statistical characteristics and vertical distributions of aerosol concentration, particle size, optical properties, including aerosol scattering coefficient (σ_{sp}), backscattering ratio (β_{sc}), Ångström exponent (α), single-scattering albedo (SSA), partially-integrated aerosol optical depth (PAOD), and black carbon concentration (BCc), were obtained and discussed. Mean values of aerosol particle number concentration (N_a), particle volume concentration (V_a), mass concentration (M_a), surface concentration (Sa), and particle effective diameter (EDa) were 854.92 cm^{-3}, 13.37 μm^3 cm^{-3}, 20.06 μg m^{-3}, 170.08 μm^3 cm^{-3}, and 0.47 μm, respectively. Mean values of BCc, σ_{sp} (450, 525, 635 nm), β_{sp} (525 nm), α (635/450), and SSA were 1791.66 ng m^{-3}, 82.37 Mm^{-1} at 450 nm, 102.57 Mm^{-1} at 525 nm, 126.60 Mm^{-1} at 635 nm, 0.23, 1.47, and 0.92, respectively. Compared with values obtained in 2013, N_a decreased by 60% and M_a decreased by 45%, but the scattering coefficients increased in different degrees. In the vertical direction, aerosol concentrations were higher at lower altitudes, decreasing with height. Vertical profiles of σ_{sp}, β_{sp}, α (635/450), and BCc measured during the six flights were examined. Two peaks in N_a were identified near the top of the boundary layer and between 2000 and 2200 m. Fine particles with EDa smaller than 0.8 μm are dominant in the boundary layer and coarse aerosols existed aloft. Aerosol scattering properties and BCc in the lowest layer of the atmosphere contributed the most to the total aerosol radiative forcing. SSA values were greater than 0.9 below 2500 m, with lower values at higher levels of the atmosphere. On lightly foggy days, SSA values were greater than 0.9, and aerosols played a cooling role in the atmosphere. On hazy days, lower level SSA values were generally greater than 0.85, with aerosols likely having a warming effect on the atmosphere. The 48-hour backward trajectories of air masses during the observation days showed that the majority of aerosol particles in the lower atmosphere originated from local or regional pollution emissions, contributing the most to the total aerosol loading and leading to high values of aerosol concentration and radiative forcing. (Cai Zhaoxin, Li Zhanqing, Li Peiren, Li Junxia, Sun Hongping, Yang Yiman, Gao Xin, Ren Gang, Ren Rongmin, Wei Jing)

1.16 Assimilation of ground-based microwave radiometer on heavy rainfall forecast in Beijing

Ground-based microwave radiometers (MWRPS) can provide continuous atmospheric temperature and relative humidity profiles for a weather prediction model. We investigated the impact of assimilation of ground-based microwave radiometers based on the rapid-refresh multiscale analysis and prediction system-short term (RMAPS-ST). In this study, five MWRP-retrieved profiles were assimilated for the precipitation enhancement that occurred in Beijing on 21 May 2020. To evaluate the influence of their assimilation, two experiments with and without the MWRPS assimilation were set. Compared to the control experiment, which only assimilated conventional observations and radar data, the MWRPS experiment, which assimilated conventional observations, the ground-based microwave radiometer profiles and the radar data, had a positive impact on the forecasts of the RMAPS-ST. The results show that in comparison with the control test, the MWRPS experiment reproduced the heat island phenomenon in the observation better. The MWRPS assimilation reduced the bias and RMSE of 2-meter temperature and 2-meter specific humidity forecasting in the 0–12 h of the forecast range. Furthermore, assimilating the MWRPS improved both the distribution and the intensity of the hourly rainfall forecast, as compared with that of the control experiment, with observations that predicted the process

of the precipitation enhancement in the urban area of Beijing.（Qi Yajie, Fan Shuiyong, Li Bai, Mao Jiajia, Lin Dawei）

1.17 How do multiscale interactions affect extreme precipitation in eastern central Asia?

The variability of extreme precipitation in the eastern central Asia (ECA) during summer (June–August) and its corresponding mechanisms were investigated from a multiscale synergy perspective. Extreme precipitation in ECA displayed a quasi-monopole increasing pattern with abrupt change since 2000/2001, which was likely dominated by increased high-latitude North Atlantic SST anomalies as shown by diagnosed and numerical experiment results. Increased SST via adjusting the quasi-stationary wave train that related to the negative North Atlantic oscillation (NAO) and the east Atlantic/western Russia (EA/WR) pattern guided the cyclonic anomaly in central Asia, deepened the Lake Balkhash trough, and enhanced the moisture convergence in ECA. These anomalies also exhibited interdecadal enhancement after 2000. On the synoptic scale, two synoptic transient wave trains correlated with extreme precipitation in ECA by amplifying the amplitude of the quasi-stationary waves and guiding transient eddies in ECA. The induced transient eddies and deepened Lake Balkhash trough strengthened positive meridional vorticity advection and local positive vorticity, which promoted ascending motions, and guided the southerly warm moisture in ECA especially after 2000. Meanwhile, additional mesoscale vortices were stimulated and strengthened near the Tianshan Mountain in front of the wave trough, which, together with the enhanced meridional circulation, further increased extreme precipitation in ECA.（Ma Qianrong, Zhang Jie, Ma Yujun, Asaminew Teshome Game, Chen Zhiheng, Chang Yi, Liu Meichen）

1.18 人工影响天气碘化银催化剂研究进展

碘化银（AgI）类催化剂是人工影响天气外场试验和业务作业中使用最广泛的催化剂，其核化效率和核化机制在很大程度上影响催化效果。在总结美国、中国和欧洲多个国家利用云室和风洞研究AgI类催化剂的核化机制、核化阈温及成核率的室内试验成果的基础上，梳理利用室内试验成果发展的AgI数值催化模式，旨在为下一步优选新型高效AgI类催化剂和改进数值催化模式提供借鉴。AgI类催化剂核化机制包括凝华核化、接触冻结核化、凝结冻结核化和浸没冻结核化，其核化过程受大气温湿条件、催化剂粒子大小、成分等多种因素影响，并与催化剂粒子的燃烧溶液法、燃烧焰剂法和爆炸法等发生方式有关。目前国内外使用的AgI类催化剂含有不同成分，有多种催化剂粒子产生方式，催化剂粒子的核化机制和成核率有很大差异。将来应重点基于高性能云室和风洞，分析不同催化剂配方的核化机制和成核率，优选新型高效催化剂，改进AgI数值催化模式。（楼小凤，傅瑜，苏正军）

1.19 青藏高原夏季对流云微物理特征和降水形成机制

青藏高原对我国天气、气候和水循环过程有重要影响。利用第三次青藏高原大气科学试验（TIPEX-Ⅲ）2014年7月在那曲地区的飞机观测数据，研究青藏高原夏季对流云和降水的微物理特征及降水形成机制。飞机探测的云系主要为初生或发展阶段的冰水混合云，云滴数浓度低于平原、海洋地区1～2个量级，云内存在大量大云滴和雨滴，过冷水含量高。大粒子（$D \geqslant 50$ μm）数浓度量级为100～101/L，云内上升气流速度集中在1～4 m/s。青藏高原云滴谱主要呈双峰型，云内冰相粒子多为密实、不透明的霰粒子，云内凇附过程显著。云内暖雨过程产生的大云滴和雨滴有利于冰相过程，尤其是凇附过程的产生，使得青藏高原云更易产生降水。此外，残留云系与对流云有着较为类似的微物理特征。（常祎，郭学良，唐洁，卢广献，亓鹏）

1.20 基于探空云识别方法的云垂直结构分布特征

云的垂直结构特征作为云重要的宏观特征之一，直接决定了云的类型，进而通过发射和吸收辐射

的方式影响着地气系统的能量收支平衡，因此对云垂直结构特征的研究一直都是云物理研究的一个重要方向。作为观测云垂直结构特征的一种方式，探空气球通过获取沿路径方向高分辨率的廓线信息，采用一定反演方法从而能够较为准确地识别云的垂直结构。本文即利用我国业务布网探空站的观测资料，采用相对湿度阈值法识别云垂直结构，并同激光云高仪、“风云四号”静止卫星和毫米波云雷达对识别的云结构特征量进行了一致性检验。在此基础上，统计分析了2015—2017年单层、两层和三层云的垂直结构分布特征、日变化和季节变化特征以及全国区域分布特征。结果表明：（1）整体分布上，单层云在垂直方向上出现的高度范围介于多层云的高度范围内，并且随着云层数的增加，云在垂直方向上更为伸展，即高层云越高，低层云越低。（2）在日变化中，中午单层和多层云中最低层云的云底高度均高于早晨，而夜间单层和多层云中最高层云的云顶高度则高于早晨和中午，同时中间层云厚的变化要小于最上层和最下层云厚的变化。（3）在季节变化中，夏季云量较其他季节更多，云体发展也更为深厚，表明温暖的大气条件更有利于云的形成和发展。（4）我国云垂直结构分布特征具有明显的纬向变化趋势，从以青藏高原为中心的西南地区的云底较高云体较薄的云，逐步过渡到以东南沿海地区为中心的云底较低云体较为深厚的云，表明不同地形和气候带的差异与不同云类型的分布直接相关。（李琦，蔡淼，周毓荃，唐雅慧，欧建军）

1.21　六盘山地区一次低槽低涡云系结构及其降水机制的数值模拟研究

六盘山是西北重要的水源涵养林基地，干旱少雨制约了该地区农业和经济发展。作为该地区人工增雨技术研究的基础，本文利用WRF模式对2018年8月21日发生在宁夏南部六盘山区的一次降水天气过程进行了数值模拟。根据模拟结果结合实测资料，分析了造成此次强降水过程的有利环流形势场，重点讨论了山区降水云系的微物理结构以及降水形成机制。结果表明：降水是在高空槽配合低涡的动力场作用下形成的，受六盘山地形的阻挡作用，低层低涡系统移速落后于高空槽；垂直方向上云系呈现“催化–供给”的分层结构，但在云系不同部位，各层水凝物配置不同，导致冷暖云过程对降水的贡献差异；六盘山东部迎风坡降水强于西坡。霰粒子融化和云水碰并是地面降水的主要来源；碰冻过冷雨水是霰增长的主要过程。迎风坡云水层深厚，含水量高，一方面促进过冷层中霰粒子的碰冻增长过程，一方面为雨滴碰并增长提供充沛的云水条件，即同时增强了冷暖云降水过程。地形对云的发展和降水的形成有明显影响，当降低地形高度后，云水量减少，暖云过程减弱，同时也影响了霰粒子的增长过程。（高亮书，姚展予，贾烁，张沛，安琳，常倬林，桑建人，赵文慧，王伟健）

1.22　祁连山春季一次层状云降水的雨滴谱分布及地形影响特征

祁连山是青藏高原东北部重要的生态屏障和冰川与水源涵养生态功能区，是黄河流域重要水源产流地，但针对该地区的云和降水过程研究很少。本文利用祁连山地区11个Parsivel2雨滴谱仪的观测数据，研究了祁连山地区春季一次层状云降水过程的雨滴谱分布及地形影响特征。此次降水过程主要受短波槽影响，降水时空差异较大。雨滴谱观测数据表明，此次降水过程的雨滴等效直径（D_m）较小，雨滴谱数浓度（N_T）与D_m随海拔高度升高分别呈增加和减小的趋势，低海拔站点$\lg N_w$（N_w为雨滴谱截断参数）和D_m分布有着明显的层状云降水特征，而整个祁连山地区在同样D_m下有着更高的N_w。低海拔站点由于碰并和小雨滴的蒸发，因此有着更少的小雨滴（＜1 mm）和更多的大雨滴，而高海拔站点由于距离云底较近或位于云内，云滴尺度小且浓度大，D_m随R（R为降水强度）增大变化趋势不明显。M-P分布和Gamma分布在低海拔站点的拟合效果要优于高海拔站点，相较于Gamma分布，M-P分布对高海拔站点的小雨滴和大雨滴浓度有一定的高估和低估，因此更适用于高海拔站点雨滴谱的描述。对比于低海拔站点，高海拔站点的μ-λ（μ、λ分别为Gamma分布的形状参数和斜率参数）关系与相关研究的结果较为接近，但在λ较小（＜40 mm^{-1}）时拟合结果较为接近。受海拔高度与云底的相对位置和地形的影响，祁连山地区的Z-R（Z为雷达反射率因子）关系与其他地区或研究有着较大的区别。（程鹏，

常祎，刘琴，王研峰，李宝梓，陈祺，罗汉）

1.23 华北地区一次气溶胶与浅积云微物理特性的飞机观测研究

2014年8月15日，山西省人工降雨防雹办公室在山西忻州开展了气溶胶和浅积云的飞机观测，本文利用机载云物理资料，详细分析了华北地区气溶胶、云凝结核（CCN）和浅积云微物理特性及其相互影响。主要结论有：（1）此次过程的边界层高度约为3600 m，不同层结情况下，0.1 ～ 3 μm尺度范围内的气溶胶粒子浓度N_a、有效直径D_a和CCN数浓度的垂直廓线明显不同，近地面N_a可达2500 cm^{-3}。（2）CCN的主要来源为积聚模态、爱根模态或者核模态的气溶胶颗粒，0.2%过饱和度下，气溶胶活化率（AR）在各高度层的结果变化不大；0.4%过饱和度下，AR随着高度增加而降低。（3）后向轨迹模式分析表明，2 km以下的气溶胶主要来自于当地城市排放，由细颗粒污染物组成；2 km以上的气溶胶主要来源于中国西北和蒙古地区的沙漠，由亚微米沙尘组成，溶解度相对较低，可作为潜在的冰核。（4）本文细致分析了两块相邻浅积云（Cu-1 和 Cu-2）的云物理特性。Cu-1云底高度约4500 m，云厚约600 m，云体松散，夹卷较多；云中液态含水量（LWC）基本保持在0.5 g/m^3，云粒子浓度N_c平均值为278.3 cm^{-3}，云滴有效直径D_e整体在15 μm以内；毛毛雨滴粒子浓度最大值为0.002 cm^{-3}，云中几乎无降水粒子；粒子谱宽随着高度增加而增大，主要集中在30 μm以内。Cu-2云底高度约3900 m，云厚约1200 m，云体密实；云中过冷水丰沛，LWC有多个超过1 g/m^3的区域，云顶附近出现冰晶，云中粒子从凝结增长状态直接进入到混合相态；积云内部粒子水平分布不均，同一高度N_c相差较大，最大可达1240 cm^{-3}。D_e随着高度增加而增大；粒子谱宽随着高度增加而拓展，最大可达1100 μm，谱型由单峰向多峰转变；降水粒子和冰晶图像大多为霰粒子、针状和板状。（蔡兆鑫，蔡淼，李培仁，李军霞，孙鸿娉，杨怡曼，任刚，高欣）

1.24 祁连山一次地形云降水微物理特征飞机观测

祁连山是我国西北地区重要的生态屏障，地形云是祁连山主要降水云系，加强对祁连山云微物理过程的认识，对科学有效开展人工增雨作业、改善生态环境具有重要意义。利用2020年8月29日祁连山一次地形云降水过程的飞机观测数据，研究祁连山地区夏季云降水过程的微物理特征。此次降水过程云系呈明显的分层结构，云底高度为4000 m，整层含水量较丰富，云水大值区出现在4500 ～ 5300 m高度，与云滴高浓度区对应，云水含量主要由粒子直径为15 ～ 20 μm的云滴粒子贡献。小云粒子和大云粒子平均浓度分别为7.54 cm^{-3}和0.86 cm^{-3}，有效直径平均值分别为11.02 μm和198.11 μm，呈现出浓度小、直径大的特征。云系翻越祁连山过程中南北坡云微物理特征有明显变化，北坡（背风坡）粒子浓度、直径和液态水含量明显大于南坡（迎风坡）。祁连山地区不同高度小云粒子谱呈单峰型分布，Gamma分布可较好拟合直径小于50 μm的云滴谱，直径大于50 μm的云粒子谱更符合幂指数分布。凝华和聚并是冰相层冰雪晶的增长机制，混合层冰晶增长以贝吉龙过程为主，并伴有凇附和聚并生长。（程鹏，罗汉，常祎，甘泽文，张丰伟，刘维成，陈祺，冒立鑫）

2 关键技术研发与业务应用转化
2 Key technology development and application

2.1 FACT: an air-ground communication framework for seeding quality control of aircraft

A new type of air-ground communication application framework named FACT (framework for air-ground communication technology with weather-modification aircraft) is presented to track and command weather-modification aircraft to perform ideal cloud seeding. FACT provides a set of solutions from three

perspectives, namely, onboard, onground and air-to-ground, with the core purpose of solving the problems of the rapid exchange of information, contract analysis and identifying potential seeding areas when flight plans and meteorological conditions change. On board, the observed data are processed centrally and transmitted downward through air-to-ground communication. The real-time application and sharing of aircraft detection data are strengthened on the ground, and potential areas of operation are automatically identified based on ground data. The communication between the air and the ground achieves a technical breakthrough by realizing double satellite links, adaptive data transmission and VPN channel encryption. Additionally, an application based on FACT is designed and implemented for the real-time command of weather-modified aircraft. This approach has become the key air-to-ground communication system support for more than 40 Chinese aircraft and the big data service support center of airborne data to ensure improved operation of weather-modification aircraft in China.（Li Dequan, Li Jiming, Zhou Xu, Hu Jinrong, Wang Xin, Duan Jing）

2.2 Seasonal variations of aerosol number concentration and spectrum distribution in Nanjing

In this paper, the diurnal variations and seasonal variations of the aerosol spectrum distribution, as well as their correlations with meteorological factors in Nanjing in different seasons, are analysed. The results show that the number concentration of ultrafine particle in size of 0.01–0.1 μm accounts for over 60% of the total particle concentration in each season. The Aitken mode (AIM) particles dominate the changes of aerosol in Nanjing, which are mainly from traffic sources. Both local emissions and external transportation make important contributions to the air pollution in Nanjing. The southerly and easterly airflows are conducive to the accumulation of pollutants. The number concentrations of the AIM and Accumulation mode (ACM) particles decrease with the increasing wind speed, while the variation trend of the Nucleation mode (NUM) particles is opposite. The removal efficiency of precipitation for the ACM particles is much lower than that on the other three modes.（Jiang Qi, Wang Fei, Ying Chun, Zhu Bin）

2.3 Increasing cloud water resource in a warming world

Under global warming, terrestrial water resources regulated by precipitation may become more unevenly distributed across space, and some regions are likely to be highly water-stressed. From the perspective of the hydrological cycle, we propose a method to quantify the water resources with potential precipitation capacity in the atmosphere, or hydrometeors that remain suspended in the atmosphere without contributing to precipitation, namely cloud water resource (CWR). During 2000–2017, CWR mainly concentrates in the middle-high latitudes which is the cold zone of the Köppen classification. In a warming world, CWR shows a significant increase, especially in the cold zone. Climate change with Arctic amplification and enhanced meridional circulation both contribute to the change of CWR through influencing hydrometeor inflow. By studying the characteristics of CWR and its influencing mechanisms, we demonstrate a potential for human intervention to take advantage of CWR in the atmosphere to alleviate terrestrial water resource shortages in the future.（Cheng Jingya, You Qinglong, Zhou Yuquan, Cai Miao, Nick Pepin, Chen Deliang, Amir AghaKouchak, Kang Shichang, Li Mingcai）

2.4 层状云催化宏微观物理响应的数值模拟研究

层状云系是进行人工增雨开发利用空中云水资源的重要对象，增雨作业需要有科学可行的技术指标来指导实际作业的科学实施，而合理准确评估人工增雨作业的效果也是需要解决的重要课题，通过数值模式合理地仿真模拟实际催化作业的过程，进而研究增雨作业后云和降水的一系列宏微观特征的变化及其机理，是建立和改进催化作业技术的必要途径，也是评估实际人工增雨作业效果的有效手段。本文使用三维中尺度冷云催化模式对2014年4月15日河北省一次层状云降水的飞机催化作业过程进行

了仿真模拟，力图对实际作业过程进行合理再现，通过对模拟结果的分析，研究飞机播撒的AgI（Silver iodide）催化剂在空中的扩散传输特征，分析催化对云和降水宏微观特性的影响，并对此次飞机催化作业的增雨效果进行评估。研究结果表明：播撒的AgI催化剂烟羽扩展的水平尺度可达数十公里以上，垂直方向上，大部分AgI粒子则主要集中在作业层上下约1 km的厚度范围内，AgI粒子的向上输送明显强于向下的输送；催化后云中的冰晶和雪粒子明显增加，导致催化模拟前期的霰增长受到抑制，之后随着霰碰并雪过程及零度层附近冰相粒子淞附过程的增强，云中霰的总量逐渐增加；催化作业后，催化云的雷达回波强度有明显增强，且随时间变化表现出不同的结构特征；催化导致地面降水出现先减少后增加的时间变化特征，催化后3 h，作业影响区向作业区下游扩展100 km以上，总体呈现减雨—增雨的区域分布特征；数值模拟评估表明，整个评估区内的净增雨量达到3.6×10^7 kg，平均增雨率为1.1%，暖层霰粒浓度和尺度的增加是降水增加的主要原因。由于作业目标云系的催化条件一般，而播撒的AgI剂量偏大，造成增雨作业效果偏低。（刘卫国，陶玥，周毓荃）

2.5　一次对流云人工消减雨作业云条件预报和作业预案合理性分析

为做好固定目标时段和区域的人工消减雨作业，利用云降水显式预报系统（CPEFS_V1.0）对云系性质和结构、移速移向及演变、降水机制等云条件进行预报。预报结果显示：2017年8月8日影响呼和浩特的云系性质为分散性对流云，具有冷暖混合云结构，云中上升气流强，对流单体水平尺度约几十公里，生命史1.5 ～ 3 h，云顶高度约10 km、云底高度约3 km，0 ℃高度约为4.3 km；微观方面冰相水凝物雪、霰含量高，暖区云水含量少，云中过冷水含量最大达0.7 g/kg，过冷水丰沛区域冰晶数浓度低，以冷云降水为主。初生在呼和浩特特定防护区西北方向的对流云团快速发展东移南压影响核心保障区，移速30 ～ 40 km/h。卫星、雷达等实况监测显示8日的云系为分散性对流云，预报对流云的生成时间比实况偏晚1 ～ 2 h，移向与实况一致，移速偏慢10 ～ 20 km/h。在5400 m高度处（–8 ℃），机载云物理探测的液水含量最大为0.6 g/m^3，预报与实况接近。根据预报的云系条件制定作业预案指出，在核心保障区的偏西北方向50 ～ 30 km处进行重点布防，适宜在5.1 ～ 7.0 km高度处实施AgI过量催化，8日上午飞机在第一道防线的弱回波区开展探测作业，地面作业集中在第三道防线对流云初生阶段实施过量播撒，以达到消减雨作业的目标。根据预案，提前24 h在核心保障区偏西北方向的第三道防线增设了5个地面移动作业点，这些作业点8日及时实施了消减雨作业。总体看来，此次云条件预报正确、预案制定合理，及时为外场实施消减雨作业提供了支撑。（史月琴，刘卫国，王飞，高扬）

2.6　基于飞机真实轨迹的一次层状云催化的增雨效果及其作用机制的模拟研究

层状云降水效率通常较低，但却具有较高的云水资源开发潜力，是人工增雨作业的重要对象。随着中国南方地区生态改善、水库增蓄、抗旱等社会需求的增加，针对这些地区降水云系的人工增雨研究显得愈发重要。使用三维中尺度冷云催化模式，对2018年10月21日湖北省一次层状云飞机人工增雨作业过程进行了数值模拟研究，并将模拟结果与卫星、降水和机载云物理观测数据进行了对比。模式合理地模拟出了云和降水的主要宏、微观特征，观测和模拟结果均显示作业云区具有较好的冷云催化条件，在此基础上，按照实际作业中的飞机播撒轨迹，完整地模拟了此次催化作业过程。对数值模拟结果的分析表明：凝结冻结核化和凝华核化是碘化银催化剂的主要核化方式；90%以上碘化银粒子的局地活化比为0.01% ～ 2%，平均活化比为0.07% ～ 0.27%；云系降水是由冷云降水和暖云降水两种机制共同作用的结果，催化作业使两种降水机制均有增强，增雨效果明显；催化后4 h，整个评估区内的累计净增雨量为2.12×10^8 kg，局地增雨率为−51.1% ～ 306.7%，区域平均增雨率为8.1%；催化作业也使部分地区出现减雨，主要是由于催化过程中的潜热释放引起过冷层动力场扰动，一部分云区的上升气流减弱，从而导致降水粒子的成长减弱，地面出现减雨；在过冷云区，碘化银核化使冰晶浓度升高，导致冰晶–雪、雪–霰的转化过程增强，雪、霰粒子总量增加，更多的雪、霰粒子从冷区落入暖区，

在暖区上层产生更多的大雨滴，从而使暖区的云雨粒子碰并过程增强，最终地面降水增加，这是此次催化作业导致增雨的主要微物理链条。（刘卫国，陶玥，周毓荃，党娟，谭超，高扬）

2.7 飞机积冰的云层特征个例分析

利用卫星、雷达、探空、飞机等观测资料和NCEP再分析资料，以及数值模拟结果，对2016年3月8—9日我国安庆地区的云系特征和飞机积冰气象条件进行了分析。结果表明，此次飞机积冰发生在寒潮天气背景下，强冷空气造成锋面逆温。实测飞机积冰现象出现在对流降雨结束后的层积云层顶部，积冰高度对应高空锋区逆温层底部，云顶高度约3.4 km，云顶温度−10 ℃，无降水和雷达回波，云中主要为过冷水，丰沛时段飞机观测过冷水平均值为0.36 g/m^3，基本无冰相粒子。当云顶高度再度抬升，冰相粒子增多时，过冷水含量减少，不利于积冰现象发生。CPEFS模式模拟出了与实测比较一致的云宏微观结构。（孙晶，蔡淼，王飞，史月琴）

2.8 新疆春季两次直升机积冰气象条件分析

利用卫星、雷达、探空、地面等观测资料和NCEP再分析资料，以及数值模拟结果，对2018年3月新疆昌吉地区两次飞机积冰探测试验过程的云系特征和积冰气象条件进行了分析。 结果表明，两次直升机积冰过程影响系统分别为500 hPa低涡和500 hPa浅槽，地面有冷锋配合。积冰时段处于低涡系统发展前期阶段和低槽系统发展中期阶段。积冰云层均为中低云云层，云顶高度为4 km，云顶温度为−15 ～ −25 ℃，云底高度为1.5 km，云层厚度为1 ～ 3 km，光学厚度大于12，雷达回波特征不明显，无回波或者回波强度在10 dBz以下。3月27日浅槽锋面过程云顶有逆温。CPEFS模式模拟云微观结构表明，积冰云层是以过冷水为主，冰相粒子含量很少。 根据直升机特性修改后的CIP初始积冰潜势算法较好地体现了这两次层积云飞机积冰特征，对于稳定性云层的积冰潜势具有指示意义。结合飞行速度等参量计算的积冰强度与实况基本吻合。（孙晶，谭超，周毓荃，刘政，黄珺，王泽林）

2.9 DMT机载云粒子图像形状识别及其应用

利用机载云粒子探测设备入云进行观测是目前获取云粒子微物理特征最直接有效的手段。国内已有多家单位引进美国DMT公司的云粒子图像探头CIP。由于其配套软件不能输出逐个粒子的详细信息，在很大程度上限制了对云粒子图像探测数据的深入挖掘和分析。基于解析粒子图像原始数据，对粒子图像数据进行质量控制，并根据粒子形状几何特征将粒子形状分为8类（微小、线状、聚合状、霰状、球状、板状、枝状和不规则状）。利用2018年12月至2019年3月河南省3次冬季航测获取的灰度CIP探测数据，分析云粒子形状及各形状粒子面积的统计特征，并对比基于不同形状粒子的质量−尺度关系与将所有粒子视作球形液滴计算所得的粒子水凝物含量，发现后者超过前者约1个量级。（张荣，李宏宇，周旭，李昊，胡向峰，夏强）

2.10 一次东北冷涡结构及云系特征分析

利用ERA5逐小时再分析资料、FY-4A卫星反演云特征参量产品、逐小时地面降水资料，分析了2020年5月16—19日一次东北冷涡降水过程的环流形势、热力不稳定条件、水汽输送及云系宏微观特征。结果显示，本次过程500 hPa低涡中心位于36° ～ 48° N，对流层中高层至低层均有气旋性环流，伴随有地面气旋，属于深厚的中偏南涡，共维持了6 d。18日辽宁东部出现区域性暴雨，24 h降水量超过100 mm的站点有15个，最大雨强达到了43.4 mm/h，暴雨区出现在冷涡成熟阶段，位于冷涡后部偏北气流影响下，来自热带低压东侧西南低空急流输送的水汽与冷涡东南部的水汽输送合并，成为了暴雨产生的必要条件。降水强度大于6 mm/h的区域，K指数基本都大于35 ℃，且整层都有较强的垂直上升运动。冷涡云系云顶高度为4 ～ 9 km，靠近冷涡中心的涡旋状云系云光学厚度大于30，云层水凝物含量丰富密实，属于冷暖混合云，降水主要出现在这些区域；远离冷涡中心的区域云系光学厚度小于

20，云层松散属于高层冰云，地面基本无降水。（史月琴，周毓荃，戴艳萍）

2.11 SPEC机载云探测系统及其云物理研究进展

在综合介绍我国机载云探测系统的发展历程、应用情况和优缺点的基础上，对新一代机载云探测系统SPEC的系统组成、探测原理、探测方法和探测范围等进行了详细说明，并探讨了近年来国内外相关研究进展。随着科学研究人员对云探测精细程度、准确度要求的日益提高，以往使用的粒子观测系统（PMS）等云探测系统已无法满足一些科学试验的需求；SPEC与很多其他云探测系统相比，在精密程度、探测粒子的信息量、分辨率等方面具有很大的探测优势，这对于云物理更深入的研究是非常重要的。国外研发并应用SPEC系统已有几十年的时间，而我国近年开始引进并越来越多地使用这套探测系统来探究云的宏微观物理特性，这必将使得对云物理的理解更加深入。（刘思瑶，赵传峰，周毓荃）

2.12 基于Ka波段云雷达的六盘山顶云特征分析

本文利用宁夏六盘山气象站2017年9月至2018 年8月的Ka波段云雷达观测资料，统计分析了六盘山顶不同云的出现频率及宏观特征。结果发现：六盘山顶云出现频率最高值出现在7月，为61%，最低值出现在12月，为26%；按云层数划分，六盘山顶出现的云主要以1层云、2层云及3层云为主，相对总云的月平均出现频率分别为68% ～ 86%、14% ～ 27%及0.4% ～ 4.8%；按云底高度及云层厚度划分，六盘山顶低云、中云、高云及直展云相对总云的月平均出现频率分别为29% ～ 53%、14% ～ 58%、6% ～ 22%及2% ～ 20%。云底高度在冬春季节高于夏秋季节，云顶高度在夏秋季节高于冬春季节，云层厚度在1.6 ～ 3.6 km 之间，年变化特征与云顶高度类似。整体来看，春、夏、秋季云厚在白天大于夜间，冬季云厚在夜间大于白天，其中夏、秋季云厚日变化特征较为明显。（田磊，桑建人，姚展予，常倬林，舒志亮，曹宁）

2.13 基于微波辐射计的宁夏六盘山西侧大气水汽变化特征

采用隆德气象站2 a德制微波辐射计与同期1 h降水量资料，利用统计法分析了六盘山脉西侧大气水汽含量以及云液态水含量的时间分布特征，并分析了92次不同降水性质、不同降水量级的降水个例，得到降水前跃增时间的变化特征。剔除降水背景结果统计表明：（1）六盘山西侧大气水汽含量和云液态水含量有明显的季节变化，其中夏季是大气水汽含量最多的季节，平均为23.44 mm，占年均水汽含量的47.7%。（2）大气水汽含量和云液态水含量日变化呈-谷-峰分布，春、夏、秋三季均在午后出现最大峰值，冬季在11:00出现峰值；大气水汽含量低值区春、夏、秋季出现在日出前后，冬季出现在22:00。（3）87.0%的降水个例在降水发生之前大气水汽含量都在12.00 mm以上，且其值随着降水的量级增大而增大。（4）降水前云液态水含量发生明显跃增现象，春、夏季表现强，根据降水性质及降水量级不同，降水前跃增时间也不同。研究结论对把握人影作业时机具有一定的参考价值。（林彤，桑建人，姚展予，舒志亮，田磊，曹宁，常倬林）

2.14 利用FY-4A卫星光学数据对中国近地面$PM_{2.5}$浓度的估算和检验分析

对FY-4A卫星的气溶胶光学厚度（AOD）产品进行检验，并根据卫星相关观测资料，通过改进后的PMRS方法，反演得到中国近地面$PM_{2.5}$质量浓度网格化分布。结果表明，FY-4A卫星反演不同站点AOD与地基观测网（AERONET）观测结果吻合较好，但存在一定的低估或高估现象，相关系数区间为0.54 ～ 0.87。将细粒子比（FMF）以0.4为界进行划分，FMF＞0.4时，拟合结果较FMF≤0.4时更接近于AERONET观测结果；但FMF≤0.4时，卫星反演的AOD稳定性优于FMF＞0.4时。通过引入AOD的大小，改进FMF＞0.4时对细粒子柱状体积消光比（VEf）的估算算法，并通过改进后的PMRS方法对中国近地面$PM_{2.5}$浓度进行逐时反演，其反演结果和地面观测结果相关较好，其中，乌鲁木齐、石家庄和徐州观测点的相关系数均高于0.7，但数值上仍存在高估或低估，误差结果由多种因素决定。空间分

布中，卫星反演的中国2019年近地面$PM_{2.5}$浓度月均值与近地面观测的结果有较好的对应关系，二者逐月演变趋势基本一致，基本可以反映出中国近地面大气细粒子的空间分布，特别是秋、冬季京津冀周边区域、汾渭平原等污染高值区均与地面观测对应较好。（江琪，迎春，王飞，张天航，何佳宝，桂海林，张碧辉，徐冉）

2.15 崇明东滩湿地与上海城市气候特征对比分析

基于2010—2019年崇明东滩湿地与同期的上海近海台站、崇明气象站及市区气象站的温度、湿度、降水观测资料，采用时间同步对比方法，分析了崇明东滩湿地与上海城市不同地区的气候特征。结果表明：东滩湿地由于其地理位置特殊，与上海其他台站比，日最高气温最低、春夏气温升幅最小，日最低气温接近或高于近海台站和崇明城镇的日最低气温，仅低于中心城区的日最低气温，湿地不易升温、也不易降温；由于东滩湿地下垫面性质及周围环境与城市其他台站的不同，没有城市热岛效应、阻碍效应引起的增雨，中雨以上降水概率明显小于其他各站的降水概率，暴雨概率及强降水次数比其他各站分别少68% ～ 75%和70% ～ 81%，表明东滩夏季雨日少于其他各站的雨日，但秋冬季雨日比其他各站多18% ～ 40%，这也是东滩湿地总雨日多的主要原因；东滩湿地不但缩小昼夜温差还缩小昼夜湿差，尤其湿地能降低雨强，致使有雨日逐年平均相对湿度反而比上海其他各站的小。（贺芳芳，毛卓成，姚展予，许建明，彭丽）

2.16 临沂市区冬季大气污染物的特征解析

基于2018年冬季临沂市区4个国控环境空气自动监测子站的SO_2、NO_2、CO、O_3、$PM_{2.5}$和PM_{10}小时浓度数据，研究了临沂市区大气污染物的特征。结果表明：$PM_{2.5}$和PM_{10}污染最为严重，其次是NO_2和CO，而SO_2和O_3污染较轻；SO_2、CO和O_3空间差异显著，NO_2、$PM_{2.5}$和PM_{10}空间差异不显著。日变化特征分析发现，SO_2、CO和PM_{10}呈双峰型，NO_2呈单谷型，O_3呈单峰型，$PM_{2.5}$呈一峰二谷型分布。O_3与其他大气污染物不同，清洁天空气质量较好，强太阳辐射会促进光化学反应生成更多O_3。气团后向轨迹聚类分析结果显示，临沂市区冬季主要受近距离的气团输送影响，同时也受到来源于蒙古国的高空远距离沙尘输送影响。（王璐，温天雪，周旭，刘旭）

2.17 全球云水量气候分布及变化趋势特征分析

采用20世纪再分析版本2c数据集的云水量逐月再分析数据，通过数理统计方法，分析了1960—2014年全球、海洋和陆地上空云水量的分布和变化特征及其与水汽通量的关系。结果表明：（1）全球云水量空间分布不均，海洋高于陆地且比例约为4∶3，中低纬海洋、陆地上空云水量变化趋势分别为0.07 g/（m^2·10a）和−0.04 g/（m^2·10a），季节性差异主要体现于夏季在热带辐合带和南半球海洋高，冬季在北半球海洋和南半球陆地高。（2）对比六大洲发现，云水量最高的南美洲有最快增加趋势，为0.46 g/（m^2·10a），同时云水量最低的非洲有最快降低趋势，为−0.59 g/（m^2·10a）。（3）中低层整层水汽通量散度场的辐合、辐散区和云水量的高、低值区相对应，云水量与水汽通量散度变化呈负相关（相关系数为−0.44），负相关关系在赤道附近的低纬地区显著。本文揭示了在全球变暖背景下，大气中云水量分布和变化的时空格局，为模式参数化和未来气候预估提供参考。（程敬雅，游庆龙，蔡淼）

2.18 云解析人工影响天气数值模式的改进、初步试验和展望

基于WRF四维资料同化和预报技术，初步发展了针对我国西北地区云微物理和播云催化技术的云解析人工影响天气模式系统（CR-WMM）。该模式耦合并改进了中国气象科学院发展的微物理方案（CAMS-MP）和碘化银（AgI）催化方案，并实现基于大涡模拟（LES）模式的飞机、地面烟炉等播撒源及毗邻区域AgI粒子扩散的精细模拟方法。选取降水案例对CR-WMM资料同化功能、CAMS-MP微物理参数化和AgI的催化数值模拟方案进行测试和评估，验证了该系统的资料同化能力、微物理参数化

和AgI催化数值模拟方案的可靠性。CR-WMM具备连续同化常规和加密气象观测，特别是针对云微物理过程的新型卫星、云雷达和人工影响天气外场作业飞机和基地的特殊观测能力，能生成全面、精确的云和降水热力、动力和微物理分析场，支撑云和降水过程及云催化技术的理论研究及优化人工播云方案辅助决策。并提出为达到这一目标，CR-WMM模式在未来5～10年应集中攻克的5个方面的科学难题。（刘玉宝，丁秋冀，史月琴，方春刚，段婧，楼小凤，李萍，霍朝阳，周永波，王昊亮，景晓琴，王新，陈添宇，陈宝君，李集明）

2.19 基于时域对象的网格降水预报的追踪诊断分析

检验和评估模式降水预报的时间和位置偏差对提高降水预报准确率有重要意义，而传统点对点的检验方法对此无能为力。基于2018年和2019年6—8月欧洲中期预报中心（ECMWF）降水预报资料，利用面向对象时域诊断分析工具（MTD），追踪模式降水预报对象的生命周期、初生、消散等预报表现。研究表明：（1）个例分析显示，时域诊断分析工具MTD能够很好的从三维降水场中提取降水对象，进而刻画降水对象的生命周期及开始结束时间，对客观描述降水对象的时间偏差具有独特的优势。（2）低阈值条件下模式预报能很好地描述降水对象的空间分布，不足在于观测降水对象较模式预报明显偏多；随着降水阈值增大，预报与观测降水对象的空间频次呈现出显著差异，表明模式对强降水的位置预报仍然需要改进。（3）采用最小卷积半径和降水阈值定义降水对象，观测和预报场中80%的降水对象生命周期小于15 h，且生命周期随着降水阈值和卷积半径的增大而减小。（4）三维对象追踪显示，预报对象的持续时间较观测偏短，移动速度较观测整体偏慢。（张宏芳，潘留杰，卢珊，巨晓璇，史月琴）

3 项目进展和观测试验
3 Project progress and observational experiments

3.1 云水资源评估研究与利用示范

云水资源评估研究与利用示范研究取得如下进展：（1）基于大气水循环过程和云物理过程及大气水分收支平衡方程，提出并完善云水资源及其11个组成量和12个特征量的概念和计算式。（2）构建多尺度三维云场诊断技术体系，建立并优化云水资源观测诊断和数值模拟两套定量估算方法，研发云水资源评估系统（V1.0），实现中国和全球近20年1°分辨率、全球近60年2.5°分辨率的云水资源诊断评估及华北示范区近5年3 km分辨率的云水资源数值精细评估，并开展对比验证。（3）利用近20年中国云水资源评估数据集，研究得到中国不同人工影响天气分区和关键典型水文流域（如黄河流域、淮河流域）的云水资源特征，利用3 km的数值评估结果，揭示华北区域的云水资源特性，利用全球云水资源评估数据集，研究得到全球云水资源的时空分布特征和变化规律。（4）在两个示范区建立并优化固定目标区云水资源开发技术体系，探索发展北方层状云飞机增雨和南方对流云地面增雨优化的方案设计及效果评估方法；建立空陆耦合云水资源开发利用全流程技术体系，攻关云水资源预报及开发效果预估等关键技术环节，并应用于重大活动保障。

3.2 人工影响天气技术集成综合科学试验与示范应用

人工影响天气技术集成综合科学试验与示范应用项目开展了3次华北多机联合观测，取得星-空-地联合观测数据集2套；完成一种浸润冻结机制冰核测量装置（FINDA）的搭建与应用，其试验结果与国际上其他学者的结论一致。梳理南方各种类型对流云个例21个；分析祁连山地形影响下的云降水演变特征与机理以及地形云降水微物理特征与降水机制，结果表明不同类型强降水的形成机制及物理量条件各有差异，地形对降水的影响效应也各不相同，揭示地形云凝华和聚并是冰相层冰雪晶的增长

机制，混合层冰晶增长以贝吉龙过程为主，并伴有淞附和聚并生长；利用DBSCAN聚类算法及Hough变换，提出一种对雷达线状或带状飑线的自动识别方法，并用5次飑线天气过程检验DBSCAN算法和Hough变换的合理性和有效性；初步试验结果认为燃气炮增雨作业有效果，但还需要开展更多的外场试验和试验分析。基于飞机观测检验微物理结构模拟，将各微物理方案模拟的IWC、冰相粒子谱、粒子数浓度和M-D关系进行了对比分析，给出各微物理方案在模拟能力上的各自优势。

3.3 新一代人工影响天气数值模式系统研发

新一代人工影响天气数值模式系统研发工作取得如下进展：（1）在WRF中建立全新三参数云物理方案并开展批量预报试验，对6月份一个月的预报结果表明，该方案可以有效预报不同云降水过程，在模式积分时间步长方面有待改进。（2）在WRF4.2动力框架中耦合了CAMS双参数云微物理方案，利用1 km水平分辨率开展不同区域、不同时间的积层混合云、对流云、层状云等多个例模拟研究，模式运行稳定，模拟的降水、云系结构特征及演变与卫星、雷达、机载云物理探测实况相符。（3）开展AgI催化方案的编制及与WRF模式中CAMS云方案的耦合试验。（4）采用分析逼近Nudging同化方法，开发雷达资料反演的水成物场及对应的潜热进行同化的方案，基于WRF模式实现对雷达资料的实时同化和模拟应用，个例对比试验表明，同化后对于模拟的降水落区范围比无同化有明显改善，更接近实况观测。（5）探索了面向对象检验（MODE）方法在云场检验方面的适用性，开展了不同检验方案（格点、邻域、对象）对预报云场的检验适用性研究，并对夏季的云场预报结果进行检验应用。

3.4 新型催化剂研发

组织召开新型催化剂研制课题2021年度工作会议，课题组开展了膨胀云室物理模拟试验能力的测试和初步试验，进一步完善云室系统的云雾参数监测系统；开展了表明活性物质作为暖云催化潜力的模拟试验；开展了华北污染背景的实验室模拟试验研究（70 m^3膨胀云室）；开展了纳米催化剂的扩散云室模拟试验研究；讨论研制了3中不同吸湿性暖云催化剂的试验配方，完成工厂加工压制和工厂性能测试，近期将送北京实验室开展模拟试验，进而筛选出效果较好的暖云催化剂型。完成发表论文1篇，申请发明技术专利1项，已进入实质性审查阶段，申报实用新型技术专利3项，其中2项得到授权，1项受理中。1项气象行业标准预研究项目通过验收。

3.5 贵州防雹外场观测试验

2021年4月，首部用于人工防雹观测的X波段双偏振相控阵雷达在贵州威宁防雹基地建成。2021年5月13日，人工影响天气中心组织开展国家（贵州）防雹外场科学试验实施方案论证会。5月27日召开2021年国家（贵州）防雹外场试验启动会，人工防雹外场试验正式启动。试验持续到9月底结束，基于X波段双偏振相控阵雷达共观测防雹个例18次，收集了多种扫描方式（体扫、扇扫和RHI扫）的防雹观测资料，为贵州威宁冰雹结构特征分析和防雹效果检验提供了直接的外场观测资料，目前正对观测资料进行整理分析。本次观测通过利用高时空分辨率的相控阵雷达资料清楚观测到贵州威宁冰雹云的发展演变过程和垂直结构特征，发现威宁冰雹发展迅速，稳定少动；雹云强回波首先出现在空中，然后向下发展加强；雹云在成熟期主要呈倾斜垂直结构，有明显的有界弱回波区，空中存在冰雹特征。高时间分辨率的相控阵雷达能对防雹效果进行检验，从相控阵雷达可以看到高炮作业后强对流的雷达回波减弱、强回波面积有所减少，特别是高炮作业量增大后，防雹作业效果比较明显。

3.6 庐山云雾降水外场观测试验

2021年，对庐山云雾降水外场观测试验进行了重新部署，开展了秋冬季外场试验。在2020年外场试验方案的基础上，根据新设备补充情况和2021年的试验需求，不断完善试验方案和实施方案，编写完成了《2021年国家（庐山）云雾物理试验基地外场观测试验方案》。2021年9月28—29日联合江

西省气象局组织和召开了2021年国家（庐山）云雾物理试验基地外场观测试验启动会，秋冬季外场观测试验正式启动。会后与江西省气象局联合编写完成《庐山云雾物理试验基地2021年外场试验工作方案》，作为工作指南。此次试验布局为以山上、山下的联合梯度观测，以及山上不同地点的同要素对比观测，依此开展包括秋冬季大气与气溶胶背景特征、云宏观及微物理特征研究。根据观测要求，新增2台雾滴谱仪、冰核采样器、云凝结核仪、PCASP-X2、雾水采集器等观测设备，并将云雾站单一的观测点扩展到云雾站和仰天坪两个观测点，在仰天坪调度和布设了自动气象站、雾滴谱仪、能见度仪、微雨雷达、云凝结核仪、冰核采样器和颗粒物仪等观测设备。2022年1月9日，庐山秋冬外场试验基本完成年度观测任务（10月1日至1月9日）。此次试验10月初开始，11月10日基本完成两个主要观测点（云雾站、仰天坪）的设备调试和部署，12月8日完成梯度观测部署（庐山市气象局），所有设备部署地点均按试验方案部署完成后，一直进行持续的加强观测。初步统计，捕捉重点天气过程约13次，包括云雾（最多）、降雨（1次）、降雪（3次）、冻雨（1次）过程。采集包括雾滴谱仪、微雨雷达、微波辐射计、云高仪、能见度仪、云凝结核计数器、颗粒物仪、自动站等数据资料约670 G；雾水样本（46份）；冰核膜采样样本（95份）。在山上两个站点（仰天坪和云雾站）重点开展了云雾、降水对比观测；此外，在仰天坪开展了冰核、云凝结核加强观测，在云雾站开展了云雾过程的雾水采集观测；同时实现了山上、山下云宏观特征的梯度对比观测。获取了多次包括冻雨等特殊天气过程的观测数据。

3.7　数据集建设

庐山云雾观测数据集建设进展。4月邀请参与过庐山观测的老专家协助解决历史数据中字迹不清楚和记录方法等问题，重新翻阅了纸质版历史资料，经过4个版本的更新，已经完成历史数据集的数字化工作。7月初经商议确定现代数据集除了csv文本格式，新增NetCDF格式数据集，确定了NetCDF格式确定数据录入信息和结构存储方式。9月在针对nc格式的专家咨询会中进一步确定了存储的细节并咨询疑问，已经完成两个版本的csv格式和NetCDF格式的数据样本。合理利用人影数据标准编码规范的同时，调整了地基特种观测数据的编码格式，改进和更新了数据集的存储和质控方案。经过一年多的建设，目前对于历史观测资料，已经完成所有资料的归整、查阅、补充扫描、内容订正等工作，完成了历史数据集的数字化。对于现代观测数据，已经完成数据的质量控制，并多次完善现代数据的编码和存储方案，阶段性的推进数据集建设，形成现代数据集样本，并正在开展数据质量评估。庐山云雾观测数据集已基本建成。同时，建设期间初步形成了一套较完整的《人工影响天气试验地面特种观测资料集数据文件编码和存储格式规范（草稿）》。

飞机观测数据集建设进展。优化改进了飞机数据处理系统，完成国家级飞机探测数据集建设项目的平台改造；初步建立了一套飞机数据集，完成2017—2020年国家级高性能飞机所得探测数据的处理和成集工作，并提供中心使用；梳理了一批典型探测个例，初步形成了一套飞机数据质控流程，为中心所承担的重大活动保障、重要应急保障以及重点科研项目所得的飞机探测数据提供质控和产品制作服务；完成了用户手册、工作报告、技术报告等文档。

3.8　云雾物理环境重点开放实验室开放课题

2021年度中国气象局云雾物理环境重点开放实验室开放课题分别在多源数据融合技术的人工影响天气应用研究、冰雹云结构及成雹机理研究、山地环境气溶胶–云雾特征及相互作用研究，以及人工增雨防雹火箭技术研究5个重点研究领域共资助11个课题，资助强度2～3万元，总经费26万元。受资助人员涵括人影业务部门、相关高校以及科研单位。

4 人工影响天气现代化建设
4 Modernization of weather modification

4.1 西北区域人工影响天气能力建设项目总体设计与实施

概要梳理了西北区域人工影响天气能力建设项目总体设计的思路，归纳了设计中所重点考虑的3个技术系统和技术措施，总结了项目建设模式与经验，可为后续区域人工影响天气项目建设提供参考和借鉴。（李集明，陈添宇，陈宝君，顾青峰，殷占福，段婧，李宏宇，李德泉，方春刚，房文，尹宪志，李林，桑建人，李抗抗）

4.2 “云+端”业务框架的西北人工影响天气指挥应用系统综述

简要阐述了面向人工影响天气业务深度融入“天擎”大数据云平台需求，在西北区域首先采用“云+端”业务系统架构模式设计并实现新型的人工影响天气指挥业务系统（SPACE-NW），为人工影响天气各类业务提供综合业务软件支撑。该系统依托“天擎”基础，提出具有普适性的人工影响天气“云+端”下的“4C+ABC”框架，实现了人工影响天气业务数据环境深度融入、产品分析与自动化制作与加工流水线的深度融入、资料分析与指挥业务流程与基础气象业务的深度融入。解决了人工影响天气部门一段时期以来的资料采集渠道多样、标准不统一、系统开放性不足、信息流转渠道不畅等业务问题。该系统在西北区域率先部署试用，发挥省级人工影响天气业务与“天擎”的深度融入的典型示范作用。（李德泉，李集明，田建兵，田显，穆建华，李宝梓，白向东，李圆圆）

4.3 西北区域人工影响天气试验示范基地设计

西北人工影响天气工程在西北地区选取重点区域建设人工影响天气试验示范基地，合理设计观测仪器设备布局，建立了涵盖中尺度水汽、风场监测、云降水宏观场监测、云降水微观场探测的大气、云和降水宏微观三维结构及湿热力、动力综合监测网；在基地科学设计外场试验区，开展外场作业试验，开展新型催化作业装备和催化剂研发。基地的建设能够有效地促进我国人工影响天气业务自主创新，为西北区域和全国人工影响天气业务发展提供有力的科技支撑，提高作业效率和水平，提高西北区域人工影响天气作业实际效益。目前该基地已基本完成观测系统以及业务平台建设，观测资料已在研究试验中得到有效应用。（方春刚，段婧，李圆圆，李宝梓，岳治国，田磊，田建兵，黄山，陈添宇，陈宝君，李集明）

4.4 西北人工影响天气工程研究试验设计与实施

西北区域人工影响天气能力建设项目通过科学设计，创新运行机制，预期利用已有和本项目即将建设的装备设施，通过有科学设计的专项研究，开展针对西北区域地形云的人工增雨（雪）试验研究。在工程项目建设中设立研究试验内容，旨在通过项目建设中同步实施试验研究，充分体现科技支撑能力在工程项目中的重要作用。本文总结了西北区域人工影响天气能力建设项目中研究试验的设计和实施过程，依据建设经验，提出提高工程项目效益的建议，为相关工程项目建设提供参考。（段婧，王自强，李圆圆，程鹏，常倬林，林春英，岳治国，史金丽，殷占福，陈宝君，陈添宇，李集明）

4.5 空中国王350增雨飞机改装与集成设计

介绍了西北区域人工影响天气能力建设项目（以下简称“西北人影项目”）建设的2架空中国王350国家级作业飞机（以下简称“西北空中国王飞机”）差异化和通用化的设计思路，以及西北空中国王飞机机载大气探测系统、机载催化作业系统、空地通信系统改装集成工作的所要遵循的原则、工作

思路和初步方案。对后续人工影响天气区域工程项目飞机改装集成工作提供相应的技术支持。（高扬，李宏宇，殷占福，戴艳萍，陈添宇，李集明）

4.6 新舟60高性能增雨飞机机载任务系统集成设计

西北区域人工影响天气能力建设项目设计建设的新舟60增雨飞机是集催化作业、云宏微观探测以及实时通信与综合集成显示功能于一体的国家高性能人工增雨飞机，该飞机系统建设中充分汲取了前期东北区域国家增雨飞机研制成果与经验，并在系统供电管理、催化作业能力、探测系统集成、卫星通信功能、设备系统和操作台布局等方面进行了针对性设计改进，通过便捷操作实现对任务系统供电与各分系统的集中控制、综合显示、数据存储共享，并且机载探测、催化、通信各分系统均采用双重或多重备份设计，既保证了机载任务系统先进性设计，同时保证任务系统运行稳定可靠和各项功能的完整实现。（张骁拓，胡颖琼，李宏宇，苏海周，周旭，高扬，张荣）

4.7 陕西渭北果业区冰雹研究进展

阐述了开展陕西渭北果业区防雹技术研究试验的重要意义，讨论了渭北果业区冰雹研究在气候、雷达回波、雹云探空、冰雹微物理、数值模拟和防雹效果等方面的进展，并对研究试验中存在的问题进行了讨论。这些研究加深了渭北冰雹形成过程的认识，对研究高效冰雹防御方法和提高冰雹防御效果有重要意义。（岳治国，陈宝君，王瑾，左爱文，李金辉，罗俊颉，朱荣增，花少烽，刘佩佩）

5 人工影响天气重大应急与重大服务保障
5 Weather modification in support of major emergency response and major event service

面对持续时间长、影响范围广的南方冬春连旱，迅速响应、国省协同、空地联合作业，全力做好抗旱增雨、森林灭火等重大应急服务保障。在日常业务发布的人工影响天气模式预报和卫星监测云条件产品基础上，针对重大活动保障和森林草原防灭火等应急人工影响天气服务保障，完善潜力预报和预案制定、条件监测和方案设计、信息收集与效果评估等全流程的6类人工影响天气专项服务指导产品，并在河南、西藏林火等重大应急和重大活动服务保障中开展应用。

采用新技术、利用新资料，老中青同心聚力完成各项重大人工影响天气专项保障服务。全年发布7种服务材料共245期，专题会商56次，2期决策服务材料报送党中央，1期获得中央领导同志的批示。积极参与国产大飞机试飞气象保障工作。与商飞密切配合，利用进博会增雨作业飞行，开展自然结冰探测。与中航工业试飞院签订关于大飞机自然结冰项目战略合作框架协议书。

6 研究型人工影响天气业务发展
6 Reseach-oriented development of weather modification operations

6.1 指挥业务精细化发展

开展精细化云预报试验。将人工影响天气业务模式水平分辨率从3 km提高至1 km并开展试用，云水资源预报在重大服务中应用。改进人工影响天气催化模式，利用WRF–AgI催化模式和对流云–AgI催化模式，实现飞机、火箭等人工增雨、消减雨和消雹催化的仿真模拟，进行了不同催化模式的催化效果比较研究。

提升国家级业务平台功能和业务支撑能力。2021年7月1日，全国人工影响天气综合信息系统正

式投入业务运行，该系统整合原有“人工影响天气作业信息采集处理系统”和“人工影响天气业务产品共享发布系统”，实现产品发布、信息上报、实时监控、业务管理和通知通报等功能。“人工影响天气综合信息系统”面向全国业务运行有效提升了人工影响天气指导产品发布的时效性和作业信息采集的规范性。

开展国家级人工影响天气核心业务系统融入“气象大数据云平台”工作。对各个业务系统账户进行了进一步的规范化管理，完善了系统的融入方案和实施进程。国家级人工影响天气平台已基本实现了从CIMISS平台过渡到云平台进行实时业务数据的采集。

6.2 人工影响天气装备安全运行

联合有关省组建国家级飞机运行技术支持团队，为国家飞机安全高效运行提供技术支持。对新疆、陕西国家飞机托管招标文件进行技术审查，把严把牢安全运行红线。对国家飞机设备系统状态及运行开展安全巡检。

配合完成“3·1”事故处理。调研编制飞机安全运行及管理模式等的决策服务材料。推进相关标准规范建设，编制《人工影响天气飞机安全检查规范（试行）》《国家人工影响天气飞机作业规程（试行）》和《国家人工影响天气飞机航材库管理办法（试行）》等3项业务规范并经减灾司印发全国执行。

完成人工影响天气弹药物联网系统运行监控和作业装备行政审批技术审核。配合减灾司做好安全生产督查工作，编制安全检查报告。

6.3 国内外交流合作

推进中泰、中韩、中阿、中沙在人工影响天气领域的合作。（1）中泰合作：2021年2月9日，通过线上视频会议的形式与泰国签署了人工影响天气技术合作协议。中泰双方在2021年7月29日以线上的形式召开了技术交流讨论会，进一步细化了双方的合作计划。（2）中韩交流：中国气象局人工影响天气中心与韩国国立气象科学院于2021年12月30日举办了2021年中韩人工影响天气技术视频交流会。双方主要讨论了人工增雨效果检验相关问题（包括对比区的选取、增加雨量的计算、增雨作业的时效性等）、冰核观测及设备相关情况，以及未来双方可以开展的合作。（3）中阿交流：2021年4月12日，中国气象局和阿联酋国家气象中心人工影响天气专家14人举行视频会议，交流人工影响天气技术研究和业务工作进展，研讨未来合作意向。（4）中沙交流：应沙特阿拉伯方面要求对其关心的我国人工影响天气领域的几个方面内容进行答复。明确了中沙合作的联系人。

组织筹办12期云雾物理开放实验室学术交流论坛，出版《全国人工影响天气技术与方法交流会论文集（2020）》《气象科技进展》西北人工影响天气专刊（2021年11月）。

参加气象科技活动周、全国林业和草原科技活动周、第18届中国–东盟博览会、国家“十三五”科技创新成就展，人工冰晶模拟系统获得2021年气象科技活动周优秀展项奖。人工影响天气中心援疆专家在政府部门开展科普讲座，使得人工影响天气工作被更多人了解和认识，取得了良好的社会反响。

6.5 人工影响天气标委会工作

积极推进项目申报和标准的编制进度。新颁布行业标准2项，国家标准1项；批复国标立项1项，国标外文版立项1项，行标7项，行标预研究1项；推荐申请国标1项；组织完成标准预审9次、正式审查10次，函审6次；组织开展标准网上征求意见工作5项。组织完成1项国标的网上立项投票。编辑印制了2003—2020年度人工影响天气领域标准文集。

消息与动态
News and Notes

2021年1月4日，气科院组织召开专家研讨会，就世界气象组织（WMO）新冠疫情工作组形成的《气候、气象和环境因素对新冠疫情影响报告》（第一版）征求意见稿展开讨论。研讨会邀请了北京大学、清华大学、复旦大学、兰州大学、南京大学、中国科学院大气物理研究所、中山大学、中国疾病控制中心及中国矿业大学（北京）的大气、公共卫生及传染病方向的专家，通过现场及网络视频会议的形式就WMO报告内容及未来关注点进行了交流与讨论。

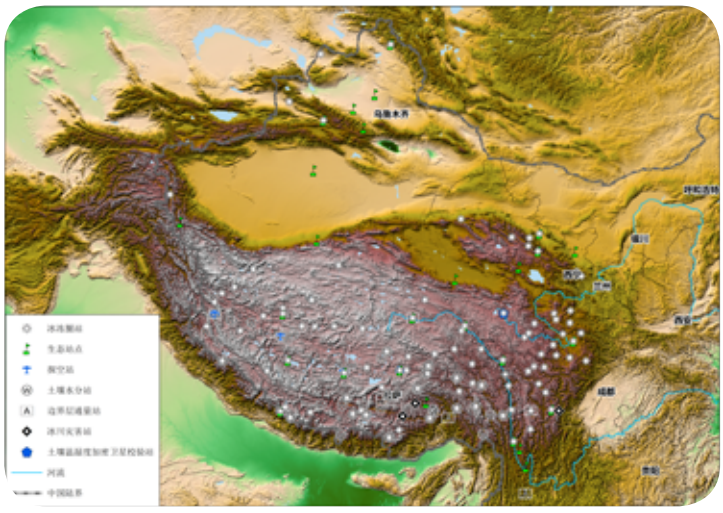

2021年1月4日，气科院牵头编制的《青藏高原冰冻圈与生态观测站网布局设计方案》由中国气象局综合观测司和中国气象局科技与气候变化司联合正式印发（气测函〔2021〕1号）。该方案自2019年初开始筹备，同年6月中国气象局综合观测司召开研讨会，正式启动该方案编制工作。气科院赵平副院长担任编写组组长，科技处协助组织，青藏高原与极地气象科学研究所、灾害天气国家重点实验室、生态与农业气象研究所相关专家承担主要编制任务，中国气象局综合观测司、科技与气候变化司以及10余家业务单位和科研院所的专家参与编写。针对青藏高原区域冰冻圈和生态系统观测站点稀少现状，编写组围绕冰冻圈、生态系统与大气圈相互作用的关键过程，组织各领域专家通过实地调研、数值模拟和素材征集汇总后，形成了冰冻圈和生态系统的站网布局设计方案初稿。在方案编制过程中，编写组多次向各方面专家征求意见和建议，在设计框架明确后，不断完善布局站点内容和观测要素。2020年10月13日方案通过专家论证会论证。《青藏高原冰冻圈与生态观测站网布局设计方案》的出台为中国气象局各级业务单位在青藏高原冰冻圈和生态观测站网布局提供了设计蓝图，将进一步增强青藏高原冰冻圈和生态系统观测站网布局的统筹规划，科学完善青藏高原区域站网建设，提升青藏高原冰冻圈和生态系统监测和评估能力。该方案为支持气候变化背景下高原大气科学研究，提供富有价值的指导和借鉴。

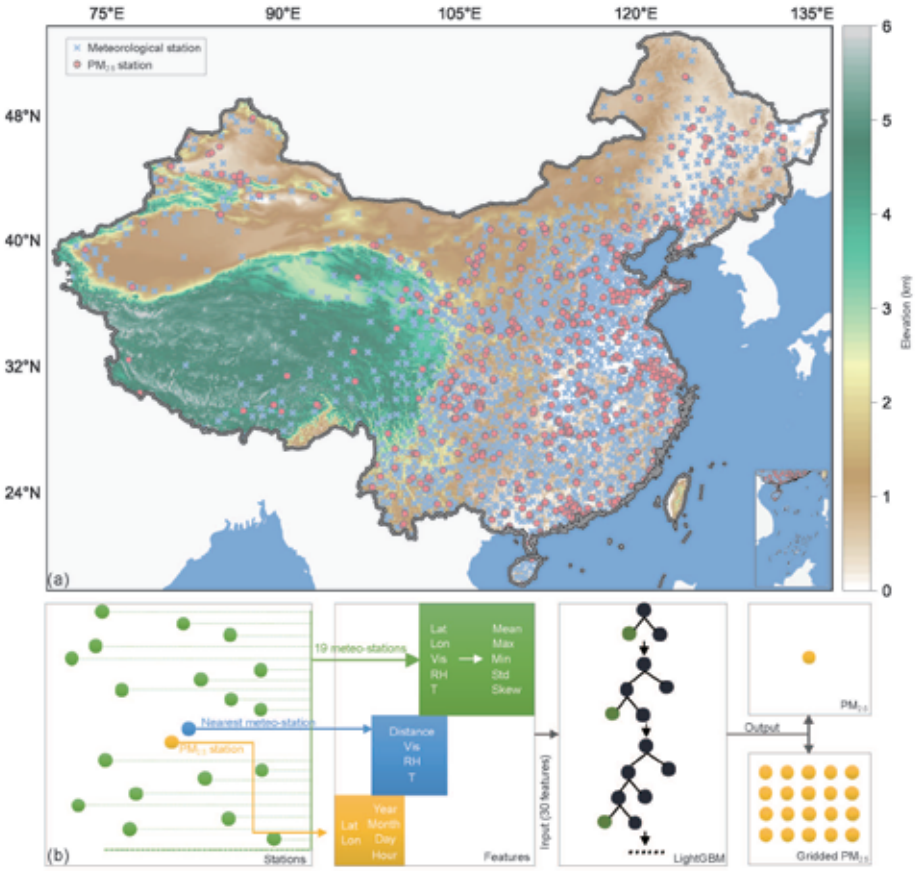

全国1440个$PM_{2.5}$国控站和2450个国家级气象观测站的空间分布(a)和空间特征提取与模型构建的概念模型(b)

2021年1月5日，*National Science Review*在线预先发表了气科院博士研究生仲峻霆（第一作者）、张小曳院士和桂柯博士（通讯作者）等人的Robust Prediction of Hourly $PM_{2.5}$ from Meteorological Data using LightGBM（基于机器学习模型LightGBM实现从气象数据中准确预估$PM_{2.5}$浓度）的文章。 2013年起，生态环境部建立了地基监测站点，开始对细颗粒物（$PM_{2.5}$）污染进行业务观测。但是，此前的历史数据难以获取，导致长序列$PM_{2.5}$数据缺失，为认识中国$PM_{2.5}$长期变化带来了挑战。为解决这一问题，气科院张小曳院士团队基于国家级地面气象观测网，抽取空间特征并结合先进的机器学习技术LightGBM，构建了考虑空间气象效应的高性能机器学习模型，能够获取20世纪60年代以来的长序列$PM_{2.5}$历史数据集。该数据集将对理解气溶胶长期变化趋势、环境和气候影响以及通过同化到化学–天气耦合模型中构建长期再分析数据具有重要价值。研究人员使用十折交叉验证方法，验证了这个模型的准确性。同时，还将交叉验证的评分与其他模型进行了比较。该模型从日到年尺度都优于其他模型，其小时尺度R^2（0.80）甚至优于其他大多数模型日尺度R^2（0.41～0.85）。研究人员将模型预测的2019年$PM_{2.5}$数值和观测的实际数值比较结果表明，该模型都能够以前所未有的预测能力准确估算$PM_{2.5}$质量浓度。该模型不仅可以对$PM_{2.5}$进行逐小时预测，在日、月、年尺度的预测能力上也都展示出相当大的优势，而这些优势主要来自于空间气象效应的引入。

2021年1月7日，由气科院牵头，联合国家气象中心、西藏自治区气象台、云南省气象科学研究所等单位共同承担的国家自然科学基金重点项目“青藏高原异常降水与孟加拉湾风暴影响的机制研究”年度学术研讨会在北京召开，中国工程院院士李泽椿和陈联寿、项目组特邀专家，以及项目参与单位的相关科技人员等160余人通过线上线下参加了会议。项目负责人李英研究员介绍了项目年度研究进展，陈联寿院士讲解了孟加拉湾气旋性风暴的特点，赵平副院长报告了青藏高原气象观测的研究进展和展望，复旦大学吴立广教授和中国科学院大气物理研究所孙继明研究员也带来了气候变暖下夏季南压高压变化以及青藏高原对流云大涡模拟的精彩报告。项目组成员就前期研究结果、业务技术需求以及下一步的研究计划进行了汇报和交流。截至2020年底，项目完成的研究成果初步揭示了孟加拉湾风暴与我国降水的相关性及其降水特征，指出风暴活动对我国青藏高原东南部、西南以及长江中下游以南地区降水具有同期显著影响，并发现孟加拉湾风暴有利于我国季风水汽输送的爆发性增长，对季风转换期间我国降水量有重要贡献。李泽椿和陈联寿院士、陆汉城教授、雷小途研究员等咨询专家指出了项目研究的重要意义，对项目下一步研究重点、具体技术方案等提出了宝贵意见，并强调做好科研工作最终应服务于天气预报、集中解决预报技术的具体需求。

2021年1月10日，由南京气象科技创新研究院与南京大学大气科学学院、中国气象局气象探测中心共同主办的 “天气雷达新技术和资料应用研讨会”在南京召开。来自中国气象局系统以及南京大学、中国科学技术大学、兰州大学等高校，中国科学院大气物理研究所、安徽光学精密机械研究所等研究院所，北京敏视达雷达有限公司、安徽四创电子有限公司、国睿科技股份有限公司等企业的专家学者500多人采用线上线下的方式出席会议。中国气象局科技与气候变化司姚学祥司长致开幕词，强调了雷达技术作为气象科学中的卡脖子问题和关键技术问题，是国家重点支持和发展的研究内容。气科院端义宏院长、中国气象局气象探测中心李良序主任和南京大学大气科学学院丁爱军院长分别代表3家主办单位致辞，指出当务之急是将国内优秀的气象雷达队伍凝聚起来，促进气象雷达技术高质量发展。会议4个学术主题为：我国气象雷达业务现状及发展趋势；多波长和双偏振雷达新技术的应用；相控阵、激光、毫米波和地波等雷达新技术的应用；气象雷达技术发展和应用专家建议。18位专家做了大会报告，与会人员与报告专家展开了热烈的讨论。专家们针对气象雷达新技术的发展和应用提出了宝贵建议，指出扩展多雷达布局、解决雷达探测关键核心技术、推动业务应用发展与培养专业人才是当前气象雷达国家发展的重点方向。

2021年1月14日，中国气象局党组书记、局长庄国泰一行到气科院调研。庄国泰局长首先参观了气科院一楼科技展厅，详细了解中国气象科技的发展史、气科院建院以来取得的成就和对中国气象事业的贡献，随后听取了气科院党委书记、院长端义宏的工作汇报。庄国泰局长充分肯定气科院在气象事业发展中发挥了重要的不可替代的作用。他指出，目前是气象科学发展的最好机遇，广大干部职工要认真学习习近平总书记对新中国气象事业70周年重要指示以及在科学家座谈会上的重要讲话精神，认真贯彻党中央关于科技创新的决策部署，遵循科学发展规律，推动科技创新成果不断涌现，要瞄准关键核心技术特别是“卡脖子”问题，要重视科技成果转化，做大做强做实气科院，形成气象发展的大格局，再现辉煌。中国气象局办公室主任宋善允、科技与气候变化司司长姚学祥、人事司司长陈振林陪同调研。气科院领导班子成员、徐祥德和张小曳院士参加调研活动。

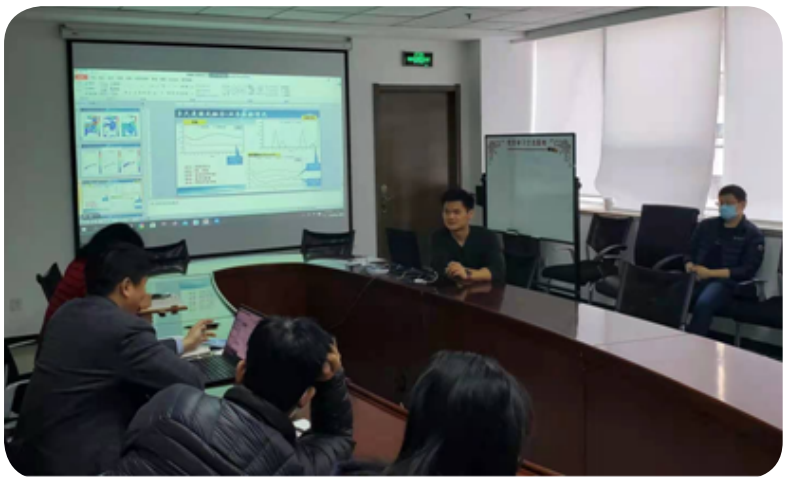

2021年1月19日，人工智能气象应用研究所邀请国家气象中心周康辉博士做了题为“基于深度学习的无缝隙强对流天气预报方法”的学术讲座，会议由王亚强所长主持。周康辉博士简要介绍了在临近短时预报广泛使用的包括光流法在内的传统方法，并从临近预报、短时预报、短期预报、深度学习可解释性分析4个方面，重点介绍了基于深度学习开展的冰雹、雷暴大风、闪电及短时强降水预报研究成果。在临近预报方面，周博士基于卫星、雷达和地闪定位数据等多源观测数据研发了LightingNet模型，可以提高闪电和短时强降水的临近预报。在短时预报方面，基于临近预报的工作基础和高分辨模式数据，通过特征融合不同来源的数据，更好地预报强对流天气现象。在短期预报方面，比较了CNN、逻辑回归等模型对ECMWF模式的分析场数据的学习能力，结果表明CNN的表现更为优异。针对深度学习可解释性方面，周博士交流了自己的工作，包括卷积核可视化、置换特征、GBDT排序特征重要性等理论。最后，现场和视频会议上的多位听众就报告内容与周博士进行了讨论和交流。

2021年1月19日，灾害天气国家重点实验室2020年度学术委员会/科学顾问委员会会议顺利召开。此次会议采取线上和线下相结合的方式，实验室学术委员会主任吴国雄院士、科学顾问委员会主任周秀骥院士、各位委员，中国气象局科技与气候变化司姚学祥司长、气科院端义宏院长、科技处金啟华副处长出席了会议。会议由吴国雄院士主持。会议首先听取了实验室2020年度进展报告，委员们对实验室的工作进展以及取得的成绩给予了充分肯定。过去几年，实验室在青藏高原大气科学试验及综合科考、华南季风降水试验及暴雨研究、多尺度大气数值模式研发、卫星资料应用研究、天气雷达探测技术及资料应用研究、雷暴云起放电过程和雷击效应研究等方面均取得了显著进展，为我国气象防灾减灾提供了强有力的科技支撑。委员们针对实验室如何瞄准当前影响业务发展的重大科学问题，着力加强新技术、成果业务转化能力，做到有亮点、有创新，做到人无我有、人有我优、人优我新，为防灾减灾气象保障能力提升发挥更大作用，给出了具体的指导意见。

2021年1月20日，南京气象科技创新研究院以远程视频形式举行2020年度团队工作进展报告会，气科院端义宏院长、高云副院长、科技处温敏处长，创新院领导班子全体成员、各团队首席、联合首席及首席助理出席会议。高影响天气团队首席孙继松研究员、多尺度气象模式团队首席李建研究员、气象探测技术团队首席翁富忠研究员、气象大数据与人工智能团队首席王亚强研究员和交通气象团队首席刘端阳研究员分别汇报了各自团队2020年的工作亮点、成果和2021年工作部署与安排。与会领导和专家对各研究团队2020年的研究进展给予了充分肯定，同时也对团队建设和未来研究工作提出了许多中肯的意见和建议。端义宏院长在肯定各研究团队工作的同时希望各研究团队首席要把握整体布局，瞄准核心任务和方向，做到科学研究与人才培养并进；作为创新院骨干的首席助理要发挥好首席与团队成员间的桥梁作用，协助做好团队各项工作；各研究团队要瞄准主攻方向，分工明确，形成自己的特色，加强人员融合和团队间交流，避免任务重叠；创新院领导班子要大力支持团队的建设与运行，给团队自主权，探索管理方式，实行动态管理，促进团队的发展和优化。

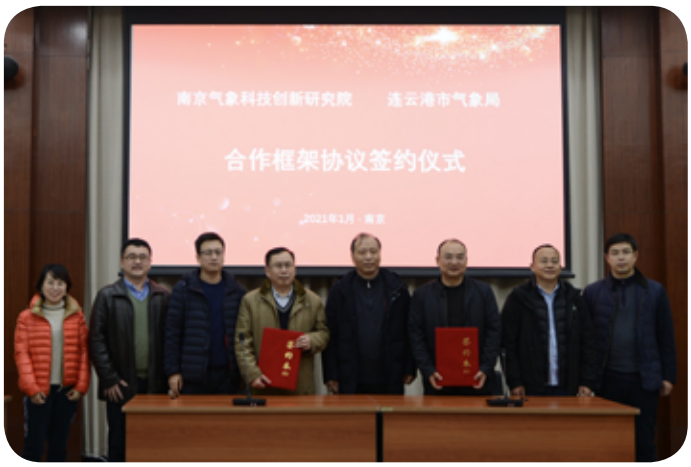

2021年1月26日，南京气象科技创新研究院与连云港市气象局合作框架协议签订及科研业务合作研讨会在南京举行，江苏省气象局严明良副局长、预报处吕军处长，连云港市气象局徐良谋局长、陈飞副局长、观测与预报处王桂臣处长，南京气象科技创新研究院副院长孙效功和刘端阳及中国气象局交通气象重点开放实验室骨干成员出席会议。此次协议的签订是在前期长达6年的合作基础上，充分发挥了创新研究院陆上交通气象特色与连云港市气象局海洋气象研究优势条件，在共建共享野外科学试验基地、联合开展海洋交通气象研究站建设及相关设备的研发、成果转化应用、项目合作、人才培养等方面达成新合作。双方的合作有助于共同推进灾害性天气、数值天气模式、交通气象研究以及科技成果的转化应用，提升连云港市气象防灾减灾能力和海洋交通气象服务能力。会议就双方单位开展后续合作进行了深入探讨。严明良副局长对创新研究院和连云港市气象局的合作表示肯定与支持，并希望充分利用好创新研究院的科研团队与连云港得天独厚的外场观测条件，将科研与业务相融合，为提升海洋气象服务能力做贡献，不断推进气象现代化建设。

2021年1月27日，中国气象局人工影响天气中心召开学术交流会。会议由中国气象局云雾物理环境重点开放实验室主任陈宝君主持，中心全体人员参加会议，会议采取线上线下结合形式举行。人工影响天气中心的22位业务、科研人员依次汇报了自己最近一年的研究成果及进展，报告涵盖了从业务应用关键技术成果到云降水物理机理研究等多方面内容。每个报告结束后，大家都针对汇报内容进行了充分的讨论。此次学术交流会促进了大家对研究成果的展示与讨论，从而达到互通有无、加强相互交流和学习的目的，推动中心全体人员进一步提升业务和科研工作水平。报告结束后，陈宝君主任对会议进行了总结，希望大家认真参考讨论的建议，加快推进研究结果的业务应用和成果产出。

2021年1月29日，气科院2021年工作会议在北京召开，会议以线下和线上结合的形式进行。会议传达了2021年全国气象局长会议精神。端义宏院长做了“实施创新驱动发展战略，担负气象科技自立自强主体责任，引领气象科技创新“的工作报告，总结2020年和“十三五”工作的同时，强调并部署了下一年的工作。气科院2021年重点工作任务：一是持续抓好党的十九届五中全会精神学习贯彻，推动全面从严治党纵深发展；二是加强关键核心技术攻关和科学理论研究；三是强化科技成果转化支撑气象业务发展和重大服务；四是加强科技创新平台建设；五是推进人工影响天气工作；六是提升综合管理，持续激发科技创新活力；七是拓展深化开放合作；八是积极推进气象学会发展。中国气象局科技与气候变化司司长姚学祥出席会议，代表中国气象局领导对气科院在2020年以及“十三五”期间取得的成绩表示祝贺，并传达了宇如聪副局长对气科院提出的“要立足新阶段、贯彻新理念、构建新格局、抓住新机遇，实现全面创新发展”的期望。气科院领导班子成员、院士以及各单位主要负责同志在主会场参会，院管理部门、各研究单位全体职工在分会场参会。工作会上还宣读了2020年全院各类获表彰名单。

2021年1月29日，中国气象局科技与气候变化司组织召开了公益性行业（气象）科研专项项目“气溶胶吸收特性测量新技术研发”结题验收会。验收会采用线上与线下相结合的方式进行，中国气象局科技与气候变化司项目处张岳主持会议。专家组听取了项目组的结题汇报，审阅了有关文档资料，经过充分质疑和讨论，认为项目完成了任务书规定的各项研究内容，实现了预期目标，一致同意通过验收。公益性行业（气象）科研专项项目“气溶胶吸收特性测量新技术研发”主持单位为气科院，联合复旦大学、北京大学、中国科学院大气物理研究所和南京信息工程大学等单位共同承担。项目设计和建立了连续、高精度测量大气气溶胶消光系数的光腔衰荡光谱仪系统（CRDS），完成了激光光腔衰荡气溶胶消光仪的样机研制，并建立了实验室定标和标定方法；组织开展了多种气溶胶光学仪器的综合对比试验，对国内外主要类型的仪器设备的观测性能和偏差等获得了较为深入的认识；研制样机及其工程化系统在多个科学试验、业务观测中得到了很好的应用，对获取高质量气溶胶光学特性观测，促进科研、业务工作起到积极作用。

2021年2月5日，中国气象局人工影响天气中心通过视频会议方式组织召开西北区域人工影响天气能力建设项目新舟60国家作业飞机交付状态验收会，中国气象局、北京大学、中国科学院大气物理研究所、北京航空工程技术中心、天驹通航公司、中飞通航公司及北京、河北、山西、甘肃、陕西等省（市）气象局专家参加了会议。与会专家听取了飞机研制、监造、任务系统验查和飞机托管交接检查等4个报告。经质询、讨论专家们一致认为，2架新舟60国家作业飞机充分借鉴东北人工影响天气项目的经验，大气探测、催化作业、空地通信、任务集成和任务电源子系统均满足初步设计和合同要求，同意通过交付状态验收。2架新舟60国家作业飞机从生产、改装、测试、试飞、查验等环节，历时2年多，实现了云微物理探测软件国产化、任务系统集成、空地视频通信等多项技术突破。相比东北人工影响天气项目建设的2架新舟60国家作业飞机，西北人工影响天气项目建设的2架新舟60国家作业飞机，作业、探测、通信、系统集成均有明显的提升。飞机投入使用后，可有效提高复杂气象条件下的作业能力，在飞行过程中可以获取实时云层状况和气象探测信息，更好地满足增雨作业业务和科研探测需求。下一步，中国气象局人工影响天气中心、相关省气象局、飞机研制单位、飞机托管单位将合力确保新舟60国家作业飞机安全高效运行，充分发挥作业效益，在西北地区生态文明建设、乡村振兴以及重大活动保障等方面做出重要贡献。

2021年2月6日，针对广东、广西、湖南、江西、浙江、福建、云南等南方省市持续干旱，部分地区存在较高的森林火险等级的情况，中国气象局局长庄国泰要求抢抓天气时机，适时开展人工影响天气作业，为缓解旱情、降低森林火险等级、保障春耕春播等提供优质服务保障；副局长余勇针对2月7—10日南方即将出现的降水过程，要求加强监测分析，开展人工增雨作业。2月7日，中国气象局人工影响天气中心，联合相关地区人工影响天气部门开展南方抗旱人工增雨作业会商。减灾司副司长赵志强、人工影响天气中心主任李集明参加会商。与会专家就南方旱区降水过程作业条件潜势预报，飞机增雨作业方案（航线设计）等作业条件和作业预案，精准、科学、有效、安全地作业及准备情况进行了讨论。2月8日上午，中国气象局人工影响天气中心组织江西、福建、广东省相关部门及赣州飞机外场基地，首次开展了赣粤闽跨省域联合增雨作业会商，精细设计了不同区域的“几”字形飞机作业方案，预计将显著提升赣粤闽跨省域联合增雨作业的效果，对缓解南方省市旱情起到十分积极的作用。自2021年1月21日中国气象局人工影响天气中心启动南方抗旱重大服务保障至今，已指导各地开展飞机人工增雨作业13架次，累积飞行时长近42 h，实施地面人工增雨作业444次，消耗炮弹20发、火箭1265枚、地面焰条330根。后续中国气象局人工影响天气中心将会积极跟进，国省联动，尽全力做好此次南方抗旱人工增雨作业服务保障工作。


2021年2月8日，南京气象科技创新研究院第一届理事会第二次会议在京宁两地采用线上线下结合方式召开。会议由宇如聪理事长主持，中国气象局、江苏省人民政府、南京市人民政府以及南京大学、国防科技大学、南京信息工程大学、河海大学、中国气象局科技与气候变化司、中国气象科学研究院、江苏省气象局各理事单位代表出席，共商创新研究院未来发展大计，构建大气科学联合研究平台发展新格局。会议审议通过了理事变更、理事会章程修订、人事任免、创新研究院2020年工作报告及2021年重点任务等事宜，并对创新研究院未来发展进行了咨询研讨。理事会肯定了创新研究院成立一年多来的工作，同时建议创新研究院要紧紧围绕重大需求和核心技术加强科技协同创新研究，加强开放合作、人才队伍建设和体制机制创新，大力推进成果转化。各位理事表示在创新研究院未来发展中给予更多的支持。


2021年2月9日，中国气象科学研究院与泰国农业和合作部皇家人工降雨和农业航空司（DRRAA）举行人工影响天气技术合作协议线上签署仪式。气科院院长端义宏、中国气象局人工影响天气中心主任李集明、中国气象局国际司双边处领导，泰国DRRAA司长Surasri Kidtimonton、副司长Panithi Samerwong、Nareeluck Wannasai及泰国农业和合作部驻华工作人员等共22人出席签署仪式。仪式上中泰双方领导致辞。Surasri Kidtimonton司长表示，中泰双方签署人工影响天气技术合作协议，是通过战略伙伴关系加强长期的友谊，是区域和平、稳定与繁荣的重要支柱。签署的合作协议以及将要开展的行动计划，将通过科技创新提高人工影响天气减轻干旱和减少灾害的能力。相信通过双方的努力，能够为两国人民带来福祉。气科院院长端义宏介绍了中国气象局人工影响天气中心近年来所做的主要工作。他表示，中泰两国在气象领域的合作源远流长，在中泰战略合作伙伴关系的背景下，在未来4年的时间里将以合作项目、人才队伍建设、人工影响天气经验交流等方式在数值模式、催化剂、催化设备、云物理探测设备及相关领域进行深入合作。希望通过合作，促进双方人工影响天气的工作交流，提高双方的技术水平，并最大限度地减轻干旱和其他自然灾害带来的社会经济损失。中泰合作协议的签订正是新春伊始之时，相信中泰两国在人工影响天气领域的合作就像初春的种子，必将生根发芽、结出累累硕果。

2021年2月24日，中国气象局人工影响天气中心召开人工影响天气与气象现代化建设需求衔接会议，中国气象局总工程师黎健、各职能司和发展规划院领导等出席会议。会议由气科院副院长、中国气象局人工影响天气中心主任李集明主持。黎健总工程师一行首先对人工影响天气中心指挥平台进行了调研，听取了人工影响天气中心指挥业务整体情况介绍。李集明主任汇报了人工影响天气“十四五”发展规划与现代化建设需求，各职能司和发展规划院领导对人工影响天气现代化工作提出了建设性的意见。黎健肯定了人工影响天气中心在业务服务、现代化建设等方面所做的工作并对未来的规划和高质量发展提出了要求：一是要站在初心使命和国家战略高度考虑人工影响天气工作，强化对全国的技术指导，增强科学性、安全性；二是要贯彻落实好《国务院办公厅关于推进人工影响天气工作高质量发展的意见》；三是要对气象发展十四五规划中的人工影响天气部分提出完整意见；四是规划要注重观测、预报、服务等工作的协同性、系统性，要有共享建设理念；五是规划要与事业单位改革、人工影响天气中心改革以及人才队伍建设相匹配；六是要进一步加强与各职能司的沟通，对规划进行修改完善。

2021年2月26日，针对冬小麦返青、春耕春播关键期我国黄淮及周边地区出现的持续旱情，为及时抓住有利的人工增雨（雪）作业条件，中国气象局人工影响天气中心采用腾讯会议形式组织山西、河北、山东、河南、安徽、江苏、浙江、江西等8省人工影响天气部门开展抗旱人工增雨作业条件及作业预案专题会商。中国气象局人工影响天气中心首先提出了会商重点、预报结论、预报理由以及作业预案建议，各省人工影响天气部门依次对2月27日至3月1日的作业条件和作业预案，以及作业和准备情况进行了充分的交流和讨论。针对此次旱情，中国气象局人工影响天气中心从2月22日以来制作发布多期作业条件预报、预案、人工影响天气服务快报等专项指导产品。此次应急会商，通过对云系演变特征和云系垂直结构的分析，精细地做出了作业潜力区预报和作业预案建议，有利于提高各地人工增雨作业的科学、精准水平，也将为此次降水过程有效缓和旱情，助力春播生产、抗旱保墒，以及为地方经济发展发挥积极作用。

2021年3月5日，国家气候中心气候模式室主任吴统文研究员访问气候与气候变化研究所，在“科技创新论坛”做了题为“次季节–季节–年际尺度一体化气候模式预测业务系统（BCC-CPSv3）及影响机制研究”的学术报告，报告会由祝从文副所长主持，李建所长和全所科研人员参加报告会。吴统文研究员现任国际次季节–季节预测计划（S2S）科学指导小组成员，长期担任中国气象局气候模式研发团队负责人和学术带头人，带领团队于2016年、2020年先后完成了我国第二代、第三代气候模式预测业务系统的研发。吴统文介绍了我国三代气候模式预测业务系统的研发历程，着重介绍了第三代系统（BCC-CPSv3）的主要构成，包括多圈层耦合模式BCC-CSM2-HR的配置和性能特点，多圈层耦合同化技术和集合预测方法研究进展，并介绍了评估BCC-CPSv3模式对月内尺度温度、降水、大气环流，次季节尺度MJO季节内振荡和季节尺度降水、温度、环流、SST和海冰等预测能力的情况，与现有模式预测业务系统对比有显著进步，在某些方面优于国际业务预测产品。气候所各研究团队人员与吴统文研究员开展了深入交流，就模式分辨率对预测效果的影响、物理过程和同化系统研发进展，以及气候模式未来的发展前景等进行热烈讨论。此次报告会对气候所多尺度模式研发、S2S变化机理与预测理论等方向研究都带来了有益启发，对了解业务进展和需求、进一步推动科研业务结合也有积极作用。

2021年2月27日至3月12日，气科院青藏高原与极地气象研究所联合中国科学院国家天文台南京天文光学技术研究所、山东师范大学等单位科技人员组成冬奥赛道科考队，前往北京延庆国家高山滑雪中心、河北崇礼云顶滑雪场和黑龙江亚布力滑雪场等地，开展冬奥气象保障工作。具体工作包括跟踪观测上一轮试验完成的赛道，评估赛道在回暖天气的维持能力，探索在相对高温下制作赛道的技术方法等。在科考工作期间，遇到了试验窗口期短、突发暴风雪天气等困难，在大家的一致努力下顺利完成了所有的预期科考项目。通过此次科考，科考队初步掌握了不同天气下赛道制作和维持的技术要点，为冬奥会雪务保障工作积累了宝贵经验。在科考工作间隙，科考队成员组织了一次有特殊意义的党小组活动。大家集中学习了北京市委书记、北京冬奥组委主席蔡奇同志关于冬奥筹办的重要指示精神。经过交流，大家一致认为要坚决保质保量完成赛道试验工作，为冬奥成果的展示与推广打下坚实基础。

2021年3月12日，科技处组织召开2021年我国夏季气候预测会商会。会议由气候与气候变化研究所副所长祝从文主持，次季节–季节研究团队与多尺度数值预报系统研发团队相关科研人员、气候预测领域专家魏凤英研究员参加了研讨交流。苏京志研究员首先做了基于气科院动力预测系统的2021年夏季气候预测意见报告。该动力预测系统基于气科院气候系统模式（CAMS-CSM）研发，于2020年3月开始逐月开展实时预测，对2020年秋冬季“拉尼娜”状态的预测与实况基本一致。根据动力预测系统预测结果，苏京志综合分析给出了2021年ENSO状态后期演变的预测意见。刘伯奇副研究员介绍了改进后的气科院统计预测自动化系统（CAMS ASPS）。改进后的CAMS ASPS系统在回报2020年梅雨期降水和2020/2021年冬季气温及降水方面预报效果有明显提高。基于CAMS ASPS系统预测结果和美国、韩国、欧洲中期天气预报中心、WMO等多家多模式集合预测产品，综合考虑热带太平洋–印度洋、北太平洋SSTA和南半球环状模（AAO）等因素的影响，给出2021年夏季我国降水和气温趋势预测意见。与会人员就预测意见开展了讨论，并建议进一步考虑中纬度环流异常对我国夏季气候预测的重要影响。

2021年3月31日，气科院青联举办2021年首次青年学术论坛暨气科院极地专题青年报告会。报告会由气科院青联主席丁明虎研究员主持，赵平副院长出席会议并致辞，线上线下一百多人参加会议。会议邀请了清华大学徐世明副教授介绍了其领衔的基于耦合模式的高分辨率多尺度海冰动力学模拟的最新研究进展，中国科学院大学耿雷教授对雪–气界面硝酸光化学过程和冰芯硝酸同位素记录解读进行了介绍，中国科学院大气物理研究所李熙晨研究员介绍了热带–极地遥相关和南极气候变化的研究成果，自然资源部海洋三所祁第研究员介绍了人为二氧化碳从南极大陆架转移到南大洋深处及其对海洋酸化的影响。与会青年科研人员和研究生对4位科学家的研究工作表示出了浓厚兴趣，并就相关问题开展了积极讨论。4位科学家从自身科研经验出发解答了线上、线下科研人员的问题与疑惑。气科院青年表示要积极学习4位科学家脚踏实地、刻苦钻研的精神，抓住机遇，尽早成为气象科技事业的中坚力量。气科院青联坚持围绕中心、服务大局，今年还将适时组织专题青年学术交流，引领和带动全院青年弘扬科学精神、钻研科学知识、创新科学方法，助力青年岗位建功。

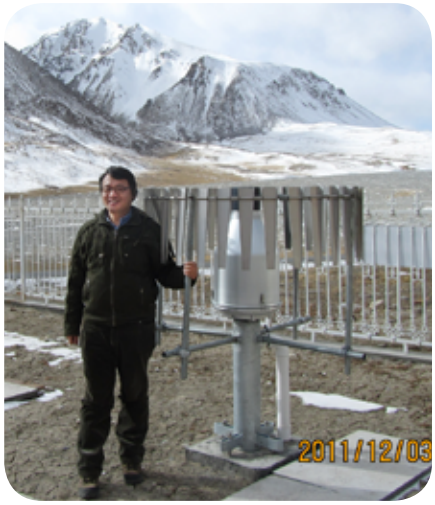


援疆纪念证书

刘洪利同志：

受中国气象局派遣于2011年1月-2014年1月在新疆气象局支援工作，特发此证，以资纪念。

新疆维吾尔自治区气象局
二〇二〇年九月


援疆纪念证书

尹金方同志：

受中国气象局派遣于2014年9月-2016年3月在新疆气象局支援工作，特发此证，以资纪念。

新疆维吾尔自治区气象局
二〇二〇年九月


援疆纪念证书

徐洪雄同志：

受中国气象局派遣于2016年3月-2017年8月在新疆气象局支援工作，特发此证，以资纪念。

新疆维吾尔自治区气象局
二〇二〇年九月

2021年3月，新疆维吾尔自治区气象局向气科院刘洪利、尹金方、徐洪雄3位援疆干部颁发了援疆纪念证书及奖章，高度赞誉并感谢他们在援疆工作中的努力和取得的优秀业绩。

• 青藏高原与极地气象科学研究所刘洪利研究员在援疆期间（2011—2014年），主要围绕乌鲁木齐市气象局的数值天气预报、雾霾天气预报和新疆地区大气污染防治、环境气象业务预报等方面开展技术研发，同时开展了技术成果应用推广和讲座培训工作，推动了乌鲁木齐市气象局相关预报技术的提升。参与并主笔撰写的新疆自治区政协“重点城市控制$PM_{2.5}$，防治汽车尾气污染”专题报告，得到自治区政协的好评，并获得自治区党委书记张春贤批示。

• 灾害天气国家重点实验室尹金方研究员在中国气象局新疆沙漠气象研究所援疆期间（2014—2016年），开展的雷达资料同化工作改善了新疆区域数值预报业务系统初始场，提高了模式预报准确率，为预报系统的业务准入给予了极大的支撑。其专题授课和技能指导，提高了沙漠所年轻科研人员科研业务能力。2017年荣获“第八批中央和国家机关、中央企业优秀援疆干部人才”称号及援疆工作记功一次。

• 灾害天气国家重点实验室徐洪雄副研究员在中国气象局新疆沙漠气象研究所援疆期间（2016—2017年），参与全国6万区域站点遴选工作，参加了进行观测模拟批量试验所需程序（脚本驱动的OSSE系统、后期站点插值以及检验模块等）的重新开发。推动气科院灾害天气国家重点实验室陆面资料在沙漠所业务模式中的使用，为观测模拟批量试验做了大量前期数据及技术准备，并参与了批量试验工作。

2021年4月1日，应赵平和高云副院长的邀请，中国科学院院士、中国科学院地理科学与资源研究所崔鹏研究员一行5人访问气科院，并就青藏高原观测站网合作事宜进行了交流和研讨。气科院高云副院长，王迎春、任宏利、丁明虎和张东启研究员，中国气象局科技与气候变化司周秉荣副处长等参加了研讨，研讨会由赵平副院长主持。崔鹏院士做了题为“青藏高原自然灾害与防灾减灾”的报告，介绍了他们对高原地表灾害的研究成果和未来高原建站观测的计划。青藏高原与极地气象科学研究所副所长任宏利研究员向崔鹏院士一行介绍了气科院在青藏高原野外观测基地的情况。随后，赵平副院长向来宾介绍了第三次青藏高原大气科学试验的主要研究成果和近年来中国气象局和气科院在高原建站和观测方面取得的进展；高云副院长介绍了气科院的基本情况，特别是气科院负责运行的科研基地的情况以及气象局系统业务观测准入制的信息，并强调将业务观测平台优势转化为科研优势是未来气科院发展的重点目标之一。双方就川藏铁路沿线冰冻圈灾害观测站的建设、在TPRCC框架下的国内外台站建设和数据共享、气科院在青藏高原科学试验基地建设规划以及墨脱国家观象台的建设方面进行了热烈的讨论，希望能继续深入沟通并委派专人对接，就合作建站、数据共享方面进行更密切的合作。

2021年4月12日，中国气象局和阿联酋国家气象中心人工影响天气专家举行视频会议，交流人工影响天气技术研究和业务工作进展，研讨未来合作意向。来自中国气象局人工影响天气中心、中国气象局国际合作司、应急减灾与公共服务司以及阿联酋国家气象中心人工影响天气项目、国际合作部门的管理人员及专家等14人出席会议。中方专家通过5个报告介绍了中国人工影响天气的发展现状，包括中国气象局人工影响天气工作总体情况、人工影响天气外场观测试验、效果检验、云模式的发展和应用、人工消雾以及声波等新技术在人工影响天气中的应用等。阿方专家介绍了阿联酋人工增雨业务工作情况及人工增雨项目（UAE-REP）进展。在交流的基础上，双方就后续合作方向、合作方式等进行了探讨。通过此次会议，中国气象局和阿联酋国家气象中心的专家加深了对双方人工影响天气领域业务、科研情况的了解，为推进双方在人工影响天气领域的进一步合作奠定了基础。

2021年4月14日，由气科院牵头、24个农业气象试验站参加的中国气象局创新发展专项“农业气象试验站区域联合试验”（CXFZ2021Z059）项目启动会采用线下和线上相结合的方式在北京召开。会议由项目负责人周广胜研究员主持，中国气象局科技与气候变化司和应急减灾与公共服务司相关领导出席会议并讲话。项目共同负责人宋艳玲研究员介绍了项目的概况、任务、试验的具体方案；周广胜研究员介绍了任务执行的具体任务、要求和工作时间节点，并重点介绍项目成果产出《气候变暖对中国主要粮食作物产量与品质的影响评估报告》的写作框架、组织与时间进程安排。主会场与24个农业气象试验站的项目骨干人员参与了会议，参会人员就区域联合试验的工作与试验进行了讨论。中国气象局职能司相关领导进一步强调了本项目的目的，希望通过项目的实施，为农业气象业务服务指标的修订、农业气象模拟模型的改进及区域应用、农业气象适用技术的开发等提供基础试验资料和科学依据，大力提升农业气象和生态气象的业务服务支撑能力和技术水平；同时为试验站培养一批懂技术、能科研的农业气象科研人才队伍，推动农业气象试验站科研业务水平的提高。

2021年4月16日，气科院组织召开了“基于铁路网络的气象与大气环境动态探测系统及应用”合作研讨会，会议由徐祥德院士主持，端义宏院长出席并讲话。气科院、中铁特货物流股份有限公司及北京瑞蒙特科技有限公司三方领导与专家重点讨论了如何利用覆盖全国的铁路网络发展气象与大气环境三维结构动态探测新技术系统及应用前景，并就三方战略合作协议初稿和青藏铁路气象观测试验方案提出了修改意见。徐祥德院士从国家战略需求角度介绍了基于铁路网络的气象与大气环境三维结构动态探测系统及应用项目的重要意义。端义宏院长表示，非常支持该项目的探索性研究，希望以此项目为契机谋划三方长期合作，为提升灾害天气的预报预警能力提供科技支撑。中铁特货物流股份有限公司副总经理顾光明、北京瑞蒙特科技有限公司总经理白钢等领导与专家认为，该项目对提高铁路部门及其他行业的气象灾害防御能力具有重要作用，希望三方尽快签署战略合作协议，未来在项目成果转化及大数据应用等方面进行深度合作。

2021年4月19日，2021年度“华南季风/台风强降水协同观测试验”启动会暨技术研讨会在北京召开。来自气科院、广东省气象局、中国气象局广州热带海洋气象研究所、广东省茂名市气象局、深圳市国家气候观象台、南京大学、中国科学技术大学等单位的专家和技术人员、气科院端义宏院长和广东省气象局熊亚丽副局长出席了会议。“华南季风/台风强降水协同观测试验”各参与单位对2020年观测试验开展情况、研究进展、存在的问题以及2021年观测试验计划进行了汇报，与会专家就如何规划好今年的观测试验进行了讨论。2021年将继续加强合作，依托“华南季风/台风强降水协同观测试验”获取的宝贵观测资料，深入开展华南强降水发生发展机制和关键物理过程研究，为提升灾害性强降水过程的监测、预警预报水平提供科技支撑。端义宏院长在会议总结时指出：为做好此次观测试验，有必要对过去几年的工作进行总结，要做好规划，围绕亟待解决的科学问题进行观测试验方案的设计；要大力推进野外科学试验数据共享平台的建设，充分实现观测资料的共享；灾害天气国家重点实验室要做好统筹，联合各参与单位，共同开展好各项试验内容。

2021年4月22日，毕业于芬兰赫尔辛基大学的李浩然博士应邀访问灾害天气国家重点实验室并做题目为“冷云降水的雷达观测研究” 的学术报告，实验室雷达团队首席刘黎平研究员主持了会议，众多单位的学者和研究生参加了本次报告会。李浩然博士在芬兰一直从事雷达气象学和云微物理的研究，其相关工作成果在多个权威国际刊物上发表。报告中，李浩然博士首先阐述了冷云降水的重要性及云内各种微物理过程的复杂性。目前，数值模式对冰相微物理过程的描述还很不充分，需要有力的观测试验增进对这些过程的理解。李博士介绍了他利用芬兰BAECC观测试验和ACTRIS观测网的多种雷达观测资料，研究了淞附、繁生等过程对降水的影响，分析了冰相微物理过程与冰晶的融化之间的联系，并首次用试验方法反演了Ka波段和W波段雷达信号的融化层衰减量等工作。这些工作对层状云降水系统的观测及如何更好地利用雷达观测资料反演云微物理过程等方面均具有重要意义。报告结束后，参会人员就报告内容与李浩然博士进行了深入的交流和讨论。

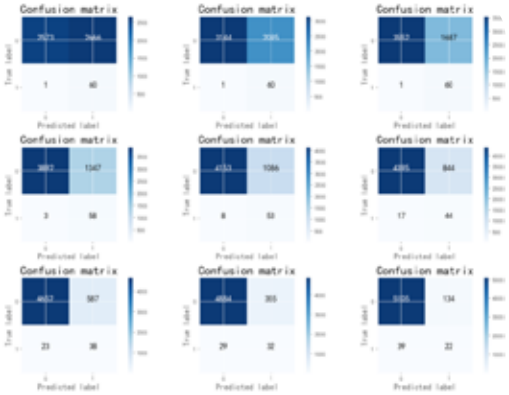

2021年4月，南京气象科技创新研究院对北极阁开放式科研基金资助的9个项目进行了验收。根据专家组意见，最终有7项通过验收，其中优秀项目2项。北极阁开放式科研基金2008年由江苏省气象局设立，面向全国相关科研院所、高校和企事业单位的科研团队，支持交通气象领域的科技创新以及多源探测资料、区域高分辨率数值模式本地化和产品释用技术为基础的灾害性、高影响天气监测预警预报方面的技术研发。此次通过验收的7个项目如下：（1）“江苏夏季雨滴谱观测特征分析及关键参数的微物理方案本地化”项目（负责人为梅海霞）。提取了符合江苏地区夏季强对流天气的雨滴谱特征参数，完成了云微物理方案中雨滴谱谱形参数诊断方法的代码改写，形成能够稳定运行的本地化改进方案。（2）“江苏省低能见度预警概率模型的建立”项目（负责人为沈沛丰）。编写了微波辐射计和风廓线雷达资料的联合应用软件客户端，能够综合展示边界层风场、水汽、热力层结特征，并投入业务试用。（3）“长江江苏段雾的生消过程及致灾机理的研究”项目（负责人为田小毅）。利用在长江江苏段沿线布设的交通气象高密度观测资料，建立了该段雾过程档案资料和雾的天气学分类模型和预警预报业务流程，提高了长江航道雾预报的准确性。（4）“江淮流域短时强降水多模式集合预报研究”项目（负责人为王坤）。使用SMOTE和LR方法构建了江淮流域短时强降水预报模型，并将其应用于单模式和多模式集合预报的短时强降水的确定性预报和概率预报产品处理，改进了江淮地区短时强降水预报能力。（5）“雾的能见度参数化方案研究”项目（负责人为祖繁）。构建了适合江苏省的能见度与湿度、雾滴数浓度和含水量的参数化方案，并应用于交通气象信息服务系统第二版TMISS2.0。（6）“华中区域高速公路大雾预报关键技术研究”项目（负责人为何明琼）。对大雾天气背景场进行了类型划分和特征概述，提炼了大雾短临预警预报技术指标，建立了预报模型，将华中区域高速公路大雾预报预警准确率提高至89.7%，预警时效比公众大雾预警时效平均提前6 h。（7）“基于道路摄像头的大雾等级智能识别技术研究”项目（负责人为苗开超）。通过采集高速公路上视频监控图像，构建了基于AlexNet网络的大雾等级识别模型，平均识别准确率为78%。

2021年5月7日，针对4月30日江苏罕见大范围雷暴大风和冰雹天气现象，南京气象科技创新研究院组织全院团队召开“4·30”大风冰雹过程研讨会，创新研究院领导班子、高影响天气研究团队首席孙继松研究员、联合首席赵坤教授，多尺度气象模式研究团队联合首席黄小刚教授，各团队首席助理及相关团队成员出席此次会议。研讨会由费建芳院长主持，他简单介绍了此次强对流天气过程及前期研究工作，按照中国气象局宇如聪副局长的指示和要求，创新研究院在气科院领导和组织下已第一时间对江苏“4·30”极端大风冰雹天气进行了初步分析并形成报告。各团队首席、首席助理依次从雷达资料、卫星资料、数值模式资料以及交通灾情统计资料等多角度分析了此次大风冰雹天气过程，专家及各团队成员对大风成因、降水及冰雹发生过程等问题展开热烈的讨论。最后，费建芳院长要求，以高影响天气团队为主、其他团队为支撑深入开展科学研究，尽可能收集各类型资料进行深层次分析，深入研究此次极端大风的形成机理，为气象防灾减灾服务提供更坚实的科技支撑。

2021年5月8日，南京气象科技创新研究院与航天新气象科技有限公司在南京召开合作研讨会并签署合作框架协议。双方将建立协同创新机制，在气象仪器及应用软件研发、项目合作、气象设备研发评估和标准规范制定、人才培养和交流等方面加强合作。创新研究院院长费建芳、新气象公司副董事长薛鸣方共同主持会议，新气象公司高允书记、王志锐副总经理及相关技术人员，创新研究院曾明剑和刘端阳副院长、高影响天气团队孙继松首席和联合首席赵坤教授携本团队及交通气象团队成员出席会议。双方代表详细介绍了各自单位及研发领域基本情况并一致认为，创新研究院与新气象公司在科学研究、气象仪器研发、成果业务转化、社会服务等方面有着很好的互补性，双方合作有助于推进气象观测能力、灾害性天气预警预报水平、防灾减灾救灾以及生态气象服务保障能力的提升。随后，曾明剑副院长与王志锐副总经理代表双方签署了合作框架协议。会议最后，与会代表就需求定位、技术要点、合作机制等方面展开深入讨论。费建芳院长表示，一方面从实处着手，加强资源整合和技术合作，集中力量开展重点攻关，联合申报各类国家级项目；另一方面展望成果应用，立足江苏、面向国家需求，将现有成果及合作成果转化，积极创造气象科技社会效益与经济效益。

2021年5月7—8日，灾害天气国家重点实验室/卫星研究与应用联合中心主办的“2021年大气海洋一体化参数反演与应用研讨会”在苏州召开。会议由翁富忠教授主持，中国气象局科技与气候变化司张跃堂二级巡视员、复旦大学金亚秋院士出席并讲话。国家卫星中心方翔副主任、气科院科技处温敏处长、南京气象科技创新研究院闫丽华副院长及其他有关专家出席会议。来自国家卫星海洋应用中心、国家卫星气象中心、复旦大学、江西师范大学、南京信息工程大学、中国气象局上海台风研究所、上海期智研究院、中国科学院上海技术物理研究所等单位的专家学者参加了研讨会。翁富忠教授明确此次会议旨在了解相关部门在大气海洋遥感方面的研究现状及能力，谋划合作方式，研究未来工作思路和重点任务。各科研院所、高校参会人员围绕快速辐射传输模式（ARMS）关键技术和卫星遥感、海洋卫星等关键技术汇报了科研进展。专家们针对卫星资料定标定位和同化技术的发展及应用展开讨论并提出了宝贵建议，指出要结合生态文明建设及环境保护的国家战略，立足顶层设计，做好底层基础工作，对标国际前沿，使中国卫星产品的算法、数据处理、信息感知达到更高水平。此次会议加强了气象、海洋不同领域学者在大气海洋一体化参数反演与应用领域的沟通与交流，促进了学科的交叉融合。5月8日下午，与会人员前往中国科学院上海技术物理研究所苏州研究院参观，就遥感科研的云计算加速技术问题进行了探讨，翁富忠教授对创建科研服务云平台给予了充分肯定并就今后发展目标提出指导性意见。

2021年5月18—19日，2021年全国夏收粮油作物产量预测会商会在山东济南召开。会议由国家气象中心主办，中国气象局应急减灾与公共服务司、国家统计局农村司、中国气象科学研究院、国家卫星气象中心以及各省市（区）相关农业气象业务单位参会。会上，山东省气象局减灾处冯桂力处长致欢迎辞并介绍了山东省气候、农业生产情况，重点介绍了目前当地开展的农业气象服务保障工程情况。中国气象局应急减灾与公共服务司姜燕调研员重申了产量预报的重要性，并期望各省气象部门对作物产量做出客观评估。国家统计局农村司的代表介绍了夏收粮食作物生产形势。国家气象中心、各省代表就2021年全国、本地区夏收粮食作物生产形势及未来产量预估做了汇报发言，最后由国家气象中心总结汇总。气科院生态与农业气象研究所马玉平副研究员做了“基于中国农业气象模式(CAMM1.0)的2021年冬小麦单产趋势预估”的报告，介绍了气科院自主研发的中国农业气象模式(CAMM1.0)及其运行平台的进展情况，给出了基于CAMM1.0模式模拟结果的2021年全国冬小麦格点单产预估，为相关作物产量预测提供了参考依据。中国农业气象模式是气科院生态与农业气象研究所近年来重点研发的科研和业务项目之一，此次马玉平副研究员参加全国夏收粮食作物产量预测会商，旨在开展模式应用检验，为下一步CAMM1.0模式应用和推广积累经验。

2021年5月19日，由工程气象研究中心承担的“北京市气候变化与风险评估研究”项目专家验收会在北京召开。国家气象中心李泽椿院士、国家气候中心肖潺研究员以及北京建筑大学、中国建筑标准设计研究院等评审专家参会。该项目综合运用面向国土空间规划的气候变化与风险评估技术，在典型气象要素、主要气象灾害和极端天气气候事件的历史变化特征及其影响分析的基础上，识别典型气象因子，并综合考虑致灾因子危险性、承灾体脆弱性和综合防范能力等方面，进行现状综合风险评估和未来气候变化情景预测，为从规划角度制定针对性的气候变化应对策略提供支撑。专家们一致认为该项目将对影响城市可持续发展的气象灾害及时采取应对措施，减缓由气候变化带来的挑战与压力，提升城市应对气候变化能力及合理制定城市发展规划提供科学支撑，具有一定的环境和社会效益。

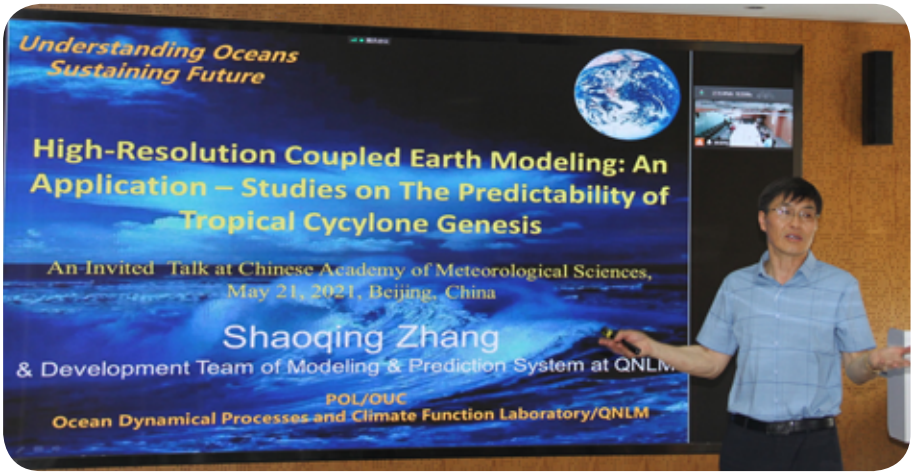

2021年5月21日，中国海洋大学张绍晴教授应邀访问灾害天气国家重点实验室并做题为“High-Resolution Coupled Earth System Modeling: An Application—Studies on The Predictability of Tropical Cyclone Genesis”（高分辨率地球耦合系统模式应用介绍——热带气旋生成可预报性研究）的学术报告，实验室副主任徐晶研究员主持了报告会。张绍晴教授为“筑峰第一层次”特聘教授、青岛海洋科学与技术试点国家实验室“鳌山人才”卓越科学家、山东省“泰山人才”特聘专家。长期从事大气-海洋耦合资料同化和初始化研究，致力于国家级的高分辨率全球和超高分辨率区域地球系统模拟和预报预测系统建设。多家单位的学者和研究生参加了报告会并与张绍晴教授进行了热烈的讨论。

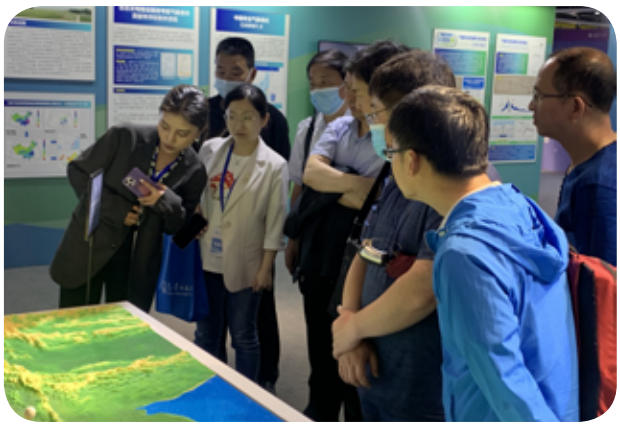

2021年5月22日，以“科技强国 气象万千”为主题的2021年气象科技活动周武汉主场活动与全国科技活动周同步启动，拉开了全国气象科技盛会的序幕。中国气象局党组书记、局长庄国泰，湖北省副省长柯俊出席启动式并致辞，中国气象局副局长宇如聪主持启动式。2021年是中国共产党成立100周年，是全面建设社会主义现代化国家新征程开启之年。本次活动充分展示了“十三五”以来气象科技发展成就和气象服务保障对全面建成小康社会的重要贡献。在武汉，以“小康社会，气象随行；伟大复兴，奋发气象”为主线的气象科技成果展，通过“国家馆”“区域馆”“长江馆”“高等院校”“企业创新”等不同版块，运用多种形式和手段集中展示气象事业科技创新取得的成果。中国气象科学研究院、南京气象科技创新研究院作为科技创新主力军参与此次展览，展区设立在“国家馆”板块，主要以展板讲解、沙盘及试验展示、视频宣传的方式多角度集中展示了气象科技创新成果。气科院主要展示的GSDART系统、台风研究、固城农业气象国家野外科学试验基地、农业气象灾害和作物苗情的全天候卫星遥感监测技术、生态文明建设绩效考核气象条件贡献率评价系统、中国农业气象模式CAMM1.0，以及创新研究院展示的人工智能强对流天气临近预报系统、遥感观测在数值天气预报中的应用、热谱地图技术研发与应用受到广泛关注。青藏高原“亚洲水塔”多圈层大气水分循环综合观测系统、第三次青藏高原大气科学试验及人工冰晶模拟试验吸引了大批公众驻足参观。

2021年5月24日，工程气象研究中心组织召开了建筑设计气象参数计算专题研讨会，天津市气象科学研究所李明财所长、中国建筑标准设计院贺静副总建筑师等相关部门专家，以及工程气象研究中心有关项目组成员参会。工程气象研究中心介绍了考虑气候变化的民用建筑节能设计气象参数与算法研究基础，中国建筑标准设计院、天津市气象科学研究所专家介绍了建筑设计用室外气象参数实用情况及实施方案。通过此次研讨，三方形成了建筑设计气象参数计算未来合作研究计划，为下一步开展建筑设计气象论证技术研发及示范应用研究打好了基础。

2021年5月27日，国家（贵州）防雹外场试验在贵州威宁正式启动，试验将由中国气象局人工影响天气中心、中国科学院大气物理研究所、成都信息工程大学和贵州省气象局等单位共同组织开展，围绕冰雹云精细化结构观测、防雹催化技术、效果评估等目前人工防雹亟待解决的关键性科学问题开展科学研究和技术攻关。国家（贵州）防雹外场试验基地设在贵州威宁，主要由中国气象局人工影响天气中心和贵州省气象局共同投资建设，现已建成以首席专家研究室、冰雹防控技术研究室、冰雹云催化数值模拟实验室、冰雹微物理结构分析室等为一体的科研基础设施和以新一代天气雷达、X波段双偏振天气雷达、风廓线雷达、GPS/MET水汽、激光雨滴谱仪等探测设备为主的立体观测网络。2019年，基地成功举办了首届“中国•冰雹减灾”论坛，在全国范围内产生较大的影响力，得到了相关领导、专家和科研人员的一致好评，此论坛被中国气象局应急减灾和公共服务司纳入“南雹（冰雹）北雨（增雨）”两大全国性论坛之一。贵州威宁处于南方多雹带核心区域，冰雹呈现生成发展快、降雹频次高、影响范围广、局部灾害重、防范难度大的特点，具有典型的山地气候特征，是开展冰雹云观测与科学研究的“天然试验场”，此次开展的试验研究对我国南方的冰雹研究而言既有代表性，也有普适性。

2021年5月27日，中国气象局科技与气候变化司在北京组织召开了公益性行业（气象）科研专项项目“人工影响天气催化剂自动化定量检测技术研究”验收会，会议采用主场与线上相结合的形式。项目由气科院牵头，联合中国兵器工业集团第209研究所和山西北方晋东化工有限公司共同承担。专家组成员来自北京大学、中国科学院大气物理研究所、中国兵器科学研究院等单位。专家组一致同意项目通过验收，并对取得的成果给予了充分肯定，认为该项目联合多家单位，通过产学研有机结合，针对我国人工影响天气催化剂检测中的自动化定量检测技术，研发了冰晶监测仪器、云室，提出了检测方案，编制相关的标准和规范，有效提升了我国人工影响天气催化剂定量检测的自动化水平。项目成果在吉林、内蒙、河北等省区人工影响天气业务、科研单位以及厂家得到推广和应用，并取得了较好的应用效果。

2021年5月，中国气象局野外科学试验基地管理服务平台正式上线运行，该平台是中国气象局“气象科学决策支撑应用集约化建设”项目的一个子系统，由中国气象科学研究院承担建设。该平台与中国气象局气政通平台集成，实现了中国气象局31个野外科学试验基地信息的在线填报、审核、管理、共享、分析和综合显示，可在线展示多个基地的全景虚拟现实和短视频。为中国气象局野外科学试验基地的科学化管理和决策提供数据支撑。

2021年5月底，从中国气象科学研究院与中国气象局广州热带海洋气象研究所联合雷电野外科学试验基地传来阶段性成果。本年度科学试验于4月20日正式展开，雷电研究团队的野外试验人员在完成前期试验设备的架设、安装和调试后，于5月29日成功实施了今年首次人工触发闪电试验，在截至发稿前已成功触发闪电5次，其中包含1次可用于研究自然闪电接地过程的空中触发闪电个例。试验中多站点、多设备协同观测，获得了高质量的同步观测数据，实现了本年度科学试验的“开门红”。为了增加雷电科学试验测试空间、提升人工触发闪电效率并扩展科学试验内容，雷电研究团队在本年度的科学试验中建设了新型人工引雷火箭发射平台。该平台可用于雷电近距离物理参量观测、防雷设备的测试以及电力系统防雷性能的检验等。此外，雷电研究团队围绕引雷试验场增加了包含7个子站的中–低频闪电放电探测阵列，进一步丰富和拓展了试验基地的多频段闪电定位方法和技术，为人工触发闪电和自然闪电的放电精细化观测以及闪电监测预警技术的完善奠定了坚实基础。试验人员克服长期持续试验造成的疲劳以及防疫管理给生活带来的不便，顶烈日、冒酷暑、主动做好试验设备的检修和维护，时刻关注雷暴天气过程，紧抓每一次开展试验的机会，以获取更多高质量的同步观测数据。

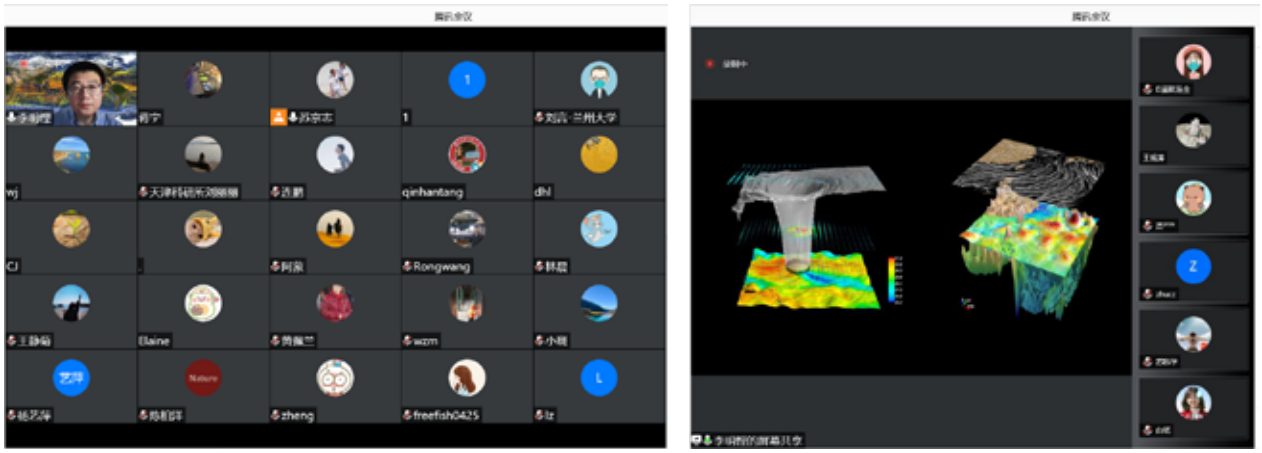

2021年6月2日，中国海洋大学李明悝副教授应邀在气科院科技创新论坛暨“气候与环境”自由论坛做了题为“Python在大气海洋科学的应用”的报告，气候与气候变化研究所苏京志研究员主持了报告会。作为大气海洋专业的一线科研人员，李明悝副教授近年来在数值模式高分辨率结果可视化方面取得一系列显示度很高的优秀成果，并出版专著《Python数据可视化》（Python在大气海洋科学的应用）等系列丛书。报告中，李明悝副教授首先向大家简要介绍了Python语言入门的常见问题，随后详细介绍了大气海洋研究中如何应用Python开展数据处理分析和可视化，内容既包括基本要点，又包括实用技巧。此次报告受到大气海洋科学研究领域科研、教学、业务人员和研究生等的积极关注，腾讯会议参会人员近240人。在互动环节，参会人员与李明悝副教授开展了热烈讨论。

2021年6月5日，在“世界环境日”中国科协生态环境产学联合体向社会发布“2020年度中国生态环境十大科技进展”。气科院赵平研究员牵头的“第三次青藏高原科学试验—边界层与对流层观测”荣幸入选十大科技进展。该活动是在中国科协指导下，31项来自高校和研究所的成果由中国科协生态环境产学联合体成员单位和两院院士推荐，经公示、初选和15位院士专家终选，产生了“2020年度中国生态环境十大科技进展”。该评选活动旨在反映生态环境科技领域前沿发展动态，引领生态环境领域技术创新，为我国生态环境保护和生态文明建设提供科技支撑。中国科协生态环境产学联合体是为贯彻落实习近平生态文明思想和全国生态环境保护大会精神，在中国科协指导下，由环境、生态、气象、地理、农、林、土壤、地质、海洋、水利、可再生能源11家全国学会，7家行业领军企业，5家代表性高校科研机构，6家公益组织于2018年9月共同发起成立，旨在联合科技界、产业界等社会各方力量，践行绿色发展理念，促进科技协同创新，服务生态治理现代化，加快推动绿色经济发展，助力打好污染防治攻坚战，促进国际交流与合作，为全球生态文明建设做出积极贡献。生态环境部部长中国环境科学学会理事长黄润秋担任首届主席，联合体秘书处设在中国环境科学学会。

2021年6月8日，华东空管局气象创新实验室主任陈志豪应邀访问南京气象科技创新研究院，并做了题为“航空气象业务与进展”的学术报告。陈志豪主任长期在民航气象业务一线工作，对航空气象业务有丰富的经验，对航空气象领域的前沿技术有深刻的了解，参与筹建了华东空管局气象创新实验室，并担任实验室主任。报告中陈志豪主任介绍了当前航空气象业务的现状，其多部门联动、社会效益明显的特征尤为突出；展示了华东民航气象中心与高校、科研院所、软件开发企业等联合，在数值预报系统建设、航空气象产品研发、强对流天气短临预报系统开发、视频反演能见度等方面开展的工作及取得的成绩。这些工作紧扣航空气象业务需求，为创新院后期开展航空气象方面的科研工作提供了良好的借鉴。报告结束后，创新研究院科研人员与陈志豪主任进行了深入的交流和讨论，双方均希望后期在针对航空气象的低能见度预警、新型探测设备应用等方面开展合作。

2021年6月9日，交通运输部路网监测与应急处置中心路网运行处蔚晓丹处长、江苏省高速公路调度指挥中心汤海学主任到访南京气象科技创新研究院，就交通气象方面开展合作事宜进行前期调研座谈，江苏省气象局服务中心副主任黄亮及创新研究院副院长、中国气象局交通气象重点开放实验室主任刘端阳，实验室骨干成员参加本次座谈。交通气象团队首席助理王宏斌博士向来访专家介绍了创新研究院整体情况及中国气象局交通气象重点开放实验室的发展历程，从夯实交通气象观测基础、开创交通气象特色优势、推动交通气象示范规范等多方面展示了交通气象实验室的科研成果与科研实力。蔚晓丹处长、汤海学主任与实验室成员针对交通运输部对气象精确预测预警需求的一些热点、难点问题开展了热烈讨论，为实验室今后的研究方向提供了思路，建议从保障路网通行安全、细化应急处置方案等具体需求出发，真正做到科研成果落地，为交通部门提供强有力的行业支撑，助力高速公路准全天候出行。

2021年6月10日，中国科学院大气物理研究所罗德海研究员访问气候与气候变化研究所，在科技创新论坛做了题为“大气环流变异的非线性多尺度相互作用理论及其应用：海温和北极海冰减少对极寒天气的影响”的学术报告，报告会由祝从文副所长主持。罗德海研究员的报告从国际上已有的外强迫、大气环流内部变化和中纬度天气气候之间联系的相关理论出发，引出了如何分析天气尺度波激发次季节大尺度环流异常的问题，介绍了大气阻塞、北大西洋涛动（NAO）和太平洋北美型（PNA）形成的行星尺度波与天气尺度波相互作用的非线性多尺度相互作用统一理论模型（简称UNMI模型），为阻塞、NAO和PNA问题的解决开辟了一条新路。基于该理论模式所提出的经向位涡（PV）梯度的大小是联系北极和中纬度的桥梁，用模式解释了北极增暖对阻塞反气旋环流等周期、强度和移动的影响。参会科研人员、研究生等围绕报告内容与罗德海研究员进行了深入交流，了解UNMI模型，将对完善和优化气候所次季节至季节预测理论研究起到积极的借鉴作用。

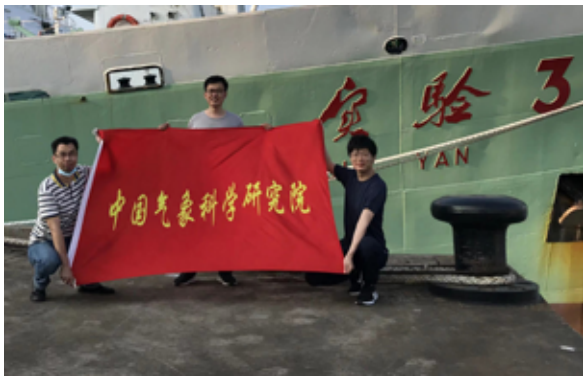

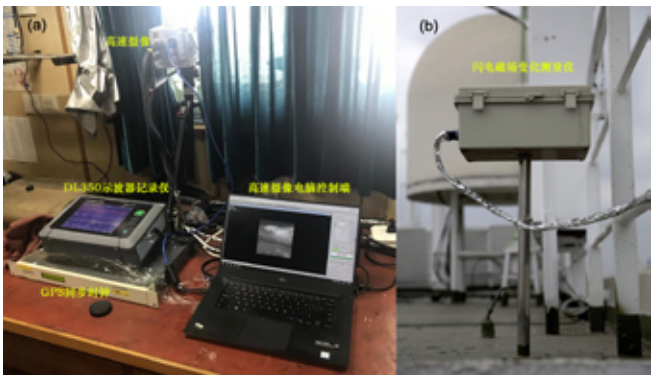

2021年4月5日至6月20日，灾害天气国家重点实验室武斌与来自不同单位的34位科考队员搭乘“实验3”号科考船赴东印度洋参加了国家自然科学基金委组织的综合科学考察。国家自然科学基金委在2010年设立了“国家自然科学基金委印度洋综合航次”共享航次计划，目的是通过对东印度洋进行多学科综合交叉调查，深入对该海域海汽过程的认识，调查海洋大气环境特征变化，增强对该海域大气环流季节特征的理解。中国科学院南海海洋研究所于2010年组织实施了首次东印度洋海洋科学考察，至今已完成12个航次任务。东印度洋海洋–大气综合科学考察极大地促进了海洋、环境、大气等多学科的交叉和融合，获取了丰富的热带海洋大气环境观测数据，并取得了丰硕的科研成果。武斌此行开展了海洋强对流闪电综合探测，这是国内首次针对海洋闪电的观测试验。此次试验主要是基于高时间分辨率高速摄像系统和高灵敏度闪电磁场变化测量仪，开展船载闪电综合观测试验，获取海洋闪电光学和磁场变化同步资料，建立海洋强对流闪电光电综合观测数据集，研究海洋强对流发生、发展演变过程中闪电活动的时空分布特征、演变规律和放电过程的细节特征，揭示海陆闪电放电特征差异及其机理。此次出海观测获取了东印度洋海域闪电光学和磁场变化同步资料，促进了闪电观测与海洋–大气研究方向的交叉和融合，还为后续开展海洋闪电精细化观测和建立两洋一海区域闪电监测网奠定了基础。

2021年6月22日，南京气象科技创新研究院举办了一场青年学术报告交流会，应气象探测团队首席助理诸葛小勇副研究员和高影响天气团队成员张树时助理研究员共同邀请，中央气象台短期预报副首席张夕迪工程师到访创新研究院并做了题为“2020年长江中下游极端梅雨特征和预报偏差分析”学术报告，创新研究院各团队成员参加了报告会。张夕迪工程师主要从事定量降水、灾害性天气以及中小尺度天气系统预报业务和研究工作。报告中，张夕迪工程师首先介绍了6—7月的极端梅雨案例，详细分析了极端梅雨的基本降水特征和大气环流特征，并从预报检验和偏差角度分析了数值模式应用的效果。张夕迪工程师表示，在日常预报工作中常用模式检验、集合预报、多模式对比应用等方法，但针对对流性降水强度和位置的预报结果仍存在较高的不确定性。今后将把研究重点放在对流强度、极端事件的分析上，为预报工作解决难点问题提供技术支撑。与会人员就报告内容与张夕迪工程师进行了深入交流与讨论。

2021年6月21—25日，生态与农业气象研究所王培娟副所长、谭凯炎、马玉平、王旗一行4人赴我国粮食主产区之一的东北三省开展调研。结合线下与线上会议座谈以及发放调查问卷的方式，调研团先后在黑龙江省气象科学研究所、吉林省气象科学研究所和辽宁省生态气象和卫星遥感中心详细了解了农业气象模式在当地气象业务服务中的应用现状、发挥的作用以及未来的应用需求等情况。调研团成员马玉平副研究员介绍了气科院自主研发的“中国农业气象模式CAMM1.0”，现场演示了模式的运行过程，并与当地农业气象业务及管理人员探讨了CAMM1.0应用推广的方式方法。调研团还参观并详细询问当地农业气象业务服务平台的相关内容。调研工作随后在当地的水利、农业等管理部门进行。在各省气象部门人员陪同下，调研团先后赴黑龙江省水利厅、黑龙江省农科院、吉林省通榆县农技推广站、辽宁省昌图县农村农业局、朝阳市农村农业局、植保站等部门，开展了当地农业种植及农田灌溉情的调研，并了解了农业生产部门或个体农户对气象精细化服务的具体需求。实地调研资料对农业气象模式的改进将发挥重要作用，未来对中国农业气象模式CAMM1.0的进一步优化也将不断展开，以期使农业气象模式成为我国粮食安全生产气象保障服务、降低农业气象灾害、确保粮食高产稳产的重要工具。

2021年6月24—26日，中国气象科学研究院–南京信息工程大学次季节–季节研究联合中心在北京召开了第六届学术研讨会。联合中心的宗旨是合作创新，打造一流科研团队，提高我国次季节–季节预测能力。会议由气科院气候与气候变化研究所主办，祝从文研究员和李天明教授共同主持，来自气科院、南京信息工程大学、北京大学、北京师范大学、中山大学、中国地质大学、中国科学院大气物理研究所、国家气候中心、天津市气候中心的科研业务人员和研究生共70余人参加了研讨会，同时开设了网络会场。夏威夷大学王斌教授、北京大学钱维宏教授、中山大学刘飞教授，中国科学院大气物理研究所凌健研究员，以及北京师范大学杨静教授应邀与会，并围绕MJO的传播理论以及模拟、中高纬度次季节波动、海气相互作用与季节内振荡的关系等方面做了特邀报告。研讨会安排口头报告22个，与会人员就MJO的物理机制及其数值模拟、数值模式次季节预报、极端事件等多个研究领域的科学问题进行了深入研讨。联合中心还为青年科研工作者的交流合作和研究生培养搭建了良好的学术平台，此次学术研讨会共有18名研究生对自己的研究成果进行了墙报展示。

2021年7月12日，南京气象科技创新研究院第一届理事会第三次会议在南京召开。中国气象局副局长、创新研究院理事会理事长宇如聪在讲话中指出，在江苏省人民政府和南京市人民政府的大力支持下，创新研究院建院开局工作稳定推进、成效显著，下一步要明确定位、砥砺前行，遵循“国际标准、国内示范、江苏先行”的定位，以高标准高质量做好气象科学研究工作。会议听取了创新研究院2021年上半年工作进展报告，审议通过了创新研究院法定代表人变更事宜，各理事会成员分别就创新研究院年度工作进行咨询并提出建议。宇如聪副局长围绕新时期气象事业高质量发展提出了具体意见，要充分促进科研和业务紧密结合，发挥自身优势，持续做好大风强对流天气和交通气象科学研究，面向各级需求、服务江苏地方经济发展。要合理规划好创新研究院科研能力建设，尽快打造出亮点成果，强化卫星遥感数据开发，加快多尺度模式成果研发及应用，在中国共产党成立100周年之际，在第二个百年奋斗目标中展现创新研究院的风采。创新研究院未来要尽快形成一套持续稳定发展的举措，关键做到管理、专家等理念一直保持先进；要充分发挥平台优势，与高校、企业建立广泛合作，强化人才培养，进一步打破唯职称、唯资历的旧标准，以能力和水平为先，不拘一格提拔人才。

2021年7月12日，气科院机关和大气成分所青年理论学习小组联合策划举办了全院青年理论学习小组联合学习报告会。张小曳院士应邀为全院青年人员做了题为“我国碳中和战略意义及气象青年使命担当”的报告，院党委副书记李慧出席活动并讲话，院机关联合青年理论学习小组领学人王皓哲副处长主持报告会，各研究所及南京气象科技创新研究院青年理论学习小组成员线上聆听了报告。张小曳院士的报告以“合道而顺德的发展之路”“绿水青山就是金山银山”“为国家需求而科研，让人生与时代环环相扣”3个主题，从气象防灾减灾、应对气候变化及绿色低碳发展等多重关系角度，结合中国气象事业的使命与担当，介绍了我国碳中和的前进方向，对今后产业格局的影响，以及科研人员在国家战略问题下的人生选择等问题。张院士从基础的科学概念切入介绍了人类活动对于天气和气候的影响，通过回顾温室气体观测背后的故事及IPCC国际关注的故事，引出我们国家碳中和目标，是通过平衡人为二氧化碳排放量与去除量，或者完全消除人为二氧化碳排放量，实现净二氧化碳零排放。张院士指出，碳中和是我国贯彻习近平生态文明思想做出的一项重大战略举措，中国气象局的科技人员尤其是气科院的科技人员应扎扎实实用习近平生态文明思想武装头脑、指导实践和推动工作，高质量推出研究成果，力争在重大问题研究上不断取得突破。碳中和中的科技问题主要集中在替代、增汇和效果评估等几大方面，他认为气科院具有扎实的科研基础、完备的科研条件，有能力也应当在碳源汇动态变化、风和光能源利用以及碳中和对天气、气候变化和环境影响等研究工作中牵头并做出巨大贡献。最后，张院士从他求学、治学的历程和感悟出发，勉励青年科研人员要培养恒心和定力，力戒浮躁浅薄，要树立远大理想，坚持为人民服务，不忘科研初心，将自己的人生选择同国家发展大势紧密结合。

2021年7月14日，应气象探测团队首席助理诸葛小勇副研究员邀请，英国雷丁大学顾剑峰博士在南京气象科技创新研究院举办的年度第2期气象科技论坛上做了题为“Intensification of Idealized Tropical Cyclones in Directional Shear Flows: Balanced Dynamics and Role of Moist Convection”（方向性切变环境中的理想热带气旋增强机制：平衡动力学及湿对流的作用）的学术报告。论坛由高影响天气研究团队首席助理王明筠副研究员主持，各单位相关科研人员通过线上线下方式参加了报告会。顾剑峰博士主要从事台风动力学、对流动力学及参数化、大涡数值模拟和大气热力学等研究，在多个大气科学权威学术期刊发表文章10余篇，主持及参与多个自然基金项目。报告主要从平衡动力学及湿对流在其中的作用两个方面阐述了理想热带气旋在方向性切变气流中的强度变化。报告指出，当环境气流的切变方向随高度发生变化时，即使深层垂直风切变完全一致，热带气旋的结构及强度变化也会呈现非常显著的差异；由方向性切变气流强迫出的随高度变化的涡旋倾斜所驱动的平衡动力学响应是影响结构差异的根本动力学机制；湿对流的组织、涡旋倾斜和移动，以及非绝热对流加热之间的反馈过程进一步放大了平衡动力学过程中的结构差异，造成热带气旋强度变化的不确定性。报告结果为理解实际台风个例中不符合经典理论的非对称结构特征提供了新的理论依据，指出强风切变下台风发生快速增强的一种新的可能途径，为进一步理解垂直风切变影响下台风强度变化的不确定性提供了新的视角。最后，参会人员就报告内容与顾剑峰博士进行了深入交流与讨论。

2021年7月15日，南京气象科技创新研究院举办2021年度第3期气象科技论坛，创新研究院副院长、交通气象研究团队首席刘端阳特邀江苏省气候中心正研级高级工程师谢志清、江苏省气象台高级工程师陈圣劼做学术报告，报告题目分别为“学习算法的中小河流暴雨洪涝风险评估预警技术”和“江苏强降雪事件成因机理及雪深影响因子研究”。此次论坛由交通气象研究团队首席助理王宏斌主持，相关业务和科研人员参加了报告会。谢志清正研级高工在报告中介绍了洪涝风险预警的业务需求以及关键科技问题和解决方法，并从气象业务实际需求探讨了机器学习算法的应用，通过致洪暴雨的天气学特征、淹没情景模拟和洪涝风险3个部分详细解释了特征因子与模型的选择，将致灾和灾损对应，努力提高洪涝风险评估智能化和自动化的水平。陈圣劼高工从预报员角度分享了她对强降雪灾害性天气的研究，以江苏强降雪事件为例分析了成因机理与积雪深度影响因子，最后与大家探讨了双偏振雷达观测数据在降雪预报中的应用。报告结束后，青年学者与2位专家展开了热烈的交流与讨论。

2021年7月16日，中国气象局人工影响天气中心在西安阎良组织召开西北区域人工影响天气能力建设项目新舟60国家作业飞机（B-651N）交付状态验收会，中国科学院大气物理研究所、空军工程大学及山西、甘肃、陕西、宁夏、青海和新疆等省（区）气象局专家参加会议。与会专家听取了项目汇报后认为，新舟60国家作业飞机（B-651N）的研制、生产、改装、试飞等过程严格按照相关规定执行，其飞行、大气和云降水探测、催化播撒、空地通信、任务系统供电、机载设备系统集成与改装性能符合项目初步设计和合同要求，可承担作业播撒、科学试验、效果评估、重大活动保障等业务科研任务。专家组一致同意通过交付验收。随着西北人工影响天气项目2架新舟60国家作业飞机的正式交付，将切实提高西北地区复杂气象条件下的飞机作业能力和空中云水资源开发利用能力。下一步，各方将继续加强协同合作，确保飞机高质量运行，建设效益达到最大化，尽快在西北地区乡村振兴、生态建设以及“十四运”等重大活动保障方面发挥经济与社会效益。

2021年6月15日至7月28日，在“第二次青藏高原综合科学考察研究项目”子专题“西风–季风协同作用与青藏高原强对流及闪电灾害”的支持下，灾害天气国家重点实验室和复旦大学雷电团队在郑栋研究员的带领下，与西藏自治区那曲市气象局合作开展了三维闪电探测网的建设和夏季高原闪电活动观测试验。那曲是高原重要的交通枢纽，也是重要的虫草产区和畜牧业区。那曲地区是高原腹地对流活动和闪电活动最为活跃的区域，其雷暴过程具有发展迅速、持续时间短、空间尺度小的特点，因此其包含闪电等灾害天气的预警预报较为困难。此次高原试验期间，实验室雷电团队携带自研的新一代电低频电场探测阵列（LFEDA）和雷电临近预警系统，在海拔4500～5000 m那曲北部雷暴和闪电活动高密度区建设了包含10个子站的闪电探测网，在那曲气象台搭建了雷电临近预警平台，初步形成了在那曲当地开展三维闪电活动观测和雷电临近预警的条件。雷电临近预警系统通过融合应用多种气象观测资料，给出0～1 h雷电发生概率产品，是国内首个专业化的雷电预警服务系统，多年来通过不断研发和完善，已经更新了多个版本。野外试验期间，实验室姚雯正研级高工为那曲市气象台安装了该系统，并进行了调试和教学培训。通过雷电临近预警系统在高原地区的试运行，雷电团队将优化系统在高原地区的参数设置，为正式投入服务奠定基础。

2021年7月30日，灾害天气国家重点实验室、国家气象中心和河南省气象局在北京联合组织召开“21•7河南极端暴雨研讨会”，围绕暴雨过程的机理、预报和服务及防灾减灾工作开展研讨。中国工程院院士李泽椿、陈联寿，中国科学院院士穆穆，来自中国气象局、应急管理部、水利部、河南省科技厅和省教育厅等单位的代表，以及北京大学、复旦大学、南京大学、郑州大学、南京信息工程大学、国防科技大学、中山大学、成都信息工程大学和中国科学院大气物理研究所等高校和科研院所的专家参会。中国气象局副局长宇如聪与会，气科院院长端义宏主持会议。会议设有河南省气象局和湖北省气象局分会场，并开通了直播，参加直播的人数超过1500人。围绕2021年7月17—22日河南省极端暴雨过程会议安排了3个主题报告，分别由国家气象中心的陈涛首席、河南省气象局应急与减灾处郑世林处长、灾害天气国家重点实验室梁旭东主任就河南极端暴雨天气实况、物理过程、预报难点和多尺度机理进行了交流，与会专家就此次极端暴雨过程分析的着眼点、下一步科研和业务工作的重点等问题提出了意见和建议。专家认为，“21•7”河南极端暴雨发生在大气环流形势异常的背景下，并受到多尺度系统和地形等影响，形成和发展过程中存在复杂的科学问题。以河南暴雨为例，在极端暴雨的形成机理、数值预报、气候变化和城市化影响等方面，亟待进一步深入研究和探索。与会专家建议，针对此次极端气象灾害过程，要利用好前期参与各项国家重大科学项目中积累的对灾害天气形成机理的科学认识，对此次过程进行系统、多角度和多方位的分析，更加深刻地认识其过程的物理特征和极端性，为以后的极端天气过程的预报预警提供参考。

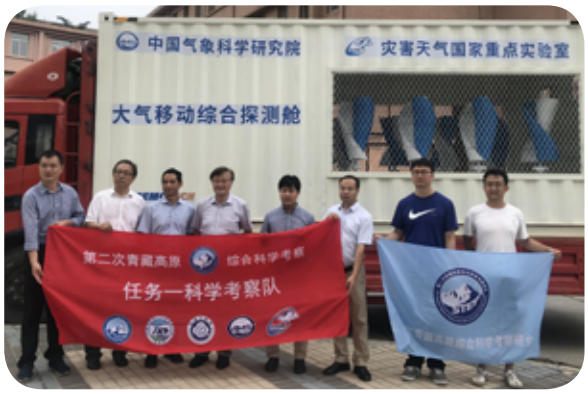

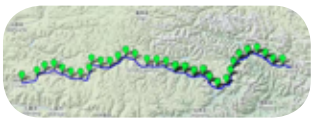

2021年7月15—31日，灾害天气国家重点实验室青藏高原研究团队组织多家单位开展了首次青藏高原气象与环境移动观测试验。参加单位包括青海省气象科学研究所、西宁市气象局、玉树州气象局、达日县气象局、拉萨市气象局、林芝市气象局、波密县气象局以及北京瑞蒙特科技有限公司、北京厚力德仪器设备有限公司。2019年初，徐祥德院士提出了大气三维结构综合动态探测思路，经过2年多的试验方案设计、仪器选型调研、观测平台研制等前期准备，实施了本次观测试验。通过搭载微波辐射计、太阳短波和长波辐射表、气溶胶激光雷达、MAX-DOAS在线监测系统、气象与环境微站等仪器设备，获取了中国东部灾害天气上游强信号区——青海和西藏东南部高时空分辨率的温湿度和水汽三维结构信息以及气溶胶光学厚度与SO_2、NO_2柱总量等大气环境动态探测资料，首次实现了青藏高原地区气象与环境的移动垂直探测，为发展“线–面”结合的大气三维结构动态探测信息群优化提取与融合同化新技术、研究青藏高原地区中小尺度天气系统的形成机理和下游地区灾害天气的预报改进技术，以及大气环境的时空演变奠定了坚实的数据基础。试验期间途经海拔高度在4700 m以上的米拉山、巴颜喀拉山、玛崩山等垭口以及天气多变的三江源、川藏公路地区，科考队员们克服缺氧、烈日和寒风等困难，及时解决仪器故障、做好观测记录，保障了观测试验的顺利进行。

2021年7月27日至8月4日，由气科院徐祥德院士任总指挥，青海省气象科学研究所所长周秉荣任副总指挥，气科院、长江科学院西宁分院、国家气象中心、国家气候中心等单位联合组成的三江源区综合科考分队，围绕第二次青藏高原综合科学考察任务，先后赴青海省的海北、海南、玉树、果洛等地开展野外科学考察。考察队一行驱车从西宁市出发，一路考察了祁连山东段的垂直植被分布、岗什卡雪峰的环境、水位连续回升的青海湖流域、共和盆地的风沙地貌，途经黄河源头、长江源头干流段的通天河、澜沧江源头支流的子曲河，翻越了海拔4800 m的巴颜喀拉山，攀登并近距离目睹海拔4700 m的阿尼玛卿雪山、冰川，历时9天圆满完成考察任务。考察队调研了中国气象局生态气象野外试验基地海北站及隆宝站等基层气象台站的冻土、土壤湿度观测等设备。重点考察了青藏高原东部不同海拔梯度下高寒植被与季节性冻土环境变化，调研了三江源及周边地区植被、生态环境、湿地面积、湖泊数量、冰川冻土等固态水体的变化现状及对“亚洲水塔”水分循环变化的影响。探讨了青藏高原东部山谷地形与河湾区云降水形成原因，分析了季节性冻土形成维持机制。考察队还探访了国家能源集团国能青海黄河玛尔挡水电开发有限公司，调研讨论了区域气候对水库布设的影响及水电调蓄对周边地区旱涝灾害及生态影响等问题。考察结束后，在西宁市召开了科考总结研讨会，会议由青海省气象局副局长高顺年主持，青海省科技厅领导到会。徐祥德院士做了“第二次青藏高原综合科学考察计划与科考进展”的报告，重点介绍了科考的内容、科学目标和取得的进展，并提出了三江源水循环及生态观测建设与布局的新思路。长江科学院西宁分院谭德宝院长做了题为“气候变化对三江源区水循环及生态环境影响科学考察与科学应对思考”的报告，提出了加强三江源区天-空-地-水立体观测的建议。青海省气象台、气候中心及气科所的负责人分别介绍了青海省气象业务和科研情况。




2021年8月初，青藏高原与极地气象科学研究所在西藏自治区嘉黎县圆满完成了边界层梯度通量观测站的建设工作。嘉黎边界层梯度通量观测站的规划建设得到了中国气象局各级主管领导的高度重视，是气科院与西藏自治区气象局联合支持“第三次青藏高原大气科学试验”计划、推动青藏高原野外观测科学试验基地建设的重要组成部分。嘉黎边界层梯度通量观测站位于西风与季风交汇地区的冰川环境背景下，在该站进行复杂下垫面边界层通量和陆气相互作用观测，有助于深入认识高原亚寒带季风湿润气候特征，补充完善青藏高原区边界层通量综合观测网，填补高原中东部那曲地区边界层科学试验观测站的空白，是中国气象局高原科学试验观测基地建设的重要一环。此次在嘉黎建立的梯度通量观测站的观测要素包括：5层空气温湿度、5层风速和风向、5层土壤温湿、土壤热通量、光合有效辐射、净辐射、雪深、CO_2/H_2O通量等。观测内容的制定前期经过专家组论证科学合理，能够实现对该典型区域陆气相互作用过程的系统性观测。

2021年8月5日，中国气象局副局长、局直属机关党委书记沈晓农同志亲临大气成分与环境气象研究所，将中央和国家机关优秀共产党员奖章、荣誉证书和奖金颁发给孙俊英同志。直属机关党委张俊霞副书记，气科院端义宏院长、李慧副书记出席。 沈晓农副局长着重介绍了中央和国家机关优秀共产党员、优秀党务工作者和先进基层党组织表彰大会的盛况，以及党和国家领导人对此次大会的重视，并殷切希望成分所党员同志向榜样看齐，再接再厉，为新时代下我国的气象事业奉献出更多更大的力量。端义宏院长也对孙俊英同志表示祝贺，赞扬其兢兢业业、长期坚守科研岗位的工作态度与作风。

2021年8月11日，北京科技大学王存海副教授应邀访问气科院，并做了题为“参与性介质内偏振辐射传输的数值解法”的学术报告。灾害天气国家重点实验室卫星团队首席科学家翁富忠教授主持报告会。王存海副教授主要从事光热辐射传输、微纳尺度导热、耦合流动传热等方面研究，主持并参与多项国家自然科学基金项目、创新研究群体项目。他从辐射光线的偏振特性进行阐述，详细分析了求解参与性介质内偏振辐射传输的多尺度数值解法，以及这些数值方法在求解非均匀介质中瞬态矢量传输的具体应用案例。相关领域的学者和研究生通过线上和线下等方式参加了此次报告会，针对王存海团队开发的参与性介质内偏振辐射传输的多种数值解法应用到中国快速辐射传输模式ARMS中的前景，气科院卫星团队成员与王存海副教授进行了热烈的讨论，并达成了初步合作意向。

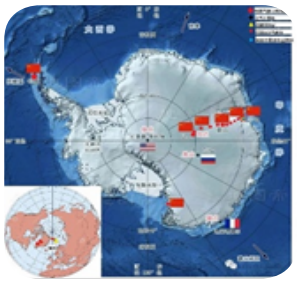

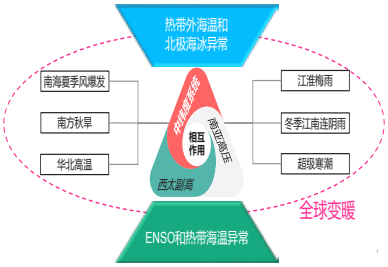

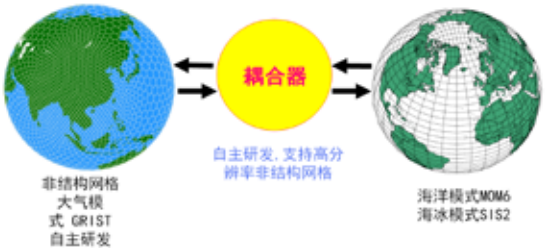

2021年8月，气科院对“极地大气科学野外观测基地”等7项基本科研业务费重点项目组织开展了验收工作，最终7项项目全部通过验收，其中“极地大气科学野外观测基地”项目获得优秀。（1）丁明虎研究员主持的“极地大气科学野外观测基地”项目建设了2个地面气象业务观测站、1个极地梯度观测站、17个低温/超低温自动气象站、1个大气本底站、1个臭氧总量业务监测站的极地综合监测体系，在超低温观测技术等方面获得突破性进展。基于此气科院在极地气候变化评估、多圈层相互作用机理、大气环境变化及其源汇特征研究等方面取得快速进展。（2）周广胜研究员主持的“固城生态与农业气象试验基地建设”项目重点解决试验基地正常运行所必须的作物灌溉给水管道改造、模拟作物适应气候变化的大型人工气候箱购置、大气成分观测场建设等，保障了业务观测、科学试验及数据传输的正常高效运行。（3）张阳研究员主持的“广州野外雷电试验基地建设及试验”项目补充及建设了人工引雷试验场和高建筑物闪电观测站的基础观测条件，研发了实时低频全闪探测网和新一代连续干涉仪，并引进了闪电成像阵列等。建立的相关观测数据集支撑并促进了雷电及雷暴的前沿研究。（4）刘伯奇副研究员主持的“次季节至季节气候预测理论和方法研究”项目揭示了三大洋海温异常共同影响东亚季风环流、中国降水和气温次季节变化的机制，建立完善了季节至次季节中国夏季降水和冬季温度多因子统计降尺度预报模型等，完善了亚洲大范围降水和气温异常成因动力诊断和数值模拟平台（VIADAS），并通过了中试项目准入申请。（5）容新尧研究员主持的“高分辨率海陆气冰耦合关键技术研究”项目完成了对CAMS-CSM模式的系统评估，建立了ESGF-node数据发布节点并成功发布CAMS-CSM的CMIP6数据，发展了基于CAMS-CSM模式的高分辨率耦合模式系统，发展海洋和大气同化系统，完成了39年气候回报试验，实现了实时滚动预报并应用于汛期气候预测。（6）周莉研究员主持的“生态文明建设绩效考核气象归因研究”项目构建了植被生态质量综合评价指标，提出了植被生态质量变化气象贡献率和人为贡献率分离的方法，发展了植被生态质量变化的气象贡献率评估技术，研制了针对生态文明绩效考核需求的气象条件贡献率评价系统。（7）楼小凤和苏正军研究员主持的“吸湿性催化剂对暖云过程影响室内试验研究”项目在国内首次开展了气溶胶和吸湿性催化剂的膨胀冷却核化过程及其对云滴谱参数影响的室内试验研究，并优选吸湿性催化剂和催化技术方法，搭建了我国研究暖云成云过程和吸湿性催化剂的实验研究平台。

2021年9月6—8日，可持续发展大数据国际研究中心成立大会暨2021年可持续发展大数据国际论坛在北京国际会议中心圆满召开，宣告全球首个以大数据服务联合国2030年可持续发展议程的国际科研机构成立。2021年是中国恢复联合国合法席位50周年，该中心的成立是中国为支持联合国在国际事务中发挥核心作用的实质举措，为全球科学家参与和推动实现可持续发展目标提供了全新的平台。开幕式当天“地球大数据促进可持续发展目标监测和评估成果展”正式开展。气科院赵俊芳研究员的案例“森林固碳作用大”入选SDG13气候行动并参加展览。SDG13气候行动的主要目标是采取紧急行动应对气候变化及其影响。展览期间，中国科学院院长侯建国院士和原院长白春礼院士、可持续发展大数据国际研究中心主任郭华东院士等领导和专家参观了赵俊芳的“森林固碳作用大”展板，并针对我国森林固碳潜力科学问题进行了讨论。

2021年9月9日，气科院举办了以“基于微波遥感的旱涝监测”为主题的科技创新论坛（第335期），邀请国家卫星气象中心李贵才研究员、北京大学万玮博士和气科院生态与农业气象研究所房世波研究员做了学术报告。来自气科院、国家卫星气象中心、国家气象中心、中国气象局气象探测中心、中国科学院植物研究所、北京大学等高校及科研单位的多名教授、学者及研究生参与了学术交流，房世波研究员主持了论坛。李贵才研究员做了题为“风云气象卫星晨昏轨道卫星及其应用潜力”的报告；万玮博士对利用GNSS-R卫星数据反演土壤湿度的方法进行了介绍；房世波研究员做了题为“干旱和涝渍的卫星遥感监测方法”的报告。与会专家围绕微波和热红外遥感的旱涝监测方面的内容进行了交流与讨论。报告会后召开了房世波研究员担任项目负责人的风云卫星应用先行计划2021项目“FY-3E微光成像和GNOS Ⅱ反射信号监测火点、洪涝和干旱”的启动会议，项目组人员就任务分解、阶段性目标和预计成果产出进行了讨论和计划落实。

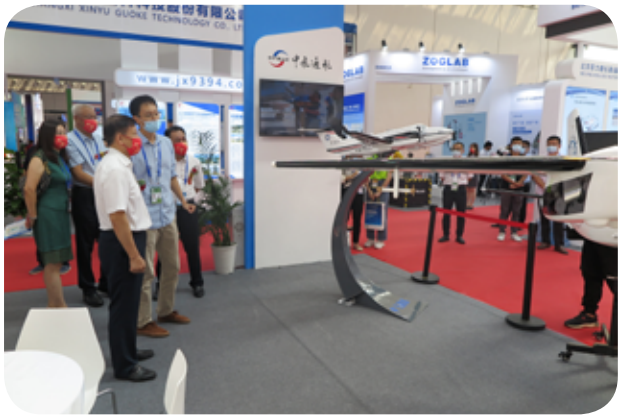

2021年9月10—13日，第18届中国–东盟博览会暨第6届中国气象装备与服务展在广西壮族自治区南宁市举办，本届展会的主题为“智慧气象服务东盟”，突出数字经济合作框架下“一带一路”国家共同防御气象灾害的理念。“人工影响天气作业装备与服务”是本届展会主题板块之一，中国气象局人工影响天气中心联合中航西飞民用飞机有限责任公司、中飞通用航空有限责任公司、三维时空三家企业共同参与，通过新舟60国家作业飞机和空中国王350国家作业飞机模型、人工影响天气作业VR虚拟体验、视频、展板、宣传册等多种方式展示了西北区域人工影响天气能力建设项目的成果。此次成果展示，吸引了中国气象局领导、行业专家、媒体以及众多观众的目光，成功展示了西北区域人工影响天气能力建设项目的成果、中国人工影响天气重大技术装备与科技水平，有助于使我国先进的气象装备“走出去”，从而不断推动中国以及东盟国家气象事业的发展与进步。

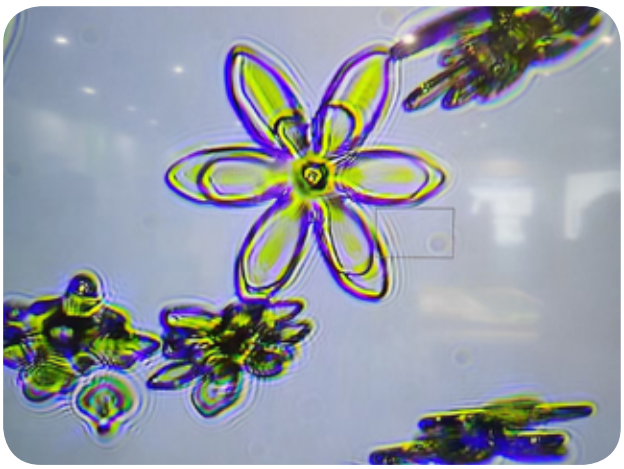

2021年9月16日，中国气象局公布了2021年气象科技活动周的优秀组织单位和优秀展项评选结果。由中国气象局人工影响天气中心和中国科学院大气物理研究所联合研发的 “人工冰晶模拟系统”被评为气象科技活动周武汉主场优秀展项。2021年5月22—28日，人工影响天气中心联合中国科学院大气物理研究所参加了气象科技活动周武汉主场活动，通过人工冰晶模拟系统向公众形象直观地展示了人工影响天气的原理。目前，我国大部分地区进行的人工增雨（雪）工作主要是针对层状云进行作业，其基本科学依据是Bergeron（贝吉龙）过程，人工冰晶模拟系统模拟和演示了此过程，可对碘化银人工催化原理和过程进行直观的展示。有趣的试验和美丽的人工冰晶吸引了很多观览者的目光，除了为公众讲解外，人工影响天气中心和中国科学院大气物理研究所也积极参与了气象科技周的网络直播活动。

2021年9月6—17日，为提升极地气象考察队员的业务能力，保障中国第38次南极考察队气象考察顺利进行，气科院联合国家海洋环境预报中心举办了为期2周的气象业务培训班。来自山东省气象局、湖北省气象局、云南省气象局和国家海洋环境预报中心的预选队员参加了培训。培训主要分为3个部分：气象观测培训、大气成分培训和南极天气预报培训。青藏高原与极地气象科学研究所卞林根、逯昌贵、汤洁、郑向东、张东启、丁明虎、田彪、张文千、朱孔驹和马文哲老中青三代参加过南极考察的“极地人”担任培训班主讲老师。在他们的讲授下，队员全面学习了极地地面气象观测业务和仪器维护维修、大气成分仪器操作、故障排除和数据处理、地基探测等气象业务知识和技能。2021年9月17日进行了结业考试，队员们以满意的答卷完成了培训，为将来为期1年的考察做好了知识和技能储备。

2021年9月23日，人工智能气象应用研究所召开学术交流会，来自宁夏回族自治区气象台的访问学者张肃诏应邀做了学术报告，会议由王亚强所长主持。张肃诏介绍了自己之前的科研工作，包括基于雷达数据的水平和质量控制算法，宁夏典型工业重污染过程和成因分析，随机森林在宁夏汛期分级降水的应用，贺兰山暴雨过程的环境客观分型特征和应用CNN-LSTM模型对暴雨的研究等，研究内容广泛，令人耳目一新。与会者针对张肃诏报告中的科学问题进行了讨论，提出了建设性的改进意见。王亚强所长结合团队的科研工作方向给予了指导和总结。

2021年9月24日，国家重点研发计划“主要经济作物气象灾害风险预警及防灾减灾关键技术”项目中期检查会在北京召开。农业农村部科技发展中心项目监督处蔡彦虹副处长、中国气象局科技与气候变化司科技项目处任颖副处长、气科院高云副院长等领导参加了会议。会上项目负责人王春乙研究员针对项目任务完成情况、重要研究进展以及下一步研究重点进行了汇报。专家组成员听取汇报后认为，项目各项研究工作达到了中期考核指标要求，通过中期检查。截至目前项目取得了丰硕的成果。研制了主要经济作物气象灾害综合风险动态评估理论与方法，构建了基于灾变过程的主要经济作物气象灾害指标体系，研发了主要经济作物气象灾害精细、动态监测预警技术，研发了主要经济作物抗逆减灾生化制剂，制定了经济作物综合减灾技术，研发了主要经济作物气象灾害天气指数保险，开发了经济作物气象灾害监测预报预警信息服务平台。根据研究成果发表论文45 篇，SCI 14篇，出版专著2部，编制图集1部，制定标准3项，获批软件著作权19项，获取专利19项。综合防控技术成果推广应用约14.67万公顷，培训人员1500人以上，制作主要经济作物气象灾害监测预警专题服务产品140余份。

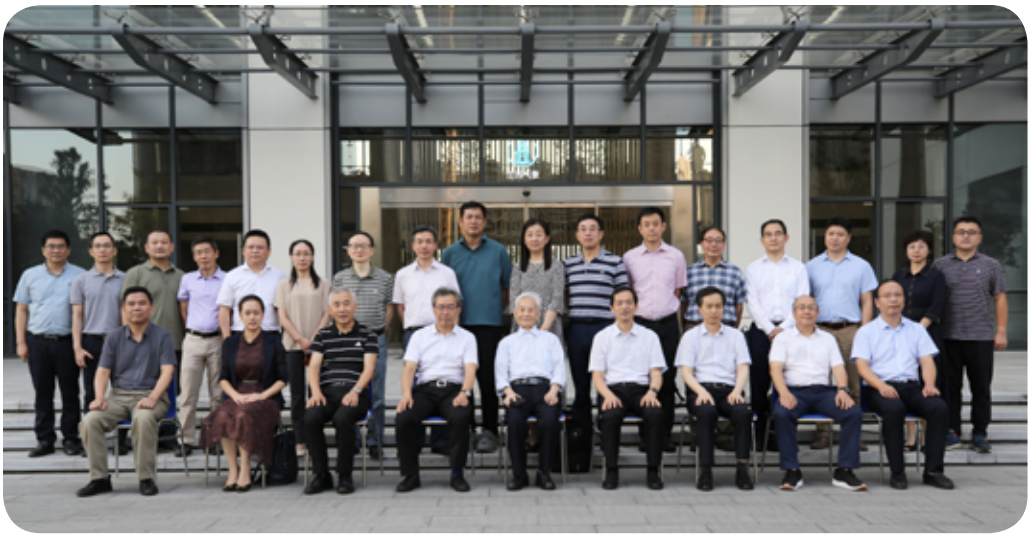

2021年9月26日，南京气象科技创新研究院第一届学术委员会第二次会议在南京召开。会议由学术委员会主任符淙斌院士主持，来自气象部门、科研院所、知名高校的学术委员会委员、特邀专家和会议承办单位领导出席会议。创新研究院副院长刘端阳做了创新研究院年度进展报告。对此，与会领导和专家在给予充分肯定的同时，针对人才队伍建设、团队协同发展、应用成果输出等方面提出了许多宝贵的意见和建议。与会专家建议，创新研究院要进一步围绕方向、凝练目标，在创新上寻求突破，在团队上加强合力，在特色上打造品牌，在应用上对标业务急需，在支持上争取多渠道，在机制上更加灵活。要更加充分利用江苏区位优势，努力打造国家级大气科学研究的创新平台，为国家气象科技创新发展提供先行先试的经验，为业务服务提供核心技术支持。

2021年9月27日，中国外交部发布了“地球大数据支撑可持续发展目标报告（2021）”。该报告围绕零饥饿、清洁饮水和卫生设施、可持续城市和社区、气候行动、水下生物、陆地生物等目标，面向可持续发展的实际场景，展示了包括单一指标进展评估和多指标综合评估的研究成果。该报告为联合国2030年可持续发展议程实现持续贡献中国科技界的一份力量。联合国可持续发展目标中设立SDG13“采取紧急行动应对气候变化及其影响”（简称:气候行动），主要聚焦减缓气候变化和适应气候变化影响，提高应对能力。气科院赵俊芳研究员的案例“气候变化对中国森林净生态系统生产力的影响”入选SDG13气候行动。案例基于国际共享数据集，利用基于个体生长过程的森林碳收支模型进行了1981年以来中国森林净生态系统生产力（NEP）的动态评估。研究结果显示，中国森林生态系统碳汇潜力巨大。其中，2011—2019年期间中国森林年平均净生态系统生产力为0.199 Pg（C）/a。案例研究结果可为准确评估森林在调节全球碳平衡以及维护全球气候等方面的碳汇作用，为中国碳中和目标的实现提供重要信息支持，也为正确评价中国森林在生态环境建设中的作用及全球气候变化研究等提供科学依据。

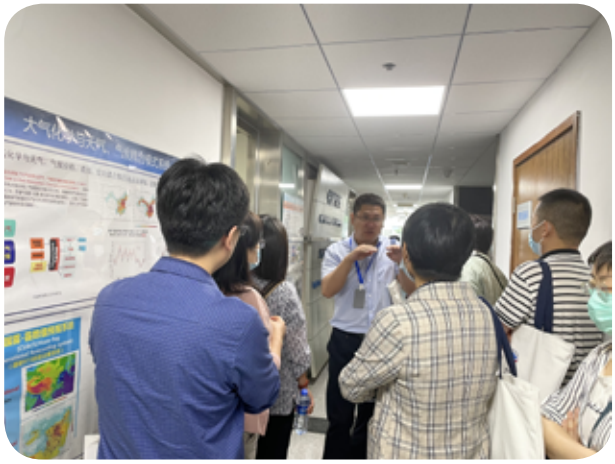

2021年9月27日，中国气象局气象干部培训学院气象部门高级专家研修班学员在气科院大气成分与环境气象研究所车慧正所长的带领下，来到大气化学重点开放实验室及14层观测平台进行了体验式教学。车慧正研究员首先详细介绍了实验室的发展历史以及成分所在基础观测、实验室分析等方面的研究现状。随后带领各位专家参观了气溶胶组分分析实验室、温室气体实验室等，介绍了各个实验室的大型仪器，并对部分研究成果进行了简要的介绍。参观过程中，专家们纷纷结合自己的研究领域与车慧正研究员进行了深入的探讨，并表示此次参观对于未来的工作具有重要的意义。

2021年9月27—28日，南京气象科技创新研究院2020—2021年度学术年会在南京召开。年会现场有来自北京大学、南京大学、南京信息工程大学、国防科技大学、河海大学、中山大学、复旦大学等多所高校的学者，中国科学院、上海台风研究所、成都高原气象研究所、中科曙光南京研究院、阿里巴巴达摩院等科研院所、有关企业和部门业务单位的专家、技术人员200余人，同时通过腾讯会议、Bilibili直播方式参会累计近万人。开幕式由创新研究院院长费建芳主持，中国气象局科技与气候变化司、江苏省科学技术厅、江苏省科协、南京市科技局等领导到会致辞。此届年会以“求是创新，协同发展”为主题，聚焦学科前沿进展、未来发展趋势，以及当下气象核心业务关键问题。主会场邀请吴国雄院士等多位知名专家学者做了特邀学术报告，内容涵盖天气气候、数值模式、卫星遥感、大气环境、灾害性天气监测预警预报技术与决策服务等方面。年会还设置了高影响天气、数值天气预报、大气探测3个分会场进行专题学术交流。此次年会学术报告精彩纷呈，提问踊跃，互动积极，学术氛围浓郁，为气象相关科研业务人员提供了一个展示科研成果、探讨学术问题的交流平台。

2021年9月28日，中山大学大气科学学院杨崧教授应邀访问了气科院，并做了题为“太平洋经向模态对ENSO作用的不确定性来源和未来预估”的学术报告。杨崧教授在全球和区域气候变化、全球季风、大气–海洋–陆地相互作用和气候可预报性等领域取得了多项具有国际影响的研究成果，创立了季风与厄尔尼诺相互作用动力学的新理论，并提出了目前全球季风研究和业务应用上最为广泛的韦伯斯特–杨崧指数。杨崧教授的最新研究发现，太平洋经向模态（PMM）的强度及其影响ENSO的效率具有正负非对称性，与风–蒸发–海温反馈和夏季深对流响应机制的正负差异有关。PMM影响ENSO的效率也受到海洋热容量先决条件的调控，即PMM对ENSO的影响主要是调制作用，并不能决定ENSO的潜在发展趋势。全球增暖能够增强风–蒸发–海温反馈的效率，从而增大PMM对ENSO的作用效果。该研究一方面明确了PMM对ENSO作用效率的正负非对称性和PMM对于ENSO发生发展的调制因子角色，为PMM应用于ENSO预测提供了参考；另一方面，发现了PMM对ENSO作用在全球变暖背景下的增强趋势，指出了PMM应用于ENSO预测的必要性。青藏高原与极地气象科学研究所副所长任宏利研究员主持会议，来自气科院、国家气候中心等多家单位相关领域的学者和研究生参加了报告会，并就报告内容及其他科学问题与杨崧教授进行了热烈的讨论。

2021年9月28日，国家卫星气象中心方翔副主任、卫星中心遥感应用室吴晓京副主任和王新研究员、卫星气象研究所寿亦萱研究员一行到南京气象科技创新研究院开展专题调研，江苏省气象局观测与网络处黄世成副处长、创新研究院曾明剑常务副院长和有关研发团队科技人员参加了座谈会。方翔副主任首先就近期中国气象局党组和庄国泰局长关于加强气象卫星在强对流、台风、暴雨等灾害性天气监测预警预报及数值模式中应用的指示精神、卫星中心目前在相关工作中的现状和下一步计划进行了简要介绍。同时介绍了风云卫星先行计划有关情况，希望通过风云卫星先行计划的实施，产生一批先进的算法和技术，提高风云卫星定量应用水平，并在执行过程中对相关的创新激励机制进行积极探索。创新研究院郑媛媛正研级高工、诸葛小勇博士、李昕博士、王宏斌博士分别就卫星资料在天气监测、短临预报、数据同化、交通气象中的应用研究进展进行了详细汇报。方翔副主任肯定了创新研究院在气象卫星应用技术研发方面取得的成绩，并就双方建立卫星遥感新技术互通合作渠道等方面提出了建议。中山大学大气科学学院闵敏教授、河南省气象台王新敏台长应邀参加了座谈会。

2021年9月29日，中国气象局人工影响天气中心和江西省气象局在江西九江联合召开了2021年国家（庐山）云雾物理试验基地外场观测试验启动会。来自北京大学，中国科学院大气物理研究所，南京信息工程大学，成都信息工程大学，32021部队，中国气象局人工影响天气中心，北京市气象局，河北省、宁夏和安徽省人工影响天气办公室，江西省气象部门的专家和技术人员，以及相关设备厂家和软件公司代表参加了会议。与会专家考察了庐山试验基地各观测点及现有设备布设情况，听取了2021年庐山外场试验方案汇报，并为今年试验顺利开展提出了宝贵的意见和建议。庐山地处典型东亚季风气候区，是良好的云雾降水观测试验场所。庐山云雾站自1959年成立以来便开始云降水和人工影响天气研究，于2015年恢复云雾–降水观测。依托正在进行的庐山云雾物理试验基地建设，2021年初完成云雾站观测平台和办公环境改造，并继续开展持续观测。庐山云雾物理试验基地由庐山云雾试验站、庐山气象局、庐山市气象局、柴桑气象局和仰天坪与小天池等多个山顶和山脚观测平台组成。此次启动的庐山云雾–降水观测试验，以庐山云雾站现有观测设备为基础，利用山上、山下其他站点现有观测能力，联合江西省气象局共同开展立体的秋冬季云雾–降水加强观测，同时将基地建设与相关科研项目结合，加强天然云雾宏微观结构研究，旨在为正在开展的庐山云雾物理试验基地建设起到积极推动作用。



2021年10月11日，科技部公布了批准建设的69个国家野外科学观测研究站名单，依托气科院建设的中国气象局固城生态与农业气象试验站位列其中。国家野外观测站是国家创新体系的重要组成部分。国家野外观测站面向社会经济和科技战略，依据我国自然条件的地理分布规律布局建设，是科技创新、学科发展和经济社会发展的有力支撑平台。2018年1月，固城生态与农业气象试验站被确定为中国气象局野外科学试验基地后，固城试验站围绕国家粮食生产安全气象保障服务需求，针对粮食作物生产的数量、质量与经济效益，以华北平原主要粮食作物生产的农业气象问题为研究对象，以农业气候资源与农业气象灾害为切入点，瞄准农业气象学、农业生态学、生态气象学国际发展前沿，以水、土、气、生等农业资源高效利用与农业环境保护为目标，利用现代新技术，重点开展主要粮食作物生产的气象条件与生态系统的野外监测和试验，研究农业气象指标、农业气象灾害影响与风险以及气候环境变化对农业生产影响适应评估的新技术与新方法；开展农业气象观测监测新方法与技术的研发、中试、示范和推广应用；开展农业气象的基础教学和在职培训以及科普工作。经过多年建设，固城试验站已形成集野外监测、科研、试验、示范、教学和科普于一体的综合支撑平台。

2021年10月14日，中国海洋大学陈显尧教授应邀访问气候与气候变化研究所，并做题为“北极快速变化可能的动力学机制”的报告，气候与气候变化研究所苏京志研究员主持报告会。陈显尧教授是国家杰出青年基金获得者，国家科技创新领军人才，主要从事海洋环流与气候变化研究，包括海洋年代际变异机制、海气相互作用、全球海平面变化、极地海洋与全球气候变化关系等方面，相关研究结果发表在*Nature*、*Science*、*Nature Climate Change*等高影响期刊上。陈显尧教授此次报告聚焦北极快速变化的成因这一国际热点问题，报告系统梳理了北极快速变化机理的研究现状、科学挑战，并给出详细解读。结合观测数据和CMIP模拟结果提出了一个新的观点：北大西洋多年代际的振荡可以通过海洋内部的热量输送影响北极海温变化，从而在全球变暖背景下，在多年代际时间尺度上调制北极变化的快慢。来自气科院多个部门的相关领域学者和研究生参加了报告会，并围绕报告主题展开热烈讨论。此次报告会对促进气候变化背景下气候系统变异成因机理研究，以及拓展对外合作将发挥积极作用。

2021年10月15日，气候与气候变化研究所召开2021/2022年冬季气候预测会商研讨会，会议由祝从文副所长主持，李建所长出席会议。基于气科院气候系统模式（CAMS-CSM）动力预测结果，蒋宁副研究员提出了未来ENSO预测意见，并根据当前海气相互作用特征和机器学习预测结果，预测2021年“拉尼娜”将继续影响。刘伯奇副研究员基于历史气候变化事实、CAMS-ASPS定量化统计预测，综合考虑北极海冰、热带太平洋和印度洋、南太平洋SSTA等因子的影响，结合CAMS-CSM动力预测结果和国际多模式集合结果、不确定性分析等，形成对2021/2022年冬季全国气温和降水异常的预测意见。基于此次会商研讨预计，2021/2022年冬季“拉尼娜”影响将持续，全国气温将以整体偏暖为主，但新疆西北部和东北北部气温可能异常偏低，同时呈现“前冬冷、后冬暖”的气候格局；降水方面全国整体以“北多南少”为主，冬季需重视全球变暖背景下“拉尼娜”事件对我国北方极端寒潮和南方干旱气候事件的可能影响。

2021年10月19—20日，由气科院生态与农业气象研究所“农业气象灾害创新团队”主办、安徽省农业气象中心承办的“农业气象创新发展学术交流会”在安徽合肥召开。来自气科院、国家气象中心、中国农业科学院、中国农业大学，宁夏、天津、上海、江苏、浙江、安徽等省区市气象局相关领导和专家80余人出席会议。安徽省气象局副局长汪克付到会致辞并宣布会议开幕。围绕“农业气象创新发展与防灾减灾”会议议题，与会专家共做了7个特邀报告、22个大会报告的深层次的交流与讨论。气科院王春乙研究员以 “农业干旱研究”为题、安徽省副局长汪克付以“新时代气象为农服务发展思考与安徽实践”为题做了特邀报告，气科院霍治国研究员以“葡萄旱涝灾变过程解析与指标构建和风险评估”为题做了大会报告。交流会研讨了农业气象研究前沿进展，气候变化与可持续发展，作物模型与数字农业气象研究与应用，农业气象灾变过程模拟与解析，农业气象灾害监测预警、风险评估与综合防控，智慧农业气象业务服务，特色农业气候资源开发利用及提质增效气象服务和长三角现代农业气象业务服务等相关问题。最后，农业气象灾害创新团队首席霍治国研究员介绍了团队在过去一年内所取得的成果。

2021年10月18—22日，由灾害天气国家重点实验室姚聃、吴翀、孙溦、胡皓、魏传文、石怡宁、张帆、范慧怡8人组成的“筑梦新气象”青年调研团，赴广东省广州、深圳、珠海等地开展为期1周的调研实践活动。本次调研的主题为“气象科技创新在灾害天气预报预警领域的应用现状与发展方向”。调研团深入走访了业务单位、科研院所、高校、科技企业和中小学。在广东省气象台、中国气象局广州热带海洋气象研究所、深圳市气象台、粤港澳大湾区气象监测预警预报中心（深圳气象创新研究院）和西涌气象观测基地，调研团深入考察了气象科技成果在业务实践中的转化和应用情况，全面了解防灾减灾一线对于气象科研的需求。在中山大学大气科学学院，调研团与青年教师和研究生代表交流座谈，共同探讨气象科技创新的发展方向以及高校与气象部门开展深入合作的前景。在珠海纳睿达气象科技有限公司，调研团考察了相控阵雷达等高新技术在气象科研业务中发挥的作用。在南方科技大学附属中学，调研团成员胡皓和吴翀分别以“气象卫星：从星辰大海守护我们的家园”和“天气雷达：灾害天气预警的重要手段”为题为中学生们做了科普讲座，并解答了充满好奇心的同学们关于气象防灾减灾的各种问题。此次调研活动不仅开拓了青年科研工作者的视野，也使他们深刻地认识到肩负的重要使命。气象学是实践性很强的自然科学，气象科技创新不应该只是坐在办公室写论文，而是应该紧密结合国家和人民群众的实际需求，用科学探索解决实际问题。

2021年10月28日，南京气象科技创新研究院与中科曙光南京计算技术有限公司战略合作签署仪式暨揭牌仪式在南京举行。创新研究院院长费建芳、中科曙光江苏公司副总裁刘华、南京大学等相关单位代表出席仪式。南京浦口经济开发区管委会营商环境部副部长程思亮在致辞中表示将全力支持双方合作，希望双方的合作为南京创新名城建设注入新活力。费建芳院长在讲话中感谢中科曙光公司为合作所做的前期工作，并简单介绍了创新研究院的定位、发展目标、团队设置等情况。刘华副总裁期待未来将在智慧气象、气象科技与人工智能应用等方面进一步实现资源共享、人才培养，实现互利双赢。创新研究院院长助理李昕与中科曙光南京计算技术有限公司总经理左洪年代表合作双方签署了战略合作协议。费建芳院长与刘华副总裁共同为“气象科技与人工智能应用联合实验室”揭牌。双方将围绕智慧气象安全可控先进计算中心和人工智能学习平台、气象高性能计算专业人才培养体系等重点内容，开展全方位和深层次共建合作，着力构建全国领先的气象科技研发中心和高性能先进计算产业。

2021年10月28日，第六届全国杰出专业技术人才表彰会在北京召开。中共中央组织部、中共中央宣传部、人力资源和社会保障部、科技部联合表彰了93名全国杰出专业技术人才和97个全国专业技术人才先进集体。气科院张小曳院士获得全国杰出专业技术人才表彰。张小曳院士曾任气科院副院长，是第一批国家万人计划-领军人才，承担国家然自然科学基金委重大项目、国家重点基础研究重点项目多项，在亚洲沙尘暴形成机制与数值预报技术、中国大气气溶胶及其气候效应、与雾-霾联系机制及雾-霾数值预报技术等方面取得系统性创新成果并得到广泛应用。2020年1月牵头组建了中国气象局温室气体及碳中和监测评估中心，作为中心主任承担着国家化学天气预报核心技术研发重任。张小曳院士在国内外学术界具有重要影响力，任世界天气研究计划/国际沙尘暴研究发展计划科学指导委员会主席、世界气象组织国际沙尘暴预警咨询系统亚洲区域科学咨询委员会主席、国际环境污染与大气化学计划科学指导委员会委员、全球大气观测计划/气溶胶科学咨询委员会委员、世界气象组织国际沙尘暴预警咨询系统科学指导委员会委员、国际开放领域专家组环境污染与大气化学计划联合科学指导委员会委员。任中国工程院大气国十条总体专家组成员、国家然自然科学基金委中国大气复合污染重大研究计划总体专家组成员、大气污染成因与治理攻关计划总体专家组成员、环保部清洁空气研究计划总体专家组成员、环保部全国环境监测技术委员会委员。获国家自然科学二等奖1项、三等奖1项、省部级一等奖4项、获诺贝尔和平奖-集体奖。完成了1项国家标准、9项行业标准、19项软件著作权。已发表学术论文400余篇，SCI收录240余篇， SCI他引1.3万余次，9篇为ESI高被引论文，过去10年间发表论文被引频次在Web of Science中位于同学科前1%，2021年入选全球前2%顶尖科学家榜单。

2021年10月29日，气科院在北京召开《青岛海洋气象研究院建设方案》研讨会。中国气象局职能司、国家级业务单位、区域海洋气象中心、科研院所等单位的20余位专家出席会议。会议重点研讨了青岛海洋气象研究院未来发展规划和建设重点任务。海洋气象研究院筹建办公室汇报了青岛海洋气象研究院建设方案。随后与会专家从功能定位、总体布局、建设内容、用人机制、交流合作等方面进行了讨论，给出了建设性的意见和建议。端义宏院长在总结讲话中表示，成立青岛海洋气象研究院是中国气象局党组为服务海洋强国战略、加强海洋气象保障和推动气象强国建设的重要举措。气科院及筹建组各成员单位希望通过听取各方对强化海洋气象研究及建设方案本身的意见，进一步明确海洋气象研究院的定位和建设任务，高起点推进海洋气象研究院的建设。感谢各位专家从不同角度对建设方案提出的宝贵意见，后续气科院与各成员单位将根据专家意见进一步完善建设方案，在职能司的指导下及业务单位和各区域海洋中心省（市）局的大力支持下，利用国家和地方的海洋科技、人才、产业聚集优势，从机制上联合部门内外优势科技力量，推动青岛海洋气象研究院建设运行，努力将其打造成国内领先、世界一流的海洋气象科技研发中心。

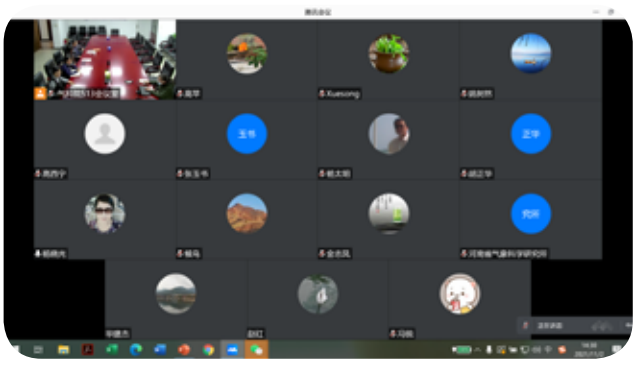

2021年11月2日，中国气象局科技与气候变化司在北京组织召开了公益性行业（气象）科研专项项目“北方冬小麦精细化土壤墒情和灌溉预报技术研究”验收会。验收专家组成员来自气科院、中国农业科学院、中国农业大学、中国气象局沈阳大气环境研究所、浙江省气候中心等多家科研业务单位。项目组汇报了项目目标任务及考核指标完成情况、取得的主要成果、成果应用效益及推广前景等。专家组认为项目完成了任务书规定的各项研究内容，实现了预期目标，一致同意通过验收。该项目确定了不同土壤类型、不同土层的土壤水分自动站标定参数；构建了基于卫星遥感数据、自动墒情资料的山东省冬小麦农田墒情实时遥感监测模式；修正了FAO-56推荐的作物系数、土壤水分胁迫指标，建立了适合北方冬小麦不同发育期的水分胁迫指标、作物系数以及模型关键参数（a、b系数），确定了基于作物根系生长的北方冬小麦不同发育期、各土层的作物蒸散系数，构建了北方冬小麦精细化逐日多层（0～10、0～20、0～30、0～50、0～100 cm）土壤墒情动态预报和灌溉预报模型。项目建立了3个省级土壤墒情和灌溉预报业务应用平台，开展了区域验证和业务应用，制作和发布多期农业气象专题服务材料，土壤墒情平均预报准确率达80%以上，平均节约农业灌溉用水达5%以上。

2021年11月4日，中国气象局科技与气候变化司在北京组织召开了公益性行业（气象）科研专项项目“人工增雨（雪）催化剂定量检测、改进与业务应用”验收会。验收专家来自北京大学，北京应用气象研究所，中国科学院大气物理研究所，北京市、河北省、天津市、河南省、山西省、山东省人工影响天气办公室等多家科研业务单位。项目组汇报了项目总体执行情况、取得的主要成果及其应用等情况。该项目针对我国人工影响天气（冷、暖）云催化剂室内试验及业务应用现状，研发了两种不同碘化银含量的新型高效的冷云催化剂，其成核率比目前国内普遍使用的催化剂高出一个量级以上；研发了一种新型高效的吸湿性催化剂，其吸湿效果明显优于国内原有暖云催化剂配方。上述两种催化剂技术已通过中国气象局科技与气候变化司组织的评审专家委员会的成果认定。制定了催化剂室内试验的检测标准和流程。上述成果已通过有关业务部门形成业务产品，在多省份人工影响天气业务中得到应用，并取得良好的作业效果。对原有高速风洞进行了技术改造，制定了含AgI催化剂动态检测规范和行业标准，为冷云催化剂动态检测提供了条件。验收专家组认为，项目完成了任务书规定的各项研究内容，实现了预期目标，一致同意通过验收。

2021年11月5日，中国第38次南极考察队中山站队员在上海乘雪龙号科考船出发。气科院选派的2位考察队员湖北省气象局陈澄和云南省气象局刘维鑫随船前往中山站，在航行过程中，他们将负责雪龙号走航断面的大气成分观测、气象观测和海冰观测任务，抵达中山站后接替第37次南极考察队员凌新锋和武维刚的工作，进行为期一年的气象观测和大气成分观测任务。另一位越冬队员山东省气象局张雪峰将于11月23日在上海乘雪龙2号科考船前往长城站，接替董剑的工作。

2021年11月11日，公益性行业（气象）科研专项项目“层状云人工增雨作业条件识别和效果分析技术”验收会在北京召开。验收专家组在听取项目汇报及质疑后，一致同意项目通过验收。该项目针对我国层状云人工增雨作业条件识别和效果分析技术开展了系列研究和业务转化，获得丰硕成果。组织开展了有设计的外场综合观测，建立了空–地配套云物理观测数据集，获得了对华北层状云宏微观结构、作业条件及作业效果的认识；建立了云结构特征参量的提取、融合反演和精细分析技术，产品实现业务化；研创了过冷水和作业条件飞机、卫星、雷达等星–空–地监测识别技术方法；提出了人工增雨多尺度概念模型和指标体系构建方案，建立了不同天气人工增雨作业潜力区指标。研创了不同催化方式催化剂扩散传输解析计算方案，实现飞机高炮火箭作业影响区计算；首创人工影响天气充分连片播撒的作业设计思路和“8”字作业设计方案；提出层状云作业效果区域动态多参量物理检验方案（K值法），获得多个例作业效果的物理统计证据；建立了水平分辨率3 km的云降水显式预报系统（CPEFSv1.0）和作业条件数值分析方法，并实现业务化；研制了人工影响天气催化作业的数值模拟仿真预报系统，初步实现作业效果数值评估；集成项目成果，升级了云降水精细处理分析核心技术形成新版系统（CPAS3.0），业务转化后率先建立了国家级和试点省、市级人工影响天气综合处理分析与指挥系统。项目注重人才培养和成果转化，取得的多项关键技术和研发的技术系统，已在全国人工影响天气业务单位推广应用。

2021年11月12日，公益性行业（气象）科研专项项目“人工增雨随机化外场试验和效果检验技术研究”验收会在北京召开，项目顺利通过专家组的验收。该项目由气科院主持，山东、福建、海南、吉林4省人工影响天气科研业务单位参加。从2014年开始攻关，项目团队设计了典型云系的地面火箭和飞机人工增雨随机化科学试验方案，在山东、福建、海南、吉林4个试验区开展人工增雨随机化科学试验，共获取了230个随机试验样本。建立了多种资料综合管理的人工增雨随机化试验样本数据库；研发了人工增雨效果统计检验和物理检验技术方法，发布了人工增雨作业效果检验技术指南，完成了基于天气雷达的对流云火箭增雨效果物理检验技术标准；给出了试验区典型云系人工增雨作业的统计检验阶段性效果和作业前后云的宏微观特征变化的物理证据；建立了人工增雨效果评估模型和作业效果检验技术系统；实现了试验区省级人工增雨作业效果评估业务化应用。项目设计的火箭和飞机人工增雨随机试验方案科学合理；提出的不同云系人工增雨效果评估概念模型指导性强；建立的人工增雨随机化试验样本数据库为全国人工影响天气科研业务人员开展效果检验相关研究提供了极大便利；建立的人工增雨作业效果检验技术方法、技术指南、技术标准和技术系统已在全国13个省市得到业务应用，效果明显，为全国人工增雨业务工作提供了重要科技支撑。

2021年11月17日，受中国气象局预报与网络司委托，气科院在北京组织召开了气象关键技术集成与应用专项项目“云条件监测识别技术和人工影响天气作业决策分析系统集成和应用”验收会。验收专家组由来自中国气象局职能司、气科院、北京大学等高校、中国科学院大气物理研究所、安徽省人工影响天气办公室等科研业务和管理单位的7位专家组成。项目组汇报了项目目标任务、主要成果等情况。该项目综合利用卫星等观测资料优化了云降水宏微观特征反演技术和产品；建立了云特征参量与不同降水的关系，提出了作业条件云特性参量识别指标；开发了云参数综合显示和融合交互分析系统，具备作业决策分析的功能；集成建立了云条件监测识别和作业决策分析业务示范系统。项目成果在各地人工影响天气业务中得到了广泛应用。研发的人工影响天气云降水特征参量静止卫星反演系统（CPPS-GSSL2.0）业务化运行，7类产品发布并在全国业务应用；提出的云特性和降水的关系及作业条件云特性识别指标，在人工影响天气业务中得到广泛应用；项目获得的多项关键技术和系统，在应用中得到不断完善和滚动发展。验收专家组认为，该项目圆满完成了任务书规定的各项研究内容，一致同意通过验收。

2021年12月3日，中国气象局人工影响天气中心在北京组织召开了2021年国家（贵州）防雹外场试验总结研讨会。来自贵州省气象局、北京大学、北京应用气象研究所、中国科学院大气物理研究所、南京大学、成都信息工程大学、中国气象局气象探测中心、北京市人工影响天气中心、河北省人工影响天气中心的专家和中国气象局人工影响天气中心的科技人员，以及相关设备厂家代表分别通过现场和网络直播方式参加了会议。与会专家听取并讨论了关于2021年国家（贵州）防雹外场试验的总结报告，肯定了防雹观测试验的成果，并为2022年试验开展提出了宝贵的意见、建议和方向。2021年国家（贵州）防雹外场试验于2021年5月在贵州威宁正式启动，试验由中国气象局人工影响天气中心和贵州省气象局联合开展，中国科学院大气物理研究所和成都信息工程大学共同参与，试验主要围绕冰雹云精细化结构特征、防雹效果和爆炸效应等目前人工防雹亟待解决的关键性科学问题开展科学研究和技术攻关。

2021年12月9日，国家卫星气象中心王劲松主任一行到访气科院，双方就加强气象卫星资料应用、科技合作、研究生培养及人才交流等工作开展座谈交流。会议由气科院端义宏院长主持，国家卫星气象中心和气科院领导、双方部分职能部门和科研业务单位主要负责人参会。气科院副院长高云详细介绍了气科院有关卫星气象的科研情况，以及构建国家重点实验室协同创新平台的工作思路及进展情况。国家卫星气象中心副主任张兴赢介绍了卫星中心及气象卫星总体情况，就气象卫星应用进展及发展计划做了详细说明，提出了双方加强合作的领域，特别是灾害天气国家重点实验室和许健民气象卫星创新中心的联合创新机制。双方就合作机制、科学技术攻关、人才交流培养、工会活动等方面进行了广泛而深入的探讨交流。

2021年12月20日，中国气象局在温室气体及碳中和监测评估中心进展交流暨学术委员会会议上宣布已建成碳监测核查支持系统（CMA.Carbon MVS v1.0）。这是由气科院张小曳院士团队建成的我国第一个自上而下反演大气二氧化碳源–汇变化的、可业务运行的全球、中国区域和省市、格点尺度四级嵌套格网碳监测同化反演核算系统。该系统依托中国气象局59个温室气体在线监测站高精度二氧化碳浓度数据，辅以碳卫星二氧化碳柱总量数据，掌握全球1° × 1°、中国区域45 × 45 km、城市5 × 5 km格点人为和自然碳通量变化。系统是在联合国政府间气候变化专门委员会（IPCC）国家清单改进指南中提出的可监测、可核查、可支撑（MVS）的方法体系下，基于气象部门建成的1个全球本底站、6个区域本底站、6个卫星地面站和46个省级站提供的高精度二氧化碳浓度数据建立的。系统可提高温室气体清单编制精确度，为全球、全国、省、市及格点尺度人为碳排放总量变化、自然碳汇变化提供客观、全面和及时的监测与核查支持，还可对比统计部门上报的省、市、区和不同行业碳排放数据，正确认识各重点排放源排放的温室气体、减排潜力，并监督其落实减排目标，更好地为政府管理决策提供全面科学的信息，有助于支撑碳排放量配额的合理分配和指导碳排放权市场交易。中国气象局副局长宇如聪表示，碳中和中心在评估已有观测数据可靠性的基础上，开展了有组织的有关碳中和科学研究和监测评估核心技术攻关，建成可业务运行的碳监测核查支持系统，将为我国实现碳达峰、碳中和目标，开展碳排放监测提供有力支持。世界气象组织（WMO）助理秘书长张文建认为，该系统精细度世界领先，起到引领和示范作用，WMO将在国际上加强发挥中国的引领作用。

2021年12月22日，由贵州省气象局和中国气象局人工影响天气中心联合主办的第二届“中国•冰雹减灾”论坛召开，中国气象局应急减灾与公共服务司、中国气象局人工影响天气中心、贵州省气象局、成都信息工程大学、毕节市人民政府等部门领导出席了开幕式。来自气科院、北京大学、成都信息工程大学、中国科学院大气物理研究所、中国气象局人工影响天气中心、北京市气象局、山东省气象局、新疆维吾尔自治区气象局、贵州省气象局等单位的专家受邀做了10个冰雹专题报告。与会专家学者围绕近年来国内外冰雹外场观测试验、冰雹形成机理、冰雹监测预警技术、冰雹防控技术等方面研究成果和业务进展等进行了交流讨论。来自全国冰雹减灾研究领域的近800余位专家和业务科技人员通过腾讯会议、网络直播方式参加了会议。本届“中国•冰雹减灾”论坛会议，聚焦冰雹研究关键科学问题，为全国冰雹减灾相关学者和技术人员提供了交流的平台，有利于提升冰雹防控技术的科技创新协同水平，为我国冰雹防控、科学研究和技术发展提供了有力的科技支撑。

2021年12月30日，为促进中韩人工影响天气技术交流，中国气象局人工影响天气中心与韩国国立气象科学院举办了2021年中韩人工影响天气技术视频交流会。会上，中国气象局人工影响天气中心和北京市人工影响天气中心的专家介绍了我国庐山和祁连山外场观测试验、室内试验和冰核观测研究成果。韩方专家报告了韩国2021年人工影响天气外场观测试验、室内试验及效果评估的研究进展。会议聚焦人工影响天气关键技术和科学问题，为中韩双方在人工影响天气领域的科技成果交流提供了平台。此次会议得到了中国气象局国际合作司、应急减灾与公共服务司和中国气象科学研究院的大力支持。

序号 No.	著作权名称 Copyright name	完成人 Accomplisher	著作权类型 Type	颁证日期 Certification date
1	大气成分历史数据自动整编软件	张小曳，张晓春（外），孙志于（外），王德英，王缅（外），李雅楠（外），吕珊珊（外），荆俊山（外），迟文学（外），温民（外）	软件著作权登记	2021-10-22
2	气溶胶光学厚度 CE-318 运行监控与数据处理软件	张小曳，张晓春（外），孙志于（外），王德英，吕珊珊（外），王缅（外），荆俊山（外），温民（外），迟文学（外）	软件著作权登记	2021-10-25
3	GRIMM 180 仪器数据采集与传输软件	张小曳，王德英，孙志于（外），张晓春（外），荆俊山（外），王缅（外）	音像制品	2021-10-22
4	多功能大气成分观测数据文件打包系统软件［简称：多功能文件打包系统软件］	张小曳，王德英，孙志于（外），张晓春（外），王缅（外），李雅楠（外），荆俊山（外），迟文学（外），温民（外）	软件著作权登记	2021-10-25
5	大气科学试验与研究平台（ASERP）2.0	高梅，张文华，李丰，王红艳，李斌，朱孔驹	音像制品	2021-01-28
6	降水预报偏差与地形高度关联评估系统	杨琳韵，陈昊明，李普曦，陆天舒	软件著作权登记	2021-12-24
7	雷达组网估算降水软件（Linux 版）	王红艳，李丰，高梅，张文华	软件著作权登记	2021-12-07
8	冰雪晶粒子图像数据智能识别标注系统	段婧，胡金蓉（外），李德泉，刘莛杨（学）	软件著作权登记	2021-06-08
9	台风路径和强度预报的全生命史检验系统 V1.0	赵大军，徐洪雄，冯佳宁	软件著作权登记	2021-11-15
10	基于物联网技术的作物无线自动监测和预警系统软件	赵艳霞，孙擎，张祎	软件著作权登记	2021-01-05
11	基于作物模型的马铃薯和甘蔗生长监测和干旱评估系统软件	赵艳霞，张祎，孙擎	软件著作权登记	2021-01-05

序号 No.	著作权名称 Copyright name	完成人 Accomplisher	著作权类型 Type	颁证日期 Certification date
12	海气 CO_2 通量评估系统 V1.0	王蕾	软件著作权登记	2021-11-17
13	全国人影飞机作业监测 APPV1.0	李德泉，李集明，周旭，李抗抗	软件著作权登记	2021-09-13
14	高分辨率卫星反演降水产品数据标准化处理软件	廖荣伟，于飞，房小怡，于瀛	软件著作权登记	2021-10-27
15	污染源反演系统 V1.0	安兴琴，王超（学），李江涛（学）	软件著作权登记	2021-07-12
16	黑碳人体健康经济损失评估系统 V1.0	安兴琴，侯青	软件著作权登记	2021-05-25
17	黑碳浓度空间分布计算平台 V1.0	安兴琴，侯青	软件著作权登记	2021-06-01
18	温度极端特征时空分布统计分析软件［简称：温度极端特征统计软件］V1.0	王培娟	软件著作权登记	2024-09-14
19	作物种植适宜度农业气候时空分析统计［简称：作物种植适宜度软件］V1.0	王培娟	软件著作权登记	2021-04-30
20	机载云粒子图像显示与形状识别软件 V1.0	张荣	软件著作权登记	2021-09-10
21	高分辨率数值模式数据标准化处理软件	廖荣伟，房小怡，于飞	软件著作权登记	2021-08-11
22	杏树春季低温冻害监测预警服务系统 V1.0	杨建莹，王培娟	音像制品	2021-08-09
23	cloudsat 卫星云数据水平空间插值软件	廖荣伟，陈军明，于飞，房小怡	软件著作权登记	2021-07-29
24	cloudsat 卫星数据云分类解码软件	廖荣伟，陈军明，于飞，房小怡	软件著作权登记	2021-02-05
25	风廓线雷达数据处理软件 V1.0	车云飞	软件著作权登记	2021-02-09


发明专利证书

发明专利证书

发明专利证书


实用新型专利证书

实用新型专利证书

实用新型专利证书

序号 No.	专利名称 Patent title	发明人 Inventor	专利类型 Type	授权日期 Authorization date
1	用于水田等土壤表面具有浅层积水环境的蒸散测定系统	赵俊芳，黄晚华（外），李明（外），吴东丽（外），房世波，谢鸿飞（学），李民华（外）	实用新型	2021-09-21
2	基于多源数据和深度学习的地表蒸散发数据降尺度方法	车向红（外），孙擎，刘纪平（外），王勇（外），徐胜华（外），罗安（外），杜凯旋（外）	发明专利	2021-12-17
3	云雾水采集器	段婧，李军（外）	实用新型	2021-06-22
4	一种传感器的双层保护装置及测量稻田蒸散量的装置	赵俊芳，黄晚华（外），李明（外），李民华（外），李涵茂（外），刘富来（外），汪天颖（外），谢鸿飞（学）	实用新型	2021-09-03
5	一种基于高时空分辨率遥感数据的植被物候提取方法	车向红（外），孙擎，刘纪平（外），王勇（外），徐胜华（外），罗安（外），刘慧慧（外）	发明专利	2021-12-21
6	一种农业用气象监测装置	赵俊芳，闫伟兄（外），杨全（外），房世波，谢鸿飞（学）	实用新型	2021-07-30
7	反演气溶胶微物理参数的方法、电子设备以及存储介质	李建，郭建平，石光明（外），李成才（外）	发明专利	2021-12-10
8	苹果花期冻害监测预警装置	霍治国，杨建莹，姚树然（外），邬定荣，王培娟，俄有浩	实用新型	2021-12-07
9	退耕地信息遥感识别方法及装置	周广胜，王树东（外），汲玉河	发明专利	2021-04-16
10	数据压缩方法、装置、终端及计算机可读存储介质	李德泉，李抗抗，段婧，李集明，马振营（外），赵婷（外）	发明专利	2021-07-20
11	一种冰晶自动取样系统	苏正军，关立友，党娟，楼小凤，方春刚，常祎	实用新型	2021-10-15
12	嵌入超图卷积层的深度学习冰晶粒子图像分类方法	段婧，廖梦媛（外），李德泉	发明专利	2021-07-27
13	一种大气监测装置的旋转定位机构	廖荣伟，赵平，房小怡，于飞	实用新型	2021-09-23
14	一种新型温湿度和 CO_2 气体浓度监测装置	廖荣伟，房小怡，于飞，赵平，赵艳霞	实用新型	2021-10-19
15	一种极度稀疏植被区域负土壤调节因子计算方法	周广胜，任鸿瑞（外），周莉	发明专利	2021-02-02
16	一种基于脉冲匹配的宽带干涉仪闪电定位方法及系统	范祥鹏，张义军（外），郑栋，姚雯	发明专利	2021-09-17
17	一种云室	苏正军，关立友，党娟，楼小凤，方春刚	实用新型	2021-08-10
18	一种新型的日光温室补光装置	廖荣伟	实用新型	2021-06-29
19	一种新型的杏树低温观测装置	王培娟，姚树然（外），董航宇（外），权畅（外），杨建莹，甄晓菊（外），霍治国	实用新型	2021-06-11


荣誉证书
授予：张小曳 同志
“全国杰出专业技术人才”
称号。
二〇二一年


证明
2020生态环境十大科技进展
进展名称：第三次青藏高原科学试验—边界层与对流层观测
第1 完成人：赵 平
二〇二一年


新时代气象高层次科技创新人才计划
证 书
祝从文 同志：
入选2021年度新时代气象高层次科技创新人才计划气象领军人才，授予“国家级首席科学家”称号。
特发此证。


新时代气象高层次科技创新人才计划
证 书
丁明虎 同志：
入选2021年度新时代气象高层次科技创新人才计划气象优秀人才，授予“青年气象英才”称号。
特发此证。


新时代气象高层次科技创新人才计划
证 书
张文娟 同志：
入选2021年度新时代气象高层次科技创新人才计划气象优秀人才，授予“青年气象英才”称号。
特发此证。


证 书
中国气象科学研究院 孙溦：
入选2021年北京市科技新星计划，
特发此证。
2022年3月


授予：傅宜聪 同志
全国气象工作先进个人

2021 年获得表彰的先进集体和个人

序号 No.	奖项名称 Award name	获奖集体 / 个人 Award-winning group/individual	授予部门 Awarding department
1	2020 年度生态环境十大科技进展	第三次青藏高原科学试验–边界层与对流层观测项目团队	中国科学技术协会
2	2020 年度全国优秀科普微视频作品：《世界屋脊探秘——气壮山河 _ 青藏高原大气科学试验》	中国气象学会（第一单位）	中国科学院办公厅
3	2020 年度中国交通运输协会科技进步奖二等奖	公路交通气象监测预警与行车安全主动防控关键技术研究及应用项目团队	中国交通运输协会
4	中国石油和化工自动化应用协会科技进步奖二等奖	大型石油罐区雷电危害防控技术研究及应用项目团队	中国石油和化工自动化应用协会
5	2020 年全国气象工作先进单位	大气成分与环境气象研究所	中国气象局
6	重大气象服务优秀集体	气候与气候变化研究所、中国气象局人工影响天气中心作业指挥与运行中心	中国气象局
7	庆祝活动气象保障服务优秀集体	中国气象局人工影响天气中心作业指挥与运行中心	中国气象局
8	第十四届全国运动会气象保障服务优秀集体	人工智能气象应用研究所、中国气象局人工影响天气中心装备研发与保障室	中国气象局
9	北京市优秀城乡规划二等奖	工程气象研究中心（第二单位）	北京城市规划学会
10	第十九届北京科技声像作品“银河杯”科普短片二等奖：《第三次青藏高原大气科学试验》	北京天禾翔云文化传媒有限公司（赵平、王欣等主创团队）	北京科技声像工作者协会
11	2020 年度国家气象中心气象科技工作奖	基于关键影响系统的江淮流域中长期强降水预报模型（KISAM）V1.0 项目团队	国家气象中心
12	2020 年度江苏省气象学会气象科技成果奖一等奖	新一代气象卫星云参数反演及预警技术项目团队	江苏省气象学会
13	2020 年度江苏省气象学会青年技术进步奖二等奖	雨滴谱数据在降水观测中的应用研究项目团队	江苏省气象学会
14	第六届全国杰出专业技术人才奖	张小曳	中共中央组织部、中共中央宣传部、人力资源和社会保障部、科技部
15	国家级青年人才计划	丁明虎等 4 名青年科学家	国家自然科学基金委等部门
16	北京市科技新星计划	孙溦	北京市科学技术委员会
17	2020 年全国气象工作先进个人	缪育聪，梁钊明	中国气象局
18	全国气象工作先进个人	梁旭东	中国气象局
19	中国气象局气象领军人才	宋丽莉，周毓荃，祝从文	中国气象局

序号 No.	奖项名称 Award name	获奖集体 / 个人 Award-winning group/individual	授予部门 Awarding department
20	中国气象局青年气象英才	丁明虎，沈小静，张文娟，诸葛小勇，缪育聪	中国气象局
21	重大气象服务优秀个人	赵大军，张骁拓	中国气象局
22	庆祝活动气象保障服务优秀个人	孙继松，姚展予，陶玥，刘卫国，李琦，原新鹏，花少烽	中国气象局
23	第十四届全国运动会气象保障服务优秀个人	王亚强，郑玉，张会，史月琴，刘卫国，李德泉，陶玥，谭超，李宏宇，周旭，李琦	
24	江苏省科协青年科技人才托举工程	诸葛小勇	江苏省科学技术协会
25	江苏省气象局气象领军人才	郑媛媛	江苏省气象局
26	江苏省气象局气象青年英才	刘希	江苏省气象局
27	江苏省双创博士	孙世玮，宇路，张树时	江苏省委组织部、江苏省人才工作领导小组办公室等 12 个部门
28	全国优秀教材：《冰冻圈科学概论（修订版）》	孙俊英，丁明虎	国家教材委员会

2021 年新项目
New Projects in 2021

序号 No.	课题名称 Title	项目类别 Project/fund	执行期间 Duration	负责人 Principal investigator
1	台风多尺度数值预报模式建立和应用示范	国家自然基金委重大项目	2022—2026	端义宏
2	植物物候变化的全气候生产要素影响机制与模拟研究	国家自然基金委重点项目	2022—2026	周广胜
3	三北工程区陆地生态系统增汇潜力及风险评估	国家自然基金委专项项目	2022—2025	周广胜
4	我国碳中和行动有效性监测评估系统构建中关键科学问题研究	国家自然基金委专项项目	2022—2025	陈报章
5	战略研究类：天气学发展战略研究	国家自然基金委专项项目	2022—2022	梁旭东
6	科学传播类：致力于防灾减灾能力提升的青少年气象科普实践	国家自然基金委专项项目	2022—2022	于玉斌
7	造成江淮地区局地风灾的强风暴精细结构演变与致灾机理研究	国家自然基金委联合基金项目	2022—2025	孙继松
8	中国东部主要流域持续性强降水多尺度演变机理和精细化预报新方法研究	国家自然基金委联合基金项目	2022—2025	翟盘茂
9	京津冀地区夏季强对流天气前期信号及适应性观测研究	国家自然基金委联合基金项目	2022—2025	郭建平
10	高密度 X 波段和 S 波段天气雷达组网方法及强降水和大风临近预报关键技术研究	国家自然基金委联合基金项目	2022—2025	刘黎平
11	适用于快速辐射传输模式（ARMS）的全极化求解方案及解析伴随模式研究	国家自然基金委联合基金项目	2022—2025	翁富忠
12	公里尺度对流分辨模式对强降水过程精细化预报的评估	国家自然基金委联合基金项目	2022—2025	陈昊明
13	基于正射校正地表反射率数据全集的作物干旱动态监测	国家自然基金委面上项目	2022—2025	王培娟
14	基于多源卫星数据的东北冷涡背景对流初生和演变研究	国家自然基金委面上项目	2022—2025	诸葛小勇
15	南海弱台风引发我国强降水的机理研究	国家自然基金委面上项目	2022—2025	魏娜
16	高空冷空气对我国近海热带气旋快速增强影响的机理研究	国家自然基金委面上项目	2022—2025	于玉斌
17	海南岛强对流触发的关键边界层过程及其作用机理研究	国家自然基金委面上项目	2022—2025	梁钊明

序号 No.	课题名称 Title	项目类别 Project/fund	执行期间 Duration	负责人 Principal investigator
18	下垫面动热力强迫对登陆后的台风强度衰减率的影响研究	国家自然基金委面上项目	2022—2025	刘璐
19	冬季北极涛动与北极气温之间的准双周正反馈机制及其在北极变暖中的作用	国家自然基金委面上项目	2022—2025	肖栋
20	高建筑物对正负地闪通道发展影响的差异及其机理研究	国家自然基金委面上项目	2022—2025	吕伟涛
21	基于索道等多源观测的庐山低云边界宏微观特征及气溶胶-云滴核化过程研究	国家自然基金委面上项目	2022—2025	段婧
22	华北农村地区霾与光化学污染之间多种反馈机制对 PAN 生成的影响研究	国家自然基金委面上项目	2022—2025	徐婉筠
23	基于化学组分和数谱分布的细颗粒物来源解析研究——两步法	国家自然基金委面上项目	2022—2025	张养梅
24	全天候无缝隙气溶胶光学厚度反演及其驱动机制研究——以华北平原为例	国家自然基金委面上项目	2022—2025	桂柯
25	北极 B-K 海周边地区与华北地区森林动态同步性及其与北极快速变化的关系	国家自然基金委青年基金项目	2022—2024	赵守栋
26	近 2000 年来北极与青藏高原多时间尺度温度变化对比研究	国家自然基金委青年基金项目	2022—2024	祁威
27	多尺度天气系统降水预报的尺度自适应集合概率匹配方法研究	国家自然基金委青年基金项目	2022—2024	乔小湜
28	江淮平原暖季大气波涌时空特征及形成机理研究	国家自然基金委青年基金项目	2022—2024	张树时
29	冬季大气内部变率对北极-欧亚地区温度异常型的影响	国家自然基金委青年基金项目	2022—2024	王赛
30	青藏高原地形对 ENSO 影响的耦合模式模拟研究	国家自然基金委青年基金项目	2022—2024	苏宝煌
31	BSISO 与青藏高原对川滇地区次季节降水的联合作用及其机理	国家自然基金委青年基金项目	2022—2024	杨琳韵
32	基于时空综合分型的 ENSO 多样性对北极海冰影响研究	国家自然基金委青年基金项目	2022—2024	王润
33	基于卫星主动遥感和客观天气分型的青藏高原云特征及其辐射强迫研究	国家自然基金委青年基金项目	2022—2024	宇路
34	基于卫星精细追踪的京津冀地区对流云时空特征及其与气溶胶的关系研究	国家自然基金委青年基金项目	2022—2024	陈田萌
35	基于被动微波遥感的热带气旋垂直结构物理约束变分反演方法研究	国家自然基金委青年基金项目	2022—2024	胡皓
36	气溶胶-云相互作用及其辐射叠加效应对霾污染的影响机制研究	国家自然基金委青年基金项目	2022—2024	郑宇
37	双波段云雷达和双偏振雷达联合反演雨滴谱垂直分布的研究	国家自然基金委青年基金项目	2022—2024	张扬
38	强对流系统中水平次网格湍流特征及其参数化方案改进研究	国家自然基金委青年基金项目	2022—2024	孙世玮

序号 No.	课题名称 Title	项目类别 Project/fund	执行期间 Duration	负责人 Principal investigator
39	极端干旱对中国北方森林、草地生态系统水分利用效率的影响研究	国家自然基金委青年基金项目	2022—2024	黄萌田
40	中国冬季区域性冷暖急转事件变化的归因及预估	国家自然基金委青年基金项目	2022—2024	廖圳
41	改进黑潮延伸体模态转变预报的目标观测网设计	国家自然基金委青年基金项目	2022—2024	耿雨
42	极地气象与冰冻圈	国家自然基金委优秀青年基金项目	2022—2024	丁明虎
43	森林草原火灾救援现场三维风场探测及预警技术与关键装备研究	科技部国家重点研发计划课题	2021—2024	王改利
44	基于国产快速辐射传输模式的大气海洋一体化参数反演与应用研究	科技部国家重点研发计划项目	2021—2025	杨俊
45	面向京津冀复合型空气污染的多源资料同化系统研发及应用	北京市科技新星计划	2021—2024	孙溦
46	基于微光成像仪的大雾、云和台风监测研究	国家卫星中心风云三号 03 批气象卫星工程地面应用系统五个领域应用系统	2021—2022	诸葛小勇
47	FY4B 和 FY3E 卫星的新型观测仪器云物理开发及在人工影响天气中的应用研究	国家卫星中心风云三号 03 批气象卫星工程地面应用系统五个领域应用系统	2021—2022	周毓荃
48	FY-3E 和 FY-4B 卫星产品在环境气象中的应用	国家卫星中心风云三号 03 批气象卫星工程地面应用系统五个领域应用系统	2021—2022	牛涛
49	基于 ARMS 的 FY-3E 和 FY-4B 辐射率资料同化关键技术研究	国家卫星中心风云三号 03 批气象卫星工程地面应用系统五个领域应用系统	2021—2022	杨俊
50	FY-3E 微波探测仪大气廓线产品反演方案研究	国家卫星中心风云三号 03 批气象卫星工程地面应用系统五个领域应用系统	2021—2022	胡皓
51	FY-3E 微光成像和 GNOS Ⅱ反射信号监测火点、洪涝和干旱	国家卫星中心风云三号 03 批气象卫星工程地面应用系统五个领域应用系统	2021—2022	房世波
52	基于 FY 数据的气象条件贡献率评价系统升级	中国气象局创新发展专项	2021—2022	周广胜
53	特定目标区的增雨减污关键技术探索研究	中国气象局创新发展专项	2021—2022	周毓荃
54	区域高分辨率模式业务能力评估及改进	中国气象局创新发展专项	2021	梁旭东

序号 No.	课题名称 Title	项目类别 Project/fund	执行期间 Duration	负责人 Principal investigator
55	农业气象试验站区域联合试验	中国气象局创新发展专项	2021	周广胜 宋艳玲
56	我国大气本底站大气臭氧观测资料标准化处理方法及质量评估	中国气象局创新发展专项	2021	张小曳
57	生态气象联网监测技术开发	中国气象局创新发展专项	2021	周莉
58	2021 年 IPCC 第一工作组支撑	中国气象局气候变化专项	2021	翟盘茂
59	“东数西算”工程对气象事业发展的意义研究	中国气象局气象软科学重点项目	2022	王郁

人才培养
Education and Training

2021年5—6月，为庆祝中国共产党成立100周年，向党的百年华诞献礼，引导青年传承红色基因，争做时代新人，气科院研究生党总支部组织拍摄歌曲《少年》视频，忆往昔峥嵘岁月，展今朝青年风采。同学们身着民国时期校服，手捧着《新青年》，吟诵着李大钊先生的《青春》，缓缓地步入镜头中，慷慨激昂的诗词一下子就把人带回了那个水深火热的年代。本次颂歌活动同学们精心选曲，刻苦排练，将党史和研究生日常学习和科研融入到视频当中，既回顾了革命先烈们的光荣历史，增强了自身爱国意识，又展现了当代气象科技工作者的良好精神风貌。习近平主席曾说过：“青年一代不怕苦，不畏难不惧牺牲，用肩膀扛起如山的责任，展现出青春激昂的风采，展现中华民族的希望。” 少年强则国强，作为当代青年当不忘初心，牢记使命，继承革命精神，坚定理想信念，为气象事业，中华民族的伟大复兴贡献青春力量。

2021年7月6日，中国气象科学研究院2021年度研究生学位授予仪式暨毕业典礼在北京举行。中国气象局党组书记、局长庄国泰，副局长宇如聪，周秀骥、丑纪范、许健民、陈联寿、徐祥德等两院院士，科技司姚学祥司长，人事司陈振林司长，华风集团张守保董事长，华云集团白海书记，气科院端义宏院长出席仪式，共同为毕业生授予学位，并颁发优秀奖项。2021年度15名博士、40名硕士毕业生及2020年度部分毕业生、部分家长、导师代表出席仪式。庄国泰局长在讲话中希望毕业生牢记习近平总书记对青年的嘱托，明大德、守公德、严私德，清清白白做人、干干净净做事。希望毕业生以学术大师为榜样，学习他们独立思考的品质、求知自觉的真诚、困厄穷途中对节操的坚持，在上下求索中找准自己的社会定位，做到自主自强，发挥应有作用。他指出，当前世界处于百年未有之大变局，气象事业发展正值重要转型时期，服务生命安全、生产发展、生活富裕、生态良好，做到监测精密、预报精准、服务精细，守好气象防灾减灾第一道防线，机遇与挑战并存。希望毕业生勇于抓住机遇，勇敢迎接挑战，把青春奋斗融入党和人民事业、融入气象事业高质量发展，不断取得新的更大成绩。

2021年7月21日至23日，气科院举办了2021年全国大气科学领域优秀大学生培训班（暑期学校）暨优秀大学生夏令营，来自兰州大学、中国海洋大学、云南大学、南京信息工程大学、成都信息工程大学等高校的43名优秀的本科三年级同学和中国地质大学（武汉）的30余名本科二年级同学在云端相聚，共叙未来。开班仪式由研究生部副主任石爱丽主持。气科院副院长赵平研究员致辞，并介绍了气科院总体情况和营期安排，同时表达了对同学们能共聚气科院的殷切期待。随后，暑期学校校长徐祥德院士介绍了气科院研究生培养制度和情况。石爱丽从中国气象局研究生教育师资力量和人才队伍、研究成果和业务贡献、科研设备和开放合作等方面展现了学位点雄厚的科研实力和研究生培养能力。最后高年级的师兄师姐们为营员们带来了包括考研、保研和研究生学习生活等方面的分享，营员们积极在线上提问，纷纷表示对未来的研究生学习生活充满了期待。夏令营为营员们组织了19场精彩的导师报告。徐祥德院士介绍了高原大气科学科考与应用研究，赵平研究员介绍了青藏高原的天气气候效应，周广胜研究员介绍了生态气象，张鹏研究员对风云三号“黎明星”进行了介绍，丁一汇院士对气候变化与西北暖湿化问题进行了探讨，王玉清教授介绍了奇妙的台风，沈学顺研究员介绍了我国数值预报的发展，翁富忠教授介绍了人工智能在卫星遥感领域中的应用，李建研究员介绍了地形与降水的关系，梁旭东研究员汇报了灾害天气监测与预报研究，王亚强研究员介绍了人工智能气象应用研究，车慧正研究员介绍了大气气溶胶的光学特性，王培娟研究员介绍了农业气象研究，任宏利研究员介绍了季节–年际气候动力学机理与气候预测研究进展，吴统文研究员介绍了地球系统模式发展与应用国际前沿，刘端阳研究员介绍了交通气象研究进展，苗世光研究员介绍了城市气象研究情况，吕伟涛研究员介绍了闪电相关研究，郑永光研究员介绍了强对流天气研究和监测预报预警。导师们的精彩讲演勾起了营员们满满的求知欲，营员们积极与老师互动提问，老师们也是知无不言，极大地满足营员们的好奇心和求知欲。为了让大家更加全面了解中国气象局和气科院，老师们播放了青藏高原大气科学试验、气科院、中央气象台、灾害天气国家重点实验室等相关视频。之后学员成果展示中，营员们多方面展示了本科的丰富经历，以及参加夏令营的感悟收获。夏令营最后的座谈会上，营员们针对自己感兴趣的方向与周秀骥院士以及8名导师代表进行了深入探讨，老师们从不同方向角度对营员们的问题进行了解答，尤其对于近期河南暴雨，极端天气事件，碳中和以及气候变化等问题展开了热烈的讨论。夏令营结束后，对营员们进行了问卷调查，绝大多数营员对于此次夏令营表示非常满意。营员们表示，能与院士和站在学术前沿的老师们面对面交流，获益匪浅，还找到了自己感兴趣的研究方向，感受到了气科院严谨的学术氛围，也体会到了愉快充实的生活氛围，更加坚定了继续探索学习的决心，期待能够携手并进，推进中国气象事业的高质量发展！

2021年9月3日，气科院研究生部组织了2021年度研究生开学典礼暨新生欢迎仪式。典礼由研究生部副主任石爱丽主持，赵平副院长、研究生部的老师和2021级69名研究生参加了开学典礼。赵平副院长在欢迎辞中指出，气科院是中国气象局高层次人才培养、学科齐全的单位，具备优秀的导师团队和良好的科研氛围，希望在研期间要积极参加社会实践，逐步了解气象业务实际情况。赵院长强调，气象工作是一件值得骄傲的事业，精准的气象预报和精细的气象服务直接关系到国家经济的生产生活，但同时预报准确率的需求高、难度大，预报水平和服务能力有待提升，鼓励同学们树立远大的科研理想和社会责任感。研究生阶段是自我学习和自我成长的阶段，石爱丽副主任介绍了研究生部老师工作分工、导师交流、学生培养、学习环境、疫情防控等情况，鼓励学生们3年学习生活期间做好规划，勇于探索，遵守规章制度，营造良好的学习氛围。研究生部的老师唐海霞刘东玥分别就培养计划、选课、学籍、就业派遣等问题与学生们进行了交流。

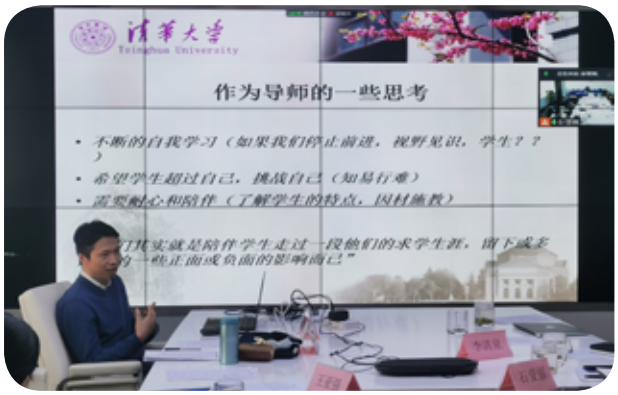

2021年11月10日，气科院研究生部在北京举办了研究生导师培训班，会议采取线上线下相结合的方式，共有近80名研究生导师参加了培训。气科院赵平副院长在致辞中介绍了气科院研究生导师总体情况和培训的重要意义，希望通过培训新评选的研究生导师能尽快了解研究生培养中的各项工作，促进所有导师在研究生培养过程中更好地履行导师职责，从建立和谐师生关系、关心学生心理健康、培养合格人才等方面共同做好研究生培养工作。此次培训邀请了4位教学经验丰富的专家，南京信息工程大学的朱彬教授以“启迪人生、追求卓越”为题讲述了导师本分、师生关系、师生卓越的培养关系；北京师范大学的龚道溢教授以“没有差的学生，只有合不合适的导师”为题，从招什么样的学生、如何培养学生及如何培养好学生等几方面分享了培养研究生的一些体会，让导师们受益匪浅。如何指导学生？如何激励学生？来自清华大学的林岩銮教授针对研究生成长和指导与各位导师们进行了交谈，并提出了有趣的“快乐科研”理论。北京师范大学的张继明副教授对如何识别和应对研究生心理健康问题进行了深入浅出的讲解，引起大家极大的兴趣。最后气科院研究生部石爱丽、唐海霞、刘东玥三位老师也分别从招生和导师管理、学位和培养、学籍和信息化管理等方面介绍气科院的研究生管理服务工作。此次研究生导师培训班的举办，是加强研究生导师管理和服务的一项举措，尤其在疫情形势下对导师们如何做好研究生科研指导工作、学生心理疏导等提供了指导，对提高研究生导师思想认识、提升研究生培养质量、构建和谐师生关系起到良好的促进作用。

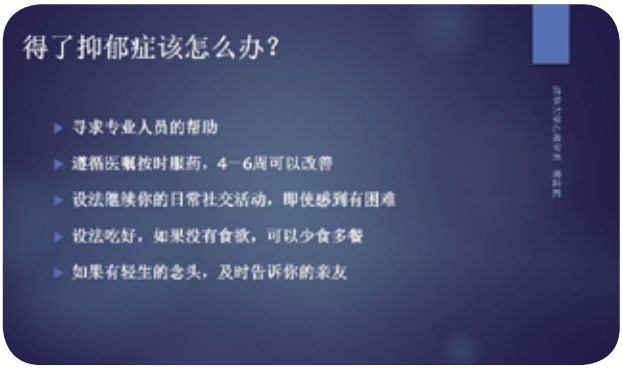

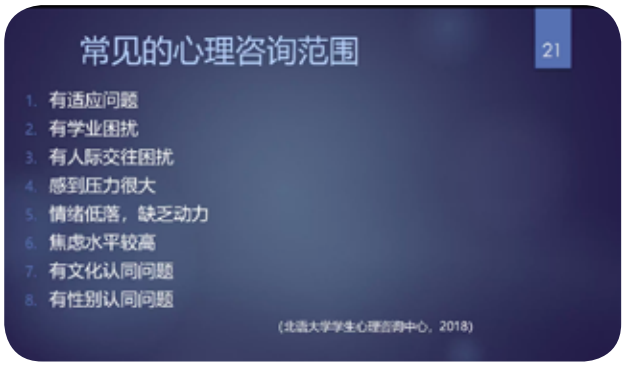

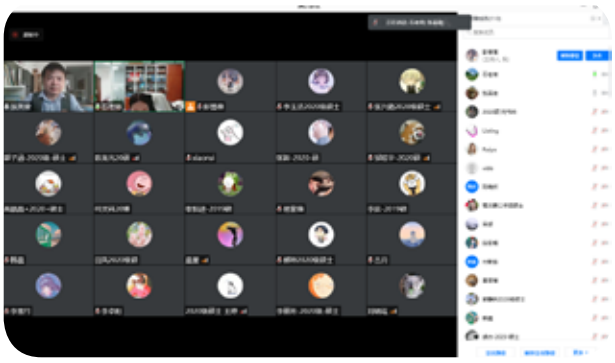

2021年11月17日，为进一步宣传普及心理健康知识，深入开展心理健康教育，气科院研究生部邀请北京师范大学的张英俊博士进行了“研究生常见的心理问题及其应对”线上心理讲座。讲座由研究生党总支书记石爱丽主持，气科院全体在读研究生参加。目前研究生群体同时面临着学业、工作、经济等各方面的压力，如何有效地进行自我心理健康的判别和自我开导尤为重要。张英俊博士首先科普了心理咨询的工作形式、范畴、目标，大众常见心理咨询和治疗，重点阐述了心理健康的判别标准和方法，抑郁和焦虑的表现形式，研究生群体如何判断心理“不正常”及哪些人需要做心理咨询，有效的精神分析治疗、认知行为治疗、人本主义治疗等形式的疗愈方式等。最后张英俊博士结合具体案例，对各位研究生如何准确识别心理问题及如何有效工作进行了特别讲解。此次讲座是气科院研究生部与北京师范大学心理健康教育与咨询中心合作的内容之一，双方合作为研究生提供了心理咨询渠道，旨在提高研究生心理素质，科学应对心理问题，促进研究生的身心健康。

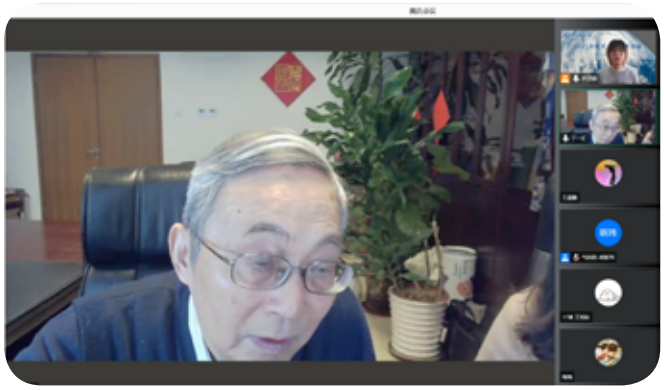

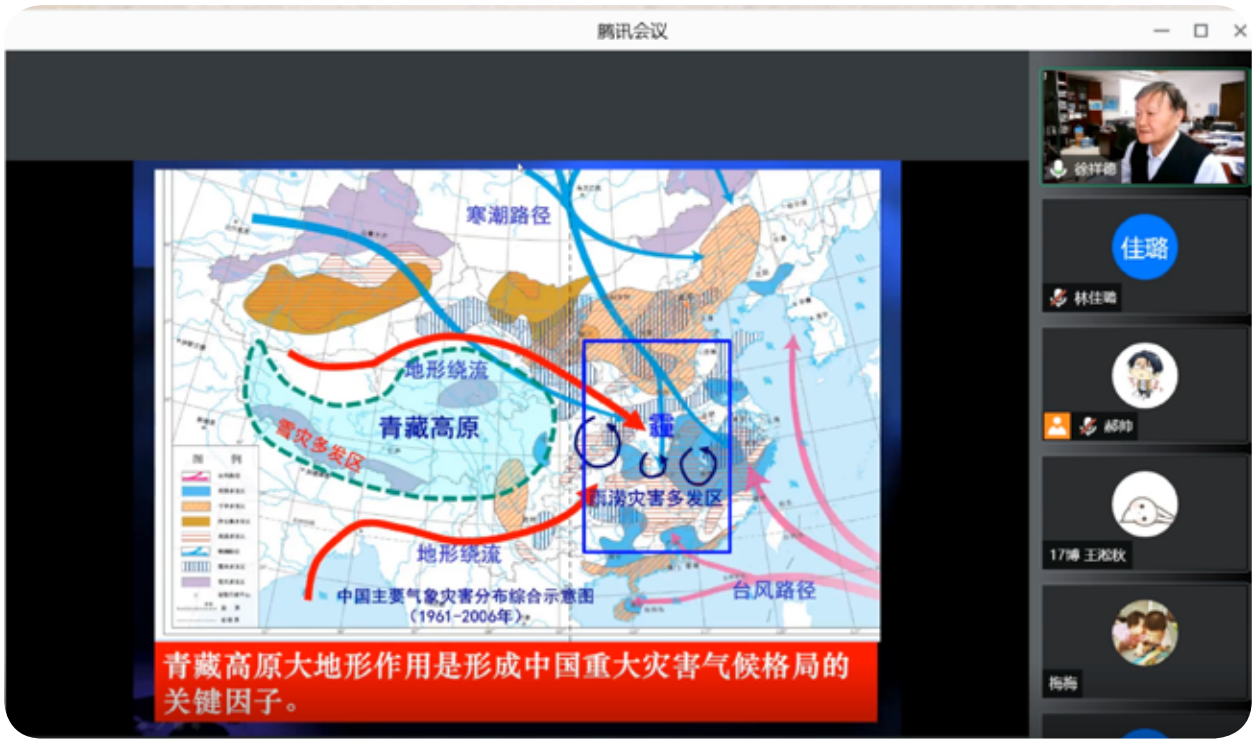

2021年12月1—7日，气科院研究生部和研究生会在线上举办了“2021年度现代大气科学论坛”。论坛邀请了丁一汇院士、徐祥德院士等国内气象学相关领域的11位知名专家教授做特邀报告，2022年即将毕业的近20位博士也在论坛上报告交流。专家学者们针对气象学热点研究做出了精彩的报告分享，与气科院的研究生们进行了深入的学术交流。专家们带来的精彩报告涵盖了气候变化、卫星遥感、数值模式、灾害性天气、气候分析等众多气象学热点研究领域，为气科院研究生们提供了一个能够系统了解、学习气象学研究现状和研究思路的宝贵机会。同时，在报告过程中老师们还充分考虑了同学们研究方向差异大的现状，不仅对各自工作的亮点、难点等进行了详尽阐述，还为同学们简明扼要地介绍了相关工作的学术背景，拓宽了同学们的学术视野。现代大气科学论坛也为学者和研究生们提供了一个学术思想碰撞的平台。尽管受疫情影响，本次论坛仅在线上进行，但这并没有影响同学们对于知识的渴望。在每轮报告结束后的提问交流环节，同学们踊跃发表对报告内容的看法，与报告人进行了深入交流。交流内容不仅涵盖研究方法、趋势上的认识，还包括软件应用、硬件发展和基本概念方面的沟通，展现了新时代研究生的良好求学风貌。报告结束后，不少研究学者和研究生深感意犹未尽，纷纷选择留下联系方式以便会后深入交流。通过举办“现代大气科学论坛”，大大加深了研究生对相关领域的了解，对激发研究生学习兴趣，拓宽学术视野提供了良好的学术氛围。

2021 年出版物
Publications in 2021

序号 No.	作者 Author (rank)	题名 Title	出版物名/出版社 Publication name or publisher	年，卷（期） Year, volume (issue)
1	An Ning, et al.	Investigating the influence of synoptic circulation patterns on regional dry and moist heat waves in North China	Climate Dynamics	2021, 57
2	An Ning, et al.	Changing structures of summertime heatwaves over China during 1961–2017	Science China: Earth Sciences	2021, 64
3	An Xingqin (2nd)	Simulated sensitivity of ozone generation to precursors in Beijing during a high O_3 episode	Advances in Atmospheric Sciences	2021, 38(7)
4	An Xingqin (2nd)	Influence of East Asian winter monsoon on particulate matter pollution in typical regions of China	Atmospheric Environment	2021, 260
5	An Xingqin (2nd)	Simulation study on regional atmospheric oxidation capacity and precursor sensitivity	Atmospheric Environment	2021, 263
6	An Xingqin (2nd)	Development of four-dimensional variational assimilationsystem based on the GRAPES-CUACE adjointmodel (GRAPES-CUACE-4D-Var V1.0) and itsapplication in emission inversion	Geoscientific Model Development	2021, 14
7	Bao Xinghua, et al.	The impact of the observation data assimilation on atmospheric reanalyses over Tibetan Plateau and western Yunnan-Guizhou Plateau	Atmosphere	2021, 12
8	Bao Xinghua, et al.	The synoptic impacts on the convection initiation of a warm-sector heavy rainfall event over coastal South China prior to the monsoon onset: A numerical modeling study	Journal of Geophysical Research: Atmospheres	2021, 126(14)
9	Cai Xiuhua, et al.	A view for atmospheric unpredictability	Frontiers in Earth Science	2021, 9
10	Cai Xiuhua, et al.	Identification of regional drought processes in North China using MCI analysis	Land	2021, 10(12)
11	Chang Yi, et al.	Characteristics of raindrop size distributions during Meiyu season in Mount Lushan, East China	Journal of the Meteorological Society of Japan	2021, 100(1)
12	Chang Yi (3rd)	Temporospatial distribution and trends of thunderstorm, hail, gale, and heavy precipitation events over the Tibetan Plateau and associated mechanisms	Journal of Climate	2021, 34(24)
13	Che Yunfei, et al.	Aerosol and cloud properties over a coastal area from aircraft observations in Zhejiang, China	Atmospheric Environment	2021, 267

序号 No.	作者 Author (rank)	题名 Title	出版物名/出版社 Publication name or publisher	年，卷（期） Year, volume (issue)
14	Chen Baozhang, et al.	An atmospheric perspective on the carbon budgets of terrestrial ecosystems in China: Progress and challenges	Chinese Science Bulletin	2021, 66(17)
15	Chen Bin (2nd)	Intensified moisture sources of heavy precipitation events contributed to interannual trend in precipitation over the Three-Rivers-Headwater region in China	Frontiers in Earth Science	2021, 9
16	Chen Bin (3rd)	Responses of heat stress to temperature and humidity changes due to anthropogenic heating and urban expansion in South and North China	Frontiers in Earth Science	2021, 9
17	Chen Tianmeng	Potential impact of aerosols on convective clouds revealed by Himawari-8 observations over different terrain types in eastern China	Atmospheric Chemistry and Physics	2021, 21
18	Chen Yang, et al.	Detectable increases in sequential flood-heatwave events across China during 1961−2018	Geophysical Research Letters	2021, 48(6)
19	Chen Yang, et al.	Detectable intensification of hourly and daily scale precipitation extremes across eastern China	Journal of Climate	2021, 34
20	Chen Yang (2nd)	The emergence of anthropogenic signal in mean and extreme precipitation trend over China by using two large ensembles	Environmental Research Letters	2021, 16
21	Chen Yang (2nd)	Detectability of the trend in precipitation characteristics over China from 1961 to 2017	International Journal of Climatology	2021, 41
22	Chen Yang (2nd)	Anthropogenic emissions and urbanization increase risk of compound hot extremes in cities	Nature Climate Change	2021, 11
23	Cheng Xinghong, et al.	A new inverse modeling approach for emission sources based on the DDM-3D and 3DVAR techniques: An application to air quality forecasts in the Beijing–Tianjin–Hebei region	Atmospheric Chemistry and Physics	2021, 21
24	Cheng Xinghong (3rd)	Development of three-cimensional variational data assimilation method of aerosol for the CMAQ model: An application for $PM_{2.5}$ and PM_{10} forecasts in the Sichuan Basin	Earth and Space Science	2021, 8(5)
25	Ding Minghu, et al.	Brief communication: Evaluation of multiple density-dependent empirical snow conductivity relationships in East Antarctica	Cryosphere	2021, 15
26	Ding Minghu (2nd)	The AntSMB dataset: A comprehensive compilation of surface mass balance field observations over the Antarctic Ice Sheet	Earth System Science Data	2021, 13
27	Ding Minghu (2nd)	On the differences in precipitation type between the Arctic, Antarctica and Tibetan Plateau	Frontiers in Earth Science	2021, 9
28	Ding Minghu (2nd)	The shallowing surface temperature inversions in the Arctic	Journal of Climate	2021, 34(9)
29	Ding Minghu (2nd)	The surface energy balance of Austre Lovénbreen, Svalbard, during the ablation period in 2014	Polar Research	2021, 40

序号 No.	作者 Author (rank)	题名 Title	出版物名/出版社 Publication name or publisher	年，卷（期） Year, volume (issue)
30	Ding Minghu (3rd)	Estimation and long-term trend analysis of surface solar radiation in Antarctica: A case study of Zhongshan Station	Advances in Atmospheric Sciences	2021, 38
31	Duan Jing, et al.	Cable-car measurements of vertical aerosol profiles impacted by mountain-valley breezes in Lushan Mountain, East China	Science of the Total Environment	2021, 768
32	Duan Jing (2nd)	Satellite estimates and subpixel variability of rainfall in a semi-arid grassland	Atmospheric and Oceanic Science Letters	2021, 14(5)
33	Duan Jing (2nd)	A hypergraph-embedded convolutional neural network for ice crystal particle habit classification	Intelligent Automation & Soft Computing	2021, 29(3)
34	Fan Xiangpeng, et al.	Radio interference observations and analysis of an energetic in-cloud pulse based on ensemble empirical mode decomposition	IEEE Transactions on Geoscience and Remote Sensing	2021, 59(12)
35	Fan Yanfeng, et al.	Electromagnetic characteristics of upward leader initiated from the Canton Tower: A comparison with rocket-triggered lightning	Journal of Geophysical Research: Atmospheres	2021, 126
36	Fan Yanfeng (3rd)	A comprehensive study on the improved radio-frequency magnetic field measurement for the initial upward leader of a negative rocket-triggered lightning flash	Remote Sensing	2021, 13
37	Fang Shibo (2nd)	Analyzing the probability of acquiring cloud-free imagery in China with AVHRR cloud mask data	Atmosphere	2021, 12
38	Fang Shibo (2nd)	Analysis of variation in reference evapotranspiration and its driving factors in mainland China from 1960 to 2016	Environmental Research Letters	2021, 16
39	Fang Shibo (2nd)	Risk analysis of wheat yield losses at the county level in mainland China	Frontiers in Environmental Science	2021, 9
40	Gao Wenhua, et al.	A study of the fraction of warm rain in a pre-summer rainfall event over South China	Atmospheric Research	2021, 262
41	Gao Wenhua (3rd)	Intensity and microphysical properties surrounding the rapid intensification in landfalling super typhoons over China during the summer and autumn seasons	International Journal of Climatology	2021, 41
42	Gong Shanling, et al.	Assessment of meteorology vs. control measures in the China fine particular matter trend from 2013 to 2019 by an environmental meteorology index	Atmospheric Chemistry and Physics	2021, 21
43	Gong Shanling (2nd)	A new parameterization of uptake coefficients for heterogeneous reactions on multi-component atmospheric aerosols	Science of the Total Environment	2021, 781
44	Gong Shanling (2nd)	Impacts of long-range transports from Central and South Asia on winter surface $PM_{2.5}$ concentrations in China	Science of the Total Environment	2021, 777

序号 No.	作者 Author (rank)	题名 Title	出版物名/出版社 Publication name or publisher	年，卷（期） Year, volume (issue)
45	Gui Ke, et al.	Three-dimensional climatology, trends, and meteorological drivers of global and regional tropospheric type-dependent aerosols: Insights from 13 years (2007−2019) of CALIOP observations	Atmospheric Chemistry and Physics	2021, 21
46	Gui Ke, et al.	A global-scale analysis of the MISR Level-3 aerosol optical depth (AOD) product: Comparison with multi-platform AOD data sources	Atmospheric Pollution Research	2021, 12(12)
47	Gui Ke, et al.	Seasonal variability and trends in global type-segregated aerosol optical depth as revealed by MISR satellite observations	Science of the Total Environment	2021, 787
48	Gui Ke (2nd)	Seasonal distribution and vertical structure of different types of aerosols in Southwest China observed from CALIOP	Atmospheric Environment	2021, 246
49	Gui Ke (2nd)	Estimating hourly surface $PM_{2.5}$ concentrations across China from high-density meteorological observations by machine learning	Atmospheric Research	2021, 254
50	Gui Ke (2nd)	Climatological variations in aerosol optical depth and aerosol type identification in Liaoning of Northeast China based on MODIS data from 2002 to 2019	Science of the Total Environment	2021, 781
51	Gui Ke (2nd)	Climatology and trends of aerosol optical depth with different particle size and shape in Northeast China from 2001 to 2018	Science of the Total Environment	2021, 763
52	Gui Ke (2nd)	Identifying the dominant local factors of 2000−2019 changes in dust loading over East Asia	Science of the Total Environment	2021, 777
53	Gui Ke (2nd)	Three-dimensional spatiotemporal evolution of wildfire-induced smoke aerosols: A case study from Liangshan, Southwest China	Science of the Total Environment	2021, 762
54	Guo Jianping, et al.	Investigation of near-global daytime boundary layer height using high-resolution radiosondes: First results and comparison with ERA-5, MERRA-2, JRA-55, and NCEP-2 reanalyses	Atmospheric Chemistry and Physics	2021, 21
55	Guo Jianping, et al.	Technical note: First comparison of wind observations from ESA's satellite mission Aeolus and ground-based radar wind profiler network of China	Atmospheric Chemistry and Physics	2021, 21
56	Guo Jianping, et al.	Satellite-derived long-term estimates of full-coverage PM_1 concentrations across China based on a stacking decision tree model	Atmospheric Environment	2021, 255
57	Guo Jianping (2nd)	Regional variability of summertime raindrop size distribution from a network of disdrometers in Beijing	Atmospheric Research	2021, 257
58	Guo Jianping (2nd)	Vertical structures of temperature inversions and clouds derived from high-resolution radiosonde measurements at Ny-lesund, Svalbard	Atmospheric Research	2021, 254

序号 No.	作者 Author (rank)	题名 Title	出版物名/出版社 Publication name or publisher	年，卷（期） Year, volume (issue)
59	Guo Jianping (2nd)	Atmospheric boundary layer height variation over mountainous and urban sites in Beijing as derived from radar wind profiler measurements	Boundary-Layer Meteorology	2021, 181(1)
60	Guo Jianping (2nd)	Spatiotemporal characteristics of atmospheric turbulence over China estimated using operational high-resolution soundings	Environmental Research Letters	2021, 16
61	Guo Jianping (3rd)	Characteristics of surface energy balance and atmospheric circulation during hot-and-polluted episodes and their synergistic relationships with urban heat islands over the Pearl River Delta region	Atmospheric Chemistry and Physics	2021, 21
62	Guo Jianping (3rd)	Contrasting effect of soil moisture on the daytime boundary layer under different thermodynamic conditions in summer over China	Geophysical Research Letters	2021, 48
63	Guo Jianping (3rd)	Long-term trend comparison of planetary boundary layer height in observations and CMIP6 models over China	Journal of Climate	2021, 34(20)
64	Guo Jianping (3rd)	Distinct spatiotemporal variation patterns of surface ozone in China due to diverse influential factors	Journal of Environmental Management	2021, 288
65	Guo Jianping (3rd)	Impacts of biomass burning in peninsular Southeast Asia on $PM_{2.5}$ concentration and ozone formation in southern China during springtime—A case study	Journal of Geophysical Research: Atmospheres	2021, 126(22)
66	Guo Lijun, et al.	Radiative effects of clouds and fog on long-lasting heavy fog events in northern China	Atmospheric Research	2021, 252
67	Han Shuangze, et al.	A skillful prediction scheme for April precipitation over central East China	Atmospheric Research	2021, 261
68	Han Shuangze, et al.	Connection between the November snow cover over Northeast Asia and the following January precipitation in southern China	International Journal of Climatology	2021, 41(4)
69	Hu Zhiqun (2nd)	Study on radar echo-filling in an occlusion area by a deep learning algorithm	Remote Sensing	2021, 13(9)
70	Hu Zhiqun (3rd)	Application of the multi-source data fusion algorithm in the hail identification	Asia-Pacific Journal of Atmospheric Sciences	2021, DOI: 10.1007/s13143-021-00265-y
71	Huang Mengtian, et al.	Achieving Paris Agreement temperature goals requires carbon neutrality by middle century with far-reaching transitions in the whole society	Advances in Climate Change Research	2021, 12
72	Huang Mengtian, et al.	Divergent responses of ecosystem water use efficiency to drought timing over Northern Eurasia	Environmental Research Letters	2021, 16
73	Huang Mengtian (2nd)	Change in drought conditions and its impacts on vegetation growth over the Tibetan Plateau	Advances in Climate Change Research	2021, 12

序号 No.	作者 Author (rank)	题名 Title	出版物名/出版社 Publication name or publisher	年，卷（期） Year, volume (issue)
74	Huang Mengtian (2nd)	Performance of the CRA-40/land, CMFD, and ERA-interim datasets in reflecting changes in surface air temperature over the Tibetan Plateau	Journal of Meteorological Research	2021, 35(4)
75	Jiang Ning (2nd)	Combined impacts of sea surface temperature in tropical Pacific and North Atlantic Oceans on the winter rainfall in southern China under decadal background	International Journal of Climatology	2021, 41(11)
76	Jiang Zhina, et al.	Two atmospheric responses to winter sea ice decline over the Barents-Kara Seas	Geophysical Research Letters	2021, 48
77	Li Dequan, et al.	Fact: An air-ground communication framework for seeding quality control of aircraft	Computer Systems Science and Engineering	2021, 41(2)
78	Li Haoran	Supercooled liquid water and secondary ice production in Kelvin-Helmholtz instability as revealed by radar Doppler spectra observations	Atmospheric Chemistry and Physics	2021, 21
79	Li Haoran	Two-year statistics of columnar-ice production in stratiform clouds over Hyytiala, Finland: Environmental conditions and the relevance to secondary ice production	Atmospheric Chemistry and Physics	2021, 21
80	Li Jian, et al.	Assessing the surface-layer stability over China using long-term wind-tower-metwork observations	Boundary-Layer Meteorology	2021, 180
81	Li Jian (2nd)	Evaluation of CMIP6 HighResMIP models in simulating precipitation over Central Asia	Advances in Climate Change Research	2021, 13(1)
82	Li Jian (2nd)	Fine-scale characteristics of summer precipitation over Cang Mountain	Journal of Applied Meteorology and Climatology	2021, 60(9)
83	Li Jianduo, et al.	Evaluation of CMIP6 global climate models for simulating land surface energy and water fluxes during 1979–2014	Journal of Advances in Modeling Earth Systems	2021, 13
84	Li Lei (2nd)	Validation of the aerosol optical property products derived by the GRASP/Component approach from multi-angular polarimetric observations	Atmospheric Research	2021, 263
85	Li Lei (2nd)	Spatio-temporal variability of aerosol components, their optical and microphysical properties over North China during winter haze in 2012, as derived from POLDER/PARASOL satellite observations	Remote Sensing	2021, 13(14)
86	Li Lun, et al.	Roles of the Tibetan Plateau vortices in the record Meiyu rainfall in 2020	Atmospheric Science Letters	2021, 22
87	Li Lun, et al.	Efect of upper-level air temperature changes over the Tibetan Plateau on the genesis frequency of Tibetan Plateau vortices at interannual timescales	Climate Dynamics	2021, 57
88	Li Lun, et al.	Regionally different precipitation trends over the Tibetan Plateau in the warming context: A perspective of the Tibetan Plateau vortices	Geophysical Research Letters	2021, 48

序号 No.	作者 Author (rank)	题名 Title	出版物名/出版社 Publication name or publisher	年，卷（期） Year, volume (issue)
89	Li Lun (3rd)	Anthropogenic influences on the extreme cold surge of early spring 2019 over the southeastern Tibetan Plateau	Bulletin of the American Meteorological Society	2021, 102(1)
90	Li Mingxin, et al.	Analysis of a record-breaking rainfall event associated with a monsoon coastal megacity of South China using multisource data	IEEE Transactions on Geoscience and Remote Sensing	2021, 59(8)
91	Li Puxi, et al.	Convection permitting modelling improves simulated precipitation over the central and eastern Tibetan Plateau	Quarterly Journal of the Royal Meteorological Society	2021, 147(734)
92	Li Puxi (3rd)	Added value of a convection permitting model in simulating atmospheric water cycle over the Asian Water Tower	Journal of Geophysical Research: Atmospheres	2021, 126(13)
93	Li Ying (2nd)	The cold avoidance of typhoons in their north turning over the South China Sea	Frontiers in Earth Science	2021, 9
94	Liang Linlin, et al.	Measurement report: Chemical characteristics of $PM_{2.5}$ during typical biomass burning season at an agricultural site of the North China Plain	Atmospheric Chemistry and Physics	2021, 21
95	Liang Xudong (2nd)	A study of extrapolation nowcasting based on IVAP-retrieved wind	Journal of Atmospheric and Oceanic Technology	2021, 38
96	Liang Zhaoming, et al.	Study of the formation of the Arctic cell associated with the two-wave middle-high latitude circulation	Atmospheric Research	2021, 258
97	Liang Zhaoming, et al.	A dynamical and numerical study of the effects of the topography of the Tibetan Plateau and westerly wind speed on the East Asian trough	International Journal of Climatology	2021, 42(1)
98	Liang Zhaoming, et al.	Organized warm-sector rainfall in the coastal region of South China in an anticyclone synoptic situation: Observational analysis	Journal of Meteorological Research	2021, 35(3)
99	Liao Rongwei, et al.	Study of wind characteristic in Tibet with numerical simulation	IOP Conference Series: Earth and Environmental Science	2021, 821
100	Liao Rongwei, et al.	Wind characteristic in the complex underlying terrain as studied with CALMET system	Journal of Physics: Conference Series	2021, 2006
101	Liao Zhen, et al.	Growing threats from unprecedented sequential flood-hot extremes across China	Geophysical Research Letters	2021, 48(18)
102	Liu Bo, et al.	Seasonal prediction skills in the CAMS-CSM climate forecast system	Climate Dynamics	2021, 57
103	Liu Boqi, et al.	Seasonal evolution of anomalous rainband over East China regulated by sea surface temperature anomalies in the Northern Hemisphere	Journal of Climate	2021, 34
104	Liu Boqi, et al.	Subseasonal-to-seasonal predictability of onset dates of South China Sea summer monsoon: A perspective of meridional temperature gradient	Journal of Climate	2021, 34

序号 No.	作者 Author (rank)	题名 Title	出版物名/出版社 Publication name or publisher	年，卷（期） Year, volume (issue)
105	Liu Boqi (2nd)	Climatological intraseasonal oscillation in the middle-upper troposphere and its effect on the northward migration of the East Asian westerly jet and rain belt over eastern China	International Journal of Climatology	2021, 41
106	Liu Ge (2nd)	Precursory signals (SST and soil moisture) of summer surface temperature anomalies over the Tibetan Plateau	Atmosphere	2021, 12(2)
107	Liu Ge (2nd)	Effect of preceding soil moisture-snow cover anomalies around Turan Plain on June precipitation over the southern Yangtze River valley	Atmospheric Research	2021, 264
108	Liu Ge (2nd)	A tripole pattern of summer surface air temperature anomalies over northern Eurasia and its precursory signals in the tropical Atlantic and northern Asian land	International Journal of Climatology	2021, 41
109	Liu Ge (3rd)	Contribution of precipitation events with different consecutive days to rainfall change over Asia during ENSO years	Theoretical and Applied Climatology	2021, 144
110	Liu Hengyi (2nd)	Lightning fatalities in China, 2009−2018	Journal of Agricultural Meteorology	2021, 77(2)
111	Liu Lei, et al.	Characteristics and potential sources of wintertime air pollution in Linfen, China	Environmental Monitoring and Assessment	2021, 193(5)
112	Liu Lei (3rd)	Comparative analysis of $PM_{2.5}$ and O_3 source in Beijing using a chemical transport model	Remote Sensing	2021, 13(17)
113	Liu Lin, et al.	Large-scale pattern of the wintertime diurnal temperature range variations over North America during 1979−2018	Atmospheric Research	2021, 257
114	Liu Lin, et al.	Evaluation of FY-3B reprocessed OLR data in the Asian-Australian monsoon region during 2011−2019: Comparison with NOAA OLR	Journal of Meteorological Research	2021, 35(6)
115	Liu Liping (2nd)	Analysis of the vertical air motions and raindrop size distribution retrievals of a squall line based on cloud radar doppler spectral density data	Atmosphere	2021, 12(3)
116	Liu Liping (3rd)	Deep learning for polarimetric radar quantitative precipitation estimation during landfalling typhoons in South China	Remote Sensing	2021, 13(16)
117	Liu Lu, et al.	The performance of three exponential decay models in estimating tropical cyclone intensity change after landfall over China	Frontiers in Earth Science	2021, 9
118	Liu Quan, et al.	Reduced volatility of aerosols from surface emissions to the top of the planetary boundary layer	Atmospheric Chemistry and Physics	2021, DOI:10.5194/acp-2021-362
119	Liu Yusi, et al.	Unexpected deep mixing layer in the Sichuan Basin, China	Atmospheric Research	2021, 249
120	Liu Yusi, et al.	Impact of residual layer transport on air pollution in Beijing, China	Environmental Pollution	2021, 271

序号 No.	作者 Author (rank)	题名 Title	出版物名/出版社 Publication name or publisher	年，卷（期） Year, volume (issue)
121	Liu Yusi (2nd)	Bypassing the NO_x titration trap in ozone pollution control in Beijing	Atmospheric Research	2021, 249
122	Liu Yusi (3rd)	The difference in the boundary layer height between urban and suburban areas in Beijing and its implications for air pollution	Atmospheric Environment	2021, 260
123	Liu Yusi (3rd)	Low particulate nitrate in the residual layer in autumn over the North China Plain	Science of the Total Environment	2021, 782
124	Lyv Weitao (2nd)	First documented downward positive cloud-to-ground lightning initiated by an upward negative lightning	Journal of Geophysical Research: Atmospheres	2021, 126
125	Luo Yali (2nd)	Effects of anthropogenic and sea salt aerosols on a heavy rainfall event during the early-summer rainy season over coastal Southern China	Atmospheric Research	2021, 265
126	Luo Yali (2nd)	General features and synoptic-scale environments of mesoscale convective systems over South China during the 2013−2017 pre-summer rainy seasons	Atmospheric Research	2021, 266
127	Luo Yali (2nd)	A statistical analysis of extreme hot characteristics and their relationships with urbanization in Southern China during 1971−2020	Journal of Applied Meteorology and Climatology	2021, 60(9)
128	Luo Yali (2nd)	On the localized extreme rainfall over the great bay area in South China with complex topography and strong UHI effects	Monthly Weather Review	2021, 149(8)
129	Luo Yali (3rd)	A double-moment SBU-YLIN cloud microphysics scheme and its impact on a squall line simulation	Journal of Advances in Modeling Earth Systems	2021, 13(11)
130	Ma Jianzhong, et al.	Ozone and aerosols over the Tibetan Plateau	Asian Atmospheric Pollution	2021, DOI: 10.1016/B978-0-12-816693-2.00008-1
131	Ma Libin, et al.	Reevaluating the impacts of oceanic vertical resolution on the simulation of Madden-Julian Oscillation eastward propagation in a climate system model	Climate Dynamics	2021, 56
132	Ma Libin, et al.	Sensitivity of ENSO simulation to the convection schemes in the NESM3 climate system model: Atmospheric processes	Frontiers in Earth Science	2021, 9
133	Ma Shuangmei, et al.	Atmospheric circulation regime causing winter temperature whiplash events in North China	International Journal of Climatology	2021, 41(2)
134	Miao Yucong, et al.	Relationship between summertime concurring $PM_{2.5}$ and O_3 pollution and boundary layer height differs between Beijing and Shanghai, China	Environmental Pollution	2021, 268
135	Miao Yucong (2nd)	Impacts of synoptic forcing and topography on aerosol pollution during winter in Shenyang, Northeast China	Atmospheric Research	2021, 262

序号 No.	作者 Author (rank)	题名 Title	出版物名/出版社 Publication name or publisher	年，卷（期） Year, volume (issue)
136	Miao Yucong (2nd)	On the heavy aerosol pollution and its meteorological dependence in Shandong Province, China	Atmospheric Research	2021, 256
137	Nan Sulan, et al.	Links between the thermal condition of the Tibetan Plateau in summer and atmospheric circulation and climate anomalies over the Eurasian continent	Atmospheric Research	2021, 247
138	Nan Sulan (2nd)	Improvement in the prediction of summer precipitation in the North China Hetao Region using the tropospheric temperature over the Tibetan Plateau in spring	Frontiers in Earth Science	2021, 9
139	Nan Sulan (3rd)	Joint influence of anomalous medium-and small-scale circulations on short-term heavy rainfall events over Beijing	International Journal of Climatology	2021, 41
140	Niu Tao (3rd)	Study on the variation of air pollutant concentration and its formation mechanism during the COVID-19 period in Wuhan	Atmospheric Environment	2021, 251
141	Niu Tao (3rd)	Study on the causes of heavy pollution in Shenyang based on the contribution of natural conditions, physical processes, and anthropogenic emissions	Atmospheric Pollution Research	2021, 12
142	Peng Xindong (2nd)	Evaluation of a flexible single ice microphysics and a Gaussian Probability-Density-Function macrophysics scheme in a single column model	Atmosphere	2021, 12
143	Peng Xindong (2nd)	High-order conservative and oscillation-suppressing transport on irregular hexagonal grids	Meteorology and Atmospheric Physics	2021, 133(3)
144	Qi Qi, et al.	Two-dimensional striking distance of lightning flashes to a cluster of tall buildings in Guangzhou	Journal of Geophysical Research: Atmospheres	2021, 126
145	Ren Hongli (2nd)	Diagnosing SST error growth during ENSO developing phase in BCC_CSM1.1(m) prediction system	Advances in Atmospheric Sciences	2021, 39
146	Ren Hongli (2nd)	Decomposition of projected summer rainfall change over East Asia based on timeslice experiments	Climate Dynamics	2021, 56
147	Ren Hongli (2nd)	Impacts of late-spring North Eurasian soil moisture variation on summer rainfall anomalies in northern East Asia	Climate Dynamics	2021, DOI:10.21203/rs.3.rs-419930/v1
148	Ren Hongli (2nd)	Understanding the causes of rapidly declining prediction skill of the East Asian summer monsoon rainfall with lead time in BCC_CSM1.1m	Climate Dynamics	2021, DOI:10.1007/s00382-021-05819-4
149	Ren Hongli (2nd)	Improving long-lead seasonal forecasts of precipitation over southern China based on statistical downscaling using BCC_CSM1.1m	Dynamics of Atmospheres and Oceans	2021, 94

序号 No.	作者 Author (rank)	题名 Title	出版物名/出版社 Publication name or publisher	年，卷（期） Year, volume (issue)
150	Ren Hongli (2nd)	ENSO phase-locking behavior in climate models: From CMIP5 to CMIP6	Environmental Research Communications	2021, 3
151	Ren Hongli (2nd)	Change of East-Asian summer precipitation associated with strong El Niño under the future emission scenarios	Frontiers in Earth Science	2021, 9
152	Ren Hongli (2nd)	Evaluation of simulation capability for multiple tropical cyclone events in the western North Pacific of the UH_HCM model	Frontiers in Earth Science	2021, 8
153	Ren Hongli (3rd)	Dynamical and machine learning hybrid seasonal prediction of summer rainfall in China	Journal of Meteorological Research	2021, 35(4)
154	Rong Xinyao, et al.	The CMIP6 historical simulation datasets produced by the climate system model CAMS-CSM	Advances in Atmospheric Sciences	2021, 38
155	Ruan Zheng (2nd)	Estimating raindrop size distributions and vertical air motions with spectral difference using vertically pointing radar	Journal of Atmospheric and Oceanic Technology	2021, 38(10)
156	Ruan Zheng (2nd)	Vertical evolution of microphysical properties during snow events in middle latitudes of China observed by a C-band vertically pointing radar	Journal of the Meteorological Society of Japan	2021, 99(3)
157	Shen Xiaojing, et al.	Enhancement of nanoparticle formation and growth during the COVID-19 lockdown period in urban Beijing	Atmospheric Chemistry and Physics	2021, 21
158	Shen Xiaojing, et al.	A novel method of retrieving low visibility during heavily polluted episodes in the North China plain	Atmospheric Environment: X	2021, X9
159	Shen Xiaojing, et al.	Long-term trend ofnew particle formation events in the Yangtze River Delta, China and its influencing factors: 7-year dataset analysis	Science of the Total Environment	2021, 807
160	Shi Xiaohui, et al.	Remote forcing effect of sea surface temperatures in the northern tropical Atlantic on tropical cyclone genesis over the western North Pacific in July	International Journal of Climatology	2021, DOI:10.1002/joc.7438
161	Shi Xiaohui, et al.	Trends in the differences between homogenized ground surface temperature and surface air temperature in China during 1961−2016 and its possible causes	Theoretical and Applied Climatology	2021, 144
162	Song Jinjie, et al.	Increasing lifetime maximum intensity of rapidly intensifying tropical cyclones over the western North Pacific	Environmental Research Letters	2021, 16
163	Song Jinjie, et al.	Slowdown in the decay of western North Pacific tropical cyclones making landfall on the Asian continent	Frontiers in Earth Science	2021, 9
164	Song Jinjie, et al.	Modulation of tropical cyclone formation over the western North Pacific by the ENSO combination mode	Geophysical Research Letters	2021, 48(5)

序号 No.	作者 Author (rank)	题名 Title	出版物名/出版社 Publication name or publisher	年，卷（期） Year, volume (issue)
165	Song Jinjie, et al.	Recent weakening of the interannual relationship between ENSO Modoki and boreal summer tropical cyclone frequency over the western North Pacific	Journal of the Meteorological Society of Japan	2021, 99(4)
166	Sun Chenghu, et al.	Diverse inter-annual variations of winter Siberian high and link with Eurasian snow in observation and BCC-CSM2-MR coupled model simulation	Frontiers in Earth Science	2021, 9
167	Sun Junying (2nd)	Simultaneous measurements of PM_1 and PM_{10} aerosol scattering properties and their relationships in urban Beijing: A two-year observation	Science of the Total Environment	2021, 770
168	Sun Qing (3rd)	The decrease in lake numbers and areas in central Asia investigated using a landsat-derived water dataset	Remote Sensing	2021, 13
169	Sun Shuang, et al.	Dryland maize yield potentials and constraints: A case study in western Kansas	Food and Energy Security	2021, DOI:10.1002/fes3.328
170	Sun Wei, et al.	Assimilation of FY-3D MWHS-2 radiances with WRF hybrid-3DVAR system for the forecast of heavy rainfall evolution associated with typhoon Ampil	Monthly Weather Review	2021, 149 (12)
171	Sun Wei (3rd)	Three-dimensional variational assimilation of Lidar extinction profiles: Application to $PM_{2.5}$ prediction in North China	Atmospheric Environment	2021, 269
172	Sun Xiaogong (2nd)	Linking ECMWF 2 m temperature forecast errors with upper-Level circulation situation: A case-study for China	Atmosphere	2021, 12
173	Wang Chunyi (2nd)	Spring phenological sensitivity to climate change in the northern hemisphere: Comprehensive evaluation and driving force analysis	Remote Sensing	2021, 13
174	Wang Fei, et al.	An airborne study of the aerosol effect on the dispersion of cloud droplets in a drizzling marine stratocumulus cloud over eastern China	Atmospheric Research	2021, 265
175	Wang Fei, et al.	Characteristics of negative leader propagation area of lightning flashes initiated in the stratiform regions of mesoscale convective systems	Journal of Geophysical Research: Atmospheres	2021, 126(3)
176	Wang Fei (2nd)	Seasonal variations of aerosol number concentration and spectrum distribution in Nanjing	International Journal of Environment and Pollution	2021, 68
177	Wang Gaili, et al.	Drop-size distribution measurements in Southeast Tibetan Plateau during STEP	Atmospheric Research	2021, 249
178	Wang Gaili, et al.	A multiscale analysis of the extreme heavy rainfall event on 14 July 2017 in northeastern China	Monthly Weather Review	2021, 173
179	Wang Gaili (2nd)	Cloud vertical structure measurements from a ground-based cloud radar over the southeastern Tibetan Plateau	Atmospheric Research	2021, 258

序号 No.	作者 Author (rank)	题名 Title	出版物名/出版社 Publication name or publisher	年，卷（期） Year, volume (issue)
180	Wang Hong (2nd)	Application of Morrison cloud microphysics scheme in GRAPES_meso model and the sensitivity study on CCN's impacts on cloud radiation	Atmosphere	2021, 12(4)
181	Wang Hong (2nd)	Impacts of PBL schemes on $PM_{2.5}$ simulation and their responses to aerosol-radiation feedback in GRAPES_CUACE model during severe haze episodes in Jing-Jin-Ji, China	Atmospheric Research	2021, 248
182	Wang Hong (2nd)	Radiative forcing of the aerosol-cloud interaction in seriously polluted East China and East China Sea	Atmospheric Research	2021, 252
183	Wang Hui, et al.	A numerical study of typhoon Megi (2010). Part II: Eyewall evolution crossing the Luzon Island	Monthly Weather Review	2021, 149 (2)
184	Wang Peijuan, et al.	Mapping threats of spring frost damage to tea plants using satellite-based minimum temperatures estimation in China	Remote Sensing	2021, 13
185	Wang Peijuan, et al.	Spring frost damage to tea plants can be identified with daily minimum air temperatures estimated by MODIS land surface temperature products	Remote Sensing	2021, 13
186	Wang Peijuan (2nd)	Standardized relative humidity index can be used to identify agricultural drought for summer maize in the Huang-Huai-Hai Plain, China	Ecological Indicators	2021, 131
187	Wang Qi, et al.	Does reduced intra-specific competition of the dominant species in intercrops allow for a higher population density?	Food and Energy Security	2021, 10
188	Wang Qi, et al.	Light interception and use efficiency differ with maize plant density in maize-peanut intercropping	Frontiers of Agricultural Science and Engineering	2021, 8(3)
189	Wang Sai	Impact of internal variability on recent opposite trends in wintertime temperature over the Barents-Kara Seas and central Eurasia	Climate Dynamics	2021, DOI:10.21203/rs.3.rs-189593/v1
190	Wang Sai, et al.	Potential mechanisms governing the variation in rain/snow frequency over the northern Antarctic Peninsula during austral summer	Atmospheric Research	2021, 263
191	Wang Yaqiang (2nd)	Classification of the circulation patterns related to strong dust weather in China using a combination of the Lamb-Jenkinson and *k*-means clustering methods	Atmosphere	2021, 12
192	Wang Yaqiang (3rd)	Reconstruction of missing data in weather radar image sequences using deep neuron networks	Applied Sciences-Basel	2021, 11
193	Wang Zhili, et al.	Reduction in European anthropogenic aerosols and the weather conditions conducive to $PM_{2.5}$ pollution in North China: A potential global teleconnection pathway	Environmental Research Letters	2021, 16
194	Wang Zhili, et al.	Incorrect Asian aerosols affecting the attribution and projection of regional climate change in CMIP6 models	Climate and Atmospheric Science	2021, 4

序号 No.	作者 Author (rank)	题名 Title	出版物名/出版社 Publication name or publisher	年，卷（期） Year, volume (issue)
195	Wang Zhili (2nd)	Responses of the East Asian summer monsoon to aerosol forcing in CMIP5 models: The role of upper-tropospheric temperature change	International Journal of Climatology	2021, 41(3)
196	Wei Ting	Reduction in extreme climate events and potential impacts by the use of technological advances	International Journal of Climatology	2021, 41(13)
197	Wei Ting (3rd)	A westward shift in tropical cyclone potential intensity and genesis regions in the North Atlantic during the last interglacial	Geophysical Research Letters	2021, 48(12)
198	Wen Min (2nd)	Relations between the quasi-biweekly oscillation over the East Asian monsoon region and the East Asian tropical monsoon	International Journal of climatology	2021, 41(2)
199	Wu Bin, et al.	A positive cloud-to-ground flash caused by a sequence of bidirectional leaders that served to form a ground- reaching branch of a pre-existing horizontal channel	Journal of Geophysical Research: Atmospheres	2021, 126(11)
200	Wu Chong, et al.	Challenges of the polarimetric update on operational radars in China-ground clutter contamination of weather radar observations	Remote Sensing	2021, 13(2)
201	Wu Chong (3rd)	Microphysical characteristics of the coexisting frontal and warm-sector heavy rainfall in South China	Journal of Geophysical Research: Atmospheres	2021, 126
202	Xia Rudi, et al.	On the diurnal cycle of heavy rainfall over the Sichuan basin during 10−18 August 2020	Advances in Atmospheric Sciences	2021, 38(12)
203	Xia Rudi (2nd)	Vorticity and moisture budget analyses on a plateau vortex that cause an intense rainfall event within the Qaidam Basin	Atmospheric Science Letters	2021, 22(e1040)
204	Xiao Dong, et al.	Climatic factors contributing to interannual and interdecadal variations in the meridional displacement of the East Asian jet stream in boreal winter	Atmospheric Research	2021, 264
205	Xiao Dong, et al.	Interdecadal changes in synoptic transient eddy activity over the Northeast Pacific and their role in tropospheric Arctic amplification	Climate Dynamics	2021, 57
206	Xiao Dong (2nd)	Role of the warming trend in global land surface air temperature variations	Science China: Earth Sciences	2021, 64
207	Xin Yufei, et al.	Modulation of snow on the daily evolution of surface heating over the Tibetan Plateau during winter: Observational analyses	Earth and Space Science	2021, 8
208	Xu Hongxiong, et al.	Effect of the vertical diffusion of moisture in the planetary boundary layer on an idealized tropical cyclone	Advances in Atmospheric Sciences	2021, 38(11)
209	Xu Hongxiong, et al.	Sensitivity of fine-scale structure in tropical cyclone boundary layer to model horizontal resolution at sub-kilometer grid spacing	Frontiers in Earth Science	2021, 9

序号 No.	作者 Author (rank)	题名 Title	出版物名/出版社 Publication name or publisher	年，卷（期） Year, volume (issue)
210	Xu Hui, et al.	The significant role of radiosonde-measured cloud-base height in the estimation of cloud radiative forcing	Advances in Atmospheric Sciences	2021, 38(9)
211	Xu Jing (2nd)	Stochastic simulation of tropical cyclones for risk assessment at one go: A multivariate functional PCA approach	Earth and Space Science	2021, 8
212	Xu Jing (3rd)	A new time-dependent theory of tropical cyclone intensification	Journal of the Atmospheric Sciences	2021, 78
213	Xu Jing (3rd)	The intensity dependence of tropical cyclone intensification rate in a simplified energetically based dynamical system model	Journal of the Atmospheric Sciences	2021, 78
214	Xu Wanyun, et al.	Aerosol promotes peroxyacetyl nitrate formation during winter in the North China Plain	Environmental Science & Technology	2021, 55(6)
215	Xu Xiangde, et al.	“Warm cover”: Precursory strong signals for haze pollution hidden in the middle troposphere	Atmospheric Chemistry and Physics	2021, 21
216	Xue Haile, et al.	A large-eddy simulation study on the diurnally evolving nonlinear trapped lee waves over a two-dimensional steep mountain	Journal of Atmospheric Sciences	2021, 78(2)
217	Xue Min, et al.	RO_x budgets and O_3 formation during summertime at Xianghe suburban site in the North China Plain	Advances in Atmospheric Sciences	2021, 38(7)
218	Xue Min (3rd)	Analysis of the effect of optical properties of black carbon on ozone in an urban environment at the Yangtze River Delta, China	Advances in Atmospheric Sciences	2021, 38(7)
219	Yan Xiaolu, et al.	Asymmetry and pathways of inter-hemispheric transport in the upper troposphere and lower stratosphere	Atmospheric Chemistry and Physics	2021, 21(9)
220	Yan Yuhan, et al.	Annual cycle of East Asian precipitation simulated by CMIP6 models	Atmosphere	2021, 12
221	Yan Yuhan, et al.	Subseasonal forecast barrier of the North Atlantic Oscillation in S2S models during the extreme Meiyu rainfall event in 2020	Climate Dynamics	2021, DOI:10.1007/S00382-021-06076-1
222	Yan Yuhan, et al.	Subseasonal predictability of South China Sea summer monsoon onset with the ECMWF S2S forecasting system	Geophysical Research Letters	2021, 48
223	Yang Jianying, et al.	Threshold-based characteristics of apricot frost exposure at young fruit in the warm temperate zone, China	International Journal of Climatology	2021, DOI:10.1002/joc.7313
224	Yang Jianying, et al.	Indicator based spatiotemporal characteristics of apple drought in North China	Natural Hazards	2021, 108(2)
225	Yang Jianying, et al.	Process-based indicators for timely identification of apricot frost disaster on the warm temperate zone, China	Theoretical and Applied Climatology	2021, 146

序号 No.	作者 Author (rank)	题名 Title	出版物名/出版社 Publication name or publisher	年，卷（期） Year, volume (issue)
226	Yin Jinfang, et al.	An investigation into the vertical structures of low-altitude atmosphere over the Central Taklimakan Desert in summer	Atmospheric Science Letters	2021, 22(9)
227	Yin Jinfang (2nd)	Evaluation of five reanalysis products with radiosonde observations over the central Taklimakan Desert during summer	Earth and Space Science	2021, 8
228	Yu Rong, et al.	Changes in summer persistent precipitation over the middle-lower reaches of the Yangtze River and associated atmospheric circulation patterns	Journal of Meteorological Research	2021, 35(3)
229	Yun Yuxing, et al.	Warm-season mesoscale convective systems over eastern China: Convection permitting climate model simulation and observation	Climate Dynamics	2021, 57
230	Zhai Panmao (2nd)	Hourly extreme precipitation changes under the influences of regional and urbanization effects in Beijing	International Journal of Climatology	2021, 41
231	Zhang Dongqi (2nd)	Monsoon clouds control the summer surface energy balance on East Rongbuk Glacier (6,523 m above sea level), the northern of Mt. Qomolangma (Everest)	Journal of Geophysical Research: Atmospheres	2021, 126
232	Zhang Gen, et al.	Simultaneous observation of atmospheric peroxyacetyl nitrate and ozone in the megacity of Shanghai, China: Regional transport and thermal decomposition	Environmental Pollution	2021, 274
233	Zhang Guo, et al.	Effects of organic soil in the Noah-MP land-surface model on simulated skin and soil temperature profiles and surface energy exchanges for China	Atmospheric Research	2021, 249
234	Zhang Guo, et al.	Effects of mosaic representation of land use/land cover on skin temperature and energy fluxes in Noah-MP land surface model over China	Journal of Geophysical Research: Atmospheres	2021, 126
235	Zhang Hua, et al.	Advances in research on the ITCZ: Mean position, model bias, and anthropogenic aerosol influences	Journal of Meteorological Research	2021, 35(5)
236	Zhang Hua (2nd)	Evaluating the impacts of cloud microphysical and overlap parameters on simulated clouds in global climate models	Advances in Atmospheric Sciences	2021, DOI:10.1007/s00376-021-0369-7
237	Zhang Hua (2nd)	Changes in anthropogenic particulate matters and resulting global climate effects since the Industrial Revolution	International Journal of Climatology	2021, 42(1)
238	Zhang Hua (2nd)	Potential driving factors on surface solar radiation trends over China in recent years	Remote Sensing	2021, 13(4)
239	Zhang Lei, et al.	Characteristics of low-level temperature inversions over the Arctic Ocean during the CHINARE 2018 campaign in summer	Atmospheric Environment	2021, 260

序号 No.	作者 Author (rank)	题名 Title	出版物名/出版社 Publication name or publisher	年，卷（期） Year, volume (issue)
240	Zhang Lei, et al.	Development of WRF/CUACE v1.0 model and its preliminary application in simulating air quality in China	Geoscientific Model Development	2021, 14(2)
241	Zhang Rong, et al.	Revisiting the size of nonspherical particles recorded by optical array probes with a new method based on the convex hull	Atmospheric and Oceanic Science Letters	2021, DOI: 10.1016/ j.aosl.2021. 100136
242	Zhang Rong (3rd)	Microphysical characteristics of precipitating cumulus cloud based on airborne Ka-band cloud radar and droplet measurements	Atmospheric and Oceanic Science Letters	2021, DOI: 10.1016/ j.aosl.2021. 100134
243	Zhang Xiaoye (2nd)	Impact of modified turbulent diffusion of $PM_{2.5}$ aerosol in WRF-Chem simulations in eastern China	Chemphyschem	2021, DOI:10.5194/ acp-2021-435
244	Zhang Xiaoye (2nd)	Application of turbulent diffusion term of aerosols in mesoscale model	Geophysical Research Letters	2021, 48(11)
245	Zhang Xiaoye (2nd)	The influence of stagnant and transport types weather on heavy pollution in the Yangtze-Huaihe Valley, China	Science of the Total Environment	2021, 792
246	Zhang Yang (2nd)	A new method for connecting the radiation sources of lightning discharge extension channels	Earth and Space Science	2021, 8
247	Zhang Yang (2nd)	Fast and fine location of total lightning from low frequency signals based on deep-learning encoding features	Remote Sensing	2021, 13
248	Zhang Yi, et al.	Increasing maize yields in Northeast China are more closely associated with changes in crop timing than with climate warming	Environmental Research Letters	2021, 16
249	Zhang Yi, et al.	AMIP simulations of a global model for unified weather-climate forecast: Understanding precipitation characteristics and sensitivity over East Asia	Journal of Advances in Modeling Earth Systems	2021, 13(11)
250	Zhang Zhengqiu, et al.	Investigation of the effects of dynamic vegetation processes on global climate simulation using the NCEP GFS and SSiB4/ TRIFFID	Journal of Meteorological Research	2021, 35(6)
251	Zhao Junfang, et al.	Integrated remote sensing and model approach for impact assessment of future climate change on the carbon budget of global forest ecosystems	Global and Planetary Change	2021, 203
252	Zhao Junfang (2nd)	Integrated remote sensing and crop model approach for impact assessment of aerosols on biomass accumulation of maize	IEEE Journal of Selected Topics in Applied Earth Observations and Remote Sensing	2021, 14
253	Zhao Junfang (2nd)	Long-term variations in solar radiation, diffuseradiation, and diffuse radiation fractioncaused by aerosols in China during 1961−2016	PLoS ONE	2021, 16(5)

序号 No.	作者 Author (rank)	题名 Title	出版物名/出版社 Publication name or publisher	年，卷（期） Year, volume (issue)
254	Zhao Junfang (2nd)	Assessment of seasonal variability of extreme temperature in mainland China under climate change	Sustainability	2021, 13
255	Zhao Shoudong, et al.	Frequent locally absent rings indicate increased threats of extreme droughts to semi-arid Pinus tabuliformis forests in North China	Agricultural and Forest Meteorology	2021, 308−309
256	Zhao Yanxia (3rd)	Evaluation and grading of climatic conditions on nutritional quality of rice: A case study of Xiaozhan rice in Tianjin	Meteorological Applications	2021, 28(4)
257	Zhao Dajun, et al.	Impact of the monsoonal surge on extreme rainfall of landfalling tropical cyclones	Advances in Atmospheric Sciences	2021, 38(5)
258	Zhao Dajun, et al.	Associations between strong earthquakes and local rainfall in China	Frontiers in Earth Science	2021, 9
259	Zhao Dajun, et al.	Monsoon surges enhance extreme rainfall by maintaining the circulation of landfalling tropical cyclones and slowing down their movement	Frontiers in Earth Science	2021, 9
260	Zheng Dong, et al.	New insights into the correlation between lightning flash rate and size in thunderstorms	Geophysical Research Letters	2021, 48(24)
261	Zheng Dong (2nd)	Association of lightning occurrence with precipitation cloud column structure at a fixed position	Atmospheric Research	2021, 267
262	Zheng Dong (2nd)	Turbulence characteristics of thunderstorms before the first flash in comparison to non-thunderstorms	Geophysical Research Letters	2021, 48(18)
263	Zheng Dong (2nd)	Winter positive cloud-to-ground lightning flashes observed by LMA in Japan	IEEG Transactions on Electrical and Electronic Engineering	2021, 16(3)
264	Zheng Dong (2nd)	Spatiotemporal lightning activity detected by WWLLN over the Tibetan Plateau and its comparison with LIS lightning	Journal of Atmospheric and Oceanic Technology	2021, 38(3)
265	Zheng Yu, et al.	Aerosol optical properties and its type classification based on multiyear joint observation campaign in North China Plain megalopolis	Chemosphere	2021, 273
266	Zheng Yu (2nd)	Global aerosol classification based on aerosol robotic network (AERONET) and satellite observation	Remote Sensing	2021, 13(6)
267	Zhong Junting, et al.	Attribution of the worse aerosol pollution in March 2018 in Beijing to meteorological variability	Atmospheric Research	2021, 250
268	Zhong Junting, et al.	Robust prediction of hourly $PM_{2.5}$ from meteorological data using LightGBM	National Science Review	2021, 8(10)
269	Zhou Baiquan, et al.	Detectable anthropogenic changes in daily-scale circulations driving summer rainfall shifts over eastern China	Environmental Research Letters	2021, 16

序号 No.	作者 Author (rank)	题名 Title	出版物名/出版社 Publication name or publisher	年，卷（期） Year, volume (issue)
270	Zhou Baiquan, et al.	Application of an improved analog-based heavy precipitation forecast model to the Yangtze-Huai River Valley and its performance in June–July 2020	Journal of Meteorological Research	2021, 35(6)
271	Zhou Chunhong (2nd)	Biological crust in sand and dust storm source areas of Asia and its impact on dust emission	Advances in Climate Change Research	2021, 12
272	Zhou Li, et al.	Increasing temperature shortened the carbon uptake period and decreased the cumulative net ecosystem productivity in a maize cropland in Northeast China	Field Crops Research	2021, 267
273	Zhou Yuquan (3rd)	Increasing cloud water resource in a warming world	Environmental Research Letters	2021, 16
274	Zhou Guangsheng (2nd)	Capability of leaf water content and its threshold values in reflection of soil-plant water status in maize during prolonged drought	Ecological Indicators	2021, 124
275	Zhou Guangsheng (2nd)	The interrelationship between water use efficiency and radiation use efficiency under progressive soil drying in maize	Frontiers in Plant Science	2021, 12
276	Zhou Guangsheng (2nd)	Critical leaf water content for maize photosynthesis under drought stress and its response to rewatering	Sustainability	2021, 13
277	Zhou Guangsheng (2nd)	Quantitative evaluation of the trade-off growth strategies of maize leaves under different drought severities	Water	2021, 13
278	Zhou Guangsheng (2nd)	Quantitative response of maize vcmax25 to persistent drought stress at different growth stages	Water	2021, 13
279	Zhu Congwen, et al.	Diversity of the coupling wheels in the East Asian summer monsoon on the interannual time scale: Challenge of summer rainfall forecasting in China	Advances in Atmospheric Sciences	2021, 38
280	Zhu Congwen (2nd)	Regulation of the subseasonal variability of winter rainfall in South China by the diversity of El Niño-Southern Oscillation	Climate Dynamics	2021, 56
281	Zuo Zhiyan (2nd)	Evaluating boreal summer circulation patterns of CMIP6 climate models over the Asian region	Climate Dynamics	2021, 58

序号 No.	作者 Author (rank)	题名 Title	出版物名/出版社 Publication name or publisher	年，卷（期） Year, Volume (Issue)
1	安兴琴（第 2）	基于 XGBoost 算法的大气化学模式 WRF-Chem 优化模拟研究	中国环境科学	2021，41(12)
2	蔡淼（第 2）	华北地区一次气溶胶与浅积云微物理特性的飞机观测研究	大气科学	2021，45(2)
3	蔡淼（第 3）	全球云水量气候分布及变化趋势特征分析	气候与环境研究	2021，26(5)
4	蔡秀华等	从界壳论探讨生态环境安全	环境生态学	2021，30(5)
5	蔡秀华等	福清厂址区域热带气旋工程参数的估算	气象科技进展	2021，11(2)
6	蔡秀华等	福清核电厂厂址区域龙卷风设计基准参数的估算	气候与环境研究	2021，26(3)
7	常祎（第 2）	祁连山春季一次层状云降水的雨滴谱分布及地形影响特征	大气科学	2021，45(6)
8	常祎（第 3）	祁连山一次地形云降水微物理特征飞机观测	应用气象学报	2021，32(6)
9	常祎等	青藏高原夏季对流云微物理特征和降水形成机制	应用气象学报	2021，32(6)
10	陈昊明（第 2）	2020 年夏季江淮流域降水 ECMWF 模式预报偏差分析	暴雨灾害	2021，40(6)
11	陈昊明（第 2）	千米尺度数值预报模式对泰山地区暖季降水预报性能的评估	气象学报	2021，79(5)
12	陈昊明等	千米尺度模式降水的检验评估进展及展望	气象科技进展	2021，11(3)
13	程宸（第 2）	北京西部生态涵养区气候承载能力初探	农学学报	2021，11(1)
14	翟盘茂等	气候变化科学方面的几个最新认知	气候变化研究进展	2021，17(6)
15	丁明虎（第 2）	南极冰盖地表能量平衡的研究进展	极地研究	2021，33(1)
16	丁明虎（第 3）	基于机器学习方法重建的过去 1000 年北半球环状模（NAM）指数	第四纪研究	2021，41(3)
17	端义宏（第 2）	台风利奇马（1909）双眼墙特征及长时间维持可能机制	应用气象学报	2021，32(3)
18	方春刚等	西北区域人工影响天气试验示范基地设计	气象科技进展	2021，11(5)
19	房世波（第 2）	基于微波数据与光学数据集成的机器学习技术在作物产量估算中的应用	地球信息科学学报	2021，23(6)
20	房小怡等	我国城市通风廊道研究与实践进展	生态学杂志	2021，40(12)
21	桂柯（第 3）	我国西南地区吸收性气溶胶时空分布	中国环境科学	2021，41(7)
22	郭建平（第 2）	山西省主要粮食作物气候资源利用率评估	生态学杂志	2021，40(5)
23	郭建平（第 2）	中国主产区玉米冠层对降水的截留研究	气象	2021，47(5)
24	郭建平等	风廓线雷达组网观测新型应用研究进展	气象科技进展	2021，11(2)
25	胡志群（第 2）	利用贝叶斯方法改进华南地区冰雹识别效果	热带气象学报	2021，37(1)
26	胡志群（第 2）	一次强雹云过程冰雹增长机制分析及防雹探讨	自然灾害学报	2021，30(5)

序号 No.	作者 Author (rank)	题名 Title	出版物名/出版社 Publication name or publisher	年，卷（期） Year, Volume (Issue)
27	黄萌田（第 3）	基于 CMIP6 模式优化集合平均预估 21 世纪全球陆地生态系统总初级生产力变化	气候变化研究进展	2021，17(5)
28	霍治国	《小麦干热风灾害等级》(QX/T 82—2019) 解读	气象标准化	2021，(3)
29	霍治国（第 2）	季节性冻土的分布与变化特征及对多样性农区农业生产的影响	中国农业资源与区划	2021，42(7)
30	霍治国（第 2）	山西省干旱灾害风险评估与区划	中国农业资源与区划	2021，42(5)
31	霍治国（第 2）	中国北方冬小麦蚜虫气候风险评估	应用气象学报	2021，32(2)
32	霍治国等	中国电线积冰灾害研究进展	应用气象学报	2021，32(5)
33	汲玉河等	2000—2019 年秦岭地区植被生态质量演变特征及驱动力分析	植物生态学报	2021，45(6)
34	姜智娜（第 2）	冬季北半球大气对巴伦支海海冰异常的敏感性研究	气象学报	2021，79(2)
35	蒋宁（第 2）	北太平洋异常高压对京津冀地区 $PM_{2.5}$ 污染影响分析	暴雨灾害	2021，40
36	李丰等	基于功率谱的风廓线雷达回波强度定标方法	应用气象学报	2021，32(3)
37	梁钊明	海风锋触发雷暴的临近预警技术研究及应用	气象出版社	2021
38	李建（第 2）	基于 GWR 模型的中国中东部降水与海拔关系特征分析	暴雨灾害	2021，40(1)
39	李建等	IPCC 第六次评估报告中的《图集》	气候变化研究进展	2021，17(6)
40	李景鑫	城市空气污染预报	气象出版社	2021
41	李琦等	基于探空云识别方法的云垂直结构分布特征	大气科学	2021，45(6)
42	李英（第 2）	川藏高原一次混合型强对流天气的观测特征	应用气象学报	2021，32(5)
43	李英（第 2）	台风“山竹”(2018) 远距离暴雨的成因分析	大气科学	2021，45(3)
44	刘黎平等	Ka/Ku 双波段云雷达反演空气垂直运动速度和雨滴谱方法研究及初步应用	大气科学	2021，45(5)
45	刘全（第 2）	基于航测的云底气溶胶活化率和过饱和度估算	应用气象学报	2021，32(6)
46	刘卫国等	层状云催化宏微观物理响应的数值模拟研究	大气科学	2021，45(1)
47	刘卫国等	基于飞机真实轨迹的一次层状云催化的增雨效果及其作用机制的模拟研究	气象学报	2021，79(2)
48	刘煜（第 2）	温室气体对亚洲夏季风影响的数值研究	应用气象学报	2021，32(2)
49	楼小凤等	人工影响天气碘化银催化剂研究进展	应用气象学报	2021，32(2)
50	罗亚丽（第 2）	1980—2017 年南海季风爆发前后华南前汛期降水统计特征对比分析	暴雨灾害	2021，40(2)

序号 No.	作者 Author (rank)	题名 Title	出版物名/出版社 Publication name or publisher	年，卷（期） Year, Volume (Issue)
51	吕俊梅（第 2）	“暖北极-冷欧亚”模态的年代际变化及其与北大西洋海温的联系	大气科学	2021，45(4)
52	吕伟涛（第 2）	广州高建筑物雷电回击光脉冲特征分析	热带气象学报	2021，37(03)
53	吕伟涛（第 2）	粤港澳大湾区两套闪电定位系统地闪探测性能的对比分析	热带气象学报	2021，37(03)
54	吕晓敏等	中国生态与农业气象研究进展	气象科技进展	2021，11(3)
55	马双梅等	2019 年 4—6 月云南持续性高温天气的大气环流异常成因	大气科学	2021，45(1)
56	马玉平等	作物发育模式重构及基于甘蔗的模拟检验	应用气象学报	2021，32(5)
57	牛涛（第 2）	阅海湿地芦苇 NPP 遥感估算及其时空变化分析	气象与环境学报	2021，37(6)
58	彭新东（第 2）	尺度自适应边界层参数化及其对一次海雾的模拟影响	气象学报	2021，79
59	祁威等	过去 2000 年北极地区气候变化特征及其对 AMO 的响应	第四纪研究	2021，41(3)
60	任宏利（第 2）	第三极地区气温和积雪的季节-年际气候预测研究	地球科学进展	2021，36(2)
61	任宏利（第 3）	BCC_CSM 北极海冰模拟性能的改进对东亚冬季气候模拟的影响	大气科学学报	2021，44(1)
62	史月琴（第 3）	云解析人工影响天气数值模式的建立、初步试验和展望	气象科技进展	2021，11(5)
63	史月琴等	一次对流云人工消减雨作业云条件预报和作业预案合理性分析	气象	2021，47(2)
64	孙继松（第 2）	山东半岛海风锋在一次飑线系统演变过程中的作用	气象学报	2021，79(5)
65	孙晶等	新疆春季两次直升机积冰气象条件分析	气象与环境科学	2021，44(4)
66	孙擎等	基于多种算法的果树果实生长模型研究——以云南昭通苹果为例	中国农业科学	2021，54(17)
67	孙爽（第 2）	葡萄生长季内需水特征	应用生态学报	2021，32(8)
68	孙爽等	华北平原不同等级干旱对冬小麦产量的影响	农业工程学报	2021，37(14)
69	孙爽等	我国北方一作区马铃薯高产稳产区分布特征	应用气象学报	2021，32(4)
70	孙爽（第 2）	气候变化对中国华北冬小麦影响研究	气象出版社	2021
71	谭凯炎等	从土壤气候视角解析农业文化遗产地的自然禀赋——以宽城传统板栗栽培系统为例	中国农学通报	2021，37(7)
72	王飞（第 3）	利用 FY-4A 卫星光学数据对中国近地面 $PM_{2.5}$ 浓度的估算和检验分析	气象学报	2021，79(3)
73	王改利等	青藏高原墨脱地区云降水综合观测及初步统计特征分析	气象学报	2021，79(5)

序号 No.	作者 Author (rank)	题名 Title	出版物名/出版社 Publication name or publisher	年，卷（期） Year, Volume (Issue)
74	王培娟（第 2）	中国大陆茶树种植气候适宜性区划	应用气象学报	2021，32(4)
75	王培娟（第 3）	物候模型支持下的杭州市春茶霜冻害时空变化及风险区划	生态学杂志	2021，40(3)
76	王培娟等	中国茶树春霜冻害研究进展	应用气象学报	2021，32(2)
77	王亚强	MeteoInfo-气象 GIS、科学计算与可视化平台	气象出版社	2021
78	王郁等	新疆地区大气环境容量系数的气候特征及其在空气质量变化中的作用	环境科学学报	2021，41(12)
79	吴翀（第 2）	双偏振相控阵雷达与业务雷达的定量对比及观测精度研究	高原气象	2021，40(2)
80	吴翀等	X 波段双偏振雷达相态识别与拼图的关键技术	应用气象学报	2021，32(2)
81	杨建莹等	中国北方苹果干旱等级指标构建及危险性评价	应用气象学报	2021，32(1)
82	杨琳韵等	次季节波动对青藏高原及其下游东亚季风区降水的影响	高原气象	2021，40(6)
83	姚雯（第 2）	不同闪电跃增算法在北京地区应用效果对比	应用气象学报	2021，32(2)
84	姚展予（第 2）	六盘山地区一次低槽低涡云系结构及其降水机制的数值模拟研究	大气科学	2021，45(2)
85	姚展予（第 3）	崇明东滩湿地与上海城市气候特征对比分析	气象与环境科学	2021，44(1)
86	姚展予（第 3）	基于 Ka 波段云雷达的六盘山顶云特征分析	气象与环境学报	2021，37(2)
87	姚展予（第 3）	基于微波辐射计的宁夏六盘山西侧大气水汽变化特征	干旱区地理	2021，44(4)
88	余荣等	关于复合型极端事件的新认识和启示	大气科学学报	2021，44(5)
89	余荣	中国气候与生态环境演变：2021（第一卷 科学基础）	科学出版社	2021
90	张根（第 2）	江西景德镇站大气 CH_4 和 CO 季节变化及源解析	中国环境科学	2021，41(12)
91	张根（第 2）	江西省冬季大气典型污染过程的气象成因研究	环境科学学报	2021，41(8)
92	张根（第 2）	长江中下游六省大气甲烷柱浓度时空分布	地球化学	2021，50(1)
93	张华等	IPCC AR6 报告解读：地球能量收支、气候反馈和气候敏感度	气候变化研究进展	2021，17(6)
94	张荣等	DMT 机载云粒子图像形状识别及其应用	应用气象学报	2021，32(6)
95	张胜军（第 2）	南海台风生成前 48 h 环流特征及热力与动力条件	应用气象学报	2021，32(3)
96	张文娟（第 2）	FY-4A LMI 观测的利奇马（2019）台前飑线闪电活动及其与对流演变的关系	遥感技术与应用	2021，36(4)
97	张文娟（第 2）	基于闪电聚类方法的西北太平洋区域 雷暴活动特征	热带气象学报	2021，37(3)
98	张文娟等	热带气旋闪电活动特征研究综述	海洋气象学报	2021，41(3)
99	张文千（第 2）	气候变化背景下中国农业干旱时空变化特征分析	中国农业气象	2021，42(1)

序号 No.	作者 Author (rank)	题名 Title	出版物名/出版社 Publication name or publisher	年，卷（期） Year, Volume (Issue)
100	张阳等	CMA_FEBLS 低频三维全闪探测技术研究及观测 10 年进展	热带气象学报	2021，37(3)
101	张养梅等	《大气气溶胶观测术语》(GB/T 31159-2014）解读	气象标准化	2021，(2)
102	张正秋等	气候动力诊断和分析系统设计与应用	应用气象学报	2021，32(5)
103	赵大军（第 3）	登陆台风影响下离地 300 m 高度内的强风特征研究	大气科学	2021，45
104	赵琳娜等	冬季稳定性降水相态预报研究进展	应用气象学报	2021，32(1)
105	赵琳娜	说个天气故事给你听	气象出版社	2021
106	赵艳霞	气象为农服务的创新模式关键技术研究	气象软科学	2021，(4)
107	赵艳霞（第 2）	基于机器学习算法的冬小麦始花期预报方法	农业工程学报	2021，37(11)
108	赵艳霞	茶树气象灾害风险管理	气象出版社	2021
109	郑栋（第 2）	华南飑线系统对流与层云区闪电起始和通道位置处的云微物理特征	热带气象学报	2021，37(3)
110	郑栋（第 2）	雷暴云特征数据集及我国雷暴活动特征	应用气象学报	2021，32(3)
111	郑栋等	雷暴闪电活动特征研究进展	热带气象学报	2021，37(3)
112	周佰铨等	IPCC 第六次气候变化评估中的气候约束预估方法	气象学报	2021，79(6)
113	周广胜（第 2）	不同灌溉量夏玉米叶绿素含量的高光谱特征及其反演	生态学报	2021，41(2)
114	周广胜（第 2）	横断山区地表真实面积与垂直投影面积差异分析——以雅江县为例	测绘通报	2021，8
115	周广胜（第 2）	温度和光周期协同作用对蒙古栎幼苗春季物候的影响	生态学报	2021，41(7)
116	周广胜（第 2）	增温背景下克氏针茅枯黄期物候对降水响应的光合生理机制	应用生态学报	2021，32(3)
117	周广胜（第 2）	中国欧亚种酿酒葡萄种植分布的主要气候影响因子与气候适宜性	生态学报	2021，41(6)
118	周广胜等	黄河水生态承载力的流域整体性和时空连通性	科学通报	2021，66
119	周莉（第 2）	辽河三角洲芦苇沼泽植物冠层内外大气中水汽的稳定同位素组成	湿地科学	2021，19(3)
120	周旭（第 3）	临沂市区冬季大气污染物的特征解析	环境污染与防治	2021，43(5)
121	周毓荃（第 3）	SPEC 机载云探测系统及其云物理研究进展	暴雨灾害	2021，40(3)
122	祝从文（第 3）	西南夏季降水多因子降维客观预测方法研究	大气科学	2021，45(3)

中国气象科学研究院年报　2021

主办单位：中国气象科学研究院
主　　编：端义宏
执行主编：袁凤杰
编辑出版：《中国气象科学研究院年报》编辑部
制作印刷：北京新华印刷有限公司
地　　址：北京中关村南大街 46 号，邮编 100081
邮　　箱：kjdt@cma.gov.cn
出版日期：2022 年 6 月

ANNUAL REPORT OF CAMS 2021

Sponsor: Chinese Academy of Meteorological Sciences
Chief Editor: Duan Yihong
Executive Chief Editor: Yuan Fengjie
Publication: *Annual Report of CAMS* Editional Division
Design and Printing: Beijing Xinhua Printing Co. , Ltd.
Address: 46 Zhongguancun Nandajie, Beijing, 100081, China
Email: kjdt@cma.gov.cn
Publication date: June 2022